

Antonio Gil  
Sophia A. Korili  
Raquel Trujillano  
Miguel Angel Vicente  
*Editors*

# Pillared Clays and Related Catalysts

 Springer

# Pillared Clays and Related Catalysts

Antonio Gil · Sophia A. Korili · Raquel Trujillano ·  
Miguel Angel Vicente  
Editors

# Pillared Clays and Related Catalysts

Foreword by Thomas J. Pinnavaia

 Springer

*Editors*

Dr. Antonio Gil  
Department of Applied Chemistry  
Public University of Navarra  
Pamplona 31080, Spain  
andoni@unavarra.es

Dr. Sophia A. Korili  
Department of Applied Chemistry  
Public University of Navarra  
Pamplona 31080, Spain  
sofia.korili@unavarra.es

Dr. Raquel Trujillano  
Department of Inorganic Chemistry  
University of Salamanca  
Salamanca 37008, Spain  
rakel@usal.es

Dr. Miguel Angel Vicente  
Department of Inorganic Chemistry  
University of Salamanca  
Salamanca 37008, Spain  
mavicente@usal.es

ISBN 978-1-4419-6669-8

e-ISBN 978-1-4419-6670-4

DOI 10.1007/978-1-4419-6670-4

Springer New York Dordrecht Heidelberg London

Library of Congress Control Number: 2010933724

© Springer Science+Business Media, LLC 2010

All rights reserved. This work may not be translated or copied in whole or in part without the written permission of the publisher (Springer Science+Business Media, LLC, 233 Spring Street, New York, NY 10013, USA), except for brief excerpts in connection with reviews or scholarly analysis. Use in connection with any form of information storage and retrieval, electronic adaptation, computer software, or by similar or dissimilar methodology now known or hereafter developed is forbidden.

The use in this publication of trade names, trademarks, service marks, and similar terms, even if they are not identified as such, is not to be taken as an expression of opinion as to whether or not they are subject to proprietary rights.

Printed on acid-free paper

Springer is part of Springer Science+Business Media ([www.springer.com](http://www.springer.com))

# Foreword

The concept of using intercalation chemistry to transform a lamellar solid into a porous analog originated more than 55 years ago in the Aberdeen University laboratory of Professor Richard M. Barrer. In a seminal 1955 paper, co-authored with graduate student D.M. MacLeod and published in the *Transactions of the Faraday Society*, Barrer described how the “replacement of inorganic cations in montmorillonite by  $N(CH_3)_4^+$  and  $N(C_2H_5)_4^+$  cations opens up the lamellae and causes profound changes in the sorption and intercalation of organic molecules.” The paper also demonstrated sorptive selectivity based on the cross-sectional molecular diameters of the adsorbates. Despite the promising molecular sieving properties of Barrer’s alkylammonium ion-exchanged forms of smectite clays, his innovation remained essentially undeveloped for two decades due primarily to the concomitant discovery of synthetic zeolites Linde Type A (LTA) and Type X (FAU). These purely inorganic molecular sieves had surface areas and pore volumes comparable to Barrer’s clay intercalates, but they were far more thermally stable in comparison to the alkylammonium ion-exchanged forms of smectic clays.

In 1977, George W. Brindley and R.E. Sempels showed that the partial replacement of  $Na^+$ -exchange cations by hydroxyaluminum cations in the galleries of the smectic clay beidellite afforded intercalates with nitrogen BET surface areas up to 500  $m^2/g$  after calcination at 325 °C. This finding presaged the 1978 W.R. Grace patent invention of David E.W. Vaughan, Roger J. Lussier, and John S. Magee, Jr. on “Pillared Interlayered Clay Materials Useful as Catalysts and Sorbents.” This breakthrough garnered the attention of the clay and zeolites research communities and spawned a flurry of research activity that persists to the current day. To date, more than 3,500 journal publications and 390 patents have been published on pillared smectite clays and related porous derivatives of lamellar compounds. Moreover, the advances in the applications of pillared materials continue to expand. The decade following the pillared clay disclosure of Vaughan et al. witnessed the publication of approximately 200 journal articles and 64 patents. In the decade of the 1990s, the numbers grew to 1,300 journal articles and 170 patents. The decade following the turn of the twenty-first century saw a sustained interest in pillared materials, as evidenced by the publication of more than 2,000 additional journal articles and 155 patents.

The decade following 2010 almost certainly will witness continued research on the applications of pillared layered materials. For this reason the present volume on pillared intercalates is an exceptionally timely contribution that will serve as a valuable reference source. Much of the contemporary interest in pillared clays and related interaction compounds is stimulated by their properties as heterogeneous catalysts for the production of fine chemicals and as selective adsorbents for molecular preparations, environmental remediation, and pollution control. The present volume provides a thorough and expert accounting of the recent advances in each of these application areas. Emphasis is understandably placed on pillared versions of smectite clays and layered double hydroxides, also known as hydrotalcites or mixed metal hydroxides, in part, because these are the most versatile and cost-effective lamellar host structures available in commercial quantities for pillaring. In addition, detailed state-of-the art evaluations are also provided for layered phosphates and porous aluminum phosphates. The 16 complementary chapters cover a very broad range of catalytic and sorptive processes of environmental and industrial relevance with little or no redundancies. The level of coverage attests to the expertise of the contributing authors in the field of pillared layered materials. The book surely will serve as an essential reference source over the next decade for workers engaged in the intercalation chemistry and materials applications of lamellar inorganic solids, particularly layered oxides and hydroxides.

University Distinguished Professor of Chemistry  
Michigan State University  
East Lansing, MI, USA

Thomas J. Pinnavaia

# Preface

The interest in all aspects related to pillared interlayered clays, such as new synthesis methods or the study of their properties and applications, has greatly increased over the last few years. Several of the papers devoted to pillared interlayered clays, both as articles and as book chapters, have reviewed various aspects of the preparation, characterization, or applications of these solids. The approach that has been commonly used in previous studies to organize such a large amount of information is mainly based on the preparation of pillared clays, as well as some aspects about the catalytic applications of these solids. As indicated earlier, the interest in these solids is so large that, since our first comprehensive review on the synthesis and catalytic applications published 9 years ago (Gil A, Gandia LM, Vicente MA (2000) Recent advances in the synthesis and catalytic applications of pillared clays. *Catalysis Reviews*, 42:145–212), more than 500 new references have appeared in the literature and interest in this field is continuously increasing. A second review deals with the porous structure developed by these materials during the intercalation process (Gil A, Korili SA, Vicente MA (2008) Recent advances in the control and characterization of the porous structure of pillared clay catalysts. *Catalysis Reviews*, 50:153–221). This is a very important aspect because the textural properties of pillared clays play a key role when these materials are used as catalysts, adsorbents, or in gas separation.

Since the first works introducing the aluminum intercalated clay family at the beginning of the 1970s, the synthesis of pillared interlayered clays has expanded enormously. The need for solids that could be used as cracking catalysts with larger pores than the zeolitic materials spurred the synthesis of new porous materials from clays. These solids are prepared by exchanging the charge-compensating cations present in the interlamellar space of the swelling clays by hydroxyl-metal polycations. On calcining, the inserted polycations yield rigid, thermally stable oxide species, which prop the clay layers apart and prevent their collapse. The intercalation and pillaring processes produce the development of a porous structure with the presence of particular surface sites. These properties determine the potential use of the solids in catalytic, purification, and sorption-based separation applications. The properties of pillared clays synthesized in the presence of microwave irradiation are compared to those prepared in the conventional way by Fetter and Bosch in

**Chapter 1.** In **Chapter 2**, Pires and Pinto present the potential use of pillared clays as selective adsorbents of natural and biogas components, such as carbon dioxide, methane, ethane, and nitrogen.

An important characteristic of the pillared clays is their acidity. The type, number, and strength of surface acid sites depend on several factors, such as the exchange of cations, the preparation method, and the nature of the starting clay. These are properties directly related to the catalytic performance. Therefore, the type of acidity can determine which type of reaction the clays can catalyze. Several types of reaction have been studied, such as alkylation, dehydrogenation, hydrocracking, and isomerization. Some examples of this type of applications are summarized in **Chapters 3** and **4**.

One of the most studied topics related to pillared clays is their use as supports for catalytically active phases, and the use of the resulting solids in several reactions, particularly in environment-friendly ones. The number of articles in this field is very extensive, including catalysts that contain Co, Cr, Cu, Fe, Mn, Ni, Pd, Pt, Rh, or V. Mishra summarizes the synthesis and applications of transition metal oxide-pillared clays in **Chapter 5**. Titanium, iron, chromium, manganese, and mixed oxides were considered, with emphasis on their future potential as catalysts. Hydrocarbon cracking and various examples related to environmental processes as photocatalysis and pollution control in gas and liquid phases are presented by the author. The use of pillared clays in catalytic waste water treatment is summarized in **Chapters 6–8**. Herney-Ramirez and Madeira reviewed the use of pillared clays in heterogeneous Fenton-like advanced oxidation processes. The effect of the main operating conditions on oxidation efficiency is considered by the authors. Special attention to the use of pillared clays in wet air catalytic oxidation (WACO), wet hydrogen peroxide catalytic oxidation (WHPCO), and photo-Fenton conversion of pollutants is considered by Perathoner and Centi. The catalytic wet peroxide oxidation of phenol using pillared clays in a continuous flow reactor is presented by Guélou et al. in **Chapter 8**. The experimental results are very promising for developing a catalytic continuous process for industrial wastewater purification. The chapter written by Zuo et al. reviews the recent developments offered from pillared clay-supported noble metals and metal oxide catalysts for complete oxidation of representative volatile organic compound (VOC) molecules such as benzene, toluene, chlorobenzene, phenol, among others. Selective reduction of NO<sub>x</sub> has been the reaction *to* environmental interest for which pillared clays have been most widely used. Recent trends, limits, and opportunities offered from pillared clays and other related materials (layered clays, layered double hydroxides (LDHs), and porous clay heterostructures (PCHs)) in this field are discussed by Belver in **Chapter 10**. Special attention is focused on the modification that led to materials with a higher or comparable activity to that described by commercial systems. In **Chapter 11**, Vicente et al. presents the use of pillared clays in catalytic oxidation reactions related to green chemistry concepts.

The book also includes four Chapters (**12–15**) dealing with treatment of other layered materials, mainly anionic clays, and mesoporous solids, comparing them with the pillared clays. The state-of-the-art in the synthesis, characterization, and



catalytic performance of layered double hydroxides (LDH) with the hydroxalcite-type structure containing several polyoxometalates (POM) in the interlayer is presented by the Rives group in [Chapter 12](#). The immobilization of polyoxometalate species in the interlayers of layered double hydroxides with the hydroxalcite-type-solids allows the preparation of homogeneous catalysts with tailored redox and acidity properties. The authors indicate that the properties of these materials can be finely tuned through the modification of the cations in the brucite-like layers and the polyoxometalate in the interlayer, in order to apply them to several catalytic processes. Other parameters such as the polarity modulation or the solvents can modify the reactivity of the LDH–POM catalysts. In [Chapter 13](#), Figueras presents the latest ideas on the modification of the basic properties of hydroxalcites by anion exchange and on the properties of solid bases as catalysts. Several examples of applications are given, with emphasis on industrial processes recently shown such as isomerization of olefins, aldolization, oxidation of ketones; supports of metal catalysts; as well as adsorbents and anionic exchangers. The synthetic pathways for obtaining mesoporous phosphate structures and aluminophosphates make up the subjects presented in [Chapters 14](#) and [15](#) by Moreno et al. and O'Malley et al., respectively. The preparation of metal-supported catalysts and their application in gas separation, adsorption, and catalysis are also reviewed.

In the final chapter, the synthesis and application to industrial catalytic reactions of macrocyclic complexes supported on clays with thermal and chemical stability are presented by the team of Kumar et al.

The editors are very grateful to all the authors for their willingness to participate in this project, and for their enthusiasm in writing the contributions, and for sharing their knowledge with the readers.

Navarra, Spain  
Navarra, Spain  
Salamanca, Spain  
Salamanca, Spain

Antonio Gil  
Sophia A. Korili  
Raquel Trujillano  
Miguel Angel Vicente

# Contents

<b>1</b>	<b>Microwave Effect on Clay Pillaring . . . . .</b>	<b>1</b>
	Geolar Fetter and Pedro Bosch	
<b>2</b>	<b>Pillared Interlayered Clays as Adsorbents of Gases and Vapors . . .</b>	<b>23</b>
	J. Pires and M.L. Pinto	
<b>3</b>	<b>Characterization and Catalytic Performance of Montmorillonites with Mixed Aluminium/Lanthanide Pillars . . .</b>	<b>43</b>
	F. González, C. Pesquera, and C. Blanco	
<b>4</b>	<b>Synthetic Hectorite: Preparation, Pillaring and Applications in Catalysis . . . . .</b>	<b>67</b>
	Chun-Hui Zhou, Dongshen Tong, and Xiaonian Li	
<b>5</b>	<b>Transition Metal Oxide-Pillared Clay Catalyst: Synthesis to Application . . . . .</b>	<b>99</b>
	Trilochan Mishra	
<b>6</b>	<b>Use of Pillared Clay-Based Catalysts for Wastewater Treatment Through Fenton-Like Processes . . . . .</b>	<b>129</b>
	J. Herney-Ramírez and Luis M. Madeira	
<b>7</b>	<b>Catalytic Wastewater Treatment Using Pillared Clays . . . . .</b>	<b>167</b>
	Siglinda Perathoner and Gabriele Centi	
<b>8</b>	<b>Fe–Al-Pillared Clays: Catalysts for Wet Peroxide Oxidation of Phenol . . . . .</b>	<b>201</b>
	Erwan Guélou, Jean-Michel Tatibouët, and Joël Barrault	
<b>9</b>	<b>Pillared Clay-Supported Noble Metal and Metal Oxide Catalysts for Complete Oxidation of VOCs . . . . .</b>	<b>225</b>
	Shufeng Zuo, Qinqin Huang, and Renxian Zhou	
<b>10</b>	<b>Clay Materials for Selective Catalytic Reduction of NO<sub>x</sub> . . . . .</b>	<b>255</b>
	Carolina Belver	

<b>11 Pillared Clay Catalysts in Green Oxidation Reactions . . . . .</b>	<b>301</b>
M.A. Vicente, R. Trujillano, K.J. Ciuffi, E.J. Nassar, S.A. Korili, and A. Gil	
<b>12 Heterogeneous Catalysis by Polyoxometalate-Intercalated Layered Double Hydroxides . . . . .</b>	<b>319</b>
Vicente Rives, Daniel Carriazo, and Cristina Martín	
<b>13 Basicity, Catalytic and Adsorptive Properties of Hydrotalcites . . . . .</b>	<b>399</b>
Francois Figueras	
<b>14 Mesoporous Phosphate Heterostructures: Synthesis and Application on Adsorption and Catalysis . . . . .</b>	<b>423</b>
Ramón Moreno-Tost, José Jiménez-Jiménez, Antonia Infantes-Molina, Celio L. Cavalcante, Jr., Diana C.S. Azevedo, María Dolores Soriano, José Manuel López Nieto, Antonio Jiménez-López, and Enrique Rodríguez-Castellón	
<b>15 Recent Advances in the Preparation and Application of Mesoporous Aluminophosphate-Based Materials . . . . .</b>	<b>447</b>
Kathleen O'Malley, Wiebke Reimann, and Teresa Curtin	
<b>16 Heterogeneous Complex Catalysts Having Ionically Macrocyclic Complex Bonded to Montmorillonite Clay for Industrial Reactions . . . . .</b>	<b>465</b>
Sunder Lal, K.S. Anisia, and Anil Kumar	
<b>Index . . . . .</b>	<b>517</b>

# Contributors

**K.S. Anisia** Department of Chemical Engineering, Indian Institute of Technology Kanpur, Kanpur 208016, India

**Diana C.S. Azevedo** Department of Engenharia Química, Universidade Federal do Ceará, Grupo de Pesquisa em Separações por Adsorção (GPSA), Campus do Pici, Bl. 709, 60.455-760 Fortaleza, CE, Brazil

**Joël Barrault** Ecole Supérieure d'Ingénieurs de Poitiers, Laboratoire de Catalyse en Chimie Organique, LACCO/UMR CNRS 6503, Université de Poitiers, 40 avenue du Recteur Pineau, 86022 Poitiers Cedex, France, joel.barrault@univ-poitiers.fr

**Carolina Belver** Instituto de Ciencia de Materiales de Madrid, CSIC., Madrid, E-28049, Spain, cbelver@icmm.csic.es

**C. Blanco** Inorganic Chemistry Group, Department of Chemical Engineering and Inorganic Chemistry, University of Cantabria, Cantabria, Spain

**Pedro Bosch** Universidad Nacional Autónoma de México, Instituto de Investigaciones en Materiales, A.P. 70360, Ciudad Universitaria, C.P. 04510 México, DF, Mexico, croqcroq@hotmail.com

**Daniel Carriazo** Instituto de Ciencia de Materiales de Madrid (ICMM), Consejo Superior de Investigaciones Científicas (CSIC), Cantoblanco, 28049-Madrid, Spain, dcarriazo@usal.es

**Celio L. Cavalcante, Jr.** Department of Engenharia Química, Universidade Federal do Ceará, Grupo de Pesquisa em Separações por Adsorção (GPSA), Campus do Pici, Bl. 709, 60.455-760 Fortaleza, CE, Brazil

**Gabriele Centi** Dipartimento di Chimica Industriale ed Ingegneria dei Materiali and CASPE (INSTM Laboratory of Catalysis for Sustainable Production and Energy), Università di Messina, Salita Sperone 31, 98166 Messina, Italy

**K.J. Ciuffi** Universidade de Franca, Av. Dr. Armando Salles Oliveira, 201-Pq. Universitario, 14404-600 Franca, SP, Brazil

**Teresa Curtin** Department of Chemical and Environmental Sciences, Materials and Surface Science Institute, SFI-SRC in Solar Energy Materials, University of Limerick, Limerick, Ireland, [teresa.curtin@ul.ie](mailto:teresa.curtin@ul.ie)

**Geolar Fetter** Facultad de Ciencias Químicas, Benemérita Universidad Autónoma de Puebla, Blvd. 14 Sur y Av. San Claudio, C.P. 72570, Puebla, PUE, Mexico, [geolarfetter@yahoo.com.mx](mailto:geolarfetter@yahoo.com.mx)

**Francois Figueras** IRCELYON-CNRS-Université Lyon, 2 avenue Albert Einstein, 69626 Villeurbanne Cedex, France, [francois.figueras@ircelyon.univ-lyon1.fr](mailto:francois.figueras@ircelyon.univ-lyon1.fr)

**A. Gil** Department of Applied Chemistry, Building Los Acebos, Public University of Navarra, Campus of Arrosadia, E-31006 Pamplona, Spain, [andoni@unavarra.es](mailto:andoni@unavarra.es)

**F. González** Inorganic Chemistry Group, Department of Chemical Engineering and Inorganic Chemistry, University of Cantabria, Cantabria, Spain

**Erwan Guélou** Laboratoire de Catalyse en Chimie Organique, LACCO/UMR CNRS 6503, Université de Poitiers, Ecole Supérieure d'Ingénieurs de Poitiers, 40 avenue du Recteur Pineau, 86022 Poitiers Cedex, France

**J. Herney-Ramírez** Departamento de Ingeniería Química y Ambiental, Universidad Nacional de Colombia, Facultad de Ingeniería, Carrera 30 No 45-03, Bogotá, DC, Colombia

**Qinqin Huang** Institute of Catalysis, Zhejiang University, Hangzhou, 310028, People's Republic of China

**Antonia Infantes-Molina** Instituto de Catálisis y Petroleoquímica, Consejo Superior de Investigaciones Científicas, 28049, Cantoblanco, Madrid, Spain

**José Jiménez-Jiménez** Departamento de Química Inorgánica, Cristalografía y Mineralogía, Unidad Asociada al Instituto de Catálisis (CSIC), Facultad de Ciencias, Universidad de Málaga, 29071 Málaga, Spain

**Antonio Jiménez-López** Departamento de Química Inorgánica, Cristalografía y Mineralogía, Unidad Asociada al Instituto de Catálisis (CSIC), Facultad de Ciencias, Universidad de Málaga, 29071 Málaga, Spain

**S.A. Korili** Department of Applied Chemistry, Building Los Acebos, Public University of Navarra, Campus of Arrosadia, E-31006 Pamplona, Spain

**Anil Kumar** Department of Chemical Engineering, Indian Institute of Technology Kanpur, Kanpur 208016, India, [anilk@iitk.ac.in](mailto:anilk@iitk.ac.in)

**Sunder Lal** Department of Chemical Engineering, Indian Institute of Technology Kanpur, Kanpur 208016, India

**Xiaonian Li** Research Group for Advanced Materials & Sustainable Catalysis (AMSC), R&D Center for Advanced Clay-Based Materials (CCM), College of Chemical Engineering and Materials Science, Zhejiang University of Technology (ZJUT), Hangzhou 310032, China

**José Manuel López Nieto** Instituto de Tecnología Química, UPV-CSIC, Av. Los Naranjos s/n, Valencia, Spain

**Luis M. Madeira** LEPAE, Department of Chemical Engineering, Faculty of Engineering, Porto University, Rua Dr. Roberto Frias, 4200-465 Porto, Portugal, mmadeira@fe.up.pt

**Cristina Martín** GIR-QUESCAT, Departamento de Química Inorgánica, Universidad de Salamanca, 37008 Salamanca, Spain

**Trilochan Mishra** ACC Division, National Metallurgical Laboratory CSIR, Jamshedpur 831007, India, drtmishra@yahoo.com

**Ramón Moreno-Tost** Departamento de Química Inorgánica, Cristalografía y Mineralogía, Unidad Asociada al Instituto de Catálisis (CSIC), Facultad de Ciencias, Universidad de Málaga, 29071 Málaga, Spain

**E.J. Nassar** Universidade de Franca, Av. Dr. Armando Salles Oliveira, 201-Pq. Universitário, 14404-600 Franca, SP, Brazil

**Kathleen O'Malley** Department of Chemical and Environmental Sciences SFI-SRC in Solar Energy Materials, Materials and Surface Science Institute, University of Limerick, Limerick, Ireland

**Siglinda Perathoner** Dipartimento di Chimica Industriale ed Ingegneria dei Materiali and CASPE (INSTM Laboratory of Catalysis for Sustainable Production and Energy), Università di Messina, Salita Sperone 31, 98166 Messina, Italy, perathon@unime.it

**C. Pesquera** Inorganic Chemistry Group, Department of Chemical Engineering and Inorganic Chemistry, University of Cantabria, Cantabria, Spain, carmen.pesquera@unican.es

**M.L. Pinto** Department of Chemistry and Biochemistry and CQB, Faculty of Sciences – University of Lisbon, Ed. C8, Campo Grande, 1749-016, Lisboa, Portugal

**J. Pires** Department of Chemistry and Biochemistry and CQB, Faculty of Sciences – University of Lisbon, Ed. C8, Campo Grande, 1749-016, Lisboa, Portugal, jpsilva@fc.ul.pt

**Vicente Rives** GIR-QUESCAT, Departamento de Química Inorgánica, Universidad de Salamanca, Salamanca 37008, Spain, vrives@usal.es

**Enrique Rodríguez-Castellón** Departamento de Química Inorgánica, Cristalografía y Mineralogía, Unidad Asociada al Instituto de Catálisis (CSIC), Facultad de Ciencias, Universidad de Málaga, 29071 Málaga, Spain, castellon@uma.es

**María Dolores Soriano** Instituto de Tecnología Química, UPV-CSIC, Av. Los Naranjos s/n, Valencia, Spain

**Jean-Michel Tatibouët** Laboratoire de Catalyse en Chimie Organique, LACCO/UMR CNRS 6503, Université de Poitiers, Ecole Supérieure d'Ingénieurs de Poitiers, 40 avenue du Recteur Pineau, 86022 Poitiers Cedex, France

**Dongshen Tong** Research Group for Advanced Materials & Sustainable Catalysis (AMSC), R&D Center for Advanced Clay-Based Materials (CCM), College of Chemical Engineering and Materials Science, Zhejiang University of Technology (ZJUT), Hangzhou 310032, China

**R. Trujillano** Department of Inorganic Chemistry, Faculty of Chemical Sciences, University of Salamanca, Plaza de la Merced, E-37008 Salamanca, Spain

**M.A. Vicente** Department of Inorganic Chemistry, Faculty of Chemical Sciences, University of Salamanca, Plaza de la Merced, E-37008 Salamanca, Spain

**Wiebke Reimann** Department of Chemical and Environmental Sciences SFI-SRC in Solar Energy Materials, Materials and Surface Science Institute, University of Limerick, Limerick, Ireland

**Chun-Hui Zhou** Research Group for Advanced Materials & Sustainable Catalysis (AMSC), R&D Center for Advanced Clay-based Materials (CCM), College of Chemical Engineering and Materials Science, Zhejiang University of Technology (ZJUT), Hangzhou 310032, China

**Renxian Zhou** Institute of Catalysis, Zhejiang University, Hangzhou 310028, People's Republic of China, zhorenxian@zju.edu.cn

**Shufeng Zuo** Institute of Applied Chemistry, Shaoxing University, Shaoxing 312000, People's Republic of China, sfzuo@usx.edu.cn

# Chapter 1

## Microwave Effect on Clay Pillaring

Geolar Fetter and Pedro Bosch

**Abstract** Pillared clays may be prepared in presence of microwave irradiation as it has been extensively used in organic chemistry syntheses. Preparation time of the conventional intercalating solution takes about 2 days, but only 15 min when the preparation mixture is microwave-irradiated. The amount of water required to disperse and to dilute the pillar precursor salts is also significantly reduced. In this work, the properties of the pillared clays prepared in presence of microwave irradiation are compared to those prepared by the conventional way. Their performance as catalysts or as adsorbents is discussed.

**Keywords** Clays · Montmorillonite · Pillars · Microwave irradiation · Microporous · Ion exchange · Adsorption · Catalysis · Aluminosilicate

### 1.1 Introduction

Catalysis and adsorption require materials with high porosity and large surface area. Although clays, as montmorillonite, present a surface area of ca. 40–70 m<sup>2</sup>/g and a porosity of ca. 0.006–0.010 cm<sup>3</sup>/g, which are low, their layered structure may be expanded through organic or inorganic pillars. Indeed, clays are cationic exchangers. The pillars may be large inorganic metalpolyoxocations intercalated between the aluminosilicate layers. These polyoxocations (Al, Zr, Cr, . . .) are, then, converted into stable metal oxide pillars through a calcination step, holding the layers permanently apart and, thus, creating microporosity. In this way, the interlamellar space, originally close to 3.0 Å, can reach a value as high as 20 Å. The porosity of the

---

G. Fetter (✉)

Facultad de Ciencias Químicas, Benemérita Universidad Autónoma de Puebla, Blvd. 14 Sur y Av. San Claudio, C.P. 72570 Puebla, PUE, Mexico  
e-mail: geolarfetter@yahoo.com.mx



pillar-interlayered clays can be tailored by changing the size, shape, and concentration of the intercalated species [1–4]. The obtained surfaces and microporosity are ca. four times larger than the values of the non-pillared clay.

In this way, pillared clays may be used, for instance, in fine chemistry as catalysts in the synthesis of biologically active multifunctional dihydropyrimidinones [5]. In hydrocracking, chromia and tin oxide-pillared clays are performing as catalysts of heavy liquid fuels [6], while in photocatalysis, titania-pillared montmorillonite has been used to remove 4-chlorophenol in water and methanol in air [7]. Otherwise, clays may be intercalated with organic compounds such as drugs. The clay acts as a drug deliverer depending on the environmental conditions [8, 9].

Among the large number of clays, montmorillonite is the most frequently used in pillaring chemistry. Indeed, it is often found in nature and the cation-exchange capacity is high (50–150 mequiv/100 g of clay). Still, other smectite clays such as saponite [10, 11], beidellite [12, 13], nontronite [14], or hectorite [15, 16] have been pillared.

The pillaring process starts with the intercalation of metalpolyoxocations which are large complexes (ca. 10 Å) constituted by clusters of oxygen and metal atoms. The corresponding charge promotes the cation exchange and the subsequent interaction with the negatively charged aluminosilicate layer. For instance, the polyoxocation of aluminum is a Keggin ion,  $[Al_{13}O_4(OH)_{24}(H_2O)_{12}]^{7+}$ , which contains 13 aluminum atoms and whose resulting charge is 7<sup>+</sup>.

The conventional preparation may be summarized as follows [2, 4]. A pillaring agent is initially prepared. Then, the suspended clay is mixed with the polyoxocation solution and maintained at ca. 80 °C for 18 h. After the intercalation process is complete, the clay is separated, washed, and then calcined (300–800 °C for 5 h), i.e., pillared. The obtained sample is often labeled as PILC (pillared clay).

Clearly, the conventional procedure is complex and time-consuming as shown in the following chapters. Furthermore, from an industrial viewpoint, in which large amounts of clay have to be prepared, this process may result uneconomic, since enormous equipments as well as the manipulation of huge volumes of water are required [17–19].

Irradiation during the solution preparation and the intercalation decreases significantly the polyoxocation formation time as well as the amount of water required as it is a source of external energy. Irradiation propitiates the required dispersion of cations in a more concentrated solution. During intercalation, it favors a fast diffusion of the exchanged species. Last but not least, irradiation may be used to dry the samples [20, 21] (Fig. 1.1).

Materials may be irradiated with a wide interval of wavelengths including microwaves. Microwaves are electromagnetic radiation, whose wavelength lies in the range of 1 mm to 1 m (frequency range of 0.3–300 GHz). Only narrow frequency windows centered at 900 MHz and 2.45 GHz are allowed for microwave heating purposes. The exact nature of microwave interaction with reactants during the synthesis is somewhat unclear and speculative. However, energy transfer from microwaves to the material is believed to occur through either resonance or relaxation, which results in rapid heating [22].

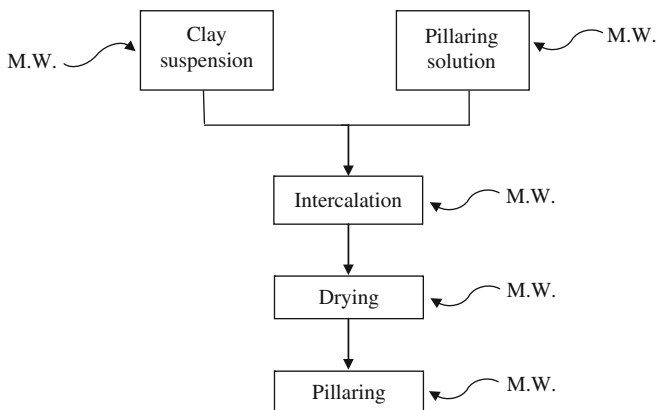


**Fig. 1.1** Preparation steps of pillared clays where microwave irradiation can be applied

In this work we review and discuss the use of microwave irradiation on clay pillaring.

## 1.2 Experimental

Microwave equipment to irradiate typically consists of an autoclave of 500 ml, which fits in a microwave oven whose power may be selected. A stirring mechanism is adapted to the autoclave so that temperature is the same all over. The frequency is always 2.45 GHz. Temperature is controlled through an infrared radiation sensor. Pressure can reach values as high as 10 atm. Laboratory apparatus are commercialized by Milestone or CEM, among other; in our case, we have used a Sistemas y Equipos de Vidrio model MIC-II apparatus (see Fig. 1.2).

Still, reproducible results have been reported using domestic ovens [23–25] but, in order to avoid explosions, the obtained amount of sample has to be very small, around 5 g. As the samples cannot be stirred, the probability of high temperature points cannot be discarded.

## 1.3 Determinant Conditions

### 1.3.1 Irradiation Time

#### 1.3.1.1 Alumina-Pillared Montmorillonite

Irradiation time is one of the most determining parameters on the sample features. Fetter et al. [25] studied the synthesis of Al-intercalated montmorillonites. If the prepared samples are irradiated for 2 min or more, during the intercalation

**Fig. 1.2** Synthesis autoclave apparatus operated with microwave irradiation



step, and compared to the conventionally prepared materials (18 h), a higher surface area is obtained (340 vs. 244 m<sup>2</sup>/g). In the microwaved samples, the  $d_{001}$  distance turns out to be 19.0 Å whereas in the conventionally prepared sample it is 19.7 Å.

De Andrés et al. [26] report a very complete characterization of Al-pillared montmorillonite prepared either by the conventional method or by microwave irradiation during the intercalation step for 2, 10, 18, or 20 min. The same samples are, then, thermally treated at 450 °C. This study is complementary of the previous one [25], as it performs thermal gravimetry analysis–differential thermal analysis (TGA–DTA), impedance spectroscopy, <sup>27</sup>Al magic angle spinning nuclear magnetic resonance (MAS NMR), and intercalative adsorption of Methylene Blue (MB) and concludes that the irradiated samples are intermediate between non-treated-intercalated samples and conventionally pillared samples. It appears that at least a fraction of the interlayer Al-polycations remain hydroxylated and linked to some

coordinated water molecules. If  $\text{Al}_2\text{O}_3$  pillars have to be anchored to the silicate layers, these microwaved materials need an additional thermal treatment to achieve the usual properties inherent to conventional aluminum-pillared montmorillonite. The proton availability, in the only microwaved materials, should be useful to catalyze acidic reactions. Their good thermal stability also supports this type of application.

Nevertheless, prolonged irradiation produces structural and textural damages. Basal spacing, specific surface area, and pore volume are of the same order of magnitude as those of conventional aluminum-pillared montmorillonite. The interlayer distances ( $d_{001} = 17.2\text{--}16.9 \text{ \AA}$ ) decrease as the microwave irradiation time increases. Specific surface areas (BET,  $\text{N}_2$ ) are in the  $300\text{--}400 \text{ m}^2/\text{g}$  range, with micropore volume in the order of  $0.15 \text{ cm}^3/\text{g}$ , which is close to values of conventional aluminum-pillared clays although they decrease from 399 to  $296 \text{ m}^2/\text{g}$  as the microwave irradiation time increases from 10 to 20 min.

A special mention has to be made to boehmite sol-intercalated smectites [21]. The intercalated smectite was dried in an oven at  $60 \text{ }^\circ\text{C}$  over a period of 24 h and also in a microwave oven of 2.45 GHz frequency and 600 W power over a range of 3–15 min. Both kinds of samples have identical thermal and electrical properties. However, the microwave-dried samples have a distinctly higher surface area of  $120 \text{ m}^2/\text{g}$ , stable up to  $650 \text{ }^\circ\text{C}$  with a marginal reduction to  $116 \text{ m}^2/\text{g}$  compared with  $94 \text{ m}^2/\text{g}$  for the oven-dried sample. Similarly, there is a clear difference in the morphological features of the two kinds of samples, the air-dried sample having a close-packed structure while the microwave ones were delaminated and porous.

### 1.3.1.2 Zirconia-Pillared Montmorillonite

If the mixture of clay and zirconium solution is irradiated (intercalation step) for 5, 10, 20, and 30 min, maintaining the ratio of zirconium to clay constant and equal to  $2 \text{ mmol/g}$ , the interlayer distances, determined by X-ray diffraction, turn out to be  $19 \text{ \AA}$  [27]. This value can be compared to the  $12.4 \text{ \AA}$  of the initial montmorillonite, showing that all samples are intercalated. Nevertheless, the intensity and broadness of the 001 diffraction peaks show an inhomogeneous stacking of the clay layers, typical of the zirconium-pillared compounds [28]. Indeed, the expected zirconium species, present among others, in solution is the hydroxocation  $[\text{Zr}_4(\text{OH})_8(\text{H}_2\text{O})_{16}]^{8+}$ , which rapidly polymerizes to form other species [29]. Then, the montmorillonites are expected to be intercalated with several zirconium species possessing different sizes causing the irregular stacking of the clay layers. There is a slight effect of the irradiation time on the pillaring of the montmorillonite; the 001 and 002 peaks, in X-ray diffraction patterns, are slightly more intense for samples irradiated for 10–30 min than those microwaved for 5 min. The conventionally prepared sample presented 001 peaks similar to those of the 5-min irradiated sample. Hence, a better pillaring is obtained if samples are microwave-irradiated.

When the Zr/clay ratio is increased to 5 mmol/g, the 001 diffraction peak turns out to be well-defined only for the samples intercalated by microwave irradiation for 10–30 min. The interlayer distances are about 19.2 Å. The amount of zirconium used in the syntheses does not alter significantly the structural parameters. Independently of the amount of zirconium, the intercalation method or the intercalation time, the surface areas are ca. 160 m<sup>2</sup>/g in the samples pillared by microwave irradiation. These surface area values are similar to those obtained with the corresponding non-irradiated samples. The comparison of the ammonia thermodesorption curves shows that all curves are similar showing that acidity features are independent of the synthesis method as well as the irradiation time for 2 or 5 mmol of zirconium/g of clay. As the ammonia desorption is carried out with water and hydroxyl radicals, not only the acidity but also the hydration degree is the same [27].

### 1.3.1.3 Titania-Pillared Montmorillonite

The intercalation of titanium in montmorillonite, in presence of microwave irradiation, provides a 001 distance from 14.0 to 22.0 Å and surface area of 281 m<sup>2</sup>/g. The advantages of irradiation, in this case, are, again, on the one hand, a significant reduction of the aging time (about 100 times, if compared to the conventional method) and, on the other, solid concentrations in the pillaring suspension are increased up to 20 times [30]. Furthermore, a higher stability of the layer stacking was verified: contact time between clay and acid pillaring solution is short and, therefore, the clay is not dealuminated.

Microwave irradiation for 15 min during the calcination step has been shown to produce Ti-montmorillonite which, used as photocatalyst, is active in the remotion of 4-chlorophenol in water and methanol in air. Microwave-calcined samples led to an activity that was less than TiO<sub>2</sub> P-25 for 4-chlorophenol removal in water but higher for methanol removal in air. This behavior might result from a higher surface area of pillared TiO<sub>2</sub> and perhaps a different distribution of pores. TiO<sub>2</sub>-pillared montmorillonite may include a smaller density of irregularities prone to behave as recombination centers of the photo-produced charges [7].

When the sample is irradiated for 30 min in a multi-mode domestic microwave oven operated at 700 W with 2.45 GHz, and then calcined at 400 °C, no 001 distance appears in the X-ray diffraction pattern. Therefore, in those conditions the pillared montmorillonite does not present a sufficiently ordered and oriented layer structure [23].

However, if titanium-pillared clays are prepared conventionally [31], either from TiCl<sub>4</sub> or Ti(OC<sub>3</sub>H<sub>7</sub>)<sub>4</sub> precursors, the 001 distance is 19.3–19.9 Å and the surface area turns out to be 229–277 m<sup>2</sup>/g [32, 33]. In fact, the 001 distance depends on the H<sup>+</sup>/Ti ratio as  $d_{001}$ , for a H<sup>+</sup>/Ti ratio of 1.2, is 14.1 Å but it is 15.9 and 26.2 Å if the ratio is 0.24. The clay prefers to be exchanged with H<sup>+</sup>.

Still, it has been reported that, after conventional intercalation, samples may not exhibit the 001 basal reflection. In such cases, a mixture of pillared structure and partially delaminated structure has been proposed [23, 34].

### 1.3.1.4 Multimetallic-Pillared Montmorillonite

Ti/Zr-pillared bentonites have been prepared using microwave irradiation in the calcination step. The sharp (001) peak of the Ti/Zr-pillared montmorillonites is found to be at  $2\theta = 4.2^\circ$  ( $d = 24 \text{ \AA}$ ) due to polycationic species of titanium and zirconium. Note that the Na-montmorillonite shows a 001 peak at  $2\theta = 10.2^\circ$  ( $d = 10 \text{ \AA}$ ). Microwave irradiation for 15 min, with a commercial oven operating at 2.45 GHz and at a power level up to 300 W, improves the photocatalytic activities of the samples in the removal of 4-chlorophenol and dichloroacetic acid in water [20]. The higher activity of microwave irradiation-calcined samples might result from a higher surface area and a different pore distribution. Indeed, a solid sample is uniformly heated in the bulk and on the surface when submitted to microwave irradiation. Consequently, the microwave drying is supposed to facilitate the transport of water molecules toward the surface, unlike a conventional heating where the heat is transferred from the surface to the bulk.

Unfortunately it seems that not many studies on complex pillaring under microwave irradiation have been published, although, many complex pillars have been synthesized conventionally. They may be constituted by two metals as: aluminum and lanthanides [35], aluminum and silicon [36, 37], or silicon and zirconium [38].

Large-pore montmorillonites pillared with aluminum–lanthanum complexes have been synthesized in presence of microwave irradiation in the pillaring solution preparation at different times and in the intercalation step for 10 min [39, 40]. The microwave treatment of the intercalation solution with a molar ratio of Al/La of 5 for 1, 3, and 5 h results in pillared clays with specific areas of 182, 226, and 245 m<sup>2</sup>/g, respectively. The interlayer distances were ca. 26.0 Å, much larger than those obtained with Keggin-type aluminum pillars (ca. 18 Å). When the Al/La ratio increased to 30 the surface area decreased to 168 m<sup>2</sup>/g and the interlayer distance turned out to be 24.7 Å. These results show that microwave irradiation applied to prepare pillaring solutions can reduce the time from 120 h by the conventional method to 3 or 5 h. The intercalation time is reduced from 18 h (conventional) [41–44] to 10 min with microwaves.

Pillars constituted by three different metals have also been reported: aluminum, zirconium, and cerium [45] or aluminum, iron, and cerium [46] into montmorillonite layers. The effect of microwave irradiation has not been established on those materials. New compounds should appear as association of metals in the pillars is expected to be different due to the strong energetic effect of microwaves.

An interesting proposition is to prepare a monometallic-pillared montmorillonite and to use it as support for other metals, for instance, a titania-pillared clay has been vanadia doped to use it in the epoxidation of allylic alcohol (*E*)-2-hexen-1-ol [33]. This catalyst was found to be more active than Ti-pillared clay for the epoxidation.

Supported vanadium-containing catalysts have been prepared by impregnation of Al-pillared clays with NaVO<sub>3</sub> precursor aqueous solutions. A montmorillonite and a saponite pillared with Al<sub>13</sub> Keggin polycations were used as supports [47]. Again, the microwave irradiation effect on those materials has to be determined.

### 1.3.1.5 Remarks

These studies show that an irradiation time of ca. 10–30 min provides the most ordered materials. Higher irradiation times only lead to disordered clays with structural and textural damages. Acidity is independent of irradiation time. The microwave irradiation guarantees short contact times between clay and the acid-pillaring solution, therefore the clay is not dealuminated. Furthermore, microwave drying is assumed to favor the water molecules transport toward surface unlike a conventional heating where heating is transported from the surface to the bulk. Such features may explain the differences in pillar distribution and catalytic performance of the microwave-irradiated and conventional samples.

## 1.3.2 Clay to Water Ratio

### 1.3.2.1 Alumina-Pillared Montmorillonite

It is known that the Al/clay ratio has a significant effect on the accessibility properties in Al-pillared clays. If highly concentrated clay suspensions (10–50 wt% of clay in water instead of the usual 0.5 wt%) is used, and the irradiation is maintained for 7 min after the clay is mixed with chlorhydrol (aluminum polyoxocation), the inter-layer distances turn out to be again 19.0 Å and the large surfaces are reproduced (335 m<sup>2</sup>/g) [17]. This result is most important as, without microwave irradiation, intercalation is very hard and the specific surface is low. Molina et al. [48] have used a dialysis technique for intercalation and washings to prepare alumina-pillared montmorillonite from a 40-wt% clay slurry. They observed that the intercalation occurs mainly during the washing step, where, indeed, the system is highly diluted.

A different approach was followed by Perez-Zurita et al. [49], who report the synthesis of Al-PILC assisted by ultrasound. They managed to reduce the intercalation time and the amount of synthesis water. The clay to water content was in this case 30% (w/w) clay in water and the amount of water was reduced by 60% if compared to conventional preparations. The obtained specific surface areas were comprised between ca. 100 and 200 m<sup>2</sup>/g depending on the ratio Al/g of clay. The conventionally prepared clay presented a 001 interplanar distance of 18 Å whereas the ultrasound-intercalated clays show distances comprised between 16 and 19 Å. The main effect of ultrasonic radiation is to reduce the size of the clay grain and, as a consequence, the Al precursor diffusion, toward the core of the particle, is improved.

### 1.3.2.2 Iron oxide-Pillared Montmorillonite

The preparation procedure of iron oxide-pillared montmorillonite has to be explained in detail, in this case, as the sample was irradiated 3 times [50]. A slurry

composed of 1 g of montmorillonite in 100 ml of water was added to the solution already irradiated for 10 min (15 mmol of iron per g of clay) and placed in a microwave oven for 10 min at low power. Distilled water was added to the resulting mixture which was placed again in the microwave oven for further irradiation for 10 min.

One of the main advantages of irradiation, which is the use of highly concentrated clay suspensions and solutions, is not explored in the Berry et al. (1994) work [50]. The water to clay ratio in iron oxide-pillared montmorillonite is 1% while in the previous alumina-pillared montmorillonite it is 10–50%. Still, iron oxide-pillared montmorillonite under those conditions can be prepared in less than 1 h by a process involving microwave heating. The iron oxide pillars are progressively reduced in hydrogen at temperatures between 300 and 600 °C. The metallic iron formed at 600 °C is unaffected by exposure to oxygen at room temperature and partially oxidized when heated in oxygen at 300 °C.

### 1.3.2.3 Remarks

Concentration of clay suspensions may be increased with the use of microwave irradiation. Highly concentrated clay suspensions, 10–50%, instead of the conventional 0.5–1%, irradiated for 7 min, provide the required dispersion of the clay. Such result is determinant for any large-scale preparation of intercalated clays as the amount of water is strikingly reduced.

## 1.3.3 Metal to Clay Ratio

### 1.3.3.1 Titanium-Pillared Clays

If conditions to pillar with titanium are compared to those of Al pillaring or Zr pillaring, the performance of the microwave irradiation method is clear [23]. In non-irradiated preparations, titanium pillaring is most difficult. Instead, if the samples are prepared in the presence of microwave irradiation, the pillaring is easily achieved, and the pillars turn out to be preferentially anatase phase. This point is most important as these materials exhibited good photocatalytic degradation performance of Methyl Orange. In the same experimental conditions, the non-irradiated samples present a ratio of anatase to rutile three times less than the irradiated preparation.

### 1.3.3.2 Zirconium-Pillared Montmorillonite

The synthesis, at different zirconia/clay ratios, of zirconia-pillared montmorillonite in presence of microwave irradiation has been reported [27]. If the metal/clay ratio is 2 mmol/g of clay the montmorillonite is expanded to a  $d_{001}$  of 19 Å. If the ratio is 5 mmol/g of clay,  $d_{001}$  turns out to be 19.2 Å. Therefore, the amount



of zirconium does not alter significantly the structural parameters. All samples, microwave-irradiated or not, present the same surface areas and acidity features. As well, if the samples are sonicated [51], the structural features are independent of the metal/clay ratio (0.2–1.3 mmol Zr/g of clay) but the specific surface area evolves from 272 to 214 m<sup>2</sup>/g.

The expected zirconium species present in solution is the hydroxocation [Zr<sub>4</sub>(OH)<sub>8</sub>(H<sub>2</sub>O)<sub>16</sub>]<sup>8+</sup>. The main pillaring species appear to be nanorods composed of several Zr<sub>4</sub> tetramers. The basic features of the tetramer structure are preserved in zirconia nanoparticles fixed between aluminosilicate layers in pillared clays. In calcined samples, those nanoparticles contain only bridging hydroxyls and/or oxygen anions responsible for bonding within pillars and between pillars and clay sheets [52].

### 1.3.3.3 Remarks

The metal–clay interaction seems to be specific of each metal although not enough work has been done in this direction with microwave irradiation. In titania-pillared montmorillonite, microwave irradiation promotes a higher anatase formation than the conventional preparations. Instead, zirconium-pillared samples in presence or not of microwave irradiation (or sonication) are similar to those prepared conventionally as acidity and interlamellar distance remain the same. The amount of intercalated metal does not alter those results, the interlamellar distance (19 Å) is the same from 2 to 5 mmol/g of clay.

### 1.3.4 Ultrasound Versus Microwave Irradiation

Although this work is centered in microwave irradiation, it is illustrative to compare the effect of microwave irradiation to other wavelengths as ultrasound or gamma irradiations, Table 1.1. The interest of sonication is exemplified by the following result. Aluminum oligomers may be introduced into Ca<sup>2+</sup>-montmorillonite using ultrasonics within 20 min at ambient temperature [53]. In the conventionally prepared pillared clay the lamellar structure is lost at around 700 °C whereas the sonication for 20 min results in a pillared clay stable up to 800 °C. The observed higher thermal stability can be explained on the basis of uniform distribution of the

**Table 1.1** Comparison of microwave, ultrasonic, and gamma irradiation features

Radiation type	Wavelength	Typical frequency (MHz)	Chemical bond energy (kcal/mol)
Gamma rays	<10 pm	$3.0 \times 10^{14}$	120
Microwaves	1 mm–1 m	2,450	4.8
Ultrasonic waves	ca. 1.5 mm	0.002	–

pillars within the layers. Ultrasonication for 20 min results in an optimum  $d$ -spacing and a very high surface area with an optimum micropore volume, 19.2 Å, 281 m<sup>2</sup>/g, 0.11 cm<sup>3</sup>/g, respectively.

The intercalation time and the water amount (<60%) are significantly reduced with ultrasonic irradiation as stated by Pérez-Zurita et al. [49]. The improvement of the Al pillar distribution is attributed to a smaller particle size, i.e., a better delamination of the aluminosilicate layers due to sonication, which may increase the space available between the layers, thus enhancing the extent of intercalation and reducing considerably the reaction time [54]. Furthermore, it has been claimed that through sonication pillars are well distributed without any non-pillared portion of the clay [55]. Strong acid sites and sufficient gallery height of Zr-PILC seem to promote the activity in alkylation of benzene with long-chain olefins to produce dialkylbenzenes.

Microwave and ultrasound irradiation effects have been combined to obtain Zr-pillared clays [24]. The pillaring solution is irradiated with microwaves (5, 10, 20, or 30 min), then, the clay is intercalated in presence of ultrasounds (5, 10, 20, 30, or 40 min). The resulting materials have been tested under microwave irradiation in the acylation of various primary, secondary, tertiary, and benzylic alcohols and mono-acylation of 1, $n$ -diols with acetic anhydride under solventless conditions. The catalysts are reactivated using again microwave irradiation. The advantages were mainly in operational simplicity, recyclability, and selectivity. The better conditions were obtained with a catalyst prepared with an ultrasonication of 30 min. Still, if the sonication is performed during the preparation of various biologically active dihydropyrimidinones, the reaction takes longer time and the product yield is lower [5].

Instead, if the irradiation is gamma, no change attributable to irradiation is observed, only a small variation in the water content is noted but it is not systematic. The effect of heavy doses (up to 200 Mrad) on the short-range structural organization in montmorillonite has been studied using infrared spectroscopy and solid-state high-resolution<sup>27</sup>Al and <sup>29</sup>Si nuclear magnetic resonance [56].

When perfect and imperfect kaolinites, palygorskite, montmorillonite, muscovite, synthetic gibbsite, or brucite are exposed to high doses of  $\gamma$ -irradiation (10<sup>5</sup>, 10<sup>6</sup>, 10<sup>7</sup>, 3 × 10<sup>7</sup> Gy) the Al<sup>3+</sup> leaching from kaolinite increases, but that of Si<sup>4+</sup> decreases; for montmorillonite and palygorskite the other way round. The irradiation dose leads to different types of defects which may be correlated with the increase of specific surface and solubility [57].

These results may be understood from the main principles of wave interaction with matter. Microwave effects in organic synthesis have been tentatively rationalized [58], whereas no clear mechanisms have been proposed for inorganic reactions. Still, details concerning the application of microwaves to chemical reactions have been proposed [59]. Two mechanisms have been advanced. Many researchers think that the observed acceleration of the reaction rates could be due to the different modes of transferring heat to the reagents and solvents. Others on the contrary suggest that absorption of microwave radiation has some specific activating (non-thermal) effect on the reagent molecules. Actually, the acceleration of reactions

by microwave exposure results from material–wave interactions leading to thermal effects (which may be easily estimated by temperature measurements) and specific (non-purely thermal) effects.

Non purely-thermal effects can be envisaged to have multiple origins. These effects can be rationalized through the Arrhenius law,  $k = A \exp(-\Delta G^*/RT)$ , and can result from modifications in each of the terms in this equation. Decrease in activation energy  $\Delta G^*$  is for sure a main effect.

Gamma irradiation is also an electromagnetic wave whose wavelength is much shorter (less than 10 pm) but the frequency is much higher ( $3.0 \times 10^{14}$  MHz) and thus, it does not heat the samples nor promotes molecular diffusion. Instead, due to the high energy of the waves, it is able to dissociate molecules. It has been used to change white topaz into blue topaz.

In this context, the comparison with sonication (ultrasound irradiation) is interesting as sonication only promotes heat transfer combined with a pressure increase. If ultrasonic energy at high power, more than  $1/3 \text{ W/cm}^2$  for water at room temperature, is applied to a liquid, cavitation takes place [60]. These conditions are very short-lived although they have been used to synthesize diamonds [61]. They may result in the generation of highly reactive species including hydroxyl, hydrogen, and hydroperoxyl radicals and hydrogen peroxide. Such radicals may initiate or promote many reduction–oxidation reactions. Reactions with organic and inorganic substrates are, then, fast and may reach the diffusion-controlled rate [62].

Assuming adiabatic bubble collapse, the maximum temperatures and pressures within the collapsed cavitation bubbles are predicted by Noltingk and Neppiras from approximate solutions of Rayleigh–Plesset equations [63]. Note that frequency has a significant effect on cavitation because it alters the critical size of the cavitation bubble. At very high frequencies, the cavitation effect is reduced. Lower frequency ultrasound produces more violent cavitation, leading to higher localized temperatures and pressures. Last but not least, there are two extremes with respect to power: the threshold power which must be surpassed and the optimum power beyond which further power increases have no effect [64].

### 1.3.4.1 Remarks

As already mentioned, the interaction of ultrasound waves or microwaves with matter follows two mechanisms which may both result in an acceleration of chemical reactions. Microwaves are electromagnetic waves with wavelengths ranging from 1 mm to 1 m, or frequencies between 0.3 and 300 GHz, whereas ultrasound waves (20–200 kHz) are cyclic sound pressure waves with a wavelength of ca. 1.5 mm. Thus, the interaction with matter is definitely different and they should be used depending on the required result. If the material has to be altered at the atomic level, gamma irradiation is recommended.

Microwave interaction with materials leads to thermal and specific effects. Sonication instead promotes heat transfer combined with a pressure increase.

## 1.4 Other Clays

### 1.4.1 Clay Synthesis

A promising method to synthesize clays using microwave irradiation has been reported. Fast microwave synthesis of hectorite has been obtained by Vicente et al. [65], according to the method reported in which brucite sheets act as crystallization nuclei of hectorite, as proposed by Granquist and Pollack (1959) [66]. A slurry, containing the brucite seeds freshly prepared, lithium fluoride, and silica, was stirred for 1 h. The resulting mixture was treated in a microwave equipment at 100 °C for 4 and 8 h or at 120 °C for 4, 8, or 16 h. Higher proportions of hectorite with higher crystallinity were achieved at longer aging time, higher temperature, and by using a more crystalline brucite. However, the highest purity was 60%. Note that the conventional method provides a 40% hectorite mixture. In summary, the hydrothermal microwave treatment provides a faster synthesis of hectorites, more than 10 times. However, such synthesis has to be improved as no successful pillaring would be achieved with low purity clays.

### 1.4.2 Aluminum-Intercalated Samples

Other clays, not only montmorillonite, have been pillared. Microwave irradiation has been found to enhance the intercalation of aluminum complexes into rectorite due to the promotion of ion exchange during synthesis. Rectorite has a 2:1 layer structure in a regularly interstratified clay mineral of dioctahedral mica layer and dioctahedral smectite layers in a 1:1 ratio. This clay consists of alternate pairs of mica-like (non-expandable) and smectite-like layer (expandable). Mica-like layers increase the thermal stability of rectorite; smectite-like layers determine its pillaring possibility. Thus, aluminum-pillared rectorites should be resistant cracking catalysts. They have been already synthesized using microwave irradiation [67].

### 1.4.3 Titania-Pillared Clays

Conventionally, titanium-pillared clays using montmorillonite, saponite, and rectorite hosts have been prepared from  $\text{TiCl}_4$ -ethanol solutions. Of course, the amount of Ti incorporated is related to the cation-exchange capacity of the host. Saponite has the highest acidity, and this is reflected in the highest conversion for cumene cracking. In the case of pentanol dehydration, however, the highest activity is seen for the rectorite sample, despite its apparent lower acidity. Similar effects have been reported previously for this reaction with alumina-pillared clays. The thermal stability decreases from rectorite through montmorillonite to saponite [32].

Microwave irradiation has been used in the sol-gel synthesis of the small titanium nanoparticles which were supported on laponite [68]. The photocatalytic

activity improves by increasing the Ti/clay ratio as a greater number of active anatase sites are provided and also by the use of hydrothermal treatment which enhanced the anatase crystallinity.

#### ***1.4.4 Chromia and Tin Oxide-Pillared Montmorillonites and Laponites***

Tin oxide-pillared laponite has been formed under ambient conditions from aryltin precursors using microwave heating [69]. The pillaring was achieved via neutral precursors rather than by sacrificial reaction of the exchanged cation. The intercalation/pillaring reactions are much more rapid (5 min) when carried out in containers in a simple domestic microwave oven. Combined  $^{119}\text{Sn}$  Mössbauer and X-ray photoelectron spectroscopic studies suggest that, in the microwave experiments,  $\text{Ph}_3\text{SnCl}$  has a higher initial affinity for the clay surface than  $(\text{Ph}_3\text{Sn})_2\text{O}$  but that the chloride undergoes hydrolysis on the surface once sorbed. Evidence for the considerable mobility of  $\text{Mg}^{2+}$  within the laponite lattice during microwave heating is provided.

Gyftopoulou et al. [6] report the preparation of chromia and tin oxide-pillared montmorillonites and laponites using both conventional and microwave-assisted methods. For the microwaved tin oxide-pillared montmorillonite, a water solution of ammonium hexachlorostannate was mixed with a bentonite suspension and irradiated at 100 W for 15 min at 100 °C. The authors find that the microwave method can be considered successful for the synthesis of tin oxide-pillared montmorillonite as, by XRD measurements, it is shown that the sample presents the same trend as the conventionally prepared ones. For the microwaved tin oxide-pillared laponite, a sodium-exchanged laponite and triphenyltin chloride were mixed with dry ethanol and irradiated for 5 min at 100 W. In this case X-ray powder diffraction is not a suitable method for characterizing pillared laponites due to the lack of first-order reflection. It is replaced by X-ray photoelectron spectroscopy, which shows that in the case of tin oxide-pillared laponites the amount of tin varies among the different preparations although no clear trend is observed relating it with the preparation conditions.

For the microwaved chromia-pillared montmorillonites two sets of experiments were performed: (1) the intermixed solution of chromium nitrate and sodium carbonate was added slowly to the clay suspension and then microwave-irradiated at different power, time, and temperature; (2) the intermixed solution of chromium nitrate and sodium carbonate was microwave-irradiated at 150 W and 105 °C for 15 min. Then, the microwave-treated solution was mixed with the clay suspension and stirred for 1.5 h. The authors [6] find that with microwave irradiation a considerably faster preparation, possibly with highly concentrated clay suspension and pillaring solutions, can be achieved, leading to large-scale production of pillared clays. The basal spacing of 20 Å is not as high as that following the conventional method (27 Å) by Pinnavaia et al. [70], but it is in agreement with other reports and confirms some pillaring [71].

The prepared PILCs were employed as catalysts in the hydrocracking of coal-derived liquids in a conventional microbomb reactor exhibiting high-quality performance and remaining active after 4 h utilization regardless of high coke deposition [6]. When reused, an increase in the total conversion was shown. Although, a range of catalysts with different structural properties depending on texture, morphology, way of preparation, nature of clay catalyst, nature of active metal, etc., were prepared, the selected hydrocracking reaction does not show any particular sensitivity to these factors.

### ***1.4.5 Saponite Pillared with Fe-Organometallic by Microwave and Ultrasound Irradiation***

Natural Na-saponite was intercalated with an iron complex:  $[\text{Fe}_8(\mu_3\text{-O})_2(\mu_2\text{-OH})_{12}(1,4,7\text{-triazacyclononane})_6]^{7+}$ , which behaves as a single molecule magnet at low temperature, by the conventional method and by microwave or ultrasound irradiation [72]. An interlayer distance of 15.6 Å is found for the irradiated samples and 13.7 Å for the sample prepared conventionally. Since the Fe-complex size is ca. 10 Å, only the microwave or ultrasound irradiation promotes the Fe-complex intercalation. This complex conserves the structure of the polycation inorganic core: connectivity seems to be maintained, while the polycations must be somewhat flattened by strain due to intercalation. Magnetization experiments appear compatible with a conservation of the polycation nuclearity.

### ***1.4.6 Pillared Anionic Clays***

#### **1.4.6.1 Polyvanadate-Intercalated Hydrotalcites**

Hydrotalcites are anionic clays, whose chemical formula is  $[\text{M}^{2+}_{1-x}\text{M}^{3+}_x(\text{OH})_2](\text{A}^{m-})_{x/m}\cdot n\text{H}_2\text{O}$ , where  $\text{M}^{2+}$  may be replaced by three-valent cations,  $\text{M}^{3+}$ , which produce positively charged layers, as described in a previous chapter. Hydrotalcite may be synthesized by precipitation or through the sol-gel method among others. They may be prepared in presence of ultrasound or microwave irradiation. Those conditions determine the properties of hydrotalcite-like compounds [73–78].

Hydrotalcites have been intercalated with decavanadate polyoxo complexes in presence of microwave irradiation during the intercalation process as well as during the hydrotalcite crystallization step. The  $d_{003}$  distances of the intercalated samples are 11.8 or 7.8 Å depending on irradiation time, 1 or 5 min, respectively. The specific surface areas turn out to be 52 and 60 m<sup>2</sup>/g for the 1 and 5 min irradiated samples. The interlayer distance of the non-pillared hydrotalcite is 7.7 Å. These compounds were tested in the aldolic condensation of acetone. As expected, the sample irradiated for 1 min, presenting a higher layer expansion, is the most active [79].

#### 1.4.6.2 $PO_4^{3-}$ and $P_2O_7^{4-}$ -Intercalated Hydrotalcites

Zhang et al. [80] report the intercalation of  $PO_4^{3-}$  and  $P_2O_7^{4-}$  species in carbonated Mg–Al- or Zn–Al-hydrotalcites by direct anion-exchange reaction in presence of microwave irradiation at 90°C for 10 min. By infrared spectroscopy it is shown that the  $CO_3^{2-}$  band of the original hydrotalcite disappears in the intercalated materials and the characteristic bands of the  $PO_4^{3-}$  or  $P_2O_7^{4-}$  species appear, confirming intercalation. The X-ray diffraction patterns of the  $PO_4^{3-}$  or  $P_2O_7^{4-}$ -intercalated Mg–Al-hydrotalcites show broader peaks compared with those of the carbonated Mg–Al-hydrotalcite. In the case of Zn–Al-hydrotalcites the 003 peak at  $2\theta = 11.6^\circ$  becomes less intense by intercalation with  $PO_4^{3-}$  and even disappears with  $P_2O_7^{4-}$  interlayered. This peak broadening has been assigned to a disturbance in the structure due to the pillaring with  $PO_4^{3-}$  or  $P_2O_7^{4-}$  species. The authors conclude that the microwave method can destroy the acting force between lamellar structures so that phosphate or pyrophosphate ions can easily exchange carbonate ions. Therefore, the microwave method cannot only make the exchange reaction possible but also shorten the interaction time dramatically to obtain crystalline products.

#### 1.4.6.3 PET–Hydrotalcite Nanocomposites

The hydrotalcite has been organically modified using dodecyl sulfate as the interlamellar anion, to overcome the lack of compatibility between the polymer and hydrotalcites containing purely inorganic anions, such as carbonate and nitrate. Then, the polyethylene terephthalate (PET) –hydrotalcite nanocomposites have been prepared as follows. The PET precursors were microwave-irradiated while the hydrotalcite is dispersed in an ultrasonic bath [81]. The authors show that in situ polymerization under microwave irradiation constitutes an alternative method for preparing PET–hydrotalcite nanocomposites. The preparation time is considerably reduced and the inorganic filler results well dispersed and exfoliated in the polymer matrix. The nanocomposites obtained are thermally more stable than original PET.

#### 1.4.6.4 Remarks

The intercalation of other clays than montmorillonite in presence of microwave or ultrasound irradiation has been reported. The thermal stability of the intercalated material seems to increase from saponite, through montmorillonite to rectorite. An interesting result is that aluminum-intercalated rectorite can be a resistant-cracking catalyst and that only microwave or ultrasound irradiations promote the Fe-complex interaction with saponite. Note that anionic clays have been intercalated in presence of microwave irradiation. The main advantages of irradiation are those already reported: faster preparation, easier preparation, and most important the use of concentrated solutions. Furthermore, irradiation improves thermal stability.

## 1.5 Conclusion

Microwave and ultrasound irradiation are available tools in the synthesis of intercalated and pillared clays, cationic or anionic. Microwave interaction with materials leads to thermal and specific effects. Sonication only promotes heat transfer combined with a pressure increase.

A microwave irradiation time of ca. 10–30 min provides ordered materials, thermally resistant and not dealuminated clays. Furthermore, microwave drying is assumed to favor the water molecules transport toward surface unlike a conventional heating where heating is transported from the surface to the bulk. Such features may explain the differences in pillar distribution and catalytic performance of the microwave-irradiated and conventional samples.

Concentration of clay suspensions may be increased with the use of microwave irradiation. Highly concentrated clay suspensions, 10–50%, instead of the conventional 0.5–1%, irradiated for 7 min, provide the required dispersion of the clay. Such result is determinant for any large-scale preparation of intercalated clays as the amount of water is strikingly reduced.

The intercalation of other clays than montmorillonite in presence of microwave or ultrasound irradiation has been reported. The thermal stability of the intercalated material seems to increase from saponite, through montmorillonite to rectorite.

**Acknowledgments** This work was developed in the frame of a sabbatical visit of G. Fetter to the Instituto de Investigaciones en Materiales, UNAM. The financial support of CONACYT is gratefully recognized.

## References

1. Gil A, Korili SA, Vicente MA (2008) Recent advances in the control and characterization of the porous structure of pillared clay catalysts. *Cat Rev Sci Eng* 50:153
2. Gil A, Gandía LM, Vicente MA (2000) Recent advances in the synthesis and catalytic applications of pillared clays. *Cat Rev Sci Eng* 42:145
3. Klopogge JT (1998) Synthesis of smectites and porous pillared clay catalysts: a review. *J Porous Mater* 5:5
4. Figueras F (1988) Pillared clays as catalysts. *Cat Rev Sci Eng* 30:457
5. Singh V, Sapeliya V, Srivastava V, Kaur S (2006) ZrO<sub>2</sub>-pillared clay: an efficient catalyst for solventless synthesis of biologically active multifunctional dihydropyrimidinones. *Catal Comm* 7:571
6. Gyftopoulou ME, Millan M, Bridgwater AV, Dugwell D, Kandiyoti R, Hriljac JA (2005) Pillared clays as catalysts for hydrocracking of heavy liquid fuels. *Appl Catal A* 282:205
7. Pichat P, Khalaf H, Tabet D, Houari M, Saisi M (2005) Ti-montmorillonite as photocatalyst to remove 4-chlorophenol in water and methanol in air. *Environ Chem Lett* 2:191
8. Aguzzi C, Cerezo P, Viseras C, Caramella C (2007) Use of clays as drug delivery systems: possibilities and limitations. *Appl Clay Sci* 36:22
9. Mott CJB (1988) Pillared Clays. Burch R (ed) *Catal Today* 2:199
10. Vicente MA, Bañares-Muñoz MA, Toranzo R, Gandía LM, Gil A (2001) Influence of the Ti precursor on the properties of Ti-pillared smectites. *Clay Miner* 36:125



11. Belver C, Bñares-Muñoz MA, Vicente MA (2004) Fe-saponite pillared and impregnated catalysts I. Preparation and characterisation. *Appl Catal B* 50:101
12. Kloprogge JT, Booy E, Jansen JBH, Geus JW (1994) Synthesis of Al-pillared beidellite and its catalytic activity in the hydroconversion of n-heptane. *Catal Lett* 29:293
13. Miehe-Brendle J, Khouchaf L, Baron J, Le Dred R, Tuilier M-H (1997) Zr-exchanged and pillared beidellite: preparation and characterization by chemical analysis, XRD and Zr K EXAFS. *Micropor Mater* 11:171
14. Gangas NHJ, Van Wonerghem J, Mörup S, Koch CJW (1985) Magnetic bridging in nontronite by intercalated iron. *J Phys C: Solid State Phys* 18:L1011
15. De Bock M, Maes N, Cool P, Heylen I, Vansant EF (1996) Theoretical evaluation of pillared clay adsorbents: part III: the total porosity and the macrostructure of Al-pillared montmorillonite and hectorite. *J Porous Mater* 3:207
16. Bergaya F, Hassoun N, Barrault J, Gatineau L (1993) Pillaring of synthetic hectorite by mixed [Al<sub>13</sub>-xFex] pillars. *Clay Miner* 28:109
17. Fetter G, Heredia G, Velázquez LA, Maubert AM, Bosch P (1997) Synthesis of aluminum-pillared montmorillonites using highly concentrated clay suspensions. *Appl Catal A* 162:41
18. Storaro L, Lenarda M, Perissinotto M, Lucchini V, Ganzerla R (1998) Hydroxy-Al pillaring of concentrated suspensions of smectite clays. *Micropor Mesopor Mater* 20:317
19. Aouad A, Mandalia T, Bergaya F (2005) A novel method of Al-pillared montmorillonite preparation for potential industrial up-scaling. *Appl Clay Sci* 28:175
20. Houari M, Saidi M, Tabet D, Pichat P, Khalaf H (2005) The removal of 4-chlorophenol and dichloroacetic acid in water using Ti-, Zr- and Ti/Zr-pillared bentonites as photocatalyst. *Am J Appl Sci* 2:1136
21. Warriar KKG, Mukundan P, Ghosh SK, Sivakumar S, Damodaran AD (1994) Microwave drying of boehmite sol intercalated smectites. *J Mater Sci* 29:3415
22. Rao KJ, Vaidhyanathan B, Ganguli M, Ramakrishnan PA (1999) Synthesis of inorganic solids using microwaves. *Chem Mater* 11:882
23. Sun S, Jiang Y, Yu L, Li F, Yang Z, Hou T, Hu D, Xia M (2006) Enhanced photocatalytic activity of microwave treated TiO<sub>2</sub> pillared montmorillonite. *Mater Chem Phys* 98:377
24. Singh V, Sapehiya V, Lal Kad G (2004) Ultrasound and microwave activated preparation of ZrO<sub>2</sub>-pillared clay composite: catalytic activity for selective, solventless acylation of 1, n-diols. *J Molec Catal A* 210:119
25. Fetter G, Heredia G, Maubert AM, Bosch P (1996) Synthesis of Al-intercalated montmorillonites using microwave irradiation. *J Mater Chem* 6:1857
26. De Andrés AM, Merino J, Galván JC, Ruiz-Hitzky E (1999) Synthesis of pillared clays assisted by microwaves. *Mater Res Bull* 34:641
27. Fetter G, Hernández V, Rodríguez V, Valenzuela MA, Lara VH, Bosch P (2003) Effect of microwave irradiation time on the synthesis of zirconia-pillared clays. *Mater Lett* 57:1220
28. Figueras F, Mattrod-Bashi A, Fetter G, Thrierr A, Zanchetta JV (1989) Preparation and thermal-properties of Zr-intercalated clays. *J Catal* 119:91
29. Yamanaka S, Brindley GW (1979) High surface-area solids obtained by reaction of montmorillonite with zirconyl chloride. *Clays Clay Miner* 27:119
30. Martínez-Ortiz MJ, Fetter G, Domínguez JM, Melo-Banda JA, Ramos-Gómez R (2003) Catalytic hydrotreating of heavy vacuum gas oil on Al- and Ti-pillared clays prepared by conventional and microwave irradiation methods. *Micropor Mesopor Mater* 58:73
31. Lin J-T, Jong S-J, Cheng S (1993) A new method for preparing microporous titanium pillared clays. *Micropor Mater* 1:287
32. Kooli F, Bovey J, Jones W (1997) Dependence of the properties of titanium-pillared clays on the host matrix: a comparison of montmorillonite, saponite and rectorite pillared materials. *J Mater Chem* 7:153
33. Arfaoui J, Boudali LK, Ghorbel A (2006) Vanadia-doped titanium-pillared clay: preparation, characterization and reactivity in the epoxidation of allylic alcohol (E)-2-hexen-1-ol. *Catal Commun* 7:86

34. Jagtap N, Ramaswamy V (2006) Oxidation of aniline over titania pillared montmorillonite clays. *Appl Clay Sci* 33:89
35. Fetter G, Salas P, Velazquez LA, Bosch P (2000) Ce-Al-Pillared clays: synthesis, characterization, and catalytic performance. *Ind Eng Chem Res* 39:1944
36. Gil A, Vicente MA, Korili SA (2005) Effect of the Si/Al ratio on the structure and surface properties of silica-alumina-pillared clays. *J Catal* 229:119
37. Fetter G, Tichit D, De Menorval LC, Figueras F (1995) Synthesis and characterization of pillared clays containing both Si and Al pillars. *Appl Catal A* 126:165
38. Han Y-S, Yamanaka S (2006) Preparation and characterization of microporous SiO<sub>2</sub>-ZrO<sub>2</sub> pillared montmorillonite. *J Solid State Chem* 179:1146
39. Trejo MA, Flores SO, Córdova I, Valenzuela MA, Fetter G (2003) Synthesis of Al-La-pillared clays using microwave irradiation. 18th North American catalysis society meeting Proceedings, Cancún, Mexico
40. Trejo M, Fetter G, Bosch P, Sánchez-Sánchez J, Alvarez LJ (2000) "Síntesis y caracterización de arcillas pilareadas con La-Al", in XVII Simposio Iberoamericano de Catálisis, Vol. I, pp. 449, Oporto, Portugal.
41. Sterte J (1991) Preparation and properties of large-pore La-Al-pillared montmorillonite. *Clays Clay Miner* 39:167
42. Booij E, Klopogge JT, Van Veen JAR (1996) Preparation, structural characteristics and catalytic properties of large-pore rare earth element (Ce,La)/Al-pillared smectites. *Clays Clay Miner* 44:774
43. Pires J, Machado M, De Carvalho MB (1998) Porosity and thermal stability of PILCs prepared with clays from different origins and different metal-polyhydroxycationic species of Al and Al/Ce. *J Mater Chem*, 8:1465
44. Rao GR, Mishra BG (2005) A comparative UV-vis-diffuse reflectance study on the location and interaction of cerium ions in Al- and Zr-pillared montmorillonite clays. *Mater Chem Phys* 89:110
45. Mishra BG, Rao GR (2005) Cerium containing Al- and Zr-pillared clays: promoting effect of cerium (III) ions on structural and catalytic properties. *J Porous Mater* 12:171
46. Carriazo J, Guélou E, Barrault J, Tatibouët JM, Molina R, Moreno S (2005) Synthesis of pillared clays containing Al, Al-Fe or Al-Ce-Fe from a bentonite: characterization and catalytic activity. *Catal Today* 107:126
47. Vicente MA, Belver C, Trujillano R, Bañares-Muñoz MA, Rives V, Korili SA, Gil A, Gandía LM, Lambert J-F (2003) Preparation and characterisation of vanadium catalysts supported over alumina-pillared clays. *Catal Today* 78:181
48. Molina R, Vieira-Coelho A, Poncelet G (1992) Hydroxy-Al pillaring of concentrated clay suspensions. *Clays Clay Miner* 40:480
49. Pérez-Zurita MJ, Pérez-Quintana GJ, Alfonso H, Maldonado A, Urbino de Navarro C, De Abrisqueta A, Scott CE (2005) Synthesis of Al-PILC assisted by ultrasound: reducing the intercalation time and the amount of synthesis water. *Clays Clay Miner* 53:528
50. Berry FJ, Rao KK, Oates G (1994) Fe-57 Mossbauer-spectroscopy study of iron-oxide pillared clays synthesized by microwave-heating. *Hyperfine Interact* 83:343
51. Awate SV, Waghmode SB, Patil KR, Agashe MS, Joshi PN (2001) Influence of preparation parameters on characteristics of zirconia-pillared clay using ultrasonic technique and its catalytic performance in phenol hydroxylation reaction. *Korean J Chem Eng* 18:257
52. Sadykov VA, Kuznetsova TG, Doronin VP, Sorokina TP, Kochubei DI, Novgorodov BN, Kolomichuk VN, Moroz EM, Zyuzin DA, Paukshtis EA, Felonov VB, Derevyankin AY, Beloshapkin SA, Matyshak VA, Konin GA, Ross JRH (2001) Structure of zirconia nanoparticles used for pillaring of clay. *Materials Research Society Symposium V* paper V13.21, Boston.
53. Katdare SP, Ramaswamy V, and Ramaswamy AV (1997) Intercalation of Al oligomers into Ca<sup>2+</sup>-montmorillonite using ultrasonics, *J Mater Chem* 7:2197; (1999), Ultrasonication: a competitive method of intercalation for the preparation of alumina pillared montmorillonite

- catalyst, *Catal Today* 49:313; (2000), Factors affecting the preparation of alumina pillared montmorillonite employing ultrasonics, *Microporous Mesoporous Mater* 37:329
54. Sivakumar S, Damodaran AD, Warriar KGK (1995) Delamination through sonication for hydroxy metal-oxide sol intercalation of montmorillonite. *Ceramics Internet* 21:85
  55. Awate SV, Waghmode SB, Agashe MS (2004) Synthesis, characterization and catalytic evaluation of zirconia-pillared montmorillonite for linear alkylation of benzene. *Catal Commun* 5:407
  56. Negron A, Ramos S, Blumenfeld AL, Pacheco G, Fripiat J (2002) On the structural stability of montmorillonite submitted to heavy gamma-irradiation. *Clays Clay Miner* 50:35
  57. Pushkareva R, Kalinichenko E, Lytovchenko A, Pushkarev A, Kadochnikov V, Plastynina M (2002) Irradiation effect on physico-chemical properties of clay minerals. *Appl Clay Sci* 21:117
  58. Perreux L, Loupy A (2001) A tentative rationalization of microwave effects in organic synthesis according to the reaction medium, and mechanistic considerations. *Tetrahedron* 57:9199
  59. Fioni A, Breccia A (1999) Chemistry by microwaves. *Pure Appl Chem* 71:573
  60. Lindley J (1990) Sonochemical aspects of inorganic and organometallic chemistry including catalysis. In: Mason TJ (ed) *Chemistry with ultrasound*, vol 28. Elsevier Applied Science, London, pp 27–64
  61. Khachatryan AKh, Aloyan SG, May PW, Sargsyan R, Khachatryan VA, Baghdasaryan VS (2008) Graphite-to-diamond transformation induced by ultrasound cavitation. *Diamond Related Mater* 17:931
  62. Adewuyi YG (2001) Sonochemistry: environmental science and engineering applications. *Ind Eng Chem Res* 40:4681
  63. Neppiras EA (1980) Acoustic cavitation. *Phys Rep* 61:159
  64. Mason TJ (1990) Introduction. In: Mason TJ (ed) *Chemistry with ultrasound*, vol 28. Elsevier Applied Science, London, pp 1–25
  65. Vicente I, Salagre P, Cesteros Y, Guirado F, Medina F, Sueiras JE (2009) Fast microwave synthesis of hectorite. *Appl Clay Sci* 43:103
  66. Granquist WT, Pollack SS (1959) Crystallization of hectorite favored by brucite nuclei. *Clays Clay Miner* 8:150
  67. Du D, Zhao X, Lu X (2005) Comparison of conventional and microwave-assisted synthesis and characteristics of aluminum-pillared rectorite. *J Wuhan Univ Tech Mater Sci Ed* 20:53
  68. Daniel LM, Frost RL, Zhu HY (2007) Synthesis and characterisation of clay-supported titania photocatalysts. *J Coll Interface Sci* 316:72
  69. Ashcroft RC, Bond SP, Beevers MS, Lawrence MAM, Gelder A, McWhinnie WR (1992) Sn-119 Mossbauer and X-ray photoelectron studies of novel tin oxide pillared laponite formed under ambient conditions from aryltin precursors - rapid intercalation reactions using microwave-heating. *Polyhedron* 11:1001
  70. Pinnavaia TJ, Tzou MS, Landau SD (1985) New chromia pillared clay catalysts. *J Am Chem Soc* 107:4783
  71. Volzone C, Cesio AM (2003) Changes in OH-Cr-montmorillonite after heating in air and nitrogen atmospheres. *Mater Chem Phys* 79:98
  72. Stievano L, Mbemba K, Train C, Wagner FE, Lambert J-F (2006) Intercalation of [Fe-8(mu(3)-O)(2)(mu(2)-OH)(12)(tacn)(6)](8+) single molecule magnets in saponite clay. *J Phys Chem Solids* 67:1363
  73. Benito P, Labajos FM, Rocha J, Rives V (2006) Influence of microwave radiation on the textural properties of layered double hydroxides. *Micropor Mesopor Mater* 94:148
  74. Benito P, Herrero M, Barriga C, Labajos FM, Rives V (2008) Microwave-assisted homogeneous precipitation of hydrotalcites by urea hydrolysis. *Inorg Chem* 47:5453
  75. Abelló S, Medina F, Tichit D, Pérez-Ramírez J, Cesteros Y, Salagre P, Sueiras JE (2005) Nanoplatelet-based reconstructed hydrotalcites: towards more efficient solid base catalysts in aldol condensations. *Chem Comm* 1453

76. Rivera JA, Fetter G, Bosch P (2006) Microwave power effect on hydrotalcite synthesis. *Micropor Mesopor Mater* 89:306
77. Rivera JA, Fetter G, Giménez Y, Xochipa MM, Bosch P (2007) Nickel distribution in (Ni,Mg)/Al-layered double hydroxides. *Appl Catal A* 316:207
78. Tichit D, Rolland A, Prinetto F, Fetter G, Martínez-Ortiz MJ, Valenzuela MA, Bosch P (2002) Comparison of the structural and acid-base properties of Ga- and Al-containing layered double hydroxides obtained by microwave irradiation and conventional ageing of synthesis gels. *J Mater Chem* 12:3832
79. Castro LV, Fetter G, Valenzuela MA, Bosch P (2004) Condensación aldólica catalizada con hidrotalcitas intercaladas. In: XIX symposium Iberoam catalysis proceedings, Mérida, Yucatán, México, Spanish, pp 2714
80. Zhang ZJ, Mei XJ, Fen LR, Lu SJ, Qiu FL (2004) Preparation of PO4<sup>3-</sup>, P2O7<sup>4-</sup> anion-pillared nanocrystalline Mg-Al and Zn-Al layered double hydroxides in microwave fields. *Chinese Chem Lett* 15:867
81. Martínez-Gallegos S, Herrero M, Rives V (2008) In situ microwave-assisted polymerization of polyethylene terephthalate in layered double hydroxides. *J Appl Polymer Sci* 109:1388

# Chapter 2

## Pillared Interlayered Clays as Adsorbents of Gases and Vapors

J. Pires and M.L. Pinto

**Abstract** This chapter reviews recent works where porous materials prepared from clays, particularly pillared interlayered clays (PILCs), were studied as gas phase adsorbents. It also includes the cases which used the adsorption of gases and vapors for the nanotextural characterization of the materials, other than the usual low temperature nitrogen adsorption. This is, for instance, the case of the adsorption of molecules of volatile organic compounds (VOCs), with various dimensions and shapes, which can be used as probe molecules for the characterization of the porosity or concerning the topic of the VOCs abatement. A similar situation occurs with water adsorption, whose results can be informative not only on the desiccant properties of the materials but also on their surface chemistry. A more recent line of studies of adsorption by materials prepared from clays, namely, the hydrocarbon purification from natural gas or biogas, was also addressed.

**Keywords** Adsorption · PILCs · PCHs · Purification · Separation · Volatile organic compounds · Landfill gases

### 2.1 Introduction

Pillared interlayered clays (PILCs) are far more studied concerning their preparation methodologies and their catalytic properties [1, 2] than what concerns their possibilities as adsorbents, particularly as selective adsorbents. PILCs present, in general, lower structural regularity than, for instance, the more usual zeolites, but PILCs structural regularity is higher than other important classes of adsorbent materials, such as activated carbons. Therefore, the lack of a precise regular structure cannot be regarded as a major drawback for PILC applications as adsorbents. Furthermore, these materials can be prepared from soils, creating added value materials from

---

J. Pires (✉)

Department of Chemistry and Biochemistry and CQB, Faculty of Sciences – University of Lisbon, Ed. C8, Campo Grande, 1749-016 Lisboa, Portugal  
e-mail: jpsilva@fc.ul.pt

natural products. This review intends to be a contribution for the study of PILCs as adsorbents of gases and vapors. And, in a certain extent also, for the use of adsorption methodologies in the study of properties of PILCs, other than the well-known and well-documented low temperature nitrogen adsorption. In this way, the adsorption of volatile organic compounds (VOCs) is studied both for textural characterization using selected VOCs as probe molecules as well as for the abatement of noxious VOCs. Also water adsorption in PILCs can be studied from the view of the characterization of the surface chemistry, namely, their hydrophobic–hydrophilic properties, and as adsorbents for water removal. Particular attention is devoted also to the potentialities of PILCs as selective adsorbents of natural and biogas components, such as carbon dioxide, methane, ethane, and nitrogen. In this work we avoided to refer data from the literature where the units for adsorbed amounts were not clear, particularly in cases where, at least apparently, some confusion could be made between the units of  $\text{cm}^3/\text{g}$  and  $\text{cm}^3\text{STP}/\text{g}$ .

## 2.2 Adsorption of Volatile Organic Compounds (VOCs)

### 2.2.1 As Probe Molecules

Concerning the characterization of the porosity of PILCs, while the gallery heights can usually be known with high accuracy from X-ray diffraction, the knowledge of the space between the pillars poses more difficulties. Micropore size distributions, evaluated from the adsorption of only one probe molecule, usually nitrogen at 77 K, have been obtained for PILCs [3–5]. The various methodologies have necessarily their advantages and drawbacks. The use of only nitrogen adsorption at 77 K is advantageous since few experiments are needed but quality data at very low pressures are mandatory. Furthermore, effects due to the surface chemistry can change the adsorption potential and, in this way, influence the obtained micropore size distribution. The use of the adsorption of various probe molecules has also been made in the characterization of the porosity of PILCs [6–10], but more experimental work is needed in this case, since several adsorbates are to be used. These adsorbates are usually organic molecules with different sizes and shapes. This methodology is also limited by the vapor pressure of the probe molecules to be used. In fact, since the experiments are normally performed at room temperature the organic molecules to be used need to have a measurable vapor pressure at this temperature. Another assumption of the use of various organic probe molecules for characterizing the porosity is that, since porous volumes are preferably expressed in liquid volume ( $\text{cm}^3/\text{g}$ ), the density of the adsorbed phase needs to be approached by the density of the liquid at same temperature. Nevertheless, this methodology was adopted by some authors who were able to propose micropore size distributions on the basis of the exclusion by molecular sizes [6, 8]. One illustrative example is given in Fig. 2.1 [8] where the micropore size distributions were proposed for three PILCs, prepared from starting clays with different origins, on the basis of the size exclusion effect of nitrogen, *n*-hexane, cyclohexane, and triethylamine [8]. This methodology can

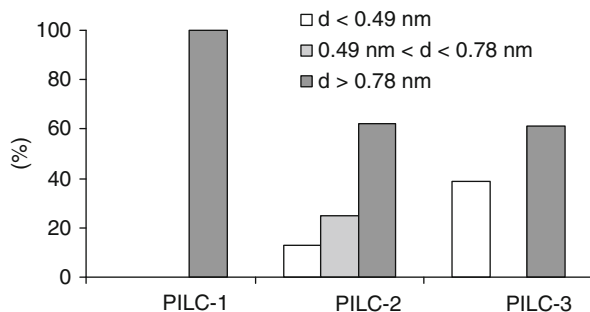


**Fig. 2.1** Micropore size distributions proposed from the adsorption of various probe molecules in three different PILCs

also give useful information for the characterization and understanding of the catalytic properties of PILCs by knowing the precise amount of a particular reactant or reaction product that can be accommodated in the material structure.

It is obviously very difficult to generalize the results published in the literature for the adsorption of molecules with different sizes and shapes in different PILCs. Nevertheless, Fig. 2.2 illustrates some interesting features. In this figure, the results obtained for the adsorption in PILCs, prepared from montmorillonites, are compared with those obtained in the well-known NaY zeolite. As expected, due to the differences in their total microporous volumes, the adsorbed amounts of the presented organic molecules are lower in the PILCs than in the NaY zeolite. Also, the shape of the isotherm is different. In the case of the NaY zeolite, the isotherm is normally more steeper for low relative pressures and a plateau is more clearly defined, as a consequence of its narrow pore sizes (0.74 nm) [11] and more uniform structure of the zeolite.

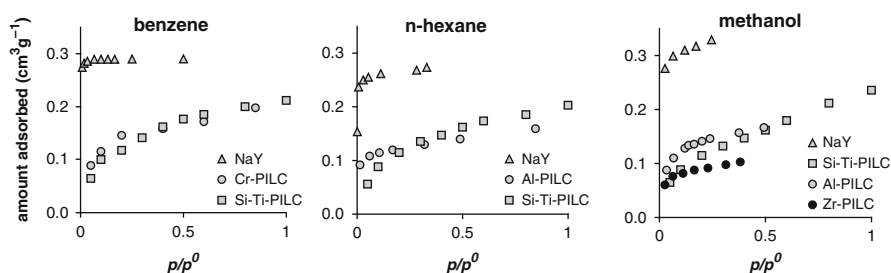


**Fig. 2.2** Adsorption isotherms of various organic molecules in PILCs and in the NaY zeolite at 298 K. Data from [7, 8, 12]

It is also interesting to note in Fig. 2.2 that PILCs prepared with rather different types of pillars, such as chromium oxide (Cr-PILC) and silicium–titanium oxides (Si–Ti-PILC), can have relatively similar adsorption isotherms in the case of benzene. Also for *n*-hexane adsorption the aluminum oxide-pillared material (Al-PILC)

presents an isotherm which is relatively similar to the Si–Ti-PILC. In the case of methanol (a zirconium oxide-pillared sample – Zr-PILC – was included in this case), probably because this is the smallest molecule of the series, the isotherms are now more different among the various solids.

When the adsorption of chlorinated or oxygenated VOCs is considered, the isotherms can be very different in the same PILC [9, 13, 14]. But, in this case and because these types of molecules have normally a high dipole moment or are highly polarizable, those differences can be entirely attributed not only to size exclusion affects but also, in a non-measurable way, to specific adsorbate–adsorbent interactions. In this way, the use of chlorinated or oxygenated VOCs as probe molecules for the characterization of the microporosity may not be adequate. The adsorption of organic gases and vapors in PILCs has been modeled according to the BET [7], Langmuir [7, 14] virial [15], Dubinin–Radushkevich [12], and Dubinin–Asthakov [14] equations.

### ***2.2.2 For Separation/Purification***

It is well known that a number of VOCs, liberated in various industrial activities, are toxic and contribute to the atmospheric pollution, with direct or indirect action on human tissues [16]. The abatement of VOCs can be made by thermal oxidation, an efficient but highly energy costly process that, additionally, is not entirely adequate for chlorinated VOCs [17]. The catalytic oxidation of VOCs is an important procedure but adsorption can, in the limit, make possible the re-use of a particular VOC [18]. Additionally, since VOCs are usually present in diluted air streams, adsorbents may be used to concentrate a diluted stream and therefore improving the efficiency of thermal or catalytic oxidation [18]. While activated carbons, due to their spread use and moderate-to-low cost, are usually considered as good candidates as adsorbents, in the field of the removal of VOCs these materials present some drawbacks since their flammability poses difficulties to their regeneration [19]. Zeolites are another family of adsorbents that can be considered for the VOCs abatement. Some limitations of zeolites, at least for the more common, are due to their hydrophilic nature, since humidity is also normally present in the streams where VOCs are to be removed. Zeolites can be prepared less hydrophilic [19], for instance, by dealumination processes [19, 20], but this is an additional preparative step and the limiting adsorbed amounts tend to be lower in the respective dealuminated samples [20]. Pillared clays have intermediate hydrophobic–hydrophilic properties between activated carbons and the more common zeolites [21] and could be an interesting alternative as adsorbents in the field of VOCs removal/abatement, at least if an appropriated methodology of making PILCs economically in large amounts is developed.

Since the removal of noxious volatile organic compounds is usually to be considered in the low pressure region, Table 2.1 includes the amounts of selected VOCs adsorbed in several PILCs at the relative pressure of 0.1.



**Table 2.1** Amounts of selected VOCs adsorbed in PILCs at the relative pressure of 0.1. When indicated in the original work, the structural formula of the clays, which were all montmorillonites, (per  $O_{10}(OH_2)$ ) is given

VOC	Type of pillars	Starting clay	Amount adsorbed ( $cm^3/g$ ) and reference
Benzene	SiO <sub>2</sub> -TiO <sub>2</sub>	(Si <sub>3.89</sub> Al <sub>0.11</sub> )(Al <sub>1.60</sub> Mg <sub>0.32</sub> Fe <sub>0.08</sub> )	0.1 [7]
Benzene	Chromium oxide		0.13 [12]
Benzene	Titanium oxide		0.14 [12]
Toluene	Aluminum oxide		0.12 [10]
Cyclohexane	SiO <sub>2</sub> -TiO <sub>2</sub>	(Si <sub>3.89</sub> Al <sub>0.11</sub> )(Al <sub>1.60</sub> Mg <sub>0.32</sub> Fe <sub>0.08</sub> )	0.065 [7]
<i>n</i> -Hexane	SiO <sub>2</sub> -TiO <sub>2</sub>	(Si <sub>3.89</sub> Al <sub>0.11</sub> )(Al <sub>1.60</sub> Mg <sub>0.32</sub> Fe <sub>0.08</sub> )	0.09 [7]
CCl <sub>4</sub>	Iron oxide-zirconium oxide	(Si <sub>4</sub> )(Al <sub>1.67</sub> Mg <sub>0.34</sub> Fe <sub>0.08</sub> )	0.31 [9]
CHCl <sub>3</sub>	Iron oxide-zirconium oxide	(Si <sub>4</sub> )(Al <sub>1.67</sub> Mg <sub>0.34</sub> Fe <sub>0.08</sub> )	0.28 [9]
Trichloroethane	Aluminum oxide		0.12 [10]
Trichloroethane	Zirconium oxide	(Si <sub>3.70</sub> Al <sub>0.30</sub> )(Al <sub>1.16</sub> Fe <sub>0.51</sub> Mg <sub>0.26</sub> )	0.07 [13]
Methanol	Aluminum oxide	(Si <sub>3.70</sub> Al <sub>0.30</sub> )(Al <sub>1.16</sub> Fe <sub>0.51</sub> Mg <sub>0.26</sub> )	0.12 [13]
Methanol	Zirconium oxide	(Si <sub>3.70</sub> Al <sub>0.30</sub> )(Al <sub>1.16</sub> Fe <sub>0.51</sub> Mg <sub>0.26</sub> )	0.08 [13]

Some studies addressed the separation of organic molecules using PILCs as selective adsorbents [13,22]. In dynamic experiments [22] separation factors for an aluminum oxide-pillared clay with values of 2.08 for *n*-hexane/benzene (at 523 K); 1.90 for *n*-hexane/*n*-heptane (at 594 K), and 2.68 for cyclohexane/benzene (at 624 K) were reported. The modeling of selective adsorption of VOCs, by a methodology based on the Dubinin-Radushkevich theory was also attempted in montmorillonites pillared with aluminum or zirconium oxide pillars [13]. Various VOCs were tested and separation factors near three (at a coverage of 0.5) for the methanol/propanone system and the methylethylketone/propanone system were obtained. The effects of the type of pillars in the separation factors were not entirely clear, although the total amounts adsorbed were highest for the aluminum oxide-pillared materials, in line with the highest specific surface area of these samples [13]. Chlorinated samples such as the 1,1,1-trichloroethane/trichloroethylene were also tested but the results were less promising in this case [13].

A limited number of studies were made considering the adsorption of H<sub>2</sub>S, which is also a noxious gaseous pollutant. These considered either the study of the effect of the pillaring with different oxide pillars, mainly of aluminum or iron [23] or the particular case of H<sub>2</sub>S removal related to the conservation of works of art [24]. In the latter case, a montmorillonite from Wyoming pillared with aluminum oxide pillars resulted to be more efficient in the removal of H<sub>2</sub>S at very low relative pressures, in spite of its lowest total microporous volume when considered with other more common adsorbents, such as sodium X or Y zeolites.

## 2.3 Adsorption of Water

Water adsorption studies in pillared clays have been made by various authors, essentially with a twofold objective: the potential use of these adsorbents in moisture removal and also the characterization of the surface of PILCs. In this section, we considered the analysis of published water adsorption results in terms of their potentialities as desiccants, using some indications in the literature that materials should have, in particular, if the envisage use is as desiccants in gas-fired cooling systems and dehumidification [25]. For this, one important criterion, although of course not the only one, is that the water adsorption isotherm must be of a “moderate” type I. Roughly, the amount adsorbed at a relative pressure of 0.1 should be about 50% the total amount adsorbed [25, 26].

Figure 2.3 collects the maximum water adsorbed amounts, estimated from the published data for relative pressures between 0.85 and 0.95 and the respective percentage of amount adsorbed at the relative pressure of 0.1. In this figure, the data for samples 1–4 are from [26], for samples 5–9 from [27], for samples 10–13 from [28], for samples 14–16 from [29], and for samples 17–22 from [12]. Samples 23 and 24 [8] are not PILCs, they are, respectively, Y and A zeolites. The latter samples were include in Fig. 2.3 to illustrate the effect of a steep type I isotherm, which is usually obtained for water adsorption in these hydrophilic zeolitic materials. In fact, for these zeolites, the amount adsorbed at a relative pressure of 0.1 is more than 80% (almost 90% for A zeolite) of the total adsorbed volume.

All materials in Fig. 2.3 have alumina-based pillars except samples 17–19 [12], which have chromium oxide pillars, and samples 20–22 [12] that have titanium

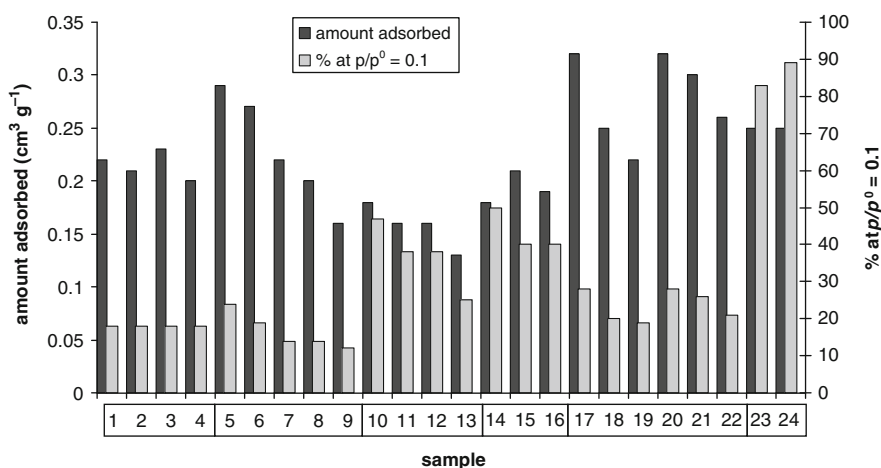


**Fig. 2.3** Adsorption capacities for water and respective adsorption at  $p/p^0 = 0.1$  for various pillared clays and zeolites (see text for references)

oxide pillars. As can be seen in Fig. 2.3, the highest water adsorption amounts seem to be registered not for PILCs that have aluminum oxide pillars but for those that have chromium or titanium oxide pillars.

In the series of samples 5–9 [27], samples 5 and 6 are also among those with the highest water adsorbed amounts. In that work the authors study the effect of the progressive increase of the calcination temperature, in steps of 100 °C between 200 °C, for sample 5, and 600 °C, for sample 9, and observed that the maximum adsorbed amount of water decreases as the calcinations temperature increases. In the case of the lowest calcination temperature (200 °C), the highest adsorbed amount observed may also be due to the fact that the oligomeric cationic species that are the precursors of the pillars can be not entirely transformed into the respective oxide and the residual OH groups may then increase the adsorption via specific interaction with the water molecules. For all samples of this series (samples 5–9) the percentage adsorbed at  $p/p^0 = 0.1$  is always well below 50%, putting in evidence the relatively low hydrophilicity of the studied samples.

In the case of the samples 1–4, the authors [26] tried to improve the properties of the PILCs for water adsorption by increasing the percentage of the amount adsorbed at  $p/p^0 = 0.1$  by varying the aging conditions of the pillaring solution. A slightly better result was obtained in the same study in a PILC, where  $\text{Ca}^{2+}$  cations were introduced after the pillaring/calcination process, where that percentage increases to 32%. Other authors have also studied the effect on water adsorption properties of PILCs by introducing cations after the preparation of the PILCs [28], by direct cation exchange at high pH, namely,  $\text{Ca}^{2+}$ ,  $\text{Na}^{2+}$ ,  $\text{Mg}^{2+}$ , and  $\text{Li}^+$  (samples 10, 11, 12, and 13, respectively). As can be seen in Fig. 2.3, the most favorable results were obtained for  $\text{Ca}^{2+}$ , while  $\text{Li}^+$  and  $\text{Mg}^{2+}$  resulted only in a modest improvement. The authors [28] interpreted the latter fact as due to the migration of the smallest  $\text{Li}^+$  and  $\text{Mg}^{2+}$  cations into the octahedral layers of the clay sheets, according to the known Hoffmann–Klemen effect.

Water is a polar molecule, and as well stated in the literature for water adsorption, the contribution of the dispersion forces to adsorption is usually small when compared with the contribution from the interactions with the dipole [30]. Therefore, water adsorption has a high degree of specific interactions with the surface. In the present review it is difficult to disclose from the published results some aspects related namely with differences in the used starting clays that could also partially explain the variation of results in Fig. 2.3. For the preparation of the aluminum oxide-pillared clays corresponding to the samples 14–16 [29] the authors used three montmorillonites from three different soil deposits. From these materials, sample 14 presented the best results, particularly concerning the value of the amount adsorbed at  $p/p^0 = 0.1$ , which approached 50% of the total amount. This sample was prepared with a montmorillonite that had a high degree of substitutions in the tetrahedral substitutions (of silicon by aluminum), while the global silicon to aluminum ratio of the three samples was much similar. The tetrahedral sheets are, of course, more exposed to the interactions with the adsorbed molecules and so specific interactions can be developed with the adsorbed water molecules. This

result seems to indicate that starting clays with high degree of tetrahedral substitutions may be beneficial when preparing PILCs for moisture adsorption, particularly for improving the adsorption properties in the initial portion of the adsorption isotherm.

## 2.4 Adsorption of Natural and Biogas Components

One important application of adsorbent materials is in gas separation processes, where a mixture of two or more gases is separated to obtain one or more purified components [31]. PILCs can be potentially used in such processes, provided that they present the adequate properties for an effective separation of a given mixture. However, comparing with other types of adsorbent materials, like activated carbons and zeolites, relatively few studies and experimental data can be found on the literature about the adsorption of permanent gases on PILCs. Works involving adsorption at pressures above the atmospheric pressure (high-pressure adsorption) are even scarcer. Nevertheless, some important and illustrative results were obtained, namely, in the study of PILCs for the purification of natural and biogas components. This section presents the published adsorption results on this topic along with a discussion and analysis of the results in the view of possible industrial applications.

PILCs have been studied for the methane/ethane separation [32, 33]. This separation has importance in the context of the natural gas extraction, since these are the two main hydrocarbon components of natural gas [34]. Ethane may be separated for use as a feedstock for steam cracking for the production of ethylene. Other higher molecular weight hydrocarbons present in natural gases are important fuels as well as chemical feedstocks and are normally recovered as natural gas liquids. An example of the methane and ethane adsorption results is presented in Fig. 2.4 for the adsorption on a zirconium oxide PILC (Zr-PILC). As expected, ethane adsorbs considerably more than methane, since it is the heavier component, and at near atmospheric pressure the adsorbed amounts of ethane are more than three times higher than those of methane. The vacancy solution theory (VST) [35–37] was used to predict the adsorption isotherms of methane/ethane binary mixtures and successfully compared them with some experimental points [32]. In Fig. 2.4, the binary adsorption isotherms predicted by VST and by the ideal adsorbed solution theory (IAST) [38–41] are also presented and as may be observed agree fairly well for the gas phase compositions compared, although VST tends to predict higher adsorption values at the same composition. It is interesting to note that, for equal composition in the gas phase (0.5 methane molar fraction), the predicted isotherms are considerably more close to the pure ethane isotherm than to the pure methane. This is a first indication that the material selectively adsorbs ethane over methane.

For a better understanding of the adsorption behavior of mixtures in an adsorbent material, at a given fixed pressure, it is useful to compare the composition of the gas phase ( $y_i$ ) with the composition of the adsorbed phase ( $x_i$ ), by constructing

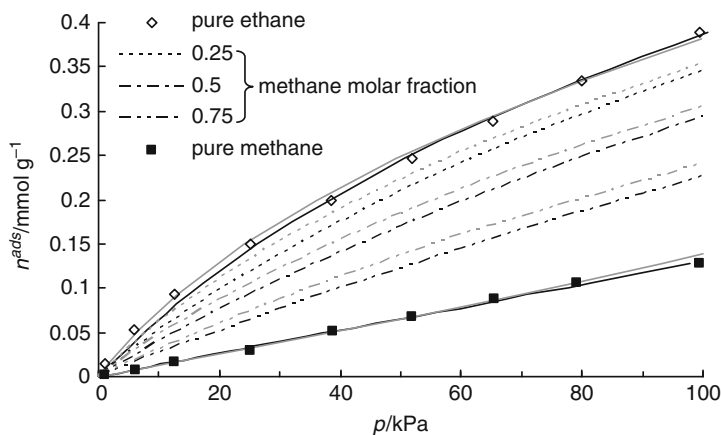


**Fig. 2.4** Comparison between IAST (*black*) and VST (*gray*) predictions of binary mixture isotherms of methane/ethane on a zirconium oxide-PILC, at 289 K. Experimental values taken from [32]

the so-called  $x$ - $y$  phase diagram [31]. For the same zirconium oxide-pillared clay presented in Figure 4.1, it is possible to obtain the diagram in Fig. 2.5 using the IAST model adjusted to the experimental results obtained at two temperatures. In this figure, the composition of methane (molar fractions) in the gas phase ( $y_1$ ) and adsorbed phase ( $x_1$ ) are represented in the axis. In this way, the composition of the adsorbed phase may be known for a given gas composition, which is a very useful information in the context of gas separation since it allows to estimate the expected purity of the separated gases. The two curves (one at each temperature) show that the gas phase is always richer in methane than the adsorbed phase, i.e., the ethane tends to adsorb on the material and the methane tends to stay in the gas phase. The sharper the knee of the curve, the more effective is the separation. In fact, if one

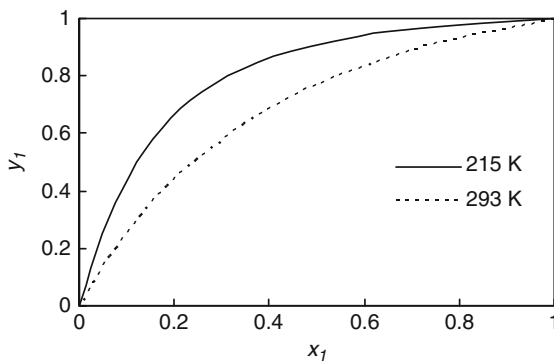


**Fig. 2.5**  $x$ - $y$  phase diagram of the methane/ethane adsorption (composition of the adsorbed and gas phases) on a Zr-PILC, at 215 and 293 K and 100 kPa

considers the gas mixture with 0.8 in methane ( $y_1$ ) it can be seen that the composition of the adsorbed phase at 215 K is about 0.3 in methane ( $x_1$ ) (i.e., about 0.7 in ethane), but increases to 0.55 in methane at 293 K. Therefore, Fig. 2.5 clearly shows that the separation is more effective at 215 K than at 293 K. Nevertheless, the results indicate that this PILC could be used for the methane/ethane separation.

The  $x$ - $y$  diagrams are useful for the evaluation of a material for a specific separation, as shown by the preceding example, but they do not give any information on the adsorbed amounts in a given mass of adsorbent. This information is also important when designing the separation equipment for a particular application, namely, for calculating the maximum adsorbed amounts of a separation column. For this purpose, the representation of the adsorbed amounts as a function of the gas phase composition is more suited, by constructing a gas phase diagram of the adsorbed phase. When using such representation for the same Zr-PILC (shown in Fig. 2.6) it becomes evident that the adsorption capacities at 215 and 293 K are significantly different. The interception of the lines for the ethane and methane amounts indicates the composition of the gas phase at which the composition of the adsorbed phase is equal in the two components. This point moves to lower  $y_1$  values when the temperatures increase, indicating that the separation becomes less effective. The results at 293 K are more significant for possible applications, since they are close to ambient temperatures and separations are normally preformed near these temperatures. In these conditions, Fig. 2.6 shows that the amounts of ethane vary from about 0.45 mmol/g of the pure ethane adsorption to about 0.16 mmol/g, at 0.79 methane molar fraction, and for higher methane concentration on the gas phase the amounts of

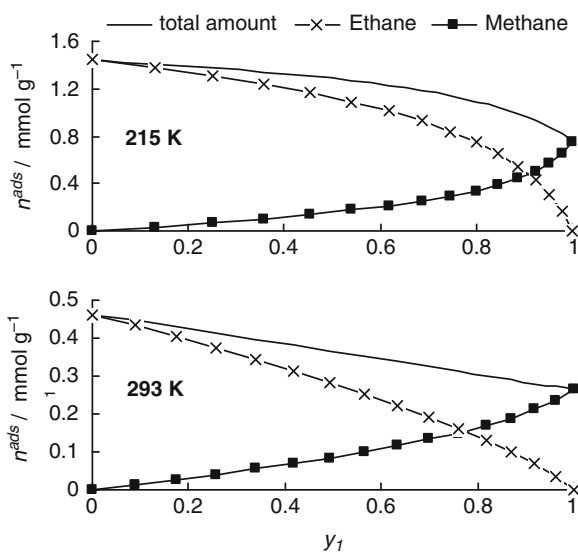


**Fig. 2.6** Phase diagrams (amounts adsorbed) at two temperatures predicted by IAST at 100 kPa, as a function of the gas phase composition, for a Zr-PILC

methane adsorbed became higher than those of ethane. This indicates the amounts of ethane that could be recovered from mixtures under these conditions, using this Zr-PILC as the adsorbent material.

The predictions shown in Fig. 2.6 may be compared with experimental values obtained for the adsorption of methane/ethane mixtures. When the predictions made using the VST are compared with the total adsorbed amount and gas phase composition determined experimentally, deviations of about 2–3% in the adsorbed amount were found [32] which is a good result considering that the experimental values have about the same uncertainty. The predictions presented in 2.6 were made by the IAST may also be compared with the experimental data, and in Fig. 2.7 the experimental point is compared with the predictions. As can be seen, the experimental point is close to the solid line of the total adsorbed amount, with a deviation of 5%. This supports the predictions made by IAST and confirms that they are close to those made by VST (already seen in Fig. 2.4). Also very important is the indication that these theories are suitable for modeling the adsorption of binary mixtures in PILC, using the pure components adsorption isotherms. In fact, the measurements of isotherms for gas mixtures are much more complicated than for pure gases, due to equilibrium problems and to the analysis of the gas phase composition. Thus, IAST or VST are important tools to the analysis of the adsorption data, especially when comparing different PILC materials for an envisaged application. More recently, an adsorption model based on statistical mechanics for the prediction of mixture isotherms on PILCs was proposed [42] with higher accuracy at very high pressures, but for the range of pressures normally used on adsorption experiments it gives similar results to IAST.

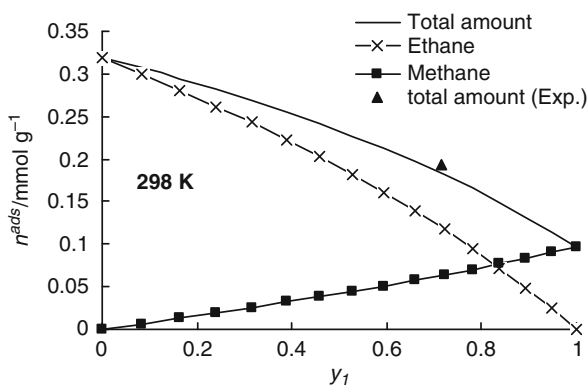


**Fig. 2.7** Comparison of the predicted adsorbed phase diagram at 73.84 kPa, with an experimental point, for a Zr-PILC

Most times, there is an interest to study the separation of a gas mixture with a specific composition and the temperature or pressure effects on the separation performance of the adsorbent materials. One way is to use the selectivity of the separation, defined as

$$S_{2,1} = \frac{x_2/y_2}{x_1/y_1} \quad (2.1)$$

and evaluate this parameter as a function of pressure or temperature. Usually a separation with selectivity higher than three is considered appropriate for industrial applications [31].

In the methane/ethane separation applied to natural gas, the abundance of ethane in the distribution gas is only about 8% (i.e.,  $y_1 = 0.92$ ), and this value can be used as reference to the evaluation of the selectivity of PILC. Figure 2.8 shows the selectivity for the separation of ethane from methane, at this reference composition, using zirconium oxide-pillared clays synthesized from two different clays [32]. One clay, labeled as PTS, is from Porto Santo (Madeira archipelago, Portugal), and the other, labeled as BEN, is from Benavila (Alentejo, Portugal). It is evident from Fig. 2.8 that selectivity toward ethane decreases, as pressures and temperatures increase, although at the higher temperature (293 K) the selectivity is almost insensitive to the pressure. It is interesting to notice that the selectivity values for BEN and PTS-pillared clays are not very different. Nevertheless, in the majority of conditions, selectivity is higher for the PTS sample, a fact that is related, most probably, to the higher heat of adsorption of ethane on this pillared clay [32]. The selectivity values calculated using IAST and VST present some discrepancies at 215 K for the same materials, being the IAST values higher than those calculated by VST. However, they qualitatively agree in the order of the expected selectivity for the separation, and at 293 K the values are identical. From the practical point of view, the potential application of pillared clays in the separation of the major hydrocarbon components of natural gas (methane and ethane) is confirmed, since the selectivity coefficients, between six and eight at 293 K, compare well with those obtained with other adsorbents [43].

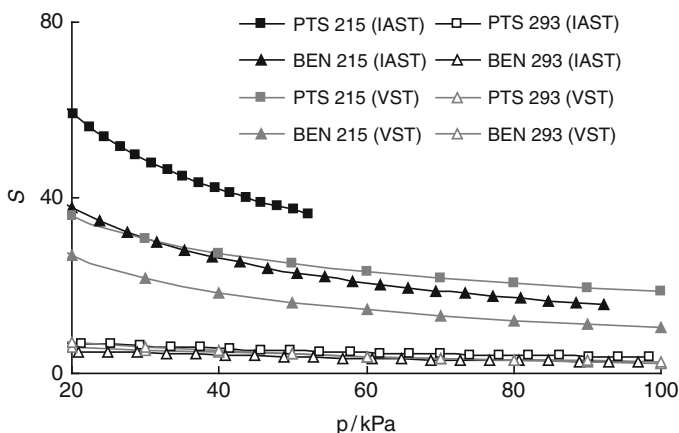


**Fig. 2.8** Selectivity of Zr-PILC (PTS and BEN) predicted by IAST (*black*) and VST (*gray*), at two temperatures, for the methane/ethane separation, at 0.92 methane molar fraction



Another important gas separation, which has also been studied using PILCs as adsorbents, is the carbon dioxide/methane separation. This separation can be applied for the purification of natural gas, biogas, and landfill gas, which are formed with a considerable amount of carbon dioxide along with the combustible part [34, 44–46]. In Fig. 2.9 the adsorption results on two PILCs using the same Porto Santo clay (PTS), but different pillars, are presented [47, 48]. The Zr-PTS present higher adsorption capacity for methane and carbon dioxide in the range of comparable values (0–100 kPa), although the two materials have about the same surface area. This indicates that the nature of the pillars strongly influences the adsorption behavior of these gases, either by differences on the chemical nature of the surface (surface charges, acidity, etc.), or by differences in the pillar's density and size (i.e., the size of the micropores). In a recent work, aluminum and zirconium oxide-PILCs prepared using Wyoming (WYO) and Benavila (BEN) clays have been studied for carbon dioxide/methane separation, up to 1,000 kPa [33]. The results showed that the zirconium PILCs presented the highest carbon dioxide adsorbed amounts per unit surface area of the studied materials, due to the more acidic nature of Zr oxide-PILCs and their interaction with the quadrupole of the carbon dioxide. However, when the comparison is made by the adsorbed amount in terms of the mass of material only, the comparison is not be so evident. In fact, some aluminum-PILC presented higher adsorbed amounts than another zirconium-PILC (Zr-BEN), due to their higher surface areas and microporous volumes. Therefore, the work concludes that the more favorable results obtained for Zr-WYO PILC is an outcome of the chemistry of  $\text{ZrO}_2$  pillars in the Wyoming clay host. This points out the difficulties of drawing some general conclusions about the pillars that are more suitable for a given separation, since they will also depend on the parent clay used in the preparation. This subject will be further discussed with more detail hereafter.

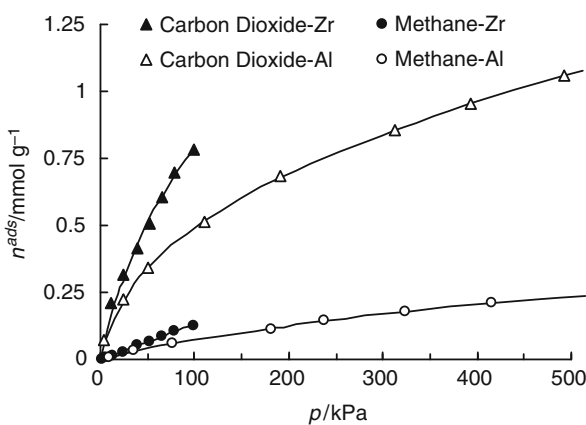


**Fig. 2.9** Carbon dioxide and methane adsorption isotherms, on PILCs obtained with Al and Zr oxide pillars at 298 K

Considering applications using pressure swing adsorption [31], which is the most used type of cyclic gas adsorption separation, the materials used in this process should be easily regenerated in the end of the adsorption step, preferably by a simple decompression of the system. The fact that the adsorption isotherms of carbon dioxide and methane on PILCs are most times slow rising curves, like those presented in Fig. 2.9, is favorable from this viewpoint. This is an advantage over many zeolites, since these usually have rectangular shaped isotherms and become almost saturated with carbon dioxide below atmospheric pressure, hampering the effective regeneration by a simple decompression step. Taking into account the example for the aluminum oxide-PILC in Fig. 2.9, one can see that the adsorption amount rises from about 0.5 mmol/g at 100 kPa (atmospheric pressure) to more than 1 mmol/g at 500 kPa, giving a working capacity of 0.5 mmol/g for that pressure cycle. Similar working capacity for pressure swing adsorption and vacuum swing adsorption results were also reported for other PILCs, supporting the possible application of PILCs for carbon dioxide/methane separation [33].

For a better analysis of the adsorption results presented in Fig. 2.9,  $x$ - $y$  phase diagrams and selectivity coefficients were calculated using the IAST and are presented in Figs. 2.10 and 2.11. Both figures show that the PILC with aluminum oxide pillars is more effective for the separation under study, since it allows obtaining methane

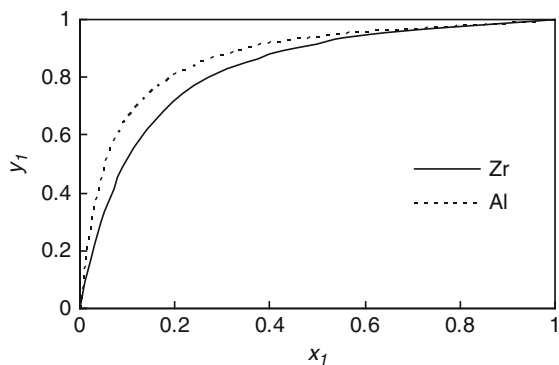


**Fig. 2.10** Zr-PTS and Al-PTS  $x$ - $y$  phase diagrams of carbon dioxide/methane mixture, at 100 kPa and 298 K (component 1 – methane)

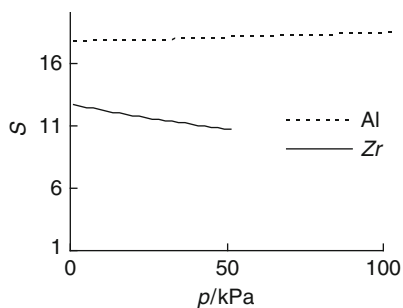


**Fig. 2.11** Selectivity coefficients as function of pressure, at  $y_1 = 0.5$  (methane), for the two PILCs prepared from PTS clay, at 298 K

with a slightly higher purity. It is interesting to note that the simple comparison of the isotherms would clearly lead to this conclusion. In fact, Zr-PTS presented the highest adsorption amounts for both methane and carbon dioxide. However, it is the relation between these two amounts that influences the selectivity of the separation. The results presented in Figs. 2.10 and 2.11 are inline with those obtained with the same type of pillars in other clays [33].

As already mentioned, most gas separations are carried at pressures above atmospheric, and there is much interest to study the adsorption of gases in this pressure range. However, there is scarce data in the literature on high-pressure adsorption of gases on PILCs. Recently, the first comparison work on the high-pressure adsorption of methane, ethane, carbon dioxide, and nitrogen on different aluminum and zirconium PILCs [33] was presented. This work was a contribution to evaluate the real applicability of PILCs for the separation of binary mixtures of the studied gases, which is important in the context of the natural, bio, and landfill gas upgrade. For the studied binary mixtures, the presented results indicate the possible application in the separation of methane/ethane, methane/carbon dioxide, nitrogen/ethane, and nitrogen/carbon dioxide. The latter separation has also interest for applications in carbon dioxide emissions abatement.

In addition to the applicability evaluation, the results obtained in a broad pressure range also give the opportunity to study the evolution of the phase diagrams, similar to those in Figs. 2.6 and 2.7, but now as function of pressure. This approach leads to tri-dimensional representation of the phase diagrams as in Fig. 2.12. This figure shows the phase diagram for a zirconium oxide-pillared clay, which presented the best results of the studied PILCs for the methane/carbon dioxide separation. The

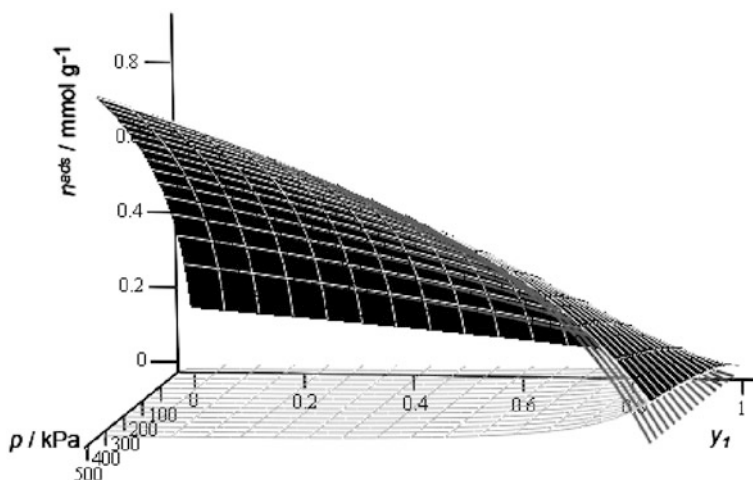


**Fig. 2.12** Phase diagram (composition of the adsorbed phase) predicted by IAST, as a function of the gas phase composition and pressure for a zirconium oxide-PILC. The *black* surface represents the total amount adsorbed, the lower *gray* mesh represents the adsorbed methane amounts and the upper *gray* mesh represents the adsorbed carbon dioxide amount

lines formed by the interception of the surfaces with the vertical  $p$ ,  $n^{\text{ads}}$  planes at  $y_1 = 0$  and  $y_1 = 1$  (methane molar fraction in the gas phase) correspond to the pure components adsorption isotherms of carbon dioxide and methane, respectively. Similarly, the lines contained in the  $p$ ,  $n^{\text{ads}}$  planes, but at intermediate compositions ( $0 < y_1 < 1$ ), correspond to the isotherms of each component and the total amount adsorbed at a given gas phase composition. The cuts obtained from the  $n^{\text{ads}}$ ,  $y_1$  plane are phase diagram representations analogous to those in Figs. 2.6 and 2.7. Observing the effect of pressure on the adsorbed amounts, Fig. 2.12 clearly shows that the increasing of the pressure favors the adsorption of  $\text{CO}_2$  and so the separation at higher pressures becomes more effective. In fact, at a gas phase composition between 0.4 and 0.6 in methane (typical of biogas and landfill gas), the composition of the adsorbed phase is about 0.05 in methane at 500 kPa, that is, the adsorbed phase is about 95% rich in carbon dioxide. This is a strong indication that these materials could be used for the upgrade of biogas or landfill gas.

Another separation that was studied using PILCs is the methane/nitrogen [33, 49, 50]. Selectivity values of 2.35 were reported for an  $\text{Al}_2\text{O}_3$ -PILC from Arizona montmorillonite [49] and for a series of Wyoming-based PILCs reported values were slightly above 5 for Al-PILC, about 2 for Ti-PILC and Fe-PILC, and close to 1 (no separation) for Cr-PILC and Zr-PILC [50]. Other results obtained at higher pressures revealed selectivity above 10 for best case (Zr-WYO) and about 2–3 in the other cases [33]. Although these values seem encouraging for the applications of PILCs in the methane/nitrogen separation, it must be taken in to account that the methane adsorbed amounts are quite low. Figure 2.13 presents adsorption isotherms of methane, at 298 K, on different PILCs, and show that the amounts are only about 0.2 mmol/g at 500 kPa. It can be observed that the amounts are relatively similar and independent of the pillars and clays used in the preparation of the materials. This is more or less expected since the methane adsorption is due to non-specific

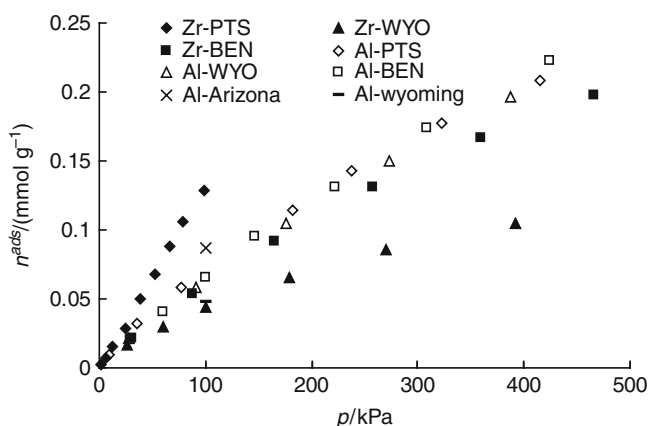


**Fig. 2.13** Adsorption isotherms of methane, at 298 K, in different pillared clays (different clays with different metal oxide pillars). Experimental results collected from the literature [33, 48, 49]

dispersion forces, and thus the chemical nature of the adsorbents surface is much less relevant. Nevertheless, some significant differences are noticed, namely, among the Zr PILCs, since these presented the lowest (Zr-WYO) and the highest amounts (Zr-PTS) in the pressure range where they are comparable. Some values reported in the literature [50] were not included in Fig. 2.13 because they seem to be inconsistent with the values for carbon dioxide adsorption and also with the values obtained by the same authors in following works. Values for methane adsorption on iron–zirconium oxide-PILC, and on an amine-modified iron oxide-PILC, higher than those presented in Fig. 2.13, but at 273 K, were reported also [9]. The small adsorption capacity of PILCs for methane stems from its relatively low surface area, when compared to other clay-based adsorbents like the porous clays heterostructures [48], which have surface areas around 1,000 m<sup>2</sup>/g. This disadvantage imposes the use of quite large amounts of adsorbent in the separation columns to achieve a minimum adsorption capacity of the separation systems.

On the contrary, PILCs usually present a considerable adsorption capacity for the adsorption of carbon dioxide. Figure 2.14 presents the adsorption isotherms obtained on different PILCs, at 298 K. In this case, the carbon dioxide molecule has a quadrupole moment (about  $3.3 \times 10^{-16}$  cm<sup>2</sup> [51]) that is capable of specific interaction with surface charges or dipoles and is expected that its adsorption is more sensitive to differences in the surface chemistry of the different PILCs. However, Fig. 2.14 does not give a clear distinction of the pillars or clays that are more suited to prepare PILCs with high adsorption capacity for carbon dioxide. In the case of the Al-PILCs, it is noticed that the adsorption of this gas is almost insensitive to the clay used in the PILC preparation. The Zr-PILCs are known to have higher acidity than Al-PILCs, but this property seems not to strongly influence the carbon dioxide adsorption. Although, Zr-PTS presented the highest adsorption capacity of the PILCs, in the comparable pressure range, the other Zr-PILCs show lower adsorption capacities than Al-PILCs. The Cr and Ti-PILCs results indicate that these materials have adsorption capacities for carbon dioxide comparable to those of Zr or Al-PILCs. The lowest values obtained for Fe-PILCs could be explained by the low

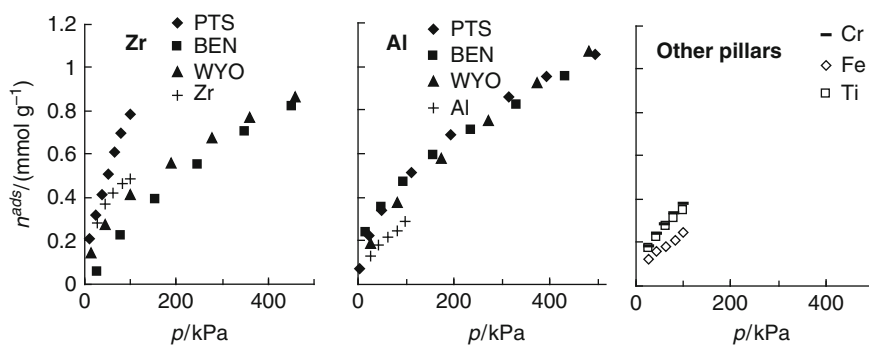


**Fig. 2.14** Adsorption isotherms of CO<sub>2</sub>, at 298 K, in different pillared clays (different clays with different metal oxide pillars). Experimental results collected from the literature [33, 48–50]

surface areas and porous volumes usually obtained in these PILCs [9]. Considering the above, the results in Fig. 2.14 strongly suggest that the variations in the surface chemistry of PILCs are not sufficient to explain the carbon dioxide adsorption. In fact, other textural parameters, like the surface area and porous volumes, are also important to explain the differences between the carbon dioxide adsorption [33]. In the preparation of PILCs, the size and charge of the oligomeric cations and the cation-exchange capacity of the clay influence the pillar's size and density. Thus is very difficult, if not impossible, to obtain PILCs from the same clay with different pillars but with the same pore size and pore volume, i.e., the same pore size distribution. This impairs any attempt of prediction on the best clay or type of pillar to use for the adsorption of carbon dioxide, since ultimately the results will depend on the particular combination of both factors.

## 2.5 Conclusion

As said in the introduction the number of published works where PILCs are considered as adsorbent materials is not very large. Therefore, the systematic of effects such as the composition of the pillars, the nature of the parent clays, or the surface chemistry versus porosity in the selective adsorption properties of PILCs is still difficult. Nevertheless, the materials prepared from natural montmorillonites, with aluminum or zirconium oxide pillars, have important adsorption properties for the adsorption of VOCs, water, and natural gas or biogas components. Having in mind the importance of preparing adsorbent materials from natural, low-added value products, in a sustainable development the study of PILCs as adsorbents surely has its place in the general field of nanoporous materials.

## References

1. Ding Z, Klopogge JT, Frost RL, Lu GQ, Zhu HY (2001) Porous clays and pillared clays-based catalysts. Part 2: a review of the catalytic and molecular sieve applications. *J Porous Mater* 8:273–293
2. Gil A, Korili SA, Vicente MA (2008) Recent advances in the control and characterization of the porous structure of pillared clay catalysts. *Catal Rev* 50:153–221
3. Gil A, Montes M (1994) Analysis of the microporosity in pillared clays. *Langmuir* 10: 291–297
4. Vansant EF, Zhu HY, Maes N, Molinard A (1994) Determination of the micropore size distribution in pillared clays by gas adsorption. *Micropor Mater* 3:235–243
5. Olivier JP, Occelli ML (2003) Surface area and microporosity of pillared rectorite catalysts from a hybrid density functional theory method. *Micropor Mesopor Mater* 57:291–296
6. Baksh MS, Kikkinides ES, Yang RT (1992) Characterization by physisorption of a new class of microporous adsorbents – pillared clays. *Ind Eng Chem Res* 31:2181–2189
7. Yamanaka S, Inoue Y, Hattori M, Okumura F, Yoshikawa M (1992) Preparation and properties of clays pillared with  $\text{SiO}_2\text{-TiO}_2$  sol particles. *Bull Chem Soc Jpn* 65:2494–2500
8. Pires J, Carvalho MB, Carvalho AP (1996) Characterisation of clays and aluminium pillared clays by adsorption of probe molecules. *Micropor Mater* 6:65–77

9. Heylen I, Vansant EF (1997) The difference in adsorption capacity between Fe-PILCs and modified Fe-BuA- and Fe-Zr-PILCs. *Micropor Mater* 10:41–50
10. Pires J, Mahboub R, Mouzdahir YE, Elmchaouri A, Carvalho A, Pinto M (2006) Characterization of a delaminated clay and pillared clays by adsorption of probe molecules. *Coll Surf A* 280:81–87
11. Meier WM, Olson DH (1992) Atlas of zeolite structure types. *Zeolites* 12:16–185
12. Sychev M, Prihod'ko R, Stepanenko A, Rozwadowski M, de Beer VHJ, van Santen RA (2001) Characterisation of the microporosity of chromia- and titania-pillared montmorillonites differing in pillar density – II. Adsorption of benzene and water. *Micropor Mesopor Mater* 47:311–321
13. Pires J, Pinto ML, Carvalho AP de Carvalho MB (2003) Adsorption of volatile organic compounds in pillared clays: estimation of the separation factor by a method derived from the Dubinin–Radushkevich equation. *Langmuir* 19:7941–7943
14. Pires J, Carvalho A, de Carvalho MB (2001) Adsorption of volatile organic compounds in Y zeolites and pillared clays. *Micropor Mesopor Mater* 43:277–287
15. Bandosz TJ, Jagiello J, Schwarz JA (1996) Adsorption of sulfur hexafluoride and propane at temperatures near ambient on pillared clays. *J Chem Eng Data* 41:880–884
16. Tancrede M, Wilson R, Zeise L, Crouch EC (1987) The carcinogenic risk of some organic vapors indoors: a theoretical survey. *Atmos Environ* 21:2187–2205
17. Wang X, Daniels R, Baker RW (2001) Recovery of VOCs from high-volume, low-VOC-concentration air streams. *AIChE J* 47:1094–1100
18. Ruddy EN, Carroll LA (1993) Select the best VOC control strategy. *Chem Eng Prog* 89:28–35
19. Clause B, Garrot B, Cornier C, Paulin C, Simonot-Grange M-H, Boutros F (1998) Adsorption of chlorinated volatile organic compounds on hydrophobic faujasite: correlation between the thermodynamic and kinetic properties and the prediction of air cleaning. *Micropor Mesopor Mater* 25:169–177
20. Pires J, Carvalho A, Veloso P, de Carvalho MB (2002) Preparation of dealuminated faujasites for adsorption of volatile organic compounds. *J Mater Chem* 12:3100–3104
21. Pires J, Pinto ML, Carvalho A, de Carvalho MB (2003) Assessment of hydrophobic–hydrophilic properties of microporous materials from water adsorption isotherms. *Adsorption* 9:303–309
22. De Stefanis A, Perez G, Tomlinson AAG (1994) Pillared layered structures vs zeolites as sorbents and catalysts. 1. Hydrocarbon separations on 2 alumina-pillared clays and  $\alpha$ -tin phosphate analog. *J Mater Chem* 4:959–964
23. Nguyen-Thanh D, Block K, Bandosz TJ (2005) Adsorption of hydrogen sulfide on montmorillonites modified with iron. *Chemosphere* 59:343–353
24. Cruz AJ, Pires J, Carvalho AP, De Carvalho MB (2005) Physical adsorption of H<sub>2</sub>S related to the conservation of works of art: the role of the pore structure at low relative pressure. *Adsorption* 11:569–576
25. Colier RK, Cole TS, Lavan Z (1986) Advanced desiccation materials assessment – final report. Gas Res Inst, Chicago
26. Malla PB, Komarneni S (1990) Synthesis of highly microporous and hydrophilic alumina-pillared montmorillonite – water-sorption properties. *Clays Clay Miner* 38:363–372
27. Yamanaka S, Malla PB, Komarneni S (1990) Water-adsorption properties of alumina pillared clay. *J Colloid Interface Sci* 134:51–58
28. Zhu HY, Gao WH, Vansant EF (1995) The porosity and water-adsorption of alumina pillared montmorillonite. *J Colloid Interface Sci* 171:377–385
29. Pires J, Carvalho MB (1997) Water adsorption in aluminium pillared clays and zeolites. *J Mater Chem* 7:1901–1904
30. Gregg SJ, Sing KSW (1982) Adsorption, surface area and porosity. Acad. Press, London
31. Yang RT (1987) Gas separation by adsorption processes. Butterworths, Boston
32. Pereira PR, Pires J, de Carvalho MB (2001) Adsorption of methane and ethane in zirconium oxide pillared clays. *Sep Purif Technol* 21:237–246

33. Pires J, Saini VK, Pinto ML (2008) Studies on selective adsorption of biogas components on pillared clays: approach for biogas improvement. *Environ Sci Technol* 42:8727–8732
34. Matar S, Hatch LF (2000) *Chemistry of petrochemical processes*, 2nd edn. Gulf Publishing Company, Houston
35. Cochran TW, Kabel RL, Danner RP (1985) The vacancy solution model of adsorption – improvements and recommendations. *AIChE J* 31:2075–2081
36. Suwanayuen S, Danner RP (1980) Gas-adsorption isotherm equation based on vacancy solution theory. *AIChE J* 26:68–76
37. Suwanayuen S, Danner RP (1980) Vacancy solution theory of adsorption from gas-mixtures. *AIChE J* 26:76–83
38. Myers AL, Prausnit JM (1965) Thermodynamics of mixed-gas adsorption. *AIChE J* 11:121–127
39. Myers AL (2003) Equation of state for adsorption of gases and their mixtures in porous materials. *Adsorption* 9:9–16
40. Siperstein FR, Myers AL (2001) Mixed-gas adsorption. *AIChE J* 47:1141–1159
41. Sircar S, Myers AL (1971) Thermodynamic consistency test for adsorption from binary liquid mixtures on solids. *AIChE J* 17:186–190
42. Ghassemzadeh J, Xu LF, Tsotsis TT, Sahimi M (2000) Statistical mechanics and molecular simulation of adsorption in microporous materials: pillared clays and carbon molecular sieve membranes. *J Phys Chem B* 104:3892–3905
43. Cochran TW, Kabel RL, Danner RP (1985) Vacancy solution theory of adsorption using Flory–Huggins activity-coefficient equations. *AIChE J* 31:268–277
44. Tsai WT (2007) Bioenergy from landfill gas (LFG) in Taiwan. *Renew Sust Energy Rev* 11:331–344
45. Desideri U, Di Maria F, Leonardi D, Proietti S (2003) Sanitary landfill energetic potential analysis: a real case study. *Energy Convers Manage* 44:1969–1981
46. Spiegel RJ, Preston JL (2003) Technical assessment of fuel cell operation on landfill gas at the Groton, CT, landfill. *Energy* 28:397–409
47. Pereira PR, Pires J, de Carvalho MB (1998) Zirconium pillared clays for carbon dioxide methane separation. 1. Preparation of adsorbent materials and pure gas adsorption. *Langmuir* 14:4584–4588
48. Pinto ML, Pires J, Rocha J (2008) Porous materials prepared from clays for the upgrade of landfill gas. *J Phys Chem C* 112:14394–14402
49. Cheng LS, Yang RT (1997) Tailoring micropore dimensions in pillared clays for enhanced gas adsorption. *Micropor Mater* 8:177–186
50. Baksh MSA, Yang RT (1992) Unique adsorption properties and potential-energy profiles of microporous pillared clays. *AIChE J* 38:1357–1368
51. Zwanzig RW (1956) Influence of molecular electric quadrupole moments on dielectric constants. *J Chem Phys* 25:211–216



# Chapter 3

## Characterization and Catalytic Performance of Montmorillonites with Mixed Aluminium/Lanthanide Pillars

F. González, C. Pesquera, and C. Blanco

**Abstract** Pillared montmorillonites with mixed Al/lanthanide pillars were prepared. The materials present characteristics that are very different from montmorillonite pillared with only aluminium. Nuclear magnetic resonance studies indicated total absence of tetrahedral aluminium in the pillars when lanthanide cations are incorporated between the clay layers. They have a high thermal stability, high specific surface area and porosity, with pores at the limit between the microporosity and mesoporosity. The textural parameters maintained high values up to 700 °C. The number and the strength of the acid sites in these materials were also high. The increase of the conversion in dehydration of 1-butanol as in hydroisomerization of *n*-heptane shows their better behaviour as acid catalysts. The Al/lanthanide-pillared samples showed increased conversion and improved the selectivity towards the products of cracking. The study of 1-butanol dehydration showed that there is an increase in the acidity, thermal stability and smaller deactivation by carbonaceous deposits in the Al/lanthanide-pillared sample.

**Keywords** Montmorillonites · Al/lanthanide · Pillared clays

### 3.1 Introduction

Pillared clays are prepared from inorganic polyoxycations, which generate a microporous structure with a high specific surface area [1–8]. The most commonly used polyoxycations as pillaring agents are species of aluminium, zirconium, titanium, chromium and iron [1–5]. Pillared montmorillonites have been proposed as potential materials for cracking catalysts of heavy oil fractions [9], as they can be prepared with pore sizes larger than zeolites. The presence of acid centres on the surface of

---

C. Pesquera (✉)

Inorganic Chemistry Group, Department of Chemical Engineering and Inorganic Chemistry, University of Cantabria, Cantabria, Spain  
e-mail: carmen.pesquera@unican.es

their layers as well as on their pillars makes these materials suitable also for use in other reactions of acid catalysis [10, 11]. As the clay layers sinter at the high temperature of the catalytic reactions, the thermal resistance of the pillars must be increased. One well-tested way of achieving this is to use mixed pillars in the materials [12–14], and the most widely used methods have been the mixing of Al-pillaring solutions with lanthanide cations [15–22]. Sterte [23] and McCauley [24] were the first researchers who incorporated lanthanide elements into the preparation of the pillaring agent.

The present study tries to review the main results obtained from the preparation and characterization of montmorillonite pillared with aluminium and lanthanide cations and also analyzes the increase of thermal stability that the pillared materials with aluminium/lanthanide cations undergo compared to the montmorillonite pillared only with aluminium. It distinguishes and analyzes the different thermal evolution of both sizes of pores generated in pillared montmorillonite with aluminium/lanthanide elements and compares it with the thermal evolution of the one single type of pores generated in the pillared montmorillonite with aluminium. We have applied classical and new models to low pressure nitrogen adsorption data to obtain a quantitative evaluation of the microporosity of the synthesized materials' evolution. The chemical reactivity of the materials generated was evaluated and compared by means of their catalytic activity as metal–acid bifunctional catalysts in the hydrocracking–hydroisomerization reaction of *n*-heptane over Pt-impregnated samples and as acid catalyst in the dehydration of 1-butanol.

## 3.2 Experimental Section

### 3.2.1 Starting Material

The clay used as the raw material was a montmorillonite from Wyoming (USA), supplied by Missouri University, and denominated here as Wy. It was purified by fractional sedimentation, with the fraction of  $<2 \mu\text{m}$  being collected. Its specific surface area is  $33 \text{ m}^2/\text{g}$  and its pore volume is  $0.042 \text{ cm}^3/\text{g}$  at  $p/p^\circ = 0.98$ . Its exchange capacity is 106 mequiv/100 g of clay.

### 3.2.2 Synthesis

#### 3.2.2.1 Preparation of the Pillaring Agents

The solutions of the pillaring agent with different Al/lanthanide (Ce, La) molar ratios (Table 3.1) were prepared by adding suitable amounts of  $\text{CeCl}_3 \cdot 7\text{H}_2\text{O}$  or  $\text{LaCl}_3 \cdot 7\text{H}_2\text{O}$  to a solution of 7.2 g of  $[\text{Al}_2(\text{OH})_5\text{Cl}_2 \cdot 3\text{H}_2\text{O}]$  in 21.6 ml of water. The final solutions, 2.5 M in Al, were transferred to a cylindrical Teflon vial that was then closed, placed in an autoclave and heated to  $130 \text{ }^\circ\text{C}$  at  $10 \text{ }^\circ\text{C}/\text{min}$  and maintained at this temperature for 72 h. After returning to room temperature and atmospheric

**Table 3.1** Amount of cations incorporated into the pillaring clay and basal spacing

Sample	Al <sup>3+</sup> incorp. (mequiv/g)	La <sup>3+</sup> or Ce <sup>3+</sup> incorp. (mequiv/g)	<i>d</i> (001), 25 °C (Å)	<i>d</i> (001), 400 °C (Å)
Al-Wy	8.5	–	20.0	18.8
AlLa-Wy-25	19.5	0.3	27.5	26.1
AlCe-Wy-25	15.6	0.3	27.2	24.7
AlCe-Wy-50	12.0	0.1	26.1	24.5
AlCe-Wy-75	7.1	0.0	20.3	17.9

pressure, the reaction mixture was diluted with 640 ml of water necessary to yield an Al concentration of 0.1 M.

### 3.2.2.2 Pillaring Process

The solutions of pillaring agent were added slowly from a glass beaker, with vigorous stirring, to clay slurry obtained by mixing 10 g of clay in 400 ml of water which had been left to stand for 72 h. The final proportion in all cases was 20 mequiv of Al/g of clay, with a solid/liquid ratio of 0.5%. The reaction mixture was stirred continuously for 24 h at room temperature. It was then dialyzed with distilled water, using 1 l of water/g of clay. Dialysis was continued, with water being renewed every 24 h until the Cl<sup>−</sup> concentrations decreased to the point where the conductivity of the aqueous phase was <30 μS. Finally, the samples were freeze dried. Samples were then calcined in air atmosphere for 2 h at 400 °C. The obtained samples are denoted as AlCe-Wy-*x*, where *x* (25, 50 and 75) is the molar ratio of Al/Ce used in the pillaring agent and AlLa-Wy-25, where 25 is the molar ratio of Al/La. The sample denominated as Al-Wy was obtained under the same conditions from a pillaring agent prepared with solution containing only aluminium.

## 3.3 Results and Discussion

Table 3.1 shows the amount of aluminium, lanthanum and cerium cations incorporated (mequiv/g) into the pillaring products. For the AlCe-Wy-75 sample, the chemical analysis indicated an absence of cerium and the amount of aluminium incorporated was similar to that in the Al-Wy sample. However, in the other two samples, cerium was incorporated and the aluminium content was at least double than on the other materials. Moreover, when lanthanum ions were incorporated into the pillars, the amount of this element was 0.3 mequiv/g clay for the AlLa-Wy-25 sample, similar to the Ce content for the same Al/Ce ratio tried. While the aluminium incorporated in this sample was higher (19.5 mequiv/g clay) than in the samples with Al and Ce ions in the pillars.

### 3.3.1 X-ray Diffraction (*Cu K $\alpha$* radiation)

Figure 3.1 shows the X-ray diffraction diagrams between 3 and 12° ( $2\theta$ ) of AlCe-Wy-25 and Al-Wy samples. The Al-Wy sample displays a  $d(001)$  peak at 20.0 Å, associated with the basal spacing between the clay layers and characteristic of clays pillared with aluminium polyoxycations (Keggin ion) [25–27]. In contrast, AlCe-Wy-25 sample displayed two peaks, at 27.2 Å and at 13.6 Å, which correspond to inorganic polyoxycations with different sizes from that of the Keggin ion. When the samples were treated at 400 °C, the basal spacing was reduced to 24.7 Å for the AlCe-Wy-25 sample and to 18.8 Å for the Al-Wy sample. The symmetry and intensity of the  $d(001)$  peaks confirm the existence of pillared materials.

**Fig. 3.1** X-ray diffraction patterns of (a) Al-Wy and (b) AlCe-Wy-25 samples

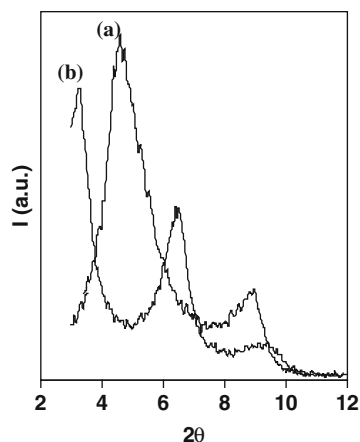
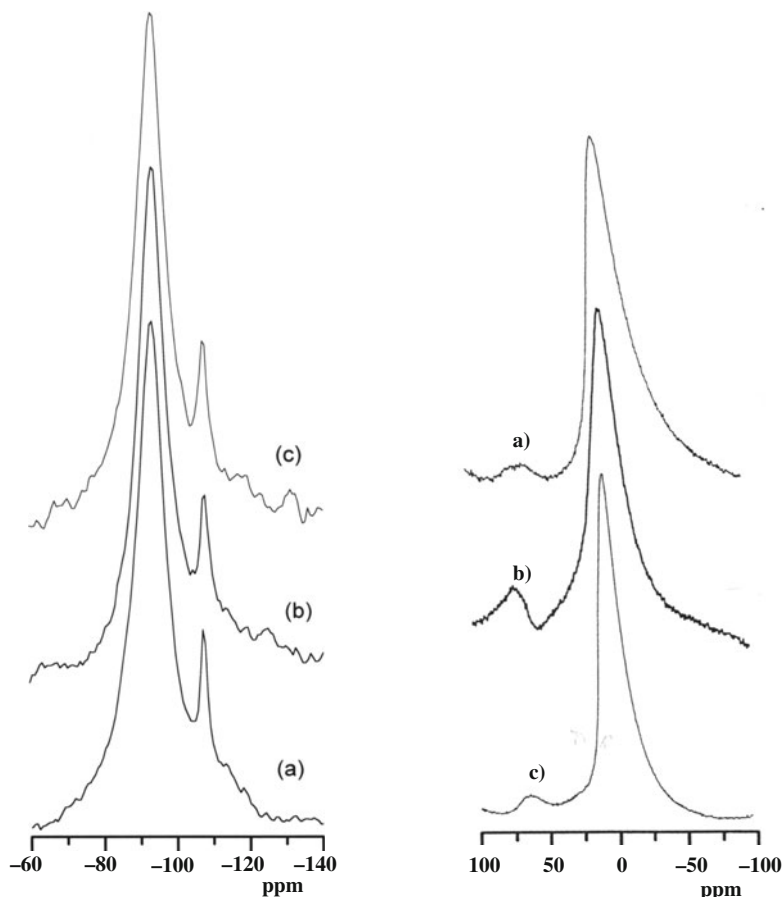


Table 3.1 gives the basal spacing data for all the samples. The samples incorporating only aluminium show similar values (lower than 20 Å), while the samples that have incorporated aluminium and lanthanide elements have higher values. This would seem to indicate the presence of inorganic polyoxycations different from the Keggin ion between the clay layers when aluminium and lanthanide elements have been incorporated.

### 3.3.2 MAS NMR Spectra

<sup>29</sup>Si MAS NMR spectra (59.60 MHz, pulse width of 4 μs, spinning rate 4.0 kHz, spectral width 20 kHz): As an example it is shown in Fig. 3.2(left) the <sup>29</sup>Si spectra obtained for AlCe-Wy-50 and Al-Wy samples, together with that of the original montmorillonite, Wy. All the spectra are very similar, showing a signal centred at 93.8 ppm. This signal is attributable to one <sup>29</sup>Si coordinated with three tetrahedral silica, Q<sup>3</sup>(OAl), as reported in the literature [28, 29] for the bidimensional framework of sheet silicates. The fact that this signal does not shift indicates that



**Fig. 3.2**  $^{29}\text{Si}$  MAS NMR spectra (*left*) and  $^{27}\text{Al}$  MAS NMR spectra (*right*): (a) Wy, (b) Al-Wy and (c) AlCe-Wy-50 samples

this bidimensional framework is maintained in the pillared materials. The signal at 107.9 ppm is attributable to one  $^{29}\text{Si}$  coordinated with four silica,  $\text{Q}^4(\text{OAl})$ . It comes from the feldspar impurities already present in the initial montmorillonite sample, Wy.

$^{27}\text{Al}$  MAS NMR Spectra (78.23 MHz, pulse width of  $4 \mu\text{s}$ , spinning rate 3.0 kHz, spectral width 50 kHz): The  $^{27}\text{Al}$  spectra of some of the samples studied are shown in Fig. 3.2(*right*). All display a central line close to 0 ppm, assigned to  $\text{Al}^{\text{VI}}$  of the octahedral layer of sheet silicates [28, 29]. The spectrum for Wy sample shows a very weak signal at around 60 ppm. This signal can be attributable to  $\text{Al}^{\text{IV}}$  due to the replacement of Si by Al in the tetrahedral layer or due to impurities in the starting materials. The Al-Wy sample, with pillars ( $\text{AlAl}_{12}$ ), clearly shows a signal of higher intensity at 60 ppm due to the presence of tetrahedral aluminium in

the central position of the oligomer ( $\text{AlAl}_{12}$ ), surrounded by 12 octahedral aluminium [25]. In contrast, in the AlCe-Wy-50 sample, this signal is not altered with respect to the initial montmorillonite. This may indicate the absence of tetrahedral aluminium in the intercalated inorganic polyoxycations between the clay sheets in this sample. Similar results are obtained for the AlLa-Wy-25 sample. Two possible explanations of this, that lanthanide cations are occupying all the tetrahedral positions in  $\text{AlAl}_{12}$ -like polycations or that polycation species different that  $\text{AlAl}_{12}$ , and without tetrahedral Al, are actually intercalated. The second option is more possible, and this may also explain the high basal spacing of these solids, because a basal spacing of 24.5 Å or higher may not be justified by the intercalation of  $\text{AlAl}_{12}$  species [30].

Figure 3.3 shows the  $^{27}\text{Al}$  MAS NMR spectra of Al-Wy and AlCe-Wy-50 samples at room temperature and subjected to thermal treatment at 400 °C. The signal corresponding to the tetrahedral aluminium in Al-Wy sample is modified (Fig. 3.3b), deforming and shifting to a lower value, whereas this signal is not altered in AlCe-Wy-50 sample. This result supports the absence of tetrahedral aluminium in the inorganic polyoxycations intercalated in AlCe-Wy-50 sample (Fig. 3.3c).

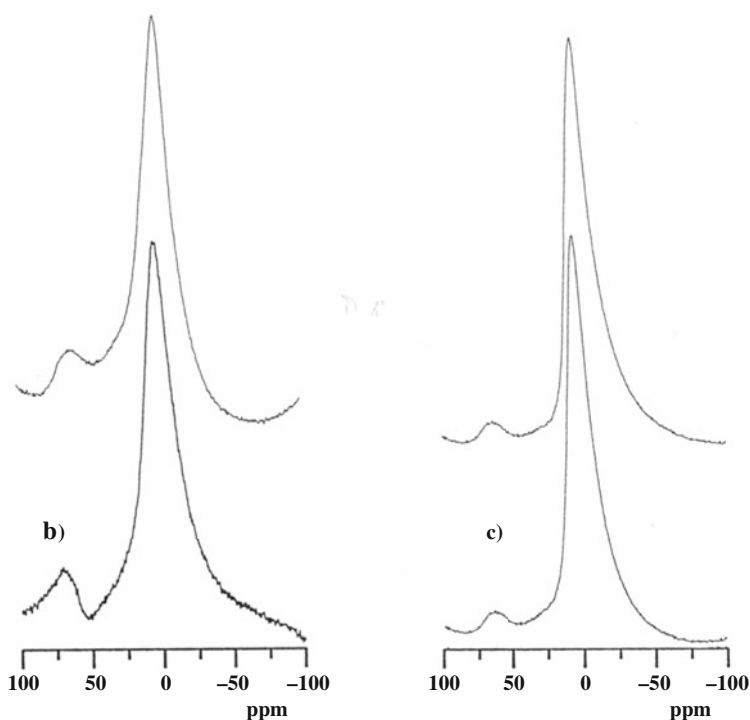


**Fig. 3.3**  $^{27}\text{Al}$  MAS NMR spectra at room temperature and at 400 °C from *bottom to top*: (b) Al-Wy and (c) AlCe-Wy-50 samples

### 3.3.3 Textural Analysis

The textural parameters of the samples were studied by means of the adsorption–desorption isotherms of  $N_2$  at 77 K. Since all the Al/lanthanide-pillared samples behave in a similar way, the AlLa-Wy-25 and Al-Wy samples have been chosen as representative in the figures.

Figure 3.4 shows the  $N_2$  isotherms at 77 K for Al-Wy and AlLa-Wy-25 samples after thermal treatment for stabilization at 400 °C. The isotherms are of type IV, corresponding to mesoporous solids. All pillared samples in the zone of low values of  $p/p^0$  ( $<0.1$ ) present Langmuir adsorption isotherms (type I), which indicate the presence of micropores, generated in the pillaring process to intercalate inorganic polyoxycations between the clay layers. All samples show a hysteresis loop type H4 in the IUPAC classification [31]. In the Al/lanthanide-pillared samples two levels of nitrogen adsorption are observed, a new increase in the volume of adsorbed nitrogen, with respect to pillared samples with aluminium alone, taking place at approximately  $p/p^0 = 0.1$ . This new step in the level of nitrogen adsorption is seen more clearly when the isotherms of nitrogen adsorption are represented in semilogarithmic scale, Fig. 3.4(*left*). The presence of two different steps at the low relative pressure of nitrogen adsorption could be due to the different sizes of polyoxycations inserted between the clay sheets. Moreover, this is reflected in the greater basal spacing, thus generating a greater space interlayer and, consequently, pores of larger diameter. This adsorption took place in micropores at the limit between microporous and mesoporous sizes corresponding to a diameter of 20 Å in the classification of Dubinin [32].

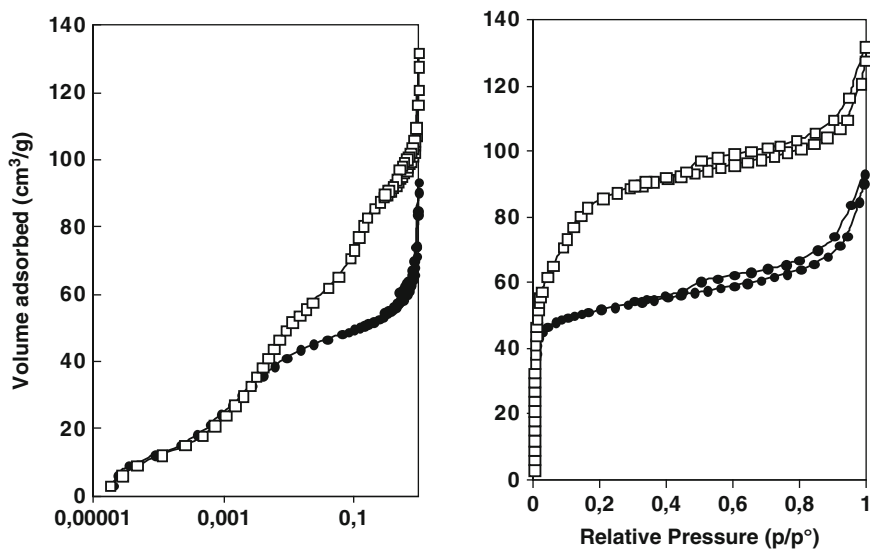


Fig. 3.4  $N_2$  adsorption–desorption isotherms at 77 K of (■) Al-Wy and (□) AlLa-Wy-25 samples. Relative pressure axes: *right*, linear; *left*, logarithmic

However, in the Al-Wy-pillared sample we observed that there is a single level of adsorption at low pressures, in Fig. 3.4(*left*) the step at approximately  $p/p^0 = 0.1$  does not appear, which indicates a unique micropore size.

Table 3.2 presents the values for specific surface area,  $S_{\text{BET}}$ , volume of  $\text{N}_2$  adsorbed at  $p/p^0 = 0.98$ ,  $V_{\text{ad}}$ , microporosity volume,  $V_{\text{mp}}$ , deduced from the  $t$ -plot, mesoporosity volume,  $V_{\text{msp}}$ , from the Barret–Joyner–Halenda method [33] and average pore diameter ( $D$ ) of the different samples after thermal treatment at 400 °C.

**Table 3.2** Textural parameters of the samples

Sample	$S_{\text{BET}}$ (m <sup>2</sup> /g)	$V_{\text{ad}}$ ( $p/p^0 = 0.98$ ) (cm <sup>3</sup> /g)	$V_{\text{mp}}$ (cm <sup>3</sup> /g)	$V_{\text{msp}}$ (cm <sup>3</sup> /g)	$D$ (Å)
Wy	33	0.042	0	0.040	50.9
Al-Wy	265	0.175	0.092	0.090	26.1
AlLa-Wy-25	349	0.293	0.207	0.110	33.6
AlCe-Wy-25	373	0.312	0.196	0.111	33.5
AlCe-Wy-50	411	0.337	0.223	0.109	32.8
AlCe-Wy-75	277	0.189	0.100	0.086	27.3

An increase both in the adsorbed volume,  $V_{\text{ad}}$ , and in the micropore volume was observed in all of the pillared samples in relation to the initial sample, Wy, which has no microporosity and a specific surface area of 33 m<sup>2</sup>/g. This is a consequence of the creation of micropores between the clay sheets in the pillaring process. This increase is much greater in the pillared samples incorporating aluminium and lanthanide elements. However, the mesopore volume showed little variation in the two types of pillared materials, and the adsorption isotherms of Al-Wy and AlLa-Wy-25 samples are parallel from  $p/p^0 > 0.2$ . This indicates that the nitrogen adsorbed from this point to  $p/p^0 = 0.98$  was similar in both types of sample. In contrast, the specific surface area of the Al/lanthanide-pillared samples increased, but to a lesser degree than the micropore volume, which showed a twofold increase over the pillared samples with only aluminium in the pillars. As a result, the average pore diameter of the Al/lanthanide-pillared samples is larger. These textural parameters indicate the presence of larger pores between the clay sheets, originating in the pillaring process, and that this correlates with the increase in basal spacing.

In order to study the different thermal evolution of both types of pores generated in the Al/lanthanide-pillared samples compared with the sample with one type of pores generated in the Al-pillared samples, we analyze the evolution of the textural parameters of these samples with thermal treatments from 400 to 800 °C.

Figures 3.5 and 3.6 show the adsorption branch of nitrogen isotherms at 77 K for AlCe-Wy-25 and Al-Wy samples, after successive thermal treatments at temperatures between 400 and 800 °C.

Figure 3.5 shows that the step at  $p/p^0 = 0.1$  present in the samples pillared with Al/lanthanide cations remained after treatments up to 700 °C, although when the temperature is increased, a decrease in intensity of the step is observed with inferior nitrogen adsorptions when the samples are treated at higher temperatures. This



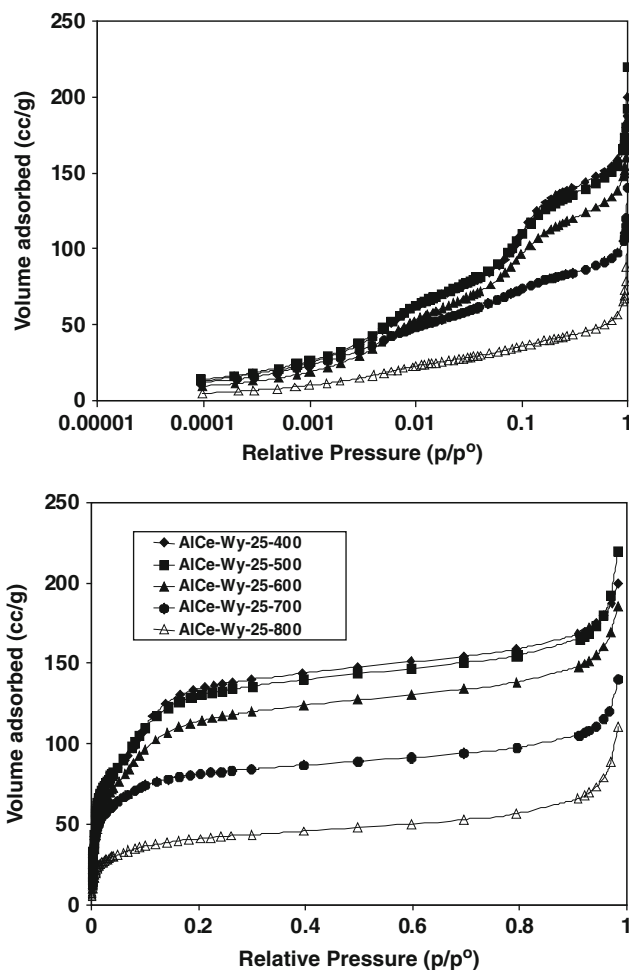
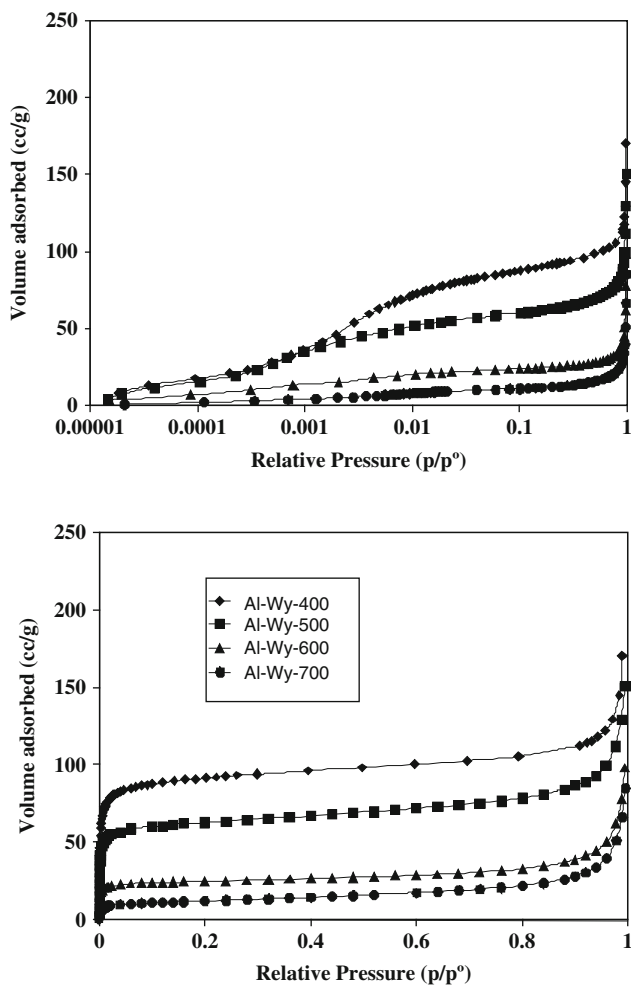


Fig. 3.5  $N_2$  adsorption isotherms at 77 K on AlCe-Wy-25-pillared sample after thermal treatments, between 400 and 800 °C. Relative pressure axes: *bottom*, linear; *top*, logarithmic

relationship between the level of nitrogen adsorption and the increase in thermal treatment is also noted in the Al-Wy sample (Fig. 3.6). The adsorption branches of the isotherms (Figs. 3.5 and 3.6), at high pressures  $p/p^\circ > 0.2$ , remain parallel to each other after the consecutive thermal treatments, which indicates that the mesoporosity of the materials is not modified, affecting the decrease in the adsorption of nitrogen at low pressure values and therefore to the microporous zone. In addition, the adsorption branches of the Al-pillared materials (Al-Wy) are seen to display lower values that decrease more quickly with the thermal treatment.

Table 3.3 shows the values of the specific surface area,  $S_{BET}$ , after thermal treatments. The Al/lanthanide pillar samples show much higher percentages of



**Fig. 3.6**  $N_2$  adsorption isotherms at 77 K on pillared sample Al-Wy after thermal treatments, between 400 and 700 °C. Relative pressure axes: *bottom*, linear; *top*, logarithmic

**Table 3.3** Surface area calculated by the BET equation

Sample	$S_{BET}$ (m <sup>2</sup> /g)				
	400 °C	500 °C	600 °C	700 °C	800 °C
Al-Wy	265	185	82	41	30
AlLa-Wy-25	349	296	237	193	101
AlCe-Wy-25	373	365	328	304	135
AlCe-Wy-50	411	312	273	270	44
AlCe-Wy-75	277	205	110	43	—

**Table 3.4** Percentage of surface conserved with respect to samples treated at 400 and 500 °C, respectively

Sample	Surface conserved (%)			
	500 °C	600 °C	700 °C	800 °C
Al-Wy	69.8	30.9	15.5	11.3
	–	44.3	17.2	16.2
AlLa-Wy-25	84.8	67.9	55.3	28.9
	–	80.1	65.2	34.1
AlCe-Wy-25	97.9	87.9	81.5	36.2
	–	89.9	83.3	37.0
AlCe-Wy-50	75.9	66.4	65.7	10.7
	–	87.5	86.5	14.1
AlCe-Wy-75	74.0	39.7	15.5	–
	–	53.7	21.0	–

conservation of the surface area than the pillared samples with only aluminium in the pillars.

In Table 3.4 the percentage of specific surface area conserved after thermal treatment is shown for each sample, at 400 °C in the first line and at 500 °C in the second line for each sample. The Al/lanthanide-pillared samples can be seen to show much higher percentages of conservation of the surface area than the Al-Wy and AlCe-Wy-75 samples. Thus the AlCe-Wy-25 sample modifies its specific surface area of 373 m<sup>2</sup>/g at 400 °C maintaining 304 m<sup>2</sup>/g at 700 °C, similar thermal behaviour is present in the AlLa-Wy-25 sample. Whereas Al-Wy sample, in the same range of temperatures, decreases from 265 to 47 m<sup>2</sup>/g. In the AlCe-Wy-50 sample, less thermal stability in the 400–500 °C range is observed, maintaining 75.9% of the percentage of conservation of surface area against 97.9% in the AlCe-Wy-25 sample. This can be attributed to the presence of a lower density of pillars of superior size given the smaller amount of cerium in the sample. Moreover, the AlCe-Wy-25 sample, which incorporates more cerium in the pillaring process and increases the basal spacing, is seen to display greater thermal stability than the samples that only incorporate Al in this process and have minor basal spacing. Therefore the percentage of conservation of the specific surface area is 81.5% at 700 °C as opposed to 15.5% in the Al-Wy sample. This percentage of conservation is even superior to the one for pillared montmorillonite with mixed Al–Ga pillars, whose percentage of conservation of the surface area at 700 °C was 70.5% [25, 27], with the same basal spacing as the Al-pillared samples.

Table 3.5 presents the micropore volume of the samples, calculated by the *t*-method, after thermal treatment at 400, 500, 600, 700 and 800 °C. From the data of Table 3.5 it can be seen that the volume of micropores remains high in the Al/lanthanide-pillared samples after the successive thermal treatments.

On the other hand, the thermal stability of the micropore volume developed after the pillaring process is lower in the Al-pillared samples, being reduced practically to zero after thermal treatment at 700 °C, whereas in the Al/lanthanide-pillared

**Table 3.5** Micropore volume deduced by *t*-plot

Sample	Vmp (cc/g) by <i>t</i> -plot				
	400 °C	500 °C	600 °C	700 °C	800 °C
Al-Wy	0.092	0.061	0.056	0.005	–
AlLa-Wy-25	0.207	0.169	0.105	0.090	0.067
AlCe-Wy-25	0.196	0.188	0.139	0.118	0.048
AlCe-Wy-50	0.224	0.137	0.126	0.116	0.006
AlCe-Wy-75	0.110	0.078	0.031	0.006	–

samples it is 0.090–0.118 cm<sup>3</sup>/g at 700 °C. To study the evolution of the microporosity of these materials with thermal treatments, the micropore size distribution and cumulative pore volume of the pillared samples have been analyzed. The Density Functional Theory (DFT) method has been applied accordingly assuming the slit-like pore model [34], taking into account the laminar structure of the samples. Figures 3.7 and 3.8 show the micropore distribution (*bottom*) and cumulative pore volume (*top*) for the AlCe-Wy-25 and Al-Wy samples after thermal treatments. The Al/lanthanide-pillared samples presented micropores of two sizes whereas, the Al-pillared sample presented micropores of only one size, which corresponds to the smallest diameter pore of the Al/lanthanide-pillared samples. Moreover, these figures also reveal that up to 700 °C, the cumulative pore volume in the AlCe-Wy-25 sample for the smaller diameter type of pore is not greatly altered, whereas in the Al-pillared sample the decrease is easily observable in this type of pore.

### 3.3.4 Acidity of Samples

The surface acidity in the starting montmorillonite and pillared clays is given in Table 3.6 as the amount of pyridine (Py) adsorbed up to saturation at different temperatures.

Comparison of the acidity data for the pillared samples (Table 3.6) with the acidity values for the starting montmorillonite shows a remarkable increase in the acid sites generated in the samples by the pillaring process. These values indicate a larger number of total acid centres, as seen in the data of micromole per gram of adsorbed Py. Table 3.6 also shows that the samples incorporating Al/lanthanide into the pillars have greater acidity than those incorporating only aluminium. As the temperature increased, the surface acidity gradually decreased, because only the strongest acid sites were able to retain the adsorbed Py. Nevertheless, at high temperatures, the samples incorporating Al/lanthanides retained more acid sites than did the samples that only fixed aluminium. This increased acidity in the Al/lanthanide-pillared samples is associated with an increase in the number of the strongest acid centres. Figure 3.9 presents the infrared spectra in the region 1700–1300 cm<sup>-1</sup> of pyridine adsorbed on Al-Wy and AlCe-Wy-50 samples. The samples treated at 200 °C after pyridine adsorption exhibit the bands at 1447 and 1615 cm<sup>-1</sup>, which are assigned

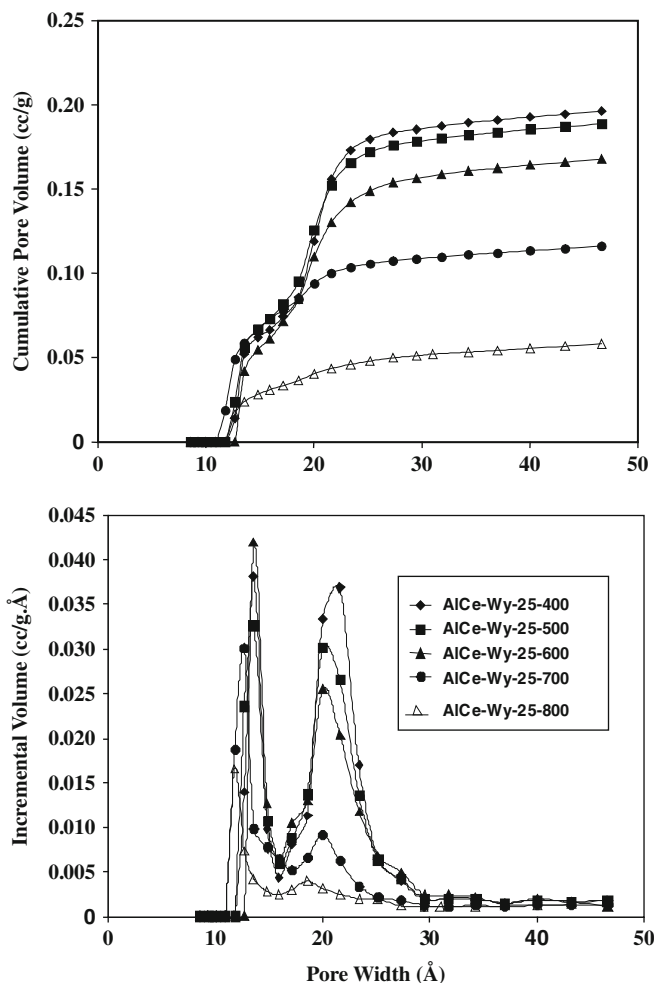


**Fig. 3.7** Distribution (*bottom*) and cumulative pore volume (*top*) by the DFT method of the pillared sample AlCe-Wy-25 after thermal treatments, between 400 and 800 °C

to Lewis centres, and a band at  $1490\text{ cm}^{-1}$ , attributed to both Lewis and Brönsted acid sites [35].

There are also small bands at  $1547$  and  $1641\text{ cm}^{-1}$  due to Brönsted acid sites. Analysis of the spectra of the pyridine adsorbed on the surface of the samples with increasing pyridine desorption temperature (200, 300 and 400 °C) reveals that the ratio of Brönsted/Lewis (B/L) centres increased in the Al/lanthanide-pillared samples, as evaluated above with regard to the intensity of the appropriate bands. From the study of the acidity of the samples, we can conclude that the Al/lanthanide-pillared samples not only present greater acidity than the samples pillared only with aluminium but also have a greater number of strong acid centres. These strong

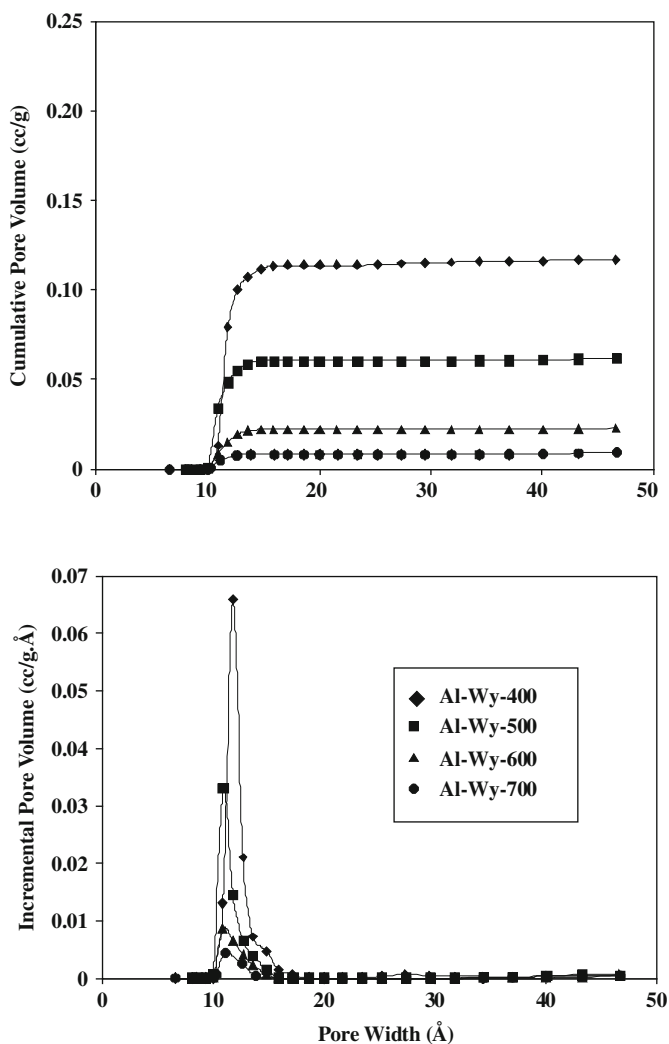


**Fig. 3.8** Distribution (*bottom*) and cumulative pore volume (*top*) by the DFT method of the pillared sample Al-Wy after thermal treatments, between 400 and 700 °C

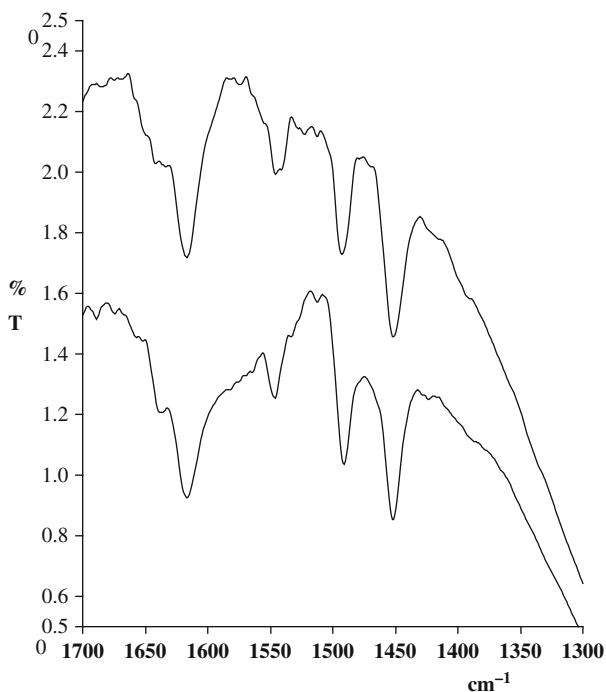
centres are linked to the Brönsted acid centres generated because the B/L ratio was greater in the pyridine spectra when desorption temperature was increased.

### 3.3.5 Catalytic Activity

In order to study the chemical reactivity of the pillared samples two catalytic tests have been assayed.

**Table 3.6** Surface acid properties of the samples

Sample	$\mu\text{mol Pyridine/g}$		
	200 °C	300 °C	400 °C
Wy	21	15	0
Al-Wy	360	241	96
AlLa-Wy-25	409	270	135
AlCe-Wy-25	391	261	129
AlCe-Wy-50	403	275	134
AlCe-Wy-75	349	230	89

**Fig. 3.9** IR spectra of adsorbed pyridine: Al-Wy (*bottom*) and AlCe-Wy-50 samples (*top*)

For the AlCe-Wy-*x* pillared samples the catalytic behaviour was evaluated and compared by the hydroisomerization and hydrocracking of *n*-heptane. For the AlLa-Wy-25 sample the catalytic activity as acid catalyst in the dehydration of 1-butanol has been studied. For the two catalytic tests the raw material and the Al-Wy samples have been used for comparative effects.

*Metal–acid bifunctional catalysts.* The catalytic performances of the pillared clays have been evaluated in the hydroisomerization–hydrocracking of *n*-heptane over samples previously impregnated with platinum tetrammine chloride solution, using the required volume to load the samples with 1 wt% of metal. The catalytic

reactions were carried out in a microreactor with continuous flow system at a pressure of 1.0 atm, with a fixed bed of 200 mg of catalyst. All samples were heated at 400 °C for 2 h under an air flow of 10 cm<sup>3</sup>/min. The circuit was purged with helium. The metal was then reduced by flow hydrogen at 400 °C under a constant flow of 10 cm<sup>3</sup>/min. After, the reactor was cooled to 175 °C. A stream of hydrogen saturated with *n*-heptane vapour was generated by passing hydrogen through a thermostated glass saturator filled with heptane and kept at 27 °C. The total flow hydrogen/heptane was 10 cm<sup>3</sup>/min. The weight hour space velocity (WHSV) was 0.9 g heptane (g catalyst h)<sup>-1</sup>. The reaction was performed under temperature-programmed conditions with a heating rate of 1 °C/min between 200 and 400 °C. The products were collected every 25 °C and were analyzed in a Varian 3000 gas chromatograph with flame ionization detector (FID). This process provides good evaluation of the number and strength of the acid sites. Two types of products can be obtained through this reaction: products of isomerization and products of cracking. In these bifunctional catalysts, the main role of the Pt is to dehydrogenate the alkane, which is then isomerized or cracked on the acid sites.

*Acid catalysts.* The test reaction, 1-butanol dehydration, was carried out at atmospheric pressure between 150 and 300 °C in a fixed bed reactor placed in a vertical furnace.

Pretreatment of the acid catalyst (pillared clays) consisted of heating in a stream of nitrogen (90 cm<sup>3</sup>/min) for 2 h at 300 °C. Nitrogen, the carrier gas, was used to introduce 1-butanol into the vapour phase from a saturator held at 55 °C (5.5 kPa butanol partial pressure). This nitrogen/1-butanol gas reaction mixture passed through the catalytic bed reactor (catalyst weight 25 mg) at a rate of 90 cm<sup>3</sup>/min. The WHSV was 3.2 g 1-butanol (g catalyst h)<sup>-1</sup>. The products were collected every 25 °C and were analyzed in a Varian 3000 gas chromatograph with FID.

In Fig. 3.10(*left*) the percentage of total conversion for AlCe-Wy-25, AlCe-Wy-50 and Al-Wy samples (data for sample AlCe-Wy-75 are not shown because they are similar to those for Al-Wy sample) is plotted as a function of the temperature in the reaction of hydroisomerization–hydrocracking of *n*-heptane. The AlCe-pillared samples present higher percentages for conversion of *n*-heptane than the sample incorporating aluminium. This is true over the whole temperature range for the AlCe-Wy-50 sample and from 300 °C for the AlCe-Wy-25 sample. This increase of the total conversion is related to the higher amount of acid sites in the Al/lanthanide-pillared samples (Table 3.6).

The greatest differences in the behaviour of the catalytic activity are seen when the process is analyzed for selectivity between cracked and isomerized products.

Figure 3.10(*right*) shows the percentage of cracking conversion for the samples in relation to reaction temperature. Table 3.7 gives the percentages for total conversion, cracking and isomerization and the percentage of cracked selectivity between 300 and 400 °C. The fact that the conversion varies over a large range could not allow making a kinetic or thermodynamic study, but it is possible to compare the different chemical behaviours of the materials. The selectivity percentage towards cracking products is greatly increased in the AlCe-pillared samples. The cracked conversion



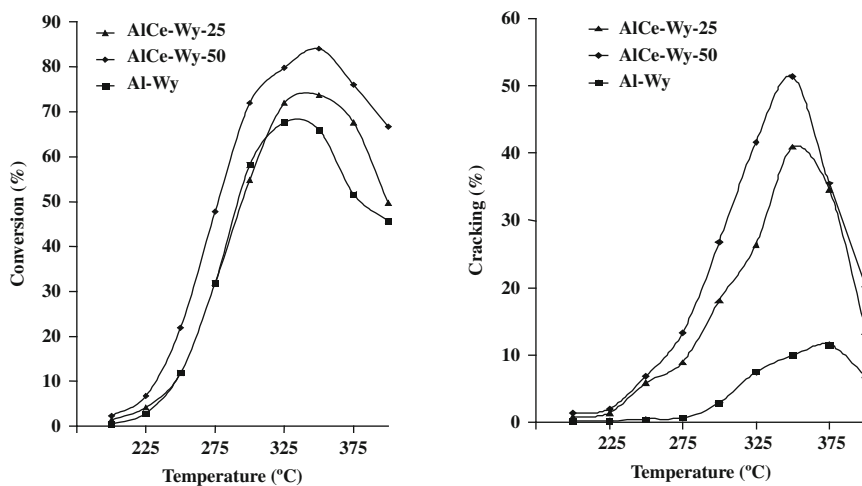


**Fig. 3.10** Total conversion of *n*-heptane versus reaction temperature (*left*), and cracking conversion of *n*-heptane versus reaction temperature (*right*)

**Table 3.7** Conversion and selectivity of the samples

Sample	Temperature (°C)				
	300	325	350	375	400
AlCe-Wy-25					
Conversion	54.9 <sup>a</sup>	72.0	73.7	67.6	49.7
Isomerization	36.8 <sup>b</sup>	45.6	32.8	32.9	36.1
Cracking	18.1 <sup>c</sup>	26.4	40.9	34.6	13.6
Selectivity	33.0 <sup>d</sup>	36.7	55.5	51.2	27.4
AlCe-Wy-50					
Conversion	71.9	79.8	84.0	76.0	66.7
Isomerization	45.2	38.2	32.7	40.5	46.6
Cracking	26.7	41.6	51.3	35.5	20.1
Selectivity	37.1	52.1	61.1	46.7	30.1
AlCe-Wy-75					
Conversion	57.1	65.3	64.9	50.7	43.9
Isomerization	52.3	56.2	54.3	40.3	37.8
Cracking	4.8	9.1	10.6	10.4	6.1
Selectivity	8.4	13.9	16.3	20.5	13.9
Al-Wy					
Conversion	58.2	67.6	65.9	51.6	45.6
Isomerization	55.2	60.1	56.0	40.1	38.9
Cracking	2.9	7.5	9.9	11.6	6.8
Selectivity	5.0	11.2	15.0	22.5	14.9

<sup>a</sup>(% mol) Total conversion of *n*-heptane

<sup>b</sup>(% mol) Conversion to isomerization products

<sup>c</sup>(% mol) Conversion to cracking products

<sup>d</sup>(% mol) Selectivity towards cracking

percentage ranges from a maximum of 11.6% for Al-Wy sample to 40.9 and 51.3% for AlCe-Wy-25 and AlCe-Wy-50 samples, respectively.

There is a significant shift of selectivity towards the cracked products over the whole range of temperatures. The largest difference (41.4%) occurs between Al-Wy sample and AlCe-Wy-50 sample at 350 °C. The presence of Ce in the samples increased both *n*-heptane conversion and selectivity towards cracking. These results must be interpreted in light of two commonly accepted assumptions. First, hydroisomerization and hydrocracking of hydrocarbons take place through the formation of carbocations as intermediate species, the number of these being formed corresponding to the number of acid centres and their strength. Second, hydroisomerization requires milder conditions of temperature and acid strength than hydrocracking [16, 36–39]. In the AlCe-pillared samples, there are a larger number of acid centres and a higher B/L ratio with increasing temperature. This indicates a greater number and strength of Brönsted acid centres, which seem a plausible explanation of the greater selectivity towards cracking.

The AlCe-pillared materials present more acid centres, the centres active in reactions catalyzed by acids. This increase is greater in the number and strength of the Brönsted acid centres. These changes are reflected in the improved reactivity of these materials in the hydroisomerization–hydrocracking reaction of *n*-heptane, with increased conversion and a greater selectivity towards the products of cracking.

The dehydration of 1-butanol is a reaction used as a probe of the acid–base properties of oxides, silicates and phosphates [40–43]. The reaction can proceed through various paths, as the intramolecular dehydration of 1-butanol to 1-butene, which occurs through the E1, E2 or E1cB mechanisms [44], or the consecutive isomerization of 1-butene to *cis/trans*-2-butene, a reaction used to test the acid or basic character of catalysts. A high *cis/trans* ratio is observed for the basic-catalyzed isomerization, in contrast to a value close to or less than one for an acid-catalyzed isomerization. Noller et al. [45] suggest that on a strong acid, catalyzing the intramolecular dehydration of 1-butanol through an E1 mechanism, 1-butene isomerizing rapidly to 2-butene will be the major reaction product. On amphoteric or basic catalysts, catalyzing the intramolecular dehydration through an E2 or E1cB mechanism, 1-butene will be the major reaction product. The intermolecular dehydration of two molecules of 1-butanol to dibutylether requires the cooperation of acid and basic surface sites [44].

Figure 3.11 shows the conversion of 1-butanol dehydration over pillared samples and raw montmorillonite under our reaction conditions, the AlLa-Wy-25-pillared sample is more active than the Al-Wy-pillared sample. In both pillared samples, at low temperatures, selectivity for dibutylether is high, indicating the prevalence of bifunctional acid–base sites capable of catalyzing the intermolecular dehydration of 1-butanol on the samples. When the temperature increases, in both pillared samples butane selectivity increases showing selectivities of 100% between 225 and 300 °C, the 1-butene is highly isomerized to *cis*-2-butene and *trans*-2-butene, as shown in Fig. 3.12, indicating an E1 mechanism and acid catalysis in the dehydration of 1-butanol.

**Fig. 3.11** Conversion of 1-butanol dehydration as a function of temperature on ( $\Delta$ ) Wy, ( $\bullet$ ) Al-Wy and ( $\square$ ) AILa-Wy-25 samples

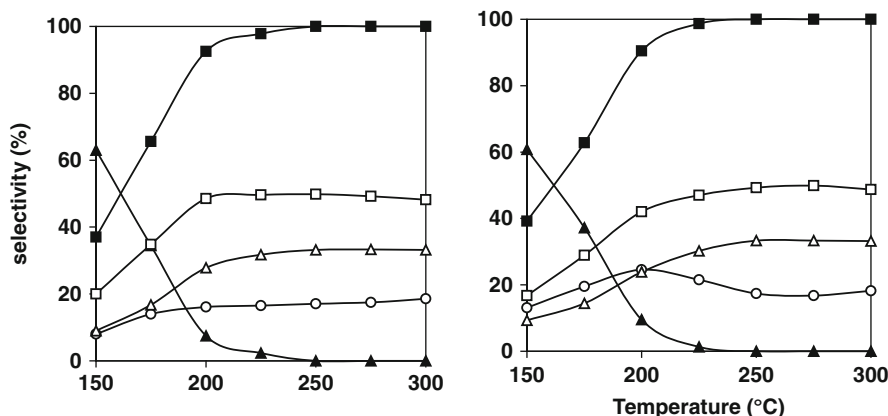
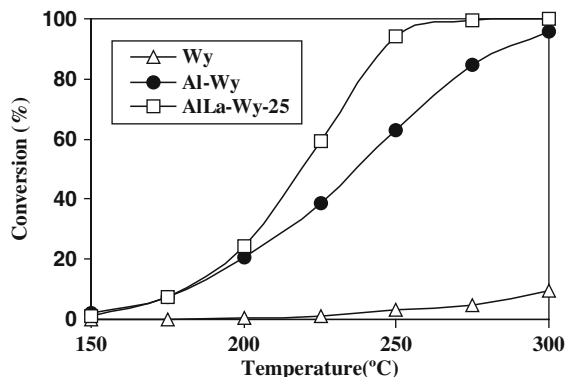
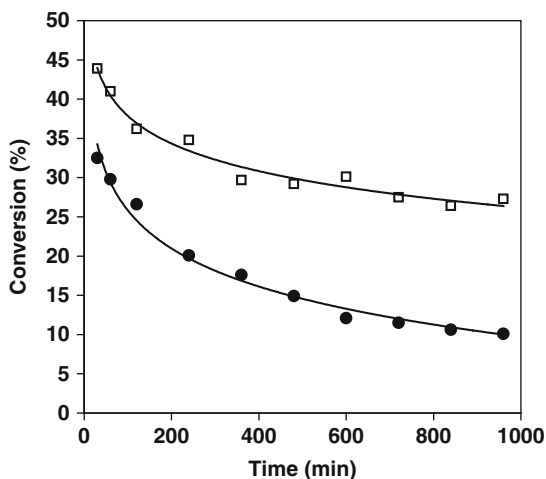


**Fig. 3.12** Selectivity of 1-butanol dehydration as a function of the reaction temperature over Al-Wy (*left*) and AILa-Wy-25 (*right*); ( $\blacksquare$ ) butenes, ( $\blacktriangle$ ) dibutylether, ( $\circ$ ) 1-butene, ( $\triangle$ ) *cis*-2-butene and ( $\square$ ) *trans*-2-butene

The greater conversion and the same selectivity in the AILa-Wy-25-pillared sample than in Al-Wy-pillared correspond to a greater number of acid centres in the first sample. Figure 3.13 shows the evolution of the catalytic activity of 1-butanol dehydration over the Al-Wy and AILa-Wy-25-pillared samples with time on stream at 215 °C. The AILa-Wy-25 sample presents a smaller deactivation, whereas in the Al-Wy sample the deactivation is of 65% with an initial conversion of 32%, after 16 h. The selectivity to dibutylether increases with time in both catalysts, from 2.2 to 18.4% in Al-Wy and from 2.5 to 13.6% in AILa-Wy-25, in parallel to the deactivation of the catalysts and their acid centres by coke deposition, the recovered catalyst presents a grey colour after testing. When the acid centres of the catalysts are deactivated with time, the ratio of basic/acid centres increases, the intramolecular dehydration by means of mechanism E1cB is increased, and

**Fig. 3.13** Conversion of 1-butanol dehydration as a function of time on stream; (■) Al-Wy and (□) AILa-Wy-25 samples



therefore greater formation of dibutylether takes place. The selectivity of butenes (1-butene, *cis*-2-butene and *trans*-2-butene) is not modified with time.

We have already indicated that the AILa-Wy-25 sample shows a greater thermal stability in its textural properties, porosity and specific surface. We wanted to show by means of the reaction of dehydration of 1-butanol that the acid characteristics of surface of the AILa-Wy-25-pillared material also present greater thermal stability than the pillared sample exclusively with aluminium. After treating thermally both samples in air atmosphere for 2 h to different temperatures, the catalytic test of dehydration of 1-butanol with the Al-Wy and AILa-Wy-25 samples, treated thermally to 700 and 800 °C, has been performed, and we have compared their activities with the previous samples, which correspond to thermal treatment of 400 °C.

In Fig. 3.14, a very important reduction in the conversion of the Al-Wy-pillared sample treated at 700 °C takes place and a practically null conversion in the sample

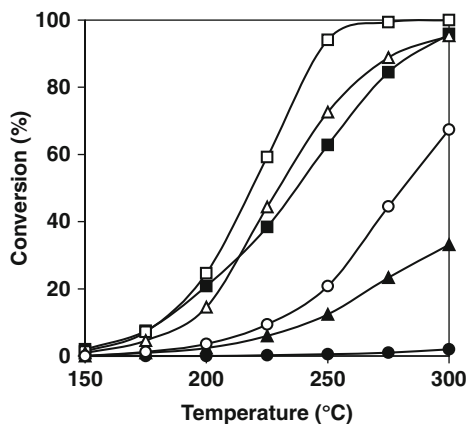


**Fig. 3.14** Conversion of 1-butanol dehydration as a function of the reaction temperature over Al-Wy (*fill*) and AILa-Wy-25 (*empty*), after thermal treatments at (□, ■) 400, (△, ▲) 700 and (○, ●) 800 °C

calcined to 800 °C can be observed. Whereas the AlLa-Wy-25-pillared sample maintains a very high catalytic activity in the calcined sample to 700 °C like in the one calcined at 800 °C, in comparison with the pillared Al-Wy treated to the same temperatures. This fact indicates that the AlLa-Wy-25 material not only conserves the texture, specific surface and microporosity in a high percentage with the thermal treatments, but that it is also able to conserve the acid centres necessary to generate catalytic activity in the dehydration of 1-butanol. The selectivity in the dehydration of 1-butanol of the thermally treated materials is not modified, which indicates that the materials maintain the typical characteristics of an acid catalyst with a great part of their active acid centres and these in the AlLa-Wy-25 sample, in a much higher percentage.

### 3.4 Conclusions

Pillared montmorillonite with mixed Al/lanthanide pillars between the clay layers with a chemical nature different from that of the aluminium polyoxycation denominated Keggin ion were prepared. The materials present characteristics that are very different from montmorillonite pillared with only aluminium. This was shown by NMR studies that indicated total absence of tetrahedral aluminium in the pillars when lanthanide cations are incorporated between the clay layers. XR diffraction also showed an increase in the basal spacing up to 26 Å.

They have a high thermal stability, high specific surface area and porosity, with pores at the limit between the microporosity and mesoporosity. The pores are larger than those generated in the Al-pillared materials, which clearly displays microporous characteristics. The textural parameters maintained high values up to 700 °C.

In addition, the number and the strength of the acid sites in these materials were also high, the centres active in reactions catalyzed by acids. The increase of the conversion in dehydration of 1-butanol as in hydroisomerization of *n*-heptane shows their better behaviour as acid catalysts. The Al/lanthanide-pillared samples showed increased conversion and improved selectivity towards the products of cracking. The study of 1-butanol dehydration showed that there is an increase in the acidity, thermal stability and smaller deactivation by carbonaceous deposits in the Al/lanthanide-pillared sample.

### References

1. Figueras F (1988) Pillared clay as catalysts. *Catal Rev Sci Eng* 30:457
2. Tichit D, Fajula F, Figueras F, Ducouraut B, Mascherpa G, Gueguen D, Bousquet J (1988) Sintering of montmorillonites pillared by hydroxy-aluminum species. *Clays Clay Miner* 36:369
3. Martin-Luengo MA, Martins-Carvalho H, Ladriere J, Grange P (1989) Fe(iii)-pillared montmorillonites – preparation and characterization. *Clay Miner* 24:495

4. Figueras F, Martrod-Bashi A, Fetter G, Thrierr A, Zanchetta JV (1989) Preparation and thermal-properties of Zr-intercalated clays *J Catal* 119:91
5. Choudary BM, Valli VLK (1990) A novel vanadium pillared montmorillonite catalyst for molecular recognition of benzyl alcohols. *J Chem Soc Chem Commun* 16:1115
6. Klopogge JT (1998) Synthesis of smectites and porous pillared clay catalysts: a review. *J Porous Mater* 5:5
7. Gil A, Gandia LM, Vicente MA (2000) Recent advances in the synthesis and catalytic applications of pillared clays. *Catal Rev Sci Eng* 42:145
8. Gil A, Korili SA, Vicente MA (2008) Recent advances in the control and characterization of the porous structure of pillared clay catalysts. *Catal Rev Sci Eng* 50(2):153
9. Mitchell IV (1990) Pillared layered structures: current trends and applications. Elsevier Applied Science, London
10. Kikuchi E, Matsuda T (1988) Shape selective acid catalysis by pillared clays. *Catal Today* 2:297
11. Mokaya R, Jones W (1995) Pillared clays and pillared acid-activated clays: a comparative study of physical, acidic, and catalytic properties. *J Catal* 153:76
12. Hernando MJ, Pesquera C, Blanco C, González F (2002) Langmuir Increase in thermal stability of the texture in montmorillonites pillared with Al/Ce polyoxocations 18(14):5633
13. Zhu HY, Vansant EF, Xia JA, Lu GQ (1997) Porosity and thermal stability of montmorillonite pillared with mixed oxides of lanthanum, calcium and aluminium. *J Porous Mater* 4:17
14. Cañizares P, Valverde JL, Sun Kou R, Molina CB (1999) Synthesis and characterization of PILCs with single and mixed oxide pillars prepared from two different bentonites. A comparative study. *Micropor Mesopor Mater* 29:267
15. González F, Pesquera C, Benito I, Mendioroz S, Poncelet G (1992) High conversion and selectivity for cracking of n-heptane on cerium-aluminium-montmorillonite catalysts. *J Chem Soc Chem Commun* 6:491
16. Hernando MJ, Pesquera C, Blanco C, Benito I, González F (1996) General, effect of Ce on catalytic properties of pillared montmorillonite with Al- and GaAl-polyoxocations. *Appl Catal A* 141:175
17. López-Ortega A, Domínguez JM, Rojas-Hernández A, Benítez-Patricio A, Salmon M (1996) Synthesis and characterization of Ln/Al pillared clays. *Mater Res Soc Conf Symp* 431:51
18. Flego C, Galasso L, Millini R, Kiricsi I (1998) General, The influence of the composition on the thermal and acid characteristics of multi-component oxide pillared montmorillonite. *Appl Catal A* 168:323
19. Pires J, Machado M, de Carvalho MB (1998) *J Mater Chem* 8:1465
20. Fetter G, Salas P, Velazquez LA, Bosch P (2000) Ce-Al-Pillared clays: synthesis, characterization, and catalytic performance. *Ind Eng Chem Res* 39:1944
21. Hernando MJ (2000) Síntesis y caracterización de montmorillonitas apilaradas con aluminio modificadas por incorporación de galio y cerio. Thesis, University of Cantabria, Santander, Spain
22. Hernando MJ, Pesquera C, Blanco C, González F (2001) Synthesis, characterization, and catalytic properties of pillared montmorillonite with aluminum/cerium polyoxocations. *Chem Mater* 13:2154
23. Sterte J (1991) Preparation and properties of large-pore La-Al-pillared montmorillonite. *Clays Clay Miner* 39:167
24. McCauley JR (1989) Stable intercalated clays and preparation method. US Patent 4,818,737
25. Hernando MJ, Pesquera C, Blanco C, Benito I, González F (1996) Differences in structural, textural, and catalytic properties of montmorillonite pillared with (GaAl<sub>12</sub>) and (AlAl<sub>12</sub>) polyoxocations. *Chem Mater* 8:76
26. Pesquera C, González F, Benito I, Mendioroz S, Pajares JA (1991) Synthesis and characterization of pillared montmorillonite catalysts. *Appl Catal* 67:97
27. González F, Pesquera C, Blanco C, Benito I, Mendioroz S (1992) Synthesis and characterization of Al-Ga pillared clays with high thermal and hydrothermal stability. *Inorg Chem* 31:727

28. Plee D, Borg F, Gatineau L, Fripiat JJ (1985) High-resolution solid-state  $^{27}\text{Al}$  and  $^{29}\text{Si}$  Nuclear Magnetic Resonance study of pillared clays. *J Am Chem Soc* 107:2362
29. Fripiat JJ (1987) High resolution solid state NMR study of pillared clays. *Catal Today* 2:281
30. Macias O, Largo J, Pesquera C, Blanco C, González F (2006) General, Characterization and catalytic properties of montmorillonites pillared with aluminum/lanthanum. *Appl Catal A* 314:23
31. Gregg SJ, Sing KSW (1991) Adsorption surface area and porosity. Academic, London
32. Sing KSW, Everett DH, Haul RAW, Moscou L, Pierotti RA, Rouquerol J, Siemieniewska T (1985) Reporting physisorption data for gas solid systems with special reference to the determination of surface-area and porosity. *Pure Appl Chem* 57:603
33. Barrett EP, Joyner LG, Halenda PP (1951) The determination of pore volume and area distributions in porous substances. I. Computations from nitrogen isotherms. *J Am Chem Soc* 73:373
34. Olivier JP (1995) Modeling physical adsorption on porous and nonporous solids using Density Functional Theory. *J Porous Mater* 2:9
35. Parry ER (1963) An infrared study of pyridine adsorbed on acidic solids: characterization of surface acidity. *J Catal* 2:371
36. Wojciechowski BW, Corma A (1986) Catalytic cracking. Marcel Dekker, New York
37. Moreno S, Sun Kou R, Poncelet G (1996) Hydroconversion of heptane over Pt/Al-pillared montmorillonites and saponites. *J Catal* 162:198
38. Wang X, Li C, Wang Y, Cai T (2004) n-Heptane isomerization over mesoporous MoOx and Ni-MoOx catalysts. *Catal Today* 93:135
39. Roldán R, Romero FJ, Jiménez-Sanchidrián C, Marinas JM, Gómez JP (2005) General, Influence of acidity and pore geometry on the product distribution in the hydroisomerization of light paraffins on zeolites. *Appl Catal A* 288:104
40. Berteau P, Ceckiewicz S, Delmon B (1987) Role of the acid-base properties of aluminas, modified gamma-alumina, and silica-alumina in 1-butanol dehydration. *Appl Catal* 31:361
41. Guiu G, Grange P (1995) Acidic and catalytic properties of  $\text{SiO}_2\text{-Ta}_2\text{O}_5$  mixed oxides prepared by the sol-gel method. *J Catal* 156:132
42. Bautista FM, Delmon B (1995) General, 1-Butanol dehydration on  $\text{AlPO}_4$  and modified  $\text{AlPO}_4$ : catalytic behaviour and deactivation. *Appl Catal A* 130:47
43. Gil A, Vicente MA, Korili SA (2005) Effect of the Si/Al ratio on the structure and surface properties of silica-alumina-pillared clays. *J Catal* 229:119
44. Delsarte S, Grange P (2004) General, Butan-1-ol and butan-2-ol of dehydration on nitrated aluminophosphates: influence of nitridation on reaction pathways. *Appl Catal A* 259:269
45. Noller H, Lercher JA, Vinek H (1988) Acidic and basic sites of main group mixed metal oxides. *Mater Chem Phys* 18:577

# Chapter 4

## Synthetic Hectorite: Preparation, Pillaring and Applications in Catalysis

Chun-Hui Zhou, Dongshen Tong, and Xiaonian Li

**Abstract** This chapter makes a comprehensive and critical overview on the preparation of hectorite-like solids, pillaring, properties and catalytic applications of pillared interlayered synthetic hectorite clays (PILCs). Hectorite, with some specific properties, is a natural mineral among the most common smectite group of clay minerals. However, hectorite in natural occurrence is scarce. The general synthesis of hectorite-like solids is by means of hydrothermal process or solid-state reaction. The synthesis variables, crystallization, structure of synthetic hectorite along with their characteristics are discussed. Using synthetic hectorite clays with tuneable composition and high purity as layered host precursors is much conducive to designed features and specific applications of PILCs, in contrast to using natural clay minerals with impurities plus other uncertain factors arising from natural deposits. The various intercalation methods and intercalated species in PILC products have been reported with an objective to improve the porous structure and properties of the resultant PILCs. Among many potential uses of pillared synthetic hectorite, the important applications concerning catalysis are emphasized. Finally, the prospects of synthetic hectorite-based materials are briefly remarked.

**Keywords** Synthetic hectorite · Pillared interlayered clays · Pillaring · Nanocomposites · Catalysis

### 4.1 Introduction

Layered clay minerals are a class of the most common naturally occurring phyllosilicate minerals on Earth's surface. They are also among the most important and useful industrial minerals in the world. Based on their specific physical and

---

C.-H. Zhou (✉)

Research Group for Advanced Materials & Sustainable Catalysis (AMSC), R&D Center for Advanced Clay-Based Materials (CCM), College of Chemical Engineering and Materials Science, Zhejiang University of Technology (ZJUT), Hangzhou 310032, China  
e-mail: catalysis8@yahoo.com.cn; clay@zjut.edu.cn



chemical properties, so far the natural clay minerals have been extensively used to produce pottery, ceramics and building materials as well as to produce paper coatings and fillings, drilling mud, foundry moulds, cat litters, pharmaceuticals, agrochemicals, polymer nanocomposites, adsorbents, catalysts or catalyst supports [1]. Among the new and improved clay-based products nowadays, pillared interlayered clays (PILCs) prepared by intercalation and pillaring of large active species into the interlayer of clay structure have shown promising application in the field of catalysis, adsorption and separation [2].

As a kind of novel porous materials, the specific properties of pillared interlayered clays are of quite general relevance to both the layered solids as hosts and the pillars as guests sandwiched between the clay layers. The most documented PILCs are generally prepared by using purified natural cationic clay minerals as starting parent materials such as montmorillonite, saponite and beidellite, vermiculite, mica and hectorite. Though using natural minerals as the hosts seemingly looks convenient and economical, there exist many uncertain aspects in natural clay minerals such as chemical composition, crystallinity, degree of isomorphous substitution, types and contents of exchangeable cations and impurities, and so forth, arising from various mineral deposits. So do the minerals even from different sites at the same deposits. All these variables readily lead to uncertainties of physical and chemical properties of resulting clay-based products. In this respect, though hectorite minerals have better colloidal properties than bentonite as to some specific use, e.g. as tactoids, the natural colloidal hectorite clays have some disadvantages. They tend to be coloured and often contain impurities which are in the form of small, gritty particles, very difficult to separate from the clay minerals because of their origin. With regard to PILCs, uncertain parent hectorite certainly leads to uncontrollable catalytic performance of resulting PILCs. Such variables as purity, composition, reproducibility, and specifically designed features and so forth can be controlled well provided that synthetic analogues are used instead of using natural clay specimens. Therefore, comparatively, as to layered host precursors for preparation of PILCs, using synthetic layered clays with well-tuneable composition and high purity as parent materials is much more conducive to obtaining the designed features in PILCs for specific applications.

Hectorite is a kind of natural mineral among the most common smectite group of clay minerals in which montmorillonite and hectorite have been extensively employed as layer hosts for PILCs. The hectorite is originally named after the locality at Hector, CA, USA [3]. Natural hectorite mineral usually occurs with bentonite minerals as an alteration product of clinoptilolite from volcanic ash and tuff with high glass content. However, hectorite is not as abundant as montmorillonite in nature. Besides the disadvantages of natural clays mentioned above, because of scarcity of hectorite in natural occurrence and its specific features, the synthesis of hectorite-like solids has received much attention for decades. Indeed, synthetic hectorite has shown promising potentials to be used as a class of hosts for preparation of PILCs and nanocomposites.

Here it is worthy of mentioning that according to the recommendations of the Association Internationale pour l'Etude des Argiles (AIPEA) nomenclature

committee by Guggenheim et al. [4], synthetic hectorite materials may as well be referred to as ‘hectorite-like’, but never as ‘hectorite’ which is the mineral name implying a naturally occurring phase. But it is permissible to use the description modifier ‘synthetic’ with a mineral name, as in ‘synthetic hectorite’, because ‘synthetic’ unambiguous and specifically negates the naturally occurring aspect of the mineral. Hereafter, the man-made hectorite-like solids are referenced as synthetic hectorites and the natural counterparts as hectorites. A commonly used commercial product, laponite RD, is a synthetic hectorite from Laporte Industries.

## 4.2 Properties and Structure of Hectorite

For the fabrication and application of PILCs as porous catalysts or molecular sieve-like catalysts, ion exchangers or adsorbents, smectite minerals, regarded as a group of expandable clays, are most employed. Smectite clay minerals are of much interest and use mainly because they have two silicate sheets sandwiching a central octahedral sheet in a so-called 2:1 arrangement, as shown in Fig. 4.1. In detail, hectorite is a tri-octahedral clay consisting of two sheets of silica tetrahedral with a central octahedral sheet containing magnesium. According to the classification scheme proposed by AIPEA, hectorite is a species among tri-octahedral subgroup in smectite group [4, 5]. In other words, hectorite belongs to tri-octahedral subgroup in smectite group, whereas montmorillonite is di-octahedral. That hectorite is tri-octahedral smectite theoretically means that all of the octahedral sites are occupied by divalent metal cations. In contrast, in the di-octahedral smectites only  $2/3$  of the sites are occupied by a trivalent metal cation and the remaining sites are vacant [6]. Hectorite can be regarded as a rather unusual smectite as it contains essentially Mg, Li, F and OH in the octahedral sheet where the substitution of  $\text{Li}^+$  for  $\text{Mg}^{2+}$  creates the negative charge on the layers [7]. Therefore, the whole magnesia-silicate sheets have a net negative charge which is compensated by exchangeable Na ions in the interlayer. The tetrahedral sheet contains mainly Si–O and in most cases it does not contribute to the layer charge as shown in Fig. 4.1.

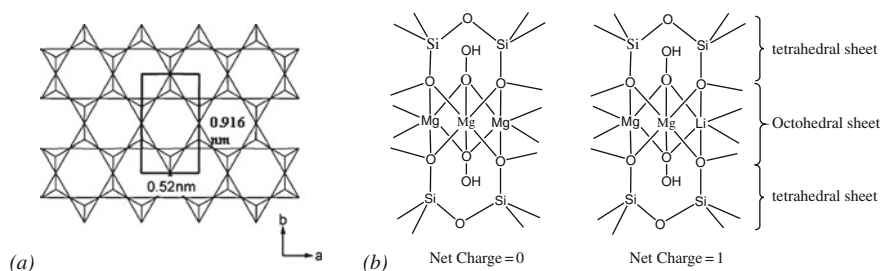


**Fig. 4.1** Schematic of the tetrahedral and the tri-octahedral sheets in the structure of hectorite. (a) Top view of Si–O hexagonal tetrahedral sheet, (b) isomorphous substitution of Li for Mg and origin of layer charge in the tri-octahedral sheet

The general characteristics of hectorite structure are 2:1 layer type with net layer charge per formula unit (p.f.u.) of 0.2–0.6 and hydrated exchangeable cations. The chemical composition of hectorite includes sodium, lithium, magnesium, silicon, hydrogen and oxygen. For instance, a typical chemical composition of natural hectorite from Hector (CA, USA) corresponds to  $(\text{Na}_{0.84}\text{Ca}_{0.08}\text{K}_{0.02})_{\Sigma=0.94}(\text{Mg}_{5.46}\text{Li}_{0.66})_{\Sigma=7.12}(\text{Si}_{7.78}\text{Al}_{0.10})_{\Sigma=7.88}\text{O}_{20}(\text{OH})_4$  [8]. The ideal hectorite composition [9] described by Grim was  $\text{Ex}_{0.66}[\text{Li}_{0.66}\text{Mg}_{5.34}\text{Si}_8\text{O}_{20}(\text{OH},\text{F})_4]$ , where Ex = exchangeable cation (Ex =  $\text{Li}^+$  or  $\text{Na}^+$ ). The lattice parameters of the *a*, *b* and *c* axes were found to be 0.52, 0.916 and 1.60 nm, respectively, and  $\beta$  is  $\sim 99^\circ$ ; Space Group belongs to  $\text{C}_2/\text{m}$ .

Hectorite is a valuable mineral for industrial applications because of its layered structure and its specific composition which yield high cation exchange capacities (CEC), surfaces areas, surface reactivity and adsorptive properties. The main properties relevant for applications are affected considerably by the composition and particle size. Exclusively, hectorite also has high viscosity and transparency in solution. Therefore, hectorite is commonly used as additive for paints and cosmetics. As to hectorite-based catalyst [10] and catalyst support of PILCs [11], just because the negatively charged magnesia-silicate layers have exchangeable cations in the interlayer space to balance the charge, such exchangeable cations provide an easy way of insertion and pillaring of inorganic or organic species with catalytic activity. Though CEC mainly arises from isomorphous substitutions of  $\text{Li}^+$  for  $\text{Mg}^{2+}$  in the octahedral layer, the cation exchange capacity is also related to the particle size which leads to quite different amounts of edges of platelets of hectorite. The structural formulae merely give the amount of negative charge per unit cell due to isomorphous substitution, i.e. the pH-independent part. At the edges of the crystals the sheet structure is broken and terminated by OH groups that may also contribute to the CEC [12].

Among the many physical and chemical features of hectorite and synthetic hectorite, the colloidal properties are of great importance in many industrial applications because of their sol gelation. Compared to montmorillonite, the hectorite clay products have much more excellent rheological, suspension and emulsion-stabilizing properties [13]. They are used in paints and coatings, ceramics and household cleaners, cosmetics, pharmaceuticals and personal care products [14, 15]. For example, the synthetic hectorite-type clays such as laponite<sup>®</sup> XLG, a synthetic layered silicate with low heavy metals content, form clear dispersions due to their high purity and very small crystallite size. The suspensions are composed of anisotropic disk-like charged particles. Upon dispersing laponite clay in water, the system comprises evenly of agglomerates of clusters of laponite. Subsequent osmotic swelling of these clusters leads to an increase in their volume fraction, responsible for slowing down of the overall dynamics of the system. As clusters fill up the space, the system undergoes glass transition [16]. The phase transition from sol to gel was observed at a clay concentration of about 0.01 g/ml. It was found that the phase transition phenomena depend on neither the types nor the concentration of salt when below a certain salt concentration. However, above a certain concentration of salt, phase separation from flocculation took place [17]. However, the origin of the gelation is still under debate.

The rheological properties and ionic conductivity are also affected by the types of exchangeable ions in synthetic hectorite and related hectorite-filled nanocomposite electrolytes. Pavlidou et al. found that significant increase of the alternating current (a.c.) conductivity of laponite can be achieved when the interlayer of synthetic hectorite was totally exchanged with potassium ions. After the change of sodium ions into potassium ions, however, the rheological properties are altered and the clay will no longer form a gel with water [18]. When exchanged with  $\text{Li}^+$ ,  $\text{Rb}^+$ ,  $\text{Cs}^+$  or  $\text{Cu}^{2+}$ , it showed no increase in the a.c. conductivity over that of the sodium form. However, the synthetic fluorolaponite produced from a sol–gel method, with increased sodium contents, gives a series of materials with enhanced a.c. conductivity, and it retains similar rheological properties to those of commercial laponite [19].

Singhal et al. prepared the electrolytes consisting of lithium-exchanged hectorite, a 2:1 layered smectite clay, dispersed in ethylene carbonate (EC) or a mixture of EC and polyethylene glycol di-methyl ether and examined the effects of Li-hectorite clay concentration and solvent composition on the conductivity and rheology of nanocomposite single-ion conductors. The results showed that all samples exhibit elastic, gel-like characteristics and room temperature conductivities of order 0.1 mS/cm. At about 25 wt% clay concentration, a maximum in conductivity is observed. The elastic modulus and yield stress increase by two orders of magnitude and the conductivity increases by one order of magnitude with increase in hectorite concentration from 5 to 25%, which indicates the significant influence of hectorite content in determining the characteristics of these single-ion conductors. The hectorite-based electrolytes have potential use in lithium-ion batteries [20].

Treatment by acids such as HCl,  $\text{HNO}_3$ ,  $\text{H}_3\text{PO}_4$  and  $\text{H}_2\text{SO}_4$  can lead to the dissolution of hectorite. Some scientists suggested that the dissolution rate of hectorite decreased in the order  $\text{H}_2\text{SO}_4 > \text{HNO}_3 = \text{HCl}$  at the same molar concentration, while others suggested the reverse order. Van Rompaey et al. claim that the differences among the three acids were rather small and that the concentration of the acids was the main parameter affecting the dissolution rate of the hectorite, in particular, in the beginning of the treatment [21].

## 4.3 Synthesis of Hectorite-Like Solids

### 4.3.1 A Brief History of Synthetic Hectorite

The synthesis of clay minerals has been reported in many papers for decades [5]. Earlier, it has been found that magnesium layer lattice silicates can be formed from aqueous solutions at reflux temperature. Just as most of the systems for synthesis of zeolite minerals, the common technique for the synthesis of hectorite-like solids is the hydrothermal reaction from mixtures of oxides and hydroxides under basic pH conditions at elevated temperature and pressure. However, there are a few investigations made into the synthesis of the clay minerals at ordinary temperature and pressure [22]. In addition, the method of solid-state reaction is reported in the literature [23–29].

As early as in the 1960s, Granquist and Pollack [23] reported the synthesis of hectorite by hydrothermal treatment of an aqueous slurry containing approximately 10% of freshly precipitated  $\text{Mg}(\text{OH})_2$ , silica gel,  $\text{LiOH}$  or  $\text{LiF}$  and various amounts of  $\text{NaOH}$ . The synthesis conditions used by these authors ranged from reflux temperature and atmospheric pressure to 573 K and approximately 83 bar.

As to the mechanism of formation of synthetic hectorite, Baird et al. [24, 25] suggested that crystallization proceeds by condensation of silica monomers onto previously formed brucite sheets. Moreover,  $\text{LiF}$  was found to speed up the crystallization of hectorite [23, 26]. Harder reported that amorphous hydroxides of Al, Fe, Mg, etc., are capable of co-precipitating silica even from very dilute solutions [27]. The formation of smectite minerals is only possible when the precipitates contain at least 6% of  $\text{MgO}$ . The precipitates remain amorphous if the magnesium content is lower. Therefore, the results suggested that magnesium seems to favour the formation of all these layer silicates, especially, the presence of magnesium particularly favours the formation of smectite minerals.

Barrer and Dicks have ever explored the synthesis of hectorite in the presence of organic species, e.g. alkylammonium, in the synthesis gels [28]. The synthetic organo-hectorites were synthesized by reflux reaction of aqueous suspension of appropriate compositions at atmospheric pressure, the gels used were for the most part of compositions  $x \text{Li}(\text{F},\text{OH})$ ,  $5.30 \text{Mg}(\text{OH})_2$ ,  $8 \text{SiO}_2 + \text{water} + x \text{ROH}$ , where  $x = 0.70$  and R is  $\text{Me}_4\text{N}$ ,  $\text{Et}_4\text{N}$ ,  $\text{Pr}_4\text{N}$  and  $\text{Bu}_4\text{N}$ . The results showed that there are close structural similarities between synthetic organo-hectorite and their counterparts prepared by ion-exchange of natural hectorite. Moreover, it has been found that alkylammonium hectorite with unhydrolyzed, interlayer quaternary ammonium can even be synthesized at 373 K. Except for tetramethylammonium hectorite, the basal spacing of the synthetic species was lower than for the corresponding ion-exchanged forms of natural species. The natural and synthetic organo-hectorite also differs in the extent to which they swelled in liquids such as acetonitrile.

Besides sol-gel and hydrothermal methods, Barrer et al. [29, 30] described a simplest and widely used solid-state reaction to synthesize fluorohectorite which is a kind of hectorite-like solid without structural hydroxyls. In solid-state reaction, reagent grade chemicals, such as pure silica,  $\text{MgO}$ ,  $\text{MgF}_2$ ,  $\text{LiF}$  and  $\text{Na}_2\text{CO}_3$  were reacted in the solid state at 1073 K within 24 h or as a melt at 1123 K within 2 h. The reaction temperature has an impact on CEC of products. When made by sintering reactions at 1073 K the fluorohectorites had exchange capacities of ca. 90 mmol per 100 g. If prepared at 1123 K with lithium fluoride melts as flux this capacity was ca. 150 mmol per 100 g. Li-fluorohectorites exchanged with  $\text{Na}^+$ ,  $\text{K}^+$ ,  $\text{Rb}^+$ ,  $\text{Cs}^+$ ,  $\text{Ca}^{2+}$ ,  $\text{Sr}^{2+}$  and  $\text{Ba}^{2+}$  were also reported therein.

Neumann and his coworkers patented a series of techniques about the synthesis of hectorite-like solids [31–34]. Hydrous magnesium silicates having a crystal structure similar to that of natural hectorite may be produced by a precipitation process in which silica is precipitated into a preformed aqueous suspension of a water-insoluble magnesium compound. The process may be operated at high concentration and the products may have good dispersibility in aqueous media and

high optical clarity when dispersed as well as good rheological properties which may be obtained by prior precipitation processes [32]. Neumann and Sampson [33] reported a hectorite-like solid with the composition of  $\text{Na}_{0.30}(\text{Mg}_{2.55}\text{Li}_{0.30}\text{vac}_{0.15})\text{Si}_4\text{O}_{9.70}(\text{OH})_{2.30}$ . This formula means that there are vacancies and Li substitutions in the synthetic products. The layer charge is apparently reduced by the presence of silanol (Si–OH) groups. Neumann also patented [34, 35] an interesting synthesis method, which comprises the formation of an aqueous slurry from water-soluble Mg salts, sodium silicate, sodium carbonate or hydroxide and lithium fluoride. This slurry was hydrothermally treated by boiling at reflux temperature under atmospheric pressure for 10–20 h. Later an improvement of the procedure was made to conduct the hydrothermal reaction in an autoclave at 10–50 bar and 458–638 K for at most 8 h. The prolonged treatment resulted in further crystallization. So for catalysts and for rheologic modifier, the extent of crystallization of synthetic hectorite can be controlled by time of hydrothermal treatment. Torii and Iwasaki [36, 37] reported another synthesis method in which the homogeneous slurries were prepared by dissolving  $\text{MgCl}_2$  in a solution of sodium silicate and nitric acid, followed by precipitation with ammonia, washing and addition of NaOH and LiOH. The resulting slurries were hydrothermally treated at 398–573 K at autogenous water vapour pressures for 1–24 h.

Laponite, a trade name, is an entirely synthetic layered silicate that resembles the natural hectorite in both structure and composition [38]. It is reportedly said that laponite is synthesized by combining salts of sodium, magnesium and lithium under carefully controlled conditions of composition and temperature. Then this produces an amorphous precipitate that is further crystallized using a subsequent high temperature treatment. After that, the resulting product is filtered, washed, dried and milled to give a fine white powder. Such laponite has both vacancies and Li substitutions. Nowadays, laponite has two functional uses commercially; as a rheology modifier for water-based systems and as a film-forming agent.

Synthetic hydrous magnesium silicates have been prepared by utilizing an intermediate derived from talc as starting material. The solid exhibits the similar crystal structure and better rheological properties to those of natural hectorite. These procedures take the advantage of using natural silicates as reactants, which are relatively cheap and readily available sources. Moreover, these procedures are less complicated and time-consuming. Neumann and his coworkers [31] utilized ‘mesotalc’ in the production of hydrous magnesium silicates by forming an aqueous suspension containing the constituents of the hydrous magnesium silicate. The intermediate, ‘mesotalc’ is the product obtained by heating a mixture of talc and sodium carbonate so as to modify the talc structure while controlling the heating to avoid destroying it. In such a synthesis procedure, at least a part of the magnesium and silicon content was provided by ‘mesotalc’ and then the suspension of the mixture was hydrothermally treated until crystal growth occurs. The resulting crystalline product generally has rheological properties better than those of natural hectorite and may be used as a basis for organophilic derivatives. Orlemann [39] have also made use of natural pure talc as a starting material to yield hectorite-like solids. First, talc was calcined between 1033 and 1253 K together with  $\text{Li}_2\text{CO}_3$ . Then the resulting solid

was hydrothermally treated together with an aqueous solution of sodium silicate and carbonate for 8–16 h at 458 K and corresponding water vapour pressure of ca. 11 bar.

Hectorite containing Zn, Cu, Co or Ni in the octahedral sheets instead of Mg was also reported. Harder [40] synthesized a zinc-containing hectorite at  $\pm 293$  K and under 1 atm, which is similar to the natural conditions on earth surface. The main reactants were the dilute solutions of zinc hydroxide and silicic acid at a pH of approximately 8. The results showed that zinc-containing hectorite was only formed when the silicic acid was present as monomers and within a small range of Zn/SiO<sub>2</sub> ratios. Otherwise zinc hydroxide plus quartz or amorphous material was readily formed. Higashi et al. showed that Zn-hectorite could be synthesized in the range of reaction temperature 373–398 K but hectorite containing Cu, Co or Ni in the octahedral sheet, under the same conditions or even at a temperature of 423 K, could not be obtained easily [41]. However, a synthetic Mn-hectorite was successfully synthesized by hydrothermal reaction using silicic acid and MnCO<sub>3</sub> mixed with aqueous solutions of NaOH or LiOH. The starting materials were treated in the temperature range of 398–473 K for 72–168 h. The best synthesis temperature was found to be 448 K. A lower Mn/Si molar composition than stoichiometric ideal composition was found to be the most effective for the formation of almost pure and crystalline phases. However, high amount of Si is apparently needed for the stability of the solids. Such manganese-hectorite showed slightly larger expandability upon glycerol treatment and lower dehydroxylation temperature in the range of 573–723 K by differential thermal analysis (DTA) and thermogravimetry analysis (TG) as compared to Zn-hectorite [42].

Due to the structural complexity and chemical variability of smectites, sorption of radionuclides involves several sorption mechanisms: (1) physical or chemical adsorption via inner-sphere and outer-sphere complexation; (2) cation exchange in the interlayer and (3) incorporation into the smectite structure. Structural incorporation of trivalent *f* elements into the framework of the tri-octahedral hectorite was also feasible [43]. Before, it was not known whether trivalent actinides such as Cm(III) and Am(III) become incorporated into the crystal structure of clay minerals like hectorite. Recently, Pieper et al. [44] have synthesized a Eu-containing and a Cm-containing hectorite by utilizing Cm(III) and chemically homologous Eu(III) coprecipitated with Mg(OH)<sub>2</sub> as precursor and have investigated the sorption mechanisms of Eu associated with the synthesized hectorite. X-ray diffraction, Fourier transform infrared spectroscopy and atomic force microscopy identified the reaction products unambiguously as hectorite. An unhydrated Eu species (fluorescence lifetime 930  $\mu$ s) and a partly hydrated Eu species (fluorescence lifetime 381  $\mu$ s) could be identified by time-resolved laser fluorescence spectroscopy (TRLFS). The unhydrated Eu species are interpreted as incorporating Eu(III) into the hectorite structure or a remaining X-ray amorphous silica phase. The spectra of Eu-hectorite and of the Eu–silica complex are too similar to permit differentiation between these species, but dialysis experiments demonstrated the close association of the unhydrated Eu species with the crystalline hectorite phase. TRLFS measurements identified the

same incorporated Eu species as long as the Eu-hectorite was stable under acidic conditions. Based on all observations it seems to be very likely that trace amounts of Cm/Eu occupy a distorted octahedral site in the hectorite.

Recently, Ogawa et al. [45] reported a kind of hectorite-like swelling silicate with controlled layer charge density and with cation-exchange capacities ranging from 60 to 90 mequiv/100 g clay. The reactants were LiF, Mg(OH)<sub>2</sub> and colloidal silica. The controlled cation-exchange capacity can be achieved by changing the composition of the starting mixture, namely, the added LiF amount successfully. The cation-exchange capacity has an influence on the nanostructures of intercalation compounds prepared by the ion exchange with dioctadecyldimethylammonium ion. Microwave-hydrothermal treatment is also used to synthesize hectorite. It is reported that synthetic hectorite has been synthesized by ageing the gel precursor by microwave-hydrothermal treatment at 393 K for 16 h. The results showed that this synthetic hectorite has higher purity (60%) than hectorite prepared by conventional heating (45%) [46].

As shown by Barrer et al. [29], synthetic organo-hectorite has also been synthesized ever since 1960s. Over the years, Carrado and coworkers have developed and patented many techniques for a series of synthetic organo-hectorite by hydrothermal treatment in the presence of organic, organometallic and polymeric intercalates [47]. In this respect, Carrado has published an excellent and very recent review article that systematically discusses preparation, characterization and material applications on synthetic organo- and polymer-clays and the readers are referred to it and references therein for more details [46]. Some organic compounds used in their reactions are listed in Fig. 4.2.

A synthetic Cs-fluorohectorite was intercalated with tetramethylammonium cations, TMA<sup>+</sup>. Under appropriate reaction conditions, a complete cation exchange is feasible while preserving the phase relationship between adjacent silicate layers. Starting from a three-dimensionally (3D) ordered and homogeneously charged synthetic Cs-hectorite it is possible to synthesize single crystals of a 3D-ordered intercalation compound TMA-hectorite [48].

Much recently, alkylammonium phyllosilicate hybrids were synthesized hydrothermally from mixtures of Mg(OH)<sub>2</sub>, LiF and Si-containing reagents without using any layered silicates [49]. Octadecyldimethyl(3-trimethoxysilylpropyl)ammonium chloride, silica sol and tetraethoxysilane (TEOS) were used as silica sources. The formation of a covalent bonding between an inorganic moiety and an organic moiety and the formation of a layered structure took place simultaneously in one pot. The inorganic moiety of the hybrids is a magnesium phyllosilicate analogous to Mg-trioctahedral smectites. The organic moiety is analogous to alkylammonium (C<sub>18</sub>H<sub>37</sub>N<sup>+</sup>(CH<sub>3</sub>)<sub>2</sub>(C<sub>3</sub>H<sub>6</sub>)) and exists between layers of the inorganic moiety, being combined with the inorganic moiety through Si–C covalent bonds. Furthermore, solid-state <sup>29</sup>Si NMR (nuclear magnetic resonance) and X-ray diffraction (XRD) revealed that there are some defects in the inorganic moiety because of substitution of CSiO<sub>3</sub> for the Si tetrahedral site. The lateral dimension of the inorganic moiety is closer to that of an Mg-trioctahedral sheet in a free state as the organic/inorganic ratio is higher.



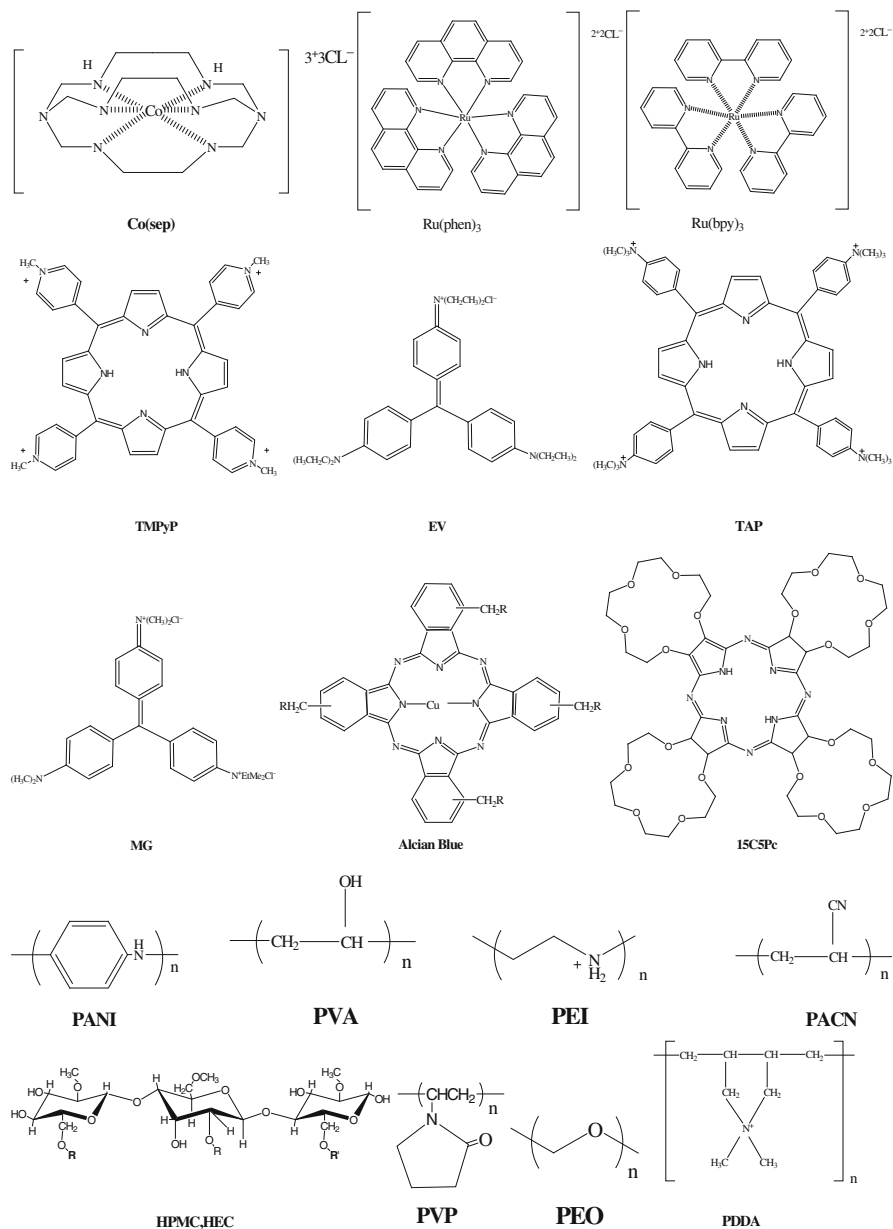


**Fig. 4.2** Structures of some organic compounds used as possible templates in hydrothermal hectorite crystallization. Reprinted from [47] with permission from Elsevier

### 4.3.2 *Synthesis Variables and Structure Characteristics*

Commonly the molar ratio of reactants for synthetic hectorite should generally be employed as the ideal composition of natural hectorite  $\text{Ex}_{0.66} [\text{Li}_{0.66} \text{Mg}_{5.34} \text{Si}_8 \text{O}_{20} (\text{OH}, \text{F})_4]$ . For example, to synthesize organo-hectorite, Carrado et al. used a typical precursor gel with the composition: 0.32 R, 1.0 LiF, 5.3  $\text{Mg}(\text{OH})_2$ ,  $8\text{SiO}_2$ ,  $n\text{H}_2\text{O}$ , where R = monovalent organic salt [50]. The typical procedure by hydrothermal reaction is as follows [28]: firstly, making fresh  $\text{Mg}(\text{OH})_2$  precipitation from magnesium salt solution and basic solution; secondly, adding wet freshly crystallized  $\text{Mg}(\text{OH})_2$  into the aqueous solution of organic-LiF with stirring; thirdly, adding silica sol into above suspension; finally, this slurry stirred and refluxed for 40–48 h and solids are isolated by centrifugation, washed and air-dried. It is worth noting that adding the magnesia to a slurry of mixed LiF and silica does not yield a clay product though the reason is still undetermined.

Recently, Zhou et al. [51] also synthesized hectorite in a hydrothermal system by using lithium fluoride, magnesium chloride, water glass and ammonium hydroxide as starting materials with a molar ratio of 1.33:5.07:7.70 of  $\text{LiF}:\text{Mg}(\text{OH})_2:\text{SiO}_2$ . First,  $\text{Mg}(\text{OH})_2$  suspension was formed from the hydrolysis of 20.00 mmol of  $\text{MgCl}_2 \cdot 6\text{H}_2\text{O}$  by 20 ml of 2 mol  $\text{l}^{-1}$   $\text{NH}_3$  solution. The hydroxide suspension was washed and then mixed with 5.20 mmol of LiF, followed by adding 30.40 mmol of silica sol. After stirring homogeneously, the gel was transferred into a PTFE Teflon<sup>®</sup>-lined stainless steel autoclave, which was then heated to 373–463 K under dynamic conditions in an oven. After 6–72 h, the products were separated from the mother mixture by centrifugation, and washed and dried.

The crystallization and structure features of synthetic hectorite can be investigated by chemical composition analysis, powder X-ray diffraction (XRD), field emission scanning electron microscopy (SEM), Fourier transform infrared spectroscopy (FTIR), thermogravimetry and differential scanning calorimetry (TG-DSC) and laser nanoparticle size analyzer, and so forth. For instance, the solid products can be effectively characterized by X-ray diffractometry to determine the basal spacing of the clay mineral platelets in the nanocomposite, impurities as well as the diameters of the crystallized particles, by electron microscopy to image the microstructures and morphologies, by absorption spectrophotometry to assess their optical band gaps, by thermoanalytical measurements to observe the structural changes that accompanied calcination and by gas adsorption analysis to determine the specific surface areas of Brunauer-Emmett-Teller (BET) and surface reactivity.

Powder X-Ray diffraction (PXRD) is a good tool to investigate the extent of crystallization, impurities, crystal particle size and the species in interlayer of synthetic hectorites. The typical pattern of natural hectorite and synthetic hectorite shows a basal (001) spacing at low angle. The peak at this value includes the thickness of a single clay layer which is 0.96 nm for typical smectite group clay minerals. Figure 4.3 shows the XRD patterns of synthetic hectorite samples for comparison of influence of time of hydrothermal treatment on products by Zhou et al. [51]. The peaks at  $5.58^\circ$ ,  $19.36^\circ$ ,  $28.87^\circ$ ,  $33.66^\circ$ ,  $36.19^\circ$ ,  $39.31^\circ$ ,  $60.45^\circ$  and  $72.67^\circ$  can be indexed to 001, 100, 005, 110, 112, 200, 300 and 222 reflections of synthetic

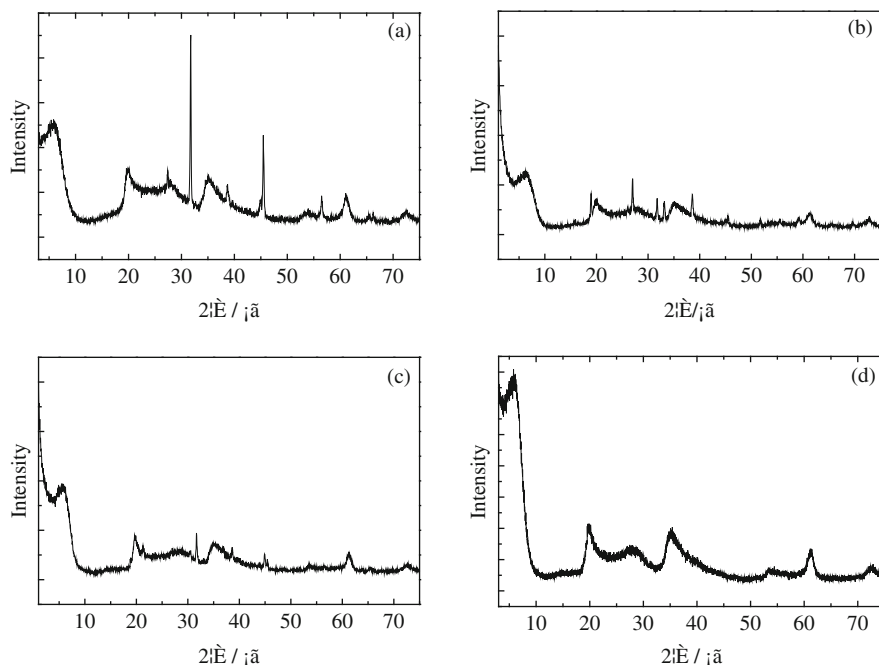


**Fig. 4.3** Powder X-ray diffraction patterns of samples at different synthesis time. (a) 6 h, (b) 32 h, (c) 49 h and (d) 72 h. Synthesis conditions: temperature = 403 K,  $\text{LiF}:\text{Mg}(\text{OH})_2:\text{SiO}_2 = 1.33:5.07:7.7$

hectorite, respectively. This even can be observed on the samples merely hydrothermally treated for 6 h, indicating that synthetic hectorite phase has formed then. However, the solid products still contain impurities such as  $\text{LiF}$  and  $\text{Li}_2\text{SiO}_3$ . As shown in Fig. 4.3, the peaks at  $26.99^\circ$ ,  $33.03^\circ$ ,  $38.60^\circ$  and  $51.68^\circ$  can be ascribed to 111, 130, 002 and 132 reflections of rhombic  $\text{Li}_2\text{SiO}_3$ . With the increase of time of hydrothermal crystallization, it is clear to see the impurities being reduced gradually. After 72 h, the only crystalline product obtained was synthetic hectorite, and the XRD pattern appeared similar to that of the natural hectorite minerals as to the peak widths and intensities of  $hkl$  reflections. The effect of the time of hydrothermal treatment on the crystallization and structure also can be clearly observed from the images of scanning electron microscopy as shown in Fig. 4.4.

The molar ratios of  $\text{Si}:\text{Mg}:\text{Li}$  and pH value in the sol–gel also play a vital role in synthesis of hectorite-like solids. Figure 4.5 displays XRD patterns for synthetic hectorite samples using different amounts of  $\text{LiF}$  under the same hydrothermal treatment for 49 h. In these patterns all of the expected peaks for synthetic hectorite are present but there are some peaks from impurities, mainly  $\text{LiF}$  and  $\text{Li}_2\text{SiO}_3$ . Interestingly, there are no peaks due to  $\text{Mg}(\text{OH})_2$  or the mineral brucite. At the stoichiometric ratio of sol–gel in terms of ideal composition of hectorite, a bit impurity is only  $\text{Li}_2\text{SiO}_3$  with the increased amount of  $\text{LiF}$ , there is an excess quantity of  $\text{LiF}$

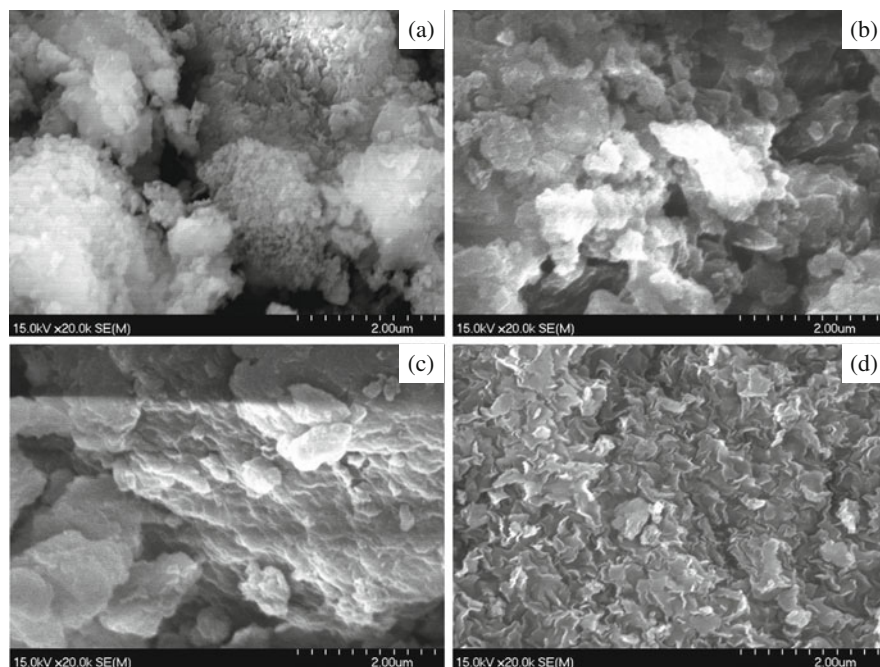


**Fig. 4.4** Scanning electron microscopy images of samples at different synthesis time. (a) 6 h, (b) 32 h, (c) 49 h and (d) 72 h

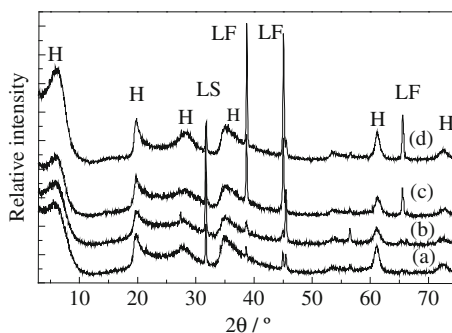
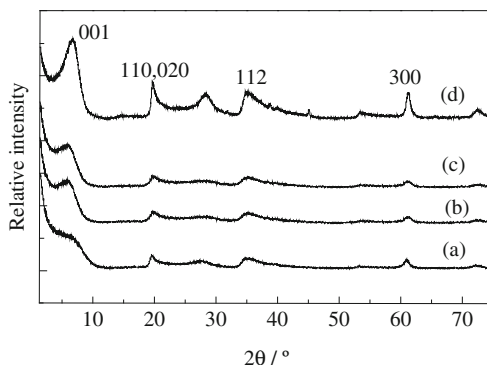


**Fig. 4.5** Powder X-ray diffraction patterns of samples at different reactant ratios of  $\text{LiF}:\text{Mg}(\text{OH})_2:\text{SiO}_2$ . (a) 1.33:5.07:7.7, (b) 2.66:5.07:7.7, (c) 3.99:5.07:7.7 and (d) 5.32:5.07:7.7. Synthesis condition: time = 49 h, temperature = 403 K (H: hectorite, LS: lithium silicate, LF: lithium fluoride)

for stoichiometric formation of hectorite-like solid with ideal composition. In fact, thus the sharp peaks at  $38.70^\circ$ ,  $44.99^\circ$  and  $65.48^\circ$  from reflections of 111, 200 and 220 of LiF are clearly observed. However, the excess of  $\text{Li}^+$  clearly facilitates the crystallization as observed from XRD patterns. After washing, LiF can be readily

**Fig. 4.6** Powder X-ray diffraction patterns of samples at different synthesis temperature. (a) 373 K, (b) 403 K, (c) 433 K and (d) 463 K. Synthesis condition:  $\text{LiF}:\text{Mg}(\text{OH})_2:\text{SiO}_2 = 1.33:5.07:7.7$ ; time = 32 h



removed from the solid samples. Increasing hydrothermal temperature is also found conducive to the formation of well-crystallized hectorite-like solids, as evidenced by XRD characterization in Fig. 4.6. Elemental analysis in the percentage by weight of Si, Mg and Li of synthetic hectorite is conducted on the samples synthesized from different reactant ratios [51]. The results showed that the silicon contents is around 57–58%, close to a theoretical amount of natural hectorite. In the case of different molar ratio of reactants, the main change takes place for the percentage of Na, Mg and Li. It is reasonable because all the amount of cations in the framework and interlayer can vary at different synthesis variables. As known from the structure of hectorite, Na and Li are exchangeable ions in the interlayer which depend on layered charge of final solids. Moreover, Mg can be substituted by Li and this consequently leads to different layer charge density. In other words, exchangeable cations and the extent of substitution certainly will depend on the synthesis conditions and composition of sol–gel precursors. Thus the controlled cation-exchange capacity can be at least achieved by changing the composition of the starting mixture.

In IR spectrum, the assignments of most peaks of synthetic hectorite can be attributed to the hectorite structure as natural hectorite, including adsorbed water. The hydroxyl-stretching region of hectorite is characterized by possibly four hydroxyl bands associated with the Mg and Li occupying two of the three possible octahedral sites [52]. Komadel et al. [53] reported only a single band at  $3675\text{ cm}^{-1}$  for hectorite from Hector, California. The peak at  $915\text{ cm}^{-1}$  corresponds primarily to Mg–O–H bond vibration and this can reflect specifically the substitution of Li for Mg as it would be expected.

Nuclear magnetic resonance (NMR) spectroscopy is very useful to probe the isomorphous substitution. Gerstmans et al. [54] have recently characterized synthetic hectorite and the corresponding surfactant-exchanged hectorite by  $^1\text{H}$ ,  $^7\text{Li}$ ,  $^{13}\text{C}$ ,  $^{23}\text{Na}$  and  $^{29}\text{Si}$  solid-state NMR spectroscopy. They found that the low-charge clays retain water more efficiently, forming aggregates without extensive drying. And the hydroxylated hectorite exhibits two  $^1\text{H}$  NMR signals near 0 ppm. The  $^{23}\text{Na}$  2D 3Q magic angle spinning (MAS) spectra of the low-charge hectorite show a single peak, the  $^{29}\text{Si}$  NMR shift depends on the interlayer charge. The isomorphous

substitutions of silicon by aluminium or boron are also possible as proven by  $^{11}\text{B}$ ,  $^{27}\text{Al}$  and  $^{29}\text{Si}$  solid-state NMR spectroscopy [55]. The addition of boron and/or aluminium compounds to the reaction mixture leads directly to boron and aluminium containing layered hectorite-type materials in a hydrothermal crystallization process without further treatment.

Passive microrheological techniques using particle tracking have been developed for the study of the gelation of hectorite suspensions [56]. By following the Brownian motion of the particles, it is possible to determine the increasing caging of the particles with time, as the system gels. Since only the Brownian motion is followed, the gelation process itself should not be affected by the measurement. As gelation proceeds the increasing heterogeneity of the particle environments can be monitored by a variety of measures, including kurtosis. An effective viscosity can be extracted from the measurements and used to indicate the gelation process. Marry et al. [57, 58] reported a quasi-elastic neutron scattering study of water dynamics confined in a model system of a synthetic hectorite with  $\text{Na}^+$ -compensating counterions. They concluded that simple isotropic analysis can only give a rough estimate about the order of magnitude of the water dynamics in the medium.

Structural incorporation of the actinide curium in the octahedral layer of the tri-octahedral Mg-rich smectite hectorite was studied using time-resolved laser fluorescence spectroscopy (TRLFS). Organo-hectorite nanoparticles were synthesized at 363 K in the presence of Cm(III). TRLFS was used to identify Cm(III) species during various synthesis steps and to characterize the structural incorporation mechanism. The formation of a Cm-containing Mg hydroxide precursor and the reaction with aqueous silica in a pH range of 9–10 to form TOT layers were identified to be key steps for trivalent actinide incorporation in hectorite via coprecipitation [59].

Electron paramagnetic resonance (EPR) spectroscopy, coupled to  $\text{NH}_3$  vapour treatment, is used to determine the chemical form and structural location of  $\text{Cu}^{2+}$  in co-precipitation with hectorite. A quick extraction with EDTA probes the structural location of  $\text{Cd}^{2+}$ ,  $\text{Cu}^{2+}$ ,  $\text{Pb}^{2+}$  and  $\text{Zn}^{2+}$  and provides information on the fraction of the transition metal ions that are loosely associated with the external surfaces of the clay mineral. As expected from the Pauling radii of the four transition metal ions,  $\text{Cu}^{2+}$  and  $\text{Zn}^{2+}$  are substituted in the mineral structure more significantly than are  $\text{Cd}^{2+}$  and  $\text{Pb}^{2+}$ . The latter metal ions may be too large to be accommodated within layer silicate structures, and therefore represent a greater challenge for stabilization by coprecipitation in clay minerals [60].

Theoretic and computer-simulated study on the synthesis and structure characteristics is also meaningful. Kang et al. [61] examined basal peak irrationalities according to boundary conditions of the hectorite basal diffraction unit (BDU), which were recognized as the total assembly of 2:1 phyllosilicate layer plus interlayer material. The hectorite basal profiles were computer-simulated using the three kinds of BDU settings identified from the middle of octahedral sheets in the nearest neighbour (centrosymmetric model), the middle of interlayers in the nearest neighbour (centrosymmetric model) and a basal oxygen plane to the margin of interlayer in contact with the next phyllosilicate layer (non-centrosymmetric model). In the results of simulations, irrationality and asymmetry of the hectorite

basal peaks relied straightforwardly on the BDU scattering modulations for the non-Bragg angles containing information on the synergic scattering events of phyllosilicate layer and interlayer material. Among the concerned BDU boundaries, the non-centrosymmetric model more effectively represented the real hectorite profile.

#### 4.4 Pillaring and Further Modification

Different from the synthetic hectorite with two-dimensional (2D) layer structures, pillared synthetic hectorites exhibiting three-dimensional network structures are normally regarded as microporous and mesoporous materials like that of zeolites and mesoporous solids. Pillared clays are also regarded as a class of nanocomposites with open and rigid structures obtained by linking robust, three-dimensional guest species to a layered host. Provided that chemical bonds are formed between the pillars and the surface oxygen atoms of the hectorite hosts, then the nanocomposite solid can be termed as cross-linked clay [62].

The pillaring process has been and continues to be an effective way of transforming 2D layered hosts into new 3D porous materials, with novel properties created and with properties complementary to those of natural clays and zeolites such as pore size and shape, acidity and redox properties. The structure and properties depend on the guests of pillars in the case of a given host, for example, here synthetic hectorite. Besides the choice of layered hosts, the properties and structure of PILCs can be well tailored by variation of guest species and pillaring conditions. Therefore, the pillaring process can be effectively used to yield pillared synthetic hectorite solids with higher surface area and higher porosity; a broad spectrum of such properties as structural, chemical, catalytic, ionic, and so forth; and tuneable internal structures, with reactive sites and/or species chosen to match particular applications or provide new kind of host porous structures for chemical or physical processes.

Many different pillaring agents can be chosen, including organic compounds, metal trischelates, organometallic complexes, metal cluster cations, metal oxide sols, and polyoxocations. Organo-pillared hectorite, e.g. pillared by large monovalent cations, can be prepared by in situ pillaring during synthesis for a synthetic hectorite. Also it can be obtained by post-ion-exchange reaction. As mentioned above, laponite is a synthetic trioctahedral smectite clay with the ideal formula  $[\text{Si}_8(\text{Mg}_{5.34}\text{Li}_{0.66})\text{O}_{20}(\text{OH})_4] \text{Na}_{0.66}$ . Introduction of tetrapropyl ammonium (TPA) and benzyltriethyl ammonium (BTEA) cations into interlayers of laponite expands the clay platelets by about 5.5 Å. Long-range face-to-face stacking of plates occurs, forming pillared hectorite with 300–350  $\text{m}^2\text{g}^{-1}$  surface area stable to about 200 °C. In contrast, the bulky ferricinium (FCN) ions can be occluded without altering the delaminated structure of the parent laponite. Increased line widths observed in the  $^{13}\text{C}$  CPMAS spectra of the pillared hectorite are attributed to chemical shifts dispersion and/or reduced mobility of the quaternary ammonium cations in the clay silicate layers. Evidence for the clay-induced distortion

of bond angles about the quadrupolar  $^{14}\text{N}$  atom could also be inferred from these spectra [63]. Hectorite intercalated with  $[\text{Cu}(\text{cyclam})]^{2+}$  (cyclam = 1,4,8,11-tetraazacyclotetradecane) has been reported and spectral simulation also shows that the  $\text{CuN}_4$  plane of  $[\text{Cu}(\text{cyclam})]^{2+}$  is parallel to the clay layers [64]. A synthetic Cs-fluorohectorite was intercalated with a large cationic pillar, 1,4-dimethyl-1,4-diazabicyclo[2.2.2] octane ( $\text{DDABCO}^{2+}$ ), and a microporous material is obtained ('pillared clay'). Under appropriate conditions, complete cation exchange is feasible and the phase relationship between adjacent silicate layers is preserved. Notably, starting with a three-dimensionally (3D) ordered and homogeneously charged Cs-hectorite, a single crystalline and 3D-ordered intercalation compound of a smectite was obtained. The characterization by structure refinement shows the results of ( $[\text{DDABCO}_{(0.25)}] [\text{Mg}_{2.5}\text{Li}_{0.5}] [\text{Si}_4](\text{O}_{10}\text{F}_2)\text{-O-TOT}$ , monoclinic,  $C2/m$ ,  $a = 5.2635(9) \text{ \AA}$ ,  $b = 9.1278 \text{ \AA}$ ,  $c = 13.984 \text{ \AA}$ ,  $\beta = 96.89(2)^\circ$ ,  $V = 667.0(2) \text{ \AA}^3$ ,  $Z = 2$ ). In other words, such products were made of two-dimensional tetrahedral (T) sheets of  $\text{SiO}_4$  units linked by an octahedral (O) sheet of  $\text{Mg}_{2.5}\text{Li}_{0.5}$  (O,OH) units, forming T–O–T layers separated by an interlayer space of  $\text{DDABCO}_{(0.25)}$ . The authors claimed that much like the inorganic  $\text{Cs}^+$  cations in the starting material, the organic pillars bridge the interlamellar space in a defined way by penetrating into the hollows on the corrugated silicate surfaces on both sides of the interlamellar space. As a result, the hexagonal cavities are forced to be arranged opposite of each other. Therefore, the pillars are arranged with their  $C$ -axes lying in the plane of the interlayer space [65].

Expansion of interlayer space of the modified clays depends on the spacers. A kind of novel nanostructured clays was synthesized from cation-exchange reaction by the intercalation of rhodium complexes with ligand spacers into clay. A unique conformation of pillar complexes was detected by cross-polarization magic angle spinning (CP MAS) NMR [66]. Recently, it was shown that attempts to intercalate phenyltin compounds onto laponite led to reaction of the organo-tin species on the clay surface and the formation of tin oxide-pillared clay [67].

Many of these organic compound-based species, however, have some drawbacks, such as low reactivity or especially lack of thermal stability. Therefore, inorganic polyoxocations and presently nanoparticles are by far the most widely employed as pillaring agents. Preparation of PILCs consists of a controlled hydrolysis reaction of pillaring precursors which can be carried out in solution or directly in the interlamellar space of the clay, the former allows better control of the nature of the polyoxocations. For instance, Fe-pillared synthetic hectorite was obtained through cation-exchange reaction and pillaring by 1 M Fe nitrate aqueous solutions partially neutralized with a carbonate solution, giving a molar ratio of  $\text{OH}^-/\text{Fe} = 2$  [68].

The difference in particle size of synthetic hectorite is also responsible for their differences in crystallinity, surface area (SA) and micropore volume ( $\mu\text{PV}$ ) and consequently for their pillared forms too. It is reported that pre-adsorption of ethylenediamine in the interlayer space of laponite can be used to reduce the important contribution of edge-to-face and edge-to-edge stacking of the clay layers and to create a more homogeneous substrate for pillaring, as is proven by using ethylenediamine-exchanged laponite as the Zr-pillaring precursors during the



pillaring reaction. Surface areas and micropore volumes of, respectively,  $482 \text{ m}^2 \text{ g}^{-1}$  and  $0.34 \text{ cm}^3 \text{ g}^{-1}$  for Zr-pillared laponite and  $171 \text{ m}^2 \text{ g}^{-1}$  and  $0.064 \text{ cm}^3 \text{ g}^{-1}$  for Zr-pillared hectorite after calcination are obtained [69].

Reaction of natural hectorite with Al, ZrAl and Zr polyoxocations generate a series of pillared hectorite materials. After heating in air at 673 K/4 h the porous materials have Langmuir surface areas of  $260\text{--}300 \text{ m}^2 \text{ g}^{-1}$  thermally stable to 873–973 K. Spectroscopic studies of adsorbed pyridine indicate that these pillared hectorites contain both Lewis and Brønsted acid sites, similar to pillared montmorillonites. But such pillared hectorites are not as active as the corresponding pillared bentonites in cracking 633–699 K boiling range gas oils but exhibit greater gasoline selectivity and minimize light gases ( $\text{C}_2\text{--C}_4$ ) generation [70]. Palinko et al. have reported that synthetic laponite was pillared by partially hydrolyzed Al, Zr and Cr salts [71, 72]. Table 4.1 lists some physical features and porosity after various pre-treatment for those pillared laponite [72]. It was found that the pillared structure survived calcination at 773 K making these materials potential shape-selective catalysts up to this temperature.

**Table 4.1** Some physical features of pillared hectorite after various pre-treatments [72]

Host	Pillars	Treatment	BET surface area ( $\text{m}^2 \text{ g}^{-1}$ )	$d_{001}$ (nm)	Reference
Laponite	None	Evacuation at 298 K for 2 h	234	1.42	[72]
	Al		348	1.68	[72]
	Zr		231	1.53	[72]
	Cr		442	1.80	[72]
Laponite	None	Calcined at 773 K for 5 h	157	1.14	[72]
	Al		170	1.44	[72]
	Zr		247	1.56	[72]
	Cr		370	1.62	[72]
Hectorite	None		10.5	$0.22 + 0.96$	[85]
	CdS	Reacting $\text{H}_2\text{S}$ gas with $\text{Cd}^{2+}$ -exchanged compounds	36.0	$0.96 + 0.96$	[85]

Mixed pillars, e.g. Al–Fe and Si–Al, were also obtained by a simple method of preparation [73, 74]. As for the preparation of mixed Al–Fe-pillared laponite, solutions of  $\text{AlCl}_3$ ,  $\text{FeCl}_3$  and  $\text{NaOH}$  were mixed with a clay suspension in adequate concentrations and kinetic conditions. Characterization by chemical analysis, XRD, NMR and  $\text{H}_2$  TPR shows that iron cations replace a few octahedral Al in the  $\text{Al}_{13}$  pillars. The mixed Al–Fe pillars present original catalytic properties with shape selectivity different from that of conventional iron catalysts [75].

The content of host in suspension is important to prepare pillared products. Often, dilute suspensions of clay are used. However, Molina et al. reported that concentrated suspensions of hectorite and montmorillonite have been successfully pillared

with base-hydrolyzed aluminium solutions with different OH/Al molar ratios. The pillared clays can be used as supports by subsequent modification. For example, over Pt-impregnated samples, these catalysts can be used in the hydroisomerization of heptane [76].

In addition to the different parameters during pillaring already mentioned, the calcination treatment also plays a key role in pillared products. Some researchers held that the method used to dry the flocculated clay layers is far more important than the choice of the pillaring reagent or the layer charge of clay hosts in determining the apparent pore size of pillared products. The differences in apparent pore openings and the dependence on the drying method are explained in terms of a clay flocculation model in which both lamellar with face-to-face structure and delaminated edge-face and edge-edge association of the layers can occur, depending in part on the morphology and the aspect ratio of the layers. Evidence for the presence of delaminated aggregates is provided by the results for laponite, which has a relatively small layer aspect ratio and a high tendency to form delaminated aggregates even under air-drying conditions. Layer delamination can have important effect on catalytic performance consequently, as demonstrated by differences in the sensitivity of air-dried and freeze-dried pillared clays to coke formation in the dealkylation of  $\beta$ -isopropyl-naphthalene [77].

With regard to the synthesis of PILCs, much attention should be paid to the delamination of hectorite because this clay is much easier to delaminate or exfoliate than other clays [78].  $\text{Cu}^{2+}$  ion-exchanged pillared clays have been prepared by using delaminated  $\text{Al}_2\text{O}_3$ -pillared laponite. The BET surface area for the delaminated  $\text{Al}_2\text{O}_3$ -pillared laponite was  $384 \text{ m}^2 \text{ g}^{-1}$ , and that of the  $\text{Cu}^{2+}$  ion-exchanged form was  $360 \text{ m}^2 \text{ g}^{-1}$ . In this case, the copper content obtained by neutron activation analysis was 2.65% by weight [79].

Both delamination and subsequent post-modification of synthetic hectorite provide more routes to make new supports and catalysts with exposed crystalline surfaces and active species. Besides in solution, even delamination can take place during freeze drying of aqueous suspensions of laponite. As observed by Lewis and Kuroda [80], the resulting low density materials were shown by scanning electron microscopy to consist of sheet-like structures made up from many individual clay sheets. Although the material obtained is sensitive towards collapse in solvents, tri-iron dodecacarbonyl was added by chemical vapour deposition. Fourier transform infrared analysis indicated that the iron complex had attached to the edge surface of the delaminated clay sheets. As an alternative to using chemical vapour deposition for the introduction of metals, the original freeze-dried clay was first stabilized towards solvents and then ion exchanged. Stabilization was carried out by treating the freeze-dried clay with gas phase tetramethyl orthosilicate. This reaction is suggested to involve cross-linking by silicon of adjacent clay sheet through edge surface hydroxyls. Palladium was subsequently introduced onto the cross-linked material by ion exchange using tetraaminepalladium(II) chloride.

With the objectives of improving the properties of pillared hectorites as catalysts or supports, PILCs can be further post-functionalized by grafting techniques. For instance, synthetic clay minerals have been transformed into Si-pillared mesoporous

structures and then grafted with SH functions for heavy metal ion trapping in polluted soils [81].

Novel mesoporous materials having exceptionally large pores were produced from hydrothermally synthesized silicate-bearing hectorite. The mesoporous material from a precursory hectorite synthesized at 423 K has a total specific surface area of  $848 \text{ m}^2 \text{ g}^{-1}$ , a pore volume of  $0.98 \text{ cm}^3 \text{ g}^{-1}$  and a pore average diameter of  $46 \text{ \AA}$ , values which are significantly higher than those of conventional pillared clays. This suggested that interlayer anisotropic silicates act as larger pillars [82]. Recently, when pillaring a well crystalline synthetic hectorite using molecular pillars, a truly microporous material that displays long-range order of the pillars and consequently a narrow pore size distribution was obtained [83].

Metal sulphides are a class of novel pillars used in PILCs. The clay can be saponite, montmorillonite, hectorite and laponite, while the metallic phase can be cobalt, nickel, zinc, cadmium or lead sulphides. The nanocomposites of layered clays and metal sulphides could be produced from reactions of the layered clay aqueous suspensions and water-soluble metal–thiourea complexes. In the nanocomposites, the clay could be incorporated with the metal sulphide pillars and metal sulphide nanoparticles [84]. Layered compound/CdS nanocomposites incorporating CdS pillars in the interlayer of layered hectorite were reportedly prepared by the stepwise ion exchange reactions of the layered compounds with  $\text{C}_3\text{H}_7\text{NH}_3^+$  and  $\text{Cd}^{2+}$  followed by the reaction with  $\text{H}_2\text{S}$  gas. The pillar height was less than 1 nm (Table 4.1) and the band gap energy was slightly larger than that of normal crystalline CdS. Although the host layered compounds were insulators or wide band gap semiconductors, CdS-pillared layered compounds showed photocatalytic activity under visible light irradiation [85]. The composites consist of CdS pillars and CdS nanoparticles which tend to increase in size as the amount of complex precursor increases. The sizes of the sulphide prepared from the same amount of complex differ due to the effect of the different clays on precursor exchange and on the subsequent nucleation and growth of CdS particles. The composites show the characteristic light absorbance of CdS and absorbance increases with the sulphide content. The composites are generally mesoporous [86].

## 4.5 Catalysis

The first industrial application of clays as catalysts dates back to 1915 [87, 88]. Acid-activated smectites have been known for more than 60 years as catalysts for oil cracking in Houdry process [89, 90]. After 1960s they were replaced by microporous crystalline zeolites due to their better catalytic activity and selectivity. As discussed above, the dissolution characteristics of hectorite in inorganic acids have also been investigated [91]. Moreover, base-treated clays have also been noticed [92]. However, besides oil refinery and petrochemical processes in which clay-based materials have been extensively used, there are a great variety of industrial processes or reactions such as organic synthesis, environment abatement, nanocomposites,

adsorption and separation. In this aspect, both layered hectorite and their synthetic analogues and the clay-based derivatives of pillared interlayered synthetic hectorite, as well as other clay minerals, undoubtedly show much promising applications with specific properties and functions [93], because of the interesting possibilities of guest–host nanocomposites, further modification and creation of porosity from 2D to 3D structure. Therefore, such materials can be chosen either as hosts or as supports to produce novel catalysts for establishing environmentally friendly catalytic processes and novel nanotechnologies. In addition, thermally treated clay can be developed as a stationary phase in liquid chromatography. For example, spray-dried, spherical synthetic hectorite particles thermally treated at 773 K for 16 h have been used by Miller and Bruno as adsorbent materials in reversed-phase liquid chromatography [94].

Because hectorite-like materials have their own features in comparison with other smectite clays, at least four classes of structural catalysts can be formed from synthetic hectorite precursors: One is ion-exchanged clays, the second synthetic hectorite with specific lattice composition for specific catalysis, the third pillared clays and the fourth delaminated clay with a proposed house-of-cards structure. Comparatively speaking, the delamination of synthetic hectorite is easier than that of other smectite minerals. But it should be noted that the delamination, in most cases, is not perfect, and then the two-dimensional layered character is partly retained despite the absence of discrete 001 X-ray reflections observed from XRD patterns.

Firstly, ion-exchanged clays can be readily obtained by simple ion-exchange reaction. In view of a given catalytic reaction, the  $\text{Na}^+$  and  $\text{Li}^+$  cations in the interlayers of hectorite and hectorite-like solids can be replaced by other alkali metal cations. This can be made either by direct synthesis or by post-ion-exchange reaction in the presence of desired metal cations. Besides, heating or calcination also has an effect on catalytic activity. Consequently, these treatments can make resultant materials exhibit either acidity and basicity, or redox properties. These increased catalytic functions can be detected by the infrared spectrum of adsorbed pyridine, adsorbed carbon dioxide or related catalytic properties. For instance, as to the catalytic conversions of 2-propanol and ethanol over synthetic hectorite and its analogues, both the dehydration and dehydrogenation products were observed by Suzuki et al. with appreciable amounts of butadiene formed besides ethylene and acetaldehyde [94]. Such catalytic performance suggested that the presence of both acidic and basic centres in the materials because the dehydration activity depended on the kind of alkali metal cations, while the dehydrogenation activity was not influenced by the nature of the alkali metal cation. Additionally, the results also suggested that the active centres for dehydration are alkali metal cations located at the entrance of the interlayer, and that the basic centres are located at the edge of the layers, plausibly oxygen anions bound to Mg cations. Suzuki et al. also claimed that synthetic fluorohectorite showed a higher activity for dehydration than hectorite [95].

Besides alkali metal cations, transition metal cations can also be exchanged with the interlayer of synthetic hectorite and its analogues. As shown by Frey et al., the hydrolysis of 4-nitrophenyl phosphate (NPP), to produce 4-nitrophenol and inorganic phosphate was catalyzed by an aqueous suspension of  $\text{La}^{3+}$  ion-bound

hectorite clay at 323 K. Sodium-exchanged hectorite does not promote the hydrolysis of NPP under the same reaction conditions, suggesting that hectorite-bound  $\text{La}^{3+}$  ions play an active role in this catalytic reaction [96].

Secondly, besides the modification by means of changing metal cations of interlayers, the composition of layers of synthetic hectorite also can be changed to meet the needs of a specific catalytic reaction. Nishiyama et al. [97] have reported the synthesis of hectorite-like smectites which contain nickel in the lattice and the catalytic behaviour of a series of synthesized hectorite-like smectites containing nickel in the decomposition reaction of 2-propanol. These synthetic nickel-containing hectorites were found to have both weak acid and base sites, the base sites being dominant. The main product of the catalytic decomposition of 2-propanol was acetone, which was accompanied by a series of dimers and trimers of propene and condensates between acetone and propene. These oligomers are believed to be formed in the interlayer of the smectites, where 2-propanol is easily accessed but propene is not. Their results also suggested that the catalytic activity depends on the composition of the smectites and those containing nickel are active, while those containing fluorine atoms lose activity.

Thirdly, nowadays it is much common in the scientific circle of clays and catalysts that some novel porous catalysts can be designed and prepared based on layered clays by pillaring processes. For instance, hectorite, montmorillonite and saponite, and other layered solids, can be made into Al-pillared forms with significant improvement of specific surface area and porosity. Such pillared clays can also be further used as supports, for example, as supports of platinum catalysts (e.g. 2.3 wt% Pt) for the catalytic combustion of acetone and methyl-ethyl-ketone [98]. Moreover, such further treatment modified the textural properties of the Al-pillared clay supports, giving rise to a significant loss of specific surface area and micropore volume.

Bodman et al. have shown that synthetic laponite can be pillared with tin, chromium and aluminium pillars. These catalysts were compared with a standard Ni/Mo catalyst supported on alumina and a dispersed catalyst,  $\text{Mo}(\text{CO})_6$ , in hydrocracking a coal extract for a short contact time of 10 min at 713 K in a microbomb reactor with tetralin solvent and hydrogen at a pressure of 190 bar. Tin-pillared laponite showed comparable catalytic performances and even the performances of such catalysts at short, long or repeated reaction times were seen to be better than that of the conventional NiMo catalyst for the hydrocracking of coal-derived materials and a petroleum residue [99].

Noble metals, which are commonly known as active species for many catalytic reactions, can also be intercalated into the interlayers of clays [100, 101]. Especially, noble metal nanoparticles can be immobilized and stabilized in layered hectorite [102]. Shimazu et al. [103] have prepared  $[\text{Pd}(\text{NH}_3)_4]^{2+}$ /hectorite and  $[\text{Pd}(\text{PDT})_3]^{2+}$ /hectorite (PDT = propane-1,3-dithiolate), using them for the hydrogenation of alkynes in dimethyl sulphoxide (DMSO). The basal spacings of  $[\text{Pd}(\text{NH}_3)_4]^{2+}$ /hectorite and  $[\text{Pd}(\text{PDT})_3]^{2+}$ /hectorite were 1.30 and 2.21 nm, respectively. When the intercalated catalysts were swelled with DMSO,  $d_{001}$  became 1.45 nm for  $[\text{Pd}(\text{NH}_3)_4]^{2+}$ /hectorite and 2.94 nm for  $[\text{Pd}(\text{PDT})_3]^{2+}$ /hectorite.

Another example is the adsorption and intercalation of the cationic luminescence probe, tris(2,2'-bipyridine)ruthenium(II) complex ( $[\text{Ru}(\text{bpy})_3]^{2+}$  or Rubpy), into hectorite and laponite host clay films [104]. Rubpy/laponite films exhibit enhanced potential for photonic and sensor applications with increased optical transparency, intense luminescence and longer luminescence lifetimes. Furthermore, co-intercalation of the cationic surfactant trimethylcetylammmonium cation promotes two-dimensional tiling of laponite tactoids and may afford selective tuning of fluorophore packing. By ion exchange, the cationic organometallic aqua complexes formed by hydrolysis of  $[(\text{C}_6\text{H}_6)\text{RuCl}_2]_2$  in water, mainly  $[(\text{C}_6\text{H}_6)\text{Ru}(\text{H}_2\text{O})_3]^{2+}$ , can also be intercalated into sodium-hectorite by replacing the sodium cations between the anionic silicate layers. The yellow hectorite thus obtained reacts in ethanol with molecular hydrogen at 50 bar and 373 K with decomposition of the organometallic aqua complexes to give a black material, in which ruthenium nanoparticles in the range of 9–18 nm are intercalated between the anionic silicate layers, the charges of which being balanced by hydronium cations. The black ruthenium-modified hectorite efficiently catalyzes the hydrogenation of benzene and toluene in ethanol at 50 bar of  $\text{H}_2$  and at 323 K, the turnover frequencies attaining 7,000 catalytic cycles per hour [105].

Finally, a delaminated synthetic hectorite catalyst can be formed by the reaction of polyoxoaluminium cations with synthetic small particle hectorite and can also show novel properties. Tested in gas oil cracking,  $\text{C}_5$ – $\text{C}_{12}$  gasoline yields obtained more nearly the same as a commercial zeolite-promoted FCC catalyst than an amorphous aluminosilicate catalyst. In addition, the delaminated clay affords higher yields of light cycle gas oil and lower yields of slurry oil than the zeolite-promoted catalyst [106].

Besides, post-functionalization of synthetic hectorite-based materials provides more routes to make catalysts for specific catalytic applications. For instance, copper acetylacetonate was immobilized directly onto laponite and then it can be treated by amine functionalization with (3-aminopropyl)triethoxysilane (APTES). The results indicated that laponite-based materials with higher metal content were obtained by direct complex anchoring, probably due to the delaminated nature of laponite which induced the particles aggregation on functionalization with APTES. All the results pointed out that the Cu complex was anchored onto the amine-functionalized clays by Schiff condensation between the amine groups of anchored APTES and the carbonyl groups of the acetylacetonate ligand, whereas direct immobilization proceeded mostly through interaction between the metal centre and the clay surface hydroxyl groups [107].

Carrado et al. put forward an idea of creating porous layered hectorite-based catalysts with mesoporosity and a unique morphology. They found that there is a certain portion of unreacted sol particles incorporated into the final matrix when using silica sol as the silicon-containing starting material. For hydrodesulphurization (HDS), the conversion of dibenzothiophene (DBT) to biphenyl was examined at 673 K using CoMoS-loaded mesostructured hectorite-based supports. No hydrogenation or hydrocracking was observed with any of the clay supports. The most active clay was derived from Ludox silica sol AS-30 with an activity of 65% DBT

conversion and 100% selectivity to biphenyl (BP). These authors suggested that the unique morphology of the mesostructured clays is important [108].

Besides conventional chemical catalysis, hectorite-based photocatalysts are one of recent interesting topics. Using hectorite clay mineral platelets and titanium dioxide nanoparticles, a kind of nanocomposites could be prepared and thus could be used as an efficient photocatalyst. Such nanocomposite material could be considered as a promising alternative for the removal of organic water contaminants. Two major methods can be employed. One involved the pre-adsorption of the titanium alkoxides into/onto the clay mineral platelets and subsequent hydrolysis and calcination. The other is that the previously crystallized titanium dioxide nanoparticles and clay mineral platelets were heterocoagulated and calcined [109]. In this aspect, Ooka et al. [110] compared four kinds of TiO<sub>2</sub>-pillared clays prepared from montmorillonite, saponite, fluorine-hectorite and fluorine mica, and their surface hydrophobicities and performances in adsorption–photocatalytic degradation of phthalate esters (di-*n*-butyl phthalate and dimethyl phthalate). It was found that surface hydrophobicity of TiO<sub>2</sub>-pillared clays largely varied with the host clay: it increased in the order saponite < fluorine-hectorite < montmorillonite < fluorine mica. The order of performance in adsorption and successive photocatalytic degradation of phthalate ester was consistent with that of surface hydrophobicity. Belessi et al. [111] evaluated the photocatalytic efficiency of the hectorite-TiO<sub>2</sub> nanocomposite catalysts using a chloroacetanilide herbicide (dimethachlor) in water as model compound. All supported catalysts exhibited good photodegradation efficiency and their overall removal efficiency per mass of TiO<sub>2</sub> was better than that of bare TiO<sub>2</sub> produced by the sol–gel method. They found that the primary degradation of dimethachlor followed pseudo-first-order kinetics according to the Langmuir–Hinshelwood model. A new titanium(IV) oxide-hectorite nanofilm photocatalyst was also prepared on quartz slides [112]. It was evaluated in the photooxidation of dibenzothiophene in non-polar organic solution (tetradecane), as a model for diesel fuel. The results indicated that the outlined process was effective in reducing sulphur levels to below 10 ppm.

Zinc oxide and SnO<sub>2</sub> nanoparticles also can be incorporated into interlayers of hectorite [113]. For example, Korosi et al. reported that SnO<sub>2</sub> nanoparticles were prepared by hydrolysis in aqueous medium and stabilized by hectorite and the photooxidative efficiency of resulting SnO<sub>2</sub>/clay photocatalysts was tested by degradation of salicylic acid [114].

## 4.6 Summary and Prospects

Clearly, synthetic hectorite and its analogues and novel synthetic hectorite-based materials with well-defined composition and specific properties have received extensive attention so far and will continuously attract attention both in academia and industry. The recent advances have shown the rapid growth of knowledge in the development of both synthetic methods and the techniques of characterization and

application [115, 116]. In addition to being used as host for preparation of PILCs, synthetic hectorite has shown promising potentials in many fields because of its specific colloidal and delamination properties with nanoscaled layered structure. Much important, it is relatively easy to synthesize hectorite-like solids by either hydrothermal process or solid-state reaction. These advances are of great significance, ranging from the tuneable composition of synthetic hectorite [117] to transformation of 2D structure to 3D pillared clays, and from hybrid with cross-linked clay particles and clay monoliths [118] to the producing of myriad nanocomposites, including the production of novel nanoparticles in the interlayer and inorganic/polymer nanocomposites [119].

As layered host precursors, synthetic hectorite with tuneable composition and high purity is much conducive to designed features and specific applications of PILCs in contrast to using natural clay minerals with impurities plus other uncertain factors arising from natural deposits. As discussed above, the specific properties of pillared interlayered clays for catalysis and adsorption depend on both the layered solids as hosts and the pillars as guests between the clay layers. In the aspects of catalysts, never before in the molecular sieve area, has one been able to control so many of the characteristics of inorganic porous solids either through framework of layers or through intercalated guest species. With these new structures of PILCs with adjustable pore sizes and compositions at hand, researchers in many fields are armed with a new arsenal of materials with which to attack the nanoscopic catalysis.

It should be noted that such kind of synthetic hectorite, not only provides a rare opportunity to construct novel catalysts, but also provides a new chance to prepare new absorbents [120, 121] and ionic conductors [122], and so forth. Nanoscaled design based on synthetic layered hectorite appears much feasible and flexible with an increasing understanding of the most likely mechanisms of synthesis and functionalization of these materials. Also, one needs to cleverly combine concepts of inorganic solid chemistry with organic and host–guest chemistry to find a niche to apply synthetic hectorite in the ever-growing area of catalysis, nanotechnology and bioengineering [123, 124].

**Acknowledgement** This work was supported by the NSF of China (Nos. 20773110; 20541002) and the NSF of Zhejiang Province of China (Nos. Y405064; Y407200; Y405025, and Zhejiang 151 Talent project) and partly financed by Zhejiang Provincial Personnel Department for Excellent Projects of Science and Technology by Returned Researchers in China from overseas. The authors also want to thank International Cooperation Project (2009C14G2020021) from the Science and Technology Department of Zhejiang Provincial Government for the related research and development.

## References

1. Murray HH (2000) Traditional and new applications for kaolin, smectite, and palygorskite: a general overview. *Appl Clay Sci* 17:207
2. Bergaya F, Theng BKG, Lagaly G (2006) *Handbook of clay science*, vol 1. Elsevier B.V, Amsterdam
3. Foshag WF, Woodford AO (1936) Bentonitic magnesian clay mineral from California. *Am Miner* 21:238



4. Guggenheim S, Adams JM, Bain DC, Bergaya F, Brigatti MF, Drits VA, Formoso MLL, Galán E, Kogure T, Stanjek H (2006) Summary of recommendations of nomenclature committees relevant to clay mineralogy: Report of the Association Internationale pour l'Etude des Argiles (AIPEA) Nomenclature. *Clays Clay Miner* 54:76
5. Klopogge JT (1998) Synthesis of smectites and porous pillared clay catalysts: a review. *J Porous Mater* 5:5
6. Güven N, (1988) Smectites. In: Bailey SW (ed) *Reviews in mineralogy*, vol 19, Hydrous phyllosilicates. Mineralogical Society of America, Washington, DC, pp 497–559
7. Newman ACD (1987) *Chemistry of clays and clay minerals*, vol 6. Mineralogical Society Monograph, London, p 480
8. <http://ruff.geo.arizona.edu/doclib/hom/hectorite.pdf>
9. Grim RE (1968) *Clay mineralogy*, 2nd edn. McGraw-Hill, New York, NY
10. Breen C (1991) Thermogravimetric study of the desorption of cyclohexylamine and pyridine from an acid-treated Wyoming bentonite. *Clay Miner* 26:473
11. Rhodes CN, Brown DR (1993) Surface-properties and porosities of silica and acid-treated montmorillonite catalyst supports-influence on activities of supported  $ZnCl_2$  alkylation catalysts. *J Chem Soc Faraday Trans* 89:1387
12. Vaccari A (1999) Clays and catalysis: a promising future. *Appl Clay Sci* 14:161
13. Plaiziervercammen J (1992) Rheological properties of laponite-xl<sub>g</sub>, a synthetic purified hectorite. *Pharmazie* 47:856
14. ITC (1998) Surface modified sodium hectorite. Technical report AMN-6000. <http://www.itcglobal.com>
15. Brindley GW, Brown G (1980) Monograph no. 5: crystal structures of clay minerals and their X-ray diffraction. Mineralogical Society, London
16. Joshi YM (2007) Model for cage formation in colloidal suspension of laponite. *J Chem Phys* 127:102
17. Mori Y, Togashi K, Nakamura K (2001) Colloidal properties of synthetic hectorite clay dispersion measured by dynamic light scattering and small angle X-ray scattering. *Adv Powder Technol* 12:45
18. Pavlidou S, Papaspyrides CD (2008) A review on polymer-layered silicate nanocomposites. *Prog Polym Sci* 33:1119
19. Greaves RC, Bond SP, McWhinnie WR (1995) Conductivity studies on modified laponites. *Polyhedron* 14:3635
20. Singhal RG, Capracotta MD, Martin JD, Khan SA, Fedkiw PS (2004) Transport properties of hectorite based nanocomposite single ion conductors. *J Power Sources* 128:247
21. Van Rompaey K, Van Ranst, E, De Coninck F, Vindevogel N (2002) Dissolution characteristics of hectorite in inorganic acids. *Appl Clay Sci* 21:241
22. Harder H (1969) *Naturwissenschaften* 56:279
23. Granquist WT, Pollack SS (1959) A study of the synthesis of hectorite. *Clays Clay Miner* 8:150
24. Baird T, Cairns-Smith AG, MacKenzie DW (1973) An electron microscope study of magnesium smectite synthesis. *Clay Miner* 10:17
25. Baird T, Cairns-Smith AG, MacKenzie DW, Snell D (1971) Electron microscope studies of synthetic hectorite. *Clay Miner* 9:250
26. Zhou C, Du ZX, Li XN, Lu CS, Ge ZH (2005) Structure development of hectorite in hydrothermal crystallization synthesis process. *Chin J Inorg Chem* 21:1327
27. Harder H (1972) The role of magnesium in the formation of smectite minerals. *Chem Geol* 10:31
28. Barrer RM, Dicks LWR (1967) *Chemistry of soil minerals*. Part IV. Synthetic alkylammonium montmorillonites and hectorites. *J Chem Soc A* :1523
29. Barrer RM, Jones DL (1970) *Chemistry of soil minerals*. Part VIII. Synthesis and properties of fluorhectorites. *J. Chem Soc A* :1531
30. Barrer RM, Craven RJB (1992) Smectite molecular-sieves .4. kinetics of intercalation in microporous fluorhectorites. *J Chem Soc Faraday Trans* 88:645

31. Neumann BS, Sansom KG (1976) Synthesis of hydrous magnesium silicates. US Patent 3,954,943
32. Neumann BS (1977) Production of magnesium silicates. US Patent 4,049,780
33. Neumann BS, Sansom KG (1970) The formation of stable sols from Laponite, a synthetic hectorite-like clay. *Clay Miner* 8:389
34. Neumann BS (1971) Synthetic hectorite-type clay minerals. US Patent 3,586,478
35. Neumann BS (1972) Synthetic clay-like minerals of the smectite type and method of preparation. US Patent 3,671,190
36. Torii K, Iwasaki T (1986) Synthesis of new trioctahedral Mg-smectite. *Chem Soc Japan Chem Lett* 1986:2012
37. Torii K, Iwasaki T (1987) Synthesis of hectorite. *Clay Sci* 7:1
38. <http://www.scprod.com/chembriefs/ChemBrief%20V1%20I2.pdf> (2009-01-07)
39. Orlemann JK (1972) Process for producing synthetic hectorite-type clays. US Patent 3,666,407
40. Harder H (1975) Synthese von Zink-Montmorin (Smektit) unter Oberflächenbedingungen. *Naturwissenschaften* 62:235
41. Higashi S, Miki K, Komarneni S (2002) Hydrothermal synthesis of Zn-smectites. *Clays Clay Miner* 50:299
42. Higashi S, Miki H, Komarneni S (2007) Mn-smectites: Hydrothermal synthesis and characterization. *Appl Clay Sci* 38:104
43. Finck N, Dardenne K, Schlegel ML, Bosbach D (2007) Structural incorporation of trivalent f elements into the trioctahedral clay mineral hectorite. *Geochim Cosmochim Acta* 71:A279
44. Pieper H, Bosbach D, Panak PJ, Rabung T, Fanghanel T (2006) Eu(III) coprecipitation with the trioctahedral clay mineral, hectorite. *Clays Clay Miner* 54:45
45. Ogawa M, Matsutomo T, Okada T (2008) Preparation of hectorite-like swelling silicate with controlled layer charge density. *J Ceram Soc Jpn* 116:1309
46. Vicente I, Salagre P, Cesteros Y, Guirado F, Medina F, Sueiras JE (2009) Fast microwave synthesis of hectorite. *Appl Clay Sci*, 43:103
47. Carrado KA (2000) Synthetic organo- and polymer-clays: preparation, characterization, and materials applications. *Appl Clay Sci* 17:1
48. Seidl W, Breu J (2005) Single crystal structure refinement of tetramethylammonium-hectorite. *Z Kristallog* 220:169
49. Fujii K, Hayashi S (2005) Hydrothermal syntheses and characterization of alkylammonium phyllosilicates containing  $\text{CSiO}_3$  and  $\text{SiO}_4$  units. *Appl Clay Sci* 29:235
50. Carrado KA, Thiyagarajan P, Elder DL (1997) Porous networks derived from synthetic polymer-clay complexes. In: Occelli ML, Kessler H (eds) *Synthesis of porous materials: zeolites, clays, and nanostructures*. Marcel Dekker, New York, NY, p 551
51. Fan NQ, Xia HS, Jiang GF, Tong DS, Lin CX, Zhou CH (2009) Investigation on controllability of metal coordination and crystallinity in synthetic cationic hectorite-like solids. In: Fiore S, Belviso C, Giannossi ML (eds) *Micro et Nano: Scientiæ Mare Magnum*, Vol.I. 14th Intl. Clay Conf., Castellana Grotte, Italy. Digilabs s.a.s Pub., Bari, Italy, P332
52. Klopogge JT, Frost RL, Hickey L (2000) Infrared emission spectroscopic study of the dehydroxylation of some hectorites. *Thermochimica Acta* 345:145
53. Komadel PM, Janek JM, Gates WP, Kirckpatrick RJ, Stucki JW (1996) Dissolution of hectorite in inorganic acids. *Clays Clay Miner* 44:228
54. Gerstman A, Urbanczyk L, Jerome R, Robert JL, Grandjean J (2008) XRD and NMR characterization of synthetic hectorites and the corresponding surfactant-exchanged clays. *Clay Miner* 43:205
55. Schwieger W, Pohl K, Brenn U, Fyfe CA, Grondey H, Fu G, Kokotailo GT (1995) Isomorphous substitution of silicon by boron or aluminum in layered silicates. *Stud Surf Sci Catal* 94:47
56. Houghton HA, Hasnain IA, Donald AM (2008) Particle tracking to reveal gelation of hectorite dispersions. *European Phys J E* 25:119

57. Marry V, Malikova N, Cadene A, Dubois E, Durand-Vidal S, Turq P, Breu J, Longeville S, Zanotti JM (2008) Water diffusion in a synthetic hectorite by neutron scattering-beyond the isotropic translational model. *J Phys Condensed Matter* 20:104205
58. Malikova N, Cadene A, Dubois E, Marry V, Durand-Vidal S, Turq P, Breu J, Longeville S, Zanotti JM (2007) Water diffusion in a synthetic hectorite clay studied by quasi-elastic neutron scattering. *J Phys Chem C* 111:17603
59. Brandt H, Bosbach D, Panak PJ, Fanghaenel T (2007) Structural incorporation of Cm(III) in trioctahedral smectite hectorite: A time-resolved laser fluorescence spectroscopy (TRLFS) study. *Geochim Cosmochim Acta* 71:145
60. Spagnuolo M, Martinez CE, Jacobson AR, Baveye P, McBride MB, Newton J (2004) Coprecipitation of trace metal ions during the synthesis of hectorite. *Appl Clay Sci* 27:129
61. Kang IM, Kim MH, Kim YJ, Moon HS, Song Y (2006) Effect of layer structure boundary on the hectorite basal diffraction. *Powder Diffraction* 21:30
62. Schoonheydt RA (1991) In: van Bekkum H, Flanigen EM, Jansen JC (eds) Introduction to zeolite. Science and practice. Chapter 6. Clays from two to three dimensions. Elsevier, Amsterdam, p 201
63. Occelli ML, Iyer PS, Sanders JV (1989) The pillaring of a synthetic hectorite with organic cations. *Stud Surf Sci Catal* 49(Part 1):469
64. So H, Jung H, Choy JH, Belford RL (2005) Electron paramagnetic resonance study of partially oriented clay platelets intercalated with copper(II) 1,4,8,11-tetraazacyclotetradecane. *J Phys Chem B* 109:3324
65. Breu J, Seidl W, Senker J (2004) Synthesis of threedimensionally ordered intercalation compounds of hectorite. *Z Anorg Allg Chem* 630:80
66. Yamaguchi N, Shimazu S, Ichikuni N, Uematsu T (2004) Synthesis of novel nano-structured clays: Unique conformation of pillar complexes. *Chem Lett* 33:208
67. McWhinnie WR, Ashcroft RC, Bond SP, Beevers MS, Lawrence MA, Gelder MA, Berry FJ (1992) <sup>119</sup>Sn Mössbauer and X-ray photoelectron studies of novel tin oxide pillared laponite formed under ambient conditions from aryltin precursors-Rapid intercalation reactions using microwave heating. *Polyhedron* 11:1001
68. Drame H (2005) Cation exchange and pillaring of smectites by aqueous Fe nitrate solutions. *Clays Clay Miner* 53:335
69. Cool P, Vansant EF (1996) Preparation and characterization of zirconium pillared laponite and hectorite. *Microporous Mater* 6:27
70. Occelli ML, Finseth DH (1986) Preparation and characterization of pillared hectorite catalysts. *J Catal* 99:316
71. Palinko I, Molnar A, Nagy JB, Lazar K, Valyon J, Kiricsi I (1997) Mixed-metal pillared layer clays and their pillaring precursors. *J Chem Soc Faraday Trans* 93:1591
72. Kollár T, Kónya Z, Pálkó I, Kiricsi, I (2001) Intercalation of various oxide species in-between Laponite layers studied by spectroscopic methods. *J Mol Struct* 563–564:417
73. Zhou C, Li XN, Ge ZH, Li QW, Tong DS (2004) Synthesis and acid catalysis of nanoporous silica/alumina-clay composites. *Catal Today* 93–95:607
74. Zhou C, Tong DS, Bao M, Du ZX, Ge ZH, Li XN (2006) Generation and characterization of catalytic nanocomposite materials of highly isolated iron nanoparticles dispersed in clays. *Topics Catal* 39:213
75. Bergaya F, Hassoun N, Gatineau L, Barrault J (1991) Mixed Al-Fe pillared laponites: preparation, characterization and catalytic properties in syngas conversion. *Stud Surf Sci Catal* 63:329
76. Molina R, Moreno S, Poncelet G. (2000) Al-pillared hectorite and montmorillonite prepared from concentrated clay suspensions: structural, textural and catalytic properties. *Stud Surf Sci Catal* 130(Part 2):983
77. Pinnavaia TJ, Tzou M-S, Landau SD, Raythatha RH (1984) Ordered forms of dianionic guanosine 5'-monophosphate with Na<sup>+</sup> as the structure director <sup>1</sup>H and <sup>31</sup>P NMR studies of

- hydrogen-bonding and comparisons of stacked tetramer and stacked dimer models. *J Mol Catal* 27:195
78. Occelli ML, Lynch J, Senders J (1987) TEM analysis of pillared and delaminated hectorite catalysts. *J Catal* 107:557
  79. Li W, Sirilumpen M, Yang RT (1997) Selective catalytic reduction of nitric oxide by ethylene in the presence of oxygen over Cu<sup>2+</sup> ion-exchanged pillared clays. *Appl Catal B* 11:347
  80. Lewis RM, Kuroda H (1989) Delaminated layered materials. *Solid State Ionics* 32–33:373
  81. Diaz M, Cambier P, Brendle J, Prost R (2007) Functionalized clay hetero structures for reducing cadmium and lead uptake by plants in contaminated soils. *Appl Clay Sci* 37:12
  82. Torii K, Iwasaki T, Onodera Y, Hatakeda K (1991) Mesoporous materials produced from hydrothermally synthesized hectorites. *Stud Surf Sci Catal* 60:81
  83. Stocker M, Seidl W, Seyfarth L, Senker J, Breu J (2008) Realisation of truly microporous pillared clays. *Chem Comm* 5:629
  84. Han ZH, Zhu HY, Shi J, Lu GQ (2006) A straightforward wet-chemical route to the nanocomposites of general layered clays and metal sulfides. *Mater Lett* 60:2309
  85. Tawkaew S, Fujishiro Y, Yin S, Sato T (2001) Synthesis of cadmium sulfide pillared layered compounds and photocatalytic reduction of nitrate under visible light irradiation. *Colloid Surf A* 179:139
  86. Han ZH, Zhu HY, Ratinac KR, Ringer SP, Shi J, Liu J (2008) Nanocomposites of layered clays and cadmium sulfide: similarities and differences in formation, structure and properties. *Micropor Mesopor Mater* 108:168
  87. Onal M, Sankaya Y (2007) Preparation and characterization of acid-activated bentonite powders. *Powder Technol* 172:14
  88. Figueras F (1988) Pillared clays as catalysts. *Catal Rev Sci Eng* 30:457
  89. Tyagi B, Chudasama CD, Jasra RV (2006) Determination of structural modification in acid activated montmorillonite clay by FT-IR spectroscopy. *Spectrochim Acta A* 64:273
  90. Fernandes C, Catrinescu C, Castilho P, Russo PA, Carrott MR, Breen C (2007) Catalytic conversion of limonene over acid activated Serra de Dentro (SD) bentonite. *Appl Catal A* 318:108
  91. Van Rompaey K, Van Ranst E, De Coninck F, Vindevogel N (2002) Dissolution characteristics of hectorite in inorganic acids. *Appl Clay Sci* 21:241
  92. Kuwahara Y (2006) In-situ AFM study of smectite dissolution under alkaline conditions at room temperature. *Am Miner* 91:1142
  93. Shabtai J (1980) Class of cracking catalysts acidic forms of cross-linked smectites. US Patent 4,238,364
  94. Miller KE, Bruno TJ (2004) Thermally-treated clay as a stationary phase in liquid chromatography. *J Chrom A* 1042:49
  95. Suzuki E, Idemura S, Ono Y (1988) Catalytic conversion of 2-propanol and ethanol over synthetic hectorite and its analogues. *Appl Clay Sci* 3:123
  96. Frey ST, Hutchins BM, Anderson BJ, Schreiber TK, Hagerman ME (2003) Catalytic hydrolysis of 4-nitrophenyl phosphate by lanthanum(III)-hectorite. *Langmuir* 19:2188
  97. Nishiyama Y, Arai M, Guo S-L, Sonehara N, Naito T, Torii K (1993) Catalytic properties of hectorite-like smectites containing nickel. *Appl Catal A* 95:171
  98. Gil A, Vicente MA, Lambert JF, Gandía LM (2001) Platinum catalysts supported on Al-pillared clays – Application to the catalytic combustion of acetone and methyl-ethyl-ketone. *Catal Today* 68:41
  99. Bodman SD, McWhinnie WR, Begon V, Millan M, Suelves I, Lazaro MJ, Herod AA, Kandiyoti R (2003) Metal-ion pillared clays as hydrocracking catalysts (II): effect of contact time on products from coal extracts and petroleum distillation residues. *Fuel* 82:2309
  100. Papp S, Dekany I (2006) Nucleation and growth of palladium nanoparticles stabilized by polymers and layer silicates. *Colloid Polym Sci* 284:1049

101. Manikandan D, Divakar D, Sivakumar T (2007) Utilization of clay minerals for developing Pt nanoparticles and their catalytic activity in the selective hydrogenation of cinnamaldehyde. *Catal Comm* 8:1781
102. Mastalir A, Szollosi G, Kiraly Z, Razga Z (2002) Preparation and characterization of platinum nanoparticles immobilized in dihydrocinchonidine-modified montmorillonite and hectorite. *Appl Clay Sci* 22:9
103. Shimazu S, Teramoto W, Iba T, Miura M, Uematsu T (1989) Selective hydrogenation of alkynes by hectorite-intercalated Pd(II) complexes. *Catal Today* 6:141
104. Hagerman ME, Salamone SJ, Herbst RW, Payeur AL (2003) Tris (2,2'-bipyridine) ruthenium (II) cations as photoprobes of clay tactoid architecture within hectorite and laponite films. *Chem Mater* 15:443
105. Suss-Fink G, Moollwitz B, Therrien B, Dadras M, Laurency G, Meister A, Meister G. (2007) Ruthenium nanoparticles intercalated in hectorite: a reusable hydrogenation catalyst for benzene and toluene. *J Cluster Sci* 18:87
106. Occelli ML, Landau SD, Pinnavaia TJ (1984) Cracking selectivity of a delaminated clay catalyst. *J Catal* 90:256
107. Pereira C, Patricio S, Silva AR, Magalhaes AL, Carvalho AP, Pires J, Freire C (2007) Copper acetylacetonate anchored onto amine-functionalised clays. *J Coll Interf Sci* 316:570
108. Carrado KA, Kim JH, Song CS, Castagnola N, Marshall CL, Schwartz MM (2006) HDS and deep HDS activity of CoMoS-mesostructured clay catalysts. *Catal Today* 116:478
109. Mogyrosi K, Dekany I, Fendler JH (2003) Preparation and characterization of clay mineral intercalated titanium dioxide nanoparticles. *Langmuir* 19:2938
110. Ooka C, Yoshida H, Suzuki K, Hattori T (2004) Highly hydrophobic TiO<sub>2</sub> pillared clay for photocatalytic degradation of organic compounds in water. *Micropor Mesopor Mater* 67:143
111. Belessi V, Lambropoulou D, Konstantinou I, Katsoulidis A, Pomonis P, Petridis D, Albanis T (2007) Structure and photocatalytic performance of TiO<sub>2</sub>/clay nanocomposites for the degradation of dimethachlor. *Appl Catal B* 73:292
112. Robertson J, Bandosz TJ (2006) Photooxidation of dibenzothiophene on TiO<sub>2</sub>/hectorite thin films layered catalyst. *J Colloid Inter Sci* 299:125
113. Szabo T, Nemeth J, Dekany I (2002) Zinc oxide nanoparticles incorporated in ultrathin layer silicate films and their photocatalytic properties. *Coll Surf A* 230:23
114. Korosi L, Nemeth J, Dekany I (2004) Structural and photooxidation properties of SnO<sub>2</sub>/layer silicate nanocomposites. *Appl Clay Sci* 27:29
115. Aldushin K, Jordan G, Schmahl WW (2006) Basal plane reactivity of phyllosilicates studied in situ by hydrothermal atomic force microscopy (HAFM). *Geochim. Cosmochim Acta* 70:4380
116. Baskaralingam P, Pulikesi M, Ramamurthi V, Sivanesan S (2006) Equilibrium studies for the adsorption of acid dye onto modified hectorite. *J Hazard Mater* 136:989
117. Karmous MS, Oueslati W, Ben Rhaïem H, Robert JL, Amara ABH (2007) Simulation of the XRD patterns, structural properties of a synthetic Na-Hectorite exchanged Cu<sup>2+</sup> and Ca<sup>2+</sup>. *Z Kristallog* 2:503
118. Bourninos AB, Jiang DD, Giannelis EP (2004) Clay-organosiloxane hybrids: a route to cross-linked clay particles and clay monoliths. *Chem Mater* 16:2404
119. Moncada E, Quijada R, Retuert J (2007) Comparative effect of metallocene and Ziegler-Natta polypropylene on the exfoliation of montmorillonite and hectorite clays to obtain nanocomposites. *J Appl Polymer Sci* 103:698
120. Schlegel ML (2008) Polarized EXAFS characterization of the sorption mechanism of yttrium on hectorite. *Radiochim Acta* 96:667
121. Baskaralingam P, Pulikesi M, Ramamurthi V, Sivanesan S (2007) Modified hectorites and adsorption studies of a reactive dye. *Appl Clay Sci* 37:207
122. Riley MW, Fedkiw PS, Khan SA (2003) Lithium hectorite clay as the ionic conductor in LiCoO<sub>2</sub> cathodes. *J Electrochem Soc* 150:A933

123. Carrado KA, Macha SM, Tiede DM (2004) Effects of surface functionalization and organo-tailoring of synthetic layer silicates on the immobilization of cytochrome c. *Chem Mater* 16:2559
124. Spagnuolo M, Jacobson AR, Baveye P (2005) Electron paramagnetic resonance analysis of the distribution of a hydrophobic spin probe in suspensions of humic acids, hectorite, and aluminum hydroxide-humate-hectorite complexes. *Environ Toxicol Chem* 24:2435

# Chapter 5

## Transition Metal Oxide-Pillared Clay Catalyst: Synthesis to Application

Trilochan Mishra

**Abstract** This chapter deals with the reviews of some important first row transition metal oxide-pillared clays. In particular, synthesis and applications of titanium, iron, chromium, manganese oxide and reported mixed oxide-pillared materials were discussed in detail with emphasis on future potential as catalysts. Use of different cationic precursors for material synthesis and their effect on stability, basal spacing and surface area are analyzed. Use of these pillared clays in some important catalytic reactions is also briefly reviewed.

**Keywords** Pillared clay catalysts · Transition metal oxide

### 5.1 Introduction

Parallel to the development of new methods for zeolite synthesis, other appropriate routes have been explored for the synthesis of porous materials for use as catalysts in the petrochemical, chemical industries and separation technologies. Pillared layered material is one of the promising porous materials which can be utilized as catalyst in a number of reactions. One of the most important concerns is the preparation of stable pillared layered structures derived from layered materials; mainly clays [1–5]. In the late 1970s, microporous clay intercalation compounds pillared with metal oxide clusters were prepared. These microporous materials were obtained by exchanging the interlayer cations of smectite clays with bulky inorganic cations followed by calcination. On heating, the intercalated cations are converted to metal oxide clusters, propping open the layers as pillars, generating interlayer space of molecular dimensions, i.e. a two-dimensional porous network. Consequently, bi-dimensional zeolite-like materials with high thermal stability and high surface

---

T. Mishra (✉)

ACC Division, National Metallurgical Laboratory CSIR, Jamshedpur 831007, India  
e-mail: drtmishra@yahoo.com

areas were made, which are called pillared interlayered clays (PILCs) or cross-linked clays. The micropore structure is tailored by the nature of the host material and of the pillaring species and may have pore sizes larger than those of zeolites and zeolite-related materials. Furthermore, intrinsic catalytic activity is induced in the pillared interlayered solids according to the nature of the pillar. Thus, the pillared derivatives have received widespread interest as a new type of microporous solid that can serve as shape selective catalysts, separating agents, supports, sorbents, etc [5]. Subsequently, various host materials other than smectite clays have also been employed to generate new catalytic materials [6–8]. However, pillared clay is found to be most interesting and studied extensively in comparison to that of other pillared layered structures.

Thirty years have passed since the first announcement of pillared interlayered clay. The preparative techniques have progressed remarkably with a wide variety of pillared solids being made. Recent advances in the synthesis of pillared clay have expanded considerably the scope of their potential catalytic applications. As a result there is now a renewed interest in the pillared material as polyfunctional catalysts and catalyst supports [9]. In particular transition metal-pillared clay can be an interesting catalytic material as the pillar itself is catalytically active due to the presence of both redox and acid–base characteristics. In these contexts first row transition metals like iron, titanium, vanadium and chromium-pillared materials are mostly studied. So there is enough scope of developing new catalytic materials for different applications by varying the transition metal oxide pillars only. This area of research is still growing and need further exploration as potential catalyst which is very limited in the literature [10–13]. This chapter will elaborate on the development and future scope of transition metal oxide-pillared clay materials as potential catalyst for number of reactions. In particular this review mainly deals with the development in synthesis and use of titanium, iron, chromium and manganese-pillared clays.

## 5.2 Pillaring Process

In general, preparation of porous pillared materials consists of a direct exchange of the interlayer cations of smectite clays by cationic precursors to form stable metal oxide pillars. In the synthesis of intercalated clays, the preparation of metal precursors is a crucial step. Cationic precursors can be categorized into four different groups, namely, (I) polynuclear metal hydroxo or oxo complex ions, (II) metal chelate complex ions, (III) metal cluster complex ions and (IV) positively charged colloidal particles. On heating, these intercalated species are converted to metal oxide pillars, propping open the smectite layers. In some cases type of pillaring species also plays an important role in material synthesis. Pore size and structure are mostly controlled by the synthesis technique and the cationic pillaring species used. Briefly speaking different types of cationic species are used to obtain stable pillared materials with increased gallery height.



### 5.2.1 Polynuclear Metal Oxo–hydroxo Cations

These are the most commonly used pillaring agents that are usually obtained by hydrolysis of metal salts at specific pH so as to obtain polymeric hydroxyl metal cationic species. Therefore initial pillared clays are limited to most of the non-transition metal oxides like alumina and silica-pillared clays. However, only a limited number of transition metals such as iron, chromium, titanium and zirconium can form stable polycationic metal precursors. Mostly the  $M_{13}$  oligomeric species formed by the base hydrolysis at specific OH/M ratio proved to be the better pillaring species. Among the transition metals iron, chromium and zirconium form  $M_{13}$  polyoxocatinic species similar to aluminium and gallium. For other transition metal elements, it is difficult to produce stable partial hydrolysis products although these oxides are quite useful as catalyst for number of reactions. This aspect promoted researchers to find some alternative method for intercalating stable transition metal oxide pillars. Subsequently this limitation was removed to some extent by use of other metal complexes by number of researchers as discussed below.

### 5.2.2 Cationic Metal Complex

Incorporation of metal chelate cations  $M(\text{chel})_3^{2+}$  ( $M = \text{Fe}, \text{Ni}$ ;  $\text{chel} = \text{phen}, \text{bpy}$ ) into smectite clays and subsequent calcination provided iron oxide and nickel oxide-pillared materials [14]. Moreover, pillared smectites with a double oxide ( $\text{LaNiOx}$ ) were prepared by intercalation of a heterobinuclear cationic chelate complex of the form  $\text{NiLa}(\text{fsaen})^+$  ( $\text{H}_4\text{fsaen} = \text{N}, \text{N-3-hydroxysalicylideneethylenediamine}$ ) into smectite followed by calcination [15]. The products after  $500^\circ\text{C}$  calcination had an interlayer spacing of  $3.8 \text{ \AA}$  and a BET surface area of  $220 \text{ m}^2/\text{g}$ . Incorporation of trinuclear acetate complex gives rise to several new transition metal oxide pillars with high thermal stability and surface area. In particular  $\text{Fe(III)}$ ,  $\text{Cr(III)}$  and  $\text{Mn(III)}$  form stable cationic complexes which can be intercalated as individual or in mixed state inside the layered material structure. Trinuclear chromium formate also forms the similar structures and can be pillared [16]. Only  $\text{Mn(III)}$  complex is not stable in aqueous solution and hence nonaqueous solution is to be used for pillaring purposes. New pillared clays like manganese oxide [17] and mixed oxides like iron–manganese-pillared clays [18] were synthesized using the said complexes as precursors. So the use of metal chelates mostly increases the number of possible metal oxide-pillared clays.

### 5.2.3 Metal Cluster Complex

This is a new approach of intercalating rare transition metal oxide pillars inside the clay structure. Pillaring of smectite with niobium and tantalum oxides was achieved with the cation exchange and subsequent oxidation of niobium and tantalum cluster

cations of the type  $M_6Cl_{12}^{n+}$  ( $n = 2,3$ ;  $M = Nb, Ta, Mo$ ). The niobium oxide and tantalum oxide-pillared clays after calcination at  $325^\circ\text{C}$  exhibited an interlayer spacing of  $9\text{ \AA}$  and BET surface area of  $60\text{--}70\text{ m}^2/\text{g}$  [19] only.

### 5.2.4 Positively Charged Colloidal Particles

Through a new approach positively charged metal oxide sols can be intercalated into the interlayer of clays by cation-exchange reactions, providing pillared materials after calcination. Although pillared materials with super galleries were made, the pore structure is not homogeneous, and the pore size distribution occurs over a broad range because the interlamellar region is stuffed with flocculated sol particles of different sizes. Using this pillaring technique,  $\text{TiO}_2$ -pillared smectites with gallery height of  $13\text{ \AA}$  and BET surface area of  $300\text{ m}^2/\text{g}$  after heat treatment at  $300^\circ\text{C}$  [20],  $(\text{SiO}_2\text{--TiO}_2)$ -pillared smectites [21],  $\text{Al}_2\text{O}_3$ -pillared smectites [22, 23] and  $\text{SiO}_2$ -pillared smectites [24] were obtained. Moreover, pillared clays with mesopores were obtained from  $(\text{SiO}_2\text{--TiO}_2)$ -pillared clays when modified by surfactant [25]. Mesoporous clay compositions were synthesized recently containing diverse well-dispersed transition metal oxides by using nanoparticles of hydroxide species as precursors by an innovative approach [26]. Oxide pillaring species of transition metals like iron, chromium, cobalt, manganese and cerium were prepared by dissolving the corresponding metal hydroxides in aqueous solution of acetic acid. These precursors were used to substitute the sodium ions in laponite clay like the way to prepare pillared clays, forming mesoporous solids with high surface areas of  $510\text{--}640\text{ m}^2/\text{g}$ . Stabilized by the adsorbed acetic acid molecules, the nanoparticle precursors of the metal oxides were well dispersed on the silicate platelets during the synthesis. The increase in the porosity after the intercalation of nanoparticles is primarily interpreted in terms of further delamination of the laponite clay caused by the reaction between the acidic metal precursor solutions and the silicate platelets. Supercritical drying of smectites intercalated with colloidal particles leads to the formation of a card-house structure, generating much larger pore volume including mesopore and macropore than air-dried samples [27, 28]. Monodispersed sol particles having the same diameter may be produced by the homogeneous precipitation method [29]. Here one must devise a technique of introducing the monodispersed particles without flocculation into the interlayer of clays.

## 5.3 Synthesis of Transition Metal Oxide-Pillared Clays

Synthesis, textural parameters and studied applications are summarized in Table 5.1 for all the reviewed transition metal oxide-pillared clays. This gives an overall picture of the so far studied materials. Here we are more concerned for the first row transition metal oxide-pillared materials like titanium, iron, chromium, manganese and their mixed oxides. Different approach of synthesis of all the materials is discussed separately below.

**Table 5.1** Textural properties and studied application of different transition metal-pillared clays

Type of pillar	Pillaring source	Basal spacing (Å)	Surface area (m <sup>2</sup> /g)	Pretreatment conditions/clay	Catalytic application	References
Titania	TiCl <sub>4</sub>	28.3	258		Nitric oxide reduction with ammonia	[124]
	TiCl <sub>4</sub>	Diffuse	263	Pillared hectorite		[84]
	TiCl <sub>4</sub>	24	200–300	Depends on preparation temperature		[38]
	Ti alkoxides	21.5–26	200–350	Depends on pretreatment temperature	Photocatalytic reaction	[45]
	TiCl <sub>4</sub>	14.2	144		Photocatalytic activity	
Iron oxide	TiCl <sub>4</sub>	Diffuse	277	Ca-montmorillonite	Degradation of Acid Red G	[37]
	Polyoxycations	–	140	1000–1200 °C	Photocatalytic degradation of airborne styrene	[48]
	Fe <sub>3</sub> (OH) <sub>4</sub> Cl <sub>5</sub>	13.8	144	Collapsed at 400 °C		[58]
	FeCl <sub>3</sub>	18–25	210–130	Surface area decreases with pretreatment temperature		[156]
	Fe(NO <sub>3</sub> ) <sub>3</sub>	26.4	217	At room temperature	NO <sub>x</sub> reduction	[124]
	Fe(III) acetate complex	21.5–16.7	300	Maximum at 350 °C	–	[60]
	Fe(III) acetate complex			Maximum at 500 °C/montmorillonite clay	Nitration	[62, 111]
	Fe salt	25–29	270–350	350 °C	Fischer-Tropsch synthesis of hydrocarbons	[55]

Table 5.1 (continued)

Type of pillar	Pillaring source	Basal spacing (Å)	Surface area (m <sup>2</sup> /g)	Pretreatment conditions/clay	Catalytic application	References
	Ferric hydroxide + acetic acid	Diffused	451–510	–	VOC decomposition	[26]
Chromium oxide	Cr(NO <sub>3</sub> ) <sub>3</sub>	18.0		Stable		[74]
	Cr(NO <sub>3</sub> ) <sub>3</sub>	27–22	430–350	Stable up to 500 °C	–	[66]
	Cr(OAc) <sub>3</sub>	20.4–15.3	350–275	Stable up to 625 °C	–	[78]
	Cr(OAc) <sub>3</sub> complex	17.8	286	Stable up to 500 °C/montmorillonite clay	Cumene cracking, alcohol dehydration	[79, 111]
	Cr(oxyformate) <sub>3</sub>	15.8–16.4	158	Stable up to 550 °C/montmorillonite clay	–	[16]
Manganese oxide Iron–chromium mixed oxide	Cr(OAc) <sub>3</sub> complex	21.2–16.8	268	Stable up to 500 °C	Nitration	[17, 111]
	Cr(oxyformate) <sub>3</sub>	22–16.8	280–252	Stable up to 500 °C/montmorillonite clay	Methanol dehydration, cumene cracking	[86]
Iron–manganese mixed oxide		16.5–16.9	268–286	Stable up to 500 °C/montmorillonite clay		
Fe–Ti	Ti-isopropoxide + Fe(NO <sub>3</sub> ) <sub>3</sub>	21.2–16.8	173	Stable up to 500 °C	Nitration	[87]

### 5.3.1 Titanium Oxide-Pillared Clays

Despite the interesting catalytic properties of  $\text{TiO}_2$ , Ti-pillared clays (Ti-PILCs) have received less attention than the other oxide-pillared clays. Generally, Ti-PILCs are prepared by exchanging charge-compensating cations between the clay layers with larger inorganic hydroxyl cations, which are polymeric or oligomeric hydroxy metal cations formed by the hydrolysis of metal salts [30, 31]. There are two traditional methods for the synthesis of the precursors of  $\text{TiO}_2$ : hydrolysis of  $\text{TiCl}_4$  [32] and  $\text{TiOSO}_4$  [30] or the sol-gel method [33]. Both methods have proven to be suitable for the preparation of Ti-PILCs, although the first one requires careful handling of  $\text{TiCl}_4$ . Miao et al. prepared a  $\text{TiO}_2$ -pillared montmorillonite via impregnating titanium tetrabutoxide into the interlayers of montmorillonite in supercritical ethanol, which showed an excellent ability to catalytically degrade Methylene Blue [34]. Ooka et al. synthesized  $\text{TiO}_2$ -pillared clay by hydrothermal treatment at different temperatures for different times and investigated the dependence of the crystallization of  $\text{TiO}_2$  pillars on the photocatalytic activity [35]. With another approach  $\text{TiO}_2$ -pillared clay was synthesized by microwave irradiation, which exhibited a good photocatalytic performance [36]. The calcination process is usually necessary for the preparation of  $\text{TiO}_2$ -PILCs. However, Zhang et al. obtained the  $\text{TiO}_2$ -pillared montmorillonite [37] with the anatase phase of  $\text{TiO}_2$  without calcination via hydrolyzing  $\text{TiCl}_4$  into an HCl aqueous solution and then intercalating titanium polycations into the interlayer of montmorillonite through cation-exchange process. Among the pillared clays, Ti-PILCs have the following remarkable characteristics: (a) they have a high thermal stability; [32, 38] (b) their large pore sizes allow further incorporation of active species without hindering pore diffusion; [39] (c) intercalating  $\text{TiO}_2$  between the  $\text{SiO}_2$  tetrahedral layers is a unique way of increasing the surface area and acidity of the  $\text{TiO}_2$  support; [40] (d) Ti-PILC-based catalysts have shown to be excellent for the selective catalytic reduction (SCR) of NO by  $\text{NH}_3$  or hydrocarbons [3, 41–43] and they have been found to be highly resistant to  $\text{SO}_2$  poisoning and also possess durability [39, 40, 44]. Del Castillo and Grange [45] determined that  $\text{Ti}(\text{OEt})_4$  (titanium tetraethoxide) gave a polycationic precursor that gave a PILC of regular structure and was stable at  $600^\circ\text{C}$ . Regulating the pillar size and distribution was difficult as it depended greatly on solution pH and reaction temperature. The acidity of the Ti-PILCs produced was determined to be mainly of the Lewis type. Unlike commonly reported microporous pillared structure, a meso-microporous delaminated structure containing pillared fragments was observed in the resulting  $\text{TiO}_2$ -pillared montmorillonite [46]. This delaminated material was synthesized through acid hydrolysis of  $\text{TiCl}_4$ . A new method [47] for the synthesis of pillared clays using supercritical carbon dioxide has been developed. This scheme consists of two steps: (1) the hydrophobitization of the clay interlayer space, using an organic ion-exchange method with interlayer cations in aqueous solution, and (2) the intercalation of a metal alkoxide dissolved in supercritical  $\text{CO}_2$  followed by hydrolysis with adsorbed water present in the interlayer space. Prepared titania-pillared montmorillonite showed better adsorbing and photocatalytic decomposition performances than conventional photocatalysts. Recent study demonstrates

the synthesis of a new type of highly thermostable titania-pillared clay [48] photocatalysts for airborne styrene decomposition in a custom designed fluidized-bed photoreactor. Highly porous layered inorganic–inorganic nanohybrids were prepared by pillaring  $\text{SiO}_2$ – $\text{TiO}_2$  nanosol particles with aluminosilicate layers [49]. This material exhibits exceptional basal spacing of 40 Å even after heat treatment at 400 °C. On the basis of the experimental findings, it was believed that the quantum-sized  $\text{TiO}_2$  and  $\text{SiO}_2$  particles are independently intercalated to form a multilayer stacking intracrystalline structure in the gallery space of aluminosilicate clay.

### 5.3.2 Iron Oxide-Pillared Clays

Earlier attempts to intercalate  $\text{Fe}^{3+}$  polymeric cations into smectites yielded products with low basal spacing ( $>14.7$  Å) and poor thermal stability [50–53]. It was inferred that in these cases the iron pillars were primarily intercalated as ‘mononuclear’  $\text{Fe}_3(\text{OH})_5^{4+}$ . However,  $\text{Fe}_{13} = [\text{Fe}_{13}\text{O}_4(\text{OH})_{24}(\text{HO})_{12}]^{7+}$ , a cationic species that is structurally analogous to the  $\text{Al}_{13}$  ion, is suggested to be formed upon base hydrolysis of iron(III) aqueous solutions [54]. This  $\text{Fe}_{13}$  ion is extremely labile and quickly decomposes, but the addition of iron(II) stabilizes the  $\text{Fe}_{13}$  ion. The interlayer spacing of the smectite intercalated with the  $\text{Fe}_{13}$  ion is ca. 9.7 Å, which is identical with the spacing of the smectite intercalated with the  $\text{Ga}_{13}$  ion. Furthermore, iron-pillared clays with large gallery heights of 13–18 Å after calcination at 350 °C were obtained by cation exchange of smectite with base-hydrolyzed solutions of iron(III) salts [55]. Even the basal spacing of 26.4 Å was reported for iron oxide-pillared delaminated clay synthesized using polyoxocationic species [56]. Tzou [57] extensively described the preparation of Fe-PILC from  $\text{FeCl}_3$ ,  $\text{Fe}(\text{NO}_3)_3$ ,  $\text{Fe}(\text{ClO}_4)_3$  and  $\text{Fe}_2(\text{SO}_4)_3$  solutions with different OH/Fe ratios, ageing times and temperatures. Sulphate gave a strong anionic effect resulting in the precipitation of the hydrolyzed iron species at low OH/Fe ratio, which was also observed by Rightor et al. [55]. In the other cases, especially from the Cl and  $\text{NO}_3$  salts, increasing the OH/Fe ratio from 0.0 to 1.0 resulted in an increase in the interlayer spacing from 3 to 14 Å. A further slow increase was observed when the OH/Fe ratio was raised to 2.5. Surface area was found to increase from 244 to 343  $\text{m}^2/\text{g}$  after calcination at 550 °C. Further it was also reported that iron oxide pillars can be converted to stable sulphide pillars without any structural changes [58]. Another route that attempted to prepare Fe-PILCs makes use of organic cage-like structures such as Fe(II)-1,10-phenanthroline [58, 59] and trinuclear aceto Fe(III) ions [60–62]. Fe(II)-1,10-phenanthroline can be formed by the reaction of aqueous solutions of ammonium ferrous sulphate and 1,10-phenanthroline. The exchange of clays with the Fe(II)-1,10-phenanthroline resulted in initially increased surface areas and high interlayer spacings at low temperature but completely collapsed at temperatures between 250 and 350 °C. Doff et al. [58] observed a basal spacing of approximately 30 Å which collapsed to 10 Å upon calcination above 300 °C. Low thermal stability again discourages the use of above complexes as precursors.

However, introduction of trinuclear acetate iron(III) cations into the interlayer space of montmorillonite has been proved to be a very useful way of obtaining stable iron intercalates that persist even after heating up to 500 °C. Iron oxide-pillared clays with an interlayer spacing of 7 Å were obtained from the reaction of trinuclear (acetatohydroxo) iron(III) complex ions with smectite followed by calcination at 500 °C [60, 61]. Similarly iron oxide-pillared clay [62] derived using Fe(III) trinuclear acetate complex yields material with gallery height of 8.4 Å and BET surface area of 284 m<sup>2</sup>/g after calcination at 500 °C. However, high-resolution transmission electron microscopy revealed the existence of isolated large iron(III) oxide particles along with the Fe<sub>2</sub>O<sub>3</sub>-pillared clays [63]. This indicates that 100% of the exchanged complexes are not intercalated rather some part remains on the surface of the clay. Martin-Luengo et al. [62] observed that almost 45% of the cation exchange capacity (CEC) still remained after the exchange of the clay with the trinuclear aceto Fe(III) ions, which might be due to incomplete saturation of the interlayer space or to partly exchangeable iron and/or protons. X-ray photoelectron spectroscopy (XPS) measurements (Fe and C peaks) indicated that the iron environment remained nearly unchanged after burning off the acetyl groups, which was confirmed by Mössbauer spectroscopy. The observed values of the quadrupole splitting and the isomer shift were consistent with the trinuclear species being preserved in the clay interlayer space. The effect of hydrolysis therefore seems to be limited to the removal of the acetyl groups. They also observed no substantial changes in the spectra after calcination at 350 °C. Complex decomposition inside the clay layer is also differs from the pattern of decomposition of pure Fe(III) complex. It was observed that the pure Fe(III) acetate complex decomposes within 235–250 °C whereas inside the clay layer the same complex decomposes within 250–340 °C indicating the partial interaction of the said complex with the clay layers [64]. This indicates the importance of material synthesis so as to obtain stable iron oxide pillars with high gallery height even at elevated temperature. In case of transition metal oxide the type of oxide phase formed inside the clay layer also plays an important role in deciding the catalytic application. Iron-pillared clay prepared from polyoxycationic species of Fe(III) gives  $\alpha$ -Fe<sub>2</sub>O<sub>3</sub> at 400 °C [56]. However, new phase formed due to thermal decomposition of intercalated Fe(III) trinuclear species is  $\gamma$ -FeOOH [64], even at 500 °C calcination. On the other hand, pure complex decomposes to Fe<sub>2</sub>O<sub>3</sub> even at 300 °C calcination. This interesting transformation behaviour of the Fe(III) complex inside the clay layer has been investigated in detail by Mössbauer spectra (Fig. 5.1). Room temperature-recorded pillared material shows clear doublet. However, clear doublets with small changes in isomer shift and unchanged quadrupole splitting in the 77 K recorded spectra (Fig. 5.1a, b) confirm the presence of  $\gamma$ -FeOOH. Interestingly, the room temperature-recorded spectra of the 300 °C calcined pure complex gave a sextet with hyperfine field of 499 kOe indicating the formation of  $\alpha$ -Fe<sub>2</sub>O<sub>3</sub>. Even pure complex (Fig. 5.1c, d) calcinated at 500 °C again shows the same hyperfine structure.

In the recent time there are several reports on the synthesis of delaminated iron oxide-pillared clay with high thermal stability [16, 65]. Thermally stable

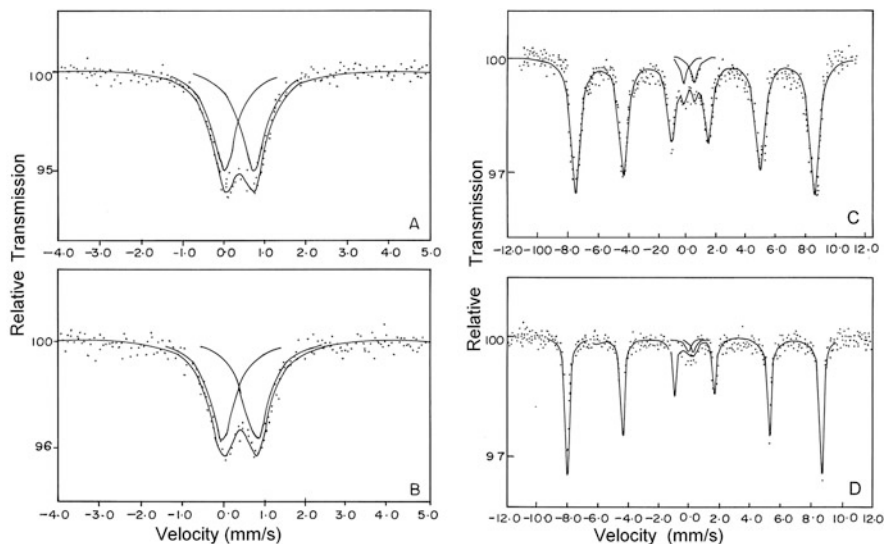


**Fig. 5.1** Mössbauer spectra of Fe(III)-pillared clay calcined at (a) 300 °C and (b) 500 °C recorded at  $-196^{\circ}\text{C}$ . Room temperature-recorded Mössbauer spectra of pure trinuclear acetato Fe(III) complex calcined at (c) 300 °C and (d) 500 °C

iron-pillared clays were also synthesized by the reaction of montmorillonite with base-hydrolyzed solutions of Fe(III) nitrate [16] with different OH/Fe molar ratio in the pillaring solution. In contrast with the classical microporous pillared structure, a novel meso-microporous delaminated structure containing pillared fragments in iron-pillared clay was obtained. BET-specific surface area and the largest porosity of the delaminated iron-pillared clays are  $215.7\text{ m}^2/\text{g}$  and  $0.29\text{ cm}^3/\text{g}$ , respectively. Mesopores in the delaminated structure make the main contribution to the total surface area and porosity, and most of them are preserved after calcination at 500 °C. Analysis of the relationship between the high d-spacing and the mesoporosity of the resultant Fe-montmorillonite provides a new insight into the structure of the PILC. The fundamental information derived from this study is of importance in developing novel catalysts or adsorbents with anion exchangeability. In my opinion there is still enough scope in the area of delaminated iron oxide-pillared clay synthesis for diverse application.

### 5.3.3 Chromium Oxide-Pillared Clays

Among many metal species, chromium oxide is a very well-known catalyst for the selective dehydrogenation of cyclohexane [66]. It has also been reported that  $\mu$ -oxotrinuclear mixed valent and mixed metal carboxylate complexes with chromium ions have been used in the catalytic oxidation of styrene and cumene



where the main products were styrene oxide and benzaldehyde [67]. Therefore, much effort has been paid to obtain highly porous pillared clays with various polycations of  $\text{Cr}^{3+}$  in the interlayer. A variety of oligomeric and polymeric chromium(III) species (dimer, trimer, tetramer and higher polymers) are formed during the base hydrolysis of chromium(III) in aqueous solution [68–72], the existence of the  $\text{Cr}_{13}$  species analogous to the tridecameric aluminum(III) and gallium(III) ions ( $\text{Al}_{13}$  and  $\text{Ga}_{13}$ ) has been suggested [73] as better pillaring precursor. Most of the early attempts to incorporate oligomeric chromium ions in the gallery of smectite made use of chromium nitrate solution hydrolyzed at room temperature. However, chromium-pillared clay synthesized by this method resulted in pillared material with low gallery height. Therefore Tzou and Pinnavaia [74] proposed the use of higher temperature for pillaring precursor formation which subsequently resulted in increased gallery height. Several kinds of Cr-pillared clays [75–77], including one with a high interlayer spacing of 18 Å at 25 °C [74], were obtained. However, these pillared clays are unstable at elevated temperatures in air due to chromium oxidation. Calcination above 200 °C in air or  $\text{N}_2$  resulted in a collapse of the pillared clay together with the segregation of Cr oxide, probably due to abrupt release of protons. Calcination under  $\text{NH}_3$ , however, resulted in stable expanded material up to 625 °C with basal spacing between 12.1 and 15.3 Å. Ammonia was thought to retain the protons released during calcination and the presence of  $\text{NH}_4^+$  apparently stabilized  $\text{Cr}^{3+}$ . Infrared (IR) spectroscopy indicated the presence of  $\text{NH}_4^+$  in the interlayer region, which is easily exchangeable by other cations. Furthermore it was shown that increasing the calcination temperature in  $\text{NH}_3$  made the pillared clay more resistant to oxidation. Chromium oxide-pillared smectites with an interlayer spacing of 6 Å after calcination under ammonia at 500 °C were obtained by the intercalation of (acetatohydroxo) chromium(III) complex ions [78]. This technique proved beneficial in increasing the surface area to 250  $\text{m}^2/\text{g}$  with the basal spacing in the range of 21–27 Å. Similar techniques resulted in thermally stable chromium oxide-pillared clay [79] with gallery height of  $\geq 17.5$  Å at 500 °C calcination. Synthesis of chromia-pillared clay was also reported using trimeric chromium oxyformate as precursor resulting in stable material with 6.2 Å gallery height and 152  $\text{m}^2/\text{g}$  of surface area after heat treatment at 400 °C [80]. It was also reported that stepwise ion-exchange process results in better intercalation compared to single-step process. Recently new chromium-pillared clay was synthesized and reported having basal spacing of 24.5 Å [81]. The chromium oligomer used for intercalation was prepared by quick addition of base and acid to Cr(III) monomeric solutions followed by reflux. The synthesized clays exhibit increased BET surface area and higher micropore volume. Pillared materials were prepared with and without reflux conditions to understand the effect of synthesis temperature. In the reflux condition the galleries received (14.6 Å) are about 50% higher and the Cr(III) uptake is increased four times compared to those received without reflux condition. Moreover, these clays possess increased BET surface and higher micropore volume. The observed microporosity is attributed to the Cr oligomers in the interlamellar space and found to increase with the gallery height. The decrease in the micropore maximum radius and the total pore volume together

with the increased Cr uptake shows that Cr(III) pillars obtained under reflux condition are more closely packed. The same results were obtained when HCl and HNO<sub>3</sub> were used instead of HClO<sub>4</sub> for the preparation of Cr(III) oligomers. On the contrary, when H<sub>3</sub>PO<sub>4</sub> or H<sub>2</sub>SO<sub>4</sub> was used the intercalation of the clay proved to be impossible. This study shows the importance of anions in the pillared clay synthesis.

### ***5.3.4 Manganese Oxide-Pillared Clay***

So far report on the pure manganese oxide-pillared clay is very much limited in the literature. However, manganese oxide doped pillared clays are well studied as oxidation catalyst by number of authors [11, 12]. In acetone decomposition reaction the effect of the nature and structure of several alumina-pillared and zirconia-pillared clays as supports of manganese oxide catalysts for the complete oxidation of acetone is studied. A significant influence of the clay-support characteristics on the catalytic performance has been found. Manganese oxide-pillared clay was synthesized [17] using trinuclear manganese(III) acetate complex as precursor in nonaqueous solvent. Both sodium exchange and acid-activated clay was used to have a comparative study on the textural and acidic properties of the materials. As far as the intercalation is concerned, the multistep ion-exchange process gave better loading of the complex in comparison to the single-step process. Presence of characteristic bands at 1548 and 1446 cm<sup>-1</sup> corresponding to the COO<sup>-</sup> asymmetric and symmetric stretching vibrations in Fourier transform infrared (FTIR) spectra confirms the presence of bidentate acetate group inside the silicate layer which decomposes at 300 °C. Materials prepared from sodium exchanged and acid-activated clays are thermally stable up to 500 °C, with basal spacing of 17.1, 16.9 Å and surface areas of 280 and 268 m<sup>2</sup>/g, respectively. Although the acid-activated pillared montmorillonite shows low uptake of the complex and low surface area, the resultant material has higher pore volume and acidity in comparison to the product from the Na-exchanged material. Samples prepared from acid-activated clays possess both micropores and mesopores (average pore diameter of 41 Å) while those prepared from Na-exchanged clays show predominately uniform small pores with an average pore diameter of 33 Å. Variation of surface area and basal spacing with respect to calcination temperature for different metal oxide pillars derived from corresponding trinuclear acetate complex is represented in Fig. 5.2. This clearly indicates that highest basal spacing is obtained for iron oxide pillars. Whereas highest surface area is found in case of chromium-pillared material.

### ***5.3.5 Mixed Transition Metal Oxide-Pillared Clay***

Limited attempts to introduce mixed transition metal oxide pillars by several methods are available. However, most of these involve oxide species such as CrOx, FeOx,

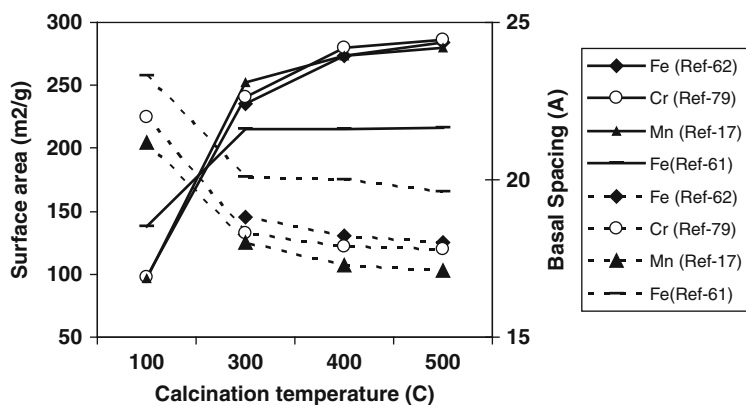


**Fig. 5.2** Variation of surface area and basal spacing with calcination temperature for various trinuclear acetate complex-pillared clay

GaOx or rare earth metal oxide with aluminium oxide [52, 82–84]. Recently Ce–Al oxide-pillared clay [85] was studied by a number of researchers. However, reports on mixed oxide transition metal-pillared clays are still limited [15, 18, 86]. In certain cases it was observed that the mixed oxide-pillared materials exhibit enhanced surface area and also surface acidity in comparison with single oxide-pillared materials. Using trinuclear acetate metal(III) complexes both iron–chromium [10] and iron–manganese-pillared clay [18] materials are synthesized having thermal stability up to 500 °C. Iron–chromium-pillared material shows basal spacing of 16.8 Å whereas iron–manganese-pillared material exhibits basal spacing of 16.9 Å after calcination at 500 °C. In both the cases it is possible to vary the metal ratio inside the clay layer by varying the complex ratio in the pillaring solution (Table 5.2). However, the metal uptake by the clay varies from complex to complex. For example, when the iron to chromium molar ratio is 10:10 in the pillaring solution, iron uptake is nearly five times more than that of chromium. Whereas when manganese to iron molar ratio is 10:10 in the solution, iron uptake is nearly two times higher than that of manganese. This indicates that the clay affinity towards the metal trinuclear acetate complexes is in the order of Fe(III) > Mn(III) > Cr(III), although size and charges of the molecules are nearly the same. Possibility of polymeric species of iron(III) due to partial hydrolysis of the complex may be the cause behind the higher intercalation. Temperature Programmed Reduction (TPR) profile of Fe–Mn-pillared clay [18] shows that the intensity of 460 °C peak is more than the peak of 350 °C indicating the formation of Mn<sub>3</sub>O<sub>4</sub> with MnO<sub>2</sub>/Mn<sub>2</sub>O<sub>3</sub> inside the clay layer during calcination. A little shifting of reduction peaks towards higher temperature was observed for the pillared materials in comparison to that of pure oxides which may be due to the restriction of the clay layers. In a recent report delaminated Fe–Cr-pillared clay was synthesized and used for the wet hydrogen peroxide oxidation of phenol in the presence of microwave irradiation [87]. It is also understood that transition metal-doped Ti-PILC possess house of cards delaminated structure with more solid acid sites

**Table 5.2** Variation of metal uptake by the clay due to the variation of molar ratio of different metal complexes in the pillaring solution

Sample	Fe:Cr added	Fe:Mn added	Total (wt%) intercalated	Fe/Cr intercalate	Fe/Mn intercalated	Surface area (m <sup>2</sup> /g)
1	0:20	–	13.0	0	–	280
2	1:19	–	11.43	0.726	–	268
3	2:18	–	13.18	1.436	–	274
4	5:15	–	13.81	3.315	–	275
5	10:10	–	14.65	5.078	–	278
6	15:5	–	15.03	6.828	–	280
7	18:2	–	14.75	8.578	–	273
8	20:0	–	14.3	–	–	268
9	–	4:16	11.24	–	–	268
10	–	8:12	11.39	–	–	272
11	–	10:10	11.73	–	–	277
12	–	12:8	12.29	–	–	282
13	–	16:4	12.77	–	–	286

in their frame [88]. In addition recently vanadia-doped Ti-PILC was synthesized with pure anatase phase having good catalytic selectivity towards H<sub>2</sub>S oxidation reaction [89]. Therefore, there is still enough scope to explore the different mixed oxide-pillared materials for diverse applications.

## 5.4 Acidity of Pillared Clay

PILCs possess both Brønsted acid (proton donor) sites and Lewis acid (electron pair acceptor) sites [90, 91]. To investigate the surface acidity on PILC samples, the most commonly used methods are the study of adsorbed ammonia or pyridine by infrared spectroscopy, temperature programmed desorption (TPD) of adsorbed ammonia [92] and base adsorption [62, 79]. By choosing adsorbed substrates with different basicities, both the number and strength of the acid sites can be determined. It is reported that 2,6-dimethylpyridine (DMPY) is selectively adsorbed on Brønsted acid sites, thus it can be used as a good probe molecule for the determination of Brønsted acidity in clays and PILCs [93, 94].

Generally, it is believed that Brønsted acidity is mainly coming from the clay layer structural hydroxyl groups, while Lewis acidity is attributed to the metal oxide pillars. In addition, the amount and strength of Brønsted and Lewis acid sites are closely related to the types of clays and metal oxide pillars. It should be noted that heating process also has strong influence on the acidity of PILC. Normally, Lewis acidity is more thermally stable than Brønsted acidity. However, upon increasing calcination temperature both Lewis and Brønsted acidities will decrease. The main interests in catalytic applications of PILCs are where they are used as acid catalysts [2]. In these reactions, the type, amount and strength of surface acidity of PILCs are critical, because they are directly related to the catalytic activities and more

importantly, they will determine which type of reaction they can catalyze. However, instead of correlating activity to a certain type of acid sites, Brønsted or Lewis acid sites, most studies reported only total acidity. In most cases, both Brønsted and Lewis acid sites are beneficial for the reaction and one of them might be dominant, thus total acidity can still be a suitable indicator for the activity.

#### ***5.4.1 Acid Activation of Clay Before Pillaring***

To date, most attempts at improving and controlling the acidity of pillared clays have concentrated on changing the type of host matrix [95]. By changing the host matrix, Brønsted acidity cannot be increased substantially, as most of the Brønsted acid sites on the pillared clays are associated with the clay layers [96, 97]. But acid treatment increases the Brønsted acidity to a very high level, which makes the clays a potential solid acid catalyst [98]. Preliminary work with low temperature (175–250 °C) catalysis has shown that acid treatment before pillaring has beneficial effects [99]. In case of iron-pillared clay when trinuclear acetate complex was used as pillaring agent, the uptake is more in case of Na-exchanged clay in comparison to the acid-activated clay [62]. This difference in the uptake may be due to the partial deformation of the clay layer due to acid treatment. Moreover, it was found that acid activation has different effects on different clay minerals. For example, it increases the acidity on pillared montmorillonite materials, but decreases the acidity on pillared saponite materials, which was explained by the reduced accessible acid sites for the probe molecules [100]. Mishra and Parida have investigated the differences in terms of the structural, acidic and catalytic activities for Cr-PILC [79] and Mn-PILC [17] prepared from Na-exchanged montmorillonite and sulphuric acid-activated montmorillonite. Their results showed that acid pretreatment of clay can efficiently enhance the Brønsted acidity. However, amount of metal oxide intercalation slightly decreases in case of acid-activated clay. Therefore the optimum level of acid treatment is to be understood for better intercalation. In addition materials prepared from acid-activated clay possess higher mesopore volume, average pore diameter and surface acidity in comparison to the material prepared from sodium-exchanged montmorillonite. In particular acid activation of clay before pillaring increases the number of Brønsted acid sites.

#### ***5.4.2 Anion-Supported Pillared Clay***

Recently, anion-supported pillared clay also attracted the attention of number of researchers due to the enhancement of acidity and catalytic activity [101–105] similar to that of sulphated metal oxides. As far as catalytic activity is concerned the regular pore size and high surface area of pillared clay have the advantage over the simple metal oxide systems. However, decreasing surface area and thermal stability

of the pillared material due to sulphate impregnation were the main bottleneck problems [102]. In this context sulphate incorporation from the precursor solution was suggested to be beneficial [105]. Stable sulphate-supported iron–chromium mixed oxide-pillared clay with enhanced catalytic activity was reported by the aqueous impregnation method using ammonium sulphate as the source [106]. Prepared materials were found to be stable up to 500 °C, having basal spacing of  $\geq 17.7$  Å. A negligible decrease in the surface area and a substantial increase in the catalytic activity were observed due to the sulphate loading of 1–2 wt%. However, a significant decrease in the surface area as well as catalytic activity was observed for the 3 wt% and above sulphate loaded samples which may be due to the partial blockage of pores by excess sulphate. Results show the importance of acidity of the material due to sulphate loading (up to 2 wt%) and thus can be used as a better acid catalyst. However, amount of sulphate loading is crucial for increasing the catalytic activity. Based on the surface area result, authors proposed a hypothesis (Fig. 5.3) on the type of interaction of the sulphate group with the pillared clay. Probably, sulphate preferentially goes to the pillars and hence a negligible decrease in the surface area for 1 and 2 wt% sulphated samples as shown in Case I. After saturation of the pillar surfaces excess sulphate probably prefers the clay surface which may result in partial blockage of the pore opening as in Case III. Hence the decreasing surface area is observed for a 3 wt% and above sulphate loading.

Authors tried to explain the increase in acidity and catalytic activity by ammonia TPD. In the TPD profile (Fig. 5.4) only two peaks were marked for all the materials (a). The initial peak (90–120 °C) which is observed in all three cases is due mostly to the presence of weak acid sites. This peak more or less remains the same even after the sulphate addition. Peak (B') observed within 300–350 °C is mostly due to the ammonia desorption from Brønsted acid sites. Interestingly, due to the sulphate addition a new intense peak (L') is observed within 450–600 °C, which may be corroborated with the presence of strong Lewis acid sites. However, the peak due to the presence of Brønsted acid site is less intense for sulphated samples. So it is concluded that strong Lewis acid sites are formed at the cost of some of the Brønsted acid sites due to the sulphate addition. In total the TPD profile of sulphated iron–chromium mixed oxide systems is quite comparable to that of sulphated metal oxide systems.

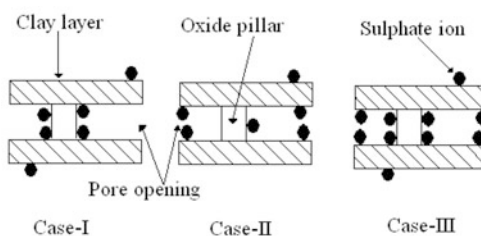
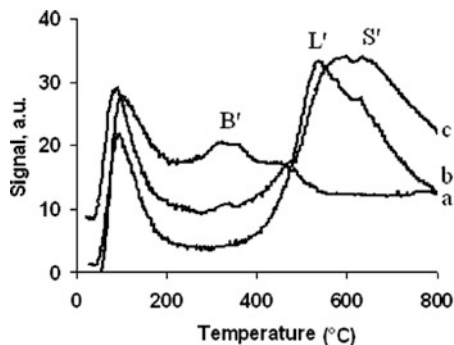


**Fig. 5.3** Proposed interaction of sulphate ions with pillared clay during impregnation. Reprinted from [106], with permission from Elsevier

**Fig. 5.4** Ammonia TPD of sulphated iron–chromium mixed oxide-pillared clay. Reprinted from [106], with permission from Elsevier



## 5.5 Catalytic Reaction

### 5.5.1 Acidic Reaction

In the mid-1930s, acid-modified smectite-type clays were widely used as commercial catalysts in petroleum-cracking reaction. Around the mid-1960s, the role of acidic clays in cracking process was taken over by Y zeolites and aluminosilicates with better thermal stability and shape selectivity. However, new reports on the successful synthesis of PILCs using inorganic complexes have renewed the interests in applying them as cracking catalysts [1, 107]. However, most of the study on catalytic cracking is based on Al, Ga and Si-pillared clays. In some cases transition oxide-pillared clays are also studied for cracking reaction. Mishra et al. showed the importance of acid activation of clay before pillaring in the catalytic cracking of cumene using chromium-pillared clay [79]. The importance of Brønsted acidity in cumene cracking processes is clearly illustrated. Zhao and co-workers showed that by incorporating Al into Cr-PILC, both the thermal stability and surface acidity for the final mixed Al/Cr-PILC were improved, resulting in a higher activity in cumene cracking [108]. Chromia-pillared laponite prepared using microwave irradiation is found to be a good catalyst for hydrocracking of heavy liquid fuels derived from coal. Catalyst is found to be active even after 4 h of reaction regardless of high coke formation. The same catalyst can be reused without any decrease in the activity [109]. In addition to the use of PILCs in catalytic cracking processes, the application of PILCs as acid catalysts in the synthesis of chemicals forms another interesting area. Different types of reactions have been studied, such as hydroxylation, [110] dehydration [45, 86], dehydrogenation [74, 79, 86], aromatic nitration [111] and disproportionation [91]. The reaction conditions are milder than that in cracking processes and the product selectivity is dependant on the type and strength of the acidity and the pore geometry of PILCs. Similar to cracking reactions, dehydration is more related to the Brønsted acidity of the catalyst. In addition, the porous structure is also crucial for the product selectivity and coke formation.

Homogeneous catalyst presents several problems like tedious work up, use of corrosive chemicals, moisture sensitivity, decreased regioselectivity etc. Therefore for better practical application solid acid catalyst is the best alternative for various alkylation and acylation reactions. Kurian and Sugunon [112] reported the use of iron-pillared montmorillonite and its transition metal-exchanged analogues for the benzylation of benzene, a typical example of Friedel–Crafts alkylations. Monoalkylated product of 100% selectivity is obtained with these catalysts. Same author also reported the use of transition metal-exchanged-pillared montmorillonites as novel catalysts for the vapour phase *tert*-butylation of phenol [113]. Iron-pillared and mixed iron-pillared systems are efficient catalysts for *tert*-butylation of phenol in the gas phase. The catalytic activities of the systems depend on the amount of acid sites on the catalyst surface and the di-substituted product selectivity depends on the amount of strong acid sites. Appreciable activity of the material even after 5 h can be ascribed to the stability of active sites under the reaction conditions. The pillars contribute to the acidic character and the catalytic behaviour is different for the different Al/Cr ratios used [114]. The results of the ethylbenzene conversion revealed that the unpillared saponite as well as saponites with alumina-rich pillars exhibited almost exclusively dehydrogenation activity, whereas the presence of chromia induced cracking activity and reduced the selectivity to styrene. An attempt has been made by Sugunon et al. to correlate the acidity determined by the two independent methods and the catalytic activity of present systems in the benzylation of toluene with benzoyl chloride [115]. Incorporation of Fe and Cr has changed the properties of Al-pillared montmorillonite. Fe-pillared systems have been found to be very good catalysts for benzylation reaction. It was reported that transition metal (Fe, Cr and Mn)-pillared clay can be used as an efficient catalyst for the nitration of chlorobenzene [111] with high *para*-selectivity. In particular acid-activated pillared montmorillonite performs better than the sodium-exchanged pure montmorillonite. This emphasized the importance of acid activation before pillaring for the development of acidic catalyst.

### 5.5.2 Redox Reaction

Recent advances in the synthesis of pillared clay have expanded considerably the scope of their potential catalytic applications. As a result there is a renewed interest in the pillared material as polyfunctional catalysts and catalyst supports [9]. In this context clays as support and transition metal-pillared clays as catalyst are also good option due to the presence of both redox and acid sites. However, till date exploration of these materials is very limited in the literature [11–13, 116]. Transition metal oxide-supported alumina-pillared clay [11] and zirconia-pillared clay [12] were studied recently as effective catalyst for the decomposition of chloro compounds. Complete oxidation of acetone on manganese oxide-supported pillared clay justifies the importance of clay as support and manganese oxide as active catalyst [13]. Particularly in case of pillared clay, dispersion of active oxide phase and the



acidity involved in the clay plays an important role because of their participation in the decomposition reaction. Recently Mishra et al. reported synthesis, characterisation and catalytic evaluation of novel manganese and iron mixed oxide-pillared clay with varying manganese to iron ratio towards the decomposition of acetone and trichloroethylene [18]. It was noticed that with a fixed manganese to iron ratio acetone decomposition is maximum even at low temperature of 200 °C. This justifies the presence of iron oxide with manganese oxide for better result. A mild and efficient method for benzylic oxidation of arylmethylenes to the corresponding carbonyl compounds in good yields is described using a catalytic amount of chromium-pillared montmorillonite and equimolar quantities of *tert*-butyl hydroperoxide [117]. The method is very selective towards monocarbonyl compounds of the substrates prone to form dicarbonyl compounds. The present heterogeneous catalyst is inert towards the branched hydrocarbons and has been put to practice to obtain *p*-isobutylacetophenone selectively from *p*-isobutylethylbenzene. A striking feature of the oxidative deprotection with the present method is the oxidative deprotection of a benzyl group from the substrates having an alkyne moiety. The study of the catalytic behaviour of phenol oxidation by hydrogen peroxide in the presence of Fe–Al-pillared clay [118] has shown that both heterogeneous and homogeneous catalytic systems behave similarly. For both systems, the reaction has been found sensitive to the pH, the highest phenol conversion and TOC abatement being obtained at a pH value close to 3.7. Pillared clays prepared with iron oxocations (Fe-PILC) have recently been used in dye mineralization [119–121] using photo-Fenton techniques. Two iron oxide-pillared catalysts prepared separately from two different-sized particle fractions of montmorillonite were tested for catalytic performance in photo-Fenton discoloration of Methylene Blue aqueous solutions [122]. An improvement of catalyst textural parameters and an increase in catalytic activity in Methylene Blue discoloration by photo-Fenton processes was found for the smaller-sized particle fraction of the starting mineral. Recently Cr–Al mixed oxide-pillared clay is also found to be good CO oxidation catalyst. Particularly, maximum conversion of CO was observed with the material when prepared from Cr/Al ratio of 0.33 [123].

### 5.5.3 Selective Catalytic Reduction (SCR) of $\text{NO}_x$

In recent years, Yang and co-workers have published a series of reports on SCR of NO to nitrogen with either ammonia or hydrocarbon as reductants [32, 124–127]. DeNO<sub>x</sub> reactions are important for treating effluent gases from combustion sources. For the SCR of NO with ammonia, V<sub>2</sub>O<sub>5</sub>/TiO<sub>2</sub> promoted by WO<sub>3</sub> is a widely used industrial catalyst because of its high activity and good resistance to SO<sub>2</sub> poisoning. The attempt of using PILC as porous support materials was first reported in 1992 [124], which showed a great potential to replace the commercial V<sub>2</sub>O<sub>5</sub>/TiO<sub>2</sub> catalyst. Some recent results of the comparative performance of different PILCs in the SCR of NO with ammonia were reviewed by Ding et al. [88]. It is obvious that

higher activity was obtained using the PILC catalysts and that these PILCs are stable in the presence of  $\text{SO}_2$  and water [32, 41, 127–128]. In addition, the product selectivity to  $\text{N}_2$  is better for the pillared clay catalyst than the  $\text{V}_2\text{O}_5/\text{TiO}_2$ -based materials. Unlike cracking processes, the reaction temperature in the SCR of NO is lower, mainly in 350–450 °C range. Therefore, the Brønsted acidity of the PILC could be preserved, which is crucial for the DeNO<sub>x</sub> reaction. Another contribution for maintaining the high Brønsted acidity in this process is coming from the ammonia reactant. It was reported that the disappearance of Brønsted acidity upon heating was mainly because of proton migration from the interlayer surface to the octahedral sheet within the clay layers and this could be prevented by the presence of ammonia [124–130]. In the latter condition, protons were attracted by ammonia, thus remaining on the interlayer surface, leading to higher Brønsted acidity. A study on the comparison of activities among Fe/Ti-PILC samples with or without acid or base pretreatment showed that the surface Brønsted acidity had a much stronger influence on the activity than the amount of active iron sites [128].

Ti-PILCs have been specifically used as catalysts for the SCR of NO<sub>x</sub> [41–42, 108, 131–132]. In particular Ti-PILCs modified with copper present a higher activity in this reaction, because of their excellent properties like high thermal stability, high surface area and appropriate acidity values. Because of the potential applications of titanium-pillared clays for Hydrocarbon based Selective Catalytic Reduction (HC-SCR), attention has been focused recently on the performance and reaction mechanism of these catalysts [133]. It is well known that the surface acidity exerts an important role in SCR reaction of NO by  $\text{NH}_3$ . Several authors attribute to the surface acid sites and specifically to the Brønsted acidity [127, 134], a relevant role in the SCR reaction. Both Lewis and Brønsted acid sites exist on Ti-pillared clays. Stronger Brønsted acid sites were observed on sulphated Ti-modified pillared montmorillonites compared to unsulphated ones [135]. The increase of sulphate content improves significantly the NO conversion. Our results strongly support that the high catalytic activity for SCR-NO process on sulphated Ti-pillared clay is directly related to the available Brønsted acid sites.

The performance of vanadia-supported sulphated Ti-pillared clay in the SCR reaction was compared to a physical mixture of pure  $\text{V}_2\text{O}_5$  with sulphated Ti-pillared clay [136]. From the results obtained, it appears that the presence of a Brønsted acid site in close proximity with the vanadia site on sulphated Ti-pillared clay results in a promoting effect on SCR-NO activity. Looking at the commercial possibility the textural and SCR of NO of Ti-pillared montmorillonites prepared at bench scale (1 kg per batch level) have been compared with those prepared at laboratory scale [137]. Despite the differences of their textural properties, from the catalytic point of view, laboratory and pilot samples showed rather similar performances. Certainly, the performance of the catalysts reported in this work for the SCR of NO is quite lower than that shown for other catalysts such as zeolites [138]. Cu/Ti-PILCs have, nevertheless, a promising advantage: the maximum conversion is obtained at temperatures 100–200 °C lower than those observed for catalysts based on zeolites, which could be interesting from an industrial point of view. Thus, if the activity of these materials could be improved, they would become a good alternative to zeolite-based catalysts.

### 5.5.4 Photocatalytic Reaction

Anatase ( $\text{TiO}_2$ ) is regarded as the titania polymorph that possesses the highest activity for photocatalytic decomposition of several organic pollutants in water and air [139–141]. Anatase photocatalysts can be used in various processes such as odour elimination from drinking water, degradation of oil spills in surface water systems and degradation of harmful organic contaminants like herbicides, pesticides and synthetic dyes. As the photocatalytic reaction takes place on the surface of anatase crystals, the catalysts composed of ultrafine anatase powders with a particle size on the nanometre scale should exhibit a superior activity because of the large specific surface area. However, ultrafine powders have a strong tendency to agglomerate into larger particles, resulting in an adverse effect on catalytic performance. To avoid the agglomeration of the fine particles and achieve structures with a large surface area of anatase, introducing a second component to partition the fine anatase particles is a feasible option. It is difficult for the light to penetrate through many clay layers to initiate the reaction even if the organic molecules could diffuse to the inner anatase sites between layers. As a result, anatase located at the inner sites between clay layers might not exhibit any photocatalytic effect. The poor activity of amorphous  $\text{TiO}_2$  pillars and the layered structure makes the  $\text{TiO}_2$ -pillared clays exhibit a moderate catalytic performance for the photodegradation of organic pollutants which are often large molecules [142]. To develop more efficient photocatalysts, it is necessary to increase the content of anatase nanocrystals and improve the accessibility of these crystals to the reactants, organic molecules and incident light. Therefore material synthesis has an important role for photocatalytic application of pillared clays.

In particular  $\text{TiO}_2$ -pillared clays (PILCs) have a mesoporous structure, high adsorption ability, stable photocatalytic activity and large specific surface area due to their nanosized  $\text{TiO}_2$  particles [36, 143], which are located as pillars between the silicate layers. The photocatalytic activity of  $\text{TiO}_2$ -PILCs is greatly affected by the concentration of the metal ion, the temperature, the preparation method, the crystalline and phase type of the nanosized  $\text{TiO}_2$  pillars [144], and the different drying methods [145]. The calcination process is usually necessary for the preparation of anatase  $\text{TiO}_2$ -PILCs. In some material UV absorption edge of the titania clay composites [37] shows a redshift in comparison to that of pure  $\text{TiO}_2$  particles. The obtained catalyst has the highest photocatalytic activity when the composite temperature is  $70^\circ\text{C}$ , which could be attributed to the synergetic effects of the adsorbability of montmorillonite and the photocatalytic property of  $\text{TiO}_2$  in it. A new structure of anatase nanocrystals attached to clay fragments has been formed by the reaction between  $\text{TiOSO}_4$  and laponite clay under hydrothermal condition [146]. This new structure exhibits superior photocatalytic properties and is more efficient for degrading organic pollutants in water; compared to the conventional titania-pillared clay. In this structure, the anatase crystals are linked to the fragments of the acid leached clay layers through chemical bonds. The new structure has a large mesoporosity and large pore aperture, which facilitate the exposure of anatase nanocrystals to the light and the diffusion of the organic molecules to the anatase surfaces. We found that the catalytic activity increases with increasing anatase crystal content, pore

volume, specific surface area and pore aperture. These properties can be tailored facilely by tuning the synthetic parameters such as the temperature of hydrothermal synthesis and the Ti/clay ratio. The knowledge acquired in this study is useful for designing photocatalysts with high efficiency. Present study [48, 147] demonstrates a new type of well-characterized, highly thermostable titania-pillared clay photocatalysts for airborne styrene decomposition in a custom-designed fluidized-bed photoreactor. This photocatalytic system is found to be capable of destroying up to 87% of 300 ppmV airborne styrene in the presence of ultraviolet (UV) irradiation. The effects of relative humidity are also studied, together with the arising physical structures like porosity and surface characteristics of the catalysts when subjected to relatively high calcination temperatures of 1000–1200 °C. Such a temperature range may be encountered in flue gas emissions. It is found that relative humidity levels of 20% retard the degradation efficiencies of airborne styrene when using highly porous catalysts. Recently non-metal-doped titania-pillared clays are also studied for visible light-sensitive photocatalysis [148–149]. Higher activity demonstrates that the much higher visible light photocatalytic activity of the photocatalyst is due to the synergistic effects of coupling doping of S and N elements to TiO<sub>2</sub>, extensive specific surface area of montmorillonite and quantum-sized efficacy between layers of montmorillonite. A considerable improvement of the photocatalytic activity was found for all the doped samples in comparison to the undoped TiO<sub>2</sub>-pillared montmorillonite catalyst for dye decomposition [149]. In addition to the pillared clay other pillared material like titania-pillared zirconium phosphates [150] are also studied as potential photocatalysts even in presence of visible light.

## 5.6 Conclusions

The aim of this review is to provide the reader with a general overview of the synthesis and physical–chemical characteristics and catalytic application of transition metal oxide-pillared clays. Future scope of these materials is also stressed so as to initiate new insight into this area of research. Synthesis of mixed oxide-pillared clay with desired metal ratio can open a new series of materials with different catalytic properties for future application. Therefore this subject needs to be explored in more detail. Both acid activation of clay before pillaring and post-anion impregnation increase the surface acidity of pillared clay making it more suitable for acid-catalyzed reactions. Most of the application till today has been conducted in the area of oil cracking and refinery. For this type of application, amount and strength of surface acidities, thermal and hydrothermal stabilities of PILC are crucial. However, for the replacement of existing commercial catalysts in commercial processes, also the price and the reliability of the new PILC-based catalysts with respect to fixed composition deactivation, coke formation and regeneration will play a major role. On the other hand increasing interest is noticed in the recent years in the application of PILCs in environmental processes including photocatalysis, particularly pollution control in both gas phase and liquid phase. Although this is a new field, the results

are very promising. Only extensive studies are available in the area of selective catalytic reduction of  $\text{NO}_x$ . Good PILC-based catalysts with a comparable or better performance than commercial catalyst can be obtained after careful selection and modification of these PILC materials. Similarly, photocatalysis is also an exciting area of application for pillared materials. Other than catalysis pillared materials are increasingly found suitable as adsorbent for environmental applications. So this new area of application is to be looked into. As a whole it can be concluded that environmental application is still an open area of research which needs more exploration. It is understood that in the last 30 years, there have not been any actual commercial uses for pillared materials yet. So it is the high time to understand the drawbacks of this material and more positively find out the specific area of application as per the suitability.

**Acknowledgments** Author thanks Mr. Noor Aman of NML and Dr. D.P. Das of IMMT, Bhubaneswar for their help during the preparation of the manuscript. Due thanks are also given to Director of NML for his permission and Dr. S. Bhattacharjee, Head ACC division, for his encouragement during the preparation. Author also acknowledges the support of CSIR network project-NWP-0010.

## References

1. Pinnavaia TJ (1983) Intercalated clay catalysts. *Science* 220:365–371
2. Burch R (ed) (1988) Pillared clays. *Catal Today* 2:185–367
3. Figueras F (1988) Pillared clays as catalysts. *Catal Rev Sci Eng* 30:457–499
4. Behrens P (1993) Mesoporous inorganic solids. *Adv Mater* 5:127–132
5. Mitchell I V (1990) Pillared layered structures: current trends and applications. Elsevier Applied Science, London
6. Alberti G, Costantino U (1982) Intercalates formed by zirconium phosphate. In: Whittingham MS, Jacobson AJ (eds) *Intercalation chemistry*. Academic, New York, NY
7. Ohtsuka K (1997) Preparation and properties of two-dimensional microporous pillared interlayered solids, reviews. *Chem Mater* 9:2039–2050
8. Olivera-Pastor P, Maireles-Torres P, Rodriguez-Castellon E, Jimenez-Lopez A, Cassagneau T, Jones DJ, Rozire J (1996) Nanostructured inorganically pillared layered metal (IV) phosphates. *Chem Mater* 8:1758–1769
9. Gil A, Gandia LM, Vicente MA (2000) Recent advances in the synthesis and catalytic applications of pillared clays. *Catal Rev Sci Eng* 42:145–205
10. Jinjun L, Zheng J, Zhengping H, Xiuyan X, Yahui Z (2005) Pillared laponite clays-supported palladium catalysts for the complete oxidation of benzene. *J Mol Catal A* 225:173–179
11. Gandia LM, Vicente MA, Gil A (2002) Complete oxidation of acetone over manganese oxide catalysts supported on alumina- and zirconia-pillared clays. *Appl Catal B* 38:295–307
12. Gil A, Vicente MA, Korili SA (2006) Effect of the nature and structure of pillared clays in the catalytic behaviour of supported manganese oxide. *Catal Today* 112:117–120
13. Papaefthimiou P, Ioannides T, Verykios XE (1999) VOC removal: investigation of ethylacetate oxidation over supported Pt catalysts. *Catal Today* 54:81–92
14. Loeppert RT, Mortland MM, Pinnavaia TJ (1979) Synthesis and properties of heat stable expanded smectite and vermiculite. *Clays Clay Miner* 27:201–208
15. Skaribas SP, Pomonis PJ, Grange P, Delmon B (1992) Controlled architecture of solids with micro- and meso-porosity obtained by pillaring of montmorillonite with an  $\text{LaNiO}_x$  binary oxide. *J Chem Soc, Faraday Trans* 88:3217–3223

16. Yoon J-B, Hwang S-H, Choy J-H (2000) Trimeric chromium oxyformate route to chromia-pillared clay. *Bull Korean Chem Soc* 21:989–994
17. Mishra T, Parida K (1997) Transition metal oxide pillared clay: 2. Comparative study of textural and acidic properties of Mn(III) pillared montmorillonite and pillared acid activated montmorillonite. *J Mater Chem* 7:147–152
18. Mishra T, Mohapatra P, Parida KM (2008) Synthesis, characterisation and catalytic evaluation of iron–manganese mixed oxide pillared clay towards VOC oxidation reaction. *Appl Catal B* 79:279–285
19. Christiano SP, Wang J, Pinnavaia TJ (1985) Intercalation of niobium and tantalum  $M_6Cl_{12}^{n+}$  cluster cations in montmorillonite: a new route to pillared clays. *Inorg Chem* 24:1222–1227
20. Yamanaka S, Nishihara T, Hattori M, Suzuki Y (1987) Preparation and properties of titania pillared clay. *Mater Chem Phys* 17:87–101
21. Yamanaka S, Inoue Y, Hattori M, Okumura F, Yoshikawa M (1992) Preparation and properties of clays pillared with  $SiO_2$ – $TiO_2$  sol particles. *Bull Chem Soc Jpn* 65:2494–2500
22. Zheng L, Hao Y, Tao L (1989) The preparation and characterization of some pillared clays. *Studies Surf Sci Catal* 49:481–488
23. Warriar KGK, Mukundan P, Ghosh SK, Sivakumar S, Damodaran AD (1994) Microwave drying of boehmite sol intercalated smectites. *J Mater Sci* 29:3415–3418
24. Moini A, Pinnavaia TJ (1988) A new strategy for the synthesis of pillared clays with super galleries: direct intercalation of metal oxide sols (DIMOS). *Solid State Ionics* 26:119–123
25. Takahama K, Yokoyama M, Hirao S, Yamanaka S, Hattori M (1991) Preparation and properties of pillared clays with controlled pore structures (part 1): effects of organic cation additives. *J Ceram Soc Jpn* 99:14–18
26. Li JJ, Mu Z, Xu XY, Tian H, Duan MH, Li LD, Hao ZP, Qiao SZ, Lu GQ (2008) A new and generic preparation method of mesoporous clay composites containing dispersed metal oxide nanoparticles. *Micropor Mesopor Mater* 114:214–221
27. Takahama K, Yokoyama M, Hirao S, Yamanaka S, Hattori M (1992) Supercritical drying of  $SiO_2$ – $TiO_2$  sol-pillared clays. *J Mater Sci* 27:1297–1301
28. Occelli M L, Peadar PA, Ritz GP, Iyer PS, Yokoyama M. (1993) The effects of supercritical drying on the properties of a montmorillonite expanded with colloidal particles. *Micropor Mater* 1:99–113
29. Matijevic E (1993) Preparation and properties of uniform size colloids. *Chem Mater* 5:412–426
30. Bovey J, Kooli F, Jones W (1996) Preparation and characterization of Ti-pillared acid-activated clay catalysts. *Clay Miner* 31:501–506
31. Hutson ND, Hoekstra MJ, Yang RT (1999) Control of microporosity of  $Al_2O_3$ -pillared clays: effect of pH, calcination temperature and clay cation exchange capacity. *Micropor Mesopor Mater* 28:447–459
32. Long RQ, Yang, RT (1999) Selective catalytic reduction of nitrogen oxides by ammonia over  $Fe^{3+}$ -exchanged  $TiO_2$ -pillared clay catalysts. *J Catal* 186:254–268
33. Ooka C, Yoshida H, Suzuki K, Hattori, T (2004) Highly hydrophobic  $TiO_2$  pillared clay for photocatalytic degradation of organic compounds in water. *Micropor Mesopor Mater* 67:143–150
34. Miao SD, Liu ZM, Han BX, Zhang JL, Yu X, Du JM, Sun ZY (2006) Synthesis and characterization of  $TiO_2$ -montmorillonite nanocomposites and their application for removal of Methylene Blue. *J Mater Chem* 16:579–584
35. Ooka C, Akita S, Ohashi Y, Horiuchi T, Suzuki K, Komai S, Yoshida H, Hattori T (1999) Crystallization of hydrothermally treated  $TiO_2$  pillars in pillared montmorillonite for improvement of the photocatalytic activity. *J Mater Chem* 9:2943–2952
36. Sun SM, Jiang YS, Yu LX, Li FF, Yang ZW, Hou TY, Hu DQ, Xia MS (2006) Enhanced photocatalytic activity of microwave treated  $TiO_2$  pillared montmorillonite. *Mater Chem Phys* 98:377–381

37. Zhang GK, Ding XM, He FS, Yu XY, Zhou J, Hu YJ, Xie J W (2008) Low-temperature synthesis and photocatalytic activity of TiO<sub>2</sub> pillared montmorillonite. *Langmuir* 24:1026–1030
38. Bernier A, Admaiai LF, Grange P (1991) Synthesis and characterization of titanium pillared clays, influence of the temperature of preparation. *Appl Catal A* 77:269–281
39. Cheng LS, Yang RT, Chen N (1996) Iron oxide and chromia supported on titania-pillared clay for selective catalytic reduction of nitric oxide with ammonia. *J Catal* 164:70–81
40. Yang RT, Cichanowicz JE (1995) Pillared interlayered clay catalysts for the selective reduction of nitrogen oxides with ammonia. US Patent 5,415,850
41. Long RQ, Yang RT, Zammitt KD (2000) Superior pillared clay catalysts for selective catalytic reduction of nitrogen oxides for power plant emission control. *J Air Waste Manage Assoc* 50:436–442
42. Cheng S (1999) From layer compounds to catalytic materials. *Catal Today* 49:303–312
43. Chae HG, Ham SW, Hong SB, Nam I (2001) Physicochemical characteristics of pillared interlayered clays. *Catal Today* 68:31–40
44. Kato A, Matsuda S, Nakajima F, Imanari M, Watanabe Y (1981) Reduction of nitric oxide with ammonia on iron oxide–titanium oxide catalyst. *J Phys Chem* 85:1710–1713
45. Del Castillo HL, Grange P (1993) Preparation and catalytic activity of titanium pillared montmorillonite. *Appl Catal A* 103:23–34
46. Yuan P, Yin X, He H, Yang D, Wang L, Zhu J (2006) Investigation on the delaminated-pillared structure of TiO<sub>2</sub>-PILC synthesized by TiCl<sub>4</sub> hydrolysis method. *Micropor Mesopor Mater* 93:240–247
47. Yoda S, Sakurai Y, Endo A, Miyata T, Yanagishita H, Otake K, Tsuchiya T (2004) Synthesis of titania-pillared montmorillonite via intercalation of titanium alkoxide dissolved in supercritical carbon dioxide. *J Mater Chem* 14:2763–2767
48. Malvim L, Zhou Y, Wood B, Zhouwang L, Rudolph V (2009) Highly thermostable anatase titania-pillared clay for the photocatalytic degradation of airborne styrene. *Environ Sci Technol* 43:538–543
49. Park JH, Yang JH, Yoon JB (2006) Intracrystalline structure and physicochemical properties of mixed SiO<sub>2</sub>–TiO<sub>2</sub> sol-pillared aluminosilicate. *J Phys Chem B* 110:1592–1598
50. Bergaya F, Hassoun N, Barrault J, Gatinneau L (1993) Pillaring of synthetic hectorite by mixed [Al<sub>13-x</sub>Fe<sub>x</sub>] pillars. *Clay Miner* 28:109–122
51. Rengasamy P, Oades JM (1977) Interaction of monomeric and polymeric species of metal ions with clay surfaces: I. Adsorption of iron II species. *Aust J Soil Res* 15:235–242
52. Lee WY, Raythatha RH, Tatarchuk BJ (1989) Pillared-clay catalysts containing mixed-metal complexes: I. Preparation and characterization. *J Catal* 115:159–179
53. Klopogge JT (1998) Synthesis of smectites and porous pillared clay catalysts: a review. *J Porous Mater* 5:5–41
54. Bradley SM, Kydd RA (1993) Comparison of the species formed upon base hydrolyses of gallium(III) and iron(III) aqueous solutions: the possibility of existence of an [FeO<sub>4</sub>Fe<sub>12</sub>(OH)<sub>24</sub>(H<sub>2</sub>O)<sub>12</sub>]<sup>7+</sup> polyoxocation. *J Chem Soc, Dalton Trans* 15:2407–2413
55. Rightor EG, Tzou MS, Pinnavaia TJ (1991) Iron oxide pillared clay with large gallery height: synthesis and properties as a Fischer–Tropsch catalyst. *J Catal* 130:29–40
56. Chen JP, Hausladen MC, Yang RT (1995) Delaminated Fe<sub>2</sub>O<sub>3</sub>-pillared clay: its preparation, characterization, and activities for selective catalytic reduction of NO by NH<sub>3</sub>. *J Catal* 151:135–146
57. Tzou MS (1983) Clay catalysts pillared by metal hydroxy polymers. Ph.D. Thesis, Michigan State University
58. Doff DH, Gangas NHJ, Allan JEM, Coey JMD (1988) Preparation and characterization of iron oxide pillared montmorillonite. *Clay Miner* 23:367–377
59. Warburton C I (1988) Preparation and catalytic properties of iron oxide and iron sulphide pillared clays. *Catal Today* 2:271–280
60. Yamanaka S, Hattori M (1988) Iron oxide pillared clay. *Catal Today* 2:261–270

61. Martin-Luengo MA, Martins-Carvalho H, Landriere J, Grange P (1989) Fe(III) pillared montmorillonites: preparation and characterization. *Clay Miner* 24:495–504
62. Mishra T, Parida KM, Rao SB (1996) Transition metal oxide pillared clay: 1. A comparative study of textural and acidic properties of Fe (III) pillared montmorillonite and pillared acid activated montmorillonite. *Colloid Interface Sci* 183:176–183
63. Mori H, Miyoshi H, Takeda K, Yoneyama H, Fujita H, Iwata Y, Otsuka Y, Muratu Y (1992) TEM observation of iron oxide pillars in montmorillonite. *J Mater Sci* 27:3197–3199
64. Parida KM, Mishra T, Das D, Chintalpudi SN (1999) Thermal transformation of trinuclear iron (III) acetato complex intercalated montmorillonite. *Appl Clay Sci* 15:463–475
65. Yuan P, He H, Bergaya F, Wu D, Zhou Q, Zhu J (2006) Synthesis and characterization of delaminated iron-pillared clay with meso–microporous structure. *Micropor Mesopor Mater* 88:8–15
66. Pinnavaia TJ, Tzou MS, Landau SD (1985) New chromia pillared clay catalysts. *J Am Chem Soc* 107:4783–4785
67. Kanai H, Hayashi H, Koike T, Ohsuga M, Matsumoto M (1992) Oxidation of styrene catalyzed by  $\mu$ -oxotrinuclear mixed valence and mixed metal carboxylate complexes. *J Catal* 138:611–616
68. Finholt, JE, Thompson, ME, Connic, RE (1981) Hydrolytic polymerization of chromium(III). 2. A trimeric species. *Inorg Chem* 20:4151–4155
69. Stunzi H, Marty W (1983) Early stages of the hydrolysis of chromium(III) in aqueous solution 1. Characterization of a tetrameric species. *Inorg Chem* 22:2145–2150
70. Stunzi H, Spiccia L, Rotzinger RP, Marty W (1989) Early stages of the hydrolysis of chromium(III) in aqueous solution. 4. The stability constants of the hydrolytic dimer, trimer, and tetramer at 25 °C and I = 1.0 M. *Inorg Chem* 28:66–71
71. Bornholdt K, Corker JM, Evans J, Rummey JM (1991) EXAFS studies of the formation of chromia pillared clay catalysts. *Inorg Chem* 30:1–2
72. Spiccia L, Marty W, Giovanoli R (1988) Hydrolytic trimer of chromium (III). Synthesis through chromite cleavage and use in the preparation of the “active” trimer hydroxide. *Inorg Chem* 27:2660–2666
73. Bradley SM, Lehr CR, Kydd RA (1993) Base hydrolysis of aqueous chromium(III) solutions: on the existence of  $[\text{Cr}(\text{OH})_4]^-$  and speculation regarding a new chromium polyoxocation. *J Chem Soc Dalton Trans* 15:2415–2420
74. Tzou MS, Pinnavaia TJ (1988) Chromia pillared clays. *Catal Today* 2:243–259
75. Brindley GW, Yamanaka S (1979) A study of hydroxy-chromium montmorillonites and the form of the hydroxy-chromium polymers. *Am Miner* 64:830–835
76. Drljaca A, Anderson JR, Spiccia L, Turney TW (1992) Intercalation of montmorillonite with individual chromium(III) hydrolytic oligomers. *Inorg Chem* 31:4894–4897
77. Volzone C, Cesio AM, Torres Sanchez RM, Pereira E (1993) Hydroxy-chromium smectite. *Clays Clay Miner* 41:702–706
78. Jimenez-Lopez A, Maza-Rodriguez J, Olivera-Pastor P, Maireles-Torres P, Rodriguez-Castellon E (1993) Pillared clays prepared from the reaction of chromium acetate with montmorillonite. *Clays Clay Miner* 41:328–334
79. Mishra T, Parida K (1998) Transition metal pillared clay 4. A comparative study of textural, acidic and catalytic properties of chromia pillared montmorillonite and acid activated montmorillonite. *Appl Catal A* 166:123–133
80. Yoon JB, Hwang SH, Choy JH (2000) Trimeric chromium oxyformate route to chromia-pillared clay. *Bull Korean Chem Soc* 21:989–994
81. Roulia M (2005) Synthesis and characterization of novel chromium pillared clays. *Mater Chem Phys* 91:281–288
82. Bergaya F, Hassoum N, Gatineau L, Barrault J, Poncelet G, Jacobs PA, Grange P, Delmon B (eds) (1991) Mixed Al–Fe pillared laponites: preparation, characterization and catalytic properties in syngas conversion. In: *Preparation of catalyst*, vol. V. Elsevier, Amsterdam, p 329



83. Sterte J, Poncelet G, Jacobs PA, Grange P, Delmon B (eds) (1991) Preparation and properties of large-pore Re/Al-pillared montmorillonite. A comparison of re-cations. In: Preparation of catalyst, vol. V. Elsevier, Amsterdam, p 301
84. Bagshaw SA, Cooney RP (1995) Preparation and characterization of a highly stable pillared clay: GaAl<sub>12</sub>-pillared rectorite. Chem Mater 7:1384–1389
85. Hernando MJ, Pesquera C, Blanco C, Gonzalez F (2002) Increase in thermal stability of the texture in montmorillonites pillared with aluminum/cerium polyoxocations. Langmuir 18:5633–5636
86. Mishra T, Parida KM (1998) Transition metal oxide pillared clay: 5. Synthesis, characterization and catalytic activity of iron–chromium mixed oxide pillared montmorillonite. Appl Catal A 174:91–98
87. Mei JG, Yu SM, Cheng J (2004) Heterogeneous catalytic wet peroxide oxidation of phenol over delaminated Fe–Ti-PILC employing microwave irradiation. Catal Comm 5:437–440
88. Ding Z, Klopogge JT, Frost RL (2001) Porous clays and pillared clays-based catalysts. Part 2: A review of the catalytic and molecular sieve applications. J Porous Mater 8:273–293
89. Bineesh KV, Cho DR, Kim SY, Jermy BR, Park DW (2008) Vanadia doped titania pillared montmorillonite clay for the selective catalytic oxidation of H<sub>2</sub>S. Catal Comm 9: 2040–2043
90. Chevalier S, Franck R, Suquet H, Lambert JF, Barthomeuf D (1994) Al-pillared saponites. Part 1. IR studies. J Chem Soc Faraday Trans 90:667–674
91. Auer H, Hofmann H (1993) Pillared clays: characterization of acidity and catalytic properties and comparison with some zeolites Appl Catal A 97:23–38
92. Zubkov SA, Kustov LM, Kazansky VB, Fetter G, Tichit D, Figueras F (1994) Study of the nature of acid sites of montmorillonites pillared with aluminum and oligosilsesquioxane complex cations; 1, Bronsted acidity. Clays Clay Miner 42:421–427
93. Liu WQ, Zhao L, Sun GD, Min EZ (1999) Saturation of aromatics and aromatization of C<sub>3</sub> and C<sub>4</sub> hydrocarbons over metal loaded pillared clay catalysts. Catal Today 51:135–140
94. Benito I, Riego AD, Martinez M, Blanco C, Pesquera C, Gonzalez F (1999) Toluene methylation on Al<sub>13</sub>- and GaAl<sub>12</sub>-pillared clay catalysts. Appl Catal A 180:175–182
95. Molina R, Schutz A, and Poncelet G (1995) Transformation of *m*-xylene over Al-pillared clays and ultrastable zeolite Y. J Catal 145:79–85
96. Ming-Huan H, Zhonghui L, Enze, M (1988) Acidic and hydrocarbon catalytic properties of pillared clay. Catal Today 2:321–338
97. Bradley SM, Kydd RA, (1993) Ga<sub>13</sub>, Al<sub>13</sub>, GaAl<sub>12</sub>, and chromium-pillared montmorillonites: acidity and reactivity for cumene conversion. J Catal 141:239–249
98. Heyding RD, Tronside ARR, Norris AR, Rryszniak RY (1960) Acid activation of montmorillonite. Can J Chem 38:1003–1016
99. Mokaya R, Jones W, (1994) Pillared acid-activated clay catalysts. J Chem Soc Chem Comm 8:929–930
100. Kooli F and W Jones (1998) Al and Zr pillared acid-activated saponite clays: characterization and properties. J Mater Chem 8:2119–2124
101. Chaabene SB, Bergaoui SL, Ghorbel A, Lambert JF (2002) Non-aggressive way using zirconium acetate for preparation of zirconium pillared clay developing high sulfur thermal stability over 830 °C. Stud Surf Sci Catal 143:1053–1062
102. Katoh M, Fujisawa H, Yamaguchi T (1994) Synthesis and catalytic properties of sulfate ion-promoted Zr-pillared clays. Stud Surf Sci Catal 90:263–268
103. Khalfallah Boudali L, Ghorbel A, Tichit D, Figueras F, Dutartre R (1994) Synthesis and characterization of titanium-pillared montmorillonites. Microporous Mesoporous Mater 2:525–541
104. Knifton JF (1993) One-step synthesis of methyl *t*-butyl ether from *t*-butanol using pillared, phosphated montmorillonite clay catalysts. US Patent 5352847

105. Benchaabene S, Bergaoui L, Ghorbel A, Lambert JF, Grange P (2003) Acidic properties of a clay prepared from the reaction of zirconyl chloride solution containing sulfate ions with montmorillonite. *Appl Catal A* 252:411–419
106. Mishra T, Parida KM (2006) Effect of sulfate on the surface and catalytic properties of iron–chromium mixed oxide pillared clay. *J Colloid Interface Sci* 301:554–559
107. Occelli ML (1985) Surface and catalytic properties of some pillared clays. In: Schultz LG, van Olphen H, Mumpton FA (eds) *Proceedings of the International Clay Conference*. The Clay Minerals Society, Denver, pp 319–323
108. Zhao D, Yang Y, Guo X (1995) Synthesis and characterization of hydroxyl Cr–Al pillared clays. *Zeolites* 15:58–66
109. Gyftopoulou ME, Millan M, Bridgwater AV, Dugwell D, Kandiyoti R, Hriljac JA (2005) Pillared clays as catalysts for hydrocracking of heavy liquid fuels. *Appl Catal A* 282: 205–214
110. Del Castillo HL, Gil A, Grange P (1996) Hydroxylation of phenol on titanium pillared montmorillonite. *Clays Clay Miner* 44:706–709
111. Mishra T, Parida KM (1997) Transition metal pillared clays: 3. A para selective catalyst for nitration of chlorobenzene. *J Mol Catal A* 121:91–96
112. Kurian M, Sugunan S (2005) Catalytic activity of iron pillared montmorillonites for benzylation of benzene with benzyl chloride. *Bull Catal Soc India* 4:88–100
113. Kurian M, Sugunan S (2006) *tert*-Butylation of phenol catalysed by metal exchanged iron pillared montmorillonites. *Catal Comm* 7:417–421
114. Vicente MA, Meyer A, Gonzalez E, Bañares-Munoz MA, Gandia LM, Gil A (2002) Dehydrogenation of ethylbenzene on alumina–chromia-pillared saponites. *Catal Lett* 78: 99–104
115. Sugunan S, Rahna KS (2002) Surface acidity and catalytic activity of mixed Fe–Al and Cr–Al pillared montmorillonites. *Indian J Chem A* 41:1355–1362
116. Jinjun L, Zheng J, Zhengping H, Xiuyan X, Yahui Z (2005) Pillared laponite clays-supported palladium catalysts for the complete oxidation of benzene. *J Mol Catal A* 225:173–179
117. Choudary B M, Prasad A D, Bhuma V, Swapna V (1992) Chromium-pillared clay as a catalyst for benzylic oxidation and oxidative deprotection of benzyl ethers and benzylamines: a simple and convenient procedure. *J Org Chem* 57:5841–5844
118. Tatibouet JM, Guelou E, Fournier J (2005) Catalytic oxidation of phenol by hydrogen peroxide over a pillared clay containing iron. Active species and pH effect. *Topics Catal* 33:225–232
119. Feng J, Hu X, Yue PL (2004) Novel bentonite clay-based Fe-nanocomposite as a heterogeneous catalyst for photo-Fenton discoloration and mineralization of Orange II. *Environ Sci Technol* 38:269–275
120. Feng J, Hu X, Yue P L (2006) Effect of initial solution pH on the degradation of Orange II using clay-based Fe nanocomposites as heterogeneous photo-Fenton catalyst. *Water Res* 40:641–646
121. Li Y, Lu Y, Zhu X (2006) Photo-Fenton discoloration of the azo dye X-3B over pillared bentonites containing iron. *J Hazard Mater* 132:196–201
122. De Leon MA, Castiglioni J, Bussi J, Sergio M (2008) Catalytic activity of an iron-pillared montmorillonitic clay mineral in heterogeneous photo-Fenton process. *Catal Today* 133–135:600–605
123. Tomul F, Balci S (2009) Characterization of Al, Cr-pillared clays and CO oxidation. *Appl Clay Sci* 43:13–20
124. Yang RT, Chen JP, Kikkinides ES, Cheng LS, Cichanowicz JE (1992) Pillared clays as superior catalysts for selective catalytic reduction of nitric oxide with ammonia. *Ind Eng Chem Res* 31:1440–1445
125. Cheng LS, Yang RT, Chen N (1996) Iron oxide and chromia supported on titania-pillared clay for selective catalytic reduction of nitric oxide with ammonia. *J Catal* 164:70–81

126. Yang RT, Tharappiwattananon N, Long RQ (1998) Ion-exchanged pillared clays for selective catalytic reduction of NO by ethylene in the presence of oxygen. *Appl Catal B* 19:289–297
127. Long RQ, Yang RT (2000) Selective catalytic reduction of NO with ammonia over V<sub>2</sub>O<sub>5</sub> doped TiO<sub>2</sub> pillared clay catalysts. *Appl Catal B* 24:13–21
128. Long RQ, Yang RT (1999) Acid- and base-treated Fe<sup>3+</sup>-TiO<sub>2</sub>-pillared clays for selective catalytic reduction of NO by NH<sub>3</sub>. *Catal Lett* 59:39–44
129. Chae HJ, Nam IS, Kim YG, Yang HS, Choi HC, Song SL (1999) Characteristics of V<sub>2</sub>O<sub>5</sub>/Ti-PILC catalyst for the reduction of NO by NH<sub>3</sub>. *Stud Surf Sci Catal* 125:595–602
130. Tilak D, Tennakoon DTB, Jones W, Thomas JM (1986) Structural aspects of metal-oxide-pillared sheet silicates. An investigation by magic-angle-spinning nuclear magnetic resonance, Fourier-transform infrared spectroscopy and powder X-ray diffractometry. *J Chem Soc Faraday Trans* 82:3081–3095
131. Valverde JL, Lucas A, Dorado F, Romero A, Garcia PB (2005) Influence of the operating parameters on the selective catalytic reduction of NO with hydrocarbons using Cu-ion-exchanged titanium-pillared interlayer clays (Ti-PILCs). *Ind Eng Chem Res* 44:2955–2965
132. Li WB, Sirilumpen M, Yang RT (1997) Selective catalytic reduction of nitric oxide by ethylene in the presence of oxygen over Cu<sup>2+</sup> ion-exchanged pillared clays. *Appl Catal B* 11:347–363
133. Shen SC, Kawi S (2001) Kinetic studies of selective catalytic reduction of nitric oxide by propylene on Pt/MCM-41 catalyst. *Catal Today* 68:245–254
134. Busca G, Lietti L, Ramis G, Berti F (1998) Chemical and mechanistic aspects of the selective catalytic reduction of NO<sub>x</sub> by ammonia over oxide catalysts: a review. *Appl Catal B* 18:1–36
135. Del Castillo HL, Gil A, Grange P (1997) Preparation and characterization of sulfated titanium-modified pillared montmorillonite. *Catal Lett* 43:133–137
136. Khalfallah Boudali L, Ghorbel A, Grange P (2006) SCR of NO by NH<sub>3</sub> over V<sub>2</sub>O<sub>5</sub> supported sulfated Ti-pillared clay: reactivity and reducibility of catalysts. *Appl Catal A* 305:7–14
137. Valverde JL, Lucas A, Dorado F, Sun-Kou R (2003) Characterization and catalytic properties of titanium-pillared clays prepared at laboratory and pilot scales: a comparative study. *Ind Eng Chem Res* 42:2783–2790
138. himokawabe M, Tadokoro K, Sasaki S, Takezawa N (1998) Temperature programmed desorption and infrared spectroscopic studies of nitrogen monoxide adsorbed on ion-exchanged copper mordenite catalysts. *Appl Catal A* 166:215–223
139. Fujishima A, Hashimoto K, Watanabe T (1999) TiO<sub>2</sub> photocatalysis: fundamentals and applications. BKC, Tokyo
140. Linsebigler AL, Lu G, Yates JT Jr (1995) Photocatalysis on TiO<sub>2</sub> surfaces: principles, mechanisms, and selected results. *Chem Rev* 95:735–758
141. Anpo M (2000) Utilization of TiO<sub>2</sub> photocatalyst in green chemistry. *Pure Appl Chem* 72:1265–1270
142. Yoneyama H, Haga S, Yamanaka S (1989) Photocatalytic activities of microcrystalline TiO<sub>2</sub>, incorporated in sheet silicates of clay. *J Phys Chem* 93:4833–4837
143. Ooka C, Yoshida H, Suzuki K, Hattori T (2004) Effect of surface hydrophobicity of TiO<sub>2</sub>-pillared clay on adsorption and photocatalysis of gaseous molecules in air. *Appl Catal A* 260:47–53
144. Valverde JL, Sanchez P, Dorado F, Molina CB, Romero A (2002) Influence of the synthesis conditions on the preparation of titanium-pillared clays using hydrolyzed titanium ethoxide as the pillaring agent. *Micropor Mesopor Mater* 54:155–165
145. Ding Z, Zhu HY, Lu GQ, Greenfield PF (1999) Photocatalytic properties of titania pillared clays by different drying methods. *J Colloid Interface Sci* 209:193–199
146. Xuzhuang Y, Yang D, Huaiyong Z, Jiangwen L, Martins WN, Frost R, Daniel L, Yuenian S (2009) Mesoporous structure with size controllable anatase attached on silicate layers for efficient photocatalysis. *J Phys Chem C* 113:8243–8248

147. Lim M, Zhou Y, Wood B, Wang LZ, Rudolph V, Lu GQ (2009) Highly thermostable anatase titania-pillared clay for the photocatalytic degradation of airborne styrene. *Environ Sci Technol* 43:538–543
148. An-ning Z, You-mei C, Zhan-Jiang Y (2008) Visible light induced TiO<sub>2</sub> pillared MMT photocatalyst coupling-doped with S and N. *J Coal Sci Eng* 14:517–519
149. Zhang G, Ding X, Hu Y, Huang B, Zhang X, Qin X, Zhou J, Xie J (2008) Photocatalytic degradation of 4BS dye by N, S-codoped TiO<sub>2</sub> pillared montmorillonite photocatalysts under visible-light irradiation. *J Phys Chem C* 112:17994–17997
150. Das DP, Parida KM (2008) Solar light induced photocatalytic degradation of pollutants over titania pillared zirconium phosphate and titanium phosphate. *Catal Surv Asia* 12:203–213

# Chapter 6

## Use of Pillared Clay-Based Catalysts for Wastewater Treatment Through Fenton-Like Processes

J. Herney-Ramírez and Luis M. Madeira

**Abstract** Clays, both natural and physical-chemically modified, are attractive materials for the preparation of supported catalysts. In this chapter, a review is made regarding the use of pillared interlayered clays (PILCs) in heterogeneous Fenton-like advanced oxidation processes. Their applications in pollutants degradation is summarized, with particular emphasis on the effect of the main operating conditions (e.g., initial  $\text{H}_2\text{O}_2$  or parent compound concentration, catalyst load, pH, or temperature) on oxidation efficiency. Special attention is also given to the type of catalyst or precursor used, to the importance and advantages of the heterogeneous versus homogeneous process, and to significant aspects like catalyst stability. Among the technological issues that are of concern, the importance of using continuous flow reactors (e.g., fixed-bed) is discussed. Finally, some mechanistic studies are reviewed as well as modeling works, based on phenomenological or semi-empiric models (e.g., using statistic tools like design of experiments).

**Keywords** Pillared clays · Catalyst · Fenton · Wastewater treatment · Advanced oxidation processes

### 6.1 Introduction

#### 6.1.1 Water Treatment with Advanced Oxidation Processes

Water and wastewater treatment is an issue of concern in our society. However, some of the typical treatment methods, for example, adsorption (e.g., using activated carbon), coagulation, or air stripping, simply transfer the aqueous organics

---

L.M. Madeira (✉)  
LEPAE, Department of Chemical Engineering, Faculty of Engineering, Porto University,  
Rua Dr. Roberto Frias, 4200-465 Porto, Portugal  
e-mail: mmadeira@fe.up.pt

to another phase leaving the contaminants undestroyed. Moreover, many of these pollutants are refractory to biological degradation or even toxic to the microorganisms; when it is not the case, these processes proceed at low rates. Therefore, during the past decades many researchers have stressed their focus on searching for direct and effective methods to solve this problem.

Advanced oxidation processes (AOPs) are known as being effective to remove non-biodegradable organic pollutants from waters/wastewaters. Their efficiency results from the fact that the in situ generated hydroxyl radicals ( $\text{HO}\cdot$ ) are highly reactive species ( $E^\circ = +2.8 \text{ V}$ ), which attack the majority of the organic molecules causing their oxidation to other products and ultimately to  $\text{CO}_2$  and  $\text{H}_2\text{O}$  [1], except for some of the simplest organic compounds such as acetic, maleic, and oxalic acids, acetone, or simple chloride derivatives as chloroform [2].  $\text{HO}\cdot$  radicals attack the organic molecules with rate constants usually in the order of  $10^6\text{--}10^9 \text{ M}^{-1} \text{ s}^{-1}$  [3]. They are also characterized by a low selectivity of attack, which is a useful attribute for an oxidant used in wastewater treatment and for solving pollution problems [4]. The radicals are produced by processes that usually operate at mild temperatures and pressures and that result from the combinations of ozone, hydrogen peroxide, UV radiation, ferrous ions and/or titanium dioxide, among others (see Fig. 6.1). Contaminants are mainly oxidized through the use of four different reagents: ozone, hydrogen peroxide, oxygen, and air or their combination. To choose the most appropriate technology some aspects, such as the concentration and nature of the pollutants and the volume of wastewater, must be considered [5].

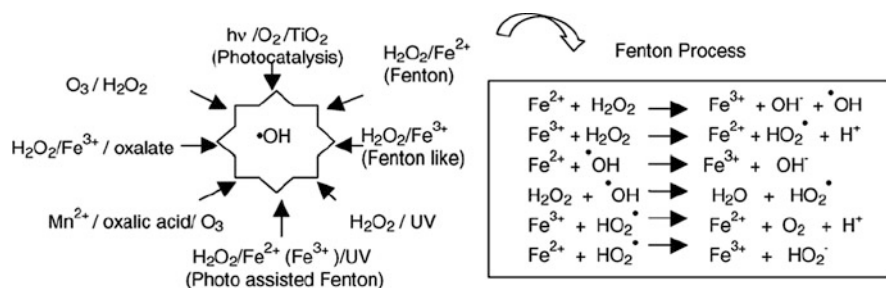


**Fig. 6.1** Sketch of some advanced oxidation processes. Reprinted from [1], with permission from Elsevier

The versatility of the AOPs is also enhanced by the fact that they offer different possible ways for hydroxyl radicals production, thus allowing a better compliance with the specific treatment requirements, as described by Andreozzi et al. [3]. Currently, the four AOPs that have been most widely studied are ozonation,  $\text{H}_2\text{O}_2/\text{UV}$ , the Fenton's reagent ( $\text{Fe}^{2+}/\text{H}_2\text{O}_2$ ), and  $\text{TiO}_2/\text{UV}$  [6]. AOPs include also other techniques, such as methods based on ultrasound, plasma, and electrohydraulic, among others, but are much less common [5]. In this chapter we will focus our attention on the use of Fenton-like processes, also often called wet hydrogen peroxide catalytic oxidation (WHPCO) or catalytic wet peroxide oxidation (CWPO), for instance. Actually, hydrogen peroxide is one of the more desirable

oxidant agents; although  $\text{H}_2\text{O}_2$  is a relatively costly reactant, it is easy to handle and the excess decomposes to environmentally safe products. Besides, as compared with ozone, for instance, it does not form any harmful by-products and is a non-toxic and ecological reactant [7]. Advantages of Fenton's reagent over other oxidizing treatment methods include also the high efficiency, simplicity in destroying the contaminants (eventually leaving no residues), stability to treat a wide range of substances, and non-necessity of special equipment. Besides, operating conditions are usually mild (atmospheric pressure and around room temperature), and the reaction rates are reasonably high due to the use of the iron catalyst.

As described in detail below, the use of this AOP aims usually at the degradation of certain compounds or complex wastewaters to meet the environmental standards before effluent's discharge. Nevertheless, its use has been often considered when coupled with biological processes. Actually, integrated catalytic-biological systems have been recently seen as cost-effective processes for the treatment of organic compounds and have become an important developing trend in practical industrial wastewater treatment. This is due to the fact that compared with typical biological treatment, AOPs such as Fenton-like normally have a much higher operating cost. Therefore, in a real industrial wastewater treatment plant, complete mineralization of the wastewater by AOPs is not cost-effective and not necessary. So, to decrease the operational cost, the use of AOPs as a pre-treatment step to enhance the biodegradability of wastewater containing recalcitrant or inhibitory compounds is an interesting approach if the resulting intermediates are easily degradable in a further biological unit. Based on this idea, the Fenton reactors can be envisaged as the pre-treatment step of wastewaters.

### ***6.1.2 The Use of Pillared Clays in Heterogeneous Fenton-Based Processes***

Fenton-like processes have been traditionally employed in a homogeneous way, i.e., with the iron catalyst salt dissolved in the aqueous solution. However, there is a major drawback: they need large amounts of Fe in solution (up to 50–80 ppm), which is well above the EU directives that allow a maximum of 2 ppm Fe in treated water to be discharged directly into the environment [8]. In addition, the application of the homogeneous treatment to large water flow rates may produce large amounts of sludge in the final neutralization step. The treatment of the sludge-containing Fe ions at the end of wastewater treatment (usually through precipitation and redissolution) is costly and needs large amount of chemicals and manpower [9].

Therefore, numerous attempts have been done to find heterogeneous systems/supports for the Fe species, so that they can be effectively applied in wastewater treatment, e.g., see Refs. [10–15]. The major advantage of the use of heterogeneous catalytic materials is their easy recovery. Unlike the homogeneous systems, these solid catalysts can be recuperated by means of a simple separation operation and re-used in the next runs. Besides, these materials should meet criteria

like high efficiency/catalytic activity, low cost, and long-term stability. In this sense, one of the principal goals is the development of stable heterogeneous catalysts with minimal leaching of the active species under the reaction conditions. Studies found in the literature refer to the use of membranes (e.g., Nafion-based), resins, zeolites, silica, alumina, or carbons. Here, we are particularly concerned with pillared clays, which have several advantages as extensively described in other chapters of this book, namely, their particular properties and structures as well as their abundance and low cost.

Clays have been widely used as ion exchangers, catalysts, and adsorbents. However, the lack of permanent high porosity limits their further application in industry [16]. To solve this problem, bulky inorganic polycations obtained from polymerization of multivalent inorganic cations (e.g.,  $\text{Al}^{3+}$ ,  $\text{Zr}^{4+}$ ,  $\text{Ti}^{4+}$ , and  $\text{Fe}^{3+}$ ) have been intercalated into the interlayer region of the clays by cationic exchange [17–19]. This is done because when clays are dispersed in water, they swell significantly owing to the hydration of the interlamellar cations that act as counter ions to balance the negative charges of the clay layers [9]. Therefore, polycations in aqueous solutions can be intercalated into the interlayer gallery by cation exchange. The intercalated polycations increase the basal spacing of the clays and, upon heating in the calcination stage at a high temperature, the intercalated species undergo dehydration and dehydroxylation and hence are converted to temperature-stable oxide pillars, propping the clay layers apart and preventing its collapse. The final pillared interlayered clays (PILCs) present a permanent two-dimensional porous network, showing a dramatic improvement in catalytic and adsorption applications [17, 18]. The final properties of PILCs can be modulated by carefully choosing the different parameters, such as nature of the pillaring agent, type of clay and particle size, pillaring procedure, and thermal treatments, thus offering a very powerful and flexible way to design tailored catalysts. Therefore, control of the pillaring process is a very promising means to obtain solids with (i) very high surface areas up to  $600 \text{ m}^2 \text{ g}^{-1}$ , (ii) a broad spectrum of properties (structural, chemical, catalytic, etc.), and (iii) controlled internal structures, with reactive sites and/or species chosen to match particular applications or provide host structures for chemical or physical processes [20, 21].

Actually, PILCs constitute one of the most widely studied materials among the new groups of microporous materials developed by molecular engineering. An extensive review on the advances in the synthesis and catalytic applications of PILCs (also known as cross-linked clays) has been published by Gil et al. [18]. One of the more studied topics related to PILCs is their use as support for active catalytic phases in the preparation of supported catalysts and the applicability of the resulting solids in several reactions, particularly environmental-friendly ones [22].

Among the intercalated clay precursors indicated above,  $\text{Fe}^{3+}$  is an ongoing one for research in heterogeneous catalysis and adsorption, being of particular relevance in Fenton-based processes which make use of Fe species as catalyst.

Several studies on the formation of Fe-PILC were carried out in the past few years, as stated by Sum et al. [16]. In particular, many researchers showed that when using bentonite and montmorillonite clays, the Fe-PILC has basal spacings of up to



10–20 Å and BET surface area reaching up to 300 m<sup>2</sup>/g [16]. Montmorillonites in particular constitute one of the most abundant smectitic clays in nature [23]. They are characterized by the substitution of Al<sup>3+</sup> by Mg<sup>2+</sup> in the octahedral sheet, resulting in a negative layer charge that is compensated by hydrated cations adsorbed in the interlamellar space. These cations can be easily substituted by others present in solution.

Another interesting material for the applications envisaged in this review is laponite. As described by Bobu et al. [17], in a diluted aqueous dispersion laponite RD (model synthetic hectorite-type smectite clay) exists as discrete plates with 20–30 nm diameter. Therefore, this clay is an ideal inorganic medium to form nanometer-scale composite structures with iron oxide particulates named Fe-Lap-RD. X-ray diffraction results revealed that the Fe-Lap-RD mainly consists of Fe<sub>2</sub>O<sub>3</sub> (maghemite) crystallites and Fe<sub>2</sub>SiO<sub>10</sub>(OH)<sub>2</sub> (iron silicate hydroxide) crystallites.

As described by Iurascu et al. [24], Fe has also been often incorporated by pillaring of smectites, yet polymerization of Fe(III) produces polyoxocations that can intercalate swellable clays by substitution of their exchangeable cations. However, intercalation pillaring with Fe has a main disadvantage because it is not easily reproducible. Differently from the Al<sub>13</sub> polycation, well known and easy to prepare, Fe forms various polycations depending on the preparation conditions. Thus, some authors, including the present ones [25, 26] and others, e.g., see Ref. [24], have used a new strategy for the preparation of Fe-clay catalysts, which involves the impregnation with Fe-salts of previously prepared Al-pillared saponite. In this way, the textural properties of the support are maintained, because of the high stability of Al-pillared saponite, and the amount of the Fe-active phase can easily be controlled.

### ***6.1.3 Pollutants Degraded or Wastewaters Treated with Pillared Clay-Based Catalysts***

As mentioned before, PILCs have been extensively used in Fenton-like processes. Table 6.1 provides an overview of the pollutants degraded by such processes and the types of PILCs used. Among the different types of substances degraded using this AOP, phenols (and their derivatives) deserved the attention of numerous studies. Actually, phenols are among the most abundant pollutants in industrial wastewaters, due to their wide utilization in several industries. The world production of phenol is estimated to be over  $3 \times 10^6$  t/year [24], being used in the synthesis of resins, dyes, pharmaceuticals, perfumes, pesticides, tanning agents, solvents, or lubricating oils. It has several concerns to human health, as long-term exposure to phenol paralyzes the central nervous system and damages kidneys and lungs. Besides, biodegradability is only 90% in surface waters after 7 days, and the aquatic toxicity of phenol (LC<sub>50</sub>) is 12 mg/l (*Daphnia magna*, 48 h) [24].

Another class of compounds that has been widely covered in the literature and reported in Table 6.1 is dyes. Over 700,000 t of approximately 10,000 types of dyes and pigments are produced every year worldwide [27]. From this amount, about

**Table 6.1** Some examples of substances degraded by Fenton-like processes using pillared clays

Type of pollutant degraded	Type of pillared clay	References
Phenol	Pillared bentonite containing iron	[32–35]
Phenol	Fe-exchanged pillared beidellite	[36]
4-Nitrophenol	Fe-modified montmorillonite	[37]
Azo-dye Orange II	Saponite clay-based catalyst	[25, 26]
Azo-dye Reactive Yellow 84	Iron-containing pillared beidellite	[38]
Cinnamic acid	Fe-pillared montmorillonite	[30]

20% are discharged without treatment [28]. So, the disposal of the large amounts of effluents from textile industry produces uncontrollable environmental hazards because they contain considerable color as well as appreciable quantities of organic compounds that are not easily eliminated by conventional wastewater treatment methods (particularly azo dyes due to their non-biodegradable nature or toxicity) [6, 27, 29].

Finally, cinnamic acids [30], which are simple aromatic compounds that result from olive cell wall degradation during oil extraction, were studied using Fe-pillared montmorillonite catalyst (see Table 6.1). These various aromatic acids are typically found in wastewaters of agricultural origin and represent a dangerous contamination. The conventional biological or physico-chemical treatments are slow or non-destructive and consequently are considered as inadequate for eliminating these types of pollutants. Attempts to develop an appropriate technology based on partial oxidation using ozone as oxidant or by applying wet air oxidation have been reported. However, these methods are considered to be either expensive or requiring a high reaction temperature [31] and so the Fenton-like might be a feasible alternative.

In the following section, we will describe this AOP in more detail, with special emphasis on the effect of the operating conditions, as well as on other technological issues that are of concern for real implementation.

## 6.2 Fenton and Fenton-Like Process

### 6.2.1 Introduction

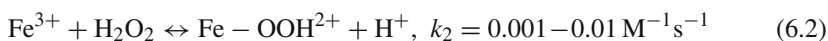
In 1894, Fenton reported that ferrous ion strongly promotes the oxidation of tartaric acid by hydrogen peroxide [39]. Forty years later, Haber and Weiss [40] discovered that the hydroxyl radical is the actual oxidant in such system. In reality, the Fenton catalyst ( $\text{Fe}^{2+}/\text{Fe}^{3+}$  system) causes the dissociation of hydrogen peroxide and the formation of highly reactive  $\text{HO}\cdot$  radicals that attack and destroy the organic compounds. This reaction is a widely used and studied catalytic process based on an electron transfer between  $\text{H}_2\text{O}_2$  and a metal (usually transition metal) acting as

a homogeneous catalyst [41, 42]. By far, the most common of these ones is iron [43, 44].

The mechanism of Fenton's oxidation involves basically the following steps. First, a mixture of  $\text{H}_2\text{O}_2$  and ferrous iron in acidic solution generates hydroxyl radicals according to the following reaction [44–47]:

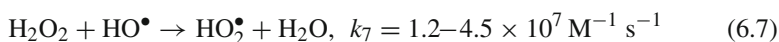
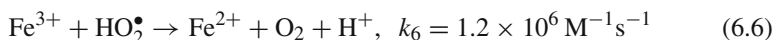
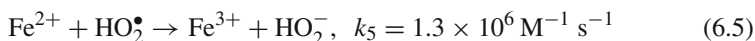
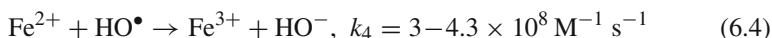


Because iron(II) acts as a catalyst, it has to be restored, which seems to occur through the following scheme:



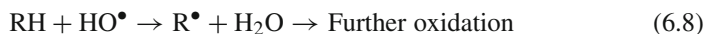
The reaction of hydrogen peroxide with ferric ions is referred to as a Fenton-like, see reactions (6.2) and (6.3) [48, 49].

The generation of the radicals involves a complex reaction sequence in aqueous solution, some of them described below. In particular, it is worth noting the scavenging of different radicals by the Fe species and also by  $\text{H}_2\text{O}_2$ , which can act as an  $\text{OH}^\bullet$  scavenger as well as an initiator (reaction (6.1)).

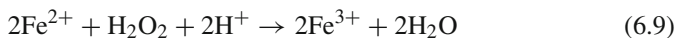


It is finally worth noting that the scheme presented herein is a simplification of those reported by several authors, where tens of equations are often considered [2, 50].

Hydroxyl radicals formed can then oxidize organics (RH) by abstraction of protons producing organic radicals ( $\text{R}^\bullet$ ), which are highly reactive and can be further oxidized [51, 52]:



Walling [44] simplified the overall Fenton chemistry (reaction (6.1)) by accounting for the dissociation water:



This equation suggests that the presence of  $H^+$  is required in the decomposition of  $H_2O_2$ , indicating the need for an acid environment to produce the maximum amount of hydroxyl radicals.

The oxidation using Fenton's reagent has proved to be a promising and attractive treatment method for the effective destruction of a large number of hazardous and organic pollutants, e.g., see Refs. [2, 3]. However, and as mentioned above (see Section 6.1.2), the homogeneous Fenton process often needs significant amounts of the metal in solution, increasing the subsequent costs for sludge's treatment and/or catalyst recovery. So, recent research trends have been focused on the incorporation of the Fe ions or Fe oxides into porous supports, particularly into PILCs for the reasons described above (cf. Section 6.1.2), namely, their particular properties and structures (with tunable pore size), as well as the abundance and low cost of natural clay minerals. Besides, they lead to active and stable solids in aqueous media, usually being very stable against leaching [38].

Table 6.2 gives a perspective of some of the studies found in the open literature in which PILCs have been employed in the Fenton/Fenton-like degradation of some compounds. The best or typical performances reached are also mentioned, as well as the corresponding operating conditions. In this concern it is important to remark that in most studies not only information on the parent compound degradation is gathered, but also information on mineralization (i.e., quantification of total organic carbon – TOC – reduction) is also of crucial importance. Actually, even if the complete degradation can be achieved, some intermediates might still be formed having eventually a higher toxic potential than the parent compound. Thus, in Table 6.2, data about TOC conversion are also included, whenever available.

## 6.2.2 Effect of the Main Operating Conditions

The heterogeneous Fenton-like process is affected by several process parameters. This will be discussed in the following sections, and some examples will be given to better illustrate such effects.

### 6.2.2.1 Effect of the Initial pH

A dependence of the reaction performance with the pH is normally observed in homogeneous and heterogeneous Fenton-like reactions. In homogeneous systems the decreased performance at lower pHs is usually attributed to the inhibition of the reaction between  $Fe^{3+}$  and hydrogen peroxide (reaction (6.2)), because the formation of the iron(III) peroxocomplexes (as intermediates) decreases when pH decreases [55]. Besides, at pH around 3.0 maximum concentration of the active  $Fe^{2+}$  species is reached along with the lowest rate of  $H_2O_2$  parasitic decomposition. By increasing the pH, the precipitation of the insoluble ferric hydroxides takes place and the decomposition of  $H_2O_2$  becomes significant [35]. This disadvantage can be avoided using a heterogeneous system; for example, Catrinescu et al. [36] observed that although an important difference in phenol removal in the 2.5–7.0 pH

**Table 6.2** Best or typical performances reached and corresponding operating conditions during wastewater treatment through Fenton and Fenton-like AOPs using pillared clays

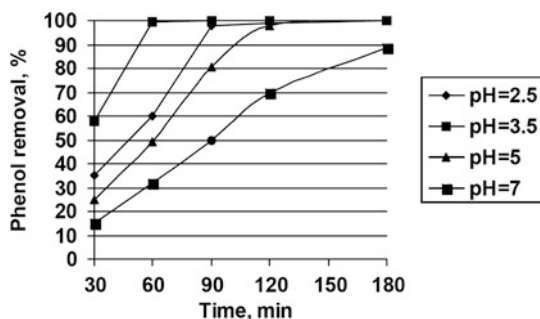
Type of pollutant degraded	Operating conditions	Best (or typical) performances reached	Observation	References
Azo-dye Orange II (OII)	$57\text{ }^{\circ}\text{C} < T < 68\text{ }^{\circ}\text{C}$ $C_{\text{catalyst}} < 43\text{ mg/l}$ or $35\text{ }^{\circ}\text{C} < T < 45\text{ }^{\circ}\text{C}$ , $C_{\text{catalyst}} > 118\text{ mg/l}$ , $\text{pH} = 3.0$ , $\text{CH}_2\text{O}_2 = 3\text{ mM}$	99% discoloration, 90% TOC removal, $t = 4\text{ h}$	0.1 mM OII, saponite clay-based catalyst	[26]
Azo-dye Orange II (OII)	$T = 70\text{ }^{\circ}\text{C}$ , $C_{\text{catalyst}} = 91.5\text{ mg/l}$ , $\text{pH} = 3.0$ , $\text{CH}_2\text{O}_2 = 6\text{ mM}$	99% discoloration, 91% TOC removal, $t = 4\text{ h}$	0.1 mM OII, saponite clay-based catalyst	[25]
Phenol	$T = 27\text{ }^{\circ}\text{C}$ , $C_{\text{catalyst}} = 1.5\text{ g/l}$ , $\text{pH} = 4.0$ , $\text{CH}_2\text{O}_2 = 4\text{ mM}$	100% degradation, $t = 3\text{ h}$	$5 \times 10^{-4}\text{ M}$ phenol, pillared clay-based catalysts, Fe-Al	[53]
Phenol	$T = 25\text{ }^{\circ}\text{C}$ , $C_{\text{catalyst}} = 5\text{ g/l}$ , $\text{pH} = 3.7$ , $\text{CH}_2\text{O}_2 = 0.1\text{ mM}$	100% conversion, 60–70% TOC removal, $t = 4\text{ h}$	$5 \times 10^{-4}\text{ M}$ phenol Al-Fe-pillared clay-based catalyst	[32]
Phenol	$C_{\text{catalyst}} = 5\text{ g/l}$ , $\text{pH} = 3.7$ , $\text{CH}_2\text{O}_2 = 0.1\text{ M}$	100% conversion, 80% TOC removal, $t = 4\text{ h}$	$5 \times 10^{-4}\text{ M}$ phenol, Al-Fe-pillared clay-based catalyst	[33]
Phenol	$T = 70\text{ }^{\circ}\text{C}$ , $C_{\text{catalyst}} = 1\text{ g/l}$ , $\text{pH} = 3.5\text{--}4.0$ , $\text{CH}_2\text{O}_2 = 0.1\text{ mM}$	100% conversion, 80% TOC removal, $t = 2\text{ h}$	$5 \times 10^{-4}\text{ M}$ phenol, Al-Fe-pillared clay-based catalyst	[34]
Phenol	$C_{\text{catalyst}} = 0.5\text{ g}$ , $\text{pH} = 3.7$ , $\text{CH}_2\text{O}_2 = 0.1\text{ mM}$	$X_{\text{phenol}} = 100\%$ , $t = 2\text{ h}$ , $X_{\text{TOC}} = 49\text{--}53\%$ , $t = 4\text{ h}$	$5 \times 10^{-4}\text{ M}$ phenol, Al-Fe-pillared bentonite catalyst	[54]
Phenol	$T = 50\text{ }^{\circ}\text{C}$ , $C_{\text{catalyst}} = 1\text{ g/l}$ , $\text{pH} = 5.0$ , $\text{CH}_2\text{O}_2 = 37.23\text{ mM}$	100% conversion, 87.9% COD removal, $t = 3\text{ h}$	250 mg/l phenol, batch reactor, Fe-exchanged Al-pillared clay-based catalyst	[36]

Table 6.2 (continued)

Type of pollutant degraded	Operating conditions	Best (or typical) performances reached	Observation	References
Phenol	$T = 70\text{ }^{\circ}\text{C}$ , $C_{\text{catalyst}} = 6.6\text{ g/l}$ , $\text{pH} = 4.0$ , $\text{CH}_2\text{O}_2 = 0.3\text{ mM}$ , atmospheric pressure	100% conversion, 50% TOC removal, $t = 4\text{ h}$	100–500 mg/l phenol, Al-Fe-pillared clay-based catalyst	[35]
Azo-dye C.I. Reactive Yellow 84	$T = 50\text{ }^{\circ}\text{C}$ , $C_{\text{catalyst}} = 1\text{ g/l}$ , $\text{pH} = 3.5$ , $\text{CH}_2\text{O}_2 = 20\text{ mM}$	99.8% discoloration, 48% TOC removal, $t = 1\text{ h}$	100 mg/l azo dye, Al-Fe-pillared clay-based catalyst	[38]
Cinnamic acid	$T = 30\text{ }^{\circ}\text{C}$ , ratio Fe/cinnamic A = 0.2 (molar), $\text{pH} = 2.9$ $\text{H}_2\text{O}_2/\text{cinnamic A} = 83$ (molar)	100% conversion, $t = 3\text{ h}$	120 mg/l cinnamic acid, Fe-pillared montmorillonite catalyst	[30]
4-Nitrophenol	$C_{\text{catalyst}} = 1\text{ g/l}$ , $\text{CH}_2\text{O}_2 = 10\text{ mM}$	100% conversion, $t = 3\text{ h}$	1 mM 4 nitro-phenol, Fe (III)-exchanged and pillared montmorillonite as catalysts	[37]

**Fig. 6.2** Phenol removal at different pH values

( $C_{\text{PILC catalyst}} = 0.5 \text{ g/l}$ ,  
 $C_{\text{Pho}} = 250 \text{ ppm}$ ;  
 $C_{\text{H}_2\text{O}_2} = 37.23 \text{ mM}$ ,  
 $T = 50 \text{ }^\circ\text{C}$ ). Reprinted from [36], with permission from Elsevier



range occurs for initial reaction times, this is attenuated after ca. 2 h, at least for pH values up to 5 (see Fig. 6.2). Besides, when  $\text{Fe}^{3+}$ -exchanged Al-pillared beidellite is used, intermediates are completely eliminated, whatever be the pH value within the 2.5–5.0 range. The catalyst remains active even at neutral pH. This is in contrast to homogeneous Fenton catalysts which show no, or negligible, activity at this pH. This activity could be related to the particular environment of Fe cations inside the pore structure of PILCs, where strong electrostatic fields are present [36]. Accordingly, by using heterogeneous catalysts, such as PILCs, it is possible to extend the range of pH values for which Fenton-type oxidation can occur.

Other authors, using pillared clay catalyst for phenol conversion [32], found that the stability of hydrogen peroxide is dependent on pH. The least decomposition of  $\text{H}_2\text{O}_2$  was found at pH values between 3 and 4. This range corresponds to the highest stability zone of  $[\text{Fe}(\text{OH})]^{2+}$ . Above pH 4, the rapid hydrogen peroxide decomposition produces molecular oxygen without formation of appreciable amounts of hydroxyl radicals in the solution. Below pH 3, more of the charged ferric ions remained as hydrated ferric ions, which accelerate not only the decomposition of the peroxide but also the competitive reaction for hydroxyl radicals' depletion. In addition, a pH lower than 3 favors leaching of the metal into the solution [35].

Other studies have also reported optimum pH values close to 3–4 in heterogeneous PILC-based systems, for instance, Tatibouët et al. [32] during phenol conversion or Ramirez et al. [25] during Orange II dye degradation. In another study [30], using Fe-pillared clay as a Fenton-type heterogeneous catalyst for cinnamic acid degradation, the pH varied between 2.9 and 5.0. Figure 6.3 shows that a lower pH led to a higher removal, both in homogeneous and heterogeneous systems. From Fig. 6.3 it can be seen that the heterogeneous Fenton reagent was more efficient than the homogeneous one in reducing concentration of cinnamic acid, the difference being particularly noticeable at pH 5. It might be the result of the affinity of the organic species for the clay surface. Furthermore, the heterogeneous catalyst activity was slightly less sensitive than that of the homogenous catalyst to pH variations in the 2.9–5.0 range after 3 h, while during the first 2 h the sensitivity in the two cases was similar. In this study, a higher elimination rate of cinnamic acid was obtained at pH = 2.9.

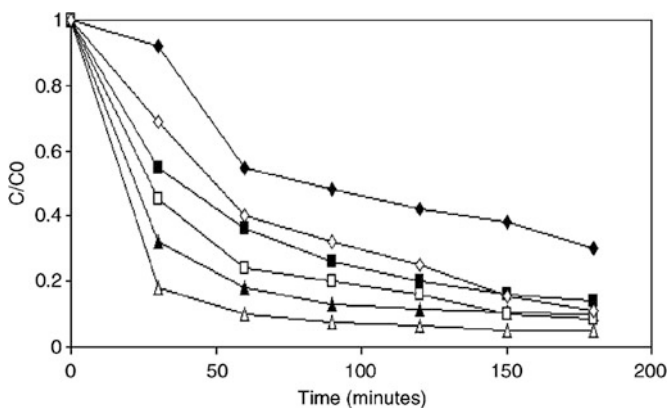


**Fig. 6.3** Influence of the pH on the disappearance of cinnamic acid as a function of time at various pHs at Fe/cinnamic acid molar ratio = 10 and  $\text{H}_2\text{O}_2$ /cinnamic acid molar ratio = 8.3. *Solid symbols* refer to homogeneous catalysis and *open symbols* to heterogeneous catalysts: (◇) pH = 5.0, (□) pH = 4.0, and (△) pH = 2.9. Reprinted from [30], with permission from Elsevier

### 6.2.2.2 Effect of the Temperature

Temperature is a very important parameter in the Fenton and Fenton-like processes, because it can affect not only the catalytic performance but also the stability of the hydrogen peroxide (and eventually of the catalyst, by acting on the leaching). Several researchers have investigated the effect of temperature on the degradation/conversion of different compounds, using PILCs. For instance, Ramirez et al. [26] have used a clay-based Fenton-like catalyst for the oxidation of Orange II and found that the reaction temperature has indeed an important effect on the dye degradation history. Total color removal can be reached in less than 30 min when working at a temperature of 73.6 °C (Fig. 6.4a), but at lower temperatures the process slows down significantly. This kind of effect was expected, since it is known that kinetic constants (either for radicals production or for iron regeneration) have exponential dependency with reaction temperature (Arrhenius law). For TOC removal (Fig. 6.4b) the same kind of effect can be seen as for dye degradation. Temperature increase leads to better TOC removal, but the difference between temperatures of 40 and 73.6 °C is not as significant as it was observed for color removal. This is probably due to the fact that  $\text{H}_2\text{O}_2$  decomposes into oxygen and water at high temperatures, affecting more strongly mineralization of all of the organics which proceed more slowly (and thus the effect is noticed at longer reaction times) than OII degradation. Similar trends were obtained by other authors [35, 36]. Finally, when the temperature increases the iron loss from the support also increases, affecting the stability of the catalyst (cf. Fig. 6.4c).

Guélou et al. [33] observed that when they changed the temperature between 18 and 70 °C, an increase, both in the rate of phenol conversion and in the TOC abatement level, was reached. The study carried out by Barrault et al. [34] over mixed (Al-Fe)-pillared clays showed results very similar to the ones obtained by



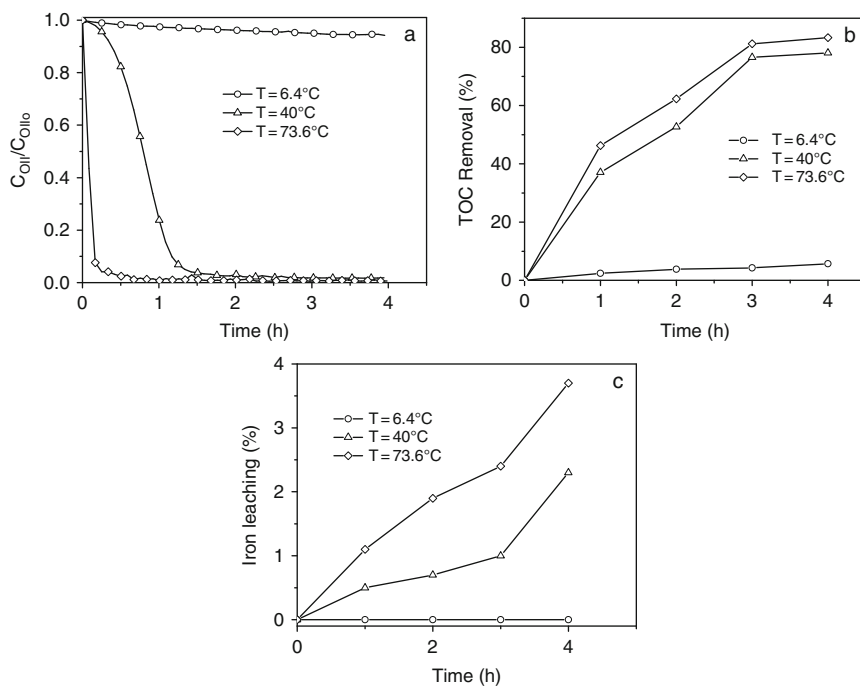


**Fig. 6.4** Temperature effect on Orange II dye degradation (a), mineralization (b), and iron loss (c);  $C_{\text{catalyst}} = 70 \text{ mg/l}$ ,  $C_{\text{H}_2\text{O}_2} = 1.3 \times 10^{-2} \text{ M}$ ,  $\text{pH} = 3$ . Reprinted from [26], with permission from American Chemical Society

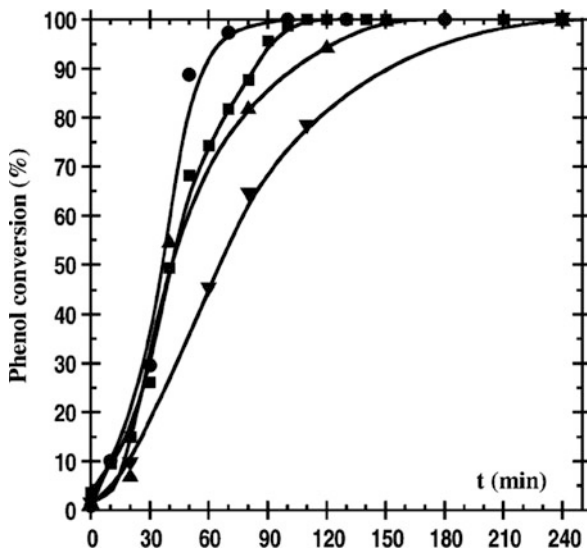
Guérou et al. [33]. It should be noticed that the catalyst leaching remains low, but in this case the effect of the temperature was the opposite to that reported in Fig. 6.4c (0.8 and 0.2 ppm after 4 h of reaction at 40 and 70 °C, respectively).

### 6.2.2.3 Effect of the Initial $\text{H}_2\text{O}_2$ Concentration

Luo et al. [53] determined that when changing the hydrogen peroxide concentration between 1.1 and 4.1 mM for phenol degradation, no significant effect was observed. Guérou et al. [33] also found that, for the oxidation of phenol but in a semi-continuous reactor, for a reaction time less than 60 min the rate of the addition of the hydrogen peroxide seems to have no important effect on the rate of phenol conversion, except for the lowest flow rate used. However, the total phenol conversion is reached for increasing times when the load of hydrogen peroxide solution decreases (Fig. 6.5). The same effect was observed for the TOC abatement, but the maximum value reached after more than 4 h of reaction remains about the same ( $\approx 80\%$ ), whatever the concentration/flow-rate of the hydrogen peroxide solution.

Guo and Al-Dahhan [35] studied the catalytic wet oxidation of phenol by hydrogen peroxide over PILCs, also continuously adding the oxidant to minimize its

**Fig. 6.5** Influence of the hydrogen peroxide addition rate on the phenol conversion ( $T = 70\text{ }^{\circ}\text{C}$ , catalyst =  $10\text{ g/l}$ ); (●)  $4 \times 10^{-4}\text{ mol/h}$ , (■)  $2 \times 10^{-4}\text{ mol/h}$ , (▲)  $1.6 \times 10^{-4}\text{ mol/h}$ , (▼)  $1 \times 10^{-4}\text{ mol/h}$ . Reprinted from [33], with permission from Elsevier



consumption and to maximize the efficiency of its use. In such a work, the authors have shown the time dependence of phenol conversion at four  $\text{H}_2\text{O}_2$  concentrations, corresponding to about 25, 50, 100, and 600% of the stoichiometric amount required for complete removal of aqueous phenol at 180 min. A higher initial rate of phenol removal results from a higher  $\text{H}_2\text{O}_2$  concentration, which means that the  $\text{H}_2\text{O}_2$  concentration needs to be considered in their kinetic expressions.

Ramírez et al. [25], in the Fenton-like oxidation of Orange II solutions using catalysts based on saponite clay, have also varied the hydrogen peroxide concentration between 3 and 24 mM. It was observed that the increase of the oxidant concentration from 3 to 12 mM leads to an increase in the reaction rate, as expected, because more radicals will be formed. Nevertheless, for a very high hydrogen peroxide concentration (24 mM) the performance decreases (Fig. 6.6). The existence of an optimum hydrogen peroxide concentration is typical and well known in Fenton's oxidation. At higher  $\text{H}_2\text{O}_2$  concentrations the scavenging of  $\text{HO}\cdot$  radicals will occur, which can be expressed by reaction (6.7). Although other radicals ( $\text{HO}_2\cdot$ ) are produced, their oxidation potential is much smaller than that of the  $\text{HO}\cdot$  species.

The existence of optimum oxidant doses has also been reported in other works [30], putting into evidence the need of a careful design to optimize process efficiency.

#### 6.2.2.4 Effect of the Catalyst Load

Luo et al. [53] in phenol oxidation with a Fe–Al-pillared clay by  $\text{H}_2\text{O}_2$  found an increase in the reaction rate when the catalyst concentration was increased, but only up to a certain load after which it becomes less efficient (Fig. 6.7).

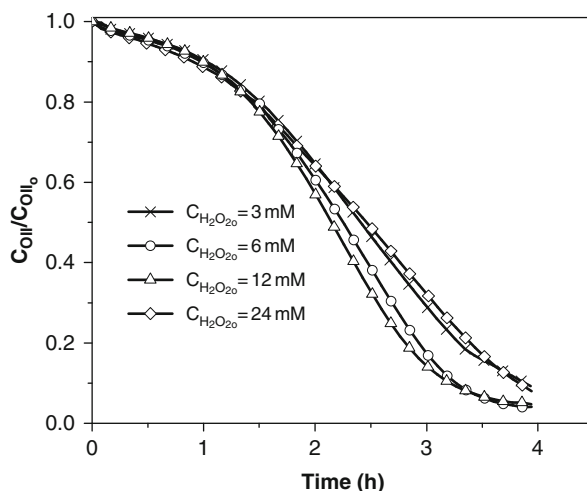


**Fig. 6.6** Effect of the hydrogen peroxide concentration on the degradation of OII solution using Fe(II) oxalate 7.5 catalysts; pH = 3,  $T = 30\text{ }^{\circ}\text{C}$ . Reprinted from [25], with permission from Elsevier

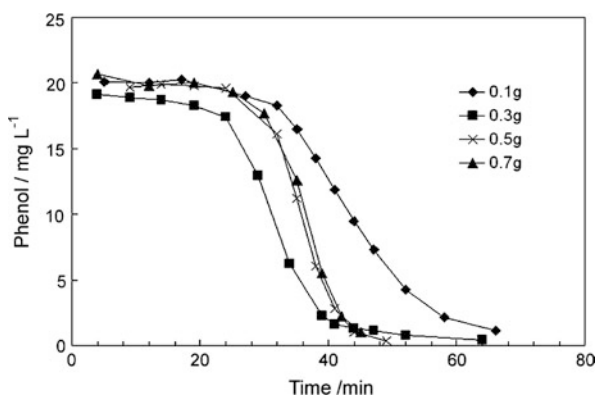


**Fig. 6.7** Effect of amount of catalyst on phenol abatement. Experimental conditions: phenol 19–21 mg/l,  $\text{H}_2\text{O}_2 = 4\text{ mM}$ ,  $T = 28 \pm 1\text{ }^{\circ}\text{C}$ , and  $\text{pH} = 4.0 \pm 0.1$ . Reprinted from [53], with permission from Elsevier

Other authors [34, 36] observed a similar behavior; Catrinescu et al. [36] studied a range of PILC catalyst concentrations between 0 and 1 g/l. Figure 6.8 shows that the chemical oxygen demand (COD) removal depends on the catalyst concentration for up to 0.5 g/l. By further increasing the amount of catalyst to 1 g/l, only a slight increase in the phenol removal and COD removal efficiency was reached. So, for the given phenol concentration, there is an optimum concentration for the PILC, which could be situated around 0.5 g/l.

**Fig. 6.8** Influence of the catalyst concentration on COD removal: 250 mg/l phenol, 50 °C, initial pH = 3.5, H<sub>2</sub>O<sub>2</sub> = 37.23 mM, 120 min. Reprinted from [36], with permission from Elsevier

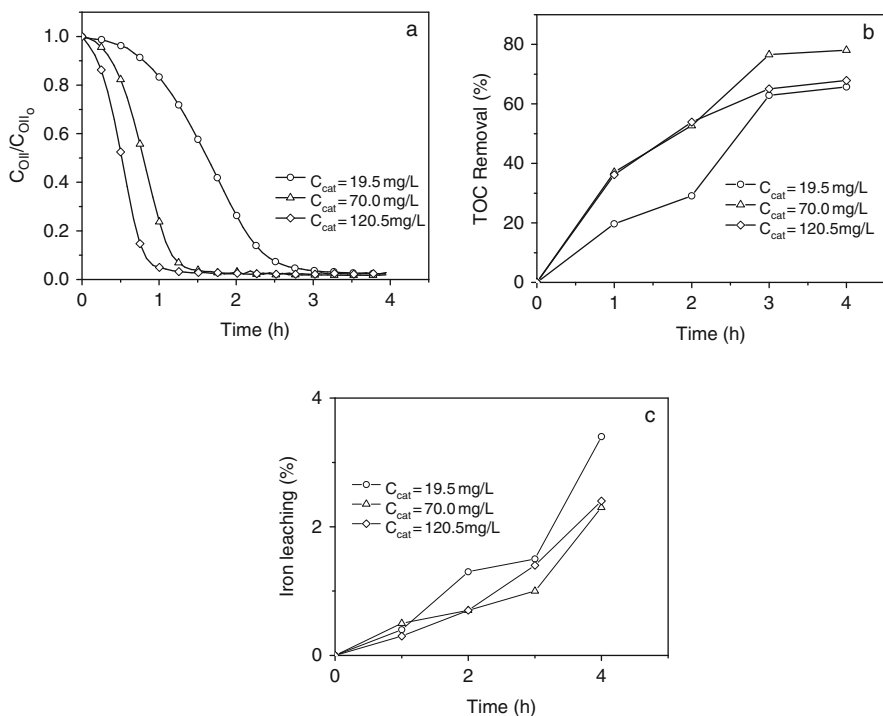
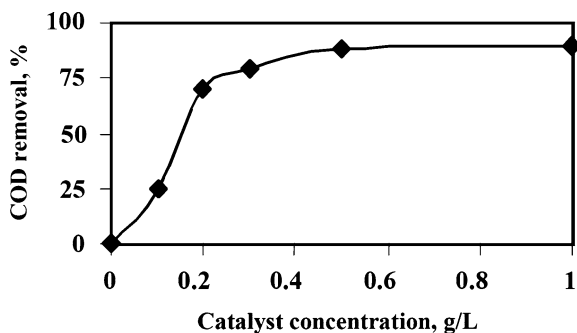


**Fig. 6.9** Catalyst concentration effect on Orange II dye degradation (a), mineralization (b), and iron loss (c);  $T = 40\text{ }^{\circ}\text{C}$ ,  $\text{C}_{\text{H}_2\text{O}_2} = 1.3 \times 10^{-2}\text{ M}$ ,  $\text{pH} = 3$ . Reprinted from [26] with permission from American Chemical Society

The effect of the catalyst concentration on the non-biodegradable azo-dye Orange II degradation histories is shown in Fig. 6.9 [26]. It can be seen that the catalyst load affects positively the dye degradation rate, as expected, because more radicals are produced, thus leading to a faster color removal. In terms of TOC removal, 70 mg/l of catalyst leads to better results as compared to catalyst loads of 19.5

and 120.5 mg/l, which provide similar TOC removals after 3 or 4 h of oxidation. This indicates, as above-mentioned, that after a certain point the catalyst load has a detrimental effect on the performance (mineralization degree in this case), which can be explained by the formation of iron complexes (iron + organics) when excess amounts of catalyst are present [26]. Other authors have also found this kind of behavior with heterogeneous systems [56, 57]. The scavenging of hydroxyl radicals (Eqs. 6.4–6.6) might also explain this effect [44], although other undesirable reactions between iron and other radicals could also be mentioned [1, 44, 58]:



Finally, in terms of percentage of iron lost from the solid, referred to the total Fe initially incorporated, Fig. 6.9c shows that the differences are small, i.e., the percentage of iron that has been leached out depends only slightly on the catalyst concentration employed in the catalytic runs. It seems, however, that higher percentages of Fe are lost from the clay support when smaller catalyst doses are used.

Other authors [30], found a similar behavior using Fe-pillared montmorillonite for cinnamic acid removal. The authors observed that the maximum removal (90%) of cinnamic acid after 1 h was obtained for the Fe/cinnamic acid molar ratio = 2 in heterogeneous medium. Beyond this ratio the degradation rate did not increase (Fig. 6.10). In the homogenous medium, it was observed that the elimination of cinnamic acid was increased by increasing the Fe/cinnamic acid ratio up to a value of 10, beyond which it became constant. In addition, it is worth noting that at all ratios of Fe/cinnamic acid the removal of cinnamic acid was lower in the homogeneous medium than in the heterogeneous medium. This behavior was explained by an

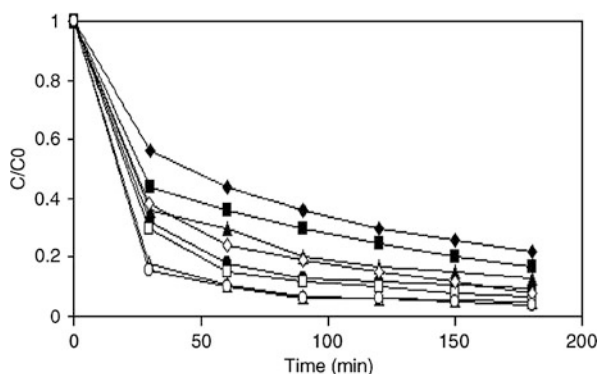


**Fig. 6.10** The effect of Fe/cinnamic acid molar ratio on cinnamic acid removal as a function of time at pH = 2.9 and  $\text{H}_2\text{O}_2/\text{cinnamic acid molar ratio} = 83$ . *Solid symbols* refer to homogeneous catalysis and *open symbols* to heterogeneous catalysts: ( $\diamond$ ) Fe/cinnamic acid molar ratio = 0.2, ( $\square$ ) Fe/cinnamic acid molar ratio = 0.5, ( $\Delta$ ) Fe/cinnamic acid molar ratio = 2, and ( $\circ$ ) Fe/cinnamic acid molar ratio = 10. Reprinted from [30], with permission from Elsevier

easier complexation with the Fe ions in the homogeneous medium by organic intermediate degradation products, such as carboxylic acids, which can in turn diminish the removal rate of cinnamic acid [30].

### 6.2.2.5 Effect of the Initial Parent Compound Concentration

Several researchers have investigated the effect of the initial concentration of phenol in solution on the degradation performance. For example, Guo and Al-Dahhan [35], reported catalytic wet oxidation of phenol by  $H_2O_2$  using a pillared clay catalyst. Figure 6.11 shows the conversion with time at four initial phenol concentrations, which demonstrate that a higher initial concentration leads to lower conversion under otherwise identical conditions. The same self-inhibiting effect of the phenol initial concentration on the oxidation rate was observed by Pintar and Levec [59]. The negative effect of the increasing parent organic compound/ $H_2O_2$  ratio on the cinnamic acid conversion was also reported by Tabet et al. [30].

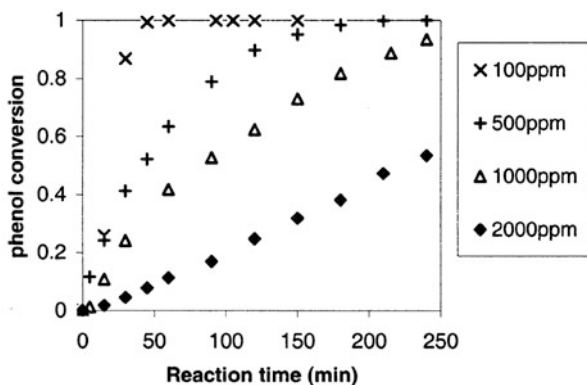


**Fig. 6.11** Effect of initial phenol concentration on its reduction by catalytic wet oxidation (70 °C, 0.3 M  $H_2O_2$ , 6.6 g/l catalyst). Reprinted from [35], with permission from American Chemical Society

### 6.2.2.6 Heterogeneous Versus Homogenous Process

The heterogeneous process has several advantages, as compared to the homogeneous one, as remarked by Tabet et al. [30]:

- It avoids the release of ferric cations into the discharged water;
- It might lead to higher removal rates of the parent compound (e.g., for cinnamic acid, by a factor of 1.5–2.5, depending on the operating conditions – cf. Figs. 6.3 and 6.10);
- It is often less sensitive to pH variations, in line with other reports, particularly in what concerns phenol and carboxylic acids degradation [31, 60].

The results obtained by Barrault et al. [34] also show that the TOC abatement obtained with the so-called FAZA catalyst, for phenol mineralization, is much higher than those observed with homogeneous iron species in the same reaction conditions. These results demonstrate unambiguously that the phenol oxidation reaction is due to the presence of a solid catalyst, the possible contribution of the homogeneous iron species arising from the catalyst leaching being likely negligible.

However, it is not very common to find reported higher activities for the heterogeneous system; actually, in most cases the opposite is observed. For instance, Tatibouët et al. [32] noticed that the phenol conversion level obtained after 2 h of reaction at pH = 3.0–3.5 is higher for the homogeneous reaction than for the catalytic heterogeneous one (using a PILC-like catalyst), although the iron content in the reactor for the heterogeneous system was more than 30 times higher than for the homogeneous one ( $\gg 15$  mg for the heterogeneous system against 0.5 mg for the homogeneous one – data not shown). This seems to be due to the induction period observed when a heterogeneous catalyst is used (Fig. 6.12), wherein catalytic performances of the same order of magnitude are reached with completely different catalyst doses (more than 30 times higher in the heterogeneous one, because one has to take into account the Fe content in the PILC sample:  $\sim 3.0$  wt%). On the other hand, the same authors reported that the homogeneous system seems to be very sensitive to pH values higher than 3.0, leading to a dramatic decrease in the conversion level, from  $\gg 80\%$  at pH = 3.0 to less than 5% at pH = 2.5, whereas the

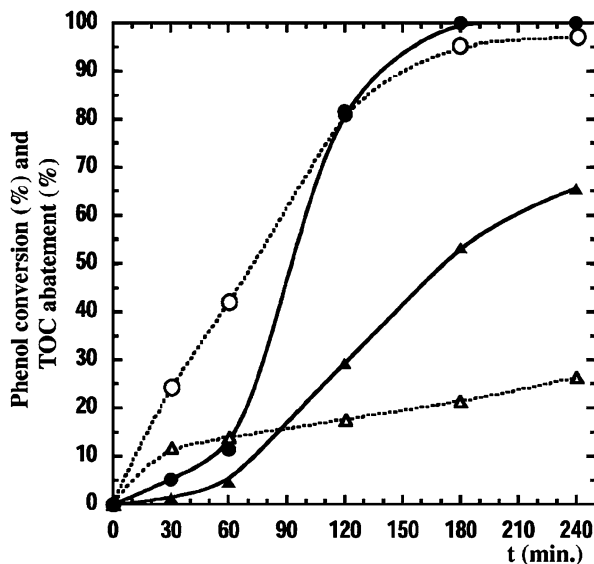


**Fig. 6.12** Phenol oxidation by hydrogen peroxide (batch reactor,  $T = 25$  °C,  $H_2O_2 = 2 \times 10^{-4}$  mol/h, pH = 3.7). Dotted lines and open symbols: homogeneous system (Fe = 5 mg/l), continuous line and solid symbols: FAZA catalyst = 5 g/l. (●) Phenol conversion, (▲) TOC abatement. With kind permission from Springer [32]

heterogeneous system shows only a slight decrease in the phenol conversion from 25 to 17% in the same pH range [32]. The heterogeneous catalytic system appears then to be less sensitive to the pH value than the homogeneous one, in line with the afore-mentioned advantages pointed by Tabet et al. [30].

The measurement of HO· species production by an ESR spin trapping technique showed that the HO· production followed the same profile in function of the pH value as the catalytic activity in phenol oxidation. This fact strongly suggests that the main active species are hydroxyl (HO·) and/or hydroperoxyl (HO<sub>2</sub>·) radicals generated by hydrogen peroxide reaction with iron species in homogeneous phase (Fenton reaction) or with iron surface species probably located in the clay porosity [32]. Then, Tatibouët et al. [32] conclude that the difference between homogeneous and heterogeneous systems could be due either to the formation of different active oxygen species from hydrogen peroxide or to the ability of the heterogeneous catalyst to adsorb on its surface the phenol and/or the reaction intermediate products, favoring their reaction with oxygen species formed by hydrogen peroxide activation. This phenomenon could be largely enhanced by the particular structure of the pillared clay where, in addition to the adsorbing properties of the pillared clay, the intermediate products of phenol oxidation could be trapped between the clay layers, favoring then their attack by the oxygenated radicals HO· and HO<sub>2</sub>·.

### ***6.2.3 Effect of the Type of Catalyst/Salt Precursor***

Ramirez et al. [25] studied the Fenton-like oxidation of Orange II solution using different heterogeneous catalysts based on saponite clay. The results obtained for the oxidation of OII solution with the 12 catalysts prepared are displayed in Fig. 6.13. Therein, the effect of the nature of the Fe-salt precursor as well as the amount of active phase used on the catalytic activity can be observed. For the catalyst with lowest (7.5 wt%) and highest (17.0 wt%) iron contents, the best results were always reached when using the oxalate precursor (Fig. 6.13a and c, respectively), while for the catalysts containing the intermediate concentration (13.0 wt%), the best sample seems to be that prepared with the acetate precursor (Fig. 6.13b). Using the clay impregnated with 13.0% of Fe(II) acetate and 17.0% of Fe(II) oxalate, degradations of 95.2 and 95.9% were obtained after 4 h, respectively.

It can also be observed in Fig. 6.13 that the influence of the iron concentration on the degradation of Orange II is not equal for all the precursors, but, in general, the final performances are not too different. The reason behind this fact is not clear, and a deeper insight regarding the mechanisms occurring in the system is required. Nevertheless, TOC elimination shows clearly that at the end of the runs it increases, for each precursor, with the iron load [25]. This increment in the mineralization with the iron concentration occurs because when the amount (concentration) of catalyst increases, more radicals are produced for the oxidation reaction (Eqs. 6.11 and 6.12, where X represents the surface of the catalyst):



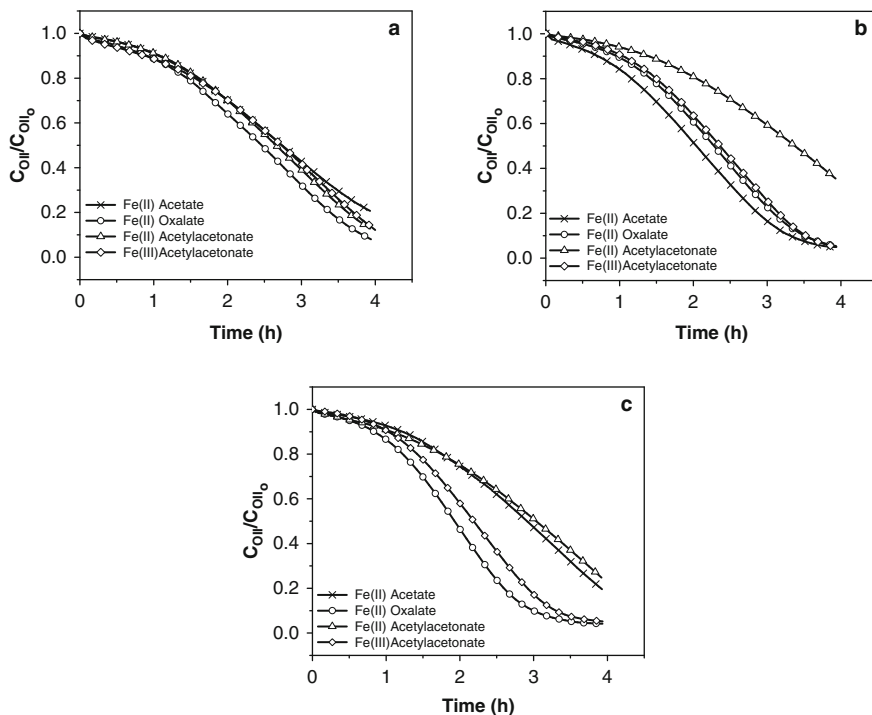
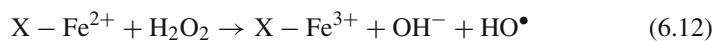
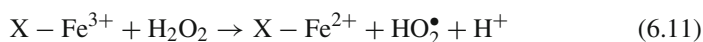


**Fig. 6.13** Effect of the precursor nature on the degradation of the OII solution for different iron loads: (a) 7.5 wt%, (b) 13.0 wt%, (c) 17.0 wt%, pH = 3,  $C_{H_2O_2} = 6 \times 10^{-3}$  M, and  $T = 30$  °C. Reprinted from [25], with permission from Elsevier



The catalytic differences observed when different precursors are used are not clear. Nevertheless, several factors might be indicated, which are known to affect the catalytic performance: (i) the iron dispersion [1], (ii) the  $Fe_2O_3$  crystalline form (hematite or maghemite-Q) [16], (iii) the location of the iron species (bonded to the aluminum pillars or engaged in small oxide clusters dispersed in the solid, inside, or outside the porosity) [34], or (iv) the oxidation states, nature, and coordination of the iron species [38].

Other authors, for example Chirchi and Ghorbel [37], carried out a study about degradation of 4-nitrophenol using various Fe-modified montmorillonite catalysts. They tested 11 different catalysts, prepared under different conditions (namely, pH) and experimental procedures and found that the best results were obtained with PILC-(Al-Fe), a pillared sample constituted by pillars of mixed Al and Fe oxides, which was selected to be the best catalyst for the heterogeneous degradation of 4-nitrophenol.

## 6.2.4 Some Technological Issues

Although some technical issues that are quite important to take into account for industrial implementation of a heterogeneous Fenton-like process have already been discussed, others need to be analyzed in detail. This will be the main focus of the following sections.

### 6.2.4.1 Catalyst Stability

For a practical implementation of a heterogeneous catalytic system, it is crucial to evaluate the stability of the catalysts. Ideally, a sample that shows a low leaching, but presenting simultaneously good catalytic performance, should be selected. In the case of a Fenton process, iron leaching should ideally be null to provide long-term stability. This is particularly interesting from the practical point of view due to the possibility of using these catalysts for a longer operation time/larger number of cycles (batch mode).

In this concern, Luo et al. [53] investigated the iron leaching from the support into the solution, for a catalytic Fenton's process using Al-Fe-pillared clay in phenol oxidation. They found that the loss of iron amounted to 0.1 mg, equivalently 0.3% of total iron of 0.3 g catalyst used. With such a low level of iron in the solution, they concluded that the homogeneous Fenton reaction is negligible. Compared to a dissolved iron concentration of 2.0 mg l<sup>-1</sup> obtained at pH 3.0–3.5 and 1.0–2.0 mg l<sup>-1</sup> at pH 3.0, the much lower iron loss in this work was attributed to the less acidic conditions (pH 3.5–4.7). Then, they studied the re-use of Fe–Al powder catalyst, employing two procedures to recycle the powder catalyst:

- (a) Centrifugal separation of the used powder and washing with plenty of water. The slurry was used for further catalysis, and alternatively
- (b) The washed slurry from procedure (a) was dried at 80 °C in an oven for 5 h. The dried powder was also used as a catalyst.

Both of the recycled catalysts were used more than three times with no obvious deactivation as shown in Fig. 6.14. However, the induction times for the re-used powder varied depending on the procedure of recovery. The induction time from procedure (a) decreased (samples denoted as “S” – slurry, in the figure), while from procedure (b) (samples denoted as “P” – powder, in the figure) it remained almost the same as with the original powder. This is probably because the slurry from procedure (a) kept the protonated surface iron species, while the dried powder from procedure (b) lost them, thus requiring a further induction period to allow them to regenerate [53].

Catrinescu et al. [36] studied a similar process, phenol degradation, but using Fe-exchanged pillared beidellite-like catalyst. They re-used the material in three consecutive experiments, with the same catalyst load at pH 3.5 and 30 °C. Between each experiment the catalyst was removed by filtration, followed by drying at 80 °C for 12 h. The results are reported in Fig. 6.15. It is obvious that the initial activity

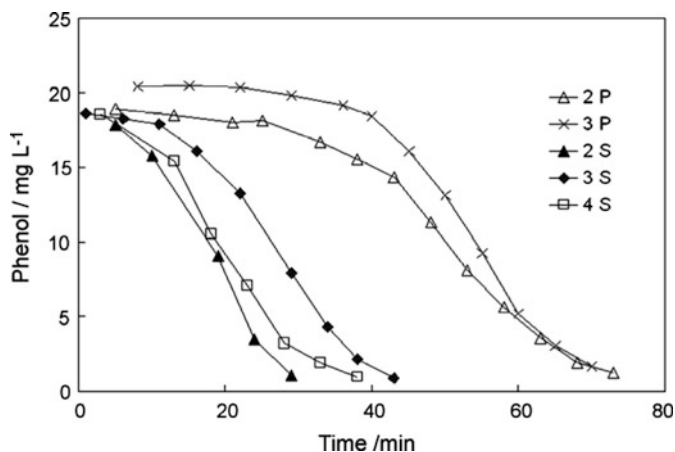


**Fig. 6.14** Re-use of catalyst in the form of either a powder slurry or a dried powder. The numbers indicated the repeated use of the catalyst, i.e., 2 means the material was used for second time. The letters refer to re-use as dried power (P) or slurry (S). Reprinted from [53], with permission from Elsevier

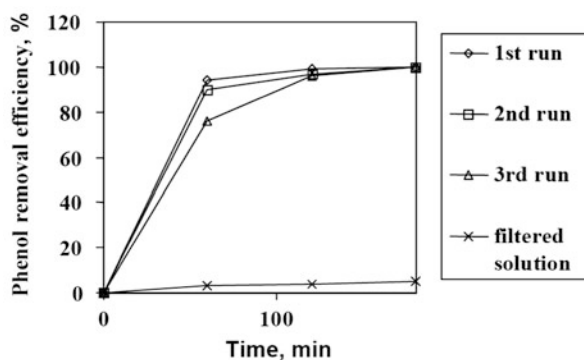
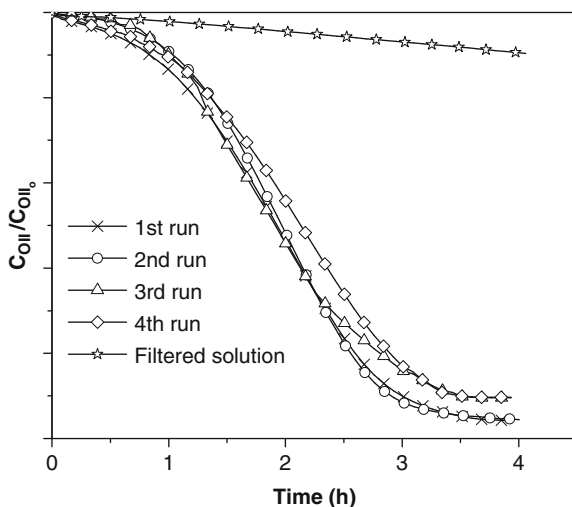


**Fig. 6.15** Conversion of phenol as function of the time of reaction in different conditions: fresh catalyst, re-used once, re-used twice, after the filtration of the catalyst and the addition of phenol and  $\text{H}_2\text{O}_2$ ; 250 ppm phenol,  $50^\circ\text{C}$ , 0.5 g/l PILC catalyst; 37.23 mM  $\text{H}_2\text{O}_2$ ; initial pH = 3.5. Reprinted from [36], with permission from Elsevier

decreased slowly during successive runs. However, at longer times, phenol removal is comparable for all the experiments. The poisoning of the active catalytic sites was considered by the authors as the reason for this initial loss of activity. The oxidation of the organic species adsorbed on the catalyst active sites may be associated with the delays observed for short reaction times. When the catalyst was used after an intermediate calcination step, its catalytic activity was restored, indicating the absence of significant deactivation, due to the loss of iron. Moreover, in the absence

of solid catalyst (after filtration) the catalytic activity is negligible, clearly demonstrating that the fraction of iron leached from the catalyst is not capable of destroying the organic pollutant [36].

**Fig. 6.16** Effect of consecutive experiments with the Fe(II) oxalate 17.0 catalyst on the degradation of OII solution. pH = 3,  $T = 30\text{ }^{\circ}\text{C}$ ,  $\text{C}_{\text{H}_2\text{O}_2} = 6 \times 10^{-3}\text{ M}$ . Reprinted from [25], with permission from Elsevier



Similar conclusions were reached in a recent study, illustrated in Fig. 6.16, which shows the performance reached in terms of OII degradation, using a clay-based catalyst in four consecutive runs [25]. To recover the catalyst, the final effluent was filtered. After the first cycle, and in order to check if the leached iron was responsible for the catalytic activity, both OII and  $\text{H}_2\text{O}_2$  were added to the solution in the same concentrations as at the beginning of the experiment. Figure 6.16 shows that in these conditions OII conversion is only a very small fraction of that recorded in the presence of the pillared clay, thus demonstrating that the Fe leached is not capable of destroying the dye, i.e., the process is essentially heterogeneous. For subsequent cycles, the filtered clay was dried overnight between consecutive runs. Even though a slight activity decay is observed, which might be due to the iron loss (ca. 1.5% per cycle that represents a final concentration smaller than 0.3 mg/l), OII conversion decreases only from 95.8 to 90.3% in 4 cycles, i.e., 16 h of operation. Regarding TOC reduction, in the 4 cycles final values were 81.6, 81.4, 78.5, and 77.1%. In practice, this small deactivation could be compensated, if required, by adapting the reaction conditions (for instance, slightly increasing the temperature along time). As already mentioned, other authors reported similar results, but they attributed the loss of activity to poisoning of the active catalytic sites due to adsorbed organic species [1, 36]. However, this could be avoided by submitting the catalyst to an intermediate calcination step, thus restoring its catalytic activity [31, 36]. Nevertheless, catalyst deactivation may occur due to a diversity of factors, as pointed by Guo and Al-Dahhan [35], including reduction of the catalyst specific surface area, poisoning of the catalytic agents by compounds formed during oxidation, surface deposition,

and strong adsorption of a polymeric carbon layer or even the dissolution of some metal oxides from catalysts into the hot acidic reaction medium. This issue should therefore be the aim of more intensive research and future work.

Other studies addressed this matter of catalyst re-use, e.g., see Refs. [34, 35], pointing very often to good stability. However, in most cases the number of cycles has been very limited, usually not exceeding ca. 4, thus not allowing true long-term catalytic activity evaluation. Other methodologies are required, for instance, testing in continuous reactors for much longer times.

#### 6.2.4.2 Use of Continuous Flow Reactors

Operation with continuous reactors is desirable for real practice, but the studies reported in the literature are limited, as compared to those employing batch reactors. One scarce example is provided in the work by Tatibouët et al. [32], whom have studied the catalytic oxidation of phenol by hydrogen peroxide over a pillared clay containing iron in a continuous flow reactor. Such reactor allowed the determination of the kinetic parameters of the reaction in steady-state conditions. In this work the authors assumed first-order kinetics for the phenol conversion rate, and thus the mass balance in a perfectly stirred reactor yields:

$$X = \frac{k\tau}{1 + k\tau} \quad (6.13)$$

with:

$X$  = phenol conversion

$k$  = rate constant ( $\text{ml min}^{-1} \text{g}^{-1}$ )

$\tau$  = catalyst weight/total flow rate ( $\text{g min ml}^{-1}$ )

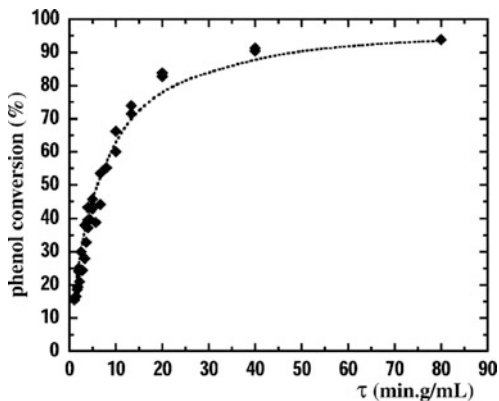
From the above equation, one obtains

$$\frac{1}{X} = 1 + \frac{1}{k\tau} \quad (6.14)$$

The rate constant  $k$  is then determined as the slope of the straight line obtained by drawing  $1/X$  as a function of  $1/\tau$ . The best fit was obtained for a constant  $k$  value equal to  $0.18 \text{ ml min}^{-1} \text{g}^{-1}$ , which was used to draw the calculated phenol conversion curve (*dotted line*) of Fig. 6.17, showing that their simple kinetic model fits very well with the experimental results, especially for a conversion lower than 70%.

Another study about oxidation of phenol, over pillared clays containing iron in a continuous flow reactor [33], was carried out by the same group. They concluded that the high stability of this pillared clay catalyst in the reaction conditions employed and its good catalytic performance in TOC abatement ( $\approx 80\%$  at  $70^\circ\text{C}$ ) would allow them to use it in a continuous process, being able to eliminate organic pollutants in industrial wastewater streams.

**Fig. 6.17** Variation of the phenol conversion as a function of residence time in the recycling continuous flow reactor ( $T = 40^\circ\text{C}$ ,  $C_{\text{phenol}} = 5 \times 10^{-4}\text{ M}$ ,  $C_{\text{H}_2\text{O}_2} = 0.01\text{ M}$ ). Dotted line: simulation for  $k = 0.18\text{ ml min}^{-1}\text{ g}^{-1}$  in Eq. 6.13. With kind permission from Springer, figure 5 [32]

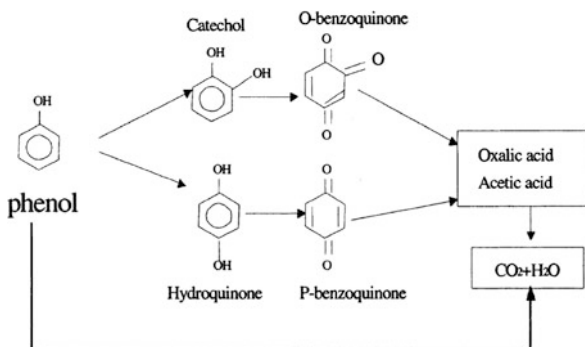


### 6.2.5 Mechanistic Studies

Up to our knowledge, there are not many studies reporting the identification/quantification of intermediates and establishing reaction mechanisms during Fenton-like processes based on PILCs. A scarce example has been reported by Guo and Al-Dahhan [35], whom identified the intermediate products of phenol oxidation by hydrogen peroxide. The main detected intermediates in the product effluent were acetic acid, catechol, and hydroquinone. Oxalic acid and benzoquinone were also identified in measurable quantities. However, malonic and formic acids were detected only as traces. No other compounds were detected in measurable amounts. In particular, no condensation products were found in the exiting solution or deposited on the catalysts. Quinone-like products such as hydroquinone, benzoquinone, and catechol were identified in the first stages of the phenol oxidation pathway [35]. These by-products need, however, to be removed because they are as toxic as phenol.

Based on the HPLC analyses and the evolution of the color along time (related with the presence of benzoquinone), a simplified reaction scheme was proposed, shown in Fig. 6.18, where the important interconnection between the presence of quinones and organic acids can be seen. The first step represents the formation of intermediate ring compounds, namely, catechol, hydroquinone, and benzoquinones, whereas the subsequent stage corresponds to the cleavage of intermediates and the formation of carboxylic acids. This scheme is in line with the conclusion of Fortuny et al. [61], except that the possibility of direct decomposition of phenol to inorganic carbon during the ring-opening reaction is also taken into account by Guo and Al-Dahhan [35].

**Fig. 6.18** Proposed reaction scheme for phenol oxidation. Reprinted from [35], with permission from American Chemical Society



## 6.3 Modeling

Modeling is a crucial issue, for instance, in the design of industrial-scale reactors. For that, degradation rate equations are required, which can be obtained via kinetic studies and subsequent phenomenological modeling. Statistical models, which we will call as semi-empiric, have also been often used for modeling purposes, allowing predicting process response and providing a tool for process optimization. Both will be described in the following sections, given their importance and the fact that have been used in modeling Fenton-like processes employing PILCs.

### 6.3.1 Phenomenological Models

#### 6.3.1.1 Langmuir–Hinshelwood Rate Equations

In the literature, different kinetic strategies can be found for the interpretation and modeling of Fenton and Fenton-like oxidation processes using PILCs, in particular using well-known Langmuir–Hinshelwood (LH) formulations. Guo and Al-Dahhan [35], assuming that the homogeneous and heterogeneous reaction rates are additive, presented a network model which was suggested to account for the significant reaction both in the liquid bulk phase and on the catalytic surface of an Al–Fe-pillared clay during Fenton-like phenol conversion. They considered a two-parallel reaction scheme for the non-catalytic oxidation and a Langmuir–Hinshelwood approach for the catalyst-mediated oxidation. In this work on phenol oxidation with hydrogen peroxide as the oxidant, experimental evidence indicates that approximately 30–40% of hydrogen peroxide homogeneously decomposes in the liquid bulk, while the other portion decomposes in contact with the clay catalyst. In Guo and Al-Dahhan's study [35], the catalyst loading term in the heterogeneous reaction rate is modified in an empirical way by including the exponent terms for both the phenol removal and the intermediate products degradation. To preserve the units of the reaction rates, it has been shown that the exponent terms have to have

the same value,  $p$  (which was determined to be 0.798), as shown in the following equations:

$$-\frac{dC_A}{dt} = r_{h,A} + r_{H,A}C_{cat}^p \quad (6.15)$$

$$\frac{dC_B}{dt} = r_{h,B} + r_{H,B}C_{cat}^p \quad (6.16)$$

where  $r_{h,A}$  represented the development of the homogeneous kinetic model (with rate  $r_h$ ) using the homogeneous experimental data, and  $r_{H,A}$  the development of the heterogeneous kinetic model (with rate  $r_H$ ) using the heterogeneous experimental data. In the latter, the homogeneous model with its fitted parameters needed also to be considered, due to leaching.

Because the reaction networks involved in wastewater treatment through AOPs are rather complex, several authors have adopted the methodology of lumped models. In this case, three basic lumps are considered in the reaction system, which are expressed in carbon concentration terms for oxidation kinetics: (1) phenol, denoted as A; (2) intermediate organic carbon, denoted as lump B, is the phenol oxidation by-product; and (3) total inorganic carbon, denoted as lump C, is the fully mineralized end products. On the basis of the carbon scale,  $C_B = \text{TOC} - C_A$  and  $C_C = C_{A0} - \text{TOC}$ .

To model the homogeneous contribution, i.e., the non-catalytic oxidation route with rate  $r_h$ , a sequential-parallel reaction scheme was proposed as in Eqs. (6.17–6.19), where the production of lump C is generated by irreversible oxidation of both A and lump B [35]. Lump B results from the irreversible oxidation of A. The homogeneous reactions are as follows:



The mass balances and reaction rates with respect to species A and B are given in the following equations:

$$-\frac{dC_A}{dt} = r_{h,A} = (k_{h1} + k_{h2})C_A C_{\text{H}_2\text{O}_2} \quad (6.20)$$

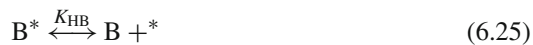
$$\frac{dC_B}{dt} = r_{h,B} = k_{h1}C_A C_{\text{H}_2\text{O}_2} - k_{h3}C_B C_{\text{H}_2\text{O}_2} \quad (6.21)$$

In the presence of catalyst, both the heterogeneous and the homogeneous oxidation reactions take place at the same time. Once the homogeneous oxidation kinetic



parameters are established and known, the parameters for the heterogeneous oxidation model are obtained by combining the heterogeneous experimental data with the fitted homogeneous reaction kinetic parameters, as explained above.

The heterogeneous elementary steps are characterized by adsorption of the reactants on the active sites of the catalyst (represented by \*), followed by surface reaction and desorption of the products back into the liquid, which can be presented as follows [35]:



In this model several assumptions are made, as explained by the authors [35]. Among them one can highlight that hydrogen peroxide is assumed to remain unadsorbed on the active sites, thus reacting directly with chemisorbed phenol. In addition, the steps of adsorption and desorption are assumed to be instantaneous as compared to surface reactions of chemisorbed phenol and its daughter intermediate products, which are the rate-controlling steps. The depletion rates of phenol and intermediate product due to the heterogeneous reaction can therefore be described by the following LH equations:

$$r_{HA} = \frac{k_{H1} K_{HA} C_A C_{H_2O_2}}{1 + K_{HA} C_A + K_{HB} C_B} \quad (6.26)$$

$$r_{HB} = \frac{k_{H1} K_{HA} C_A C_{H_2O_2}}{1 + K_{HA} C_A + K_{HB} C_B} - \frac{k_{H2} K_{HB} C_B C_{H_2O_2}}{1 + K_{HA} C_A + K_{HB} C_B} \quad (6.27)$$

where  $K_i$  stands for adsorption equilibrium constant of species  $i$ .

Model parameters were obtained following the criteria described by Guo and Al-Dahhan [35]. The comparison between the model and the experimental results can be observed in the following figures, for either homogeneous or heterogeneous experiments. Reasonably good fits of the desired reactant (Fig. 6.19) and product compositions (data not shown for brevity) were achieved for the homogeneous reaction. The prediction results based on the catalytic reaction model also agree well with the experimental measurements of A and lump B obtained at temperatures from 30 to 90 °C, as shown in Figs. 6.20 and 6.21. Consequently, the homogeneous–heterogeneous approach demonstrated to be a feasible and useful tool in the kinetic analysis for such complex reaction systems.

Compared to the non-catalytic route, the catalytic one should reduce the activation energies or increase the pre-exponential factors. The activation energies

**Fig. 6.19** Measured and predicted time profiles for phenol removal in the homogeneous reaction at different temperature (500 ppm phenol, 0.3 M  $H_2O_2$ ). Reprinted from [35], with permission from American Chemical Society

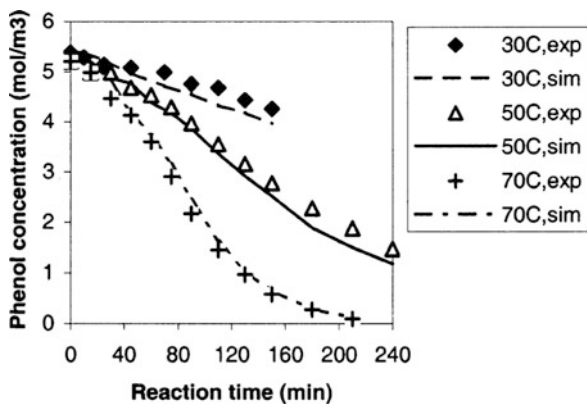


**Fig. 6.20** Measured and predicted time profiles of phenol removal at different temperatures (6.6 g/l catalyst, 500 ppm phenol, 0.3 M  $H_2O_2$ ). Reprinted from [35], with permission from American Chemical Society

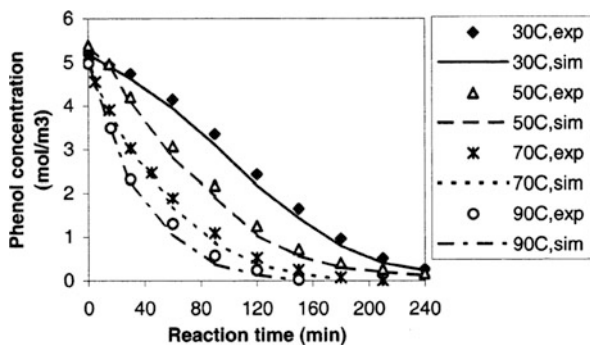
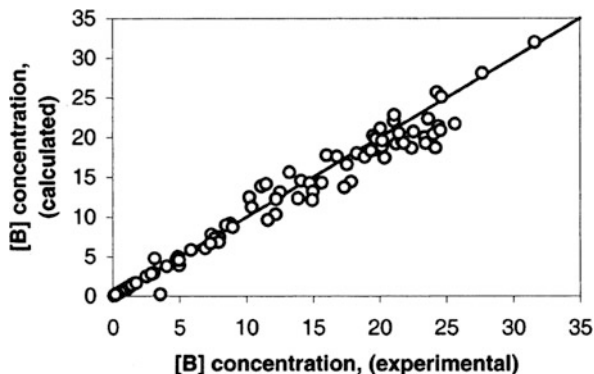


**Fig. 6.21** Parity plot for lump B concentration (mol/m<sup>3</sup>) in the heterogeneous reaction. Reprinted from [35], with permission from American Chemical Society



obtained for the degradation of phenol into intermediate products and the mineralization of the latter were 6.447 and 8.437 kJ/mol in heterogeneous reaction and the counterparts in homogeneous reaction were 13.157 and 44.596 kJ/mol, respectively [35]. In addition, the high value of the activation energy for the mineralization of intermediate products without catalyst demonstrates their recalcitrance nature.

### 6.3.1.2 Apparent First-Order Rate Equations

Most often, apparent rate equations have been adopted, usually of the first-order type. Actually, these equations are not really phenomenological, but since they are not obtained via statistic methods, we decided to include them in this section. We call them apparent because several processes can contribute to the overall conversion of the parent compound, even though the extent of each one might be quite different. For example, the following steps can occur simultaneously: adsorption on the catalyst and oxidation by radicals (hydroxyl and others) coming from the heterogeneous or homogeneous process.

One example is the Fenton-like 4-nitrophenol (NP) degradation by  $\text{H}_2\text{O}_2$  reported by Chirchi and Ghorbel [37], who have used a Fe-modified montmorillonite catalyst. The authors found a first-order model to be useful to fit the experimental values (considering thus a steady-state OH radical concentration during the degradation). In addition, the kinetic plot for the degradation of NP as a function of the concentration of  $\text{H}_2\text{O}_2$  showed a reaction order of 0.5, suggesting in their opinion that dissociation of  $\text{H}_2\text{O}_2$  into two radicals (HO), probably on the surface of the catalyst, could be the rate-determining step. The reaction rate for the degradation was thus as follows:

$$-\frac{dC_{\text{NP}}}{dt} = kC_{\text{NP}}C_{\text{H}_2\text{O}_2}^{0.5} \quad (6.28)$$

### 6.3.2 Non-Phenomenological Models

As mentioned before, statistical models have been often used for modeling purposes, allowing predicting process response and providing a tool for process optimization. This has been achieved, for instance, using design of experiments (DoE) approaches and also neural networks.

In the case of Fenton-like processes this is particularly important because several independent variables affect process performance, as described along this chapter. Thus, process optimization is not straightforward. Although many researchers have usually only focused on the single-factor-at-a-time approach, studying the effect of each experimental parameter on the process performance while keeping all other conditions constant, this approach does not take into account the cross-effects from the factors considered, is time-consuming and leads to a poor optimization result. When a multifactor system is present, it is more appropriate to employ statistically

based optimization strategies to achieve such a goal, with a minimum number of experiments. An example of using such methodology is provided in a paper by our group. Therein, Ramirez et al. [26] developed semi-empirical models with the goal of predicting and then maximizing color and total organic carbon removal, while minimizing the iron loss from the support during Orange II degradation using a clay-based Fenton-like catalyst.

First, models for each response ( $Y$ ) have to be developed, by fitting second-order equations of the type:

$$Y = a_0 + \sum_{j=1}^n a_j X_j + \sum_{j=1}^n a_{jj} X_j^2 + \sum_{i>j}^n \sum_{j=1}^n a_{ji} X_j X_i \quad (6.29)$$

to the experimental data. In Eq. (6.29), the independent variables ( $X_i$ ) considered were the temperature,  $H_2O_2$  concentration, and catalyst load. The terms  $a_i$  were determined by least squares analysis. In most cases, all the cross-effects and

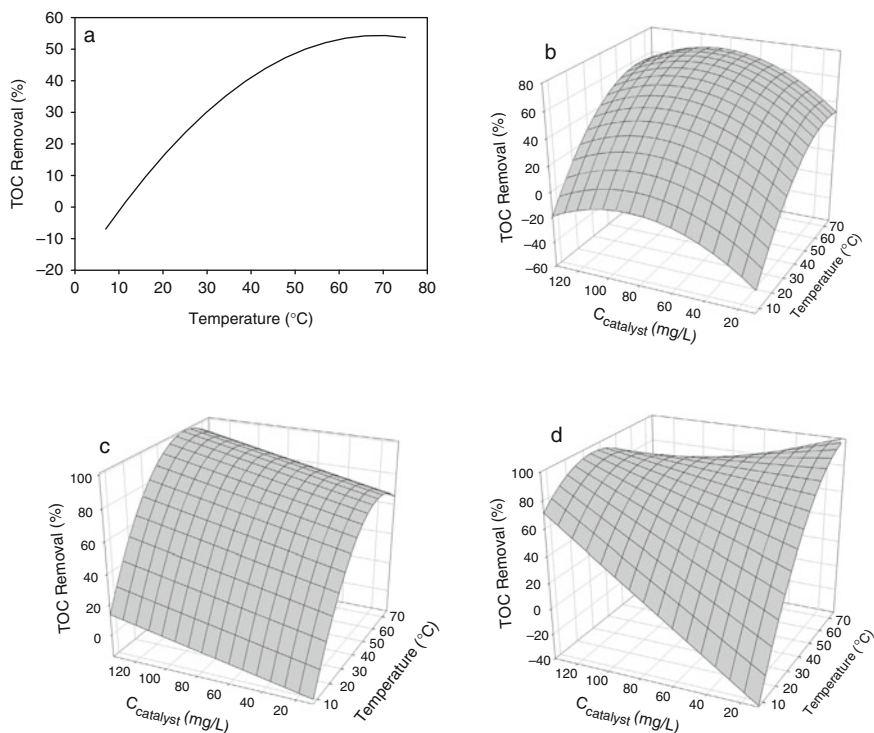


**Fig. 6.22** Effect of the process variables in the TOC removal at different reaction times. (a) 1 h, (b) 2 h, (c) 3 h, and (d) 4 h. Reprinted from [26], with permission from American Chemical Society

quadratic effects obtained with statistical meaning were negative [26], suggesting that optimum values must exist for each parameter, as shown below.

Following the establishment of the semi-empirical models for each response and the subsequent validation against experimental data using commonly employed statistic criteria, one can represent graphically the corresponding surfaces. This can also be done at different reaction times, because the responses considered (color removal –  $Y_1$ , TOC reduction –  $Y_2$ , and iron leaching –  $Y_3$ ) vary along time (batch reactor operation).

As an example, Fig. 6.22 shows the results obtained in terms of TOC removal for 1–4 h of operation. A significant influence of the temperature, and in some cases of the catalyst concentration, is evident, the process being practically independent of the  $H_2O_2$  concentration. For short times the principal variable that affects the TOC removal is the temperature, while for long times the catalyst concentration becomes also important. Thus, in such circumstances the presence of catalyst to improve reaction performance, that is, to obtain a good mineralization degree, is required. Although the highest TOC conversions are achieved at relatively high temperatures, there is an optimal point for TOC removal, which is due to the predominant non-efficient peroxide decomposition. In some cases one can also see an optimum in terms of catalyst concentration, which can be due to a loss of radicals by scavenging reactions in the presence of excess of iron and the formation of iron complexes with organics [26].

Similar plots were obtained for the other responses, which allowed obtaining optimal conditions, at different reaction times [26].

## 6.4 Conclusions

The homogeneous Fenton and Fenton-like processes require complementary steps like precipitation and re-dissolution to prevent water contamination, recover the catalyst, and enable its re-use. This might increase the cost of the processes, not only in terms of supply of chemicals, but also on labor requirements, increasing also the number of process items. So, several attempts have been made to develop efficient supports for the transition metal (namely, iron), so that the resulting catalysts should be catalytically active and stable, in particular making use of pillared clays (PILCs).

Indeed, PILCs represent a diversified range of materials, which can be tailored to achieve success for a particular application. PILCs are attractive as adsorbents, catalysts, or catalyst support due to their high specific surface area, justifying their potential as supports in the Fenton and Fenton-like processes, as described in this chapter, for wastewaters treatment. Besides, these materials can be also produced at large scale, enlarging the interest of use of natural clays for application in catalysis, increasing so the added value of this abundant natural resource.

With the goal of optimizing the Fenton-based processes performance, one should understand what kind of process variables are involved, and what are the expected effects; this has been extensively analyzed along this chapter. However, one should

also take into account other important technological issues, like catalyst stability. In fact, as a further development in this field, more active and robust catalysts, in which metal leaching is absent, are highly desirable.

For industrial application of these AOPs, the use of continuous flow reactors should be considered, e.g., of the fixed-bed type.

Depending on the type of application envisaged, these AOPs can be considered as a stand-alone process, but more often as a final polishing step or as a preliminary one. In any case, the possible generation of toxic compounds should be investigated and oxidation products formed analyzed.

Finally, for process optimization, statistic-based methodologies proved already to be efficient. However, for scale-up and reactor design, more elaborated phenomenological models are required, which is in part limited by the complexity of the reaction scheme. This could be circumvented with more detailed kinetic studies. Even so, modeling strategies adopted so far have already proved to be of usefulness.

## References

1. Carriazo J, Guelou E, Barrault J, Tatibouët JM, Molina R, Moreno S (2005) Synthesis of pillared clays containing Al, Al-Fe or Al-Ce-Fe from a bentonite: characterization and catalytic activity. *Catal Today* 107-108:126-132
2. Pera-Titus M, García-Molina V, Baños MA, Giménez J, Esplugas S (2004) Degradation of chlorophenols by means of advanced oxidation processes: a general review. *Appl Catal B Environ* 47:219-256
3. Andreozzi R, Caprio V, Insola A, Marotta R (1999) Advanced oxidation processes (AOP) for water purification and recovery. *Catal Today* 53:51-59
4. Malato S, Blanco J, Vidal A, Richter C (2002) Photocatalysis with solar energy at a pilot-plant scale: an overview. *Appl Catal B Environ* 37:1-15
5. Liotta LF, Gruttadauria M, Di Carlo G, Perrini G, Librando V (2009) Heterogeneous catalytic degradation of phenolic substrates: catalysts activity. *J Hazard Mater* 162:588-606
6. Sum OSN, Feng J, Hu X, Yue PL (2005) Photo-assisted Fenton mineralization of an azo-dye acid black 1 using a modified laponite clay-based Fe nanocomposite as a heterogeneous catalyst. *Top Catal* 33:233-242
7. Najjar W, Azabou S, Sayadi S, Ghorbel A (2007) Catalytic wet peroxide photo-oxidation of phenolic olive oil mill wastewater contaminants. Part I. Reactivity of tyrosol over (Al-Fe)PILC. *Appl Catal B Environ* 74:11-18
8. Sabhi S, Kiwi, J (2001) Degradation of 2,4-dichlorophenol by immobilized iron catalysts. *Water Res* 35:1994-2002
9. Feng J, Hu X, Yue PL, Zhu HY, Lu GQ (2003) A novel laponite clay-based Fe nanocomposite and its photo-catalytic activity in photo-assisted degradation of Orange II. *Chem Eng Sci* 58:679-685
10. Gemeay AH, Mansour IA, El-Sharkawy RG, Zaki AB (2003) Kinetics and mechanism of the heterogeneous catalyzed oxidative degradation of indigo carmine. *J Mol Catal A: Chem* 193:109-120
11. Ishtchenko VV, Huddersman KD, Vitkovskaya RF (2003) Part 1. Production of a modified PAN fibrous catalyst and its optimization towards the decomposition of hydrogen peroxide. *Appl Catal A: Gen* 242:123-137
12. Letaief S, Casal B, Aranda P, Martín-Luengo MA, Ruiz-Hitzky E (2003) Fe-containing pillared clays as catalysts for phenol hydroxylation. *Appl Clay Sci* 22:263-277
13. Tachiev G, Roth JA, Bowers AR (2000) Kinetics of hydrogen peroxide decomposition with complexed and free iron catalysts. *Int J Chem Kinet* 32:24-35

14. Neamtu M, Zaharia C, Catrinescu C, Yediler A, Macoveanu M, Kettrup A (2004) Fe-exchanged Y zeolite as catalyst for wet peroxide oxidation of reactive azo dye Procion Marine H-EXL. *Appl Catal B: Environ* 48:287–294
15. Dantas TLP, Mendonça VP, Jose HJ, Rodrigues AE, Moreira RFP (2006) Treatment of textile wastewater by heterogeneous Fenton process using a new composite Fe<sub>2</sub>O<sub>3</sub>/carbon. *Chem Eng J* 118:77–82
16. Sum OSN, Feng J, Hu X, Yue PL (2004) Pillared laponite clay-based Fe nanocomposites as heterogeneous catalysts for photo-Fenton degradation of acid black 1. *Chem Eng Sci* 59:5269–5275
17. Bobu M, Yediler A, Siminiceanu I, Schulte-Hostede S (2008) Degradation studies of ciprofloxacin on a pillared iron catalyst. *Appl Catal B: Environ* 83:15–23
18. Gil A, Gandía LM, Vicente MA (2000) Recent advances in the synthesis and catalytic applications of pillared clays. *Catal Rev Sci Eng* 42:145–212
19. Vicente MA, Bañares-Muñoz MA, Gandía LM, Gil A (2001) On the structural changes of a saponite intercalated with various polycations upon thermal treatments. *Appl Catal A: Gen* 217:191–204
20. Vaccari A (1999) Clays and catalysis: a promising future. *Appl Clay Sci* 14:161–198
21. Centi G, Perathoner S (2008) Catalysis by layered materials: a review. *Micropor Mesopor Mater* 107:3–15
22. Gil A, Korili SA, Vicente MA (2008) Recent advances in the control and characterization of the porous structure of pillared clay catalysts. *Catal Rev Sci Eng* 50:153–221
23. De León MA, Castiglioni J, Bussi J, Sergio M (2008) Catalytic activity of an iron-pillared montmorillonitic clay mineral in heterogeneous photo-Fenton process. *Catal Today* 133: 600–605
24. Iurascu B, Siminiceanu I, Vione D, Vicente MA, Gil A (2009) Phenol degradation in water through a heterogeneous photo-Fenton process catalyzed by Fe-treated laponite. *Water Res* 43:1313–1322
25. Ramirez JH, Costa CA, Madeira LM, Mata G, Vicente MA, Rojas-Cervantes ML, Lopez-Peinado AJ, Martin-Aranda RM (2007) Fenton-like oxidation of Orange II solutions using heterogeneous catalysts based on saponite clay. *Appl Catal B: Environ* 71:44–56
26. Ramirez JH, Lampinen M, Vicente MA, Costa CA, Madeira LM (2008) Experimental design to optimize the oxidation of Orange II dye solution using a clay-based Fenton-like catalyst. *Ind Eng Chem Res* 47:284–294
27. Chen Q, Wu P, Li Y, Zhu N, Dang Z (2009) Heterogeneous photo-Fenton photodegradation of Reactive Brilliant Orange X-GN over iron-pillared montmorillonite under visible irradiation. *J Hazard Mater* 168:901–908
28. Carneiro PA, Pupo Nogueira RF, Zaroni MVB (2007) Homogeneous photodegradation of C.I. Reactive Blue 4 using a photo-Fenton process under artificial and solar irradiation. *Dyes Pigment* 74:127–132
29. Yip ACK, Lam FLY, Hu X (2005) Chemical-vapor-deposited copper on acid-activated bentonite clay as an applicable heterogeneous catalyst for the photo-Fenton-like oxidation of textile organic pollutants. *Ind Eng Chem Res* 44:7983–7990
30. Tabet D, Saidi M, Houari M, Pichat P, Khalaf H (2006) Fe-pillared clay as a Fenton-type heterogeneous catalyst for cinnamic acid degradation. *J Environ Manage* 80:342–346
31. Centi G, Cimino G, Grasso G, Perathoner S, Romeo G, Toscano VG (2001) Catalytic wet H<sub>2</sub>O<sub>2</sub> oxidation of olive oil mills wastewater: development of a Fe/ZSM-5 catalyst system, CPS, Chemeng/0011003. [www.Chemweb.com](http://www.Chemweb.com). Accessed 10 October 2009
32. Tatibouët JM, Guelou E, Fournier J (2005) Catalytic oxidation of phenol by hydrogen peroxide over a pillared clay containing iron. Active species and pH effect. *Top Catal* 33:225–232
33. Guérou E, Barrault J, Fournier J, Tatibouët JM (2003) Active iron species in the catalytic wet peroxide oxidation of phenol over pillared clays containing iron. *Appl Catal B Environ* 44:1–8
34. Barrault J, Abdellaoui M, Bouchoule C, Majesté A, Tatibouët JM, Louloudi A, Papayannakos N, Gangas NH (2000) Catalytic wet peroxide oxidation over mixed (Al–Fe) pillared clays. *Appl Catal B Environ* 27:225–230

35. Guo J, Al-Dahhan M (2003) Catalytic wet oxidation of phenol by hydrogen peroxide over pillared clay catalyst. *Ind Eng Chem Res* 42:2450–2460
36. Catrinescu C, Teodosiu C, Macoveanu M, Brendle JM, Le Dred R (2003) Catalytic wet peroxide oxidation of phenol over Fe-exchanged pillared beidellite. *Water Res* 37:1154–1160
37. Chirchi L, Ghorbel A (2002) Use of various Fe-modified montmorillonite samples for 4-nitrophenol degradation by H<sub>2</sub>O<sub>2</sub>. *Appl Clay Sci* 21:271–276
38. Catrinescu C, Neamtu M, Brendlé JM, Garcia MG, Kettrup A (2006) Catalytic wet peroxide oxidation of reactive azo dyes over iron-containing pillared beidellite catalyst. In: Suárez M, Vicente MA, Rives V, Sánchez MJ (eds) *Materiales Arcillosos: de la Geología a las Nuevas Aplicaciones*, Salamanca, pp 87–98. Sociedad Española de Arcillos, ISBN: 84-689-6471-9
39. Fenton HJH (1894) Oxidation of tartaric acid in presence of iron. *J Chem Soc* 65:899–910
40. Haber F, Weiss J (1934) The catalytic decomposition of hydrogen peroxide by iron salts. *Proc R Soc Lond* 147:332–351
41. Lücking F, Köser H, Jank M, Ritter A (1998) Iron powder, graphite and activated carbon as catalysts for the oxidation of 4-chlorophenol with hydrogen peroxide in aqueous solution. *Water Res* 32:2607–2614
42. Safarzadeh-Amiri A, Bolten JR, Cater SR (1996) The use of iron in advanced oxidation processes. *J Adv Oxid Technol* 1:18–26
43. Bigda RJ (1995) Consider Fenton chemistry for wastewater treatment. *Chem Eng Proc* 91: 62–66
44. Walling C (1975) Fenton's reagent revisited. *Acc Chem Res* 8:125–131
45. Kitis M, Adams CD, Daigger GT (1999) The effects of Fenton's reagent pretreatment on the biodegradability of non-ionic surfactants. *Water Res* 33:2561–2568
46. Yoon J, Lee Y, Kim S (2001) Investigation of the reaction pathway of OH radicals produced by Fenton oxidation in the conditions of wastewater treatment. *Water Sci Technol* 44:15–21
47. Lu MC, Lin CJ, Liao CH, Ting WP, Huang RY (2001) Influence of pH on the dewatering of activated sludge by Fenton's reagent. *Water Sci Technol* 44:327–332
48. Walling C, Goosen A (1973) Mechanism of the ferric ion catalysed decomposition of hydrogen peroxide: effects of organic substrate. *J Am Chem Soc* 95:2987–2991
49. De Laat J, Gallard H (1999) Catalytic decomposition of hydrogen peroxide by Fe(III) in homogeneous aqueous solutions: mechanism and kinetic modeling. *Environ Sci Technol* 33:2726–2732
50. Gallard H, De Laat J (2000) Kinetic modelling of Fe(III)/H<sub>2</sub>O<sub>2</sub> oxidation reactions in dilute aqueous solution using atrazine as a model organic compound. *Water Res* 34:3107–3116
51. Walling C, Kato S (1971) The oxidation of alcohols by Fenton's reagent: the effect of copper ion. *J Am Chem Soc* 93:4275–4281
52. Lin SH, Lo CC (1997) Fenton process for treatment of desizing wastewater. *Water Res* 31:2050–2056
53. Luo M, Bowden D, Brimblecombe P (2009) Catalytic property of Fe–Al pillared clay for Fenton oxidation of phenol by H<sub>2</sub>O<sub>2</sub>. *Appl Catal B Environ* 85:201–206
54. Sanabria N, Alvarez A, Molina R, Moreno S (2008) Synthesis of pillared bentonite starting from the Al–Fe polymeric precursor in solid state, and its catalytic evaluation in the phenol oxidation reaction. *Catal Today* 133–135:530–533
55. Pignatello J (1992) Dark and photoassisted Fe<sup>3+</sup>-catalyzed degradation of chlorophenoxy herbicides by hydrogen peroxide. *Environ Sci Technol* 26:944–951
56. Zazo JA, Casas JA, Mohedano AF, Rodriguez JJ (2006) Catalytic wet peroxide oxidation of phenol with a Fe/active carbon catalyst. *Appl Catal B Environ* 65:261–268
57. Molina R, Martínez F, Melero JA, Bremner DH, Chakinala AG (2006) Mineralization of phenol by a heterogeneous ultrasound/Fe-SBA-15/H<sub>2</sub>O<sub>2</sub> process: multivariate study by factorial design of experiments. *Appl Catal B Environ* 66:198–207
58. De Laat J, Le TG (2006) Effects of chloride ions on the iron(III)-catalyzed decomposition of hydrogen peroxide and on the efficiency of the Fenton-like oxidation process. *Appl Catal B Environ* 66:137–146



59. Pintar A, Levec J (1992) Catalytic oxidation of organics in aqueous solutions: kinetics of phenol oxidation. *J Catal* 135:345–357
60. Fajerweg K, Debellefontaine H (1996) Wet oxidation of phenol by hydrogen peroxide using heterogeneous catalysis Fe-ZSM-5: a promising catalyst. *Appl Catal B: Environ* 10:229–235
61. Fortuny A, Ferrer C, Bengoa C, Font J, Fabregat A (1995) Catalytic removal of phenol from aqueous phase using oxygen or air as oxidant. *Catal Today* 24:79–83

# Chapter 7

## Catalytic Wastewater Treatment Using Pillared Clays

Siglinda Perathoner and Gabriele Centi

**Abstract** After introduction on the use of solid catalysts in wastewater treatment technologies, particularly advanced oxidation processes (AOPs), this review discussed the use of pillared clay (PILC) materials in three applications: (i) wet air catalytic oxidation (WACO), (ii) wet hydrogen peroxide catalytic oxidation (WHPCO) on Cu-PILC and Fe-PILC, and (iii) behavior of Ti-PILC and Fe-PILC in the photocatalytic or photo-Fenton conversion of pollutants. Literature data are critically analyzed to evidence the main direction to further investigate, in particular with reference to the possible practical application of these technologies to treat industrial, municipal, or agro-food production wastewater.

**Keywords** Catalytic waste · Pillared clays · Photocatalysis

### 7.1 Introduction

There is an increasing research and applicative interest in using advanced nanotech catalysts and materials for the purification/remediation of contaminated surface or groundwater and municipal or industrial wastewater [1–9]. Solid catalysts are used in promoting many water treatment and remediation technologies [6], such as in (i) various advanced oxidation processes (AOPs) (photocatalytic treatment of wastewater, wet air catalytic oxidation (WACO), wet hydrogen peroxide catalytic oxidation (WHPCO), catalytic ozonation), (ii) selective reduction of pollutants in water (nitrate and nitrite catalytic reduction, catalytic hydrodehalogenation), (iii) catalytic permeable reactive barriers, and (iv) other less commonly used wastewater

---

S. Perathoner (✉)

Dipartimento di Chimica Industriale ed Ingegneria dei Materiali and CASPE (INSTM Laboratory of Catalysis for Sustainable Production and Energy), Università di Messina, Salita Sperone 31, 98166 Messina, Italy  
e-mail: perathon@unime.it

treatment technologies (supercritical water oxidation, sonochemical degradation, water treatment using non-thermal plasma or e-beam irradiation). The use of solid catalysts offers several potential advantages [6]:

- operation in milder reaction conditions,
- better engineering of the process,
- possibility of selective conversion of specific target chemicals, and
- combined removal by adsorption with catalytic regeneration in a separate step.

In addition, in photocatalytic technologies semiconductors such as titania are required to generate by photo-induced processes the active species (hydroxyl radicals) responsible for the degradation of the pollutants. The use of catalysts is also often indispensable to convert recalcitrant contaminants, such as endocrine-disrupting chemicals (EDCs): hormonally active agents, xenobiotics, pharmaceutically active compounds, effluent-derived microcontaminants, and persistent organic pollutants. EDCs are pollutants with estrogenic or androgenic activity at very low concentrations and are emerging as a major concern for water quality [10]. The concentration of these microcontaminants in water is continuously increasing, and great endeavors have been done on the removal of EDCs in wastewater, because conventional water treatment technologies are not effective in their elimination. AOP methods, in combination with solid catalysts, are the most effective technologies for the treatment of wastewaters containing pharmaceuticals, personal care products (PPCPs), and especially EDCs [11].

There are many other very relevant areas in which catalytic AOP methods are between the most promising technologies, although it should be commented that in water treatment technologies a combination of technologies (“technology train”) is typically necessary to realize the optimal compromise between cost and effectiveness. In particular, the integration between catalysis and membrane is a very relevant area to mention for the development of novel water treatment technologies and in general more sustainable processes [12]. Examples of areas of application of catalytic AOP methods are the following [5]:

- Pulp Mill Effluents
- Dyeing and Printing Wastewater
- Oil Refinery Wastewater
- Distillery Wastewater
- Food Industries
- Leather Industries
- Municipal and Natural Wastes

In addition, an area of application which will fast increase in a near future will be the wastewater treatment from biorefineries. In comparison to oil-based refineries and chemical processes, the production of fuels and chemicals from biomass produces an order of magnitude higher volume of wastewater effluents with very large

amounts of contaminants [13]. The development of novel technologies for the treatment of these large volume effluents is one of the conditions for the success of a bio-based economy.

### ***7.1.1 Issues in Using Solid Catalysts in Wastewater Treatment***

Notwithstanding the large potential field of application of catalytic AOP methods, the largest part of the studies is still often limited to model compounds such as phenols [2, 3], although phenol itself is a relevant industrial contaminant. However, the wastewater typically never contains a single contaminant and it is known that in the presence of complex mixtures completely different results and/or fast deactivation may be observed with respect to that observed using single model chemicals [6]. There are increasing examples in literature on catalytic AOP studies using realistic streams, even if this type of studies should be further incentivized.

The use of solid catalysts in AOP methods requires different characteristics of the solid with respect to those typically used in environmental catalysis applications [6]. Limited attempts have been made often to tailor solid catalysts for the water treatment applications, but more attention to this issue has been given recently. There are problems of

- pore structure design (intraparticle diffusivity is usually an issue determining the catalytic performances),
- leaching (often driven from the reaction products and thus depending on the progress of the reaction), and
- stability (related, but not only depending on the possible leaching) and selectivity (typically, quite complex mixtures should be treated in practical applications).

As a consequence catalyst design for water treatment is different from that of most of other applications and even in the screening of the sample this aspect should be considered, as generally valid for the development of multiphase reaction processes [14]. New microstructured and nanostructured materials (fibers, nanotubes, multilayer composite materials) are available for a more effective catalyst design in water treatment technologies [14]. They offer also the possibility of a better reactor design. The efficient integration between catalyst and reactor design in wastewater treatment technologies is another of the critical factors to increase the use of solid catalysts in these technologies [6]. A further general issue in design of solid catalysts for AOP methods regards the fact that the effective oxidizing species are very reactive and short living, such as radical species ( $H\cdot$ ,  $HO\cdot$ ,  $HO_2\cdot$ , etc.). There is little knowledge on the catalyst design necessary to optimize performances in the presence of these very reactive species.

However, literature data on the catalytic AOP methods are often mainly phenomenological and based on the screening of different catalysts and analysis of the

effect of the reaction conditions. Another limit in current literature, from the application point of view, regards the scarce data on the toxicological effects on humans and the environment of both used catalysts (in relation to possible leaching of some of the components – metal ions, particularly – and/or formation of suspended fine particles) and of the products of degradation of pollutants, in addition to the lack of use of more realistic streams. Oxidation of pollutants may give rise to intermediates which can be more toxic than the starting chemicals. It is thus necessary to put attention on the toxicological evaluation of the quality of treated wastewater, as well as the integration of the catalytic step with downstream technologies. For example, the catalytic technology is often a pre-treatment step before biological aerobic or anaerobic processes or to a membrane separation [15–17]. Quality of water required in these cases is different, as well as often the level of conversion necessary for an optimal integration with the downstream technology.

### ***7.1.2 PILCs and Catalytic AOP Methods***

This chapter will focus the discussion on the use of pillared clays (PILCs) in AOP methods for wastewater treatment. In general, layered materials offer many attractive characteristics for their use as catalysts [18]. Their structure consisting of stacked sheets represents an interesting opportunity for developing new materials with a tailored nanodesign, controlled accessibility to the sites and properties, tunable pore size and volume, and high surface area. The use of layered materials (layered perovskite, anionic clays, pillared clays) in catalytic reactions spans from new processes for environmental protection, including wastewater treatment, to petrochemistry and fine chemicals production and refinery/biorefinery as well [18]. More specifically, pillared clays (PILCs), due to their more precise tuning of the microporous structure, possibility of multifunctional design, and improved thermal stability find application in many acid-catalyzed reactions, as well as redox reactions (selective reduction of NO<sub>x</sub>, complete oxidation of volatile organic compounds (VOCs) or chlorofluorocarbons (CFCs), and wet catalytic oxidation of waste) after introduction of suitable transition metals into the pillars or exchangeable positions [18–21]. PILCs allow a fine control of the microstructure developed in it by adjusting the several parameters involved in the synthesis process [19].

With respect to other layered catalytic materials, PILCs are characterized from the presence of oxide pillars between the layers. They are prepared by exchanging the charge-compensating cations present in the interlamellar space of the swelling clays by hydroxy-metal polycations. During calcination, the inserted polycations give rise to rigid, thermally stable oxide pillars, which limit the possibility of thermal collapse between the two-dimensional clay layers. The pillaring procedure of the clay thus allows to produce relatively stable layered materials with a tunable interlayer spacing by adjusting the several parameters involved in the synthesis process of alumina-pillared clays. The interlayer spacing typically ranges between 0.6 and 1.8 nm, e.g., situates in between microporous and mesoporous materials.

For these reasons, they were originally developed to prepare thermally stable acid catalysts that are able to crack larger molecules than those addressed by microporous (zeolitic) materials [22, 23].

This structure shows interesting characteristics to develop advanced catalytic materials for AOP applications. The interlayer distance is influenced by the nature of the intercalant species, their length, and their degree of polymerization. They can be controlled during the synthesis by the pH, the temperature, and the time of aging [19]. The most widely used intercalating agents are polymeric or oligomeric cations produced by the base hydrolysis of Al, Zr, Ti, Cr, Fe, and Ga salts. It is thus possible:

- To control the interlayer space and tailor the access to inner sites. This is important to allow access of relatively large molecules (often present in wastewater), but avoiding at the same time the humic substances that cause fouling of the active sites, e.g., to provide longer-term activity in the presence of real wastewater.
- To introduce different transition metals into the pillars/or exchangeable positions, e.g., develop multifunctional catalysts (with Brönsted and Lewis acidity, as well as redox properties) to tailor the catalytic behavior in wet oxidation.
- To control the hydrophilic character of the inner space between the layer, another important characteristic to control the catalytic performances in wet oxidation.

There are three main areas of use of PILCs in catalytic AOP methods. They are as follows:

- *Wet air catalytic oxidation* (WACO), e.g., the oxidation of organic compounds by oxygen at high temperatures (typically in the 150–250 °C temperature range) and under pressure (usually, in the 20–40 bar range) in autoclave reactors. It is a widely used technology, especially in the treatment of industrial wastewater or sludges. The use of catalysts allows operating at lower reaction temperatures, an important aspect not only to reduce operative costs, but also to mitigate corrosion problems related to the formation of acetic acid as the main by-product. Due to these corrosion problems, often special materials for the construction of the reactor (Ti, for example) are necessary, significantly increasing the fixed capital costs.
- *Wet hydrogen peroxide oxidation* (WHPCO; alternative names are catalytic wet peroxide oxidation – CWPO, and wet peroxidation or wet oxidation by hydrogen peroxide) uses H<sub>2</sub>O<sub>2</sub> (hydrogen peroxide, HP) as oxidant instead of oxygen. It operates at significantly milder reaction conditions (temperature lower than 100 °C, atmospheric pressure) and do not require costly autoclave reactors, e.g., significant lower operative and fixed capital costs. However, HP is a more costly reactant than oxygen (air). It is based on the Fenton chemistry, where transition metals such as iron and copper are able to react with HP to generate hydroxyl radicals (HO·), which are the effective oxidizing agents. The original Fenton studies, and still many investigations and applications, are based on the use of homogeneous catalysts (Fe<sup>2+</sup> and Cu<sup>+</sup> salts) [24–26], but the use of solid catalysts containing iron or copper is increasing [27–33] (heterogeneous Fenton). UV radiation is also able to catalyze the formation of these hydroxyl radicals from HP by

homolytic splitting and thus the combination of solid catalysts with UV radiation is used (photo-Fenton) [34–41].

- *Photocatalytic elimination of pollutants in water*, using semiconductor nanoparticles (typically  $\text{TiO}_2$ ) immobilized within PILC layers or using titania-pillared clays ( $\text{TiO}_2$  PILCs), e.g., when the pillars of the clay are consisted from the semiconductor photo-active element [42–46].

It should be mentioned that PILCs are used often for the removal of pollutants in water by adsorption, either organic substances [47–52] or toxic heavy metal ions [53–56]. However, we will limit our discussion here to the use of PILCs as catalysts in water treatment technologies.

It should be also mentioned that there is an increasing R&D interest on organic-pillared clays, e.g., organic–inorganic nanocomposites [57]. Although the use of these hybrid clays as advanced materials for the removal of pollutants from industrial wastewaters have been proposed from long time [58], new methods have been proposed more recently [59–61] to prepare microporous clay mineral with organic–inorganic hybrid pillars having very high surface area (about  $500 \text{ m}^2 \text{ g}^{-1}$ ) [60]. These organophilic-pillared clays (organoclays) may be prepared with different kinds of organic materials in the interlayers, and due to the better tuning the hydrophobic properties, these materials show enhanced selective adsorption toward some pollutants [62, 63]. Their applicability for catalytic AOP methods, particularly regarding stability, has to be verified, although they were proposed to prepare highly active titania-pillared clays for cleaning up the water polluted by the toxic organic compounds with poor polarity such the endocrine-disrupting chemicals [64].

## 7.2 Wet Air Catalytic Oxidation (WACO)

The number of publications on the use of PILCs in WACO applications is significantly lower than that of using PILC catalysts for wet oxidation using hydrogen peroxide (WHPCO). The motivation is related mainly to the fact that the reaction mechanism in WACO is different from that in WHPCO. In the latter, short-living hydroxyl radical species are generated which are highly reactive, as discussed later. In WACO, a combined redox and heterogeneous free radical mechanism is present.

Metal oxides are capable of initiating free radicals by activating reactant molecules directly and facilitates their decomposition into radicals, or by accelerating the decomposition into radicals, with the hydroperoxides either being present in the system or forming slowly by the first mechanism [65]. Oxygen may participate in a reaction either as an adsorbed species on the catalyst surface or as a part of the lattice oxygen presented in the metal oxides. The presence of catalysts creates an ionic environment that enhances heterolytic reactions. Both free radical (homolytic) and ionic (heterolytic) oxidation reaction mechanisms have been proposed for WACO [65].

The consequence of this difference in the reaction mechanism is that the amount of active catalyst in WACO should be higher than in WHPCO. Metal oxide should be present in PILCs essentially in the pillars to avoid a fast leaching, as discussed later. Therefore, the amount of metal oxide which can be introduced in PILCs to have a stable wet oxidation activity is limited. This amount is typically not enough for active WACO catalysts (e.g., other oxide-based catalysts have typically better performances), but can be good in the case of WHPCO. Although these aspects are not considered in discussing the catalytic behavior of PILC catalysts in wet oxidation, they should be taken into account to consider literature results and the applicability of this class of catalysts in water treatment technologies.

### 7.2.1 PILC-Based Catalysts for Wet Oxidation

The first report on the use of PILC catalyst in the wet air oxidation was of Guo and Al-Dahhan [66] who investigated the kinetics of conversion of phenol as model compound using Al-Fe-pillared clay in the form of extrudates (cylindrical, approximately  $2 \times 8$  mm). Reaction temperatures were in the range of 90–150 °C and air pressure range was 0.8–2.5 MPa. The variables studied included reaction temperature, air pressure, solution pH, initial phenol concentration, and catalyst loading. The results were compared with those obtained using hydrogen peroxide oxidation [67]. The same catalyst has been used in both types of tests, e.g., an Al-Fe-PILC prepared by NTUA (National Technical University of Athens, Greece), starting from bentonite (Zenith-N). The main composition (wt%) was as follows: SiO<sub>2</sub> 52.50, Al<sub>2</sub>O<sub>3</sub> 27.56, Fe<sub>2</sub>O<sub>3</sub> 7.02. In addition, the kinetics in both wet oxidation with air or H<sub>2</sub>O<sub>2</sub> was investigated [66, 67]. Therefore, it is one of the few cases in literature in which a good comparison between the performances in catalytic oxidation with wet air or H<sub>2</sub>O<sub>2</sub> (WACO and WHPCO, respectively) of the same catalyst is possible. This PILC catalyst (indicated with the acronym FAZA (Al-Fe-PILC)) based on bentonite (Zenith-N) was used also by other authors in wet oxidation with H<sub>2</sub>O<sub>2</sub> [68–70]. Furthermore, it has been used in various other catalytic applications, such as alkylation [71] and conversion of various alcohols [72], and its characteristics extensively discussed [73].

Reported in Fig. 7.1 is the behavior of FAZA in phenol conversion under WACO and WHPCO conditions. The reaction conditions, apart from the reaction temperature, are comparable. It should be mentioned, however, that for WACO the further increase in the air partial pressure above 1.5 MPa has minimal effect on the rate of reaction (e.g., O<sub>2</sub> concentration in solution maintains close to saturation during the batch reactor tests), while for WHPCO the increase in the H<sub>2</sub>O<sub>2</sub> concentration above 0.3 M significantly improves the reaction rate. The results reported in Fig. 7.1 clearly indicate that FAZA is more active in WHPCO than in WACO. By extrapolating the results at the same temperature (70 °C), the rate in WHPCO is from 20 to 100 times higher than that of WACO, depending on H<sub>2</sub>O<sub>2</sub> concentration. By comparing the reaction rates at 70 °C for WHPCO and 110 °C for WACO,



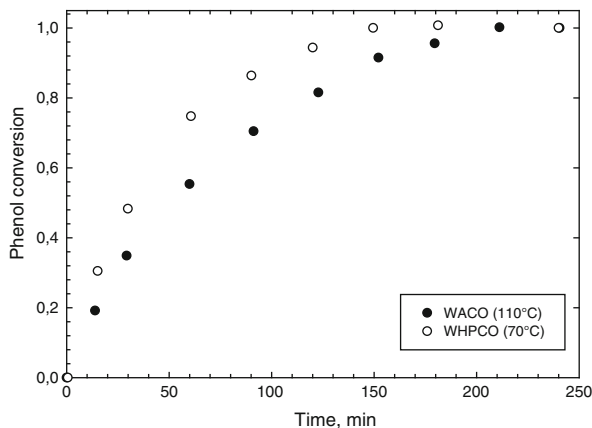
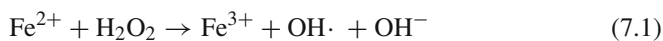


**Fig. 7.1** Behavior of FAZA (Al-Fe-PILC) catalyst in WACO and WHPCO conversion of phenol. Experimental conditions: 500 ppm phenol in distilled water, 10 g/l catalyst, batch reactor – 600 ml, 1.5 MPa air (WACO) or 0.3 M H<sub>2</sub>O<sub>2</sub> – continuous fed (WHPCO), temperature 110 °C (WACO) or 70 °C (WHPCO), natural pH. Adapted from Guo and Al-Dahhan [66, 67]

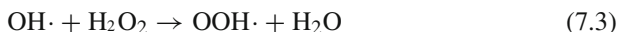
the former is about 2 times higher than the latter. For an air pressure of 1.5 MPa and a reaction temperature of 110 °C, the oxygen concentration in water is about 0.2 M [74]. It increases by lowering the reaction temperature. The concentration of O<sub>2</sub> and H<sub>2</sub>O<sub>2</sub> in solution, in the tests in Fig. 7.1, is thus quite comparable. The different reactivity of the catalyst in WHPCO and WACO is thus related to a different rate of generation of active oxygen species able to give oxidative degradation of phenol.

Guo and Al-Dahhan in their kinetic analysis of WACO and WHPCO of phenol [66, 67] concluded that in WACO the rate-controlling step was the surface reaction between adsorbed reactant species, while in WHPCO the reaction takes place to a significant extent both in the liquid phase and on the catalyst surface. However, the discrimination between the different reaction models was not based on a correct statistical methodology, such as the *F*-test. In addition, the rate equations were partially phenomenological, being a mixed between an LH (Langmuir–Hinshelwood) modeling and power law. The rate of phenol disappearance is the product of a term derived from LH approach (single or dual site surface mechanism) and the concentration of the catalyst elevated to a factor of 0.8–0.9. Therefore, reliable mechanistic indications from this type of kinetic approach cannot be derived.

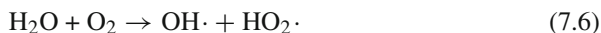
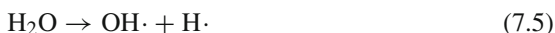
In WHPCO the active oxidizing species (hydroxyl radicals or other reactive species) are generated by the reaction of H<sub>2</sub>O<sub>2</sub> with the catalyst iron sites, according to the well-known Fenton reaction mechanism:



Side reactions are the following:



In wet air catalytic oxidation (WACO), the main reactions are described in Eqs. (7.5–7.12). Hydroxyl radicals are produced from the dissociation and oxidation of water according to Eqs. (7.5 and 7.6). Hydroperoxyl radicals are formed from the oxidation of water (Eq. 7.6) and the target compound RH (Eq. 7.10). Hydroxyl radicals are also produced from hydrogen peroxide (Eq. 7.8) and from the reaction of atomic oxygen with the target compound (Eq. 7.12). Hydrogen peroxide is produced by the recombination of hydroperoxyl radicals (Eq. 7.7) or by the reaction of hydroperoxyl radicals with the target compound (Eq. 7.11). Atomic oxygen is produced from the dissociation of oxygen (Eq. 7.9). Although the hydroperoxyl radical is less reactive than the hydroxyl radical (their relative oxidation power is 2.06 and 1.25, respectively, with respect to  $\text{Cl}_2$  put equal to 1), it plays an important role because of its relative abundance.



In addition, during catalytic wet oxidation, oxygen may participate in reaction either as an adsorbed species on the catalyst surface or as a part of the lattice oxygen present in metal oxides [65]. We may simplify the difference between WHPCO and WACO mechanisms in the case of Al–Fe–PILC catalyst (FAZA), indicating that in the former the rate of reaction depends on the redox reaction of  $\text{H}_2\text{O}_2$  with iron to form the active radical species, while in WACO the rate depends on electrophilic character of the catalyst, e.g., its rate of generation of surface radical species. Although also this property depends on the presence of redox sites, the Fenton mechanism (Eqs. 7.1 and 7.2) is much more effective to

close the cycle. Therefore, in WACO it is necessary to delocalize more effectively the charge than in WHPCO, e.g., (iron)oxide nanocrystals are necessary with respect to nearly isolated iron sites for the Fenton mechanism. The former may be instead negative for WHPCO, because it catalyzes the decomposition of hydrogen peroxide.

In conclusion, although apparently the same Fe-PILC catalyst is active in WACO and WHPCO reactions, the nature of the active sites in the two reactions is different and as a consequence the optimal characteristics and design of the catalyst to optimize the performances. The difference in the nature of the active sites and reaction mechanisms to activate  $\text{H}_2\text{O}_2$  and  $\text{O}_2$  explains the different observed reactivity, which is instead typically attributed to only the latter aspect.

More recently, Najjar et al. [75] have investigated similar Fe–Al-pillared clays, but prepared from Wyoming montmorillonite, in gallic acid wet air oxidation in mild conditions (90 °C, 5 bar). Gallic acid is a phenolic compound used as model chemicals for the polyphenolic fractions present in olive oil milling wastewater (OMW). Good performances were observed, with over 90% gallic acid conversion, although for the samples showing the higher iron leaching (15%). These samples contain iron oxide hydroxide ( $\text{FeHO}_2$ ), which forms  $\alpha\text{-Fe}_2\text{O}_3$  (hematite) by calcination. This is in agreement with the previous comments on the need for small iron oxide particles to obtain more active Fe-PILC catalysts in WACO reaction, although evidences show that these particles are more prone to be leached during the catalytic reaction. The same catalysts were also studied in the catalytic photo-oxidation with  $\text{H}_2\text{O}_2$  of tyrosol, another representative compound of the polyphenolic fraction in OMW [76]. In the presence of  $\text{H}_2\text{O}_2$  and UV radiation (which favors the homolytic cleavage of hydrogen peroxide to two hydroxyl radicals) complete conversion of tyrosol may also be obtained at room temperature, with good results also in terms of toxicity of the effluent. They conclude that this methodology using (Al-Fe)-PILC heterogeneous catalysts is a promising technique for the pre-treatment of OMW before biological treatment, in order to enhance biodegradability and reduce biotoxicity of polyphenolic fraction.

No other studies have been reported on the wet air oxidation using pillared clays, apart from further aspects on the phenol oxidation by Guo and Al-Dahhan [77, 78], mainly in relation to reactor and catalyst engineering.

### 7.3 Wet Hydrogen Peroxide Catalytic Oxidation (WHPCO)

More studies have been dedicated to the use of PILC catalysts in wet oxidation using hydrogen peroxide. In this case, in addition to the use of model compounds, several studies have also reported the behavior using real or more complex solutions which allow evaluating the applicability of these catalysts and technology to practical cases. In few cases, also indications on the stability of the catalysts have been reported, because this is one of the critical issues. Indication on the biotoxicity of

the treated effluents, another critical aspect, has been also reported in some cases. Therefore, although most of the studies have mainly an academic character, there are some indications on the applicability of the catalysts and wastewater treatment technology. Barrault et al. [79, 80] were between the first reporting the good performances of mixed (Al–Cu)-pillared clays prepared from a crude bentonite sample (H) (Tunisia deposit) in phenol oxidation with hydrogen peroxide (indicated as CWPO reaction; as noted before, often different acronyms are used for this reaction). They evidenced that the introduction of copper in pillaring position results in more effective catalysts, although the amount of copper which can be introduced was limited to less than 0.5 wt%. They also evidenced that copper introduced in this position results stable against leaching and the catalyst is reusable in successive batch reactor tests.

Barrault et al. [68, 69, 81] were also between the first reporting the excellent behavior of mixed (Al–Fe)-pillared clays (FAZA) in WHPCO conversion of phenol [69]. In mild reaction conditions, about 80% of the initial amount of phenol was transformed into CO<sub>2</sub>, at 70 °C, in 2 h under atmospheric pressure. They evidenced that the reaction is heterogeneous and that the TOC (total organic carbon) abatement obtained with the FAZA catalyst is much higher than that observed with homogeneous iron species in the same reaction conditions. The little amounts of leached iron (less than 1 ppm) give a negligible contribution to the phenol oxidation. The catalyst leaching remains very low and catalyst performance is stable, even after three cycles of reaction.

Some years later, Barrault et al. [32] discussed the nature of the iron species active in the reaction. The characterization by electron spin resonance (ESR) of the iron species contained in the Al-Fe-pillared clay (FAZA) has shown that three different iron species were present:

- Isolated iron species in highly distorted octahedral symmetry, located in the layer of the clay, probably in substitution of Al atoms.
- Iron species belonging to oxide clusters.
- Isolated iron species in octahedral symmetry, present only in the catalyst pillared by AlFe mixed complexes, probably belonging to the pillars as extra-framework species or by substituting the Al atoms of the pillars.

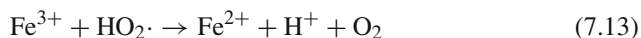
The latter species are those active in the total phenol oxidation by hydrogen peroxide. These species are also rather stable against leaching. The authors also reported long-time (350 h) catalytic experiments in a continuous flow reactor which showed the high stability of the Al-Fe-pillared clay. After these tests, the total amount of leached iron was less than 5 wt% of the initial value. This long-term result, in addition to demonstrate the suitability of the catalyst for application, evidences that a heterogeneous mechanism occurs, although it does not allow to discriminate whether it is a truly heterogeneous mechanism or the solid acts as catalyst to activate only H<sub>2</sub>O<sub>2</sub>.

### 7.3.1 Heterogeneous Versus Homogeneous Reactions

The question of heterogeneous versus homogeneous reaction in phenol oxidation by hydrogen peroxide in the presence of Fe-PILC catalysts was discussed specifically few years later by the same authors [82]. Both heterogeneous and homogeneous catalytic systems behave similarly. In both cases, the highest phenol conversion and TOC abatement being obtained at a pH value close to 3.7. However, the heterogeneous catalytic system results were less sensitive to the pH and more efficient in TOC abatement than the homogeneous one. The measurement of OH· production by an ESR spin trapping technique using 5,5-dimethylpyrroline-N-oxide (DMPO) as trapping agent showed that the OH· production followed the same profile in function of the pH value than the catalytic activity in phenol oxidation. This indicates that the main active species are hydroxyl (OH·) and/or hydroperoxyl (HO<sub>2</sub>·) radicals generated by hydrogen peroxide reaction with iron species in both homogeneous and heterogeneous systems. The main difference between homogeneous and heterogeneous systems is not the formation of different active oxygen from hydrogen peroxide, but the ability of the heterogeneous catalyst to adsorb on to its surface the phenol and/or the reaction intermediate products, favoring then their reaction with oxygen species formed by hydrogen peroxide activation.

These indications are in line with those reported by Perathoner and Centi [29] discussing the WHPCO of organic waste in agro-food and industrial streams. They also indicated that the adsorption of reactants on the solid and the different properties of iron or copper ions (or species) anchored on solid matrices (with respect to the same ions in solution) pointed out a difference between homogeneous and solid Fenton-type catalysts, notwithstanding the analogies in the behavior. The limited information in literature on the radical mechanisms in the presence of solid Fenton-type catalysts were also evidenced, as well as the little knowledge on the mass/heat diffusion aspects inside microporous materials during these fast radical-type reactions as and when hydroxyl radicals are generated.

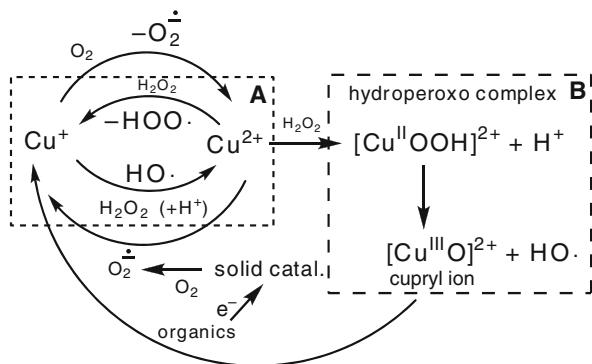
Another aspect evidenced, which usually was neglected in literature, is the oxygen formation during the reactions:



as well as that derived from the direct H<sub>2</sub>O<sub>2</sub> decomposition to water and oxygen influences the catalytic behavior. In fact, it competes with hydrogen peroxide to reoxidize the reduced Fe<sup>2+</sup> or Cu<sup>+</sup> species which are those which generate hydroxyl radicals on reaction with H<sub>2</sub>O<sub>2</sub> (Eq. 7.1). In addition, a gas cap may form on the catalyst surface, especially in micropores, such as in PILC. The formation of this gas cap depends on the hydrophobic character of the catalyst, but may significantly affect the intraparticle mass diffusion in addition to quenching the reduced iron or copper species.

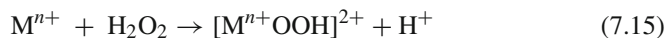
The issue of homogeneous versus heterogeneous catalytic reactions to eliminate organics from wastewater using  $\text{H}_2\text{O}_2$  was discussed in detail by Perathoner et al. [83] with specific reference to  $\text{Cu}^{2+}$ -pillared clays. Homogeneous ( $\text{Cu}^{2+}$  ions) and heterogeneous ( $\text{Cu}^{2+}$ -PILC) Fenton-like catalysts were compared in the conversion of *p*-coumaric acid, another model compound of polyphenolic fractions of OMW. The performances of the two classes of catalysts are similar for an analogous amount of copper, but there are some relevant differences in terms of (i) the presence of an induction time, (ii) the turnover frequency, (iii) the efficiency in the use of  $\text{H}_2\text{O}_2$ , (iv) the initial attack of *p*-coumaric acid (hydroxylation on the aromatic ring or oxidative attack on the double bond of the lateral chain), and (v) the effect of dissolved oxygen on the removal of total organic carbon (TOC) [83].

**Scheme 7.1** Reaction mechanism for the generation of radical oxygen species by interaction with  $\text{H}_2\text{O}_2$ , with copper ions in solution or on the solid catalyst. Adapted from Perathoner et al. [83]

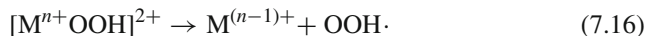


Scheme 7.1 shows an overview of the possible reaction pathways in the Fenton and Fenton-like mechanisms [83]. We indicate here Fenton mechanism that starting from  $\text{Cu}^+$  and/or  $\text{Fe}^{2+}$  ions, while Fenton-like mechanism that starting from  $\text{Cu}^{2+}$  and/or  $\text{Fe}^{3+}$  ions which reduces to the active Fenton species by reaction with organics. For solid heterogeneous catalysts, Fenton-like mechanism is prevailing. Scheme 7.1 is reported for copper ions, but it is well equivalent for the  $\text{Fe}^{2+}/\text{Fe}^{3+}$  couple. Besides the “classic” redox cyclic mechanism involving  $\text{Cu}^+$  and  $\text{Cu}^{2+}$  species (indicated with A in Scheme 7.1), an additional pathway with formation of a copper hydroperoxo complex intermediate which transforms then to cupryl ion generating an hydroxyl radical is possible (indicated with B in Scheme 7.1). The two pathways are characterized by a different turnover frequency as well as efficiency in  $\text{H}_2\text{O}_2$  use. Starting from  $\text{Cu}^{2+}$  ions (Fenton-like catalysts), the presence of the pathway A or B depends on the energetic stability of the hydroperoxo complex, which in turn depends on the ligand effect of the substituents.

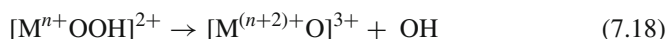
For the Fenton-like reagents ( $\text{Cu}^{2+}$ ,  $\text{Fe}^{3+}$ ), initially no O–O bond breaking takes place, but instead a metal hydroperoxo intermediate is formed as the first step via hydrolysis:



This intermediate might be able to react with organic substrates or break up into smaller active species in the second step. The metal hydroperoxo may homolyze either at the Fe–O bond generating  $M^{(n-1)+}$  and producing the reactive  $\text{HOO}\cdot$  radical or at the O–O bond producing the  $M=O$  species (example ferryl species) and an  $\text{HO}\cdot$  radical:



Alternatively, O–O bond heterolysis could take place, producing the highly reactive  $M^{(n+1)+}$  species:



Static density functional theory (DFT) calculations on the hydrated Fenton-like reagent in vacuo,  $[\text{Fe}^{\text{III}}(\text{H}_2\text{O})_5(\text{H}_2\text{O}_2)]^{3+}$ , and ab initio molecular dynamics (AIMD) simulations of the Fenton-like reagent in aqueous solution,  $\text{Fe}^{3+}/\text{H}_2\text{O}_2(\text{aq})$  [84], showed that the first reaction step consists of the donation of the  $\alpha$ -proton of hydrogen peroxide to the solvent shortly after the hydrogen peroxide coordinates to iron(III) (Eq. 7.15), and the second step involves probably the O–O bond homolysis producing the ferryl ion and a hydroxyl radical. A strong solvent effect was noted indicating that in the presence of ligands, particularly those inducing a low-spin iron(III)hydroperoxo intermediate, the pathway of transformation can be different.

This suggests that in solid Fenton catalysts such as Fe-PILC a significant change in the pathway of transformation is expected. The formation of the ferryl intermediate, e.g.,  $[\text{Fe}^{\text{IV}}\text{O}]^{2+}$ , was also suggested to be a key step in the reaction mechanism over Fe-ZSM-5 Fenton-type solid catalysts [85], but forming by oxidation of a Fe(III)–OH intermediate, not from the peroxo  $[\text{Fe}^{\text{III}}\text{OOH}]^{2+}$  species. It is likely that this ferryl (or analogous cupryl) species plays a critical role also in Fe-PILC or Cu-PILC catalyst. Therefore, Fenton and Fenton-like chemistry which is generally believed to proceed via similar mechanisms instead probably follows different reaction pathways, intermediates, and reactive species.

In Cu-PILC, the preferable pathway involves thus the formation of the  $\text{Cu}^{2+}$  hydroperoxo complex (pathway B in Scheme 7.1). Further transformation gives rise to the formation of hydroxyl radicals and cupryl ions. The latter may oxidize organic molecule thereby reducing to  $\text{Cu}^+$  ions. The change from aquo to organic ligands in the copper complex may change the stability of the hydroperoxo complex. It is therefore reasonable to suggest that in the homogeneous catalyst the initial Fenton mechanism involves the hydroperoxo complex (route B), while in the progress of the reaction the mechanism changes to the “ $\text{Cu}^+ \rightleftharpoons \text{Cu}^{2+}$ ” cyclic one (route A) as a consequence of the change in the formation of products of reactions (oxalic acid, for example) which substitute water molecules in coordinating the copper ions. This explains the presence of an induction time and the related change in the turnover frequency.

Theoretical studies [84, 86–88] have shown that the Fe(II)–aquo complex dissociates fast after coordination of H<sub>2</sub>O<sub>2</sub> to a hydroxo group coordinated to iron and an HO· radical which attacks a solvent water molecule that was hydrogen bonded to the hydrogen peroxide. In fact, the generated hydroxyl radical has a short life-time which restricts its effective range of action to a few nanometers. When the organic substrate concentration is high there is a good chance that the hydroxyl radical may react with the organic molecule in the neighborhood of the iron complex where the hydrogen peroxide is coordinated. Therefore, the HO· radical contributes to the oxidation reactions, because the radical transfer could find a path along an H bond attached to an organic substrate molecule if the latter is close enough. Otherwise, the radical passage can go via a few solvent water molecules and end up with hydrogen abstraction from one of the water ligands of the same iron complex, resulting in the formation of a dihydroxo complex:



The iron(IV)dihydroxo complex is in equilibrium with its conjugate base:



After few picoseconds, one of the water ligands leaves the first solvation shell, but the formed complex  $[(\text{H}_2\text{O})_3\text{Fe}^{\text{IV}}\text{O}(\text{OH})]^{+}$  undergoes no more spontaneous chemical changes in the next picoseconds [88]. In other words, if the hydroxyl radical formed by the Fe(II)–aquo complex and H<sub>2</sub>O<sub>2</sub> does not encounter an organic molecule in the neighborhood, the process leads to a quenching of the hydroxyl radical. However, if the pentaqua iron(II)hydrogen peroxide complex would be in the neighborhood of a hexaaqua iron(II) complex, the HO· radical passage might be, via two or three solvent water molecules, to a water ligand of the hexaaqua iron(II), with two mono-hydroxo pentaqua iron(III) complexes as the result. Their further transformation generates new radical species. For higher iron concentrations, there is thus an additional pathway of reaction of the short-living hydroxyl radicals. The hydroxyl radical reaction with a neighboring iron complex extends its area of action. Therefore increases the probability that the hydroxyl radical reacts with an organic molecule and the efficiency of the use of H<sub>2</sub>O<sub>2</sub>. It is known, on the other hand, that optimal iron/H<sub>2</sub>O<sub>2</sub> and iron/organic ratios exist to maximize the Fenton and Fenton-like processes, in agreement with the above mechanistic interpretation.

Inside the layer of Cu-PILC or Fe-PILC catalyst, a similar mechanism exists, but further complicated from the presence of radical quenching mechanisms, due to the interaction with the solid or possible enhancement effects, related to the specific microenvironment. This short discussion evidences the high complexity of the issue of discussing homogeneous versus heterogeneous reactions in wet oxidation with hydrogen peroxide using PILC-based solid catalysts. We may note, however, that some indications on the reactivity are consistent with above indications on the reaction mechanism. For example, the observation [83] that a reduction of the TOF

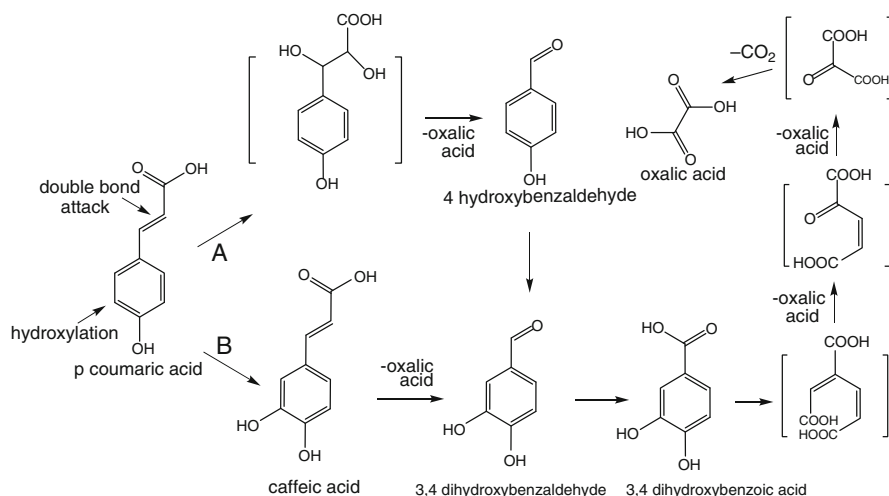


is observed together with an increase in the efficiency in  $H_2O_2$  use increases the copper concentration in Cu-PILC catalysts. In fact, increasing copper concentration decreases the  $H_2O_2/Cu^{2+}$  ratio, but increases the probability to have two neighboring copper complexes and thus the possibility of limiting the quenching of the generated hydroxyl radicals.

### 7.3.2 Mechanism of Organic Transformation

An aspect which is often not well discussed regards the mechanism of organic transformation in WHPCO using PILC-based catalysts. The mechanism is highly depending on the type of organic, but let us to exemplify the problematic using as an example the reaction mechanism in the conversion of *p*-coumaric acid [83]. This model compound exemplifies the problematic in the conversion of polyphenolic compounds in OMW and in general of aromatic substances in wastewater.

The reaction network of *p*-coumaric acid degradation is summarized in Scheme 7.2 [83]. There are two main pathways for the conversion of *p*-coumaric acid: (i) hydroxylation of the aromatic ring resulting in the formation of caffeic acid (CA) and (ii) epoxidation of the double bond of the lateral chain with the intermediate formation of the corresponding diol which is then quickly converted to 4-hydroxybenzaldehyde (4HB) with the elimination of oxalic acid. There are various possible pathways of subsequent degradation. Scheme 7.2 reports a pathway which appears to be the most probable.



**Scheme 7.2** Reaction mechanism in the conversion of *p*-coumaric acid. The compounds in the bracket were supposed as reaction intermediate, but not identified analytically. Adapted from Perathoner et al. [83]

After caffeic acid formation it is possible to have the attack on the double bond of the lateral chain to form the 3,4-dihydroxybenzaldehyde which can also be formed by hydroxylation of the aromatic ring of 4HB. Oxidation of the 3,4-dihydroxybenzaldehyde gives 3,4-dihydroxybenzoic acid and further conversion of this compound gives a sequence of intermediate products, such as triacids, which are difficult to identify analytically. Finally, the degradation of these intermediates gives oxalic acid as stable product recalcitrant to further conversion and transformation to  $\text{CO}_2$ .

According to this reaction scheme, two different oxidizing attacks are possible on *p*-coumaric acid, the epoxidation on the double bond of the lateral chain which forms 4HB as first identified product and the hydroxylation of the aromatic ring which gives CA.

There is a different trend with respect to the time on stream of the CA/4HB ratio for the homogeneous and heterogeneous cases. In the latter CA is mainly formed almost immediately, while in the homogeneous case the CA takes some time (around 15 min) to reach its maximum formation. This suggests an evolution in the nature of the active sites in the homogeneous case which agrees with the previous discussion about the mechanism responsible for an induction time in *p*-coumaric acid conversion.

The attack on the double bond of the lateral chain first followed by the hydroxylation of the aromatic ring (pathway A in Scheme 7.2) is due to the route involving the hydroperoxo complex formation, while the pathway B (first hydroxylation of the aromatic ring and then attack on the lateral chain) involves the " $\text{Cu}^+ \rightleftharpoons \text{Cu}^{2+}$ " cyclic mechanism. The first mechanism (via hydroperoxo complex) initially dominates the conversion in the homogeneous case, but then there is a progressive change to the " $\text{Cu}^+ \rightleftharpoons \text{Cu}^{2+}$ " cyclic mechanism. This explains an experimentally observed initial increase in the CA/4HB ratio in the homogeneous case after the induction time [83]. The ligand effect of the oxide in the case of the Cu-PILC, instead, inhibits the pathway via the hydroperoxo complex. Therefore, the " $\text{Cu}^+ \rightleftharpoons \text{Cu}^{2+}$ " cyclic mechanism is already the dominant route and CA/4HB ratio is already high at the beginning. The ratio then decreases due to the conversion of the caffeic acid itself.

This discussion further evidences the differences in the reaction pathways in the generation of the radical oxygen species between homogeneous and heterogeneous Fenton reaction on solid PILC-based catalysts.

### ***7.3.3 A Survey of Literature Data on the Use of PILC-Based Materials***

Detailed studies on the WHPCO reaction mechanism of PILC-based catalysts are lacking and most of the studies are limited to the analysis of the performances of PILC catalysts in the conversion of different substrates. Chirchi and Ghorbel [89] have investigated the conversion of 4-nitrophenol by  $\text{H}_2\text{O}_2$  with

iron(III)-exchanged and pillared montmorillonite as catalysts. The aspects investigated were the influence of different types of catalysts, their amounts, and the  $\text{H}_2\text{O}_2$  concentration. Ramaswamy et al. [90] have investigated phenol conversion using alumina-pillared montmorillonite (Al-PILC) on which copper–tetra decachlorophthalocyanine (Cu–Cl14Pc) complex was immobilized. Catrinescu et al. [91] have investigated the effect of different reaction parameters (pH, temperature, catalyst concentration) as well as catalyst stability in the WHPCO of phenol solutions. They used Fe-exchanged Al-pillared synthetic beidellite. Delaminated Fe-exchanged Ti-pillared interlayered montmorillonites (Fe–Ti-PILC) were instead used by Mei et al. [92] again in the WHPCO of phenol solutions. Carriazo et al. [93, 94] used instead a Colombian bentonite pillared with mixed polyhydroxocationic solutions of Al–Fe or Al–Ce–Fe again in the WHPCO of phenol solutions. They observed that the incorporation of Ce in the solids showed a favorable effect in the pillaring of the materials, allowing the increase of the basal spacing and enhancing the catalytic activity of the solids. Catalysts based on pillared clays with Al, Zr, and Al–Fe and Zr–Fe (starting from commercial bentonite) have been investigated also in WHPCO of phenol by Molina et al. [95]. The Al–Fe-pillared clay showed a higher activity than the Zr–Fe one for phenol oxidation, because the second was more active for  $\text{H}_2\text{O}_2$  decomposition. Luo et al. [96] also investigated recently clay pillared with Fe–Al for Fenton oxidation of phenol by hydrogen peroxide. As original results cited that (i) the pillaring process altered the basal space of clay, (ii) the catalytic activity is related to the accessible iron species, (iii) the Fenton reaction exhibited an induction period, and (iv) the rate of the oxidation process depends on the concentrations of phenol and  $\text{H}_2\text{O}_2$ , the amount of catalyst, pH, and temperatures. As commented above, these catalysts (Fe–Al-pillared clays) and almost all the findings were already well established in previous literature. Recently, Timofeeva et al. [97] also investigated Fe,Al-pillared clays (obtained from Mukhortala (Buryatia) montmorillonites) in phenol oxidation, although extending the investigation to also monoazo dye acid chrome dark-blue (ACDB). Most of the results were again analogous to those previously reported. The effect of  $\text{OH}/(\text{Fe} + \text{Al})$  ratio, aging time, and calcination temperature was examined. The state of iron atoms can be controlled by Al/Fe and  $\text{OH}/(\text{Fe} + \text{Al})$  ratios, aging period of Fe,Al-pillaring solution, and calcination temperature. The increase in Al/Fe ratio and calcination temperature from 400 to 500 °C decreases in the formation of oligomeric iron species. The increase in aging time decreases iron leaching and increases the reaction rate, due to the formation of isolated iron species. The same authors [98] also investigated the use of mixed Fe,Cu,Al clays. The introduction of copper ions results in an increase in the reaction rate, according to what discussed above.

This brief survey of literature results evidences that notwithstanding the continuous and also recent publications on the use of PILC catalysts in WHPCO reaction limited new information are available to produce better catalysts and/or develop on a commercial scale a process based on these catalysts. Different starting clays were used as raw materials, but without a rational choice. In addition to phenol, and the cited results on 4-nitrophenol [89] and *p*-coumaric acid [83], few other molecules were tested in WHPCO using PILC catalysts. Tabet et al.

[99] investigated Fe-pillared montmorillonite for the removal of cinnamic acid in water. The influences of the cinnamic acid, catalyst and  $\text{H}_2\text{O}_2$  concentrations, and pH on the removal rate of cinnamic acid have been studied. The results show that the efficiency of Fe-pillared montmorillonite is higher than that of the Fe ions in the homogeneous phase, and less sensitive to pH, in agreement with the results for other organic pollutants, as discussed above. Herney-Ramirez et al. [100, 101] analyzed the degradation and mineralization of Orange II solutions using catalysts based on pillared saponite impregnated with different iron salts. In the best conditions and after 4 h of oxidation, 99% of dye degradation with 91% of total organic carbon (TOC) reduction (at 70 °C), using only ca. 90 mg of clay catalyst per liter of solution was observed; 96% of dye removal with 82% of mineralization was also reached at 30 °C. The amount of iron released into the final solution was lower than 1 ppm. Copper-supported-pillared clay catalysts were investigated in the conversion of tyrosol in batch and continuous reactors [102, 103]. Stable performances were observed. Around 84 and 53% substrate and TOC conversion, respectively, were obtained for 120-h reaction. Total elimination of TOC is difficult since oxalic acid, as the main intermediate, is resistant to WHPCO. The same authors [104] also investigated the catalytic wet hydrogen peroxide oxidation of *p*-coumaric acid over Al-Fe-pillared clay. It was found that the distribution of the intermediate compounds was strongly dependent on the pH of the solution.

Few results have been reported in WHPCO using PILC catalysts for treating real wastewater streams. One of the first results has been reported by Kim et al. [105, 106] who investigated the WHPCO of real dyehouse effluents in both batch reactor and continuous flow pilot plant-scale reactor by using  $\text{Cu}/\text{Al}_2\text{O}_3$  and Al-Cu-PILC catalysts. The removal of TOC and color was strongly related to the consumption of  $\text{H}_2\text{O}_2$ . Copper components in the catalysts, especially in the Al-Cu-PILCs, showed successful activity toward complete removal of TOC and color. In addition the Al-Cu-PILC catalysts were extremely stable against copper leaching.

Copper-based and iron-based pillared clays (Cu-PILC, Fe-PILC) have been studied and compared in the WHPCO of both model phenolic compounds (*p*-coumaric and *p*-hydroxybenzoic acids) and real olive oil milling wastewater (OMW) by Caudo et al. [107]. These two catalysts show comparable performances in all these reactions, although they show some differences in the rates of the various steps of reaction. In particular, Cu-PILC shows a lower formation of oxalic acid (main reaction intermediate) with respect to Fe-PILC. Both catalysts show no leaching of the transition metal differently from other copper-based catalysts prepared by wetness impregnation on oxides (alumina, zirconia) or ion-exchange of clays (bentonite) or zeolite ZSM-5. No relationship was observed between copper reducibility in the catalyst and the performance in WHPCO, as well as between the rate of copper leaching and catalytic behavior. Cu-PILC shows a comparable activity to dissolved  $\text{Cu}^{2+}$  ions, although the turnover number is lower assuming that all copper ions in Cu-PILC are active. Cu-PILC shows a high resistance to leaching and a good catalytic performance, which was attributed to the presence of copper essentially in the

pillars of the clay. A high efficiency in  $\text{H}_2\text{O}_2$  use in the first hour of reaction with the participation of dissolved  $\text{O}_2$  in solution was also shown. For longer reaction times, however, the efficiency of  $\text{H}_2\text{O}_2$  use considerably decreases.

The behavior of Cu-PILC in the pre-treatment of OMW was compared with that of Cu-zeolites (MFI structure) by Giordano et al. [108]. Both the catalysts showed a high conversion in the oxidation of polyphenols and were able to drastically reduce the chemical oxygen demand, the biochemical oxygen demand, and the non-biodegradability of the olive oil mill wastewaters. However, the Cu-PILC shows better stability. More recently, the performances of Cu-PILC for agro-food wastewater purification with  $\text{H}_2\text{O}_2$  were discussed more in depth [109]. These catalysts were studied in the treatment of various real wastewaters from agro-food production: (i) deriving from citrus juice production, (ii) extracted concentrated polyphenolics fraction from olive oil milling (OMW), and (iii) OMW derived from three different sources. In the latter cases, tests were made both in a lab-scale reactor and in a larger volume (about 10 l) reactor. The results showed that Cu-PILC might be used to treat real wastewater from agro-food production, and not only simple model chemicals as typically made in the literature. In all cases, using a semi-batch slurry-type reactor with a continuous feed of  $\text{H}_2\text{O}_2$ , the behavior both in TOC (total organic carbon) and in polyphenols abatement may be described using pseudo-first-order reaction rates. Using real wastewater the rate constants are one to two orders of magnitude lower than using model molecules, and a decrease in the ratio between rate constant of phenols conversion and rate constant of TOC abatement is observed. However, this ratio maintains over 1 in all cases. A typical value is around 2, but the composition of wastewater and reaction conditions influence this ratio. Scaling-up to a larger volume semi-continuous slurry-type reactor causes a further lowering of one order of magnitude in the rate constants of TOC and polyphenols depletion, due to fouling of the catalyst related to the preferential coupling of the organic radicals and deposition over the catalyst with respect to their further degradation by hydroxyl radicals generated from  $\text{H}_2\text{O}_2$  activation on the copper ions of the catalyst. The use of a different reactor to overcome this problem was suggested.

The application of WHPCO for the treatment of complex effluents from electronic industry was also discussed by Perathoner and Centi in reviewing the use of iron-based or copper-based solid catalysts for the treatment of industrial waste aqueous streams [29]. To note that in this case, homogeneous Fenton catalysts were completely inactive due to the harsh reaction conditions (many complexing chemicals present in the feed), while relatively good performances were obtained using the solid catalysts.

In conclusion, this short survey on the use of PILC-based catalysts for WHPCO reaction has evidenced that these materials show interesting and stable performances. They can be used for practical applications, although data on their practical use are limited. Most of the literature data focused on the use of only model compounds. In addition, often data for a more rational design are limited and published results were mainly related to the analysis of the effect of the reaction conditions and/or catalyst composition, sometimes also rediscovering older results. This section has evidenced that it is necessary for a much more in depth understanding of

the reaction mechanism and in particular the catalytic chemistry inside the microporous clay layer. The generation of short-living and highly reactive radical species (hydroxyl radicals, for example) changes significantly the picture with respect to conventional liquid–solid catalytic chemistry. It is thus necessary to put attention on these aspects, as well as on other critical aspects, such as the hydrophobic characteristics of the inner layered structure and the formation of gas caps inside the layers.

## 7.4 Photocatalytic Behavior of Ti-PILC and Fe-PILC

### 7.4.1 Ti-PILC

The first attempt to prepare photocatalysts based on titania-pillared clays (Ti-PILCs) has been reported by Ding et al. [42]. They used a sol–gel method and different drying methods (air drying, air drying after ethanol extraction, and supercritical drying), because they have significant effect on the photocatalytic efficiency for the oxidation of phenol in water. Ti-PILC obtained by supercritical drying has the highest external and micropore surface area, largest amount and smallest crystallite size of anatase, and exhibited the highest photocatalytic activity. It should be noted, however, that these materials are not truly titania-pillared clays, but should be better described as layered materials with deposited TiO<sub>2</sub> nanocrystals. In parallel to the work of Ding et al. [42], Ooka et al. [110] reported a study on the synthesis of pillared montmorillonite with crystallized TiO<sub>2</sub>. The TiO<sub>2</sub> pillars in pillared montmorillonite were crystallized to anatase by hydrothermal treatment, while retaining the porosity of the pillared clay. The size of the crystallized TiO<sub>2</sub> pillars and the average pore diameter could be controlled in the range ca. 0.4–0.9 nm by changing the treatment conditions. These materials were studied in the photocatalytic degradation of trichloroethylene in water. The hydrothermal crystallization enhances the catalytic activity both per unit weight of TiO<sub>2</sub> and per exposed unit surface area of TiO<sub>2</sub>. The catalytic activity of the TiO<sub>2</sub> pillars was also enhanced by quantum-size effects: as the TiO<sub>2</sub> pillar size decreased, the pillared montmorillonites exhibited higher catalytic activity and showed larger blueshifts in their UV absorption spectra. The same group [111] also reported that titania-pillared clay could adsorb dibutyl phthalate (DBP), one of the endocrine disruptors, and degrade it photocatalytically.

These initial studies started a relevant activity for the preparation of Ti-PILC-based photocatalysts. The main motivations are related to the possibility of having highly dispersed nanosized TiO<sub>2</sub> pillars which acting as photo-active centers in a microenvironment (the inner layer of the clay) could control the access of pollutants and prevent deactivation by fouling. Worth to note is the possibility to control the hydrophobic character of the PILC and use this property to control the selective behavior in the photocatalysis. For example, Shimuzu et al. [112] investigated the selective photo-oxidation of benzene and cyclohexane using TiO<sub>2</sub>-pillared clays (mica, montmorillonite, and saponite). In an aqueous environment, TiO<sub>2</sub>-pillared

clays showed higher selectivity to oxygenates than  $\text{TiO}_2$  (Degussa P25). The product distribution among oxygenates also depends on the type of the clay host. For the cyclohexane photo-oxidation,  $\text{TiO}_2$ -pillared clay showed much higher selectivity than  $\text{TiO}_2$ , because of the hydrophobic nature of pillared clay.

Awate and Suzuki [113] investigated the use of titania-pillared montmorillonite clay prepared by two different routes (ion-exchange method and hydrothermal treatment after ion-exchange) in the photocatalytic oxidation of two dyes (Methylene Blue and Victoria Pure Blue). The Ti-PILC prepared by post-hydrothermal route has shown enhanced adsorption capacity and photocatalytic oxidation. Different other groups were active in the photocatalytic degradation of dyes and other pollutants using  $\text{TiO}_2$ -pillared clays: (i) 2,4-dichlorophenol and Orange II [114], (ii) benzene and cyclohexane [115], phthalate esters (di-*n*-butyl phthalate and dimethyl phthalate) [44], 4-chlorophenol [115], Methyl Orange [116], decabromodiphenyl ether (BDE 209) [117], dimethyl phthalate ester, as model of endocrine disruptor [118], the dye acidic fuchsine [119], phenol [120, 121], 4BS dye [122], textile azo dye (Solophenyl Red 3BL) [123, 124], and azoic dyes (Congo Red) [125, 126]. A larger variety of substrate was thus investigated using Ti-PILC photocatalysts with respect to the previously discussed case of WHPCO, although the use of many different substrates is typical of photocatalytic studies. Most of the studies were also in this case limited to the analysis of the effect of the reaction conditions and catalyst characteristics. Nevertheless, some clear direction could be evidenced.

Several authors put attention on the issue of hydrophobic characteristics of PILC to control the reactivity. Ooka et al. [44] investigated four kinds of  $\text{TiO}_2$ -pillared clays prepared from different raw clays (montmorillonite, saponite, fluorine hectorite, and fluorine mica) and put in relation their surface hydrophobicities with the performances in adsorption-photocatalytic degradation of phthalate esters. The surface hydrophobicity of  $\text{TiO}_2$ -pillared clays largely varies with the host clay: it increases in the order saponite < fluorine hectorite < montmorillonite < fluorine mica. The order of performance in adsorption and successive photocatalytic degradation of phthalate ester was consistent with that of surface hydrophobicity. Using the host clay that enhances surface hydrophobicity of the  $\text{TiO}_2$ -pillared clay, such as fluorine mica, it is possible to obtain highly active photocatalysts for photodegradation of organic compounds in water. The performances could be increased by improving  $\text{TiO}_2$  nanoparticle crystallinity using a treatment with aqueous hydrogen peroxide at room temperature [127]. Inorganic/organic-pillared clays (Ti/cetyltrimethylammonium bromide-pillared clays) could be prepared for some scope of controlling hydrophobic character and enhance photocatalytic activity in the removal of non-polar organics in water [128].

Other authors [129] have investigated the use of cetyltrimethylammonium bromide (CTAB) to modify the characteristics of  $\text{TiO}_2$ -pillared montmorillonite photocatalysts. The “growth” of the hydrated Ti-polycations within clay interlayers could be regulated and controlled by the surfactant CTAB. An et al. [117] also prepared  $\text{TiO}_2$ -immobilized hydrophobic montmorillonite photocatalysts via ion-exchange reaction between sodium montmorillonite with cation surfactant,

cetyltrimethylammonium bromide (CTAB). These materials were designed for the oxidation of persistent organic pollutants in water, by combining the pre-adsorption and concentrated effects for aqueous microorganic pollutants with the photocatalytic destruction of organic pollutants. Ding et al. [118] also prepared  $\text{TiO}_2$ -pillared montmorillonites by introducing  $\text{Ti}^{4+}$  into a layer of montmorillonite modified with or without cetyltrimethylammonium bromide. However, in studying the photocatalytic degradation of dimethyl phthalate ester they observed that the hydrophobic photocatalyst was slightly less active than the hydrophilic one. The same authors [130] analyzed the role of acid (acetic acid and hydrochloric acid) in catalyzing hydrolysis of titanium hydrate sols during the preparation of hydrophobic montmorillonite clay treated with organic cationic surfactant (hexadecyltrimethylammonium bromide). Hydrophobic  $\text{TiO}_2$ -pillared clay prepared with acetic acid as the acid hydrolysis catalysts possesses higher photocatalytic activity than that with hydrochloric acid. Organoclays having titania nanocrystals in interlayer hydrophobic field [64], prepared by intercalating the cetyltrimethylammonium cations to the montmorillonite layer and introducing Ti by cation-exchange, were also shown to exhibit higher photocatalytic activity for BPA (bisphenol A) degradation, due to their hydrophobic character.

Therefore, many studies focused on the role of hydrophobic character of inner microenvironment in PILC materials to have a preferential concentration of non-polar pollutants close to the active photocatalyst, usually  $\text{TiO}_2$  nanoparticles either present as pillars or as simple deposits inside the layers. The latter situation, however, gives rise to less stable photocatalysts, even if this aspect was typically not well investigated.

Some authors claimed a novel architecture for the Ti-PILC photocatalysts, although the novelty is questionable. Yang et al. [120], for example, discussed a new photocatalyst design to increase the content of anatase nanocrystals and improve the accessibility of these crystals to reactants (UV photons, organic contaminant molecules, and oxygen molecules), in order to enhance the photocatalytic performance. However, the proposed new synthesis strategy involves reaction of clay suspensions with  $\text{TiOSO}_4$ , which leads to formation of anatase nanocrystals attaching to leached clay layers through Ti–O–Si bonds. They also claimed to have discovered that the crystal size, the pore size, and the specific surface area of the catalysts can be tailored by manipulating the acidity, the ratio of Ti/clay, and the hydrothermal temperature of the synthesis systems. Although there are some differences with respect to the conventional approach of pillared intercalated layered clays, the resulting materials are not largely different from those earlier reported and discussed above. The photocatalytic performances in the conversion of phenol also do not appear rather spectacular, with about 50% conversion in 4–5 h of a highly diluted (25 ppm) phenol solution.

Xuzhuang et al. [121] also claimed for a new composite structure with superior photocatalytic activity for phenol decomposition, by reaction between  $\text{TiOSO}_4$  and a synthetic layered clay laponite. The authors claimed a superior photocatalytic activity due to the unique structure of the composite, in which anatase nanocrystals were attached on leached laponite fragments. These photocatalysts take about



2 h to convert 25 ppm phenol using UV light source. Although this result is better than that of the “traditional” pillared clay used as reference, it is still a rather poor result with respect to “conventional” photocatalysts in the same reaction, taking also into account that only phenol conversion and not TOC removal was reported.

The “superior” photocatalytic activity derives from a hydrothermal treatment which partially destroys the clay (making thus more accessible) and especially make more crystalline the anatase  $\text{TiO}_2$  nanocrystals. This aspect is that probably determining the higher performances, together with the fact that the  $\text{TiO}_2$  content in the most active samples is very high (about 60 wt%). The destruction of the characteristic pillaring structure eliminates the possibility of controlling the microenvironment and thus to have a selective photocatalysis, as discussed above. On the other hand, in terms of absolute photocatalytic performances these “novel” materials appear rather poor with respect to well-optimized  $\text{TiO}_2$  photocatalysts. It is thus difficult to support the authors claim that the knowledge acquired in their study is useful for designing photocatalysts with high efficiency.

We have discussed more in depth this specific example, although similar remarks may be made to also other published papers, to evidence that also for the use of Ti-PILC catalysts most of the studies have limited practical objectives. Being well established the fields of photocatalysis using semiconductor materials, the questions to address while studying Ti-PILC photocatalysts are the following:

- What kind of advantages (in terms of performances per unit weight or catalyst cost, considering the low cost of  $\text{TiO}_2$ ) is offered from using Ti-PILC materials?
- There are specific characteristics which can make unique these materials.

In terms of absolute photocatalytic properties, Ti-PILC does not compete with well-optimized  $\text{TiO}_2$  (note that the often used Degussa P-25 is not always the best, depending on the substrate to convert), in terms of activity per unit weight and unit cost. The reasons are related to lower amount of  $\text{TiO}_2$  (with respect to pure  $\text{TiO}_2$ ), the difficulty in obtaining well-crystallized nanocrystals, and the quantum-size effect, when small  $\text{TiO}_2$  nanocrystals are present, e.g., a blueshift in the absorption edge. This is a shift in the opposite direction to what necessary to have activity with visible light. The main problem in using photocatalytic methodologies for the elimination of pollutants is the need to operate with highly diluted solutions (few ppm), which greatly limit their possible application in practical cases. For this reason, the use of solar light is essentially required in photocatalytic waste treatment, as the use of UV lamps is not being feasible. Therefore, the issue is to analyze how to use the PILC structure to promote visible light activity. The other possible approach is to use the hydrophobic microenvironment of PILC to absorb the non-polar pollutants and then make periodic photocatalytic regeneration, e.g., to not use in a continuous illumination mode. Some authors have used the latter route, as discussed above. This would imply, however, to preserve the layered structure and optimize the inner hydrophobic properties.

Few authors have instead investigated how to use the PILC structure to promote visible light activity. Zhang et al. [122] used nitrogen and sulfur co-doped TiO<sub>2</sub>-pillared montmorillonite for the degradation of 4BS dye under visible light irradiation ( $\lambda > 400$  nm). The absorption edge of the doped samples shows a red-shift as compared to that of pure TiO<sub>2</sub>. Their photocatalytic activity is comparable to that of Degussa P25 under visible light irradiation, although it is forgotten that dyes adsorbing in the visible region are self-sensitizer. The use of dyes adsorbing in the visible region is not a suitable test to analyze the photocatalytic properties of materials in the visible region. In addition, it is well known that the issue is the complete conversion of the dye and not its partial conversion, e.g., to evaluate TOC and not dye conversion, due to this self-sensitizer effect. Yang et al. [119] also investigated the use of TiO<sub>2</sub>-pillared montmorillonite composite photocatalyst for the degradation reaction of acidic fuchsine by sunlight. Similar remarks to those evidenced above could also be made in this case.

In conclusion, several papers have been published on the use of Ti-PILC as advanced photocatalysts, and they were utilized in the conversion of many pollutants, although essentially in academic studies. Their practical applicability is still questionable and suitable data do not exist to forecast their use. On the other hand, it should be remarked that not enough effort has been made in literature to evaluate the specific features of these catalysts in relation to practical use and to optimize their design in relation to these characteristics.

#### ***7.4.2 Fe-PILC for Photo-Fenton***

From the practical point of view, more interesting prospects exist on the use of Fe-PILC for the photo-Fenton reaction, e.g., the combination of use of H<sub>2</sub>O<sub>2</sub> and light. With respect to photocatalytic oxidation, it is necessary to use a more expensive reactant (H<sub>2</sub>O<sub>2</sub>), but the higher reaction rates and the possibility to address wastewater containing higher concentrations of pollutants (the typical case) make this technology preferable. Many reviews have discussed the advantages and limits of this technology and their applicability in the treatment of hard degradable wastewater from dye, phenols, explosive, pesticide, paper-making, and some other industries [34, 41, 131–137].

Sum et al. [138] were the first in reporting the behavior of pillared laponite clay-based Fe nanocomposites in the photo-Fenton (H<sub>2</sub>O<sub>2</sub> + UV radiation) mineralization of azo-dye Acid Black 1 (AB1); 100% mineralization could be achieved, while only trace amounts of leached ferric ions were detected. Liu et al. [139] applied Fe-pillared bentonite in the photo-Fenton degradation of an organic azo-dye (Orange II). They also evidenced that the rate of the heterogeneous photo-Fenton process is much faster than that of homogeneous photo-Fenton process. The catalyst can also be easily recovered, regenerated, and re-used. Bobu et al. [140, 141] used iron-pillared laponite for the photodegradation of two important phenyl urea herbicides: Monuron and Isoproturon. However, the mineralization degree of both

herbicides was only around 10–20%. The same authors applied this catalyst in the photo-assisted Fenton mineralization of ciprofloxacin (CFX), a broad-spectrum antibiotic used in human and veterinary medicine. The effects of reaction parameters such as  $\text{H}_2\text{O}_2$  concentration, catalyst loading, and initial pH of the solution on the mineralization of CFX were investigated. It was found that at the optimal reaction conditions (60 mM  $\text{H}_2\text{O}_2$ ,  $1.0 \text{ g l}^{-1}$  catalyst, initial solution pH 3.0) complete CFX degradation and over 57% total organic carbon (TOC) removal of CFX can be achieved after 30 min of reaction. Also these authors observed very limited leaching of iron and stable performances.

De León et al. [142] investigated the photo-Fenton conversion of Methylene Blue using Fe-PILC catalysts with two different-sized particle fractions (<250  $\mu\text{m}$  and within the range of 250–450  $\mu\text{m}$ , respectively). Both catalysts showed activity in the discoloration of aqueous dye solution, but the differences in catalyst performance were correlated with textural parameters.

All these tests were made using  $\text{H}_2\text{O}_2$  and UV light, but recently the possibility of using visible light was reported. Chen et al. [143] reported the decolorization and mineralization of reactive brilliant orange X-GN under visible light irradiation ( $\lambda \geq 420 \text{ nm}$ ) by using iron-pillared montmorillonite(Fe-Mt/ $\text{H}_2\text{O}_2$ ) as the heterogeneous photo-Fenton reagent. The characterization of these materials suggested that small-sized hydrolyzed iron successfully intercalates into the interlayer spaces of the clay via pillaring. The catalytic results showed that at a reaction temperature of 30 °C, pH 3.0, 4.9 mmol/l  $\text{H}_2\text{O}_2$ , and 0.6 g/l catalyst dosage, 98.6% discoloration and 52.9% TOC removal of X-GN were achieved under visible irradiation after 140 min of treatment. Furthermore, the maximum concentration of dissolved iron ions was 1.26% of the total iron content in the Fe-Mt catalyst after photocatalysis.

Therefore, although results on Fe-PILC catalysts for photo-Fenton conversion are still limited, the performances and preliminary stability indications are promising. However, it is necessary to pass from batch to continuous reactor tests, evaluate the performances using real waste solutions, and develop/test the performances in the form of thin supported films, because from a practical point of view the use of slurry-type photoreactors is not possible.

## 7.5 Conclusions

The use of solid catalysts for wastewater treatment, particularly by AOP method, is a fast growing area, from both the scientific and applicative perspectives. Pillared clays, particularly containing Fe, Cu, and Ti as active elements, show some interesting perspectives, although most of the reported publications still give a too limited attention on the critical aspects for application. Also from the scientific perspective, often results are essentially phenomenological, e.g., the effect of the reaction conditions and catalyst composition/characteristics, more than focused at giving a more scientific approach toward the understanding of the critical issues governing the reactivity, kinetics, and reaction mechanism. Due to the formation of short-living

and highly reactive oxidizing species, such as the hydroxyl radical, the catalytic chemistry is quite different from that present in “conventional” liquid–solid catalytic reactions. This aspect, and the relevance for the design of improved catalysts, has received limited attention in literature.

There are limited, but relevant differences between the use of these heterogeneous catalysts and homogeneous catalysts, as discussed more specifically for wet oxidation with hydrogen peroxide. These differences and the implications in terms of reaction mechanism should be considered for a better catalyst design.

From the practical perspective, the use of PILC-based catalysts is promising using  $H_2O_2$  as the reactant (WHPCO or photo-Fenton) on iron-pillared or copper-pillared clays. These materials combine good activity with stable performances, although data on long-term stability in continuous flow reactors are quite limited. The problem of controlling the hydrophobic microenvironment within the layers of the pillared clays is an important issue to improve the performances, but was mainly investigated for the Ti-PILC materials for the photocatalytic oxidation of pollutants. The applicability of the latter reaction is questionable, and in general the limited attention given in literature to consider the key questions for their use and design has to be remarked. The use of PILC catalysts in wet oxidation with air also shows limited perspectives from the application point of view.

## References

1. Theron J, Walker JA, Cloete TE (2008) Nanotechnology and water treatment: applications and emerging opportunities. *Crit Rev Microbiol* 34:43–69
2. Busca G, Berardinelli S, Resini C, Arrighi L (2008) Technologies for the removal of phenol from fluid streams: a short review of recent developments. *J Hazard Mater* 160:265–288
3. Liotta LF, Gruttadauria M, Di Carlo G, Perrini G, Librando V (2009) Heterogeneous catalytic degradation of phenolic substrates: catalysts activity. *J Hazard Mater* 162:588–606
4. Kwon S, Fan M, Cooper AT, Yang H (2008) Photocatalytic applications of micro- and nano- $TiO_2$  in environmental engineering. *Crit Rev Environ Sci Tech* 38:197–226
5. Bhargava SK, Tardio J, Prasad J, Föger K, Akolekar DB, Grocott SC (2006) Wet oxidation and catalytic wet oxidation. *Ind Eng Chem Res* 45:1221–1258
6. Centi G, Perathoner S (2005) Use of solid catalysts in promoting water treatment and remediation technologies. In: Spivey JJ (ed) *Catalysis*, vol 18. Royal Society of Chemistry Publishing, Cambridge, UK, pp 46–71
7. Gogate PR, Pandit AB (2004) A review of imperative technologies for wastewater treatment II: hybrid methods. *Adv Environ Res* 8:553–597
8. Oliviero L, Barbier J Jr, Duprez D (2003) Wet air oxidation of nitrogen-containing organic compounds and ammonia in aqueous media. *Appl Catal B: Environ* 40:163–184
9. Imamura S (1999) Catalytic and noncatalytic wet oxidation. *Ind Eng Chem Res* 38:1743–1753
10. Liu Z-h, Kanjo Y, Mizutani S (2009) Removal mechanisms for endocrine disrupting compounds (EDCs) in wastewater treatment – physical means, biodegradation, and chemical advanced oxidation: a review. *Sci Total Environ* 407:731–748
11. Esplugas S, Bila DM, Krause LGT, Dezotti M (2007) Ozonation and advanced oxidation technologies to remove endocrine disrupting chemicals (EDCs) and pharmaceuticals and personal care products (PPCPs) in water effluents. *J Hazard Mater* 149:631–642

12. Rios GM, Belleville MP, Paolucci-Jeanjean D, Sanchez J (2009) Membrane technologies at the service of sustainable development through process intensification. In: Centi G, Trifiró F, Perathoner S, Cavani F (eds) Sustainable industrial processes, **Chapter 4**. Wiley, Weinheim, Germany, pp 257–278
13. Centi G, van Santen RA (2007) Catalysis for renewables. Wiley, Weinheim, Germany
14. Centi G, Perathoner S (2003) Novel catalyst design for multiphase reactions. *Catal Today* 79–80:3–13
15. Centi G, Perathoner S (1999) Recycle rinse water: problems and opportunities. *Catal Today* 53:11–21
16. Centi G, Gotti M, Perathoner S, Pinna F (2000) Rinse water purification using solid regenerable catalytic adsorbents. *Catal Today* 55:51–60
17. Marco A, Esplugas S, Saum G (1997) How and why combine chemical and biological processes for wastewater treatment. *Water Sci Technol* 35:321–327
18. Centi G, Perathoner S (2008) Catalysis by layered materials: a review. *Micropor Mesopor Mater* 107:3–15
19. Gil A, Korili SA, Vicente MA (2008) Recent advances in the control and characterization of the porous structure of pillared clay catalysts. *Catal Rev Sci Eng* 50(2): 153–221
20. Ding Z, Klopogge JT, Frost RL, Lu GQ, Zhu HY (2001) Porous clays and pillared clays-based catalysts. Part 2: a review of the catalytic and molecular sieve applications. *J Porous Mater* 8:273–293
21. Cheng S (1999) From layer compounds to catalytic materials. *Catal Today* 49:303–312
22. Pinnavaia TJ (1983) Intercalated clay catalysts. *Science* 220:365–371
23. Figueras F (1988) Pillared clays as catalysts. *Catal Rev Sci Eng* 30:457–499
24. Suty H, De Traversay C, Cost M (2004) Applications of advanced oxidation processes: present and future. *Water Sci Technol* 49:227–233
25. Vandevivere PC, Bianchi R, Verstraete W (1998) Treatment and reuse of wastewater from the textile wet-processing industry: review of emerging technologies. *J Chem Tech Biotechnol* 72:289–302
26. Neyens E, Baeyens J, Weemaes M, De Heyder B (2003) Pilot-scale peroxidation (H<sub>2</sub>O<sub>2</sub>) of sewage sludge. *J Hazard Mater* 98:91–106
27. Centi G, Perathoner S, Romeo G (2001) Fe/MFI as a new heterogeneous Fenton-type catalyst in the treatment of wastewater from agroindustrial processes. *Stud Surf Sci Catal* 135:5156–5163
28. Centi G, Perathoner S, Torre T, Verduna MG (2000) Catalytic wet oxidation with H<sub>2</sub>O<sub>2</sub> of carboxylic acids on homogeneous and heterogeneous Fenton-type catalysts. *Catal Today* 55:61–69
29. Perathoner S, Centi G (2005) Wet hydrogen peroxide catalytic oxidation (WHPCO) of organic waste in agro-food and industrial streams. *Top Catal* 33:207–224
30. Chakinala AG, Gogate PR, Burgess AE, Bremner DH (2009) Industrial wastewater treatment using hydrodynamic cavitation and heterogeneous advanced Fenton processing. *Chem Eng J* 152:498–502
31. Li D, Qu J (2009) The progress of catalytic technologies in water purification: a review. *J Environ Sci* 21:713–719
32. Guélou E, Barrault J, Fournier J, Tatibouët J-M (2003) Active iron species in the catalytic wet peroxide oxidation of phenol over pillared clays containing iron. *Appl Catal B: Environ* 44:1–8
33. Carriazo JG, Guelou E, Barrault J, Tatibouët J-M, Moreno S (2003) Catalytic wet peroxide oxidation of phenol over Al–Cu or Al–Fe modified clays. *Appl Clay Sci* 22:303–308
34. Sirtori C, Zapata A, Oller I, Gernjak W, Agüera A, Malato S (2009) Solar photo-Fenton as finishing step for biological treatment of a pharmaceutical wastewater. *Environ Sci Technol* 43:1185–1191

35. Andreozzi R, Canterino M, Di Somma I, Lo Giudice R, Marotta R, Pinto G, Pollio A (2008) Effect of combined physico-chemical processes on the phytotoxicity of olive mill wastewaters. *Water Res* 42:1684–1692
36. Kanmani S, Raja A (2008) Pilot plant treatment of distillery wastewater by solar photo-Fenton process. *Indian J Environ Prot* 28:218–226
37. Pérez M, Torrades F, Domènech X, Peral J (2002) Fenton and photo-Fenton oxidation of textile effluents. *Water Res* 36:2703–2710
38. Bauer R, Fallmann H (1997) The photo-Fenton oxidation – a cheap and efficient wastewater treatment method. *Res Chem Intermediates* 23:341–354
39. Kiwi J, Pulgarin C, Peringer P (1994) Effect of Fenton and photo-Fenton reactions on the degradation and biodegradability of 2 and 4-nitrophenols in water treatment. *Appl Catal B Environ* 3:335–350
40. Jain DM (2005) Photo Fenton degradation for environmental application. *J Ind Pollut Control* 21:181–194
41. Malato S, Fernández-Ibáñez P, Maldonado MI, Blanco J, Gernjak W (2009) Decontamination and disinfection of water by solar photocatalysis: recent overview trends. *Catal Today* 147:1–59
42. Ding Z, Zhu HY, Lu GQ, Greenfield PF (1999) Photocatalytic properties of titania pillared clays by different drying methods. *J Colloid Interface Sci* 209:193–199
43. Li J, Chen C, Zhao J, Zhu H, Ding Z (2002) Photodegradation of dye pollutants on TiO<sub>2</sub> pillared bentonites under UV light irradiation. *Sci China B* 45:445–448
44. Ooka C, Yoshida H, Suzuki K, Hattori T (2004) Highly hydrophobic TiO<sub>2</sub> pillared clay for photocatalytic degradation of organic compounds in water. *Micropor Mesopor Mater* 67:143–150
45. Romero A, Dorado F, Asencio I, García PB, Valverde JL (2006) Ti-pillared clays: synthesis and general characterization. *Clays Clay Miner* 54:737–747
46. Damardji B, Khalaf H, Duclaux L, David B (2009) Preparation of TiO<sub>2</sub>-pillared montmorillonite as photocatalyst. Part II. Photocatalytic degradation of a textile azo dye. *Appl Clay Sci* 45:98–104
47. Danis TG, Albanis TA, Petrakis DE, Pomonis PJ (1998) Removal of chlorinated phenols from aqueous solutions by adsorption on alumina pillared clays and mesoporous alumina aluminum phosphates. *Water Res* 32:295–302
48. Wibulswas R, White D, Rautiu R (1998) Removal of humic substances from water by alumina-based pillared clays. *Environ Technol* 19:627–632
49. Tahani A, Karroua M, El Farissi M, Levitz P, Van Damme H, Bergaya F, Margulies L (1999) Adsorption of phenol and its chlorine derivatives on PILCS and organo-PILCS. *J Chimie Physique et de Physico Chimie Biol* 96:464–469
50. Konstantinou IK, Albanis TA, Petrakis DE, Pomonis PJ (2000) Removal of herbicides from aqueous solutions by adsorption on Al-pillared clays, Fe–Al pillared clays and mesoporous alumina aluminum phosphates. *Water Res* 34:3123–3136
51. Bouras O, Houari M, Khalaf H (2001) Using of surfactant modified Fe-pillared bentonite for the removal of pentachlorophenol from aqueous stream. *Environ Technol* 22(1): 69–74
52. Zeng XQ, Liu WP (2005) Adsorption of direct green B on mixed hydroxyl-Fe–Al pillared montmorillonite with large basal spacing. *J Environ Sci* 17:159–162
53. Ortiz-Polo A, Richards-Urbe RM, Otazo-Sánchez EM, Prieto-García F, Hernández-Ávila J, Acevedo-Sandoval O, Gordillo-Martínez A (2008) New organo-inorganic materials for water contaminants remediation. In: Barbé C, Laine RM, Sanchez C, Schubert U (eds) *Organic/Inorganic hybrid materials-2007*, Mater Res Soc Symp Proc, Volume 1007. Warrendale, PA, pp.1007-S04-38.
54. Guerra DL, Airoidi C, Lemos VP, Angélica RS (2008) Adsorptive, thermodynamic and kinetic performances of Al/Ti and Al/Zr-pillared clays from the Brazilian Amazon region for zinc cation removal. *J Hazard Mater* 155:230–242

55. Bhattacharyya KG, Gupta SS (2008) Adsorption of a few heavy metals on natural and modified kaolinite and montmorillonite: a review. *Adv Colloid Interface Sci* 140:114–131
56. Karamanis D, Assimakopoulos PA (2007) Efficiency of aluminum-pillared montmorillonite on the removal of cesium and copper from aqueous solutions. *Water Res* 41:1897–1906
57. Zhu JX, He HP, Guo JG, Yang D (2002) Recent advances in research on organic pillared montmorillonite. *Bull Mineral Petrol Geochem* 21:234–237
58. Srinivasan KR, Fogler HS (1990) Use of inorgano-organo-clays in the removal of priority pollutants from industrial wastewaters: structural aspect. *Clays Clay Miner* 38:277–286
59. Georgakilas V, Gournis D, Petridis D (2001) Organoclay derivatives in the synthesis of macrocycles. *Ang Chemie Int Ed* 40:4286–4288
60. Nakatsuji M, Ishii R, Wang Z-M, Ooi K (2004) Preparation of porous clay minerals with organic–inorganic hybrid pillars using solvent-extraction route. *J Colloid Interface Sci* 272:158–166
61. Bergaya F, Mandalia T, Amigouët P (2005) A brief survey on CLAYPEN and nanocomposites based on unmodified PE and organo-pillared clays. *Colloid Polym Sci* 283:773–782
62. Zhou Q, He HP, Zhu JX, Shen W, Frost RL, Yuan P (2008) Mechanism of *p*-nitrophenol adsorption from aqueous solution by HDTMA<sup>+</sup>-pillared montmorillonite – implications for water purification. *J Hazard Mater* 154:1025–1032
63. López-Cortés C, Osorio-Revilla G, Gallardo-Velázquez T, Arellano-Cárdenas S (2008) Adsorption of vapor-phase VOCs (benzene and toluene) on modified clays and its relation with surface properties. *Can J Chem* 86:305–311
64. Sasai R, Hotta Y, Itoh H (2008) Preparation of organoclay having titania nano-crystals in interlayer hydrophobic field and its characterization. *J Ceram Soc Jpn (Nippon Seramikkusu Kyokai Gakujutsu Ronbunshi)* 116:205–211
65. Matatov-Meytal YI, Sheintuch M (1998) Catalytic abatement of water pollutants. *Ind Eng Chem Res* 37:309–326
66. Guo J, Al-Dahhan M (2003) Kinetics of wet air oxidation of phenol over a novel catalyst. *Ind Eng Chem Res* 22:5473–5481
67. Guo J, Al-Dahhan M (2003) Catalytic wet oxidation of phenol by hydrogen peroxide over pillared clay catalyst. *Ind Eng Chem Res* 42:2450–2460
68. Barrault J, Tatibouët J-M, Papayannakos N (2000) Catalytic wet peroxide oxidation of phenol over pillared clays containing iron or copper species. *Comptes Rendus - Series IIC - Chem* 3:777–783
69. Barrault J, Abdellaoui M, Bouchoule C, Majesté A, Tatibouët J-M, Louloudi A, Papayannakos N, Gangas NH (2000) Catalytic wet peroxide oxidation over mixed (Al–Fe) pillared clays. *Appl Catal B: Environ* 27:L225–L230
70. Guélou E, Barrault J, Fournier J, Tatibouët J-M (2003) Active iron species in the catalytic wet peroxide oxidation of phenol over pillared clays containing iron. *Appl Catal B: Environ* 44:1–8
71. De Stefanis A, Perez G, Tomlinson AAG, Bergström C (2001) Alkylation process. WO 2001–055061 assigned to Optatech Corp, Finland
72. Raimondo M, De Stefanis A, Perez G, Tomlinson AAG (1998) PLS vs. zeolites as sorbents and catalysts. 5. Evidence for Brønsted/Lewis acid crossover and high acidity in conversions of C1-3 alcohols in some alumina-pillared smectite clays. *Appl Catal A: Gen* 171:85–97
73. Tomlinson AAG (1998) Characterization of pillared layered structures. *J Porous Mater* 5:259–274
74. Tukac V, Hanika J (1998) Catalytic wet oxidation of substituted phenols in the trickle bed reactor. *J Chem Tech Biotechnol* 71:262–266
75. Ksontinia N, Najjar W, Ghorbel A (2008) Al–Fe pillared clays: synthesis, characterization and catalytic wet air oxidation activity. *J Phys Chem Solids* 69:1112–1115
76. Najjar W, Azabou S, Sayadi S, Ghorbel A (2007) Catalytic wet peroxide photo-oxidation of phenolic olive oil mill wastewater contaminants. Part I. Reactivity of tyrosol over (Al–Fe) PILC. *Appl Catal B: Environ* 74:11–18

77. Guo J, Al-Dahhan M (2005) Catalytic wet air oxidation of phenol in concurrent downflow and upflow packed-bed reactors over pillared clay catalyst. *Chem Eng Sci* 60:735–746
78. Guo J, Al-Dahhan M (2006) Activity and stability of iron-containing pillared clay catalysts for wet air oxidation of phenol. *Appl Catal A: Gen* 299:175–184
79. Barrault J, Bouchoule C, Echachoui K, Frini-Srasra N, Trabelsi M, Bergaya F (1998) Catalytic wet peroxide oxidation (CWPO) of phenol over mixed (AlCu)-pillared clays. *Appl Catal B: Environ* 15:269–274
80. Abdellaoui M, Barrault J, Bouchoule C, Srasra NF, Bergaya F (1999) Catalytic wet peroxide oxidation of phenol over mixed [Al–Cu]-pillared clays. *J Chimie Phys et de Physico Chimie Biol* 96:419–429
81. Barrault J, Bouchoule C, Tatibouët JM, Abdellaoui M, Majesté A, Louloudi I, Papayannakos N, Gangas NH (2000) Catalytic wet peroxide oxidation over mixed (Al–Fe) pillared clays. *Stud Surf Sci Catal* 130A:749–754
82. Tatibouët JM, Guélou E, Fournier J (2005) Catalytic oxidation of phenol by hydrogen peroxide over a pillared clay containing iron. Active species and pH effect. *Top Catal* 33:1–4
83. Caudo S, Centi G, Genovese C, Perathoner S (2006) Homogeneous versus heterogeneous catalytic reactions to eliminate organics from waste water using H<sub>2</sub>O<sub>2</sub>. *Top Catal* 40:207–219
84. Ensing B, Buda F, Baerends EJ (2003) Fenton-like chemistry in water: oxidation catalysis by Fe(III) and H<sub>2</sub>O<sub>2</sub>. *J Phys Chem A* 107:5722–5731
85. Kuznetsova EV, Savinov EN, Vostrikova LA, Parmon VN (2004) Heterogeneous catalysis in the Fenton-type system FeZSM-5/H<sub>2</sub>O<sub>2</sub>. *Appl Catal B: Environ* 51:165–170
86. Ensing B, Buda F, Blöchl PE, Baerends EJ (2002) A Car–Parrinello study of the formation of oxidizing intermediates from Fenton’s reagent in aqueous solution. *Phys Chem Chem Phys* 4:3619–3627
87. Ensing B, Buda F, Blöchl P, Baerends EJ (2001) Chemical involvement of solvent water molecules in elementary steps of the Fenton oxidation reaction. *Ang Chemie* 113:2977–2979
88. Ensing B (2003) Chemistry in water. First principles computer simulations. PhD Thesis, Vrije Universiteit Amsterdam, The Netherlands
89. Chirchi L, Ghorbel A (2002) Use of various Fe-modified montmorillonite samples for 4-nitrophenol degradation by H<sub>2</sub>O<sub>2</sub>. *Appl Clay Sci* 21:271–276
90. Ramaswamy V, Krishnan MS, Ramaswamy AV (2002) Immobilization and characterization of copper chlorophthalocyanine on alumina-pillared montmorillonite. *J Mol Catal A: Chem* 181:81–89
91. Catrinescu C, Teodosiu C, Macoveanu M, Míche–Brendlé JL, Dred R (2003) Catalytic wet peroxide oxidation of phenol over Fe-exchanged pillared beidellite. *Water Res* 37:1154–1160
92. Mei JG, Yu SM, Cheng J (2004) Heterogeneous catalytic wet peroxide oxidation of phenol over delaminated Fe–Ti–PILC employing microwave irradiation. *Catal Comm* 5:437–440
93. Carriazo J, Guélou E, Barrault J, Tatibouët JM, Molina R, Moreno S (2005) Catalytic wet peroxide oxidation of phenol by pillared clays containing Al–Ce–Fe. *Water Res* 39:3891–3899
94. Carriazo JG, Molina R, Moreno S (2008) A study on Al and Al–Ce–Fe pillaring species and their catalytic potential as they are supported on a bentonite. *Appl Catal A: Gen* 334:168–172
95. Molina CB, Casas JA, Zazo JA, Rodríguez JJ (2006) A comparison of Al–Fe and Zr–Fe pillared clays for catalytic wet peroxide oxidation. *Chem Eng J* 118:29–35
96. Luo M, Bowden D, Brimblecombe P (2009) Catalytic property of Fe–Al pillared clay for Fenton oxidation of phenol by H<sub>2</sub>O<sub>2</sub>. *Appl Catal B: Environ* 85:201–206
97. Timofeeva MN, Khankhasaeva ST, Chesalov YA, Tsybulya SV, Panchenko VN, Dashinamzhilova ET (2009) Synthesis of Fe,Al-pillared clays starting from the Al,Fe-polymeric precursor: effect of synthesis parameters on textural and catalytic properties. *Appl Catal B: Environ* 88:127–134



98. Timofeeva MN, Khankhasaeva ST, Talsi EP, Panchenko VN, Golovin AV, Dashinamzhilova ET, Tsybulya SV (2009) The effect of Fe/Cu ratio in the synthesis of mixed Fe,Cu,Al-clays used as catalysts in phenol peroxide oxidation. *Appl Catal B: Environ* 90:618–627
99. Tabet D, Saidi M, Houari M, Pichat P, Khalaf H (2006) Fe-pillared clay as a Fenton-type heterogeneous catalyst for cinnamic acid degradation. *J Env Manage* 80:342–346
100. Herney-Ramirez J, Costa CA, Madeira LM, Mata G, Vicente MA, Rojas-Cervantes ML, López-Peinado AJ, Martín-Aranda RM (2007) Fenton-like oxidation of Orange II solutions using heterogeneous catalysts based on saponite clay. *Appl Catal B: Environ* 71:44–56
101. Herney-Ramirez J, Lampinen M, Vicente MA, Costa CA, Madeira LM (2008) Experimental design to optimize the oxidation of orange II dye solution using a clay-based Fenton-like catalyst. *Ind Eng Chem Res* 47:284–294
102. Achma RB, Ghorbel A, Dafinov A, Medina F (2008) Stability of copper supported pillared clay catalysts during oxidation of model pollutant tyrosol in batch and continuous reactors. *Stud Surf Sci Catal* 174B:1355–1358
103. Achma RB, Ghorbel A, Dafinov A, Medina F (2008) Copper-supported pillared clay catalysts for the wet hydrogen peroxide catalytic oxidation of model pollutant tyrosol. *Appl Catal A: Gen* 349:20–28
104. Najjar W, Ghorbel A, Perathoner S, Centi G (2008) Oxidation intermediates and reaction pathways of wet hydrogen peroxide oxidation of *p*-coumaric acid over (Al–Fe)PILC catalyst. *Stud Surf Sci Catal* 174B:1063–1068
105. Kim SC, Kim DS, Oh SS, Lee DK, Yang YK (2002) Catalytic wet oxidation of dyehouse effluents with Cu/Al<sub>2</sub>O<sub>3</sub> and Cu–Al pillared clay. *Stud Surf Sci Catal* 145:355–358
106. Kim SC, Lee DK (2004) Preparation of Al–Cu pillared clay catalysts for the catalytic wet oxidation of reactive dyes. *Catal Today* 97:153–158
107. Caudo S, Centi G, Genovese C, Perathoner S (2007) Copper- and iron-pillared clay catalysts for the WHPCO of model and real wastewater streams from olive oil milling production. *Appl Catal B: Environ* 70:437–446
108. Giordano G, Perathoner S, Centi G, De Rosa S, Granato T, Katovic A, Siciliano A, Tagarelli A, Tripicchio F (2007) Wet hydrogen peroxide catalytic oxidation of olive oil mill wastewaters using Cu-zeolite and Cu-pillared clay catalysts. *Catal Today* 124:240–246
109. Caudo S, Genovese C, Perathoner S, Centi G (2008) Copper-pillared clays (Cu-PILC) for agro-food wastewater purification with H<sub>2</sub>O<sub>2</sub>. *Micropor Mesopor Mater* 107:46–57
110. Ooka C, Akita S, Ohashi Y, Horiuchi T, Suzuki K, Komai SI, Yoshida H, Hattori T (1999) Crystallization of hydrothermally treated TiO<sub>2</sub> pillars in pillared montmorillonite for improvement of the photocatalytic activity. *J Mater Chem* 9:2943–2952
111. Yoshida H, Kawase T, Miyashita Y, Murata C, Ooka C, Hattori T (1999) Effect of hydrothermal treatment of titania-pillared montmorillonite for photocatalytic degradation of dibutyl phthalate in water. *Chem Lett* 8:715–716
112. Shimizu KI, Kaneko T, Fujishima T, Kodama T, Yoshida H, Kitayama Y (2002) Selective oxidation of liquid hydrocarbons over photoirradiated TiO<sub>2</sub> pillared clays. *Appl Catal A: Gen* 225:185–191
113. Awate SV, Suzuki K (2001) Enhanced adsorption capacity and photo-catalytic oxidative activity of dyes in aqueous medium by hydrothermally treated titania pillared clay. *Adsorption* 7:319–326
114. Li J, Chen C, Zhao J, Zhu H, Ding Z (2002) Photodegradation of dye pollutants on TiO<sub>2</sub> pillared bentonites under UV light irradiation. *Sci China B* 45:445–448
115. Pichat P, Khalaf H, Tabet D, Houari M, Saidi M (2005) Ti-montmorillonite as photocatalyst to remove 4-chlorophenol in water and methanol in air. *Environ Chem Lett* 2:191–194
116. Liu S, Yang JH, Choy JH (2006) Microporous SiO<sub>2</sub>–TiO<sub>2</sub> nanosols pillared montmorillonite for photocatalytic decomposition of methyl orange. *J Photochem Photobiol A: Chem* 179:75–80
117. An T, Chen J, Li G, Ding X, Sheng G, Fu J, Mai B, O’Shea KE (2008) Characterization and the photocatalytic activity of TiO<sub>2</sub> immobilized hydrophobic montmorillonite photocatalysts. Degradation of decabromodiphenyl ether (BDE 209). *Catal Today* 139:69–76

118. Ding X, An T, Guiying L, Chen J, Sheng G, Jiamo F, Zhao J (2008) Photocatalytic degradation of dimethyl phthalate ester using novel hydrophobic TiO<sub>2</sub> pillared montmorillonite photocatalyst. *Res Chem Intermediates* 34:67–83
119. Yang W, Cheng LY, Xue ZL, Guo H, Gao JZ (2008) Preparation of TiO<sub>2</sub> pillared montmorillonite photocatalyst and its photocatalytic activity to degradation reaction of acidic fuchsine by sunlight. *Spectrosc Spectral Anal (Guang Pu Xue Yu Guang Pu Fen Xi)* 28:1122–1125
120. Yang X, Zhu H, Liu J, Gao X, Martens WN, Frost RL, Shen Y, Yuan Z (2008) A mesoporous structure for efficient photocatalysts: anatase nanocrystals attached to leached clay layers. *Micropor Mesopor Mater* 112:32–44
121. Xuzhuang Y, Yang D, Huaiyong Z, Jiangwen L, Martins WN, Frost R, Daniel L, Yuenian S (2009) Mesoporous structure with size controllable anatase attached on silicate layers for efficient photocatalysis. *J Phys Chem C* 113:8243–8248
122. Zhang G, Ding X, Hu Y, Huang B, Zhang X, Qin X, Zhou J, Xie J (2008) Photocatalytic degradation of 4BS dye by N,S-codoped TiO<sub>2</sub> pillared montmorillonite photocatalysts under visible-light irradiation. *J Phys Chem C* 112:17994–17997
123. Damardji B, Khalaf H, Duclaux L, David B (2009) Preparation of TiO<sub>2</sub>-pillared montmorillonite as photocatalyst. Part I. Microwave calcination, characterisation, and adsorption of a textile azo dye. *Appl Clay Sci* 44:201–205
124. Damardji B, Khalaf H, Duclaux L, David B (2009) Preparation of TiO<sub>2</sub>-pillared montmorillonite as photocatalyst. Part II. Photocatalytic degradation of a textile azo dye. *Appl Clay Sci* 45:98–104
125. Dvininov E, Popovici E, Pode R, Coheci L, Barvinschi P, Nica V (2009) Synthesis and characterization of TiO<sub>2</sub>-pillared Romanian clay and their application for azoic dyes photodegradation. *J Hazard Mater* 167:1050–1056
126. Pode R, Popovici E, Vasile A, Coheci L, Dvininov E (2009) Sorption and photocatalytic degradation of azoic dyes on TiO<sub>2</sub>-pillared montmorillonitic clay. *Revue Roumaine de Chimie* 54:313–321
127. Ooka C, Yoshida H, Takeuchi S, Maekawa M, Yamada Z, Hattori T (2004) Hydrogen peroxide improving crystallinity of TiO<sub>2</sub> nanoparticle in layer compound. *Catal Comm* 5:49–54
128. Yuan XT, Yu J, Liu HZ, Li WJ (2004) Synthesis and characterization of novel organic/inorganic pillared clays. *Acta Chimica Sinica* 62:1049–1054
129. Yan SF, Yu J, Liu HZ, Sun TC (2007) Preparation of Ti-pillared montmorillonite tailored by surfactant. *Chin J Process Eng (Guocheng Gongcheng Xuebao)* 7:90–94
130. Ding X, An T, Li G, Zhang S, Chen J, Yuan J, Zhao H, Chen H, Sheng G, Fu J (2008) Preparation and characterization of hydrophobic TiO<sub>2</sub> pillared clay: the effect of acid hydrolysis catalyst and doped Pt amount on photocatalytic activity. *J Colloid Interface Sci* 320:501–507
131. Li D, Qu J (2009) The progress of catalytic technologies in water purification: a review. *J Environ Sci (Beijing, China)* 21:713–719
132. von Sonntag C (2008) Advanced oxidation processes: mechanistic aspects. *Water Sci Technol* 58:1015–1021
133. Litter MI (2005) Introduction to photochemical advanced oxidation processes for water treatment. In: Hutzinger O (ed) *Environmental photochemistry. Part II (series The Handbook of Environmental Chemistry)*, vol 2 M. Springer, Berlin, pp 325–366
134. Augugliaro V, Litter M, Palmisano L, Soria J (2006) The combination of heterogeneous photocatalysis with chemical and physical operations: a tool for improving the photoprocess performance. *J Photochem Photobiol C: Photochem Rev* 7:27–144
135. Jain DM (2005) Photo Fenton degradation for environmental application. *J Ind Pollut Control* 21:181–194
136. Waite TD (2002) Challenges and opportunities in the use of iron in water and wastewater treatment. *Rev Environ Sci BioTechnol* 1:9–15

137. Suty H, De Traversay C, Cost M (2004) Applications of advanced oxidation processes: present and future. *Water Sci Technol* 49:227–233
138. Sum OSN, Feng J, Hu X, Yue PL (2004) Pillared laponite clay-based Fe nanocomposites as heterogeneous catalysts for photo-Fenton degradation of acid black. *Chem Eng Sci* 59:5269–5275
139. Liu Y, Li YM, Wen LH, Li HY (2005) Fe pillared bentonite and photo-catalytic degradation of dye-Orange II. *J Funct Mater (Gongneng Cailiao)* 36:136–138
140. Bobu MM, Siminiceanu I, Lundanes E (2008) Mineralization of two phenyl urea herbicides in water by a heterogeneous photo-Fenton process. *Environ Eng Manage J* 7:37–40
141. Bobu M, Yediler A, Siminiceanu I, Schulte-Hostede S (2008) Degradation studies of ciprofloxacin on a pillared iron catalyst. *Appl Catal B: Environ* 83:15–23
142. De León MA, Castiglioni J, Bussi J, Sergio M (2008) Catalytic activity of an iron-pillared montmorillonitic clay mineral in heterogeneous photo-Fenton process. *Catal Today* 133–135:600–605
143. Chen Q, Wu P, Li Y, Zhu N, Dang Z (2009) Heterogeneous photo-Fenton photodegradation of reactive brilliant orange X-GN over iron-pillared montmorillonite under visible irradiation. *J Hazard Mater* 168:901–908

# Chapter 8

## Fe–Al-Pillared Clays: Catalysts for Wet Peroxide Oxidation of Phenol

Erwan Guélou, Jean-Michel Tatibouët, and Joël Barrault

**Abstract** Catalytic phenol oxidation with hydrogen peroxide (CWPO) was performed over iron containing clays, pillared with Al or mixed Fe–Al complexes. This study deals with the better conditions for the oxidation reaction (temperature, pH, hydrogen peroxide concentration, atmosphere, etc.) in the presence of homogeneous or heterogeneous catalysts. The reaction was performed in a dynamic fixed-bed reactor, which gave the effect of the main experimental variables and an estimation of the kinetic parameters. The catalysts were characterized by classical techniques and by electron spin resonance (ESR). From ESR experiments the reaction mechanism involving hydroxyl radicals was also investigated.

**Keywords** Catalysis · Fe–Al-pillared clays · Catalytic phenol oxidation

### 8.1 Introduction

Domestic and agricultural activities and industrial processes generate a lot of aqueous wastes containing numerous organic pollutants, which must be treated before reuse or discharge. Due to the new rules concerning ecological and environmental aspects, specific and complete treatments must be done. Usual oxidation processes are not as efficient as expected for deep purification of wastewaters. Catalytic wet air oxidation (CWAO) processes (air or pure oxygen as oxidant) allow high pollutant conversions but unfortunately severe conditions (high temperature and pressure) [1] are needed inducing increasing costs for water treatment. The use of a liquid oxidant (like hydrogen peroxide/CWPO) and ambient experimental conditions should reduce these costs.

---

J. Barrault (✉)

Ecole Supérieure d'Ingénieurs de Poitiers, Laboratoire de Catalyse en Chimie Organique, LACCO/UMR CNRS 6503, Université de Poitiers, 40 avenue du Recteur Pineau, 86022 Poitiers Cedex, France

e-mail: joel.barrault@univ-poitiers.fr

Homogeneous processes, such as Fenton processes known for a century [2], are very effective in converting pollutants. However, the use of a homogeneous catalyst needs a rather costly flocculation–filtration step. This last phase increases the cost of the final treatment. In order to improve the Fenton process, the homogeneous catalyst should be immobilized over a support and the resulting material must be as active as a homogeneous catalyst and stable (without leaching).

A large amount of pollutants are known among drugs, pesticides and tension-active agents, and phenol is chosen as a model because (i) phenol and derivatives must be eliminated from various effluents and (ii) the main oxidation pathways to carbon dioxide are well described by Devlin and Harris [3].

Fenton and Fenton-like processes are well known for phenol oxidation with hydrogen peroxide over iron catalysts but rather few studies describe the use of a stable heterogeneous catalyst. Among all the solids used for that reaction, iron was supported on many different oxides (alumina [4], silica [5], activated carbon [6], zeolites [7, 8], mesoporous materials [9], perovskites [10] or clays [11, 12]). The clays were selected as support in our study, because of their availability and also the possibility of pillaring.

From electron spin resonance (ESR) the iron species of the catalyst (paramagnetic properties of  $\text{Fe}^{\text{III}}$ ) can be characterized. In the same time, hydroxyl radicals probably the active species in phenol oxidation processes can be also detected from ESR experiments [13]. But because of the very short lifetime of hydroxyl radicals (nanosecond), spin trapping detection with dimethyl pyroline oxide (DMPO) was used [14] since the resulting radical adduct has a half-lifetime higher than 1 h [14–16].

The aim of this chapter concerns mainly Fe–Al-pillared clays and their catalytic properties in the phenol oxidation with hydrogen peroxide. The effect of temperature, hydrogen peroxide concentration and pH was investigated. Moreover, clay catalysts were used in a continuous flow reactor to check the stability of those materials in long duration experiments. All that materials were characterized by X-ray diffraction (XRD), Brunauer–Emmett–Teller (BET), Mössbauer and ESR, and as mentioned above hydroxyl radicals formation was studied by ESR.

## 8.2 Experimental

### 8.2.1 Catalysts

Pillared clays were prepared from pillaring a commercial Greek bentonite (Zenith-N) by Al pillars (sample AZA for Al Zenith Argile (clay in French)) or mixed Fe–Al pillars (sample FAZA for Fe–Al Zenith Argile). The preparation route for FAZA was first developed at a laboratory scale and is now scaled up to 1 kg batch quantity [17]. A Zenith-N clay suspension in water (2 wt%) was prepared. The pillaring solution was prepared by titration of an  $\text{Al}^{3+}/\text{Fe}^{3+}$  cationic solution

with 0.2 mol l<sup>-1</sup> NaOH. The cationic solution contained, respectively, 0.18 and 0.02 mol l<sup>-1</sup> of AlCl<sub>3</sub> and FeCl<sub>3</sub> for FAZA catalysts (0 mol l<sup>-1</sup> of FeCl<sub>3</sub> for AZA catalyst). The NaOH solution was slowly added to the cationic solution at 70 °C until the OH/cation (mole ratio) was equal to 1.9. The pillaring solution was added to the clay suspension under stirring. The final (Al+Fe) content corresponds to 3.8 mol kg<sup>-1</sup> of dry clay. After ageing for 24 h, the pillared clay precursor was washed until total elimination of chloride ions, dried at 60–70 °C and finally calcinated at 500 °C for 2 h.

The FAZA-1 and FAZA-2 catalysts correspond to different preparations according to the same procedure. From the iron content measurement (Table 8.1), the FAZA-2 sample should contain less iron associated with the pillars than the FAZA-1 sample. The BET-specific surface area was measured by nitrogen adsorption at -196 °C. The *d*<sub>001</sub> spacing was determined by XRD analysis. The iron content of these catalysts and the iron quantity leached out after the oxidation reaction were determined by chemical analysis at the ‘Service Central d’Analyse du CNRS’, Vernaison, France. The main characteristics of the catalysts are tabulated in Table 8.1. FAZA catalysts were also shaped as pellets of 1 mm diameter and 5 mm length. The FAZA-1 catalyst called ‘used’ was obtained from an experiment in a continuous flow reactor (described elsewhere).

**Table 8.1** Some characteristics of the catalysts

Catalyst	BET surface area (m <sup>2</sup> g <sup>-1</sup> )	<i>d</i> <sub>001</sub> spacing (Å)	Fe content (wt%)	Fe in the pillars <sup>a</sup> (wt%)	Fe clusters <sup>b</sup> (wt%)	Fe clusters <sup>b</sup> (wt%)	Pore volume (cm <sup>3</sup> g <sup>-1</sup> )	Mean pore diameter (Å)	TOC abatement <sup>c</sup> %
AZA	111	18.0	2.45	0	0	0.08	29	36	0.3
FAZA-1 fresh	180	17.5	3.01	0.56	0.05	0.24	53	62	0.2
FAZA-1 used	200	17.0	2.96	0.51	0	0.25	44	64	0.3
FAZA-2	183	17.0	2.67	0.22	0	0.23	50	61	0.6

<sup>a</sup>Calculated from subtracting Fe content of AZA catalyst to Fe content of the catalyst

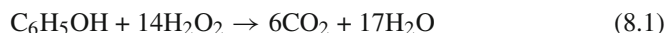
<sup>b</sup>Calculated from subtracting Fe content of FAZA-1 fresh to Fe content of FAZA-1 used

<sup>c</sup>Results obtained in a batch reactor after 4 h of reaction (*T* = 25 °C; catalyst = 5 g l<sup>-1</sup>; H<sub>2</sub>O<sub>2</sub> = 2 × 10<sup>-4</sup> mol h<sup>-1</sup>)

## 8.2.2 Catalytic Phenol Oxidation

### 8.2.2.1 Reaction

The complete mineralization of phenol with hydrogen peroxide occurs according to the following and general reaction:



### 8.2.2.2 Batch Reactor

The phenol oxidation was carried out in a thermostated stirred tank Pyrex reactor (250 ml) in isothermal conditions. The temperature of the reactor was controlled by the circulation of a thermal fluid whose temperature is regulated by a cryothermostat. The reactor was equipped with a pH electrode to continuously monitor the pH value of the reaction solution. The pH value was maintained by the addition of small amounts of diluted  $\text{H}_2\text{SO}_4$  solution, close to its optimum value ( $\text{pH} \approx 3.7$ ) as previously demonstrated [18] (value confirmed by results coming from spin trapping detection of the present study). The catalyst (0.5–1.0 g) was put into 100 ml of an aqueous phenol solution ( $5 \times 10^{-4} \text{ mol l}^{-1}$ ) under continuous stirring, 15 min before the beginning of the hydrogen peroxide addition. The hydrogen peroxide solution ( $0.1 \text{ mol l}^{-1}$ ) was added continuously to the phenol solution containing the catalyst ( $5\text{--}10 \text{ g l}^{-1}$ ) from a dosimeter (Dosimat 725 Metrohm) with a constant flow rate of  $2 \text{ ml h}^{-1}$ . In this case, after 4 h of reaction, the hydrogen peroxide in excess was about 1.14 with regards to the stoichiometry of reaction (8.1).

The reaction was performed under an airflow ( $2 \text{ l h}^{-1}$ ) bubbling directly through the solution in order to get the greatest amount of dissolved oxygen and then to increase the catalytic activity [18]. Small samples of the reaction solution were analyzed with a high performance liquid chromatography (Waters HPLC) equipped with a Bio-Rad Aminex HPX-87H column heated at  $45^\circ\text{C}$  to determine the phenol conversion and the products formed during the reaction. The total organic carbon (TOC) content was measured by a DC-190 Dohrmann TOC metre. The iron leaching was estimated by analysis of the filtrated solution after 4 h of reaction.

### 8.2.2.3 Dynamic Fixed-Bed Reactor

The reactor is a cylindrical Pyrex tube of 20 mm inner diameter and 200 mm long (volume = 62.8 ml), equipped with a sintered glass to maintain the catalyst (1–4 g of pellets). The total flow of water containing phenol and hydrogen peroxide passing through the reactor (from the bottom to the top) is obtained by a mixture of two different water solutions containing, respectively, phenol and hydrogen peroxide, delivered by means of 2 dosimeters (Dosimat 725 Metrohm).

The initial concentrations of phenol and hydrogen peroxide at the entrance of the reactor are, respectively,  $5 \times 10^{-4}$  and  $0.01 \text{ mol l}^{-1}$ . These concentrations correspond to a stoichiometric excess of hydrogen peroxide of 1.43 according to reaction (8.1).

A peristaltic pump (Masterflex C/L 77120-62) was used to maintain a high recycling ratio ( $>10$ ). As for the batch reactor, the pH is continuously monitored and can be adjusted to the desired value by addition of a diluted  $\text{H}_2\text{SO}_4$  solution with a titrimer (Titrino 719S Metrohm). The temperature of the reactor is controlled by an external circulation of water whose temperature is adjusted by a cryothermostat.

Air was continuously flowed through the catalyst bed in order (i) to maintain an oxygen saturation of the water solution and (ii) to gently move the catalyst pellets and then to improve the removal of the gaseous CO<sub>2</sub> formed by the reaction from the catalyst bed where large CO<sub>2</sub> bubbles, isolating the catalyst particles from the water, are visible in the absence of air flow.

The analytical procedure was the same as that used for experiments in a batch reactor. The phenol conversion and TOC abatement remained approximately constant with time and were measured after 24 h of reaction as 80 and 42%, respectively. These values correspond to a phenol conversion rate and TOC abatement of, respectively,  $4.8 \times 10^{-6}$  and  $2.5 \times 10^{-6}$  mol h<sup>-1</sup> g<sup>-1</sup>.

### 8.2.2.4 Mössbauer Spectroscopy

The Mössbauer spectra were recorded at the ‘Institut des Matériaux de Nantes, France’ with a constant acceleration automatic folding Elscint-type spectrometer using a room temperature <sup>57</sup>Co source in transmission geometry and a triangular reference signal. Iron was used as reference. The spectra were recorded at 300 K and computed with a least squares routine using Lorentzian lines.

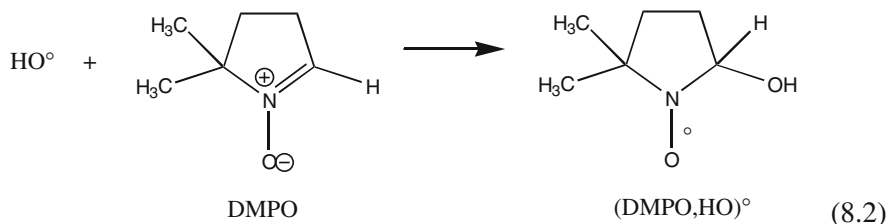
### 8.2.2.5 ESR Spectroscopy

The ESR spectra of catalysts were recorded at the ‘Laboratoire de réactivité de surface, Université P. et M. Curie, Paris, France’ on a Bruker ESP-300E spectrometer with the following settings: central field 4,100 G, sweep width 8,000, microwave frequency 9.25 GHz (X band), modulation amplitude 10.25 G, time constant 40.96 ms and gain  $2 \times 10^3$ .

The ESR spectra were recorded at -196 °C under vacuum after an outgassing at room temperature for 1 h.

The ESR spectra of aqueous solutions were recorded at 298 K with the same spectrometer in the field range of 3390–3450 Gauss, at the microwave frequency of 9.25 GHz (X band).

As previously mentioned, the direct recording of HO• radicals by ESR was not possible due to their too short lifetime. The use of DMPO (5,5-dimethylpyrroline-*N*-oxide), which rapidly reacts with HO• radicals (see Eq. (8.2)) to form stable radical adducts DMPO/HO• (half-lifetime > 1 h) [14–16], allows to detect the HO• radicals formation by ESR and then to estimate their concentration by performing a double integration of the ESR signal of the radical adducts DMPO/HO•.





The HO• measurement was performed by contacting a solution of hydrogen peroxide with the catalyst in the presence of DMPO, in such conditions that the radical's concentration is close to that used for the catalytic reaction.

The reaction was carried out in a Pyrex reactor (25 ml) at 25 °C, isolated from the day light to avoid photooxidation of the DMPO or superoxide ion formation by photoreduction of the dissolved oxygen [19, 20]. The reactor was equipped with a pH electrode to continuously monitor the pH value of the reaction solution. The catalyst (40 mg) was put into 4 ml of bi-distilled water under continuous stirring, 5 min before the addition of 2 ml of hydrogen peroxide (0.04 mol l<sup>-1</sup>) and 2 ml of a DMPO solution (0.1 mol l<sup>-1</sup>) prepared by diluting the pure commercial product (Aldrich). The resulting mixture composition was then: catalyst = 0.5 g l<sup>-1</sup>; H<sub>2</sub>O<sub>2</sub> = 0.01 mol l<sup>-1</sup>; DMPO = 0.025 mol l<sup>-1</sup>. Addition of DMPO was considered as the zero time of the reaction. Then samples were taken at 5, 30 and 60 min for immediate ESR analysis. It was generally observed that the ESR signal of the DMPO/HO• adduct remained approximately stable at its maximum level after 30 min of reaction. This stable value was used to estimate the hydroxyl radicals production.

Blank experiments were performed in the same conditions but without catalyst in order to estimate the spontaneous degradation of hydrogen peroxide. The quantity of HO• radicals produced by the reaction was then calculated by subtracting to the total quantity of HO• radicals measured in presence of the catalyst, the value obtained from the blank experiment.

The experiments were reproduced at least three times in order to estimate a possible error interval.

## 8.3 Results and Discussion

### 8.3.1 Phenol Oxidation

#### 8.3.1.1 Batch Reactor

##### Classical Catalytic Experiment

A typical catalytic reaction behaviour is shown in Fig. 8.1a. After a short induction period (generally 1 h at 25 °C), the phenol conversion grows rapidly until the complete phenol conversion. In the same time, the TOC abatement increases with time until it reaches a plateau in the 60% range. The conversion figure looks like an auto-catalyzed reaction due to the balance of Fe<sup>III</sup>/Fe<sup>II</sup> necessary for Fenton or Fenton-like system. At the end of the reaction, the main product detected by HPLC is oxalic acid.

Surprisingly, the phenol conversion profile obtained with the AZA catalyst (Fig. 8.1a) corresponds to a catalytic activity as high as those of the FAZA catalysts, whereas the TOC abatement is about half of those of the FAZA samples. The

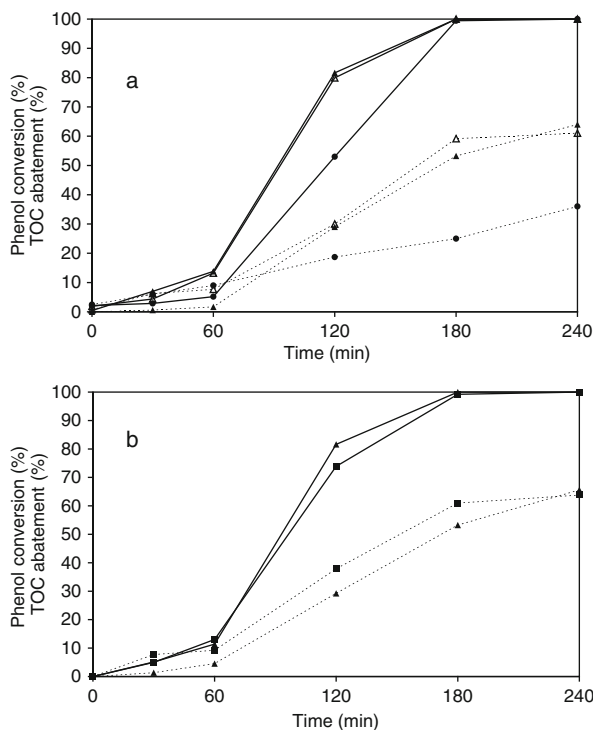


**Fig. 8.1** Phenol oxidation with hydrogen peroxide – effect of catalyst ( $T = 25^\circ\text{C}$ ; catalyst =  $5\text{ g l}^{-1}$ ;  $\text{H}_2\text{O}_2 = 2 \times 10^{-4}\text{ mol h}^{-1}$ ); (—) phenol conversion; (---) TOC abatement; (●) AZA; (▲) FAZA-1 (fresh); (■) FAZA-1 (used); (△) FAZA-2 (a) fresh catalyst; (b) used catalyst

FAZA-2 catalyst is as active as the FAZA-1 catalyst, despite the difference in iron amount of the two catalysts (see Table 8.1).

As already observed with such catalyst [18], a very low leaching of iron is observed ( $0.2\text{ mg l}^{-1}$ ) (see Fig. 8.8), corresponding to  $<0.15\%$  of the initial iron content in the catalyst (Table 8.1).

The same catalytic behaviour was observed with a reused catalyst showing that the catalyst does not deactivate with time (Fig. 8.1b). Obviously, a FAZA-1 (used) catalyst has a better TOC abatement level from the beginning of the reaction, compared to a FAZA-1 (fresh) catalyst. After 4 h of reaction the two FAZA-1 catalysts reach the same TOC abatement. This better activity of the FAZA-1 (used) catalyst could be due to the iron leached during the reaction in a continuous flow reactor. The ‘gangue of iron clusters’ surrounding the active sites (isolated iron: see section ESR catalyst) could be extracted during the continuous reaction, permitting thus the accessibility of these active sites and explaining the better TOC abatement curves of FAZA-1 (used) catalyst than the fresh one.

In order to evaluate the activity and the stability of our heterogeneous catalysts, we compared the results of phenol conversion and TOC abatement to those obtained

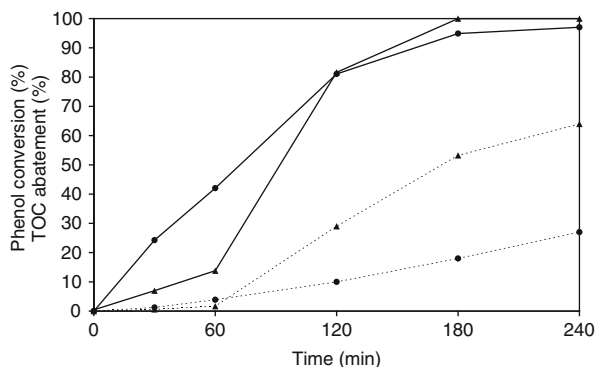


**Fig. 8.2** Phenol oxidation with hydrogen peroxide – effect of the immobilization of Fe<sup>III</sup> over a catalyst ( $T = 25\text{ }^{\circ}\text{C}$ ; catalyst =  $5\text{ g l}^{-1}$ ;  $[\text{Fe}^{\text{III}}] = 5\text{ mg l}^{-1}$ ;  $\text{H}_2\text{O}_2 = 2 \times 10^{-4}\text{ mol h}^{-1}$ ); (●) homogeneous catalyst (Fe<sup>III</sup>); (▲) heterogeneous catalyst (FAZA-1)

with an iron salt ( $\text{Fe}(\text{NO}_3)_3$ ) ( $5\text{ mg l}^{-1}$ ). Figure 8.2 shows that the phenol oxidation is greater with a homogeneous reaction than with a heterogeneous one: Fe<sup>III</sup> is immediately active for the oxidation compared to a FAZA-1 catalyst and there is no induction period. Unfortunately, the phenol conversion is not complete and reaches a plateau at 97%. In the same time, the TOC abatement is lower in the presence of homogeneous Fe<sup>III</sup> than over a FAZA-1 catalyst. Then even if the phenol oxidation rate is higher in the presence of a soluble iron salt, the TOC abatement is greater over iron immobilized on a support.

If there is some iron leaching during the catalytic test it is also important to know the influence of the homogeneous reaction in the presence of a solid catalyst. A standard experiment in which the catalyst was quickly separated from the aqueous media by filtration after various reaction times (45 and 90 min) was done and the reaction was performed in the presence of the filtrated aqueous medium. In the same time, the reaction was also evaluated without catalyst.

The results (Fig. 8.3) clearly show that after the catalyst removal (but in the presence of the leached iron) the phenol conversion does not increase with time. In the same time Fig. 8.3 also shows that without catalyst there is no reaction between phenol and hydrogen peroxide. So, after extraction of the catalyst, curves of phenol conversion look like to that of a reaction without catalyst. The conversion observed seems to be due to a natural degradation of hydrogen peroxide.

From all that results obtained from a homogeneous catalytic reaction in using  $5\text{ mg l}^{-1}$  of dissolved Fe<sup>III</sup>, we can assume that the homogeneous reaction contribution to the observed phenol conversion and TOC abatement is quite negligible.

### Effect of Oxygen

In order to know the impact of dissolved oxygen in the oxidation process the effect of carrier gas ( $\text{N}_2$  or  $\text{O}_2$ ) was investigated. As expected, we can see in Fig. 8.4 that

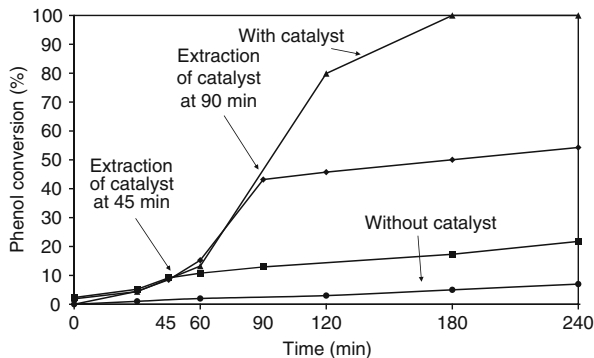


**Fig. 8.3** Phenol oxidation with hydrogen peroxide – effect of the presence of a catalyst ( $T = 25\text{ }^\circ\text{C}$ ; catalyst =  $5\text{ g l}^{-1}$ ;  $\text{H}_2\text{O}_2 = 2 \times 10^{-4}\text{ mol h}^{-1}$ ); (●) without catalyst; (■) FAZA-1 catalyst removed at 45 min; (◆) FAZA-1 catalyst removed at 90 min; (▲) FAZA-1

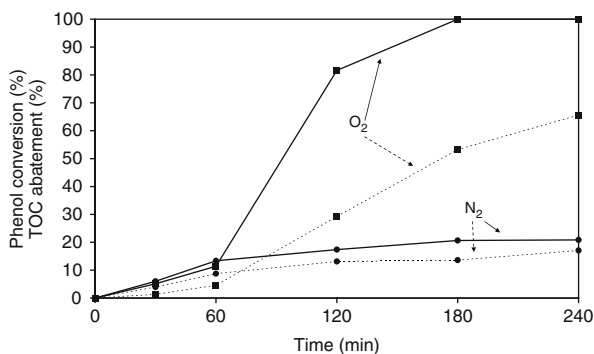


**Fig. 8.4** Phenol oxidation with hydrogen peroxide – effect of dissolved oxygen ( $T = 25\text{ }^\circ\text{C}$ ; catalyst =  $5\text{ g l}^{-1}$ ;  $\text{H}_2\text{O}_2 = 2 \times 10^{-4}\text{ mol h}^{-1}$ ); (—) phenol conversion; (---) TOC abatement; (●) N<sub>2</sub> atmosphere; (■) O<sub>2</sub> atmosphere

oxygen has a great influence over both the phenol conversion and TOC abatement. These results demonstrate the necessity of dissolved oxygen for phenol oxidation.

### Effect of Temperature

In Fig. 8.5, the reactions were performed in the same experimental conditions with a fresh catalyst for each experiment, while the temperature varied from 18 to 70 °C. As expected for an activated oxidation reaction, when the reaction temperature increases, the rate of phenol conversion also increases. Simultaneously, an increase of the TOC abatement level, which reaches a plateau, is observed (55–80% for, respectively, a temperature of 18–70 °C).

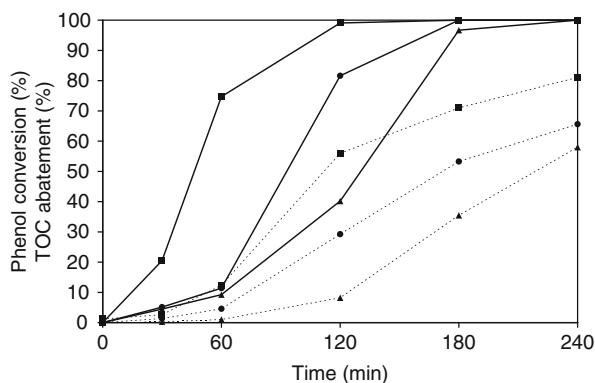


**Fig. 8.5** Phenol oxidation with hydrogen peroxide – effect of temperature (FAZA-1 =  $5 \text{ g l}^{-1}$ ;  $\text{H}_2\text{O}_2 = 2 \times 10^{-4} \text{ mol h}^{-1}$ ); (—) phenol conversion; (---) TOC abatement; (■)  $70^\circ\text{C}$ ; (●)  $25^\circ\text{C}$ ; (▲)  $18^\circ\text{C}$

### Effect of the Hydrogen Peroxide Concentration

The catalytic reaction was performed with a  $10 \cdot 10^{-1}$  concentration of FAZA-1 catalyst, at  $70^\circ\text{C}$  in adding a hydrogen peroxide solution with a concentrations varying from  $0.05$  to  $0.2 \text{ mol l}^{-1}$ , at the same flow rate of  $2 \text{ ml h}^{-1}$ . The results are shown in Figs. 8.6 and 8.7 (phenol conversion and TOC abatement). For a reaction time  $<60$  min, the rate of the addition of the hydrogen peroxide has no important effect on the rate of phenol conversion, except for the lowest rate used. For a greater reaction time, the rate of phenol conversion follows the rate of hydrogen peroxide addition. The total phenol conversion is achieved for a longer time when the hydrogen peroxide concentration decreases.

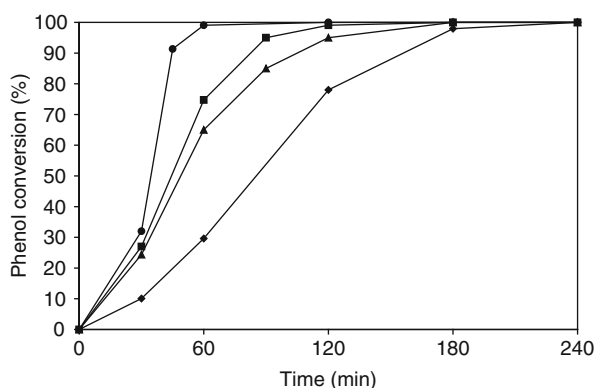


**Fig. 8.6** Phenol oxidation with hydrogen peroxide – effect of hydrogen peroxide concentration on the phenol conversion ( $T = 70^\circ\text{C}$ ; FAZA-1 =  $10 \text{ g l}^{-1}$ ); (●)  $\text{H}_2\text{O}_2 = 4 \times 10^{-4} \text{ mol h}^{-1}$ ; (■)  $\text{H}_2\text{O}_2 = 2 \times 10^{-4} \text{ mol h}^{-1}$ ; (▲)  $\text{H}_2\text{O}_2 = 1.6 \times 10^{-4} \text{ mol h}^{-1}$ ; (◆)  $\text{H}_2\text{O}_2 = 1 \times 10^{-4} \text{ mol h}^{-1}$

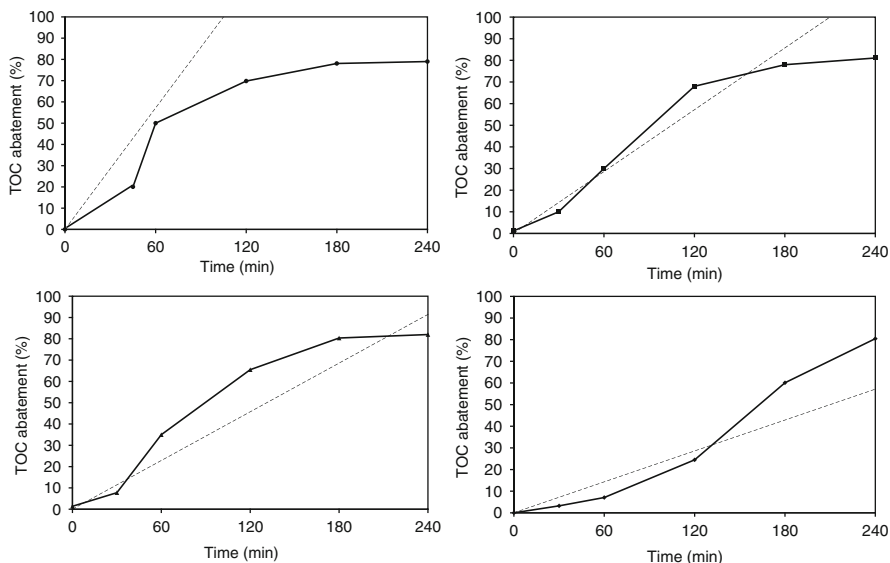


**Fig. 8.7** Phenol oxidation with hydrogen peroxide – effect of the hydrogen peroxide concentration on TOC abatement ( $T = 70\text{ }^{\circ}\text{C}$ ; FAZA-1 =  $10\text{ g l}^{-1}$ ); (●)  $\text{H}_2\text{O}_2 = 4 \times 10^{-4}\text{ mol h}^{-1}$ ; (■)  $\text{H}_2\text{O}_2 = 2 \times 10^{-4}\text{ mol h}^{-1}$ ; (▲)  $\text{H}_2\text{O}_2 = 1.6 \times 10^{-4}\text{ mol h}^{-1}$ ; (◆)  $\text{H}_2\text{O}_2 = 1 \times 10^{-4}\text{ mol h}^{-1}$ ; (—) experimental values; (- -) theoretical values

The same effect is observed for the TOC abatement, but an 80% plateau is reached after more than 4 h of reaction, whatever be the hydrogen peroxide concentration. According to reaction (8.1), it is possible to estimate the theoretical TOC abatement, which should be reached for an ideal use of the hydrogen peroxide. For example, in the standard conditions ( $[\text{H}_2\text{O}_2] = 0.1\text{ mol l}^{-1}$ ;  $F = 2 \times 10^{-4}\text{ mol h}^{-1}$ ), the stoichiometric amount of hydrogen peroxide needed for a complete phenol conversion to carbon dioxide is reached after 210 min. So, for a hydrogen peroxide concentration varying from 0.05 to  $0.2\text{ mol l}^{-1}$ , the theoretical total TOC abatement must be obtained at 105–420 min. The results presented in Fig. 8.7 clearly show that for a hydrogen peroxide concentration varying from 0.05 to  $0.2\text{ mol l}^{-1}$ , experimental TOC abatements are higher than theoretical ones (except for the  $0.2\text{ mol l}^{-1}$  experiment for which the theoretical value is obtained). It is suggested that these results evidence the activation and the participation of the oxygen dissolved in the solution besides the action of hydroxyl radicals [21].

### Effect of pH

The oxidation reactions were carried out, either in homogeneous conditions with a phenol solution containing  $5\text{ mg l}^{-1}$  of  $\text{Fe}^{\text{III}}$  (from nitrate) or in standard catalytic heterogeneous conditions (FAZA-1:5  $\text{g l}^{-1}$ ) at different pH values from 2 to 4.5. The

phenol conversion after 2 h of reaction and the TOC abatement after 4 h of reaction are shown, respectively, in Figs. 8.8 and 8.9. After each catalytic experiment (4 h of reaction), the iron leached in the solution was also measured by atomic absorption (Fig 8.8).

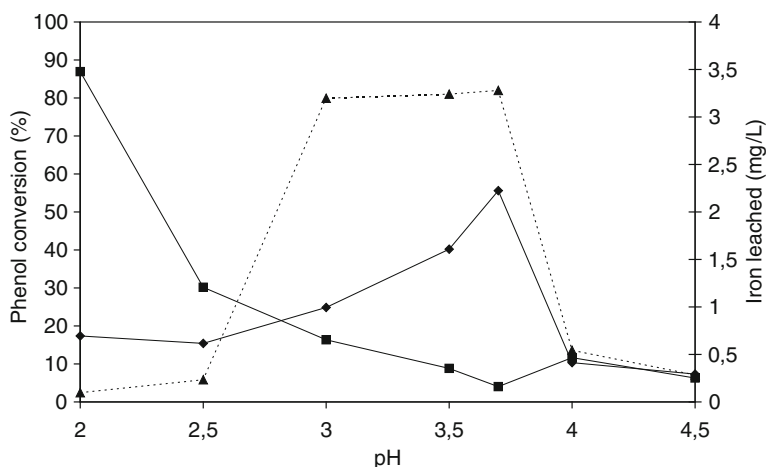


**Fig. 8.8** Phenol oxidation with hydrogen peroxide – effect of pH on phenol conversion and iron leaching ( $T = 25^{\circ}\text{C}$ ; FAZA-1 =  $5 \text{ g l}^{-1}$ ;  $[\text{Fe}^{\text{III}}] = 5 \text{ mg l}^{-1}$ ); (—) catalyst; (---) homogeneous  $\text{Fe}^{\text{III}}$ ; (◆) phenol conversion after 2 h of reaction with FAZA-1; (▲) phenol conversion after 2 h of reaction with homogeneous  $\text{Fe}^{\text{III}}$ ; (■) iron leaching after 4 h of reaction with FAZA-1 catalyst

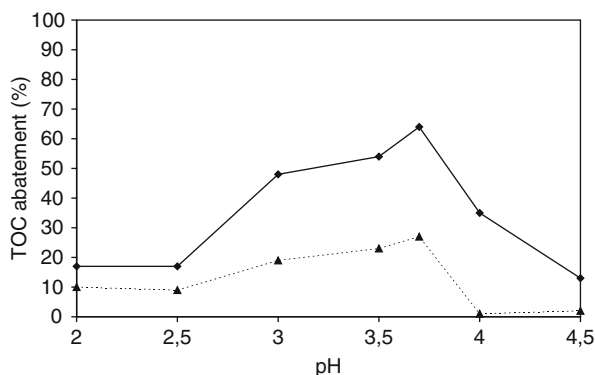


**Fig. 8.9** Phenol oxidation with hydrogen peroxide – effect of pH on TOC abatement after 4 h of reaction ( $T = 25^{\circ}\text{C}$ ; FAZA-1 =  $5 \text{ g l}^{-1}$ ;  $[\text{Fe}^{\text{III}}] = 5 \text{ mg l}^{-1}$ ); (—◆—) FAZA-1; (---▲---) homogeneous  $\text{Fe}^{\text{III}}$

A broad maximum is observed for the phenol conversion (Fig. 8.8) in the pH range of 3–3.7 for the homogeneous reaction, whereas for the heterogeneous catalytic reaction, a sharp maximum centred at a pH value of 3.7 is observed. We should notice that the phenol conversion level obtained after 2 h of reaction at pH 3–3.7 is more important for the homogeneous reaction than for the catalytic heterogeneous one although the iron content in the reactor for the heterogeneous system was 30 times greater than for the homogeneous one (15 mg for the heterogeneous system against 0.5 mg for the homogeneous one). This observation seems to be due to the induction period observed when a heterogeneous catalyst is used (see Fig. 8.1). The homogeneous system seems to be very sensitive to pH values lower than 3, leading to a drastic decrease in the conversion level from 80% at pH 3 to <5% at pH 2.5. On the other hand the heterogeneous system shows only a slight decrease in the phenol conversion from 25 to 17% in the same pH range. Then the heterogeneous catalytic system appears to be less sensitive to the pH value than the homogeneous one.

The TOC abatement (Fig. 8.9) after 4 h of reaction varies in function of the pH, similar to the phenol conversion. But it should be emphasized that the TOC abatement value is always greater for the heterogeneous catalyst than for the homogeneous system. However, for both systems, a marked maximum is also observed for a pH value close to 3.7.

#### Experiments in a Fixed-Bed Dynamic Reactor

According to the preceding results, all the experiments done in a dynamic reactor were performed at the optimum pH value of 3.7. The recycling ratio was maintained at a value higher than 10 so that the reactor behaves as a perfectly stirred reactor [22]. Figure 8.10 shows a typical behaviour of the continuous flow reactor. After a stabilization period due to (i) the filling up of the reactor (4 h), (ii) before the

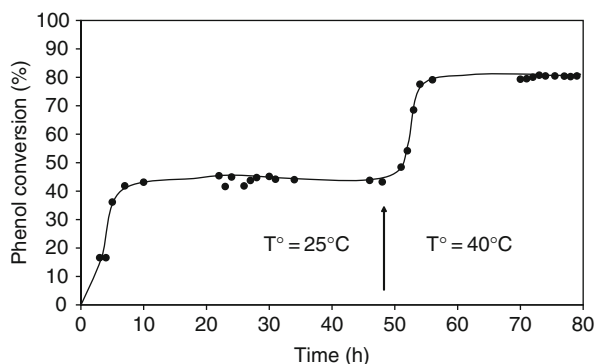


**Fig. 8.10** Phenol conversion versus time in function of temperature in a continuous flow reactor ( $[\text{phenol}] = 5 \times 10^{-4} \text{ mol l}^{-1}$ ;  $\text{H}_2\text{O}_2 = 10^{-2} \text{ mol l}^{-1}$ ; FAZA-2 = 4 g;  $\text{flow}_{\text{phenol}} = \text{flow}_{\text{hydrogen peroxide}} = 0.132 \text{ ml min}^{-1}$ )



connection of the peristaltic pump (1 h) and (iii) the stabilization of the conversion (2 h), we can see a great stability of the catalyst since the phenol conversion stays at a value of 44% during 41 h (at 25 °C). After 48 h, the temperature is increased to 40 °C and it is observed that a stabilization period of 6 h is needed to reach a plateau at 80%. This experiment demonstrates the performances of iron immobilized in a heterogeneous catalyst (activity and stability during a catalytic cycle of 80 h).

From the values (phenol conversion versus temperature) the activation energy ( $E_a$ ) of the reaction is estimated. The kinetic law for the phenol conversion is as following (see elsewhere):

$$1/X = 1 + 1/k\tau$$

or

$$k = (X/(1 - X)) \times (1/\tau)$$

and according to Arrhenius law:  $k = A \times e^{(-E_a/RT)}$  the activation energy obtained is about 85 kJ mol<sup>-1</sup> a value quite similar to those referenced in the literature for catalytic wet air oxidation [23, 24].

The variation of the phenol conversion with the residence time ( $\tau$ ), which was changed in modifying the flow rate and/or the catalyst weight, is shown in Fig. 8.11.

The low deviation of the experimental points from the mean experimental phenol conversion curve shows that the phenol reaction rate is not limited by some diffusional phenomena (low external mass transfer). Moreover, a batch experiment performed in using a catalyst either in pellets or in powder form has not shown any significant variation in phenol conversion and TOC abatement suggesting that in such experimental conditions there are no kinetic limitations due to internal mass transfer.

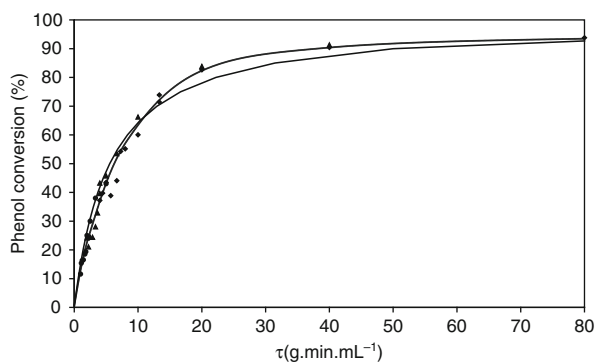


**Fig. 8.11** Phenol conversion versus residence time in a continuous flow reactor ( $T = 40^\circ\text{C}$ ; [phenol] =  $5 \times 10^{-4}$  mol l<sup>-1</sup>;  $\text{H}_2\text{O}_2 = 10^{-2}$  mol l<sup>-1</sup>); catalyst weight: ( $\square$ ) 4 g; ( $\Delta$ ) 2 g; ( $\circ$ ) 1 g; (---) experimental curve; (—) simulation curve for  $k = 0.18$  ml min<sup>-1</sup> g<sup>-1</sup>

If the kinetic order for the phenol is close to 1 the rate of phenol conversion in a perfectly stirred reactor can be expressed as follows:

$$X = k\tau/(1 + k\tau)$$

with:

$X$  = phenol conversion

$k$  = rate constant ( $\text{ml min}^{-1} \text{g}^{-1}$ )

$\tau$  = catalyst weight/total flow rate ( $\text{min g}^{-1} \text{ml}^{-1}$ )

(The density of our catalyst bed is approximately  $1 \text{ g ml}^{-1}$ , so that  $\tau$  represents also the residence time in min. In this latter case, the rate constant is then expressed in  $\text{min}^{-1}$ .)

Then,

$$1/X = 1 + 1/k\tau$$

where the rate constant  $k$  is easily determined from the slope of the straight line ( $1/X$  in function of  $1/\tau$ ) (see Fig. 8.12).

The best fit was obtained for a value of the  $k$  constant equal to  $0.18 \text{ ml min}^{-1} \text{g}^{-1}$ , which was used to evaluate the phenol conversion curve of Fig. 8.11, showing that our simple kinetic model fits very well with the experimental results, especially for a conversion lower than 70%.

These results strongly suggest that the reaction preferentially occurs on the catalyst surface where phenol and intermediate reaction products are strongly adsorbed.

It must be also noticed that the FAZA catalyst is highly stable in the reaction conditions since the iron content of the catalyst decreased only by 2% of the initial content (Table 8.1). After more than 550 h of use, the catalytic activity remains

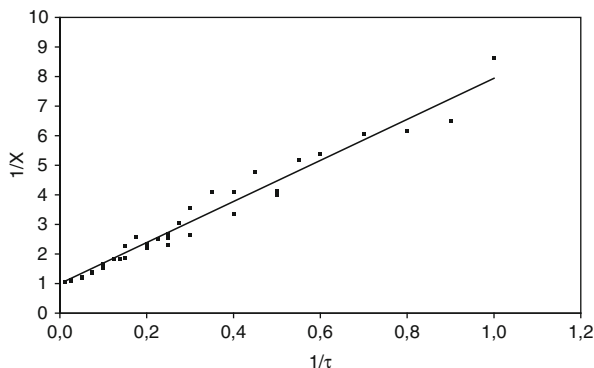


**Fig. 8.12** Determination of  $k$  constant;  $X$ : phenol conversion;  $\tau$ : residence time

almost constant. Moreover, a batch reaction, performed with the same used catalyst has not shown a different behaviour of the one observed with a fresh catalyst (see Fig. 8.1b).

## 8.3.2 Catalyst Characterizations

### 8.3.2.1 Mössbauer

Mössbauer spectra were recorded for FAZA-1 (Fig. 8.13a) and FAZA-2 (Fig. 8.13b) catalysts. Whatever be the catalyst, the spectra present a doublet signal characterized

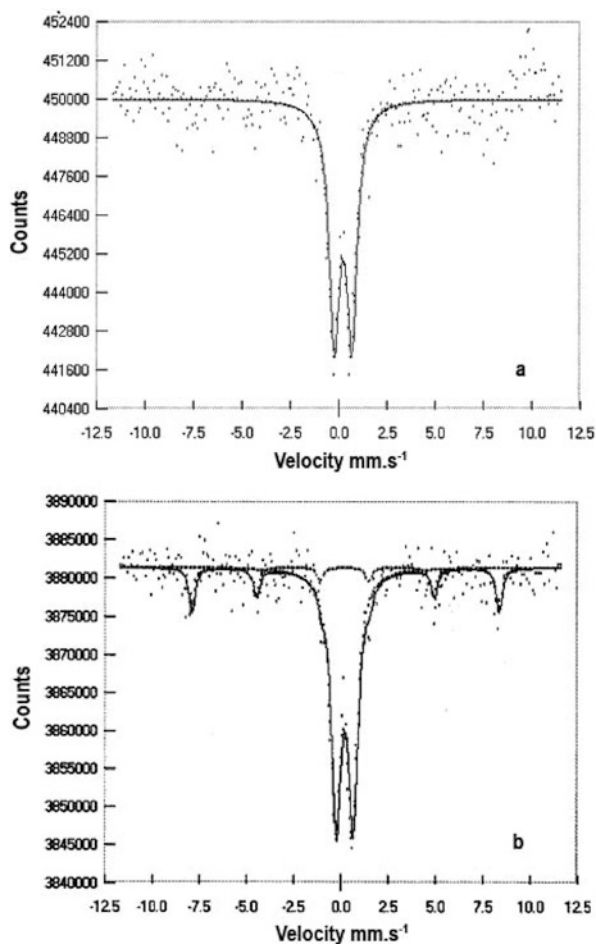


**Fig. 8.13** Mössbauer characterization of FAZA catalysts. (a) FAZA-1 catalyst and (b) FAZA-2 catalyst

by an isomeric shift of  $0.34 \text{ mm s}^{-1}$  and a quadrupole splitting of  $0.9 \text{ mm s}^{-1}$  which are in favour of the presence of  $\text{Fe}^{\text{III}}$  species in distorted octahedral symmetry [25–28]. The spectra of the FAZA-2 catalyst also present a sextuplet with an isomeric shift of  $0.36 \text{ mm s}^{-1}$  and a hyperfine interaction of 504 kGauss characteristic of an internal magnetic field, attributed to hematite.

It must be noticed that the presence of this magnetic hematite in the FAZA-2 sample does not change the catalytic activity (see Fig. 8.1a). Castelein et al. [29] showed that these particles were rapidly leached during a washing cycle (or a catalytic test).

In fact, a majority of  $\text{Fe}^{\text{III}}$  species is in octahedral coordination and as it was suggested by Palínko et al. [30] these  $\text{Fe}^{\text{III}}$  species are in Al–Fe clusters either linked or inside the pillars.

### 8.3.2.2 ESR

#### Characterization of the Solid Catalyst

Figure 8.14a shows the spectra recorded at 77 K of the AZA, FAZA-1 and FAZA-2 catalysts; and Fig. 8.14b shows the spectra recorded at 77 K of the FAZA-1 catalysts

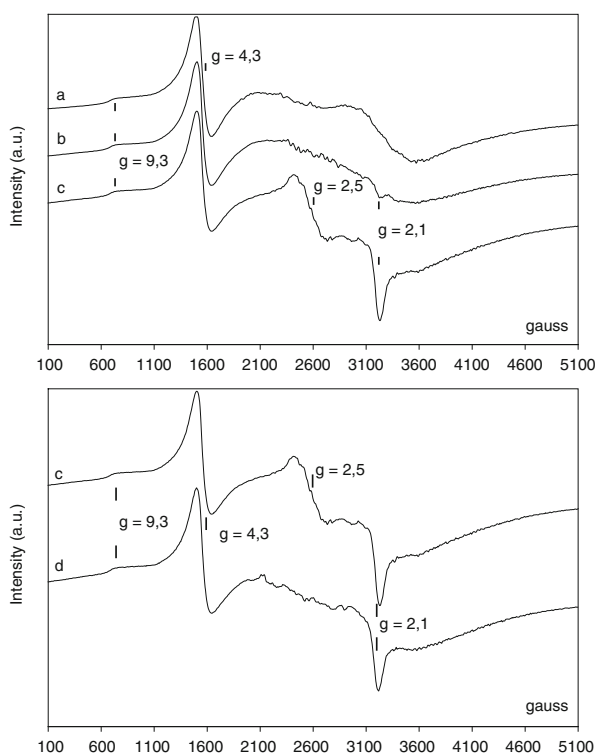


**Fig. 8.14** ESR spectra recorded at 77 K under vacuum of (a) AZA, (b) FAZA-2, (c) FAZA-1 (fresh) and (d) FAZA-1 (used 550 h)

before (fresh catalyst) and after 550 h of catalytic reaction in a continuous flow reactor (used catalyst).

FAZA-1 catalyst presents an ESR spectrum, which can be roughly described by two narrow signals and a broad one, respectively, centred at  $g \approx 4.3$ , 2.1 and 2.5. The spectrum of the AZA catalyst shows only the sharp signal at  $g \approx 4.3$ . The spectrum of the FAZA-2 catalyst is similar to that of the FAZA-1, but only with a low intense and narrow signal centred at  $g \approx 2.1$ . A very weak signal is also visible on the four spectra at  $g \approx 9.3$ .

According to previous results reported in the literature,

- the signal at  $g = 4.3$ , already mentioned by authors for a large number of microporous or layered materials [31–36] is generally assigned to the presence of isolated highly distorted octahedral or tetrahedral  $\text{Fe}^{\text{III}}$  species, with a rhombic-like symmetry [37–42].
- The weak signal observed at  $g \approx 9.3$  is associated with the presence of the signal at  $g = 4.3$ .
- As mentioned by Kucherov and coworkers [41, 42], the narrow signal centred at  $g = 2.1$  could be assigned to the presence in our catalysts of isolated octahedral  $\text{Fe}^{\text{III}}$  species in low field environment [35]. This signal is present only in the spectra of the FAZA catalysts and could then result to the Fe species initially present in the Al–Fe complexes, since the AZA catalyst was not prepared from Al–Fe mixed complexes. One may then expect that the resulting pillars of the AZA catalyst are only formed by aluminium oxide species, whereas the pillars of the FAZA catalysts, prepared from Al–Fe complexes, probably contain iron species either from aluminium isomorphic substitution or as extra-pillar species.
- The broad features, visible in the 1,500–4,000G field range and approximately centred at  $g \approx 2.5$ , are assigned to clustered iron oxide or oxyhydroxide phases [37, 41, 42]. In this domain, a slight difference is observed between the ESR spectra of the fresh and the used catalyst as a narrow superimposed signal centred at  $g \approx 2.5$  on the fresh FAZA-1 catalyst spectrum. This signal has disappeared for the used catalyst (Fig. 8.14b).
- However, the narrow signal centred at  $g = 2.1$  assigned to symmetrical  $\text{Fe}^{\text{III}}$  in octahedral coordination is not present in the ESR spectrum of the AZA clay. This catalyst was prepared by following the same procedure than for FAZA, except for the intercalation step where only Al complexes (without Fe) were used. We may then expect that in the AZA sample, the pillars are only formed by Al oxide and that the iron species detected by ESR comes from the Fe previously contained in the clay precursor (Zenith N) and are probably located in the clay layers.

If we assume that the differences between the iron content of AZA and FAZA catalysts after pillaring by Al–Fe complexes correspond to the amount of iron associated with the pillars (see Table 8.1), we can deduce that the FAZA-1 catalyst contains about 2.5 times more of iron species associated with the pillars than the FAZA-2.

This result is then very consistent with the lower intensity of the ESR narrow signal centred at  $g = 2.1$  observed in the FAZA-2 ESR spectrum. The narrow signal centred at  $g = 2.1$  could then be assigned to iron species belonging to the pillars either from aluminium atoms substitution or as extra-pillar species.

Finally, three kinds of iron species are identified in the FAZA catalysts. Two of them are isolated ones and the third one concerns oxide clusters. The catalytic behaviour of the AZA and FAZA catalysts indicates that the TOC abatement obtained after 4 h of reaction with the AZA catalyst was about half of those observed with the FAZA catalysts and seems to be associated with the amount of iron in the pillars (Table 8.1). This result shows that such iron species associated with the pillars are much more reactive for the phenol mineralization than the other iron species included in the pillared clays. Moreover these isolated iron species are highly stable since no deactivation and no changing of  $\text{Fe}^{\text{III}}$  species are observed after 550 h of reaction.

The disappearance of the small signal centred at  $g \approx 2.5$  after a long time of reaction in the fixed-bed reactor (FAZA-1 used) shows that iron leaching is mainly coming from free oxide clusters. Nevertheless the very low iron leaching observed in the present study ( $0.2 \text{ mg l}^{-1}$ ) suggests that the amount of species leading to those phenomena is very low (approximately 0.05% of initial iron content, Table 8.1).

#### Characterization of $\text{HO}^\bullet$ Radicals

The  $\text{HO}^\bullet$  production (measured from ESR spectra) in function of the pH value is shown in Figs. 8.15 and 8.16, for respectively, the homogeneous and heterogeneous

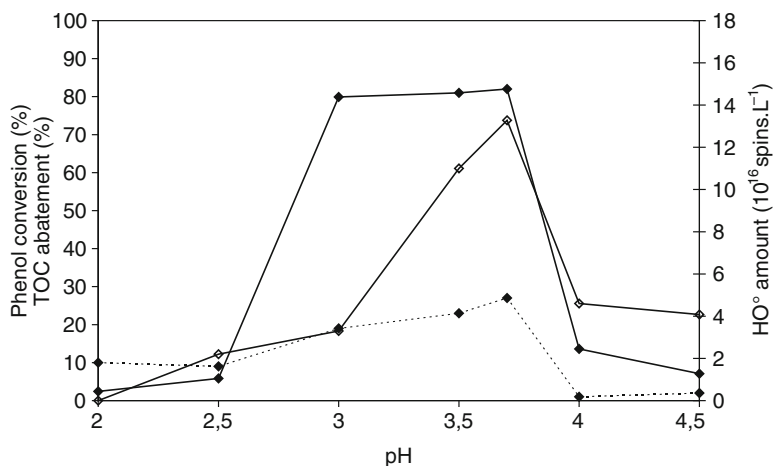


**Fig. 8.15** Phenol conversion and TOC abatement versus hydroxyl radicals production for homogeneous  $\text{Fe}^{\text{III}}$  ( $T = 25^\circ\text{C}$ ;  $[\text{Fe}^{\text{III}}] = 5 \text{ mg l}^{-1}$ ); (—◆—) phenol conversion after 2 h of reaction; (- - ◆ - -) TOC abatement after 4 h of reaction; (—◇—) hydroxyl radicals production after 1 h of reaction

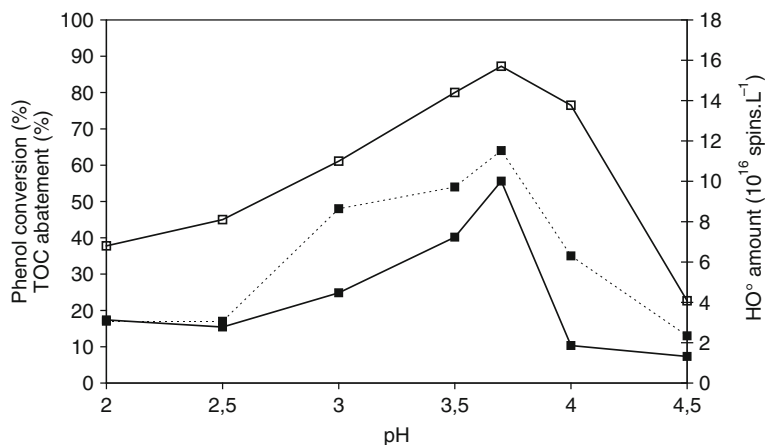


**Fig. 8.16** Phenol conversion and TOC abatement versus hydroxyl radicals production for heterogeneous FAZA-1 ( $T = 25^\circ\text{C}$ ; FAZA-1 =  $5 \text{ g l}^{-1}$ ); (—■—) phenol conversion after 2 h of reaction; (- - ■ - -) TOC abatement after 4 h of reaction; (—□—) hydroxyl radicals production after 1 h of reaction

systems. A maximum in the hydroxyl radicals production is observed for a pH value around 3.7 for both systems. The same behaviour than in the catalytic oxidation reaction is observed for the hydroxyl radicals formation, the heterogeneous catalytic system being less sensitive to the pH than the homogeneous one.

According to these results, a relationship can be established between the amount of DMPO/ $\text{HO}^\bullet$  adduct measured by ESR and the catalyst activity in phenol oxidation (Figs. 8.15 and 8.16). However, the nature of the active oxygen species responsible of the reaction remains questionable since various oxygen species such as  $\text{HO}^\bullet$ ,  $\text{HO}_2^\bullet$  and  $\text{O}_2^{\bullet-}$  can lead to the final formation of the DMPO/ $\text{HO}^\bullet$  adduct, directly or after transformation of the initial adduct [15, 43].

The DMPO/ $\text{HO}_2^\bullet$  adduct was found to be highly unstable in aqueous solution, especially in the presence of a transition metal [15, 43, 44], since it is rapidly transformed to DMPO/ $\text{HO}^\bullet$ .

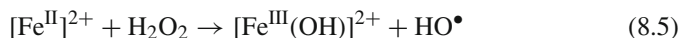
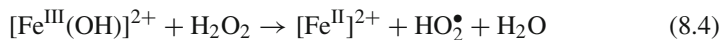
The superoxide ion ( $\text{O}_2^{\bullet-}$ ) formation could also be possible as in the photooxidation processes [44, 45], but for a rather acidic pH, the superoxide species are rapidly transformed into  $\text{HO}_2^\bullet$  by the following reaction (involving  $\text{H}^+$ ) [20]:



Moreover, the possible DMPO/ $\text{O}_2^{\bullet-}$  adduct has a too short half-lifetime (<60 s) compared to that of DMPO/ $\text{HO}^\bullet$  (<160 min) [15, 43, 44] to be detected in experimental conditions of that study.

From the preceding results,  $\text{HO}^\bullet$  and  $\text{HO}_2^\bullet$  radicals appear as the more probable active species in the phenol oxidation.

According to the stability of various iron species in water [46] it appears that the main species that should exist in the pH range (2.5–4.5) of that study are  $[\text{Fe}^{\text{III}}(\text{OH})]^{2+}$  and  $[\text{Fe}^{\text{II}}]^{2+}$ . The following reactions can then occur for homogeneous or heterogeneous systems:



However, it seems difficult to unambiguously give the same conclusion for both the heterogeneous and the homogeneous catalysts since the catalytic behaviours appear to be slightly different. Over the heterogeneous catalyst, the reaction starts after an induction period (not observed for the homogeneous system) and the TOC abatement after 4 h of reaction is largely greater than that observed for the homogeneous reaction.

Nevertheless, according to the similar shape between the  $\text{HO}^\bullet$  production and the catalytic activity, it seems highly probable that the  $\text{HO}^\bullet$  and/or  $\text{HO}_2^\bullet$  species mainly participate in the reaction mechanism of the homogeneous reaction.

The high TOC abatement observed in the presence of the FAZA catalyst which was associated with the presence of specific iron sites (isolated iron species belonging to mixed pillars) clearly showed that the  $\text{HO}^\bullet$  or  $\text{HO}_2^\bullet$  radicals production is not enough to explain the catalytic behaviour observed in the presence of that catalyst.

The difference between homogeneous and heterogeneous systems could be due either to the formation of different active oxygen from hydrogen peroxide (some species such as iron peroxo or hydroperoxo species can also exist at the catalyst surface and play a role in the catalytic phenol oxidation) or to the ability of the heterogeneous catalyst to adsorb the phenol and/or the reaction intermediate products and then increasing the reaction rate with surface oxygen species formed. These phenomena could be largely enhanced by the particular structure of the pillared clay where in addition of the adsorbing properties, the intermediate products of the phenol oxidation could be trapped between the clay layers, favouring their attack by the oxygenated radicals  $\text{HO}^\bullet$  and  $\text{HO}_2^\bullet$ . This behaviour could explain the unusual selectivity to oxalic acid observed during the experiments in a fixed-bed reactor, the larger molecules than oxalic acid formed from the phenol oxidation being trapped inside the clay porosity where they can be more easily transformed.

## 8.4 Conclusion

The study of the catalytic behaviour of Al–Fe-pillared clays (FAZA) for the phenol oxidation by hydrogen peroxide has shown the excellent performances of these materials. In room conditions (but at controlled pH) these catalysts are active and stable without use of a large excess of hydrogen peroxide.



The characterization of the Al–Fe-pillared clays by ESR clearly showed that three different iron species were present in the catalysts:

1. Isolated iron species in highly distorted octahedral symmetry located in the layer of the clay probably after isomorphous substitution of Al atoms.
2. Iron species belonging to oxide clusters.
3. Isolated iron species in octahedral symmetry, present only in the catalyst pillared with Al–Fe mixed complexes, probably belonging to the pillars but as extra-framework species or as mentioned above from isomorphous substitution of Al atoms of the pillars.

It appears that these latter species constitute very active sites for the total phenol oxidation into carbon dioxide with hydrogen peroxide.

Moreover, the high stability of these pillared clay catalysts in the conditions of that study and the catalytic performances in TOC abatement ( $\approx 80\%$  in  $<4$  h at  $70^\circ\text{C}$ ) allow the use of that catalysts in a continuous process for the elimination of organic pollutants from various wastewaters.

The study of catalytic phenol oxidation with hydrogen peroxide in the presence of iron has shown that both heterogeneous and homogeneous catalytic systems behave similarly. In both cases the highest phenol conversion and TOC abatement are obtained at a pH value close to 3.7. However, the heterogeneous catalytic system appears to be less sensitive to the pH and more efficient in TOC abatement than the homogeneous one, which is a quite important result.

The measurement of  $\text{HO}^\bullet$  production by an ESR spin trapping technique using DMPO as trapping agent clearly showed that the  $\text{HO}^\bullet$  production followed the same profile in function of the pH value than the catalytic activity in phenol oxidation. This result strongly suggests that the main active species are hydroxyl ( $\text{HO}^\bullet$ ) and/or hydroperoxyl ( $\text{HO}_2^\bullet$ ) radicals generated by hydrogen peroxide reaction with iron species in homogeneous phase (Fenton reaction) or with iron surface species probably located in the clay porosity. In the heterogeneous process the differences in catalytic activity could come from the adsorptive properties of solid catalysts as well as of the existence of other active species?

The very low amount of iron dissolved during the reaction ( $<2\%$  of the initial content) after more than 550 h of work in a continuous flow reactor is a very promising result for the development of a catalytic continuous process for industrial wastewater purification.

**Acknowledgments** P. Palvadeau (Institut des Matériaux de Nantes, France), B. Morin and J. Fournier (Laboratoire de Réactivité de Surface, Paris, France) and N. Papayannakos (National Technical University of Athens, Greece) are warmly acknowledged for, respectively, Mössbauer experiments, the ESR spectra recording and the clay materials supply.

## References

1. Luck F (1996) A review of industrial catalytic wet air oxidation processes. *Catal Today* 27:195–202
2. Fenton HJH (1894) Oxidation of tartaric acid in presence of iron. *J Chem Soc* 65:899–910

3. Devlin HR, Harris IJ (1984) Mechanism of the oxidation of aqueous phenol with dissolved oxygen. *Ind Eng Chem Fundam* 23:387–392
4. Al-Hayek N, Dore M (1990) Oxydation des phenols par le peroxyde d'hydrogene en milieu aqueux en presence de fer supporte sur alumine. *Wat Res* 24–8:973–982
5. Tagawa T, Seo Y-J, Goto S (1993) Liquid-phase oxidation of benzene to phenol over supported iron salts. *J Mol Cat* 78:201–210
6. Majesté-Labourdenne A (2000) Etude de la réactivité et de la nature des espèces actives dans l'oxydation en milieu aqueux du phénol par le peroxyde d'hydrogène, en présence de catalyseurs à base de fer déposé sur support carboné. Thesis of, Université de Poitiers
7. Centi G, Perathoner S, Torre T, Verduna G (2000) Catalytic wet oxidation with H<sub>2</sub>O<sub>2</sub> of carboxylic acids on homogeneous and heterogeneous Fenton-type catalysts. *Catal Today* 55:61–69
8. Fajerwerg WK, Debellefontaine H (1996) Wet oxidation of phenol by hydrogen peroxide using heterogeneous catalysis Fe-ZSM-5: a promising catalyst. *Appl Catal B: Env* 10: L229–L235
9. Gabelica Z, Charriot A, Vataj R, Soulimane R, Barrault J, Valange S (2009) Thermal degradation of iron chelate complexes adsorbed on mesoporous silica and alumina. *J Thermal Anal Calorim* 95:445–454
10. Faye J, Guélou E, Barrault J, Tatibouët JM, Valange S (2009) LaFeO<sub>3</sub> perovskite as new and performant catalyst for the wet peroxide oxidation of organic pollutants in ambient conditions. *Top Catal* 52:1211–1219
11. Carriazo JG, Molina R, Moreno S (2008) A study on Al and Al–Ce–Fe pillaring species and their catalytic potential as they are supported on a bentonite. *Appl Catal A: Gen* 334:168–172
12. Luo M, Bowden D, Brimblecombe P (2009) Catalytic property of Fe–Al pillared clay for Fenton oxidation of phenol by H<sub>2</sub>O<sub>2</sub>. *Appl Catal B: Env* 85:201–206
13. Kremer ML (2000) Is °OH the active Fenton intermediate in the oxidation of ethanol? *J Inorg Biochem* 78:255–257
14. Finkelstein E, Rosen GM, Rauckman EJ (1980) Spin trapping. Kinetics of the reaction of superoxide and hydroxyl radicals with nitrones. *J Am Chem Soc* 102:4994–4999
15. Finkelstein E, Rosen GM, Ranckman EJ (1980) Spin trapping of superoxide and hydroxyl radical: practical aspects. *Arch Biochem Biophys* 200:1–16
16. Pezerat H, Zalma R, Guignard J, Jaurand MC (1989) Production of oxygen radicals by the reduction of oxygen arising from the surface activity of mineral fibres. *IARC Scien Pub* 90:100–111
17. Kaloidas V, Koufanos CA, Gangas NH, Papayannakos NG (1995) Scale-up studies for the preparation of pillared layered clays at 1 kg per batch level. *Mic Mat* 5:97–105
18. Barrault J, Abdellaoui M, Bouchoule C, Majesté A, Tatibouët JM, Louloudi A, Papayannakos NG, Gangas NH (2000) Catalytic wet peroxide oxidation over mixed (Al–Fe) pillared clays. *Appl Catal B: Env* 27:L225–L230
19. Sawyer DT, Valentine TS (1981) How super is superoxide? *Accounts Chem Res* 14:393–400
20. Liu G, Zhao J, Hidaka H (2000) ESR spin-trapping detection of radical intermediates in the TiO<sub>2</sub>-assisted photo-oxidation of sulforhodamine B under visible irradiation. *J Photochem Photobiol A: Chem.* 133:83–88
21. Debellefontaine H, Chakchouk M, Foussard JN, Tissot D, Striolo P (1996) Treatment of organic aqueous wastes: wet air oxidation and wet peroxide oxidation®. *Environ Pollut* 92:155–164
22. Villermaux J (1993) Génie de la réaction chimique – Conception et fonctionnement des réacteurs. Tec & Doc, Lavoisier, Paris
23. Fortuny A, Bengoa C, Font J, Castells F, Fabregat A (1999) Water pollution abatement by catalytic wet air oxidation in a trickle bed reactor. *Catal Today* 53:107–114
24. Pintar A, Levec J (1992) Catalytic oxidation of organics in aqueous solutions : I. Kinetics of phenol oxidation. *J Catal* 135:345–357
25. Kuang Y, He N, Wang J, Xiao P, Yuan C, Lu Z (2001) Investigating the state of Fe and La in MCM-41 mesoporous molecular sieve materials. *Colloids Surf A* 179:177–184

26. Fejes P, Nagy JB, Lazar K (2000) Heat-treatment of isomorphously substituted ZSM-5 (MFI) zeolites: an ESR and Mössbauer spectroscopy and kinetic study. *J Halasz Appl Catal A* 190:117–135
27. Bakas T, Moukarika A, Papaefthymiou V, Ladavos A, Gangas NH (1994) Redox treatment of an Fe/Al pillared montmorillonite; a Moessbauer study. *Clays Clay Miner* 42:634–642
28. Ratnasamy P, Kumar R (1991) Ferrisilicate analogs of zeolites. *Catal Today* 9:329–416
29. Castelein O, Aldon L, Olivier-Fourcade J, Jumas JC, Bonnet JP, Blanchart P (2002)  $^{57}\text{Fe}$  Mössbauer study of iron distribution in a kaolin raw material: influence of the temperature and the heating rate. *J Euro Ceram Soc* 22:1767–1773
30. Palfinko I, Lazar K, Kiricsi I (1997) Cationic mixed pillared layer clays: infrared and Mössbauer characteristics of the pillaring agents and pillared structures in Fe,Al and Cr,Al pillared montmorillonites. *J Mol Struc* 410–411:547–550
31. Bensimon Y, Deroide B, Dijoux F, Martineau M (2000) Nature and thermal stability of paramagnetic defects in natural clay: a study by electron spin resonance. *J Phys Chem Solids* 61:1623–1632
32. Chung H-H, Jung J, Yoon J-H, Lee M-J (2001) Catalytic activity of clay from tidal flat sediments in the decomposition of perchloroethylene by gamma-rays. *Catal Lett* 76:247–248
33. Komadel P, Doff DH, Stucki JW (1994) Chemical stability of aluminium–iron- and iron-pillared montmorillonite: extraction and reduction of iron. *J Chem Soc Chem Commun* 1243–1244
34. Goodman BA (1978) An investigation by Moessbauer and EPR spectroscopy of the possible presence of iron-rich impurity phases in some montmorillonites. *Clay Minerals* 13:351–356
35. Olivier D, Védrine JC, Pézerat H (1977) Application de la RPE à la localisation des substitutions isomorphiques dans les micas: Localisation du  $\text{Fe}^{3+}$  dans les muscovites et les phlogopites. *J Solid State Chem* 20:267–279
36. Wloch E, Sulikowski B, Dula R, Serwicka EM (1996) Cation environment and migration in iron-exchanged zeolite Na—Y studied by ESR. *Collide Surf A* 115:257–265
37. Parmaliana A, Arena F, Frusteri F, Martinez-Arias A, Lopez Granados M, Fierro JLG (2002) Effect of Fe-addition on the catalytic activity of silicas in the partial oxidation of methane to formaldehyde. *Appl Catal A* 226:163–174
38. Prasad S (1997) Characterization of iron in Fe-VPI-5 and its thermally transformed product, FAPO-8. *Micropor Mater* 12:123–130
39. Lee CW, Ahn DH, Wang B, Hwang JS, Park S-E (2001) Hydroxylation of phenol over surface functionalized MCM-41 supported metal catalyst. *Micropor Mesopor Mater* 44–45:587–594
40. Goldfarb D, Bernardo M, Strohmaier KG, Vaughan DEW, Thomann H (1994) Characterization of iron in zeolites by X-band and Q-band ESR, pulsed ESR, and UV-visible spectroscopies. *J Am Chem Soc* 116:6344–6353
41. Kucherov AV, Montreuil CN, Kucherova TN, Shelef M (1998) In situ high-temperature ESR characterization of FeZSM-5 and FeSAPO-34 catalysts in flowing mixtures of NO,  $\text{C}_3\text{H}_6$ , and  $\text{O}_2$ . *Catal Lett* 56:173–181
42. Kucherov AV, Shelef AM (2000) Quantitative Determination of Isolated  $\text{Fe}^{3+}$  Cations in FeHZSM-5 Catalysts by ESR. *J Catal* 195:106–112
43. Buettner GR, Oberley LW (1978) Considerations in the spin trapping of superoxide and hydroxyl radical in aqueous systems using 5,5-dimethyl-1-pyrroline-1-oxide. *Biochem Biophys Res Commun* 83:69–74
44. Hadjur C, Wagnie`res G, Ihringer F, Monnier P, van den Bergh H (1997) Production of the free radicals  $\text{O}_2^{\bullet-}$  and  $\bullet\text{OH}$  by irradiation of the photosensitizer zinc(II) phthalocyanine. *J Photochem Photobiol B: Biol* 38:196–202
45. Liu G, Zhao J, Hidaka H (2000) ESR spin-trapping detection of radical intermediates in the  $\text{TiO}_2$ -assisted photo-oxidation of sulfurhodamine B under visible irradiation. *J Photochem Photobiol A: Chem* 133:83–88
46. Pourbaix M (1963) Atlas d'équilibres électrochimiques. Gauthier-Villars, Paris.

# Chapter 9

## Pillared Clay-Supported Noble Metal and Metal Oxide Catalysts for Complete Oxidation of VOCs

Shufeng Zuo, Qinqin Huang, and Renxian Zhou

**Abstract** Pillared clays (PILCs) have porous structure, high surface area, special surface acidity, and thermal stability. Due to their properties, PILCs are very suitable to be used as support for active catalytic phases in the preparation of supported catalysts, and the resulting solids can be applied in several reactions, particularly in environmental-friendly reactions. Volatile organic compounds (VOCs) have contributed significantly to air pollution. The deep catalytic oxidation of these pollutants has been identified as one of the most efficient ways to destroy VOCs. This review examines recent developments in the complete oxidation of VOCs over PILC-supported noble metal and metal oxide catalysts.

**Keywords** Pillared clays · Volatile organic compounds – VOCs · PILC

### 9.1 Introduction

Volatile organic compounds (VOCs) emitted from industrial processes and automobile exhaust emissions are recognized as major contributions to air pollution because of their toxic properties and their involvement in the formation of photochemical smog. The most commonly used methods for VOC removal include thermal incineration and catalytic oxidation. From an economical point of view, the catalytic oxidation is an interesting technology for the destruction of VOCs, especially when the VOC concentration is low, as it can treat the effluents at low/moderate temperatures, avoiding high energy costs [1–3].

In general, noble metal catalysts are mainly for non-halogenated VOC destruction, while the metal oxide catalysts are used for halogenated VOCs [1]. Supported precious metals as Pt and Pd are well established as efficient catalysts for the oxidation of different VOCs [4–6]. However, for obvious reasons, cheaper catalytic

---

R. Zhou (✉)

Institute of Catalysis, Zhejiang University, Hangzhou 310028, People's Republic of China  
e-mail: zhorenxian@zju.edu.cn

materials, involving base metal oxides, are of ever-increasing importance. Metal oxides can be more active than noble metal catalyst in function of the nature of the VOCs. The oxidation of ethyl acetate took place at lower temperature on  $\text{MnO}_2$  than on the  $\text{PtO}_2$  catalysts. Moreover, the metal oxide catalysts are more resistant to poisoning by compounds containing sulfur or chlorine. Thus, efforts have been made to develop transition metal-based catalysts with high catalytic activity [7–10]. The selection between a metal oxide and a noble metal is generally influenced by several factors such as the nature of the gaseous stream to be treated and the presence of contaminants. However, it is generally accepted that noble metals are more active than metal oxides but the latter are more resistant to poisoning [11].

Moreover, the choice of support is also important, as support materials play important roles in efficiency improvement of the catalyst by providing large pores and surface areas to disperse the active particles, particularly in oxidation reactions [12–15]. Noble metals and metal oxides, deposited in conventional supports such as  $\text{Al}_2\text{O}_3$  and  $\text{SiO}_2$ , have shown to be efficient for this reaction. Pillared clays (PILCs) are considered to be a new generation of materials with a microporous three-dimensional structure of molecular dimensions [16]. PILCs are usually adopted as supports in order to maintain favorable dispersion of active metal to achieve valid utilization [17–22].

The purpose of this review is to examine literature concerning PILC-supported noble metal and metal oxide catalysts dealing with the heterogeneous catalytic oxidation of volatile organic compounds (VOCs).

## 9.2 Pillared Clay-Supported Noble Metal Catalysts for Complete Oxidation of VOCs

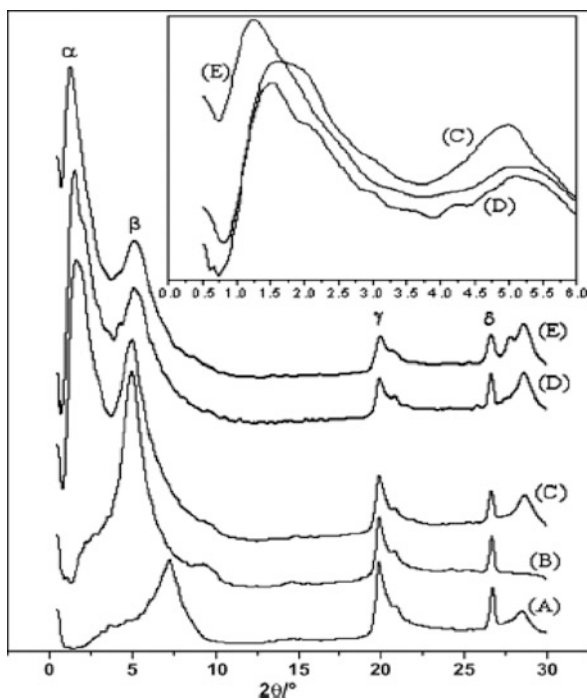
Catalytic oxidation is a well-established technology for controlling VOCs and odor emissions which has been successfully applied in a wide range of commercial installations [23, 24]. Noble metals, typically Pt or Pd in monometallic form, bimetallic Pt–Pd mixtures, or noble metals in combination with some metal oxides, are usually the preferred active phases as VOC combustion catalysts [8, 25, 26]. This is mainly due to their high specific activity that generally allows lower operating temperatures and higher space velocities for a given VOC destruction efficiency compared to the transition metal oxide-based catalysts. A large number of supports have been reported in literature. Among them  $\gamma\text{-Al}_2\text{O}_3$  has been widely used. PILCs are also a good carrier with high surface area, special surface acidity, and thermal stability. In spite of the very interesting properties of PILCs, there are few papers dealing with noble metal catalysts supported on PILCs.

Zuo et al. [27, 28] have studied the influence of synthesis conditions on pore structure of montmorillonite-based Al-PILC and the relationship between structure of the supports and catalytic properties in the deep oxidation of benzene of low concentration (about 150 ppm). Al-PILC and a series of 6%Ce/Al-PILC(A;T;R) were prepared and used as supports of Pd catalysts (0.2 wt%), where A, T, and

R represent aging time, aging temperature, and OH/Al molar ratio of the pillaring solutions, respectively.

The phase composition of the samples was determined by means of X-ray powder diffraction (XRD). XRD diagrams between  $0.5^\circ$  and  $30^\circ$  ( $2\theta$ ) of Na-montmorillonite (Na-mmt), Al-PILC, and some 6%Ce/Al-PILC are shown in Fig. 9.1. And the basal spacing data and the value ratio of peak  $\alpha$ /peak  $\beta$  for all the supports are given in Table 9.1. XRD results show that basal spacing is greatly enlarged after Al pillaring and doping with Ce on Al-PILC yielded a super structure (Fig. 9.2). For 6%Ce/Al-PILC, it is of great interest that peak  $\alpha$  is found between  $2\theta$  angles of  $0.66^\circ$  and  $1.80^\circ$ , and it is found that the value ratio of peak  $\alpha$ /peak  $\beta$  is about 3, 4, 7, and 8. They deduced that four, five, eight, and nine orderly arranged clay layers formed a super structure.

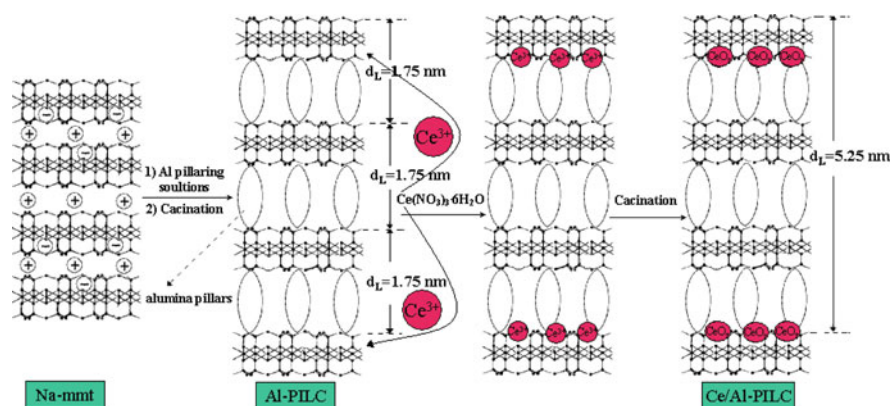
**Fig. 9.1** XRD patterns of (a) Na-mmt, (b) Al-PILC (2;60;2.4), (c) 6%Ce/Al-PILC (2;60;2.4), (d) 6%Ce/Al-PILC (8;60;2.4), and (e) 6%Ce/Al-PILC (12;60;2.4)



Concerning the formation process of the super structure, they considered that Na-mmt is modified by introducing large Al polyoxycations into its interlayer regions, after calcination the Al polyoxycations are converted to metal oxide clusters by dehydration and dehydroxylation processes. These metal oxide clusters (alumina pillars) between the clay layers permanently keep apart the layers, generating an interlayer space of molecular dimensions [29]. The migration of various cations into the clays is affected little by the charge or polarizing power of the cation and

**Table 9.1** XRD patterns and the value ratio of peak  $\alpha$ / peak  $\beta$  of all supports calcined at 500 °C for 2 h

Supports	Peak $\alpha$ $2\theta/d$ (nm)	Peak $\beta$ $2\theta/d_{001}$ (nm)	Value ratio of peak $\alpha$ /peak $\beta$
Na-mmt	–	7.28/1.22	–
Al-PILC (2;60;2.4)	–	4.96/1.77	–
Al-PILC (8;60;2.4)	–	4.97/1.78	–
6%Ce/Al-PILC (2;60;2.4)	1.68/5.25	5.04/1.75	3.0
6%Ce/Al-PILC (4;60;2.4)	1.24/7.12	5.12/1.72	4.1
6%Ce/Al-PILC (8;60;2.4)	1.65/5.35	5.10/1.73	3.1
6%Ce/Al-PILC (12;60;2.4)	1.27/6.94	5.13/1.72	4.0
6%Ce/Al-PILC (16;60;2.4)	1.60/5.51	5.18/1.70	3.2
6%Ce/Al-PILC (8;80;2.4)	1.80/4.90	5.30/1.66	3.0
6%Ce/Al-PILC (8;60;1.6)	1.32/6.68	5.26/1.68	4.0
6%Ce/Al-PILC (8;60;2.0)	0.66/13.4	5.15/1.71	7.8
6%Ce/Al-PILC (8;60;2.8)	0.70/12.6	4.90/1.80	7.0
6%Ce/Al-PILC (8;60;3.2)	1.23/7.17	4.96/1.77	4.1

**Fig. 9.2** Schematic of the mechanism for the preparation of Ce/Al-PILC and a super structure

most cations do not migrate to octahedral sites but, instead, to hexagonal Si–O cavities within the interlayer space [30, 31]. So they deduced that Ce cations migrate to hexagonal Si–O cavities and the cations in this location are more tightly held because they are closer to the locus of the charge deficiency. After calcination, the Ce cations are converted to  $\text{CeO}_2$ , which results in a disordered structure of some clay layers and a super structure.

Contact mode atomic force microscopy (AFM) images of three-dimension of Na-mmt, Al-PILC (8;60;2.4), and 6%Ce/Al-PILC (8;60;2.4) are shown in Fig. 9.3. Na-mmt has a layered structure and a two-dimension porous structure with basal spacing small and irregular. For Al-PILC (8;60;2.4), the degree of layered structure regularity was greatly increased and the basal spacing was greatly increased. Doping

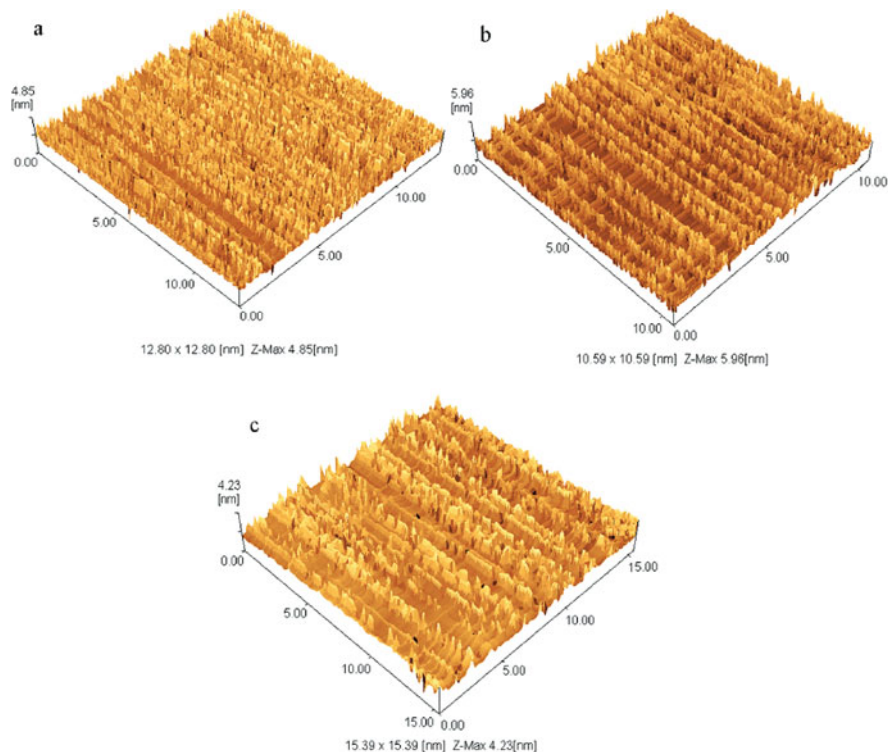


**Fig. 9.3** Contact mode AFM images of three-dimension. (a) Na-mmt, (b) Al-PILC (8;60;2.4), and (c) 6%Ce/Al-PILC (8;60;2.4)

with Ce resulted in a small decrease in the degree of layered structure regularity of Al-PILC, which might arise from the fact that  $\text{CeO}_2$  existed in the hexagonal Si–O cavities within the interlayer space.

The catalytic activity of Pd/Na-mmt, Pd/Al-PILC, Pd/6%Ce/Na-mmt, Pd/6%Ce/Al-PILC (8;60;2.4), and Pd/6%Ce/Al-PILC(8;60;2.4) for deep oxidation of benzene is shown in Fig. 9.4. It can be found that the temperature for the complete oxidation of benzene with Pd catalysts supported by Al-PILC (or ceria-modified Al-PILC), except Pd/6%Ce/Al-PILC (8;60;2.4), is about 40 °C lower than that with Na-mmt. The temperature for the complete oxidation of benzene with Pd catalyst supported by Na-mmt (or Al-PILC) modified with Ce is about 60 °C lower than that without Ce. The activity of the catalysts decreases in the order: Pd/6%Ce/Al-PILC (8;60;2.4)>Pd/6%Ce/Al-PILC (2;60;2.4)>Pd/Al-PILC (8;60;2.4)>Pd/6%Ce/Na-mmt>Pd/Al-PILC (2; 60;2.4)>Pd/Na-mmt.

Zuo et al. summarized that catalytic activity of Pd catalysts in benzene oxidation is greatly dependent on the type of supports. Pd supported on Al-PILC catalysts presents considerably higher activities than that on Na-mmt, which is due to the fact that pillaring is a process that converts thermally unstable clay minerals into PILCs



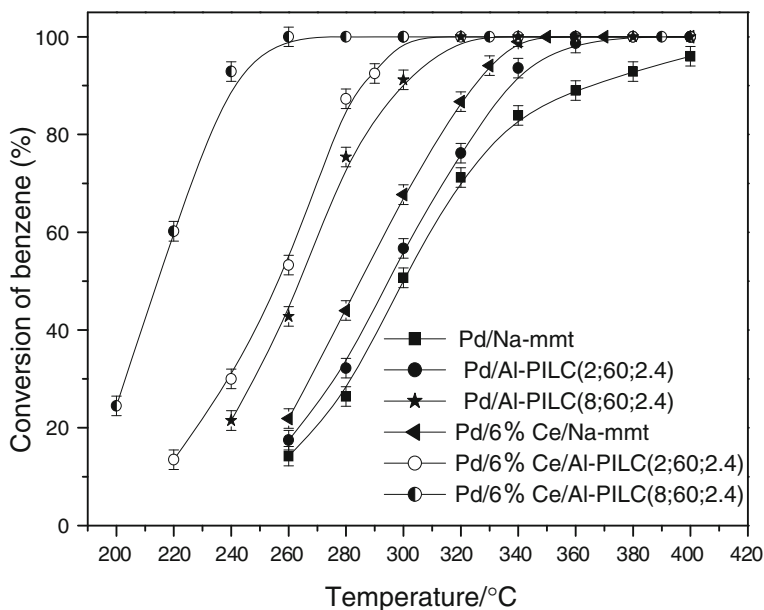


**Fig. 9.4** The catalytic activity of Pd/Na-mmt, Pd/Al-PILC (2;60;2.4), Pd/Al-PILC (8;60;2.4), Pd/6%Ce/Na-mmt, Pd/6%Ce/Al-PILC (2;60;2.4), and Pd/6%Ce/Al-PILC(8;60;2.4)

with highly porous and stable structures. And the highly porous structure of the support increases the active sites of Pd catalyst. The role of  $\text{CeO}_2$  is to stabilize Pd in a high oxidation state through an interaction via surface oxygen in oxidation reactions [32, 33], and the existence of  $\text{CeO}_2$  can improve the dispersion of Pd particles. So  $\text{CeO}_2$ , acting as a promoter in benzene oxidation, can improve the catalytic activity of Pd catalysts. The synthesis conditions of Al-PILC have a significant impact on the surface area and pore structure, and the optimized structure can strengthen the interaction between  $\text{CeO}_2$  and Al-PILC. So pillaring, optimized synthesis conditions of pillaring solution, and addition of Ce can enhance the catalytic activity of catalysts for the deep oxidation of low concentration of benzene.

Li et al. [34] used Al-, Ce- and Zr-pillared laponite clays (Al-Lap, Ce-Lap, Zr-Lap) as supports of Pd catalysts (0.3 wt%) for the complete oxidation of benzene. They found that Pd catalysts supported on the PILCs are much more active than those supported on conventional alumina. Pd/Zr-Lap, in particular, could catalyze the complete oxidation of benzene at a temperature as low as 210 °C. The effect of calcination temperature on the catalytic activity was investigated. The optimal calcination temperature was found to be 400 °C for Pd/Al-Lap catalysts and 600 °C for Pd/Zr-Lap and Pd/Ce-Lap catalysts. At optimal calcination temperatures, palladium crystallites of proper size could be formed in PILCs and showed a higher activity than those calcined at other temperatures. The activity of the catalysts depends, to a great extent, on the temperature of calcination, as indicated in Fig. 9.5. Lowering the calcination temperature would shift the conversion curves

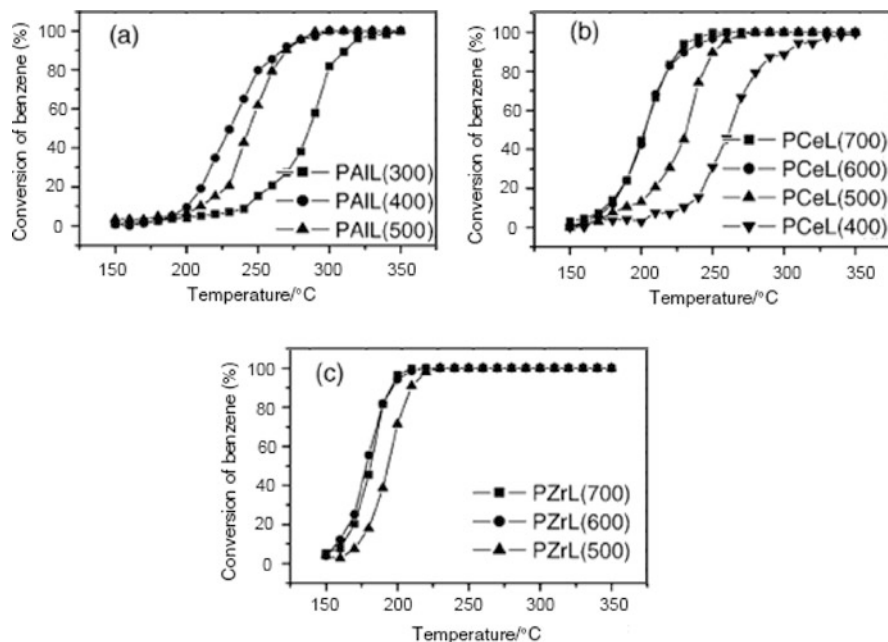


**Fig. 9.5** Conversion curves for benzene oxidation over catalysts calcined at various temperatures. (a) Pd/Al-Lap; (b) Pd/Ce-Lap, (c) Pd/Zr-Lap

toward higher temperatures. They suggested that, as a rule, calcination at too high a temperature would often induce agglomeration of the noble metals, thus resulting in a diminution of the catalyst activity.

To evaluate the stability of the catalytic activity, a series of long-term stability tests over the three types of PILC-supported catalysts were performed. And the evolutions of benzene conversion with time-on-stream are shown in Fig. 9.6. The conversion of benzene over Pd/Zr-Lap catalyst was well sustained at about 86.7% ( $\pm 0.7\%$ ) for 70 h, and no noticeable deactivation was observed. In contrast, the activity of Pd/Ce-Lap was sustained at about 83% ( $\pm 0.8\%$ ) only for the first 50 h, then it began to decrease, and the conversion value fell down to about 74.5% after 70 h. Regard to Pd/Al-Lap catalyst, the conversion value increased to 97% in the first 20 h, then gradually decreased to about 91% ( $\pm 1\%$ ), further decrease began after the test run had been operated for about 50 h, and the conversion value after 70 h was about 86.5%.

Chen et al. [35] prepared novel Pd catalysts (0.1 wt%) supported on Ce, La, Pr, and Zr-pillared montmorillonite (mmt) for the catalytic combustion of toluene, acetone, and ethyl acetate. Catalytic activity of Pd/CZM, Pd/LZM, and Pd/PZM for toluene, acetone, and ethyl acetate oxidation is shown in Fig. 9.7. Firstly, the tested catalytic activity of raw mmt clay is quite low; the  $T_{98}$  of raw mmt for toluene, acetone, and ethyl acetate is at 520, 500, and 560 °C; and the  $T_{98}$  of Zr/mmt is, respectively, at 420, 380, and 430 °C, indicating that the activity of Zr/mmt is

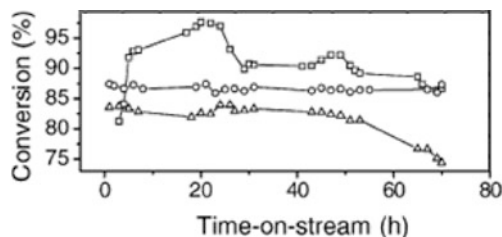


**Fig. 9.6** Stability tests of benzene conversion with time-on-stream over various catalysts. (○) PZrL (600) at 200 °C; (□) PAIL (400) at 220 °C; (△) PCeL(600) at 235 °C

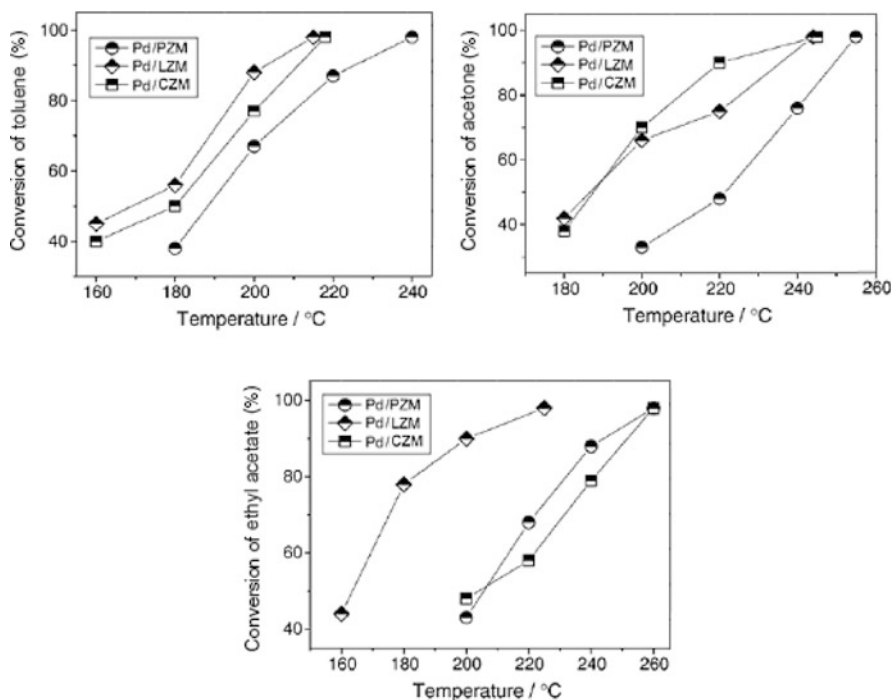


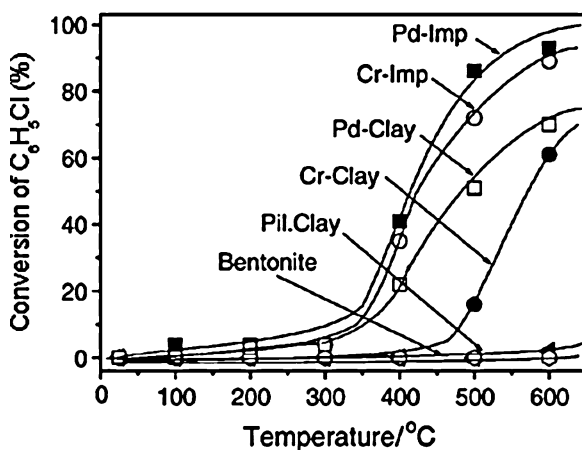
**Fig. 9.7** Catalytic activity of Pd/CZM, Pd/LZM, and Pd/PZM for toluene, acetone, and ethyl acetate oxidation, respectively

higher than that of raw mmt. It can be seen that the conversion of toluene oxidation reaches 98% at 210 °C lower temperature on Pd/LZM sample. At this temperature, toluene conversion for Pd/CZM catalyst is about 90% and is about 75% for Pd/PZM catalyst. The catalytic activity of the three catalysts for acetone was in this sequence: Pd/LZM $\approx$ Pd/CZM>Pd/PZM. And for ethyl acetate oxidation, Pd/LZM also exhibits higher activities in comparison with Pd/CZM and Pd/PZM. This fact denotes that Pd supported on La/Zr-mmt is more active for the total oxidation of the three VOCs than that supported on Ce/Zr-mmt and Pr/Zr-mmt.

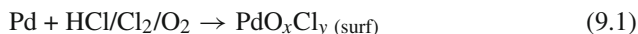
Oliveira et al. [36] investigated the catalytic behavior of Cr and Pd-impregnated Al-PILC for the oxidation of aromatic VOCs, i.e., chlorobenzene or xylene. Cr or Pd content was 5 wt% and catalysts were labeled as Cr-imp and Pd-imp, respectively. The Cr-imp showed high activity for the total oxidation of chlorobenzene and xylene but the materials were completely deactivated during the reaction at 600 °C. For the Pd/Al-PILC, the impregnation procedure completely destroyed the Al-pillars but produced a very active and stable catalyst to oxidize aromatic contaminants. However, in the case of chlorobenzene almost 20% yield of the hazardous hexachlorobenzene was obtained likely by an oxychlorination process.

The catalytic oxidation studies were carried out using chlorobenzene as a probe molecule. The Al-PILC and the original bentonite alone did not present any catalytic activity for the oxidation of chlorobenzene up to 600 °C (Fig. 9.8). The Cr or Pd-imp showed catalytic activity from 300 °C reaching more than 90% oxidation at 600 °C. If Cr or Pd were impregnated directly on the original bentonite without pillar a much lower activity was observed for both metals.

**Fig. 9.8** Conversion of chlorobenzene in the presence of Cr-imp, Pd-imp, PILC, and the original bentonite



Although the mechanism for the formation of the polychlorinated aromatic compound is not clear, the oxidation of chlorobenzene to  $\text{CO}_2$ ,  $\text{H}_2\text{O}$ , and  $\text{HCl}/\text{Cl}_2$  can produce a palladium oxychloro surface species:



This Pd oxychloro species can then chlorinate chlorobenzene to hexachlorobenzene and water.



The catalytic activity of Pd-imp was maintained for more than 70 h during reaction with chlorobenzene or xylene. The Cr-imp catalyst was completely deactivated after 10 h reaction with chlorobenzene at 600 °C (Fig. 9.9).

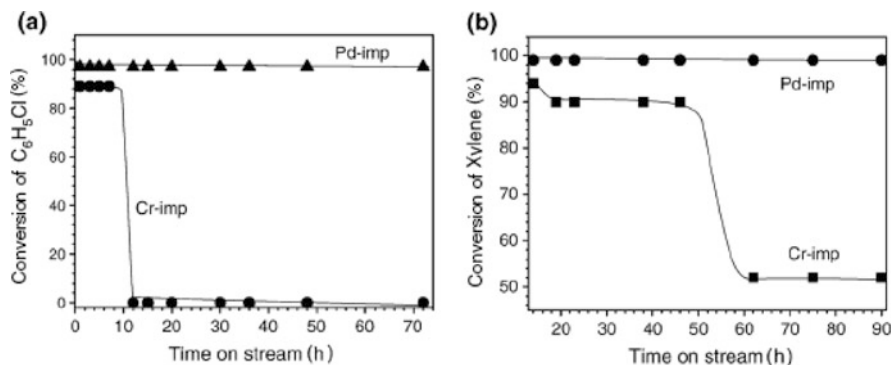


**Fig. 9.9** Life time of the catalysts in the reaction with chlorobenzene (a) and xylene (b)

Gil et al. [19] used a hectorite, a montmorillonite, and a saponite, all of them in their Al-pillared forms, as well as unpillared saponite as supports of Pt catalysts (2.3 wt% Pt) for the catalytic combustion of acetone and methyl-ethyl-ketone (MEK). Good activity and stability performances were found under the reaction conditions used. Whatever be the catalyst considered, MEK resulted easier to oxidize than acetone, a fact which has been related to the strength of the weakest C–H bond in these ketones. Remarkable differences in catalytic activity arose depending on the pillared or unpillared character of the support and the nature of the starting smectite clay used. Regardless of the ketone molecule, the following order of decreasing catalytic performance was established with respect to the support nature: unpillared saponite > Al-pillared montmorillonite > Al-pillared saponite > Al-pillared hectorite.

The light-off curves for acetone and MEK combustion over the Pt/SBhec-Al and Pt/CHmont-Al catalysts are shown in Fig. 9.10. In the same way, the results obtained in the combustion of the two ketones over the Pt/BAsap-Al and Pt/BAsap catalysts are plotted in Fig. 9.11. It can be seen that the temperatures required for total combustion of acetone range between 352 °C over Pt/BAsap and 452 °C over Pt/SBhec-Al. In the case of MEK, the temperatures vary from 317 °C over Pt/BAsap to 447 °C over Pt/SBhec-Al.

It is clear from the results in Figs. 9.10 and 9.11 that MEK is easier to oxidize than acetone over the Pt/Al-PILC catalysts. Indeed, taking the temperature at which a ketone conversion of 50% ( $T_{50}$ ) is achieved as the light-off temperature [37], it can be seen that the temperatures required for light-off range from 212 to 292 °C and from 245 to 302 °C for MEK and acetone combustion, respectively. The largest difference (33 °C) between the  $T_{50}$  values for acetone and MEK combustion is obtained over the Pt/BAsap catalyst, which is also the most active, whereas this difference is only 10 °C in the case of Pt/SBhec-Al, the least active of the four catalysts in this work.

To prevent the clay layers from sintering at the high temperature of the catalytic reactions, the stability of the pillars must be increased. One way to achieve this is to

**Fig. 9.10** Light-off curves for acetone combustion over Pt/SBhec-Al ( $\circ$ ) and Pt/CHmont-Al ( $\square$ ) and MEK combustion over Pt/SBhec-Al ( $\bullet$ ) and Pt/CHmont-Al ( $\blacksquare$ )

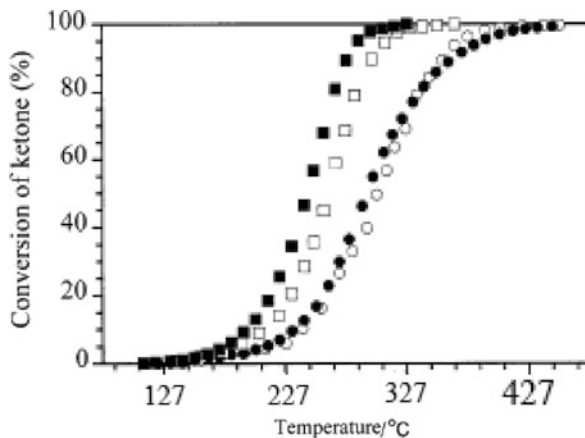
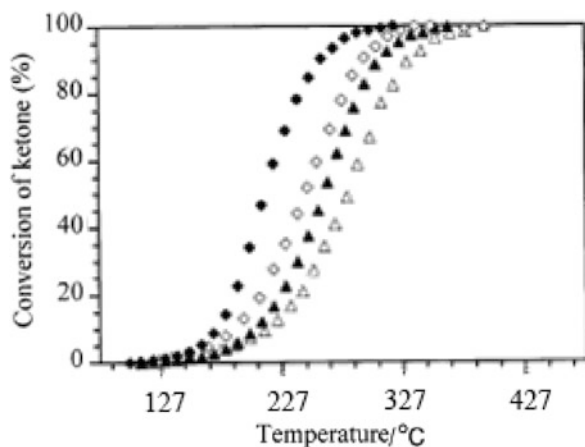


**Fig. 9.11** Light-off curves for acetone combustion over Pt/BAsap-Al ( $\Delta$ ) and Pt/BAsap ( $\diamond$ ) and MEK combustion over Pt/BAsap-Al ( $\blacktriangle$ ) and Pt/BAsap ( $\blacklozenge$ )



introduce mixed pillars into the materials [38–41]. Sterte [42] and McCauley [43] found that the incorporation of rare earth into the preparation of the pillaring agent resulted in material whose basal spacing is larger than that in conventional materials.

Zuo et al. [44] used Al/Rare Earths (REE: Y, Ce, La, Pr, and Nd) PILCs to support Pd (0.2 wt%) for deep oxidation of benzene (about 150 ppm). Activity tests show that after pillaring the optimized structure (such as large basal spacing, high  $S_{\text{BET}}$  and porosity) can enhance the catalytic activity of Pd catalysts. Compared to Al-PILC, PILC-containing REE further increase  $S_{\text{BET}}$  and  $V_{\text{mic}}$ , which causes increase in active sites of Pd catalysts and enhancement in the activity. For Pd/AlCe-PILC, in particular, the temperature of complete oxidation is about 280 °C, exhibiting the highest catalytic activity.

The light-off curves of benzene deep oxidation over Pd catalysts are shown in Fig. 9.12. For Pd impregnated directly on Na-mmt without pillars, a much

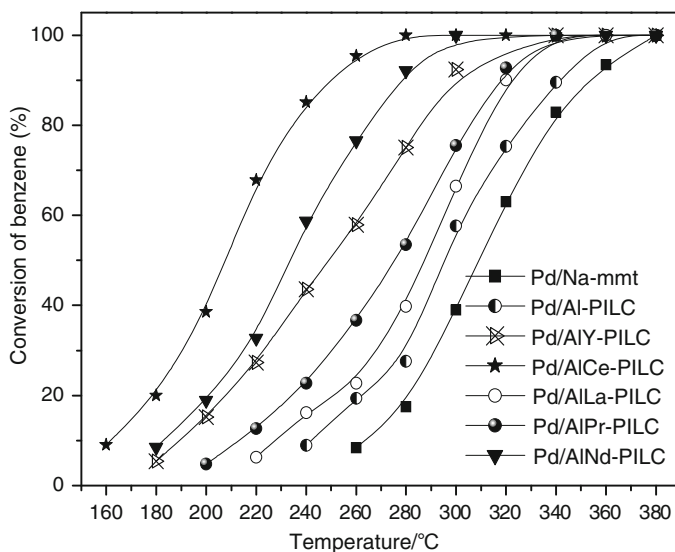


**Fig. 9.12** Light-off curves for benzene deep oxidation over Pd/Na-mmt, Pd/Al-PILC, and Pd/AlREE-PILC

lower activity is observed, the conversion is less than 20% at a reaction temperature of about 260 °C and temperature of complete oxidation is about 380 °C. For Al-PILC and AlREE-PILC-supported Pd catalysts, the catalytic activity has a considerable enhancement compared to that of Pd/Na-mmt. Especially for Pd/AlCe-PILC, the conversion is more than 80% at a reaction temperature of 240 °C and temperature of complete oxidation is about 280 °C, exhibiting the highest catalytic activity. The activity of all catalysts is observed to follow the sequence: Pd/AlCe-PILC > Pd/AlNd-PILC > Pd/AlY-PILC > Pd/AlPr-PILC > Pd/AlLa-PILC > Pd/Al-PILC > Pd/Na-mmt.

In the research of Zuo et al. [45], large pore AlCe-PILC was synthesized by hydrothermal treatments carried out in Teflon-coated stainless steel pressure vessels and used as supports for Pd catalysts in deep oxidation of benzene. These catalysts were labeled as Al-PILC and AlCe-PILC(R;T), where R and T represent Al/Ce molar ratio and hydrothermally treated time of the pillaring solutions, respectively. BET surface area, total pore volume, and  $A_{mes}$  for all the supports are reported in Table 9.2.

Basal spacings of Al-PILC and AlCe-PILC are 1.72 and 1.79–2.83 nm, respectively, while that of Na-mmt is only 1.22 nm. BET surface areas of Al-PILC and AlCe-PILC are 202.8 and 343.6–377.4 m<sup>2</sup>/g, respectively, while that of Na-mmt is only 61.9 m<sup>2</sup>/g. The above results suggest that the basal spacing is greatly enlarged and BET surface area is obviously increased after Al or Al/Ce pillaring.

The high-resolution transmission electron microscopy (HRTEM) images of Na-mmt and AlCe-PILC (5;30) are depicted in Fig. 9.13. It can be learned that

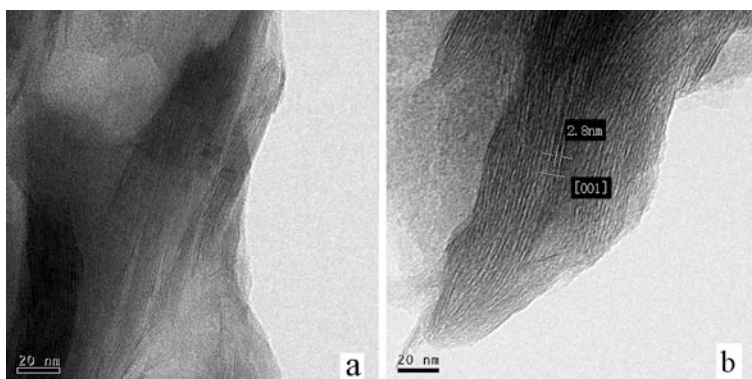
**Table 9.2** Surface area, total pore volume,  $A_{mes}$ , and basal spacing for all supports

Supports	BET surface area (m <sup>2</sup> /g) <sup>a</sup>	Total pore volume (cm <sup>3</sup> /g) <sup>b</sup>	$A_{mes}$ (m <sup>2</sup> /g) <sup>c</sup>	$2\theta$ (°)/basal spacing (nm)
Na-mmt	61.9	0.1196	61.8	7.28/1.22
Al-PILC	202.8	0.1677	88.3	5.41/1.72
AlCe-PILC (5;5)	343.6	0.2270	127.4	4.82/1.83
AlCe-PILC (5;10)	354.6	0.2361	138.6	4.78/1.85
AlCe-PILC (5;20)	360.7	0.2287	206.5	4.16/2.12
AlCe-PILC (5;30)	366.4	0.2023	279.7	3.12/2.83
AlCe-PILC (2.5;30)	377.4	0.2440	136.5	4.86/1.82
AlCe-PILC (7.5;30)	371.2	0.2244	223.7	3.90/2.26
AlCe-PILC (10;30)	377.4	0.2421	199.5	4.26/2.07
AlCe-PILC (20;30)	372.8	0.2411	184.5	4.94/1.79

<sup>a</sup>Calculated by BET surface area.

<sup>b</sup>Calculated from the Barrett-Joyner-Halenda (BJH) method.

<sup>c</sup>Calculated from the  $t$ -plot.

**Fig. 9.13** HRTEM images of (a) Na-mmt and (b) AlCe-PILC (5;30)

Na-mmt has a layered structure and a two-dimension porous structure with small basal spacing. For AlCe-PILC (5;30) the layers were obviously kept apart, obtaining large pore structures, and the basal spacing between two neighboring fringes is about 2.8 nm, corresponding to the  $d_{001}$  spacing.

The light-off curves of benzene deep oxidation over Pd catalysts are shown in Fig. 9.14. It can be concluded that the catalytic activity of Pd catalysts in benzene deep oxidation is greatly dependent on the type of supports. The activity of Pd supported on Na-mmt is very low, and the temperature for the complete benzene conversion exceeds 400 °C. Pd supported on Al-PILC and AlCe-PILC presents considerably higher activities than that on Na-mmt. The temperature for the complete benzene conversion decreases in the order: Pd/Na-mmt(>400 °C)>Pd/Al-PILC(340 °C)>Pd/AlCe-PILC (≤300 °C). This indicates that pillaring and addition of Ce are very important for improving the activity of catalysts.



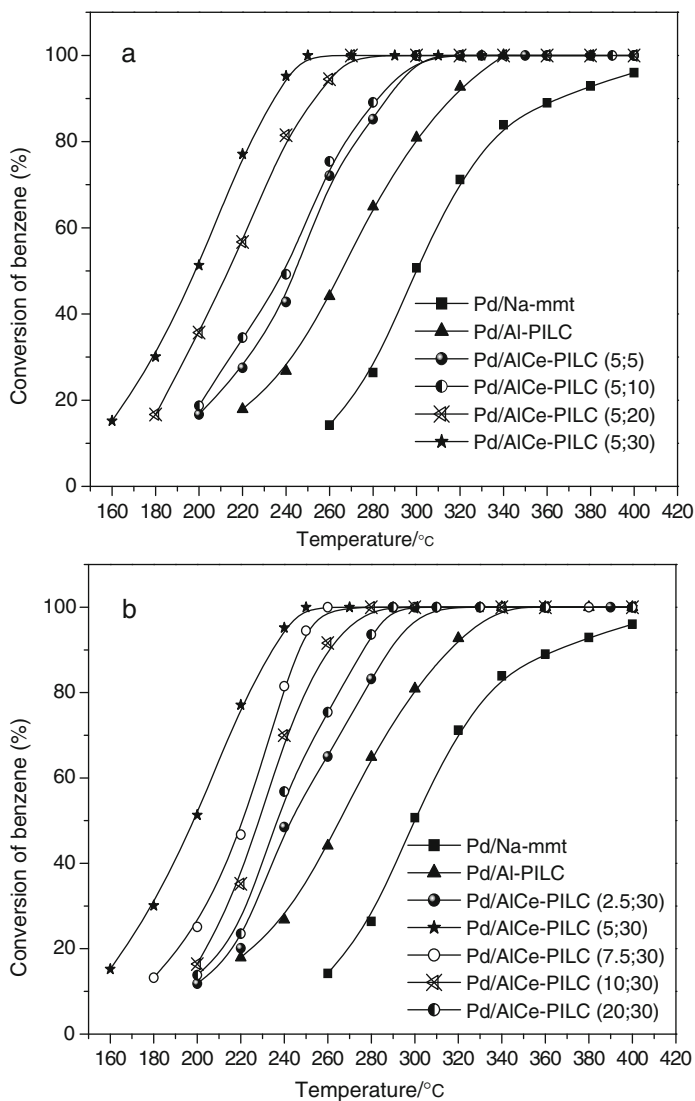


**Fig. 9.14** Light-off curves for benzene deep oxidation over (a) Pd/Na-mmt, Pd/Al-PILC, and Pd/AlCe-PILC ( $R = 5$ ;  $T = 5, 10, 20, 30$ ) and (b) Pd/Na-mmt, Pd/Al-PILC, and Pd/AlCe-PILC ( $R = 2.5, 5, 7.5, 10, 20$ ;  $T = 30$ )

The hydrothermally treated time and different loadings of Ce of Al/Ce pillaring solution obviously influence the activity of Pd/AlCe-PILC catalysts for benzene oxidation. Activity of the catalysts with different hydrothermally treated time decreases in the order: Pd/AlCe-PILC (5;30) > Pd/AlCe-PILC (5;20) > Pd/AlCe-PILC (5;10) > Pd/AlCe-PILC (5;5), and the activity of the catalysts with different

loadings of Ce decreases in the order: Pd/AlCe-PILC (5;30)>Pd/AlCe-PILC (7.5;30)>Pd/AlCe-PILC (10;30)>Pd/AlCe-PILC (20;30)>Pd/AlCe-PILC (2.5;30). So they suggest that high  $A_{mes}$  and large pore structures of the supports are the key factors in improving the activity of Pd/AlCe-PILC catalysts for benzene deep oxidation.

The evolution with time-on-stream of benzene conversion at 300 °C for Pd/Na-mmt, Pd/Al-PILC, and at 240 °C for Pd/AlCe-PILC(5;30) is reported in Fig. 9.15. It can be learned that the activity of the catalysts was measured within 24 h time-on-stream and during this period, no significant catalyst deactivation was observed. At temperatures of around 250 °C the benzene conversion efficiency with Pd/AlCe-PILC (5;30) remained above 99% and no deactivation of catalyst occurred after 100 h of operation. This result indicated that in the present study, the Pd catalysts supported on different type of supports exhibit a good maintenance of catalytic activity.

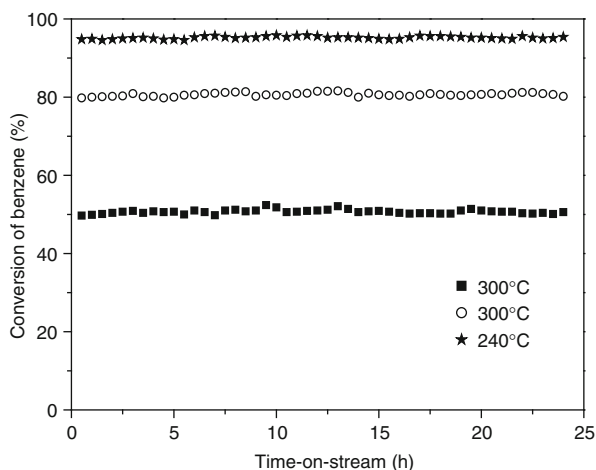


**Fig. 9.15** Evolution of benzene conversion with time-on-stream for Pd/Na-mmt (■) at 300 °C, Pd/Al-PILC (○) at 300 °C, and Pd/AlCe-PILC(5;30) (★) at 240 °C

### 9.3 Pillared Clay-Supported Metal Oxide Catalysts for Complete Oxidation of VOCs

Recently, metal oxide-based catalysts such as  $\text{Cr}_2\text{O}_3$  and  $\text{CuO}$  [46, 47] are increasingly applied in combustion systems in order to reduce costs associated with catalyst invention. Several studies have shown that manganese oxides,  $\text{MnO}_2$ ,  $\text{Mn}_3\text{O}_4$ , and  $\alpha\text{-Mn}_2\text{O}_3$ , absorb oxygen in oxidizing atmospheres and are active and stable catalysts for the combustion of organic compounds [48–50]. Among metal oxides, it is well known that  $\text{CeO}_2$  is a structural-promoting component. It enhances the metal dispersion and participates in stabilization of the support against thermal

sintering [51, 52]. CeO<sub>2</sub>-based catalysts are used for environmental purposes due to the unusual redox behavior of ceria and its high oxygen storage/transport capacity (OSC) [53].

In their researches, Li et al. [54] introduced an innovative approach to synthesize mesoporous clay compositions containing diverse well-dispersed transition metal oxides by using nanoparticles of hydroxide species as precursors, which were prepared by dissolving the corresponding metal hydroxides in aqueous solution of acetic acid. The prepared metal oxide–clay composites have surface areas of 510–640 m<sup>2</sup>/g. The reaction between the acidic precursor solutions and the silicate platelets resulted in a more delaminated structure in the products, leading to the increase of the surface areas and pore volumes of the clay. Co-containing clay composite prepared by the introduced method is more active than the impregnated cobalt catalysts in the deep oxidation of benzene. The fine dispersion of the nanoparticles and the developed mesoporosity of the composites are proposed to be responsible for its good catalytic behavior.

Figure 9.16 shows the ignition curves for the deep oxidation of benzene over clay composite catalysts containing cobalt oxide. Though the content of cobalt in Co-Lap is only ca. 2%, its activity toward the oxidation of benzene is much more superior to the impregnated cobalt catalysts supported on alumina–clay composites with a loading of even up to 10%. On Co-Lap, complete oxidation of benzene can be achieved at less than 300 °C, in contrast, on the other catalysts, complete conversion of benzene was not obtained even when the reaction temperature was raised to 400 °C. Impregnation is one of the most commonly used methods to prepare catalysts. However, this method has a drawback that metal oxides aggregate during the evaporation of impregnated solutions. In addition, the aggregated metal species can cause the blockage of the porosity of the support materials, exhibiting hindrance for the reaction molecules to approach the inner active phases [55]. In

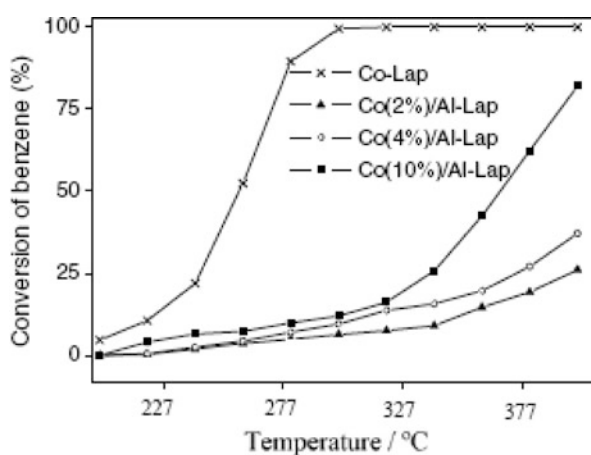
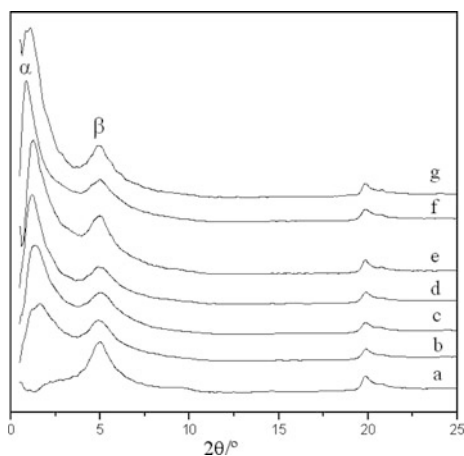


Fig. 9.16 Conversion curves of benzene over various cobalt-containing catalysts

contrast, the growth of the metal oxides was effectively controlled in the synthesis of clay composites by the new method, which insured a large active surface area or other special properties [56–58]. Moreover, the clay composites have developed mesoporosity, which favors the diffusion of reaction molecules. Thus the Co-Lap composite is fairly active in the deep oxidation of volatile organic compounds in comparison to the impregnated cobalt catalysts.

Zuo et al. used Al-PILC to support transition metals ( $M = \text{Cr, Mn, Fe, Co, Ni, and Cu}$ ) and Ce (8 wt%) for the deep oxidation of benzene and investigated the effect of Ce addition to M/Al-PILC. Activity tests show that Mn-based catalysts were the most active among the transition metals and adding Ce obviously improved the activity of M/Al-PILC. Moreover, Ce content had a great effect on the activity of MnCe/Al-PILC. MnCe (18:1)/Al-PILC exhibited the highest activity, and the temperature for the complete benzene conversion using this catalyst was about 310 °C.

Figure 9.17 shows the XRD patterns of M/Ce (6:1)/Al-PILC between 0.5 and 25°. Table 9.3 gives the basal spacing data and value ratios of peak  $\alpha$ /peak  $\beta$ . The



**Fig. 9.17** XRD patterns of the catalysts between 0.5 and 25°. (a) Al-PILC, (b) CuCe (6:1)/Al-PILC, (c) CrCe (6:1)/Al-PILC, (d) MnCe (6:1)/Al-PILC, (e) NiCe (6:1)/Al-PILC, (f) FeCe (6:1)/Al-PILC, and (g) CoCe (6:1)/Al-PILC

**Table 9.3** XRD patterns and value ratios of peak  $\alpha$ / peak  $\beta$  of the samples calcined at 500 °C for 2 h

Samples	Peak $\alpha$ ( $2\theta/d$ ) (nm)	Peak $\beta$ ( $2\theta/d_{001}$ ) (nm)	Value ratio of peak $\alpha$ /peak $\beta$
Al-PILC	–	4.97/1.78	–
CrCe (6:1)/Al-PILC	1.36/8.82	5.02/1.76	5.0
MnCe (6:1)/Al-PILC	1.18/7.48	4.90/1.80	4.1
FeCe (6:1)/Al-PILC	0.84/10.5	4.96/1.78	5.9
CoCe (6:1)/Al-PILC	0.98/9.0	4.92/1.79	5.0
NiCe (6:1)/Al-PILC	1.24/7.12	4.96/1.78	4.0
CuCe (6:1)/Al-PILC	1.62/5.45	4.90/1.80	3.0

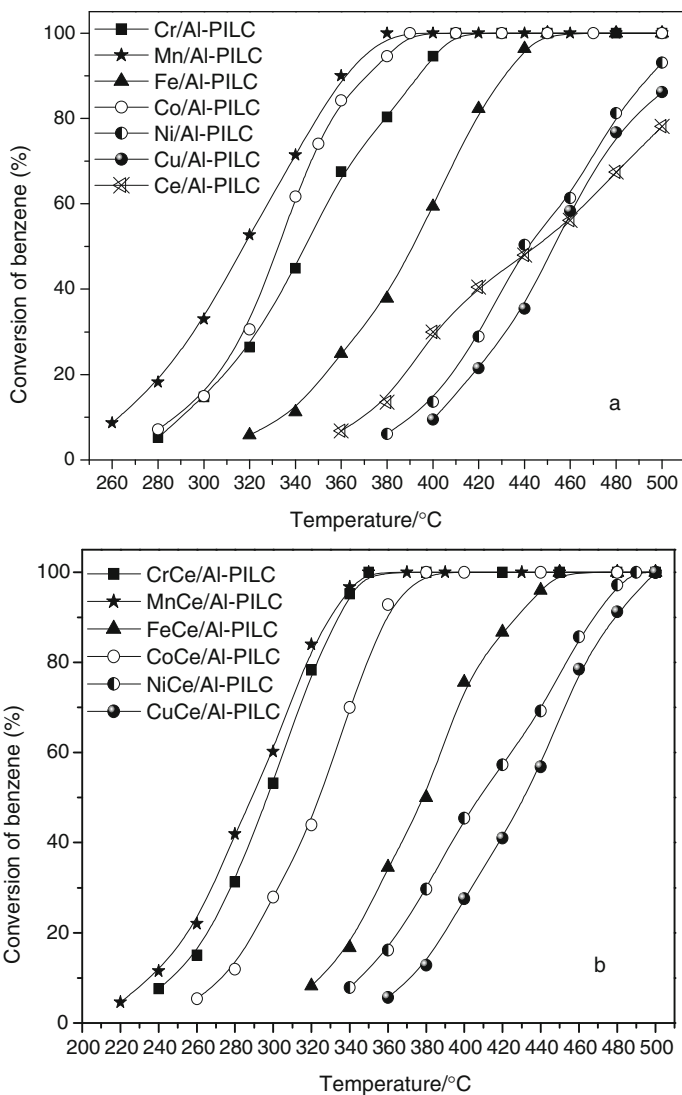


**Fig. 9.18** Benzene conversion as a function of temperature on M/Al-PILC (a) and M/Ce (6:1)/Al-PILC (b)

values of peak  $\beta$  ( $d_{001}$ ) of M/Ce (6:1)/Al-PILC were similar to that of Al-PILC, which indicates that the layered structure is well preserved. It is interesting that, after impregnating transition metals and Ce, a peak was observed between  $2\theta$  angles of  $0.84^\circ$  and  $1.62^\circ$ , and what's more, value ratios of peak  $\alpha$ /peak  $\beta$  were about 3, 4, 5, and 6. Based on the previous research [28], it could be deduced that four, five, six, and seven orderly arranged clay layers formed a super structure (Fig. 9.2). And the super structure could strengthen the interaction between the active species and the support.

To survey the most active catalyst among (Cr, Mn, Fe, Co, Ni, Cu and Ce)/Al-PILC, complete oxidation reactions of benzene were performed and the conversion as a function of temperature was shown in Fig. 9.18a. In the case of Ce/Al-PILC, Cu/Al-PILC, and Ni/Al-PILC, the conversions were negligibly low and they were less than 95% even at a reaction temperature of 500 °C. In the case of Mn/Al-PILC, Co/Al-PILC, and Cr/Al-PILC, the conversions were 52.7, 30.6, and 26.4%, respectively, at a reaction temperature of 320 °C and more than 98% at a reaction temperature of 400 °C. The activity of M/Al-PILC with respect to metal was observed to follow the sequence: Mn>Co>Cr>Fe>Ni>Cu>Ce.

Figure 9.18b shows benzene conversion as a function of temperature on M/Ce (6:1)/Al-PILC. Adding Ce obviously improved the activity of M/Al-PILC. The authors suggested that introduction of Ce into M/Al-PILC improved the dispersion of transition metals, especially for Mn-based catalyst, and induced the formation of anionic vacancies which increases the ability of the catalysts to accumulate oxygen and improves an oxygen exchange at low temperatures. So during the reaction process, CeO<sub>2</sub> could provide the active oxygen species to metal oxide, thus enhancing the oxidation ability of metal oxide.

Figure 9.19 shows the effect of Mn/Ce molar ratios on benzene deep oxidation over MnCe/Al-PILC. From these results, it is deduced that Mn/Ce molar ratios have a significant impact on the catalytic activity of MnCe/Al-PILC. The catalysts exhibited a relatively low activity when Mn/Ce ratio <6, which is caused by the fact that Mn is the active species while Ce acts as a promoting component. The catalyst activity was slightly decreased when Mn/Ce molar is >18, which is due to the fact that decrease of the amount of CeO<sub>2</sub> results in the lack of oxygen vacancies. Therefore, catalyst with high content of Mn and proper Ce content exhibits high activity. MnCe (18:1)/Al-PILC exhibited the highest activity, and the temperature for the complete benzene conversion using this catalyst was about 310 °C.

H<sub>2</sub>-Temperature programmed reduction (H<sub>2</sub>-TPR) profiles of MnCe/Al-PILC with different Mn/Ce ratios are shown in Fig. 9.20. As exemplified, no significant reduction processes take place in the case of Al-PILC support (not shown). The reduction of Mn/Al-PILC starts at about 200 °C and two strong overlapped reduction peaks at 371 and 455 °C are observed. Kapteijn et al. [59, 60] and Boot et al. [61] reported that for the catalysts prepared from impregnation with Mn (II) nitrate solutions, both MnO<sub>2</sub> and Mn<sub>2</sub>O<sub>3</sub> are reduced, without intermediate transformation, first in one step to Mn<sub>3</sub>O<sub>4</sub> and in a second step to MnO. In the case, it is found that an O/Mn stoichiometry for Mn/Al-PILC from TPR is about 1.6, which is between those of MnO<sub>2</sub> and Mn<sub>2</sub>O<sub>3</sub> and suggests a relatively high presence of Mn<sub>2</sub>O<sub>3</sub> in the catalyst.

Compared with Mn/Al-PILC, the reduction peaks of MnCe/Al-PILC with different Mn/Ce ratios systematically shift to lower temperatures, indicating that, on the one hand, Mn oxides with higher dispersion and smaller crystal size are easily reduced; on the other hand, Ce addition can change the redox properties of Mn oxide and make it easier to be reduced by the interaction between the two oxides, increasing lattice oxygen lability [62] with the promotion of the oxidation activity. Moreover, the area ratio of first to second peak also increases after adding Ce, revealing that more manganese oxide species are in higher oxidation states. So, Zuo

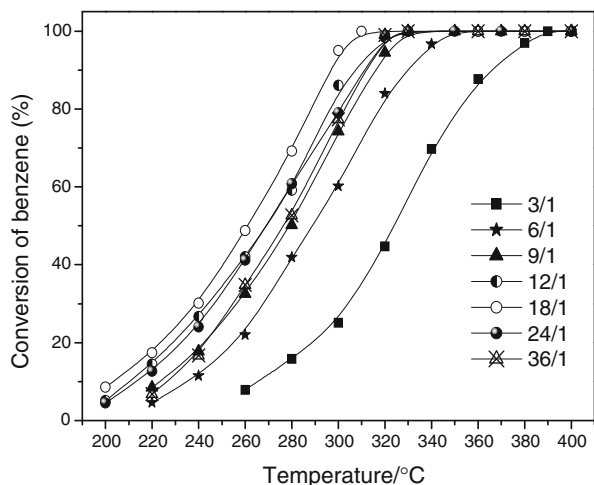
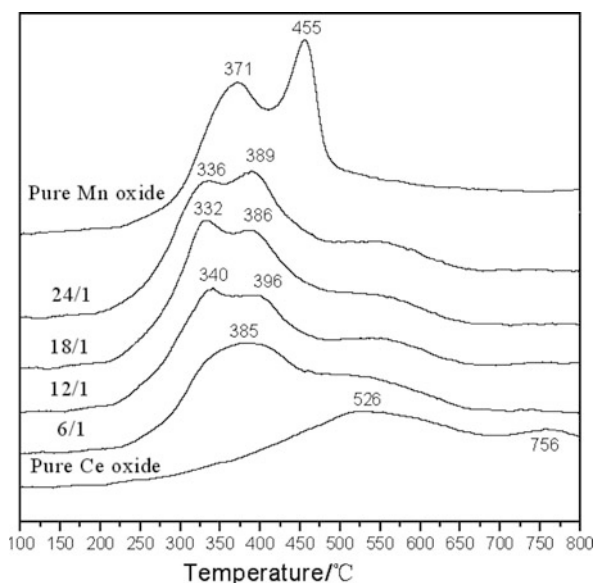
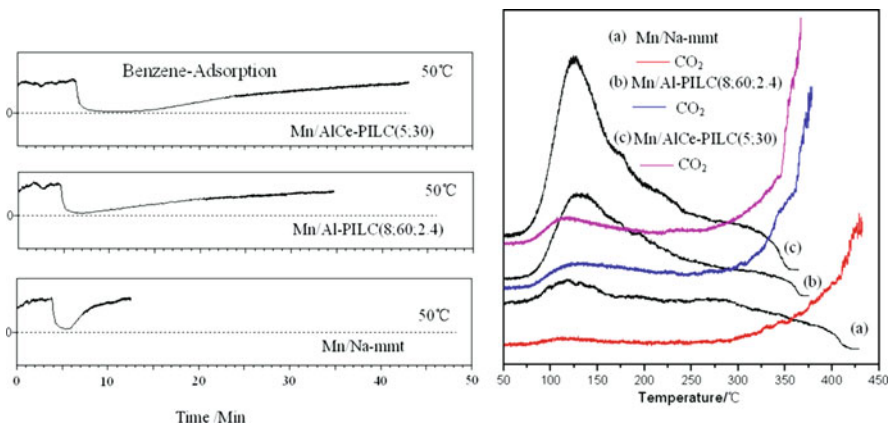


Fig. 9.19 Effect of Mn/Ce molar ratios on benzene deep oxidation over MnCe/Al-PILC

Fig. 9.20 TPR profiles for MnCe/Al-PILC with different Mn/Ce ratios. Consecutively from *bottom* to *top*, supported samples are pure Ce oxide, Mn/Ce 6/1, Mn/Ce 12/1, Mn/Ce 18/1, Mn/Ce 24/1, and Mn oxide ( $\text{Mn}_2\text{O}_3$  and  $\text{MnO}_2$ )



et al. concluded that the trend of the area ratio of the first to the second peak and the reduction temperatures are related to catalyst oxidation activity. That is, MnCe/Al-PILC catalysts with higher manganese oxide state and lower reduction temperature in TPR experiment have higher catalytic activities.



**Fig. 9.21** TPSR profiles of the catalysts calcined at 500 °C for 2 h

Figure 9.21 is the temperature-programmed surface reaction (TPSR) carried out in the same apparatus as the catalytic activity test analysis. It can be seen that the benzene adsorption ability of the catalysts is greatly dependent on the type of supports, and after pillaring, Al-PILC and AlCe-PILC have a pronounced increase in porosity and surface area compared to Na-mmt, and thus in adsorption. Zuo et al. [63] found that the temperature of desorption appears between 75 and 250 °C, and the peak temperature is at about 150 °C. The process of the catalytic oxidation is in accordance with activities of the catalysts.

In order to investigate the adsorption/desorption properties of the catalysts, Ar-TPD experiments are carried out. The results of adsorption in Ar and in Air (Fig. 9.21) atmosphere are in good agreement, which suggests that the existence of

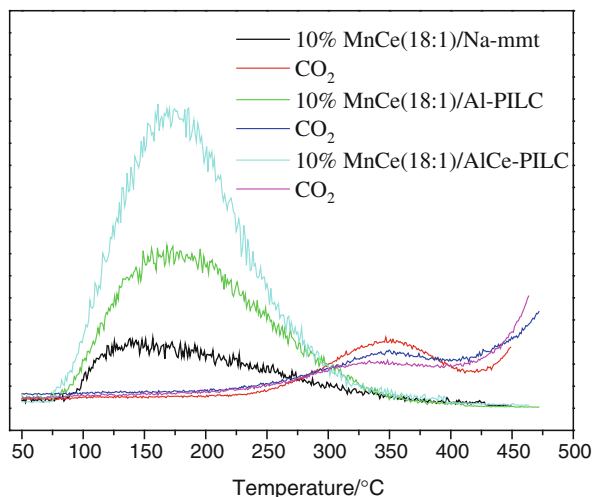


**Fig. 9.22** TPD profiles of the catalysts calcined at 500 °C for 2 h



CO<sub>2</sub> has no influence on the adsorption performance of the catalysts. Figure 9.22 shows the results of TPD experiment over the clays with different porous structure-supported Mn and Ce catalysts. It can be seen that the desorption temperature is between 75 and 250 °C, and the peak temperature is at about 175 °C, which is about 25 °C higher than that of the situation with 150 ppm benzene. This phenomenon illuminates that the interaction is very strong between the catalysts and benzene located in the sites of the interlayer space of clays. And it is very interesting that CO<sub>2</sub> peaks appear at about 230 °C, that is, catalytic oxidation takes place during the process of benzene desorption, which indicates that benzene catalytic oxidation occurs in Ar atmosphere due to the existence of the higher active lattice oxygen. This proves the oxidation reaction between the lattice oxygen and VOCs.

Huang et al. [64] investigated the catalytic activity of supported catalysts of five different supports (Na-mmt, Al-PILC, Zr-PILC, Ti-PILC, and 6%Al<sub>2</sub>O<sub>3</sub>/Ti-PILC) impregnated with an aqueous of Cr(NO<sub>3</sub>)<sub>3</sub>·9H<sub>2</sub>O and Ce(NO<sub>3</sub>)<sub>3</sub>·6H<sub>2</sub>O for deep oxidation of *n*-butylamine as a model molecule for VOCs. They found that the different catalytic activity is clearly related to the nature of the catalysts, and on the other hand, to the nature of the supports. In fact, porous structure and acidity of the catalysts play a crucial role in deep oxidation of VOCs.

In Fig. 9.23A, it can be seen that the activities of CrCe/M-PILC catalysts are obviously improved compared with CrCe/Na-mmt. Especially for 8%CrCe(6:1)/Ti-PILC and 8%CrCe(6:1)/6%Al<sub>2</sub>O<sub>3</sub>/Ti-PILC, they show much higher catalytic activity than the other three catalysts. The light-off temperatures (at ca. 10% conversion) of these two catalysts occur at about 120 °C, while for the other three ones occur at about 140 °C. The catalytic activity of these catalysts, on the base of T<sub>98</sub>, decreases in the order: CrCe (6:1)/6%Al<sub>2</sub>O<sub>3</sub>/Ti-PILC (260 °C) ≈ CrCe (6:1)/Ti-PILC (260 °C) > CrCe (6:1)/Zr-PILC (270 °C) > CrCe (6:1)/Al-PILC (280 °C) > CrCe (6:1)/Na-mmt (320 °C).

As is known, NO<sub>x</sub> is the common by-product during the deep oxidation of *n*-butylamine, which is the origin of photochemical smog that is harmful to human being and environment. So, NO<sub>x</sub> was monitored to confirm the catalytic activity of these catalysts. Figure 9.23B shows that at T<sub>98</sub>, the yield of NO<sub>x</sub> over all the catalysts is low, even the reaction temperature rises 50 °C, the yield remains below 2%, which indicates that all the catalysts have a good restraint ability of NO<sub>x</sub>.

They summarized, among the catalysts, that Ti-PILC and 6%Al<sub>2</sub>O<sub>3</sub>/Ti-PILC with (a) more mesopore structure, which favors high dispersion of active phases; (b) more weaker acid sites, as a result of highly dispersion of active phases on supports with Lewis acid sites show higher catalytic activity than the other three catalysts.

In the work of Gil et al. [21, 65], complete oxidation of acetone has been studied over a series of manganese oxide catalysts (about 10 wt%) supported on the unpillared and the Al- and Zr-pillared forms of two natural clays of the smectite class (a montmorillonite and a saponite). The temperatures required for total combustion of acetone over the several catalysts ranged from 337 to 387 °C at the relatively low Mn/F<sub>in</sub> ratio of 0.40 gMn min mmol<sup>-1</sup> acetone used. A significant influence of clay supports characteristics on the catalytic performance has been found.

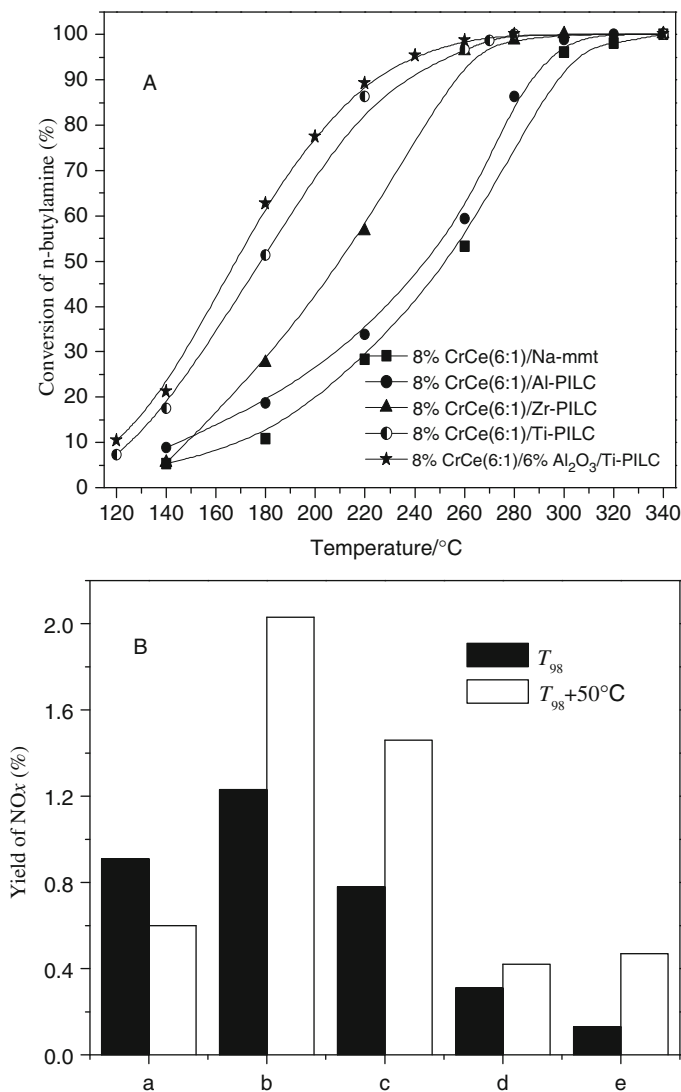
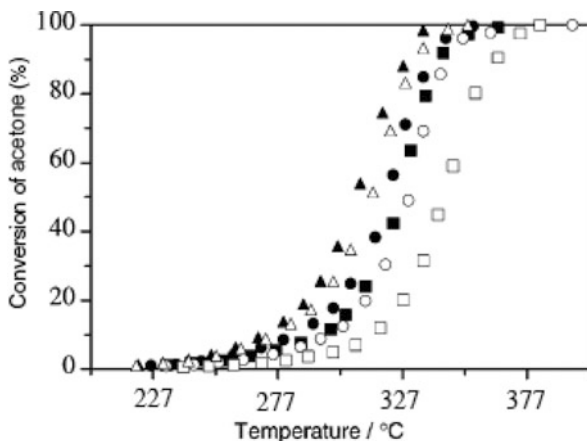


**Fig. 9.23** (A) Light-off curves for deep oxidation of *n*-butylamine and (B) column graph of NO<sub>x</sub> yield over (a) 8%CrCe (6:1)/Na-mmt; (b) 8%CrCe (6:1)/Al-PILC; (c) 8%CrCe (6:1)/Zr-PILC; (d) 8%CrCe (6:1)/Ti-PILC; (e) 8%CrCe (6:1)/6%Al<sub>2</sub>O<sub>3</sub>/Ti-PILC

The light-off curves for acetone complete oxidation over the several manganese oxide catalysts are shown in Fig. 9.24. The acetone conversion values plotted in this figure were calculated through the CO<sub>2</sub> appearance data and they were in very good accordance with the ones obtained from the acetone removal data. As it can be seen, the temperatures required for total combustion of acetone range between 337 °C over Mn/GAmont-Zr and 365 °C over Mn/GAmont-Al. For Ballarat saponite-based

**Fig. 9.24** Light-off curves for acetone combustion over Mn/GAmont (●), Mn/GAmont-Al (■), Mn/GAmont-Zr (▲), Mn/BAsap (○), Mn/BAsap-Al (□), and Mn/BAsap-Zr (◻)



catalysts, these temperatures vary from 352 °C over Mn/BAsap-Zr to 387 °C over Mn/BAsap.

The light-off curves included in Fig. 9.24 reveal some interesting differences between the performances of the several Mn/PILC catalysts. It can be seen that the temperatures required to reach complete acetone conversion are somewhat lower over the manganese oxide catalysts supported on Gador montmorillonite than on Ballarat saponite. According to the general behavior of the various catalysts throughout the light-off experiments, the following order of improving catalytic performance can be established with respect to the pillars composition: Al-PILC < unpillared clays < Zr-PILC.

This effect is more pronounced in the case of the Ballarat saponite-based series of catalysts, as shown by the corresponding values of the temperature ( $T_{50}$  or light-off temperature) at which the conversion of the organic molecule reaches 50%. In fact, the temperature required to achieve acetone light-off is 315 °C over Mn/BAsap-Zr and 345 °C over Mn/BAsap-Al, whereas the difference between the light-off temperatures of the Mn/GAmont-Zr (310 °C) and Mn/GAmont-Al (325 °C) catalysts is reduced to 15 °C. Similarly,  $T_{10}$  and  $T_{90}$  can also be defined for the temperatures at which the acetone conversion reaches 10 and 90%, respectively.

Storaro et al. [66] studied the catalytic behavior of Cr-doped Al-PILC (ACrPA) and a series of Cr-PILC materials (XSCr) for the deep oxidation of methylene chloride. Both types of catalysts showed a high activity (conversion >80%) at  $T > 350$  °C. The ACrPA sample showed a virtually constant catalytic activity (conversion >99%) in the 300–400 °C temperature range while the activity of the XSCr samples markedly increased with the temperature reaching an almost total conversion at 400 °C. The metal oxidation state of the two chromium-based systems seemed to be important in determining the catalytic activity. The increase of the activity with the Cr content in XSCr samples suggested that the acid sites in these catalysts were located on the chromia pillars.

## 9.4 Pillared Clays as Catalysts for Complete Oxidation of VOCs

In the work of Gil et al. [67], Cr–Al-pillared saponites were used as catalysts in the deep oxidation of acetone. All Cr, Al-pillared saponites were active catalysts for the complete oxidation of acetone, reaching 100% conversion at temperatures ranging from 400 to 340 °C. A significant effect of the  $\text{Al}^{3+}/\text{Cr}^{3+}$  ratio of the pillared clay on the catalytic activity has been found. The combined effect of this ratio on the Cr dispersion and PILC-specific surface area as well as the saponite intrinsic activity seem to be the main factors that control catalytic activity.

Mata et al. [68] prepared Cr-saponite catalysts by two synthesis procedures. The first method consisted in the intercalation of the saponite with solutions containing Al and Cr oligomers with various molar ratios, while the second one consisted in the incipient wetness impregnation of Al-pillared saponite with several chromium salts, ammonium chromate, Cr (II) acetate, and Cr (III) nitrate (8 wt% of  $\text{Cr}_2\text{O}_3$ ). The catalysts have been tested in the oxidation of propene, showing a catalytic behavior according to the Mars-van Krevelen mechanism, the performance not depending on the method in which Cr was incorporated into the clay.

The results obtained for the oxidation of propene, in presence of oxygen, are shown in Fig. 9.25. The conversion of propene reaches values of 100% for all the catalysts studied at 400 °C independent of the amount of Cr incorporated into the clay in the pillaring or impregnation processes. The effect of Cr amount only is apparent at lower temperatures. At 300 °C the increase of Cr percent slightly improves the propene conversion. This suggests that low amounts of Cr are effective for the propene oxidation reaction. The catalytic performance of Al-pillared clay is very low, even at high temperatures, indicating that the behavior of the catalysts evaluated is mainly due to the Cr species incorporated to the pillared clay. The pillared and the impregnated solids have the same behavior, indicating that

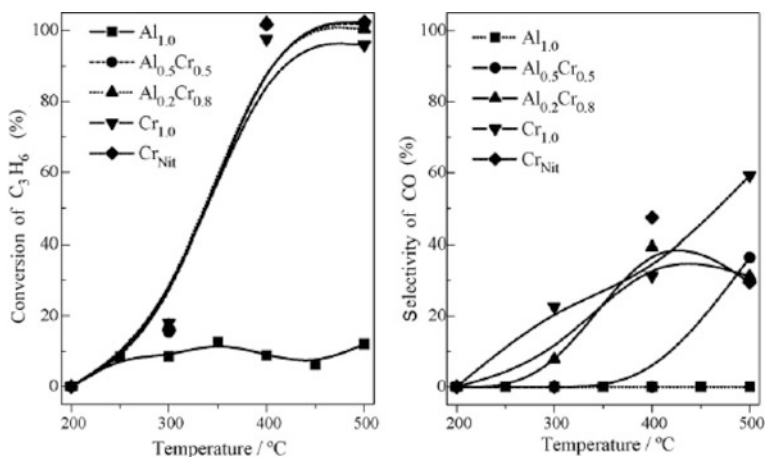
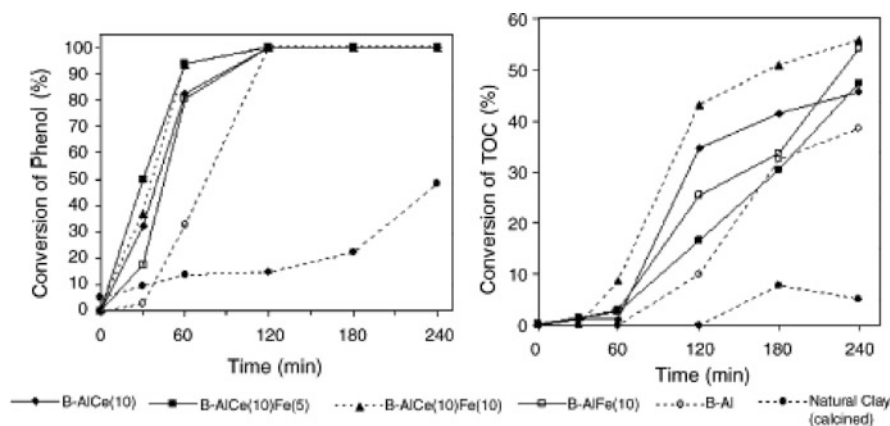


Fig. 9.25 Conversion of propene and selectivity to CO for propene oxidation

the catalytic performance does not depend on the method in which Cr was incorporated. This element acts as the active phase in oxidation reactions, both if it is mainly located in the interlayer region and on the external surface of the clay. At 350 °C CO is detected together with CO<sub>2</sub> as reaction products. The CO selectivity reached at 500 °C is 40% for all the samples studied, except for the Cr1.0–500 sample, which reached 60% CO selectivity.

In the study of Carriazo et al. [69, 70], a Colombian bentonite was modified by intercalation with polyhydroxocationic solutions of Al<sup>3+</sup> containing Fe<sup>3+</sup> and Ce<sup>3+</sup>. Addition of these solutions led to the formation of PILCs with important catalytic properties in three environmental impact reactions: phenol oxidation in diluted aqueous medium, oxidation of CO, and 2-propanol oxidation in gas phase. The catalytic tests revealed the activity of the introduced iron species and the promoter effect of the cerium on the catalytic activity of these species.

Figure 9.26 shows the main results of the catalytic activity for solids in the phenol oxidation reaction. The starting natural clay presents a very low activity (phenol conversion) and no selectivity to CO<sub>2</sub>, due to the absence of active sites. Synthesized solids are excellent catalysts with an almost total transformation of phenol in less than an hour. The TOC conversion levels are high (up to 55%), giving proof of the almost complete mineralization of phenol and its intermediaries up to CO<sub>2</sub> and water. It is clear that the introduction of iron species leads to obtain more active solids, being BAlCe(10)Fe(10) sample the most active one. In this sense, it is well known that iron species (oxides or oxyhydroxides) are active species for this reaction [70–72]. However, the selectivity of these catalysts toward CO<sub>2</sub> and H<sub>2</sub>O is the lowest one among those obtained with modified solids, which could reveal differences in the distribution of the active species with respect to that of Fe-modified materials.



**Fig. 9.26** Catalytic activity for PILCs in the oxidation of phenol (phenol conversion and TOC conversion) in diluted aqueous medium at atmospheric pressure and at 20 °C

## 9.5 Conclusions

In this review, we have examined some cases to discuss recent developments offered from pillared clay (PILC)-supported noble metal and metal oxide catalysts for deep oxidation of representative VOCs. Researches carried out up to now indicate that one of the more studied topics related to PILCs is their use as support for active catalytic phases in the preparation of supported catalysts, and the applicability of the resulting solids in environmental-friendly reactions. However, at the same time new challenges for catalysis given by these new applications have stimulated research to find new innovative solutions and technologies which will benefit all areas of catalysis as well as other industries.

**Acknowledgments** We gratefully acknowledge the financial supports from the Ministry of Science and Technology of China (no. 2004 CB 719504) and Nature Science Foundation of China (no. 20577043).

## References

1. Spivey JJ (1987) Complete catalytic oxidation of volatile organics. *Ind Eng Chem Res* 26:2165
2. Armor JN (1991) New catalytic technology commercialized in the USA during the 1980's. *Appl Catal* 78:141
3. Spivey JJ, Butt JB (1991) Literature review: deactivation of catalysts in the oxidation of volatile organic compounds. *Catal Today* 11:465
4. Dégé P, Pinard L, Magnoux P, Guisnet M (2000) Catalytic oxidation of volatile organic compounds: II. Influence of the physicochemical characteristics of Pd/HFAU catalysts on the oxidation of *o*-xylene. *Appl Catal B* 27:17
5. Wu JC-S, Lin Z-A, Pan J-W, Rei M-H (2001) A novel boron nitride supported Pt catalyst for VOC incineration. *Appl Catal A* 219:117
6. Carpentier J, Lamonier J-F, Siffert S, Zhilinskaya EA, Aboukaïs A (2001) Characterisation of Mg/Al hydrotalcite with interlayer palladium complex for catalytic oxidation of toluene. *Appl Catal A* 234:91
7. Kim SC (2002) The catalytic oxidation of aromatic hydrocarbons over supported metal oxide. *J Hazard Mater B* 91:285
8. Prasad R, Kennedy LA, Ruckenstein E (1984) Catalytic combustion. *Catal Rev Sci Eng* 26:1
9. Łojewska J, Kołodziej A, Żak J, Stoch J (2005) Pd/Pt promoted  $\text{Co}_3\text{O}_4$  catalysts for VOCs combustion: preparation of active catalyst on metallic carrier. *Catal Today* 105:655
10. Chen M, Zheng X-M (2004) The effect of K and Al over  $\text{NiCo}_2\text{O}_4$  catalyst on its character and catalytic oxidation of VOCs. *J Mol Catal A* 221:77
11. López-Fonseca R, Gutiérrez-Ortiz JI, Gutiérrez-Ortiz MA, González-Velasco JR (2002) Catalytic combustion of chlorinated ethylenes over H-zeolites. *J Chem Technol Biotechnol* 78:15
12. Okumura K, Kobayashi T, Tanaka H, Niwa M (2003) Toluene combustion over palladium supported on various metal oxide supports. *Appl Catal B* 44:325
13. Dong G, Wang J, Bao Y, Chen S (1999) A novel catalyst for CO oxidation at low temperature. *Catal Lett* 58:37
14. Kapoor MP, Ichihashi Y, Shen W, Matsumura Y (2001) Catalytic activity of palladium supported on mesoporous zirconium oxide in low-temperature methanol decomposition. *Catal Lett* 76:139

15. Lin W, Lin L, Zhu Y, Xie Y, Scheurell K, Kemnitz E (2005) Novel Pd/TiO<sub>2</sub>-ZrO<sub>2</sub> catalysts for methane total oxidation at low temperature and their <sup>18</sup>O-isotope exchange behavior. *J Mol Catal A* 226:263
16. Gil A, Vicente MA, Gandía LM (2000) Main factors controlling the texture of zirconia and alumina pillared clays. *Micropor Mesopor Mater* 34:115
17. Narui K, Yata H, Furuta K, Nishida A, Kohtoku Y, Matsuzaki T (1999) Effects of addition of Pt to PdO/Al<sub>2</sub>O<sub>3</sub> catalyst on catalytic activity for methane combustion and TEM observations of supported particles. *Appl Catal A* 179:165
18. Gandía LM, Vicente MA, Gil A (2000) Preparation and characterization of manganese oxide catalysts supported on alumina and zirconia-pillared clays. *Appl Catal A* 196:28
19. Gil A, Vicente MA, Lambert J-F, Gandía LM (2001) Platinum catalysts supported on Al-pillared clays: application to the catalytic combustion of acetone and methyl-ethyl-ketone. *Catal Today* 68:41
20. Yang L, Shi C, He X, Cai J (2002) Catalytic combustion of methane over PdO supported on Mg-modified alumina. *Appl Catal B* 38:117
21. Gil A, Vicente MA, Korili SA (2006) Effect of the nature and structure of pillared clays in the catalytic behaviour of supported manganese oxide. *Catal Today* 112:117
22. Marín-Astorga N, Alvez-Manoli G, Reyes P (2005) Stereoselective hydrogenation of phenyl alkyl acetylenes on pillared clays supported palladium catalysts. *J Mol Catal A* 226:81
23. Jennings MS, Krohn NE, Berry RS, Palazzolo MA, Parks RM, Fidler KK (1985) Catalytic incineration for control of VOC emissions. Noyes Publications, Park Ridge, NJ American Institute of Chemical Engineers, New York, NY
24. Mukhopadhyay N, Moretti EC (1993) Current and potential future industrial practices for reducing and controlling volatile organic compounds, center for waste reduction technologies. American Institute of Chemical Engineers, New York, NY
25. Spivey JJ (1989) Catalysis, vol 8. The Royal Society of Chemistry, Cambridge, UK, p 157
26. Zwinkels MFM, Järås SG, Menon PG, Griffin TA (1993) Catalytic materials for high-temperature combustion. *Catal Rev* 35:319
27. Zuo S-F, Zhou R-X (2006) Al-pillared clays supported rare earths and palladium catalysts for deep oxidation of low concentration of benzene. *Appl Surf Sci* 253:2508
28. Zuo S-F, Zhou R-X (2008) Influence of synthesis condition on pore structure of Al pillared clays and supported Pd catalysts for deep oxidation of benzene. *Micropor Mesopor Mater* 113:472
29. Gandía LM, Vicente MA, Gil A (2000) Preparation and characterization of manganese oxide catalysts supported on alumina and zirconia-pillared clays. *Appl Catal A* 196:281
30. Tettenhorst R (1962) Cation migration in montmorillonites. *Am Mineral* 47:769
31. Hutson ND, Gualdoni DJ, Yang RT (1998) Synthesis and characterization of the microporosity of ion-exchanged Al<sub>2</sub>O<sub>3</sub>-pillared clays. *Chem Mater* 10:3707
32. Wu X, Xu L, Weng D (2004) The thermal stability and catalytic performance of Ce-Zr promoted Rh-Pd/ $\gamma$ -Al<sub>2</sub>O<sub>3</sub> automotive catalysts. *Appl Surf Sci* 221:375
33. Descorme C, Taha R, Mouaddib-Moral N, Duprez D (2002) Oxygen storage capacity measurements of three-way catalysts under transient conditions. *Appl Catal A* 223:287
34. Li J-J, Jiang Z, Hao Z-P, Xu X-Y, Zhuang Y-H (2005) Pillared laponite clays-supported palladium catalysts for the complete oxidation of benzene. *J Mol Catal A* 225:173
35. Chen M, Qi L-Y, Fan L-P, Zhou R-X, Zheng X-M (2008) Polyamine/Li<sub>0.25</sub>Ni<sub>0.5</sub>LaxFe<sub>2.25-x</sub>O<sub>4</sub> nanocomposites: preparation and tailoring the magnetic property. *Mater Lett* 62:3646
36. Oliveira LCA, Lago RM, Fabris JD, Sapag K (2008) Catalytic oxidation of aromatic VOCs with Cr or Pd-impregnated Al-pillared bentonite: byproduct formation and deactivation studies. *Appl Clay Sci* 39:218
37. Pina MP, Irusta S, Menéndez M, Santamaría J, Hughes R, Boag N (1997) Combustion of volatile organic compounds over platinum-based catalytic membranes. *Ind Eng Chem Res* 36:4557

38. Ocelli ML (1986) New routes to the preparation of pillared montmorillonite catalysts. *J Mol Catal* 35:377
39. Bradley SM, Kydd RA (1991) A comparison of the thermal stabilities  $\text{Ga}_{13}$ ,  $\text{GaAl}_{12}$  and  $\text{Al}_{13}$ -pillared clay minerals. *Catal Lett* 8:185
40. Tang X, Shu WQ, Shen YF, Suib SL (1995) Preparation and characterization of pillared gallium aluminum clays with enriched pillars. *Chem Mater* 7:102
41. Hernando M.J, Pesquera C, Blanco C, Benito I, González F (1996) Differences in structural, textural, and catalytic properties of montmorillonite pillared with  $(\text{GaAl}_{12})$  and  $(\text{AlAl}_{12})$  polyoxycations. *Chem Mater* 8:76
42. Sterte J (1991) Preparation and properties of large-pore La-Al-pillared montmorillonite. *Clays Clay Miner* 39:167
43. McCauley JR (1988) Stable intercalated clays and preparation method. US Patent 4,818,737
44. Zuo S-F, Huang Q-Q, Zhou R-X Synthesis and characterization of Al and Al/REE pillared clays and supported Pd catalysts for benzene oxidation. Unpublished results
45. Zuo S-F, Huang Q-Q, Zhou R-X (2008) Al/Ce pillared clays with high surface area and large pore: synthesis, characterization and supported palladium catalysts for deep oxidation of benzene. *Catal Today* 139:88
46. Rotter H, Landau MV, Carrera M, Goldfarb D, Herskowitz M (2004) High surface area chromia aerogel efficient catalyst and catalyst support for ethylacetate combustion. *Appl Catal B* 47:111
47. Mazzocchi C, Kaddouri A (2003) On the activity of copper chromite catalysts in ethyl acetate combustion in the presence and absence of oxygen. *J Mol Catal A* 204–205:647
48. López-Fonseca R, Elizundia U, Landa I, Gutiérrez-Ortiz MA, González-Velasco JR (2005) Kinetic analysis of non-catalytic and Mn-catalysed combustion of diesel soot surrogates. *Appl Catal B* 61:150
49. Döbber D, Kiebling D, Schmitz W, Wendt G (2004)  $\text{MnO}_x/\text{ZrO}_2$  catalysts for the total oxidation of methane and chloromethane. *Appl Catal B* 52:135
50. Tang X, Xu Y, Shen W (2008) Promoting effect of copper on the catalytic activity of  $\text{MnO}_x$ - $\text{CeO}_2$  mixed oxide for complete oxidation of benzene. *Chem Eng J* 144:175
51. Dictor R, Roberts S (1989) Influence of ceria on alumina-supported rhodium: observations of rhodium morphology made using FTIR spectroscopy. *J Phys Chem B* 93:5846
52. Martínez-Arias A, Fernández-García M, Salamanca LN, Valenzuela RX, Conesa JC, Soria J (2000) Structural and redox properties of ceria in alumina-supported ceria catalyst supports. *J Phys Chem B* 104:4038
53. Trovarelli A, Boaro M, Rocchini E, De Leitenburg C, Dolcetti G (2001) Some recent developments in the characterization of ceria-based catalysts. *J Alloys Compd* 323:584
54. Li J-J, Mu Z, Xu X-Y, Tian H, Duan M-H, Li L-D, Hao Z-P, Qiao S-Z, Lu G-Q (2008) A new and generic preparation method of mesoporous clay composites containing dispersed metal oxide nanoparticles. *Micropor Mesopor Mater* 114:214
55. Li J-J, Xu X-Y, Jiang Z, Hao Z-P, Hu C (2005) Nanoporous silica-supported nanometric palladium: synthesis, characterization, and catalytic deep oxidation of benzene. *Environ Sci Technol* 39:1319
56. Somorjai GA, Borodko YG (2001) Research in nanosciences – great opportunity for catalysis science. *Catal Lett* 76:1
57. Roucoux A, Schulz J, Patin H (2002) Reduced transition metal colloids: a novel family of reusable catalysts. *Chem Rev* 102:3757
58. Henry CR (2000) Catalytic activity of supported nanometer-sized metal clusters. *Appl Surf Sci* 164:252
59. Kapteijn F, Dick van Langeveld A, Moulijn JA, Andreini A, Vuurman MA, Turek AM, Jehng J-M, Wachs IE (1994) Alumina-supported manganese oxide catalysts: I. Characterization: effect of precursor and loading. *J Catal* 150:94
60. Kapteijn F, Singoredjo L, Andreini A, Moulijn JA (1994) Activity and selectivity of pure manganese oxides in the selective catalytic reduction of nitric oxide with ammonia. *Appl Catal B* 3:173



61. Boot LA, Kerkhoffs MHJVB, van der Linden Th, Jos van Dillen A, Geus JW, van Buren FR (1996) Preparation, characterization and catalytic testing of cobalt oxide and manganese oxide catalysts supported on zirconia. *Appl Catal A* 137:69
62. de Leitenburg C, Goi D, Primavera A, Trovarelli A, Dolcetti G. (1996) Wet oxidation of acetic acid catalyzed by doped ceria. *Appl Catal B* 11:L29
63. Zuo S-F, Huang Q-Q Zhou R-X (2009) Promoting effect of Ce added to metal oxide supported on Al pillared clays for deep benzene oxidation, *Appl Catal B* 91:204
64. Huang Q-Q, Zuo S-F, Zhou R-X (2010) Catalytic performance of pillared interlayered clays (PILCs) supported CrCe catalysts for deep oxidation of nitrogen-containing VOCs, *Appl Catal B* 95:327
65. Gandía LM, Vicente MA, Gil A (2002) Complete oxidation of acetone over manganese oxide catalysts supported on alumina- and zirconia-pillared clays. *Appl Catal B* 38:295
66. Storaro L, Ganzerla R, Lenarda M, Zanoni R, Antonio J, López J, Olivera-Pastor P, Castellón ER (1997) Catalytic behavior of chromia and chromium-doped alumina pillared materials for the vapor phase deep oxidation of chlorinated hydrocarbons. *J Mol Catal A* 115:329
67. Gil A, Vicente MA, Toranzo R, Bañares MA, Gandía LM (1998) Preparation, characterization and catalytic activity in the deep oxidation of acetone of Cr, Al-pillared saponites. *J Chem Technol Biotechnol* 72:131
68. Mata G, Trujillano R, Vicente MA, Belver C, Fernández-García M, Korili SA, Gil A (2007) Chromium-saponite clay catalysts: preparation, characterization and catalytic performance in propene oxidation. *Appl Catal A* 327:1
69. Carriazo JG, Centeno MA, Odriozola JA, Moreno S, Molina R (2007) Effect of Fe and Ce on Al-pillared bentonite and their performance in catalytic oxidation reactions. *Appl Catal A* 317:120
70. Carriazo JG, Guélou E, Barrault, J, Tatibouët J-M, Molina R, Moreno S (2005) Synthesis of pillared clays containing Al, Al-Fe or Al-Ce-Fe from a bentonite: characterization and catalytic activity. *Catal Today* 107–108:126
71. Catrinescu C, Teodosiu C, Macoveanu M, Miehé-Brendlé J, Le Dred R (2003) Catalytic wet peroxide oxidation of phenol over Fe-exchanged pillared beidellite. *Water Res* 37:1154
72. Chirchi L, Ghorbel A (2002) Use of various Fe-modified montmorillonite samples for 4-nitrophenol degradation by H<sub>2</sub>O<sub>2</sub>. *Appl Clay Sci* 21:271

# Chapter 10

## Clay Materials for Selective Catalytic Reduction of NO<sub>x</sub>

Carolina Belver

**Abstract** Interest in pillared interlayered clays (PILCs) has over the past decades been centered on their prospective industrial utilization in catalysis, sorption, and separations (air – gas mixtures, small hydrocarbons, multicomponent hydrocarbon mixtures, large organic molecules). In this chapter, the application of PILCs materials and other related ones (layered clays, LDHs, PCHs) in selective catalytic reduction of NO<sub>x</sub> will be tackled in detail.

**Keywords** Pillared clays · PILCs · Layered clays · LDHs · PCHs

### 10.1 Introduction

#### 10.1.1 NO<sub>x</sub> Definition

Urban air pollution, mostly generated by vehicles, industry, and energy production, is estimated to kill some 800,000 people yearly. This value has been estimated by the World Health Organization in the world death distribution map shown in Fig. 10.1 [1]. Deaths from urban air pollution are estimated to grow over the next 30 years because of the world's population growth, which occurs in cities and towns of poor countries. In Asia, for example, the region will see an absolute increase of a billion people in urban areas over the next 3 decades. Today, many developing and developed countries are faced with severe levels of urban air pollution and are trying to improve air health and the environment. Europe, for example, aims to reduce exposure to air pollution by reducing emissions and setting limits and target values for air quality. In this sense, the National Emission Ceiling Directive imposes emission ceilings (or limits) for four key air pollutants—nitrogen oxides, sulphur dioxide,

---

C. Belver (✉)

Instituto de Ciencia de Materiales de Madrid, CSIC., Madrid E-28049, Spain  
e-mail: cbelver@icmm.csic.es

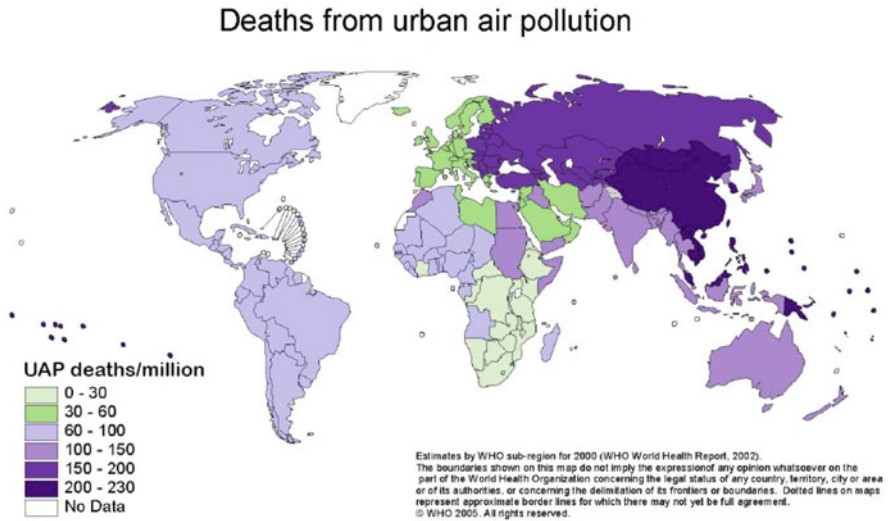


**Fig. 10.1** World death distribution map from urban air pollution estimated by the World Health Organization (2005) [1]. Reproduced with permission of the World Health Organization

nonmethane volatile organic compounds, and ammonia—that harm human health and the environment [2].

### 10.1.2 $\text{NO}_x$ Origin

Nitrogen oxides are classified as key air pollutants. The two main oxides of nitrogen are nitric oxide (NO) and nitrogen dioxide ( $\text{NO}_2$ ); both jointly are known as  $\text{NO}_x$ . The main origin of both species is the combustion process. Typically, more than 90% of the combustion of  $\text{NO}_x$  is in the form of NO, but since this is readily oxidized to  $\text{NO}_2$  in the atmosphere by  $\text{O}_2$ , both are considered together as key pollutants.  $\text{NO}_x$  formation occurs in two different ways, as thermal  $\text{NO}_x$  and as fuel  $\text{NO}_x$  [3, 4]. Thermal  $\text{NO}_x$  are formed by the oxidation of  $\text{N}_2$  with elemental oxygen, which are both present in the air that is supporting the combustion process when the temperature reaches 1000 °C, yielding increasing NO concentrations at rising temperatures. On the other hand, fuel  $\text{NO}_x$  are generated from nitrogen fuel during its combustion process. Bear in mind that the nitrogen content in fuels is 0.5–1.5% in oil and coal, and more than 2% in tar sands and bitumen.

The  $\text{NO}_x$  emission sources are different, being 70% of anthropogenic origin, see Fig. 10.2 for an example of  $\text{NO}_x$  distribution emissions in Europe (EU27) during 2006 [2]. Nature causes a small percentage, for example, the  $\text{NO}_x$  given off from nitrifying bacteria. The main anthropogenic sources are burning of fossil fuels, distributed amongst coal, oil, and diesel; power stations make up around 5%, and road transport contributes nearly half, of  $\text{NO}_x$  emissions. Other human activities which

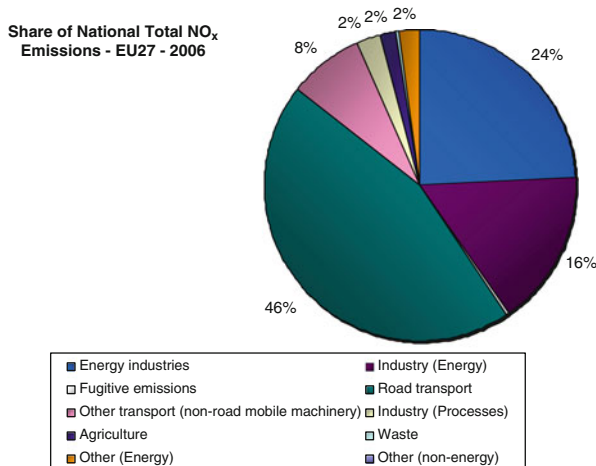


**Fig. 10.2** Share of national total  $\text{NO}_x$  emissions from EU27 in 2006 (data from European Environment Agency [2])

contribute are soil release, biomass burning (wood fuel, agricultural refuse), municipal waste, nuclear explosions, and high-flying aircraft. The latter two promote an additional damage to the environment, because the  $\text{NO}_x$  emitted remain in the stratosphere (the atmospheric region at 15–60 km height). In this region,  $\text{NO}_x$  catalyze the ozone layer decomposition; thus the emissions from ultrasonic transports and thermonuclear explosions bring about a threat to the ozone layer [5].

### 10.1.3 $\text{NO}_x$ Environmental Effects

Nitrogen oxides are poisonous to the respiratory system, provoking lung infections and allergies, and they also cause damaging effects to the environment, mainly having a hand in the creation of photochemical smog and ground-level ozone. The chemistry that underlies the formation of these effects can be quite complicated, involving radical reactions, being sensitive to the presence of volatile organic compounds (VOCs), and dependent on geographical and meteorological variations [5, 6]. The main chemical processes occurring in air pollution in which  $\text{NO}_x$  are involved have been summarized in Fig. 10.3.

$\text{NO}$  reacts with atmospheric  $\text{O}_2$  generating  $\text{NO}_2$  in periods from minutes to hours, depending on the  $\text{NO}$  concentration, being further accelerated by sunlight. The  $\text{NO}_2$  created can absorb blue and UV radiation decomposing back to  $\text{NO}$  and  $\text{O}$  atomic. The latter is highly reactive with  $\text{O}_2$  giving rise to  $\text{O}_3$  (ozone). This ozone is generally recognised as ground-level ozone, one of the most significant pollutants in terms of health impacts. Long-term and peak exposure can lead to several health consequences, ranging from minor effects on the respiratory system to

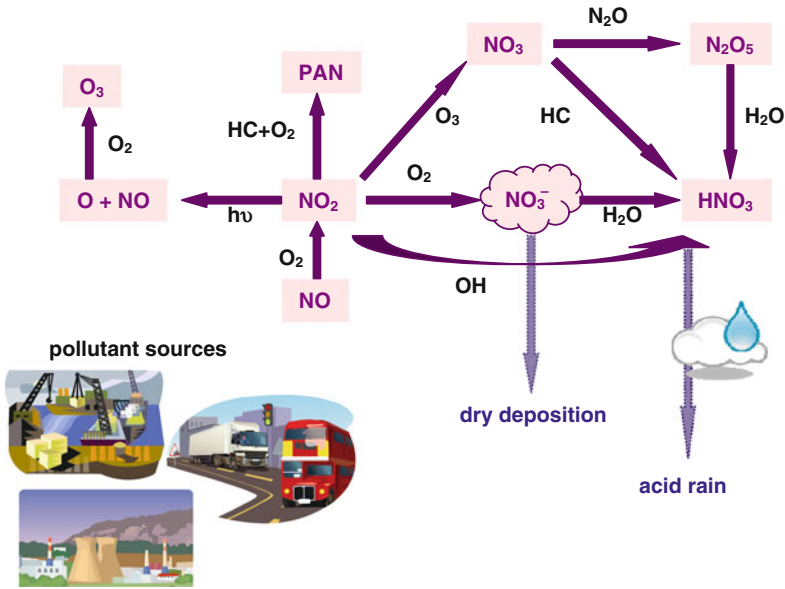


**Fig. 10.3** Chemical transformations suffered by NO<sub>x</sub> related to air pollution

premature mortality [6, 7]. On the other hand, NO<sub>x</sub> can also react with nonmethane volatile organic carbons (NMVOCs) present in the air as pollutants released from many sources, including motor vehicles, refineries, crude oil terminals, adhesives, and building paints. The organic compounds, mainly aldehydes and ketones (RR'C=O), can produce nitroorganic compounds by photochemical oxidation of carbonyl compounds in the presence of NO<sub>x</sub>—for example, the peroxyacetyl nitrate (CH<sub>3</sub>COO<sub>2</sub>NO<sub>2</sub>, named PAN) produced from acetaldehyde which reaches concentration values ca. 5–10 ppb in cities and which is responsible for eye irritations in humans and the destruction of photosynthetic pigments of plants [5, 6]. This compound presents an additional damaging effect. PAN is slightly soluble in water, hence its removal by precipitation is not effective. Its elimination occurs by thermal decomposition, which generates NO<sub>x</sub> and the peroxyacetyl radical. This decomposition has a time constant of several months, which allows its transport over long distances before it is released, generating NO<sub>x</sub> in areas far from the pollutant sources [3].

NO<sub>2</sub> can also be converted to nitric acid by different reactions (indicated in Fig. 10.3), such as: oxidation by O<sub>2</sub> and ulterior solubility in water; oxidation by OH in the daytime; reaction of NO<sub>3</sub> radicals (formed by NO<sub>2</sub> oxidation with O<sub>3</sub>) with hydrocarbons; or reaction of N<sub>2</sub>O<sub>5</sub> with water, coming this oxide from the combination of the NO<sub>3</sub> radical and NO<sub>2</sub> [3]. Nitric acid, because of its high solubility in water, composes acid rain, which causes important damage to natural environments and buildings. The acid species can also be settled over the earth's surface by dry deposition from winds. Thus these species can spread over 100 km from the

pollution focus, causing lixiviation of soils, biological death of rivers and lakes, and degradation of forests.

### ***10.1.4 Legislative Aspects***

Diverse environmental action programs, developed by several countries, aim to achieve levels of air quality that do not result in extensive damage to human health and the environment [8]. These countries have taken different regulations: for example, the 1999 CLRTAP Gothenburg Protocol caps EU15  $\text{NO}_x$  emissions in 2010 at 2.02 Mt as N, emission ceilings nor successfully reduce by many EU15 countries at the moment [2]. The legal restrictions affect several industrial sectors (see Fig. 10.2), transport being the sector most affected because over half of the  $\text{NO}_x$  emissions are from vehicles. In order to limit pollution caused by road vehicles, different regulations have been introduced by the various governments. The EU adopted a generation of standards known as Euro 5, entering into force in 2009, and created the next generation Euro 6 to be applied in 2014; whereas the U.S. adopted the EPA's Tier 2 requirements [9, 10].  $\text{NO}_x$  emission limits depend on the weight of the vehicle and its type of engine (diesel or gasoline). Therefore, the spectacular increase in the number of diesel engines (preferred by heavy-duty applications worldwide), which produce higher  $\text{NO}_x$  emissions because of higher combustion temperatures, has promoted more severe caps for the next standards. For example, emissions from vehicles intended to be used for transport will be capped at 80 mg/km (an additional reduction of more than 50% compared to the actual standard [11]).

Other industrial sectors must be also controlled to reduce  $\text{NO}_x$  emissions. Recently special limits have been applied to airports, harbors, and shipping. For example, for a ship manufactured between 2000 and 2010, the limit established is 17 g/KWh of energy supplied by the engine, a value that must be reduced progressively to 3.4 g/KWh by 2016. This fact is quite important because the total merchant shipping fleet of the world is believed to release about 10 million tons per year of  $\text{NO}_x$  [4, 12].

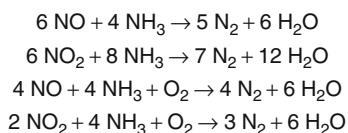
### ***10.1.5 $\text{NO}_x$ Reduction Ways***

The continuous restrictive standards regulations force novel developments and trends to reduce  $\text{NO}_x$  emissions, the technologies of which may be classified into two main groups: primary measures, or combustion control; and secondary measures, or postcombustion control. Primary ways directly try to avoid  $\text{NO}_x$  formation, whereas secondary measures attempt to reduce the emission of  $\text{NO}_x$  into the atmosphere after its formation [8, 13]. Primary technologies focus on controlling the nitrogen content of fuel by adjusting the engine and modifying the combustion process. Nowadays, special efforts are centered on modifying fuels, performing for

example the denitrogenation of actual fuels, or on looking for novel environmental fuels. Burner optimization and low  $\text{NO}_x$  burners are now employed to minimize the formation of  $\text{NO}_x$  during combustion. In this case, the combustion chamber is designed to slow the rate at which fuel and air are mixed and burned, working then under reducing conditions, so that the nitrogen from the fuel forms  $\text{N}_2$  rather than  $\text{NO}$ . These burners can be retrofitted to existing plants and have the capacity to reduce  $\text{NO}_x$  by 40% [3]. The application of a reburning process or exhaust gas recirculation is a new development in primary measures. A proportion of the post-combustion gas is returned to the cylinder. Thus, the temperature difference between cylinder and surroundings is reduced, enhancing the conversion of heat to work, requiring lower temperatures for combustion, and generating lower  $\text{NO}_x$  emissions [14].

The secondary measures developed for postcombustion control are mainly based on catalytic technologies [8, 15]. Some noncatalytic processes were developed some years ago, but none appear to be ready for large-scale and mobile sources applications because of their disadvantages. For example, selective noncatalytic reduction (SNCR) was developed by Exxon for plants, reducing  $\text{NO}_x$  by injection of ammonia into the furnace at high temperatures. Its main disadvantage is the corrosion caused by ammonium salts and the emission of unreacted ammonia and resulting products from the ammonia oxidation [13, 16]. In this way, catalytic approaches are widely applied in different industrial sectors, and there is ongoing R&D by motor manufacturers. These processes can be classified as: (i) selective catalytic reduction of  $\text{NO}_x$  with ammonia (SCR- $\text{NH}_3$ ); (ii) selective catalytic reduction of  $\text{NO}_x$  with hydrocarbons (SCR-HC); (iii) catalytic reduction of  $\text{NO}_x$  with CO; and (iv) direct catalytic decomposition of  $\text{NO}_x$  [7, 8, 13, 17].

The SCR- $\text{NH}_3$  process has been understood since the 1970s, applied to effluent residual gases from several industries, such as power stations, waste incinerators, gas turbines, and chemical industrial plants (nitric acid manufacturers [15]). With this technology,  $\text{NO}$  and/or  $\text{NO}_2$  are reduced to  $\text{N}_2$  by using liquid ammonia as a reductant agent, which is injected into the residual gas before the catalytic reaction takes place [13]. The reactions indicated hereinafter occur during the process, happening in a wide range of temperatures [18]:

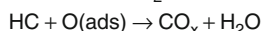
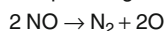


The presence of oxygen favors the  $\text{NO}_x$  reduction, according to the reactions indicated above, although high oxygen amounts can oxidize the ammonia to undesired nitrogen oxides ( $\text{NO}_2$ ). The presence of  $\text{SO}_2$ , CO, or HCl causes the consumption of  $\text{NH}_3$ , giving rise to corrosive byproducts, such as sulphate, sulphite, and carbonate ammonium salts [15, 19]. Unfortunately, although this procedure is currently the most widespread method for the cleanup of flue-gas from stationary sources, the practical use of ammonia as a reducing agent for vehicles has been discarded

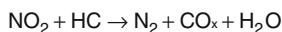
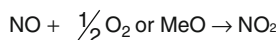
because NH<sub>3</sub> is toxic and corrosive. Alternatively, urea has been evaluated as a reductant precursor (SCR-urea) that is hydrolyzed on site to ammonia and CO<sub>2</sub>, avoiding the ammonia toxicity. This technology appears promising for car manufacturers in order to decrease NO<sub>x</sub> emissions from diesel engines. Nevertheless, special attention must be paid to design an optimum reaction system able to work with a urea aqueous solution [20, 21].

Another promising way to eliminate nitrogen oxides is selective catalytic reduction with hydrocarbons (SCR-HC). In this case, a hydrocarbon acts as reductant, replacing the ammonia and avoiding the dangers of storage, leakage, and transport of liquid NH<sub>3</sub>. In the process, NO<sub>x</sub> are reduced to elemental nitrogen by the hydrocarbon that is oxidized to CO<sub>2</sub> and H<sub>2</sub>O at the same time. The main advantage of this technology lies in the use of a similar gas mixture to that found in exhaust streams, using the same unburnt hydrocarbons as reductant agents. This technology was announced by Nissan to be developed in its vehicles [8, 18]. The main mechanisms and reactions occurring in this process are compiled in the next scheme [22].

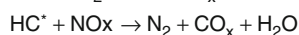
NO decomposition and subsequent regeneration by the hydrocarbon



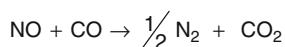
NO oxidation to NO<sub>2</sub> which acts as an oxidant



Partial oxidation of the hydrocarbon

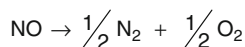


The catalytic reduction of NO<sub>x</sub> using CO and the direct NO decomposition are the latest secondary measures referred to previously. The first uses CO as the reductant agent developed for mobile sources, especially for automotive manufacturers, being an important reaction for three-way catalysts (TWC) [15, 17]. In this case, the nitrogen oxides are reduced by the CO from the same exhaust gas; thus, both pollutants are removed at the same time, yielding CO<sub>2</sub> and N<sub>2</sub>.



In the catalytic decomposition process, NO is decomposed to oxygen and nitrogen over a catalyst, mainly a precious metal, which permits reducing the activation energy of the NO decomposition reaction. This procedure appears to be an attractive solution in NO<sub>x</sub> emission control because the reaction is thermodynamically favorable. Thus, it does not require the addition of another reactant to the NO exhaust gas and could potentially lead to the formation of only N<sub>2</sub> and O<sub>2</sub> [7, 15, 20].





The severe restrictions imposed by some countries have promoted the development of these technologies as well as the appearance of novel control technologies. In this sense, the car industry has improved the  $\text{NO}_x$  abatement, performing the next processes: the selective  $\text{NO}_x$  recirculation (SNR), and the  $\text{NO}_x$  storage and reduction (NSR). Both of these are based on the adsorption of  $\text{NO}_x$  on a sorbent (called  $\text{NO}_x$  traps) where they remain as  $\text{NO}_3^-$  species, the difference being the way that nitrogen species are decomposed. In SNR technology, two adsorbents operate in parallel in the exhaust system, coordinated by upstream and downstream valves in order to operate in adsorption-desorption mode. The principle lies in concentrating and recirculating  $\text{NO}_x$  into the combustion chamber, where the nitrogen compounds are decomposed thermally [23].

NSR technology is an important advance in  $\text{NO}_x$  removal under the highly oxidizing conditions of a lean-burn engine exhaust. This procedure was developed by Toyota [24] for gasoline and diesel engines, which operate with a lean air/fuel ratio (when  $\text{O}_2$  is in excess with respect to the stoichiometric one during combustion) at cruising speeds and with stoichiometric ratios when more power is required [20]. During a fuel-lean stage, the  $\text{NO}_x$  produced are stored or retained by chemical binding to a solid. Then, when the adsorption capacity of the material is reached and the engine is switched to fuel-rich operation, the resulting exhaust compounds, hydrocarbon and CO remaining unoxidized, reduce the stored  $\text{NO}_x$  into harmless compounds and then regenerate the system [25]. The mechanism of performance for these systems is described in the diagram shown in Fig. 10.4. The effectiveness of  $\text{NO}_x$  traps depends on the material's characteristics. Different compounds have been tested as catalyst and store. They are mainly constituted by a support (metal oxides, spinels, zeolites, cuprates, etc.), [4, 23], incorporating alkaline earth sites as storage phases and noble metals as reductant compounds [5, 26]. The actual strategy used in industry involves storing  $\text{NO}_x$  on BaO in the vicinity of Pt (111), with most of the oxide being converted to nitrate. The reducing conditions created accelerate the decomposition of the nitrate phase into a homogeneous catalyst and can reduce the  $\text{NO}_x$  produced at the surface [27]. Nevertheless, the aim of other researchers is to search for novel materials that could be used as NSR catalyst/store, mainly based on

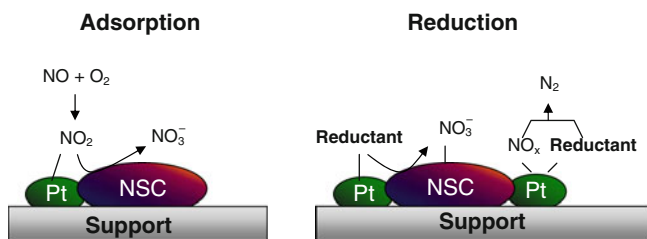


**Fig. 10.4** Adsorption and reduction of  $\text{NO}_x$  by NSR technology ( $\text{NO}_x$  Storage and Reduction) NSC:  $\text{NO}_x$  storage compounds

perovskites [28] and/or mixed oxides with transition metals instead of noble metals, such as oxo-anionic Ca-Cu/Al<sub>2</sub>O<sub>3</sub> [29] or hydrotalcites [30].

All the technologies described above have been carried out in both industrial and academic environments, because of the importance of limiting the NO<sub>x</sub> emission for environmental protection. This is the reason why numerous research laboratories are devoting time to these subjects, publishing in the literature a large number of reviews and patents each year. Nevertheless, many efforts are necessary to reach the emission ceilings set by governments. Industry and manufacturers are checking out the best ways to get higher NO<sub>x</sub> removal efficiencies, lower capital investments, and greater simplicity, even studying the possibility of combining several processes in an integrated procedure [13]. It is noteworthy that the best removal techniques (with higher removal capacities) are catalytic processes, indicated commonly as DeNO<sub>x</sub>. Selective catalytic reduction (SCR) has been the most studied of these techniques, because it can be applied to both stationary and mobile sources. Other DeNO<sub>x</sub> processes, such as decomposition and adsorption, have not been applied commonly on a commercial scale [20]. There are many examples of DeNO<sub>x</sub> technologies in industry, such as the SCR-NH<sub>3</sub> reaction included in power stations of the EON Company, or the catalytic converters used in automotive manufacture [4, 27, 31]; and in scientific and academic fields [5, 7, 8, 15–18, 21]. The abundant scientific literature related to catalytic removal of NO<sub>x</sub> and catalytic materials undertakes to dedicate an issue to these technologies.

### **10.1.6 NO<sub>x</sub> Removal by Catalytic Technologies**

The catalytic removal of NO<sub>x</sub> is divided into four categories: selective catalytic reduction with ammonia, selective catalytic reduction with hydrocarbons, catalytic reduction with CO, and catalytic decomposition, which have been described previously. All these methods have been dealt with at length, especially selective catalytic reduction (SCR), the nature of the catalyst being an important element in their development. Basically all categories of inorganic materials have been tested as DeNO<sub>x</sub> catalysts: metals, metal-supported, mixed phases, oxides, mixed oxides, zeolites, alloys, heterostructures, etc. [7, 32]. Their industrial use and development are associated with the type of reaction, reductant, and reaction conditions.

#### **10.1.6.1 Selective Catalytic Reduction with Ammonia**

A wide range of catalytic materials have been investigated for SCR of NO<sub>x</sub>. Several reports (and references therein) from the 1970s reviewed the catalysts used in the SCR of NO<sub>x</sub> with ammonia [7, 32, 33]. More than a thousand compositions have been evaluated in this reaction, oxides being the most studied even as supports of other oxides. V<sub>2</sub>O<sub>5</sub>, Fe<sub>2</sub>O<sub>3</sub>, CuO, Cr<sub>2</sub>O<sub>3</sub>, TiO<sub>2</sub>, Al<sub>2</sub>O<sub>3</sub>, and WO<sub>3</sub> are some base oxides employed in this reaction, vanadium oxide being the most active and selective catalyst, working over a wide range of temperatures (200–550 °C). The deposition of V<sub>2</sub>O<sub>5</sub> in other oxides, such as TiO<sub>2</sub>, SiO<sub>2</sub>, and Al<sub>2</sub>O<sub>3</sub>, leads to an

increase in the catalytic activity. The active sites are related to the presence of both redox (vanadyl species) and acid sites at the surface of the catalyst [34]. The activity of these systems can be promoted by adding other oxide species.  $\text{WO}_3$  enhances the activity, together with resistance towards deactivation by  $\text{SO}_2$ ; other oxides ( $\text{MoO}_3$ ,  $\text{CeO}_2$ ,  $\text{ZnO}_2$ ) cause a similar effect and reduce the reaction temperature to  $150^\circ\text{C}$  [7, 35]. Other materials have also been tested with this technology. In the beginning, noble metals, from the platinum and palladium groups, were studied both as pure metals and as metal-supported on oxides ( $\text{SiO}_2$  and  $\text{Al}_2\text{O}_3$ ). In general terms, these systems were preferable for their low-temperature activity ( $200^\circ\text{C}$ ), although their limited temperature window of operation and low stability in the presence of sulphur reduced their industrial application in stationary sources [20].

The discovery of porous solids at the beginning of the nineties and the development of novel synthetic procedures had an enormous impact in the development of new catalysts; hence other classes of catalysts were examined for the SCR- $\text{NH}_3$  reaction [7, 20]. Zeolite types with narrow pores have proved to be suitable for this reaction. Different metal-exchanged zeolites have been tested as catalysts, evaluating the influence of several parameters, such as the metal (nuclearity, content, and nature), the synthesis way, and the zeolite framework [36]. Iron and copper-exchange ZSM-5 have received much attention because of their promising activity in the SCR- $\text{NH}_3$  process [37]. These transition metals, together with chromium and manganese, have been introduced by cation exchange into different zeolitic cavities, using mainly X, Y, and ZSM5 zeolites [38, 39]. However, many researchers are nowadays improving these zeolite systems in order to enhance their low-temperature activity, hydrothermal stability, and resistance to poisons, in accordance with legal restrictions.

Up to now, catalysts based on tungsten- or molybdenum-promoted vanadium-titanium oxides have been well established in industry [34]. Moreover, a number of other metal oxides have been reported to be active and more or less selective for this reaction. Among these compounds, pure  $\text{V}_2\text{O}_5$  and  $\text{V}_2\text{O}_5$ -supported on oxide carriers ( $\text{Al}_2\text{O}_3$ ,  $\text{SiO}_2$ ,  $\text{ZrO}_2$ , and  $\text{TiO}_2$ ) have been deeply investigated. Other formulations have been evaluated as catalysts in this reaction, such as pure, supported, and/or mixed Fe [40–42], Cu [43, 44], Cr [44, 45], and Mn [44, 46, 47] oxides. Much effort is being dedicated to enhance the activity of these systems, although the debate on the mechanistic and chemical aspects of the reaction is still open. As with zeolites, metal oxides possess some disadvantages for this reaction because they are quite sensitive to different poisons usually present in exhaust streams ( $\text{H}_2\text{O}$ ,  $\text{SO}_2$ , and particles). Hence, the technological incentives are dedicated to improve the resistance against poisoning and the mechanical and thermal stability of catalysts, and triggering the activated carbon [48, 49], supported metal oxides [17, 31, 34], and pillared clays as potential solutions [50]. Therefore, a challenge for the future is to provide new experimental data more directly related to “real” conditions, working at space velocities and with composition feeds more similar to typical commercial operations.

On the other hand, as has been indicated in Section 10.1.5, ammonia is an expensive reductant with serious disadvantages, including corrosion, toxicity, and

byproducts. Therefore, the research aims at other reductants (urea, ammonium carbamate, or melamine) that are cheaper and less toxic, which means searching for new catalysts for this purpose. Recently, for example, Moreno-Tost et al. evaluated copper catalysts supported on porous phosphate heterostructures (PPH) as active catalysts in the SCR-urea process, showing better catalytic behavior than well-known zeolitic systems (CuZSM5), even when H<sub>2</sub>O and SO<sub>2</sub> were added to evaluate their deactivation [51].

#### 10.1.6.2 Selective Catalytic Reduction with Hydrocarbons

In the nineties, the pioneering works by Held et al. [52, 53] and Iwamoto et al. [54, 55], independently, showed that either alkanes or alkenes were able to reduce NO<sub>x</sub> on copper ion-exchange zeolites. Therefore, the SCR-HC technology appeared as a promising way to reduce NO<sub>x</sub> pollutants from exhaust gases; an extensive patent literature exists about this technology [56]. Since then, much research has been undertaken and reported in the literature, and nowadays the types of catalysts and the possible reductants are extremely varied [57]. The main active catalysts can be divided into three groups: zeolites, metal oxides, and noble metals.

Metal ion-exchanged zeolites have been extensively evaluated for the SCR-HC reaction, testing different parameters, such as the structure of the zeolite, the nature of the metal, the influence of the synthesis conditions, the nature of the hydrocarbon, and so on. Because of the influence of those parameters, it is hard to determine the uniform order relating to the performance of NO<sub>x</sub> reduction by zeolites [22]. Concerning the zeolite structure, the ZSM-5 framework has been extensively studied [5], although MFI, FER, and beta structures have also been tested [7]. Different studies indicate that the catalytic behavior of these systems depends on the next structural parameters: (i) the silicon/aluminum ratio, (ii) the acidity, and (iii) the geometrical positions where the metal is incorporated. With regard to metal nature and loading, different cations can be considered as the active species [58]. Copper has been extensively studied and used in many cases as a reference. It is a selective catalyst in the reduction of NO in the presence of C<sub>2+</sub> hydrocarbons, although it loses its efficiency in the presence of O<sub>2</sub> [56, 59]. Other metals have been checked out as active sites in ion-exchange zeolites: V, Cr, Mn, Fe, Co, Ni, Zn, Ga, In, Zr, Mo, La, and Ce [22]. Cobalt and gallium, for example, were able to reduce NO using methane as the hydrocarbon rather than copper, which is unable to perform the reaction with short chain hydrocarbons [60–62]. Much research effort has been devoted to the combination of Co with other metals, such as noble metals, alkali-earths, rare earths, and transition metals (Mn, Ni, Cu, Zn, etc.) [22]. Cerium-exchanged zeolites reached the best conversion values compared with other metals (La, Pr, Nd, Ln, In, Pb, or Si), even better than copper under the same experimental conditions [63]. Iron has also been incorporated into zeolites, forming oxide clusters, exhibiting a high activity in the SCR of NO in the presence of propene because of the redox process between Fe<sup>2+</sup> and Fe<sup>3+</sup> [64]. The addition of promoters (Ce, La, Na, etc.) can tune the catalyst performance, limiting and making reversible the deactivation

caused by H<sub>2</sub>O [22, 65]. The activity of precious metal ion-exchange zeolites (Pt, Pd, Rh, Ru, and Ir) has also been analysed. Pt-zeolites display a good performance in the reduction of NO<sub>x</sub> when water vapor is introduced into the effluent, although its major problem consists of Pt's tendency to convert NO to the undesired N<sub>2</sub>O [22, 66, 67].

More recently, the investigations have tended to produce automotive catalysts from metal ion-exchange catalysts. For this task, the reaction temperature window and the effluent composition must be borne in mind in order to simulate the "real" operational conditions of an engine; thus methane, ethane, propane, or even methanol have been used as reductant agents [68]. Different systems have been tested, mainly based on ZSM-5 and Co, Mn, Ni, Cu, Fe, or Pd as metal phases. Some investigations performed over various cation-ZSM-5 catalysts at 450 °C using methane showed that NO conversions followed this order: Co > Mn > Ni > Cu > H. The activity of these systems depends on the nature of the reduction hydrocarbons, decreasing in the order aromatics > olefins > paraffins [68]. From those systems, Co-beta zeolite appeared as a promising catalyst to perform under real conditions of diesel engines [69]. For automotive purposes, special attention has been paid to the synergistic effect between different metals. For example, the conversion rates of Pd-Mo-ZSM-5 were superior to the sum of the conversions of Pd-ZSM-5 and Mo-ZSM-5 [70]. In other reports, Kikuchi and coworkers showed the beneficial effect caused by incorporating different metals as additives over the activity of several M-ZSM-5 [71]. Comparing the incorporation of several metals to In-H-ZSM5, Pt, Rh, and Ir showed positive effects on the catalytic activity of the zeolite using CH<sub>4</sub> as a reductant, even in the presence of water (comparison shown in Fig. 10.5), attributed to the active behavior of these metal sites. In other work, Rh, Ag, Ce, and Fe caused promotional effects on the catalytic durability of Pd/H-ZSM-5 [72].

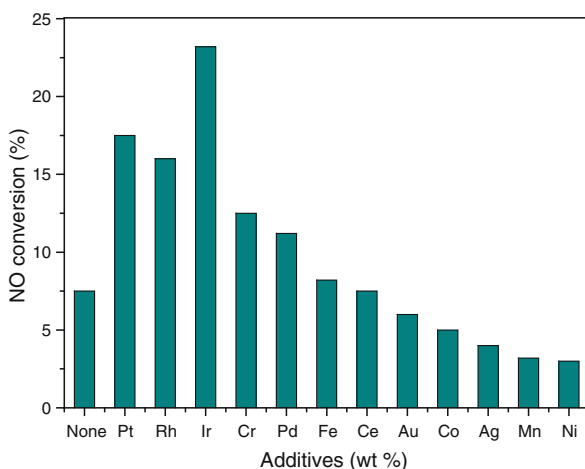


**Fig. 10.5** Effects caused by metallic additives to In-H-ZSM-5 over the NO conversion (results compiled from Kikuchi et al. [71])

Metal oxides are another class of SCR-HC catalysts, though their activities are generally low at high space velocities. Many investigations have been dedicated to metal oxide-based catalysts, mainly divided into simple oxides and supported transition metal oxides [7, 73–75]. A large number of oxides have been considered as catalysts: SiO<sub>2</sub>, V<sub>2</sub>O<sub>5</sub>, Cr<sub>2</sub>O<sub>3</sub>, MnO<sub>2</sub>, Fe<sub>2</sub>O<sub>3</sub>, and CoO—although Al<sub>2</sub>O<sub>3</sub>, Ga<sub>2</sub>O<sub>3</sub>, and ZrO<sub>2</sub> have been the most active [76], even more when they were treated with SO<sub>4</sub><sup>2-</sup> species [77, 78]. The combination of several metal oxides has also been evaluated [75]. The incorporation of transition metal ions with redox properties into the metal oxides increased the activity of the resulting catalyst. Different mixed metal oxides have been described in the literature, prepared by coprecipitation methods in order to get well dispersed metal ions. Cu, Ni, Mn, Co, and Fe were incorporated into ZrO<sub>2</sub>. The M-Zr-O linkage enhanced the activity of the catalysts, Cu-Zr-O being the most active. The design of these systems depends on the metal loading, the metal dispersion, the textural properties, and the reductant agent [79]. The Ga<sub>2</sub>O<sub>3</sub>-Al<sub>2</sub>O<sub>3</sub> mixed oxide also showed a high performance in this reaction (with methane), attributed to the presence of Ga cations at surface tetrahedral sites, which are more unsaturated than octahedral sites and provide more accessible locations for gaseous molecules [73, 75].

The incorporation of metals (other than noble metals), i.e., V, Cr, Co, Cu, Fe, Mn, Ni, Fe, and Ag, over different oxides has also been studied for SCR reaction. Different reviews offer examples of this kind of catalyst, although it is quite hard to compare them because of the catalyst preparation method (metal precursor, synthesis way, thermal treatment) and the different reaction parameters used by each author (nature of reductant, temperature, presence of oxygen or water, etc.) [5, 7, 73, 75, 76]. Al<sub>2</sub>O<sub>3</sub> is among the most suitable supports, because of its high thermal stability and its capability for the formation of isolated transition metal cations. The activities described by M-Al<sub>2</sub>O<sub>3</sub> are higher than for other oxides (TiO<sub>2</sub>, SnO, rare earth oxides), attributed to the formation of active aluminate species [74, 80]. ZrO<sub>2</sub> and Ga<sub>2</sub>O<sub>3</sub> were considered as supports exhibiting competitive activities, in some conditions higher than alumina. ZrO<sub>2</sub> received special attention because the incorporation of Cu or Co by coprecipitation generated effective catalysts with a behavior similar to the well-known Cu-ZSM-5 [76]. Their activity was related to a correct metal distribution and to the M-ZrO<sub>2</sub> bonds formed. More recently, CeO<sub>2</sub> has been proposed as a suitable carrier to support metal active sites [81]. Cu, Fe, Co, and Cr have been shown to be promoting elements. It should be noted that these metals lowered the active temperature window of Al<sub>2</sub>O<sub>3</sub> support, while Cu and Fe increased the catalytic activity [82]. Nevertheless, these metals should be deactivated by water, lowering their activity. The incorporation of Ag (Ag/Al<sub>2</sub>O<sub>3</sub>) has been demonstrated to be appropriate for avoiding the water deactivation, holding high NO conversion values (>75% at 450 °C). This system is a promising catalyst for SCR-C<sub>3</sub>H<sub>6</sub> in real conditions [69], yielding to high NO conversions in the presence of hydrocarbons with up to four carbons and with oxygenated hydrocarbons, alcohols, and ketones [83], although M/Al<sub>2</sub>O<sub>3</sub> catalysts prepared by other authors were less effective [84].

Tabata et al. considered other metals (Sn, W, Mo, Ga, Bi, and Sb), looking into the improvement of the alumina activity using alcohol as the reductant ( $\text{CH}_3\text{OH}$ ) [85]. From all these metals, only Sn was effective for  $\text{NO}_x$  reduction, because the others promoted the methanol oxidation.  $\text{Sn}/\text{Al}_2\text{O}_3$  showed excellent  $\text{DeNO}_x$  activity even in the presence of  $\text{SO}_2$ , a deactivation compound mainly present in diesel exhausts, due probably to the interaction between Sn and  $\text{Al}_2\text{O}_3$ . Considering the activity of these supported transition metal oxides, the researchers found promoters capable of improving the catalytic performance of these supported catalysts. Therefore, the incorporation of two metals appeared to be an efficient way to enhance the activity. Thus, bimetallic catalysts can be found in the literature, such as  $\text{Cu}/\text{Cr}/\text{CeO}_2$  [75, 81] and  $\text{Cs}/\text{Cu}/\text{Al}_2\text{O}_3$  [86].

Trends towards nonzeolitic catalysts also considered supported noble metals over metal oxide supports [7, 74, 80, 87]. Pt, Pd, Rh, Ru, and Ir have been studied as active sites for SCR-HC because of their redox properties. Pt and Rh supported over  $\text{Al}_2\text{O}_3$  displayed the best  $\text{NO}_x$  conversion and  $\text{N}_2$  selectivity values, both in model hydrocarbon mixtures and in real diesel exhaust mixtures, being active at relatively low temperatures (200–350 °C) [88, 89]. Initially, Pt catalysts were the most studied, trying to clarify the mechanism and parameters that control the reaction with noble metals. In this sense, it has been proved that metal precursor and loading considerably affect the temperature of the maximum conversion and the level of activity [90, 91]. Although Pt catalysts exhibited optimum activity and stability, they have a rather narrow temperature operating window [92]. Therefore, the investigations were focused on enhancing this effect—for example, by studying alumina-supported Rh catalysts [93]. The combination of Pt and Rh has also been borne in mind. In a recent work, special care has been taken regarding the synthesis method [94]. The catalysts containing alumina and precious metal atoms incorporated Rh–Al, Pt–Al, and Pt–Rh–Al phases-isostructural with  $\text{Al}_9\text{Rh}_2$  and  $\text{Al}_2\text{Pt}$  alloys. In these systems, the NO conversion to  $\text{N}_2$  began at low temperatures. Because of the NO adsorption over metal atoms and alloys occurred between 80 and 350 °C, and a synergistic effect existed between both metals. Although  $\text{Al}_2\text{O}_3$  has been extensively used as support because of a cooperative effect between noble metal and alumina [74], the influence of the nature support was also investigated [88, 92, 95].  $\text{CeO}_2$  and  $\text{ZrO}_2$  have been evaluated. These supports were capable of activating adsorption and partial oxidation of propylene on its surface by providing oxygen species, following the partial oxidation hydrocarbon mechanism described in the previous section [96]. More recently, ceria-zirconia systems have received special attention, to make the best use of ceria oxygen storage capacity [97]. Thus, novel Pd, Pt, and Rh supported over  $\text{Ce}_x\text{Zr}_y\text{O}_2$  mixed oxides have been considered, yielding catalysts with high  $\text{N}_2$  selectivity, resistance to water deactivation, and optimum activities [98–101].

The SCR-HC technology possesses limited incentives to research into stationary sources. Nevertheless, for mobile sources, in particular for diesel engines, much effort is being dedicated to reduce  $\text{NO}_x$  emissions in this way, applying this technology to actual automotive catalytic converters [102]. The catalytic removal of  $\text{NO}_x$  under lean conditions (when  $\text{O}_2$  is in excess during combustion with respect to

the stoichiometric value) is still a relevant target in the catalysis field and an open problem to meet future exhaust emission regulations.

### 10.1.6.3 Catalytic Reduction with CO

NO reduction by CO is a primary reaction in three-way catalysis (TWC) [15, 102]. The introduction of a catalytic treatment for automotive exhausts implies the removal of incomplete combustion products (CO, NO<sub>x</sub>, and residual hydrocarbons) all together. Many reviews and researches are summarized in the scientific and industrial literature about TWC technology. The number of catalysts developed and all investigations related to TWCs are too many to be included in this issue. Thus, we will dedicate this section for giving an introduction to the most relevant materials employed in NO reduction by CO alone, leaving TWC catalysts and reactions for other contributions.

Much information about catalysts for this reaction can be found in the literature. Different transition metal oxides have been tested since the 1970s, e.g., Fe<sub>2</sub>O<sub>3</sub>, CuO, Cr<sub>2</sub>O<sub>3</sub>, NiO, Al<sub>2</sub>O<sub>3</sub>, and V<sub>2</sub>O<sub>5</sub>; iron, copper, and chromium oxides being the best catalysts in terms of selectivity, activity rates, and low temperature of reaction [7]. Copper was extensively considered, either alone, supported over alumina, or forming complex catalysts with other metals [103]. The activity of these systems was attributed to the redox properties of copper. Cu and Cu<sup>+</sup> species acted as adsorption sites of NO and CO, and in the same manner Cu<sup>+</sup> and Cu<sup>2+</sup> species behaved as recipient sites of the O atom from NO dissociation [104]. Nevertheless, the low stability of metal oxides in this reaction led the investigation on. Recent researches are focusing on TiO<sub>2</sub>, CuO, and ZnO as catalysts [105–107], although CeO<sub>2</sub> has shown high activity mixed with other metal oxides (NiO, CuO, Al<sub>2</sub>O<sub>3</sub>). The presence of Ce<sup>3+</sup>–Ce<sup>4+</sup> active sites favors the activity; they can even interact with the pair of other metals (Ce<sup>4+</sup>–Cu<sup>+</sup> → Ce<sup>3+</sup>–Cu<sup>2+</sup>) participating in the formation of active metal complexes. Likewise, cerium oxide acts as an “oxygen storage” compound and enhances the stability of catalysts [108, 109].

Current catalytic converters are nonetheless constituted by supported noble metals. Many studies have been carried out on Pt, Pd, Rh, and Ir metals [15, 102, 110]. The principal factor that controls NO reduction in the presence of CO is the nature of the noble metal and the support, but the size of the supported metal and the reaction temperature are both very important parameters. Several authors have argued in favor of the use of rhodium [27]. Shelef and Graham, for example, showed that other metals (Pt or Pd) are less able to dissociate NO than Rh [111]. The combination of different metals has also been studied [112, 113]. These have been mainly supporting on ceria or ceria-zirconia systems, because the addition of cerium compounds brings on the oxygen storage effect, in addition to a good metal distribution [102, 114]. More recently, single crystal creation has provided valuable information that can be used to develop these catalysts. For example, Rh (100) and Rh (110) have been evaluated for this purpose [115], just like the Pt (100) surface that exhibited a large NO dissociation [116].



#### 10.1.6.4 Catalytic Decomposition

Direct decomposition of  $\text{NO}_x$  into its elements is the best technical solution for nitrogen oxides exhaust and is certainly more desirable than adding a reductant to remove  $\text{NO}_x$  from fluent gases. This reaction is thermodynamically favorable, although it is inhibited by its high activation energy, for which reason it is necessary to employ a catalyst. Research in this field is extensive [5, 7, 17, 54]. Therefore in this section a short review about catalysts will be given, splitting into three groups, i.e., precious metals, oxides, and zeolites.

The majority of decomposition studies carried out on precious metals have been focused on the platinum metal group supported over alumina, considering several metallic systems: metal alone, bimetallic, or alloys, these latest incorporating a transition metal [5]. The mechanism of reaction more accepted for these systems involves first the NO adsorption, followed by its dissociation into nitrogen and oxygen atoms, the oxygen desorption being important in order to avoid oxidation reactions. The NO decomposition depends on surface temperature, surface coverage, and surface defects. For example, there has been shown the important effect caused by the oxygen-metal interface, indicating that the support is not inert [117].

Metallic oxide compounds have been extensively studied as catalysts for NO decomposition [54]. More than 40 metallic oxides have been evaluated for this reaction in the temperature range from 500 to 800 °C [5, 118]. Among them, cobalt oxide ( $\text{Co}_3\text{O}_4$ ) displayed high activity, which is attributed to its spinel structure ( $\text{Co}^{\text{II}}$  and  $\text{Co}^{\text{III}}$ ) bringing it redox properties. The addition of promoters, such as alkali metals, to this system enhanced the activity. It is considered that the interface between alkali metals and  $\text{Co}_3\text{O}_4$  serves as an active site, where all the reaction steps would take place [119, 120]. Nevertheless, the presence of  $\text{O}_2$  should inhibit the reaction, because  $\text{O}_2$  retards the decomposition of NO by competing for the same surface centers; thus the activity of these systems depends on the strength of the metal–oxygen bond in the lattice. In this connection, metal-supported ceria catalysts have recently been studied for this reaction, because they prevent the oxygen “self-poisoning” effect due to an oxygen spillover effect from the metal to the reduced surface of the ceria [121].

The decomposition of NO over metal-exchanged zeolites has been studied since the pioneering works of Iwamoto et al., in particular by using Cu-ZSM-5 zeolites [122]. Since then, many investigations have been performed to attain suitable NO decomposition catalysts. Several factors have been considered, such as the nature of zeolite, the nature of metal, its loading, etc. [7, 54]. Comparative studies using different zeolite frameworks have proved the superiority of the ZSM-5 as support, the main influences being both the location of the metal in the zeolite structure and the bond between the metal and the zeolite lattice [123]. For a long time, much effort has been focused on getting to the bottom of understanding Cu-ZSM-5 activity. This process occurs via a redox mechanism, starting with the NO adsorption. The process can be schematized as:  $\text{Cu}^{2+} + \text{NO} \rightleftharpoons |\text{Cu}^+ \text{NO}^+|$ . Copper undergoes an oxygen desorption yielding to reduced copper, which is consequently oxidized by NO, generating oxidized copper and nitrogen [54]. This behavior has been corroborated by

different techniques, such as IR, ESR, XANES and EXAFS, XPS, and theoretical calculations [7, 124]. Nowadays, the efforts try to avoid the inhibition effect caused by both the presence of oxygen and water in the reaction mixture.

$\text{NO}$  decomposition over metal surfaces, oxides, or zeolites has some serious difficulties in practice.  $\text{NO}$  decomposition process is a high temperature phenomenon, which is undesirable. Likewise, catalysts suffer deactivation by oxygen. So a reductant is required to scavenge the dissociated oxygen. From an exhaust catalysis view, it is not sufficient to dissociate  $\text{NO}$ ; other pollutants like  $\text{CO}$  and hydrocarbons ( $\text{HC}$ ) should also be oxidized. Therefore,  $\text{NO}$  reduction by  $\text{CO}$ ,  $\text{HC}$ ,  $\text{H}_2$ , or  $\text{NH}_3$  is more attractive for  $\text{NO}_x$  abatement.

The identification of a suitable catalyst, or a combination of various catalysts, is still a matter of debate. The actual and future environmental regulations should require looking for efficient and low-cost materials. Fortunately, clay minerals have many properties, such as fine particle size, large surface area, high-charge surfaces, good adsorptive properties, and others, that make them logical materials for use in many environmental applications. These materials also have the advantage of tailoring by many methods, acid or basic treatment, pillaring or swelling by different molecules, etc.; therefore clays appear as likely catalysts for a potentially benign chemical process [125].

## 10.2 Pillared Clays as $\text{DeNO}_x$ Catalysts

Metal oxide pillared clays are especially important among clay derivatives that have relevant properties to chemical catalysis [50, 126]. These materials are described in detail in other chapters of this book. They are microporous materials created by replacing interlayer cations in the pristine material by bulk metallic polycations that act as a pillar precursor. The dimension of these hydroxycations provides a possibility of tailoring a porous structure. Upon calcination, the intercalated polycation is turned into a metal oxide nanoparticle with a structure that resembles a bulk oxide. These particles are anchored to clay layers, keeping them separated. Many pillar compositions have been prepared, including oxides of aluminum, gallium, titanium, and other transition metals [127–129]. Catalytic applications of pillared clays are mainly related to the nature and distribution of pillars, in addition to their surface properties [130–132]. In this section, applications of PILCs in the abatement of nitrogen oxides will be discussed, arranging the view according to the catalytic technologies described before.

### 10.2.1 $\text{NO}_x$ Reduction with Ammonia

Pillared interlayered clays containing  $\text{Cr}_2\text{O}_3$ ,  $\text{Fe}_2\text{O}_3$ ,  $\text{TiO}_2$ ,  $\text{ZrO}_2$ , or  $\text{Al}_2\text{O}_3$  were investigated in the 1990s and claimed as a promising new class of catalysts for SCR of  $\text{NO}$  by  $\text{NH}_3$  [131]. They were prepared by the ion-exchange/intercalation

procedure, employing montmorillonites as raw clays. The original interlayered cations were replaced by corresponding metal oligomers, prepared by controlled hydrolysis of metal salts. After heating, these precursors were transformed into the corresponding oxidic phases, yielding the formation of pillars. These systems displayed higher SCR activities than tungsten- or molybdenum-promoted vanadium–titanium oxides used in industry, mentioned in the previous section [50, 133]. In turn, they exhibited no activity for ammonia oxidation, an undesirable reaction, and resistance to water deactivation and  $\text{SO}_2$  poisoning (except for  $\text{Cr}_2\text{O}_3$ -PILC), Fe-pillared clay being the most promising catalyst in this regard because it showed no  $\text{SO}_2$  effect. The catalytic behavior of these materials was claimed to be related to Brønsted acid sites and to the bimodal pore structure created by the pillaring process. This pore structure is outlined in Fig. 10.6. Macropores created in interparticle spaces act as feeder pores to micropores and as filters; whereas the intraparticle micropores containing the active species carry out the catalytic action in the SCR reaction without any inhibition by the presence of poisoning agents [134].

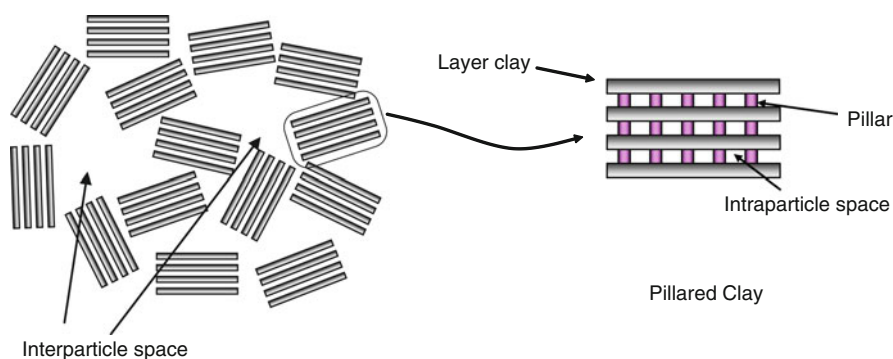


**Fig. 10.6** Bimodal pore structure created in pillared interlayered clays

The results reported by Chen et al. showed that Fe-pillared clay was a promising SCR catalyst, exhibiting good activity and the greatest poisoning resistance [134, 139]. The authors studied in parallel the activity of delaminated Fe-pillared clay [135]. This system did not exhibit long-range layer stacking, proved by the absence of (001) x-ray reflections; although a short-range stacking remained, describing an overall structure known as a “house of cards” [136,137]. Delaminated Fe-pillared clay under reaction conditions without water or  $\text{SO}_2$  exhibited higher catalytic activities than tungsten vanadium–titanium oxide and other iron oxide supported catalysts (supported on alumina or titania). When water and  $\text{SO}_2$  were included in the reaction stream, some inhibition was observed, although the system held NO conversion values around 86%. The inhibition process was reversible, exhibiting conversion rates of 95–98% when water and  $\text{SO}_2$  were switched off the stream. This behavior was related to the porous structure of this delaminated PILC system, composed by micro- and macropores, and to their Brønsted acid sites, probably as a result of interactions between iron oxide and clay. The activity of delaminated pillared clays

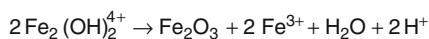
was also described by Chmielarz et al. for delaminated titania-pillared montmorillonite [138]. The temperature window of performance was between 240 and 450 °C, reaching NO conversion values of ca. 96%. These systems presented a large concentration of strong acid sites. Thus, the NO reaction took place after NO adsorption at the surface, giving rise to nitrate ions which were subsequently decomposed.

Ti-pillared clays were also evaluated by del Castillo et al. [139]. The authors confirmed the high activity of these systems and showed their great resistance to the presence of SO<sub>2</sub>. All tested catalysts achieved higher NO conversion values after contact with SO<sub>2</sub> than when fresh systems were employed. They even extended the study to evaluate the relevance of Brønsted sites for this reaction. Ti-pillared clay treated with sulphuric acid showed high SO<sub>2</sub> resistance at 400 °C, associated with its slightly greater acidity.

An additional active material can be introduced into pillared clays in order to enhance their activities. The incorporation of isolated metals has been studied since the 1990s [140]. Perathoner and Vaccari incorporated copper on Al<sub>2</sub>O<sub>3</sub>- and Al<sub>2</sub>O<sub>3</sub>/Fe<sub>2</sub>O<sub>3</sub>-PILCs by the ion-exchange method [141]. These systems exhibited higher activities than other copper catalysts (Cu-ZSM-5 or CuO/Al<sub>2</sub>O<sub>3</sub>) at high temperatures, because of the reduced rate of undesirable ammonia combustion. Preliminary tests showed that the surface properties of these pillared clays played an important role in their catalytic activity. Fe<sup>3+</sup>, Cr<sup>3+</sup>, Mn<sup>2+</sup>, Co<sup>2+</sup>, Cu<sup>2+</sup>, V<sup>3+</sup>, and Ni<sup>2+</sup> were incorporated to Fe<sub>2</sub>O<sub>3</sub>, TiO<sub>2</sub>, ZrO<sub>2</sub>, SiO<sub>2</sub>, and Al<sub>2</sub>O<sub>3</sub>-pillared clays by Yang et al., providing patented catalysts for the SCR reaction in power plants [142]. These systems were prepared by ion-exchange and showed remarkable activity for this reaction. Compared with commercial catalysts, these invented catalysts yielded higher activity, lower SO<sub>2</sub> conversion to SO<sub>3</sub>, and less undesirable N<sub>2</sub>O formation. The same authors have paid special attention to Fe<sup>3+</sup>-ion-exchange TiO<sub>2</sub>-pillared clays (from montmorillonites), because they exhibited higher SCR activities than the commercial-type V<sub>2</sub>O<sub>5</sub>-WO<sub>3</sub>/TiO<sub>2</sub> catalyst [143]. These systems were characterized by a delaminated pillared structure without structural evidences of iron oxide formation (even with high iron contents, ca. 20%); all of them suffered the loss of the (001) stacking during the intercalation procedure. This delaminated structure usually shows a larger pore diameter than pillared structures, hence the authors obtained samples with a bimodal macropore distribution. The SCR activities were higher than commercial catalysts at temperatures higher than 350 °C, showing better N<sub>2</sub> selectivity and little or no evidence of N<sub>2</sub>O generation. The authors studied the effect caused by the incorporation of O<sub>2</sub>, SO<sub>2</sub>, and H<sub>2</sub>O. Oxygen played a significant promoting role in the reaction, at low concentrations causing an increase over NO<sub>x</sub> conversion that did not change when the oxygen amount was enhanced. The authors suggest that this effect is due to the presence of oxygen species adsorbed over the material surface [143]. The incorporation of water decreased their activity, while SO<sub>2</sub> or SO<sub>2</sub>+H<sub>2</sub>O improved the catalytic behavior at high temperatures, contrary to what the vanadium–titanium catalysts exhibited.

The ion-exchange synthetic process employed by Yang and coworkers to prepare the Fe-TiO<sub>2</sub>-PILC consists of replacing TiO<sub>2</sub>-PILC cations, mainly H<sup>+</sup>, Na<sup>+</sup>, or K<sup>+</sup>, by iron cations, mainly Fe<sup>3+</sup> and Fe<sub>2</sub>(OH)<sub>4</sub><sup>2+</sup>. When the pillaring process takes

place, by heating at 400 °C, the hydroxide cations decompose to Fe<sub>2</sub>O<sub>3</sub> and Fe<sup>3+</sup> by the following reaction:



Samples prepared with low iron content (4–6%) had mainly isolated Fe<sup>3+</sup>. However, for catalysts with higher iron amounts, the iron ions hydrolyzed to hydroxide ions, yielding iron oxide. Since catalysts with low iron percentages exhibited higher SCR activities, it was concluded that isolated iron ions were more active than iron oxide [143].

Yang and coworkers also evaluated the relationship between the catalytic activity of Fe-TiO<sub>2</sub>-PILCs and their surface acidity [143, 144]. It has been accepted that the presence of Brønsted or Lewis acid sites plays an important role in the SCR reaction with ammonia. NH<sub>3</sub> is adsorbed on the Brønsted or Lewis acid sites to form, respectively, ammonium ions or coordinated ammonia. These adsorbed species react, subsequently, with gaseous or adsorbed nitric oxides, generating nitrogen and water [33, 145]. Comparing catalysts with different acidity showed that NH<sub>4</sub><sup>+</sup> ions (adsorbed on Brønsted sites) were more stable than coordinated NH<sub>3</sub>, which is more easily oxidized by oxygen, generating undesirable nitrogen oxides. Thus, the presence of Brønsted sites should involve better SCR activities [143]. Pillared clays have both Brønsted and Lewis acid sites [146], the proportion of Brønsted acid sites being larger in TiO<sub>2</sub>- and ZrO<sub>2</sub>-pillared clays [147]. Lewis acidity is created by pillars incorporated between layers [127]. Brønsted acidity, on the other hand, is due to the structural hydroxyl groups present on clay layers and to protons derived from the decomposition of metal oligomers, formed during the heating process, when they are transformed to metal oxide pillars, releasing protons that migrate to the clay layer [143, 148]. The acidity of Fe-TiO<sub>2</sub>-PILCs was modified in order to enhance their activity, obtaining greater results when the pillared clay was subjected to acid treatment [144]. The treatment with strong acids usually caused the reduction of magnesium and aluminum content from the clays [149, 150], inferring an increase in the number of Brønsted acid sites. Hence, Fe-TiO<sub>2</sub>-PILC treated with H<sub>2</sub>SO<sub>4</sub> exhibited higher acidity and subsequently rose in activity. Another optimum way to enhance the Fe-TiO<sub>2</sub>-PILC acidity was its treatment with a flow of SO<sub>2</sub> + O<sub>2</sub> + H<sub>2</sub>O at 400 °C [143, 144]. In these conditions, SO<sub>2</sub> was oxidized to SO<sub>3</sub>

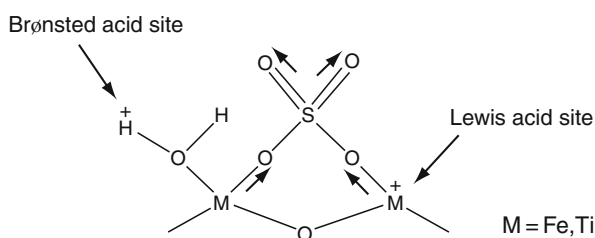
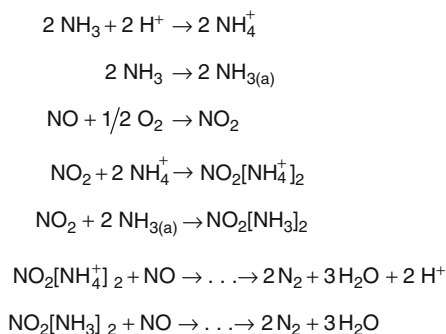


**Fig. 10.7** Model for Brønsted and Lewis acid sites on sulphated Fe-TiO<sub>2</sub>-PILC

by oxygen, leading to sulphate species formation, which remained adsorbed at the surface, increasing the acidity. The model of the acid sites created by this treatment is shown in Fig. 10.7, inferred by Yang and coworkers [143]. The presence of water causes the transformation from Lewis to Brønsted acid sites, giving rise to an increase in the acidity and therefore the catalytic activity.

The mechanism of SCR-NH<sub>3</sub> over Fe-TiO<sub>2</sub>-pillared clays has also been reported, suggesting the following steps [151]:



The initial step was adsorption of ammonia on neighboring acid sites, as has been indicated above [143, 144], generating adsorbed ammonium anions (on Brønsted sites) and adsorbed ammonia (on Lewis sites). Therefore, NO molecules were oxidized by the oxygen incorporated with the reactants, leading to the formation of NO<sub>2</sub> that stayed adsorbed on the catalyst. Then these NO<sub>2</sub> species reacted with adsorbed ammonia, generating an active intermediate that finally reacted with NO to produce nitrogen and water [151].

The incorporation of promoters into Fe-TiO<sub>2</sub>-pillared catalysts has been evaluated more recently by the same researchers. The promoters included rare earth metals, such as Ce, La, Pr, Tb, or Nd, and mixtures thereof, with a range of approximately 1–2 wt% preferred [142]. These rare earth doped Fe-TiO<sub>2</sub>-PILCs were prepared by incipient wetness impregnation, using metal nitrates as precursors [152]. The best SCR activities were described when CeO<sub>2</sub> or PrO<sub>1.83</sub> was added, being more than three times as active as the commercial tungsten promoted vanadium-titanium oxide. The activity of these systems was controlled by the incorporated amount of promoter, an optimum dispersion of it being beneficial. Thus, when the dopant amount was below 2 wt% no aggregation of the promoter was detected, enhancing the NO conversion. The beneficial effect of the promoter was not related to an increase of the acidity; the surface acidity of doped Fe-TiO<sub>2</sub>-PILC was almost unchanged. However, bearing in mind the mechanism proposed by Yang and coworkers (see scheme above), the promoter caused an increase of the oxidation of NO to NO<sub>2</sub> by O<sub>2</sub>, and thus improved the SCR activity, favoring one of the main mechanism steps. As occurred in previous metal ion-exchanged PILCs, these doped systems were also effective in the presence of H<sub>2</sub>O plus SO<sub>2</sub>. Again, this behavior was possible thanks to an increase of surface acidity due to sulphate species formation [143, 144].

Other researchers have also dedicated many efforts to develop SCR-NH<sub>3</sub> catalysts from pillared clays. Chmielarz et al. incorporated copper and iron in alumina-, titania- and zirconia-pillared clays [138]. Pillared clays were synthesized by a conventional ion-exchange/intercalation procedure with the corresponding metal oligomers. In a second step, either copper or iron was incorporated into the dried intercalated clays by the ion-exchange method, holding the intercalated clay in constant stirring with a metal solution at 60 °C. Their catalytic performance for NO reduction with ammonia strongly depended on the nature of both the pillar and the additional metal. Titania-pillared montmorillonites were the most active catalysts, higher than ZrO<sub>2</sub> and Al<sub>2</sub>O<sub>3</sub>, the system with iron being less active than the copper-TiO<sub>2</sub> pillared clay. The introduction of metals also influenced the N<sub>2</sub> selectivity, increasing for titania- and zirconia-pillared clays, but decreasing for alumina-pillared clays. The behavior of these systems depended on the Lewis acid sites created during the synthetic procedure, the centers where the ammonia could be chemisorbed, and the sites where the NO adsorption took place. Nitric oxide formed at least two types of surface species: relatively weakly sorbed NO, which desorbs at temperatures below 250 °C, and nitrates that are stable to about 450 °C. Therefore, Cu-TiO<sub>2</sub>-pillared montmorillonite described NO adsorption at low temperatures (below 200 °C), yielding the direct decomposition of NO to O<sub>2</sub> and N<sub>2</sub>. This process disappeared in other solids and was related to the greater activity of this catalyst. The same authors also studied the incorporation of the active metal and the polycation (precursor of the pillar) together. They described the synthesis and activity of Co and Cu over TiO<sub>2</sub> and Al<sub>2</sub>O<sub>3</sub>-pillared clays [153]. The simultaneous insertion of pillars and metals was less effective than the synthesis in two steps. It was mainly related to the worse textural properties obtained by this method. These studies showed that modified PILCs were very complex materials, and that under reaction conditions NO can be converted in different ways. In the low-temperature region (T < 250 °C) the chemisorbed ammonia over acid sites can react with NO molecules preadsorbed, while at higher temperatures (T > 250 °C) chemisorbed NH<sub>3</sub> molecules may react with surface nitrate anions. The suitable activation of ammonia molecules over Lewis acidic centres is probably a crucial factor, which determines the activity of clay catalysts in DeNO<sub>x</sub> processes [154].

Pillared clays described up to now as promising and active SCR catalysts are based on smectites, because of their high diversity and activity in many chemical treatments. Nevertheless, other clays have recently been tested as promising catalysts by Chmielarz and coworkers. Vermiculites [155] and phlogopites [156] have been studied for SCR purposes. These clays are both trioctahedral 2:1 sheet silicates with a negative sheet charge higher than smectites [157, 158]. Vermiculites have a layer charge close to 0.6–0.9 that should be compensated by Mg<sup>2+</sup>-hydrated ions. These cations are positioned between the bases of the aluminum tetrahedron, influencing the organization of the interlayer water molecules and conferring lower swelling properties than smectites [158]. Moreover, phlogopites belong to the true mica group with a charge close to 1, because of Si<sup>4+</sup> substitution for Al<sup>3+</sup> in a 3:1 ratio, which is compensated by nonhydrated monovalent cations (commonly K<sup>+</sup>) that are located between TOT layers. Their position coincides with the center of

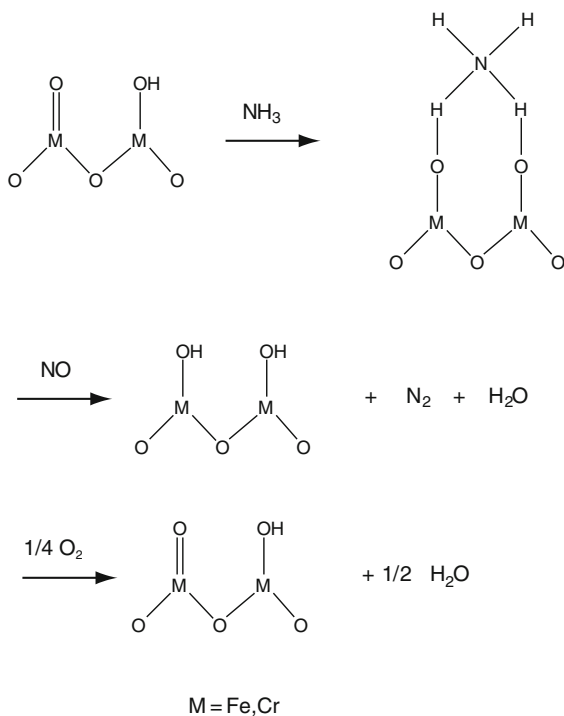
hexagonal rings formed by tetrahedrons of the T sheet, conferring a strong stabilization of the structure [159]. The direct pillaring of these clays is not as effective as for smectites, because their structural characteristics they need a previous treatment to reduce the charge of layers. Chmielarz et al. applied several acid treatments to leach aluminum cations from the tetrahedral sheet, reducing the charge of the layer [155, 156]. Controlling the process, it was able to arrange phlogopite and vermiculite in order to prepare aluminum pillared clays by intercalation/ion-exchange with Keggin ions. A posterior Cu<sup>2+</sup> or Fe<sup>3+</sup> incorporation was performed by the ion-exchange method, similar to the pillared smectites described before. The resulting Al<sub>2</sub>O<sub>3</sub>-pillared clays, modified with copper or iron, were found to be active and selective catalysts in the SCR process with ammonia. Fe-containing catalysts were more active at lower temperatures than copper samples (for both phlogopite and vermiculite starting clays); behavior related to the presence of oligomeric and bulky oxide species that were catalytically more active at low-temperature range. All systems exhibited great N<sub>2</sub> selectivity (ca. 90%) and NO conversion values; although at high temperatures (>450 °C) their effectiveness was reduced because of the undesired process of ammonia oxidation by oxygen. Nevertheless, the advantages of these systems compared with other clays are their high selectivity to nitrogen, their effectiveness at lower temperatures, and their stability.

Another way to enhance the pillared clay activity was the addition of metal oxides instead of isolated metals. Doping TiO<sub>2</sub>-montmorillonite with Fe<sub>2</sub>O<sub>3</sub> and Cr<sub>2</sub>O<sub>3</sub> yielded high activity, twice greater than the vanadia–titania commercial system [160]. Their SCR activity was related to the presence of both metal-oxygen species (M=O and M–OH) and Brønsted sites. The mechanism proposed for these systems is shown in Fig. 10.8, analogous to that proposed for the vanadia–titania commercial catalyst. Moreover, since the activity of these systems depended on the oxygen presence, the M–OH species could be oxidized to M=O by O<sub>2</sub>, increasing the activity. In addition, Fe-Cr/TiO<sub>2</sub>-PILCs caused a low SO<sub>2</sub> oxidation to undesirable SO<sub>3</sub> products, which was another advantage for these systems.

MnO<sub>x</sub> were also borne in mind, joining with ZrO<sub>2</sub>-montmorillonites through treatment with water solutions [161]. The resulting manganese oxide/hydroxide species acted as promoters for the NO conversion, obtaining practically 100% of N<sub>2</sub> selectivity. Nevertheless, as has been indicated before, the acidity of the resulting catalysts played an important role in SCR reaction. MnO<sub>x</sub> species were not acid centers, thus it was necessary to control the preparation conditions in order to form new acid sites, the previous acid activation with HCl being a promising route. Nevertheless, the metal oxide most studied in pillared clays has been vanadium oxide, mainly because of the superior activities described for other supports (metal oxides, zeolites, etc.), as discussed in the foregoing. Different V<sub>2</sub>O<sub>5</sub> percentages were incorporated into TiO<sub>2</sub>-PILCs (based on bentonites) by incipient wetness impregnation [162], and by ion-exchange with VO<sup>2+</sup> species [163]. The vanadia content influenced the activity of these systems: for V<sub>2</sub>O<sub>5</sub>/TiO<sub>2</sub>-PILCs increasing the vanadium amount raised the NO conversion at temperatures below 350 °C; whereas at higher temperatures the maximum value was exhibited by the 4.4% V<sub>2</sub>O<sub>5</sub>/TiO<sub>2</sub>-PILC [162]. The NO degraded was mainly converted to N<sub>2</sub>; all

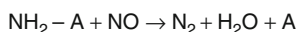
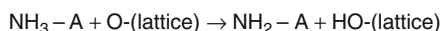
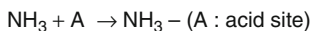


**Fig. 10.8** Scheme for the mechanism of the SCR reaction on Fe–Cr/TiO<sub>2</sub> pillared clay, where M can be Fe or Cr (adapted from Cheng et al. [160])



systems exhibited nitrogen selectivity greater than 97%. The authors demonstrated that V<sub>2</sub>O<sub>5</sub> incorporation raised the amount of Brønsted acid sites associated with V<sup>5+</sup>-OH species [163]. The acidity of these V<sub>2</sub>O<sub>5</sub>/TiO<sub>2</sub>-PILCs has also been modified by means of treating the TiO<sub>2</sub>-PILC with sulphate species, which created Brønsted acidity [164]. The activity of these samples was greater than sulphated-TiO<sub>2</sub>-PILC, and even greater than V<sub>2</sub>O<sub>5</sub>/TiO<sub>2</sub>-PILC; although it can be noticed that sulphation increased NO conversion, but decreased the N<sub>2</sub> selectivity for vanadium contents close to or higher than 3%. The presence of both sulphate and low vanadia amounts (2 wt%) in titanium-pillared clay allowed a good balance between redox and acid sites, leading to an excellent catalyst for SCR-NH<sub>3</sub> [165]. The high performances of these systems have been explained in terms of the structural combination between acid sites and redox sites, bearing in mind the mechanism described by these systems [166]. The SCR reaction occurred after the ammonia adsorption on acid sites (see following scheme), followed by its dissociation at the surface. Then gaseous NO molecules reacted with the activated NH<sub>3</sub> species to form N<sub>2</sub> and H<sub>2</sub>O that were desorbed. This process involved the reduction of vanadia active sites that were later reoxidized by oxygen [164, 166]. Therefore, the presence of Brønsted acid sites in close proximity with vanadia sites resulted in a promoting effect on SCR-NH<sub>3</sub> activity, as occurred on vanadia-sulphated titanium pillared clay.

The activity of these vanadia-doped titania-pillared clays has led to further investigations, appearing of interest to research about the influence of Ti-precursors



in the preparation of these catalysts. Titanium alkoxides were the best precursors to get effective catalysts [167]. The organic polyoxocations were able to go right through the clay layers, yielding the formation of mesoporosity and high surface areas. These textural properties were responsible for a good dispersion of vanadia species, resulting in efficient SCR catalysts.

During recent years, pillared and un-pillared clays have been modified with carbon deposits, leading to active SCR- $\text{NH}_3$  catalysts [168]. Different preparative ways have been described to obtain mineral-carbonaceous nanocomposites, although not so many have been focused on pillared clays. Chmielarz et al. treated several  $\text{ZrO}_2$ -PILCs with a polymer (polyacrylamide) by sorption in aqueous solution [169, 170]. The polymer was then turned into a carbonaceous species by carbonization under nitrogen, and subsequently manganese was incorporated by adsorption with saccharose. The presence of these carbon deposits improved the SCR- $\text{NH}_3$  activity of zirconia-pillared clays. The NO conversion values increased from 20–80% at temperatures lower than 400 °C. Supporting this work, Grzybek et al. [171] studied the influence of preparative steps on the structure of carbon-pillared clays, selecting polyacrylamide as the polymer and making the carbonization in the way described above [169]. The structural study showed the presence of carbon deposits on the inner surface of the pillared clays without changes in the PILC structure. These carbon deposits also generated micropores and acidity on the pillared clays, converting them into promising SCR- $\text{NH}_3$  catalysts. Following these researches, Motak studied the influence of copper incorporation over  $\text{Al}_2\text{O}_3$ - and  $\text{ZrO}_2$ -pillared montmorillonites treated with carbon deposits [172]. As described before, pillared clays were treated with polymer and carbonized under nitrogen at 500 °C. Subsequently, copper was introduced by incipient wetness impregnation, reaching a 5 wt%. The addition of copper to carbon-pillared clays increased  $\text{NO}_x$  conversion without modifying the  $\text{N}_2$  selectivity, thus promotion by both polymer and copper species increases as a promising way to get effective SCR- $\text{NH}_3$  catalysts.

### 10.2.2 $\text{NO}_x$ Reduction with Hydrocarbons

The interest in finding alternative reductants to ammonia for the  $\text{NO}_x$  reduction involved the development of catalysts based on layered clays [50]. The researches in this field took over the running of selective catalytic reduction with ammonia, studying similar active centers. Some investigations were performed using smectites directly, incorporating the active phase by exchanging the exchangeable cations in the smectite by Fe, Mn, Co, Ni, Cu, or Ag [173]. The efficiency of these

materials was evident only using oxygenated hydrocarbons as reductants (acetone or propanol); methane, ethane, and propane were not so effective.

The same pillared clays developed for SCR by ammonia were assessed using hydrocarbons as an ammonia substitute. These pillared clays were mainly synthesized by intercalation/pillaring with metal polyoxocations, and the active site incorporation was performed by ion-exchange or impregnation procedures. Perathoner et al. [141] evaluated the activity of Cu-Al<sub>2</sub>O<sub>3</sub>-PILC and Cu-Al<sub>2</sub>O<sub>3</sub>/Fe<sub>2</sub>O<sub>3</sub>-PILCs, comparing ammonia and propane as reductants. The activity with ammonia was satisfactory; but using propane, under the same reaction conditions, no activity was observed. A similar conclusion was drawn by Yang et al., comparing the activity of Cu-TiO<sub>2</sub>-PILC with several reductants [174]. NH<sub>3</sub> was more effective than C<sub>2</sub>H<sub>4</sub> and CH<sub>4</sub>, even being inactive under the latter. Despite the lower effectiveness of ethylene as a reductant compared with ammonia, the authors studied different pillared clay systems using that hydrocarbon as the reductant. For all catalysts, the NO<sub>x</sub> conversion by C<sub>2</sub>H<sub>4</sub> increased with increasing temperature, reached a maximum, and then decreased again. Comparing the pillared clay nature, M-TiO<sub>2</sub>-PILC was the most active catalyst with ethylene at low reaction temperatures (300–350 °C), whereas a delaminated Al<sub>2</sub>O<sub>3</sub>-pillared laponite was the most effective at higher temperatures (>400 °C) [175]. These effects were related to the porosity and the pore size of these materials. For delaminated Al<sub>2</sub>O<sub>3</sub>-pillared laponite, the macroporosity performed by delamination was partially responsible for its higher peak temperatures. Different metal active species were incorporated into these pillared clays: Cu, Fe, Co, Ce, Ag, and Ga; the copper form being the most active for both reactions, the NO reduction and the ethylene oxidation [140, 174].

The incorporation of Ag over Al<sub>2</sub>O<sub>3</sub>-, ZrO<sub>2</sub>- and TiO<sub>2</sub>-pillared montmorillonites (by the ion-exchange method) was also studied by Chmierlaz et al. [176]; but the NO reduction with C<sub>2</sub>H<sub>4</sub> was not so effective, because the oxygen from the stream oxidized NO to form undesired NO<sub>2</sub>. Therefore, the copper content and the methodology to introduce it were also studied. Growing Cu amounts increased the activity until the loading reached 6%; after that the activity decreased because of the reduction of the surface area and pore volume of the catalyst. Regarding the synthesis methodology, the ion-exchange incorporation was more efficient than wetness impregnation. This effect was associated with the copper species generated. The first method generated isolated Cu<sup>2+</sup> species, whereas the second produced CuO aggregates; the first being more easily reducible, which favored the redox cycle of the SCR reaction [174].

Other hydrocarbon reductants have been used more recently. Valverde et al. studied several M-TiO<sub>2</sub>-PILCs (M= Fe, Cu, or Ni) using C<sub>3</sub>H<sub>6</sub> as a reductant [177]. All systems showed an increase on the NO<sub>x</sub> conversion with increasing temperature, reaching a maximum (ca. 55% NO<sub>x</sub>) and decreasing after. This behavior was previously related to the combustion of the hydrocarbon. The oxidation of hydrocarbon, which reduces the amount of reductant, became dominant at higher temperatures, reducing the NO<sub>x</sub> conversion [174]. Again, copper-pillared clay appeared to be the most active catalyst, and the ion-exchange synthesis method was the optimum way for copper incorporation because it permits the formation of three types of copper species, i.e., isolated Cu<sup>2+</sup>-ions anchored at pillars, Cu<sup>2+</sup> clusters as patches of

amorphous CuO, and CuO [177]. Operating parameters have an important influence over pillared clay activity. Selecting Cu-TiO<sub>2</sub>-PILC, internal diffusion was negligible for particle sizes inferior to 1500  $\mu\text{m}$ . The increase of the hydrocarbon concentration caused positive effects when total combustion occurred, and the oxygen concentration effect depended on the called critical oxygen concentration. The water presence inhibited the reaction, although it was fully reversible [178]. The mechanism followed by this system required the adsorption of both reactants, generating several reaction intermediates, such as  $\text{NO}_3^-$ ,  $\text{C}_3\text{H}_7\text{-NO}_2$ , and acetate species. The decomposition of nitrate species by reaction with carbon intermediates generated nitrogen and carbon dioxide [179]. Similar conclusions have been described for Cu-Fe<sub>2</sub>O<sub>3</sub>-PILCs prepared by the ion-exchange methodology [180, 181] and for Cu-Al<sub>2</sub>O<sub>3</sub>/CeO<sub>2</sub>-PILCs prepared by impregnation and treated later with sulphate ions to increase the acidity [182]. Moreover, copper has an adequate redox cycle to perform the  $\text{NO}_x$  reduction by  $\text{C}_3\text{H}_6$ , controlling the operating conditions, the nature of the copper species, and the formation of reaction intermediates. The relevance of these systems is also evident in the recent work of Koch et al. [183], who have patented the methodology to produce catalytic active silicates based on copper-pillared clays.

$\text{C}_3\text{H}_6$  was also chosen as a reductant for M-ZrO<sub>2</sub>-PILCs. Titania-pillared clays have been extensively described above, but Tretyakov et al. also obtained satisfactory results for the SCR reaction using zirconia-pillared clays [184]. Zirconia-pillared montmorillonites containing transition metal cations and Ag were promising SCR-HC catalysts because of their high thermal stability, high catalytic activity, and high selectivity in the presence of oxygen. The catalytic properties of ZrO<sub>2</sub>-pillared clays were studied in detail, evaluating the intermediate species formed over these systems [185]. ZrO<sub>2</sub> existed as nano-sized particles in pillared clays and over them two nitrate species (bidentate and bridging) and isopropoxide species were formed after NO and  $\text{C}_3\text{H}_6$  adsorption, respectively, this being the first step for the SCR reaction. These species can later be consumed in the interaction with surface NO<sub>2</sub> complexes, yielding the decomposition of these surface species to the reaction products. On the other hand, platinum and copper incorporation into these systems generated high performances in the SCR reaction using decane or propylene as the reductant, even in the presence of SO<sub>2</sub> and H<sub>2</sub>O [186]. The combination of both active components allowed ensuring high N<sub>2</sub> selectivity, typical for Cu systems, and high conversion levels at low temperatures, characteristic of Pt catalysts. The inclusion of metals modifies the adsorption complexes formed at the surface [187]. The number of sites capable of forming nitrate complexes increases, and the concentration of surface hydrocarbon compounds (i.e., isopropoxide, acetone, and acetate complexes) changes. These species are able to form nitroorganic complexes (e.g., dinitropropane) that operate as reaction intermediates. Thus, the concentration of these species and their decomposition were responsible for the activity of Pt,Cu-ZrO<sub>2</sub>-PILCs compared to unmodified pillared clays.

Alumina-pillared clays and derivatives have also been evaluated for  $\text{NO}_x$  SCR reactions by  $\text{C}_3\text{H}_6$ . Iron and chromium were incorporated into Al<sub>2</sub>O<sub>3</sub>-pillared smectites by two different methods [188–190]: (i) copillaring; synthesizing polyoxocations of Fe/Al or Cr/Al that were intercalated by ion-exchange; and

(ii) incipient wetness impregnation of the corresponding metal solutions. The incorporation of iron exhibited the best  $\text{NO}_x$  and hydrocarbon conversion values around  $450^\circ\text{C}$ , although  $\text{O}_2$  contents higher than 0.6% caused a decrease in activity. Different metal loadings were studied, showing enhanced activities according to increased metal contents, reaching a maximum of ca. 10% [191]. The systems were constituted by Fe (III) cations or dispersed phases with a distorted local symmetry responsible for the catalytic activity. In this work, the copillaring synthesis appeared as an optimum way to incorporate active metals into pillared clays. The activity of  $\text{Al}_2\text{O}_3/\text{Fe}_2\text{O}_3$ -pillared clays was analogous to that described by  $\text{Fe}_2\text{O}_3$ - $\text{Al}_2\text{O}_3$ -pillared clays prepared by impregnation (see Fig. 10.9). Thus, the copillaring process appears a promising way to obtain active catalysts, avoiding the detrimental effect caused by the impregnation method over the textural properties of these materials. Nevertheless, not all active metals can be incorporated by copillaring procedures, depending on their acid–base properties. This occurs for instance with nickel catalysts. Nickel did not form optimum polycations to be intercalated between clay layers. Thus, nickel pillared clays were synthesized by impregnation and encapsulation procedures using  $\text{Al}_2\text{O}_3$ -pillared smectites as supports [192]. The resulting materials showed catalytic behavior similar to nickel catalysts based on zeolitic supports, attributed to the presence of  $\text{NiO}$  and  $\text{Ni}_2\text{AlO}_4$  spinel species.

The majority of metal pillared clays described up to now have been based on transition metals; nevertheless noble metals have also been studied as active centers for  $\text{NO}_x$  SCR reactions with pillared clays. Pd, Rh, and Pt were added to  $\text{Al}_2\text{O}_3$ -pillared

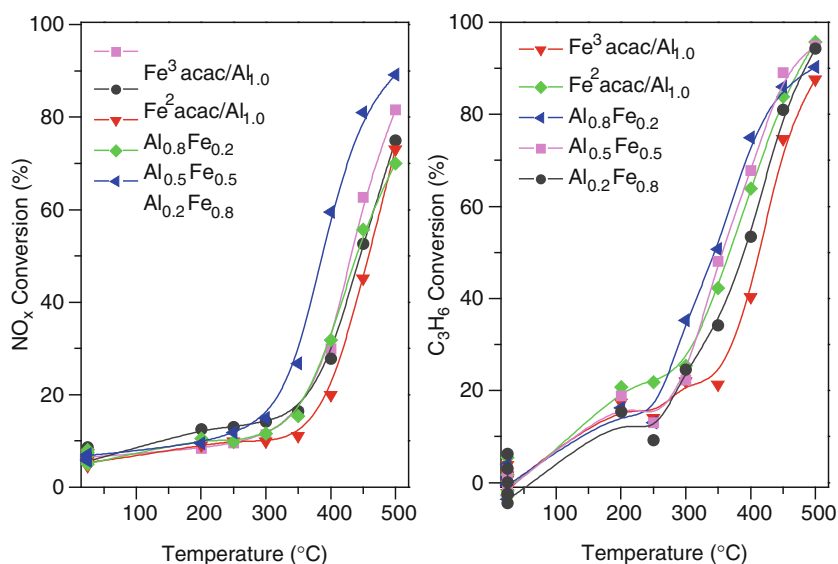


**Fig. 10.9**  $\text{NO}_x$  and  $\text{C}_3\text{H}_6$  conversion values for aluminum and iron pillared clays synthesized by copillaring ( $\text{Al}_x\text{Fe}_y$ ) and impregnation procedures (iron salt/ $\text{Al}_{1.0}$  pillared clay) (adapted from Belver et al. [191])

montmorillonites, previously extruded in monoliths, by incipient wetness impregnation, performing the catalytic studies by using methane as the reductant [193]. Rh-Al<sub>2</sub>O<sub>3</sub>-PILC exhibited the best catalytic activity at 400 °C, higher than M-ZrO<sub>2</sub> catalysts, mainly because of their surface acidity and porous structure. Nevertheless, more recent studies with Pd and Rh have demonstrated the importance of the synthetic process over the activity of these monoliths. Pd, for example, was active as Pd<sup>2+</sup>, whereas PdO clusters favored the undesired hydrocarbon combustion. Thus, the precursor nature played an important role in catalyst activity [194]. Concerning Rh systems, the incorporation of the metal by ion-exchange led to higher activities than the impregnation synthesis. Ion-exchange allowed obtaining neighboring Rh<sup>3+</sup> species and Lewis acid centers, which enhanced the catalytic activity [195]. NO<sub>x</sub> must be activated over rhodium species, whereas methane must be chemisorbed over Lewis acid centers. Subsequently, both species reacted with adsorbed NO<sub>2</sub> to produce nitrogen and carbon dioxide. Therefore, both species must be located nearby to enhance the SCR activity.

### ***10.2.3 NO<sub>x</sub> Catalytic Reduction with CO and NO<sub>x</sub> Catalytic Decomposition***

Pillared clays have been studied to a lesser extent for other DeNO<sub>x</sub> technologies, such as catalytic reduction with CO, and direct catalytic decomposition. Based on other active catalysts, noble metals have been embodied into pillared clays in order to perform the reduction of NO and CO emissions. Rh was supported by the impregnation procedure over different Al<sub>2</sub>O<sub>3</sub>- and Al<sub>2</sub>O<sub>3</sub>/Fe<sub>2</sub>O<sub>3</sub>-pillared clays (montmorillonites and saponites) [196, 197]. Up to 320 °C, all studied catalysts exhibited similar NO conversion values; but at lower temperatures the Rh-Al<sub>2</sub>O<sub>3</sub>-saponite was more active because of the presence of Rh sites more easily reduced. The activity was influenced by the starting clay and the pillaring process, achieving catalysts more efficient than the Rh-Al<sub>2</sub>O<sub>3</sub> typically used in automotive exhaust catalytic converters. On the other hand, Pd was also evaluated in the active phase for NO reduction with CO and H<sub>2</sub>, supporting the metal over several pillared clays, ZrO<sub>2</sub>-, Fe<sub>2</sub>O<sub>3</sub>-, Al<sub>2</sub>O<sub>3</sub>-, and TiO<sub>2</sub>-, prepared by conventional ion-exchange/intercalation procedures [198]. The NO conversion rates described two peaks as the temperature increased, at 140 and 240 °C, related to the reaction of in situ intermediates as the reaction took place. Among all PILCs studied, Pd-TiO<sub>2</sub>-PILCs achieved the highest conversion values. Their textural properties and the presence of oxygen vacancies were the reasons proposed for their higher activity. These catalysts exhibited high selectivity to N<sub>2</sub> at low temperatures, in contrast to other Pd/TiO<sub>2</sub> catalysts.

The direct catalytic decomposition of NO was studied in a complementary way to selective catalytic reduction reactions, in order to understand the catalytic behavior of those SCR catalysts described before. Copper incorporated by ion-exchange into an alumina-pillared laponite was subjected to direct catalytic decomposition [199].

Its behavior was similar to that described by Cu-ZSM-5 for the same reaction, N<sub>2</sub> being the major product.

### 10.3 HDL as DeNO<sub>x</sub> Catalysts

We consider next the second family of clays for possible environmental applications, the so-called hydrotalcites, layered double hydroxides (LDHs), or anionic clays [131, 132]. Briefly, LDHs are analogous to smectite clays, insofar as the layers are positively charged; thus between layers an exchangeable gallery of anions are intercalated. LDHs composition can be tailored in advance. It is possible to design both the positive charge of layers by incorporating different metal ions and, subsequently, the nature of intercalated anions [200, 201]. The diverse chemical composition and the porous network formed are especially attractive from a catalytic standpoint, representing an interesting way to create bifunctional redox catalysts or to control the acid–base properties of these catalysts [132, 202, 203]. These materials have been used for different catalytic applications, either as the catalyst itself or as a precursor to the catalyst. For example, they have been employed in the use or manufacture of syn gases (steam reforming, methanation reaction, or Fischer–Tropsch synthesis), and for the synthesis of fine chemicals [131, 204]. Although in a lesser manner, LDHs or anionic clays have also been evaluated for NO<sub>x</sub> removal technologies.

Selective catalytic reduction of NO with methane and direct catalytic decomposition of NO was a subject of interest of Detellier et al. using hydrotalcite as a precursor for catalysts. Hydrotalcites with different compositions (Mg(II), Fe(III)), (Cu(II), Al(III)), (Ni(II), Al(III)), and (Co(II), Al(III)) were heated to afford an amorphous mixed oxide losing the characteristic layered structure of the LDH precursor [205]. The direct decomposition of NO was evaluated over these materials. The conversion of nitric oxide was about 25%, except for the Ni/Al system that reached about 50%, increasing in all cases the formation of N<sub>2</sub> regularly with time. This fact suggested that the NO reduction occurred through N<sub>2</sub>O as an intermediate. Subsequently, the (Ni(II), Al(III)) system was studied for SCR with methane [206]. The reduction by methane was more effective than the direct NO decomposition, reaching NO conversion values close to 95%. This behavior remained after incorporation of oxygen to the gas stream, without N<sub>2</sub>O detection. These materials were tested under recycle conditions in order to check their continued activity. Thus, although their activity was reduced after three cycles, their conversion values remained at 70%, appearing as optimum catalysts for SCR purposes.

At the same time, Vaccari et al. created novel copper-containing catalysts from hydrotalcites for SCR reaction with ammonia [207]. The Cu<sub>x</sub>Mg<sub>(71.0-x)</sub>Al<sub>29.0</sub> hydrotalcites were prepared by coprecipitation and then calcined to decompose the LDH layered structure, obtaining the mixed oxide desired. Another sample was prepared by impregnation of a copper salt over Mg/Al hydrotalcite, previously calcined to get the corresponding Mg/Al mixed oxide. The first synthetic way demonstrated the efficiency of the method for obtaining the cubic mixed oxide without segregation of copper oxide. The catalytic behavior of CuMgAl mixed oxides in the presence of

excess O<sub>2</sub> showed differences according to the copper content. The catalysts with higher Cu loading exhibited the best NO conversion and N<sub>2</sub> selectivity values. The activity of the catalyst with 12.5% of CuO was even similar to that of the commercial catalyst up to 350 °C, with slightly better selectivity values. The catalytic activity of these systems was related to the presence of octahedrally coordinated Cu<sup>2+</sup> ions, well dispersed and stabilized in the mixed oxide matrix.

In recent years, legal restrictions imposed on NO<sub>x</sub> abatement have promoted the growth of novel technologies and materials. In this regard, several works have been reported in the scientific literature about the development of hydrotalcites as catalysts/adsorbents for NO<sub>x</sub> storage and reduction technology, commonly called NSR, which has previously been described in Section 10.1.5. The main objective in these studies was to replace commercial Pt/Ba/alumina catalysts with novel materials that exhibit higher effectiveness at low temperatures.

Centi, Vaccari, et al. synthesized Pt-Cu catalysts by impregnation over a commercial Mg/Al hydrotalcite, previously calcined to obtain the corresponding mixed oxide [30]. Reported results showed that hydrotalcite derivatives exhibited a promoted low-temperature NSR activity (below 200 °C) and a better SO<sub>2</sub> deactivation resistance than reference (Pt,Ba/alumina catalyst), although their behavior at higher temperatures (~500 °C) was slightly worse. Both effects were related to the different basicity of these supports. Mg(Al)O mixed oxide has a lower basicity than alumina because of the higher electronegativity of Mg. The lower basicity caused a better resistance to SO<sub>2</sub> and a higher amount of stored NO<sub>x</sub>. The relevance of the support was also tested, obtaining different Mg/Al mixed oxides by using several commercial hydrotalcites [208]. Outwardly, the degree of crystallinity influenced the NSR activity because the amount of well dispersed Mg(O) species and bulky Mg(O) species varied. The explanation given by the authors was that the first species were more active at lower reaction temperatures, but less stable at higher temperatures, while the second were less active at lower temperatures, but formed more thermodynamically stable species. Therefore, the suitable behavior required the presence of both types of species. On the other hand, the presence of copper was also profitable for these catalysts, because it caused a stabilization effect against hydrothermal and SO<sub>2</sub> deactivations. This fact was related to the creation of a copper-containing surface mixed oxide that stabilized the material against the formation of an undesired spinel phase, although in a later report these effects were related to the formation of Pt–Cu alloys [209]. The industrial interest of these metal-hydrotalcite precursors has been demonstrated by Vaccari et al. patenting the synthesis, and by the catalytic performance of several (M<sub>n+a</sub>Mg<sub>2+b</sub>Al<sub>3+c</sub>(OH<sup>-</sup>)<sub>2</sub>)<sub>z</sub><sup>+</sup>(A<sub>x</sub><sup>-</sup>)<sub>z/x</sub> mH<sub>2</sub>O systems, using different noble metals (Rh, Ru, Pt, Pd, and/or Ir) and varying their compositions [210].

Transition metals, leaving aside noble metals, have also been borne in mind to generate active mixed oxides from layered double hydroxides [211]. Ca<sub>x</sub>Co<sub>3-x</sub>Al hydrotalcite-like compounds (varying *x* from 0 to 3) were prepared by coprecipitation and then calcined to derive the mixed oxide with a spinel structure [212]. These materials appeared as three-functional for NO<sub>x</sub> abatement, whose behavior has been schematized in Fig. 10.10.



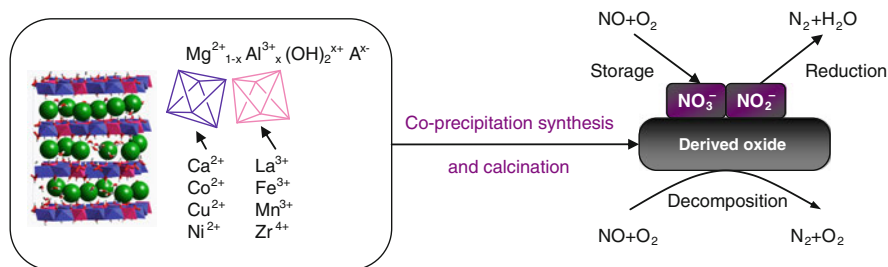


**Fig. 10.10** Representation of the multifunctional behavior of LDHs-derived catalysts for  $\text{NO}_x$  direct decomposition, storage, and reduction

LDHs-derived oxides may also behave as catalysts for the direct decomposition of NO in the presence of  $\text{O}_2$ , generating molecular nitrogen and oxygen.  $\text{Ca}_x\text{Co}_{3-x}\text{Al}$ -oxides systems reached up to 55% of NO at 300 °C, some even 75%, proving to be more active than other oxide catalysts designed for NO decomposition (see Section 10.1.6.4). On the other hand, these materials can also capture NO at the surface, describing a high NO storage capacity and reaching the steady state equilibrium after ca. 30 min. For example, the  $\text{Ca}_2\text{Co}_1\text{Al}$ -oxide was able to trap NO for 750 s, and capture 12.88  $\text{mg g}^{-1}$  of NO within 30 min. The last function of these derived oxides consists of providing the reduction of the NO trapped. For this aim, hydrogen is usually included in the stream, and thus the derived oxides behave as catalysts for NO reduction. The performance in this function of  $\text{Ca}_x\text{Co}_{3-x}\text{Al}$ -oxides was comparable to that of the commercial noble metal catalysts [212]. The scientific literature demonstrates that the activity of these materials could be improved by

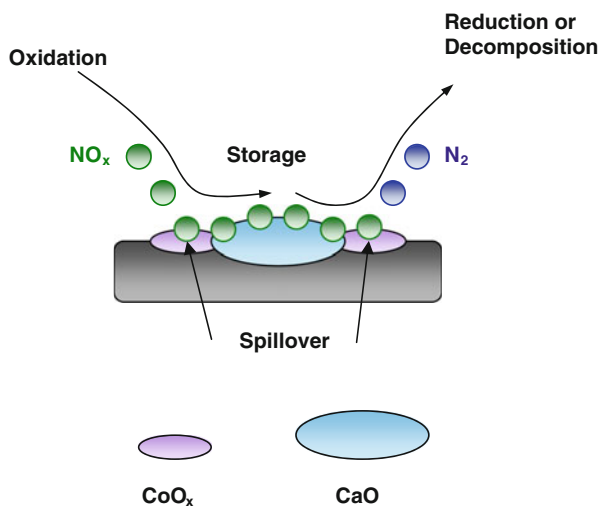


**Fig. 10.11** Schematic representation of the mechanism proposed for  $\text{CaCoAl}$ -derived oxides for  $\text{NO}_x$  storage and reduction

adding other elements (Fe, La, Zr, or Mn) to form a quaternary mixed oxide [213]. The added metal should replace the Al<sup>3+</sup> from the hydrotalcite-phase, thus it could remain well distributed and modify the reducibility of the neighboring cations. La-containing catalyst excelled over all other catalysts, mainly in its NO storage capability. The NO adsorption/desorption mechanism proposed for these materials is schematically shown in Fig. 10.11 [211–213]. NO<sub>x</sub> is oxidized on the catalytic redox region (Co species), generating various kinds of nitrites and nitrates that migrate to the storage region (Ca species), where they remain until H<sub>2</sub> is incorporated into the stream for reducing them. The migration depends on the distance between the redox and storage regions; therefore the storage site must be located near the catalytic redox site. Thus it is that the synthesis must be controlled to produce suitable catalysts, requiring a considerable study at nanometer scale. In any case, layered double hydroxides turn out to be promising precursors to generate (LDH)-based mixed oxides for NO decomposition, storage, and reduction, achieving an excellent catalytic activity by the elegant combination of normal transition metals.

#### 10.4 Porous clay Heterostructures (PCH) as DeNO<sub>x</sub> Catalysts

Layered clays have been described as interesting materials for catalytic and adsorption properties [50]. Clays can be modified by pillaring procedures to obtain a new generation of microporous materials. Pillared clays modified with noble and transition metals have been found to be active and selective for DeNO<sub>x</sub> technologies, described in detail in previous sections. Nevertheless, a new group of porous materials, named porous clay heterostructures (PCH), have been obtained from layered clays. PCH are mesoporous molecular sieves produced by templated synthesis [214, 215]. The intercalation of surfactants in the interlayer space of clays, followed by the incorporation of aqueous silicate species, leads to an interlayer silica framework. The surfactant is withdrawn by calcination, resulting in a mesoporous solid with thermally stable pores. These porous clay heterostructures are applied for patterning heterogeneous catalysts [216].

Porous clay heterostructures were synthesized from several smectites (saponite, montmorillonite, and vermiculite), incorporating copper and iron as active species in order to be evaluated for the selective catalytic reduction with ammonia [217, 218]. The porous clay heterostructures were synthesized according to the scheme presented in Fig. 10.12, divided into the following steps: (i) surfactant and cosurfactant are intercalated in the interlayer space of the clay by ion-exchange, generating micelles between layers; (ii) the silica source is added and its *in situ* polymerization takes place around the micelle, generating silica pillars; and (iii) the organic templates are removed by calcination or extraction (with a suitable solvent), yielding materials with high surface area and porosity.

Porous clay heterostructures are characterized by high thermal and hydrothermal stability, significant surface acidity, ion-exchange properties, and combined micro- and mesoporous structure. These properties depend on the type of the parent clay

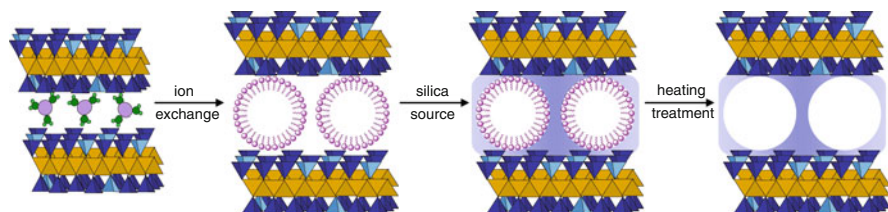


**Fig. 10.12** Scheme of the synthetic procedure employed for the preparation of porous clay heterostructures [218]

used for their synthesis, although the porous structure is also controlled by the surfactant and cosurfactant as well as the synthesis conditions. Chmielarz et al. obtained in this way porous clay heterostructures with surface areas superior to  $750 \text{ m}^2 \text{ g}^{-1}$ , comprised of micro- and mesoporosity [217, 218]. The deposition of transition metals (Cu, Fe) was made by the ion-exchange method, which permitted the control of the metal loading on these systems. Copper catalysts contained both isolated  $\text{Cu}^{2+}$  cations and oligonuclear  $[\text{Cu}-\text{O}-\text{Cu}]$  species, whereas iron-catalysts had isolated  $\text{Fe}^{3+}$  cations and oligonuclear  $(\text{FeO})_n$  species. Surface acidity of  $\text{DeNO}_x$  catalysts have been described in Section 10.2.1 as an important factor influencing their activity and selectivity. Thus, the PCH presented in this section were characterized by both Brønsted and Lewis acid sites. Brønsted sites were related to protons compensating the negative charge of the smectite layers, appearing as  $\text{Si}-\text{OH}-\text{Al}$  bridges whose location and accessibility depended on the clay and its modification. Lewis acid sites were due to the presence of aluminum in tetrahedral and octahedral sheets of clay, although the incorporation of transition metals also generated Lewis acid sites.

The catalytic activity of these PCHs has been compiled in Fig. 10.13, according to the results of Chmielarz et al. [217, 218]. All Cu,Fe-PCH catalysts were active, selective, and stable in the SCR- $\text{NH}_3$  process. The best catalytic behavior was shown by Fe-PCH from saponite, obtaining high nitrogen selectivity (97%) at lower temperatures ( $<275 \text{ }^\circ\text{C}$ ). This behavior was attributed to the presence of iron as small oligomeric  $\text{Fe}_x\text{O}_y$  species and bulky  $\text{Fe}_2\text{O}_3$  clusters, which were easily reducible at lower temperatures than isolated  $\text{Fe}^{3+}$  ions or oligomeric iron oxide species, which constituted the other iron samples. Copper systems exhibited different catalytic behavior, mainly the Cu-PCH from montmorillonite, which was due to the type of copper species deposited on the support surface as well as its acidity. Common to all catalysts was the competitive ammonia oxidation by  $\text{O}_2$ , which caused the decrease of the NO reduction when temperatures rose above  $450 \text{ }^\circ\text{C}$ . The studied catalysts operated successfully when water and  $\text{SO}_2$  were incorporated into the gas stream. The activity and selectivity of these Cu-PCH samples were nearly the same before and after treatment with  $\text{SO}_2$ . The Fe-PCH catalysts were slightly affected by  $\text{SO}_2$ , Fe-PCH from saponite suffering the highest deactivation effect: about a 2% decrease in the NO conversion. The catalytic  $\text{DeNO}_x$  performance of porous clay heterostructures demonstrated the efficiency and stability of

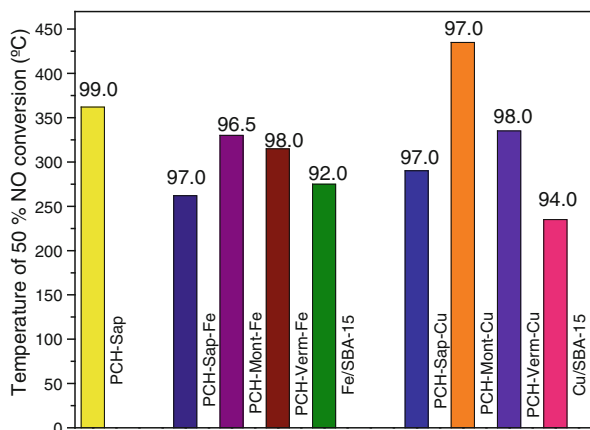


**Fig. 10.13** Catalytic performance of Cu, Fe-PCHs materials in DeNO<sub>x</sub> process: bars = temperatures needed for 50% of NO conversion; numbers above bars = selectivity to N<sub>2</sub> at these temperatures [217, 218]

these derivative clay materials, turning them into promising heterogeneous porous catalysts.

## 10.5 Concluding Remarks

This chapter first briefly discussed the different NO<sub>x</sub> sources and the relevant legislation existing in various countries. The diverse mechanisms developed to decrease its formation, the relevance of the catalytic technologies for its removal, and the contribution of clay systems to those technologies have been discussed in detail.

Currently, catalytic technologies for the removal of NO<sub>x</sub> from emission gases are the most employed: mainly, the TWCs, developed for mobile sources that use gasoline; and the SCR, applied to stationary sources such as power plants and lean-burn engines. Many different materials have been tested as catalysts for these purposes: zeolites, metal oxides, noble metals, clays, and derivatives; and the parameters that control the activity, mainly related to the synthesis pathway and the reaction conditions, have been studied.

Clays and derivatives are an interesting class of materials that can be modified in different ways, resulting in systems with different texture, acidity, and chemical (redox) properties. In this chapter, some cases have been examined to discuss recent trends, limits, and opportunities offered by these materials as DeNO<sub>x</sub> catalysts. Attention was focused on the modifications that led to materials with activity higher or comparable to that described by commercial systems. The aim of this chapter was to offer a personal view about the importance of clay materials in the removal of nitrogen oxides by catalytic technologies. A great number of publications (since the 1990s) can be found in the scientific literature about this line of research; but

the main point is that currently there are researchers focusing their investigations to produce new and better catalysts for DeNO<sub>x</sub> technologies from clay materials, mainly related to pillared clays, hydrotalcites, and porous clay heterostructures, with the same objective: to obtain competitive catalysts with a significant economic and environmental benefit.

**Acknowledgments** Support of this work is provided by the *Spanish Ministry of Science*, MAT2007-66439-C02-01. The author is indebted to the *Spanish Research Council* (CSIC) and the *European Social Fund* for a postdoctoral contract, JAE-Doc, in the *Materials Science Institute of Madrid*.

## References

1. Health and environment linkages in the urban environment (2009) World Health Organization. <http://www.who.int/heli/risks/urban/urbanenv/en/index.html>. Accessed 08 August 2009
2. About air pollution (2009) European Environment Agency. <http://www.eea.europa.eu/themes/air/> about-air-pollution. Accessed 08 August 2009; Policy context (2009) European Environment Agency. <http://www.eea.europa.eu/themes/air/policy-context>. Accessed 08 August 2009
3. Colls J (2002) Air pollution. Taylor & Francis Group, Spon Press, London
4. Jones JC (2008) Atmospheric pollution. Ventus Publishing Aps, Aberdeen
5. Fritz A, Pitchon V (1997) The current state of research on automotive lean NO<sub>x</sub> catalysis. *Appl Catal B Environ* 13:1–25
6. Sillman S (1999) The relation between ozone, NO<sub>x</sub> and hydrocarbons in urban and polluted rural environments. *Atmos Environ* 33:1821–1845
7. Pârvolescu VI, Grange P, Delmon B (1998) Catalytic removal of NO. *Catal Today* 46: 233–316 (and references herein)
8. Van Diepen AE, Makkee M, Moulin JA (2001) Emission control from mobile sources Otto and diesel engines. In: Janssen FJJG, van Santen RA (eds) *Environmental catalysis*. Imperial College Press, London
9. Christen K (2005) EU proposes new PM and NO<sub>x</sub> emission limits. NRC finds hydrogen economy on track. *Environ Sci Technol* 39:398A
10. EURO 5 and 6 emissions standards for cars and vans (2006) European Federation for Transport and Environment. Position paper. <http://www.transportenvironment.org>. Accessed 22 June 2010
11. Regulation (EC) No 715/2007 of the European Parliament and of the Council (20 June 2007). *Official Journal of the European Union*. L 171/1-L 171/16
12. International Maritime Organization (October 2008) Resolution mepc.176(58) from The Marine Environment Protection Committee. <http://www.imo.org/environment>
13. Bosch H, Janssen F (1988) Control technologies. *Catal Today* 2:381–401
14. Smoot LD, Hill SC, Xung H (1998) NO<sub>x</sub> control through reburning. *Prog Energy Combust* 24:385–408
15. Heck RM (1999) Catalytic abatement of nitrogen oxides—stationary applications. *Catal Today* 53:519–523
16. Radojevic M (1998) Reduction of nitrogen oxides in flue gases. *Environ Pollut* 102:685–689
17. Roy S, Hegde MS, Madras G (2009) Catalysis for NO<sub>x</sub> abatement. *Appl Energy* 86: 2283–2297
18. Janssen F (2001) Emission control from stationary sources. In: Janssen FJJG, van Santen RA (eds) *Environmental catalysis*. Imperial College Press, London
19. Bosch H, Janssen F (1988) Effect studies. *Catal Today* 2:433–455
20. Centi G, Perathoner S (2007) Introduction: state of the art in the development of catalytic processes for the selective catalytic reduction of NO<sub>x</sub> into N<sub>2</sub>. *Stud Surf Sci Catal* 171:1–24

21. Trichard JM (2007) Current tasks and challenges for exhaust after-treatment research: an industrial viewpoint. *Stud Surf Sci Catal* 171:211–232
22. Traa Y, Burger B, Weitkamp J (1999) Zeolite-based materials for the selective catalytic reduction of NO<sub>x</sub> with hydrocarbons. *Micropor Mesopor Mat* 30:3–41 (and references herein)
23. Gómez-García MA, Pitchon V, Kiennemann A (2005) Pollution by nitrogen oxides: an approach to NO<sub>x</sub> abatement by using sorbing catalytic materials. *Environ Int* 31:445–467
24. Kato K, Nohira H, Nakanishi K, Igushi S, Kihara T, Muraki H (1993) Exhaust emission control device in internal combustion engine. *European Patent* 0573672 A1
25. Matsumoto S (1996) DeNO<sub>x</sub> catalyst for automotive lean-burn engine. *Catal Today* 29:43–45; Misono M, Inui T (1999) New catalytic technologies in Japan. *Catal Today* 51:369–375
26. Forzatti P, Casstoldi L, Lietti L, Nova I, Tronconi E (2007) Identification of the reaction networks of the NO<sub>x</sub> storage/reduction in lean NO<sub>x</sub> trap systems. *Stud Surf Sci Catal* 171:175–208
27. Bowker M (2008) Automotive catalysis studied by surface science. *Chem Soc Rev* 37: 2204–2211
28. Hodjati S, Vaezzadeh K, Petit C, Pitchon V, Kiennemann A (2000) Absorption/desorption of NO<sub>x</sub> process on perovskites: performances to remove NO<sub>x</sub> from a lean exhaust gas. *Appl Catal B Environ* 26:5–16
29. Cremona A, Fornasari G, Livi M, Petrini G, Trifiro F, Vaccari A, Vogna E (2008) Removal NO<sub>x</sub> from lean exhaust gas by absorption on oxi-anionic materials. *Catal Lett* 125:386–391
30. Fornasari G, Trifiro F, Vaccari A, Prinetto F, Ghiotti G, Centi G (2002) Novel low temperature NO<sub>x</sub> storage-reduction catalysts for diesel light-duty engine emissions based on hydrotalcite compounds. *Catal Today* 75:421–429
31. Shelef M, McCabe RW (2000) 25 years after introduction of automotive catalysts: what next? *Catal Today* 62:35–50
32. Janssen F, Meijer R (1993) Quality control of DeNO<sub>x</sub> catalysts performance testing, surface analysis and characterization of DeNO<sub>x</sub> catalysts. *Catal Today* 16:157–185
33. Bosch H, Janssen F (1988) Catalyst testing. *Catal Today* 2:403–431
34. Busca G, Lietti L, Ramisa G, Berti F (1998) Chemical and mechanistic aspects of the selective catalytic reduction of NO<sub>x</sub> by ammonia over oxide catalysts: a review. *Appl Catal B Environ* 18:1–36
35. Nakajima F, Hamada I (1996) The state-of-the-art technology of NO<sub>x</sub> control. *Catal Today* 29:109–115
36. Brandenberger S, Kröcher O, Tissler A, Althoff R (2008) The state of the art in selective catalytic reduction of NO<sub>x</sub> by ammonia using metal-exchanged zeolite catalysts. *Catal Rev* 50:492–581
37. Long RQ, Yang RT (2000) Characterization of Fe-ZMS-5 catalyst for selective catalytic reduction of nitric oxide by ammonia. *J Catal* 194:80–90
38. Centi G, Perathoner S (1995) Nature of active species in copper-based catalysts and their chemistry of transformation of nitrogen-oxides. *Appl Catal A Gen* 132:179–259
39. Komatsu T, Nunokawa M, Moon S, Takahara T, Namba S, Yashima T (1994) Kinetic studies of reduction of nitric oxide with ammonia on Cu<sup>2+</sup>-exchanged zeolites. *J Catal* 148: 427–437
40. Apostolescu N, Geiger B, Hizbullah K, Jan MT, Kureti S, Reichert D, Schott F, Weisweiler W (2006) Selective catalytic reduction of nitrogen oxides by ammonia on iron oxide catalysts. *Appl Catal B Environ* 62:104–114
41. Weisweiler W, Mallonn E, Gorke O (2003) Removal of nitrogen oxides by the NH<sub>3</sub>-SCR process: catalysts based on industrial residues containing iron(III) oxide. *Chem Ing Tech* 75:72–76
42. Ramis G, Larrubia MA, Busca G (2000) On the chemistry of ammonia over oxide catalysts: fourier transform infrared study of ammonia, hydrazine and hydroxylamine adsorption over iron-titania catalyst. *Top Catal* 11:161–166
43. Sullivan JA, Doherty JA (2005) NH<sub>3</sub> and urea in the selective catalytic reduction of NO<sub>x</sub> over oxide-supported copper catalysts. *Appl Catal B Environ* 55:185–194

44. Pena DA, Uphade BS, Reddy EP, Smirniotis PG (2004) Identification of surface species on titania-supported manganese, chromium, and copper oxide low-temperature SCR catalysts. *J Phys Chem B* 108:9927–9936
45. Schneider H, Maciejewski M, Kohler K, Wokaun A, Baiker A (1995) Chromia supported on titania. Properties of different chromium oxide phases in the catalytic reduction of NO by NH<sub>3</sub> studied by in situ diffuse reflectance FTIR spectroscopy. *J Catal* 157:312–320
46. Wu Z, Jiang BO, Liu Y (2008) Effect of transition metals addition on the catalyst of manganese/titania for low-temperature selective catalytic reduction of nitric oxide with ammonia. *Appl Catal B Environ* 79:347–355
47. Kang M, Park ED, Kim JM, Yie JE (2007) Manganese oxide catalysts for NO<sub>x</sub> reduction with NH<sub>3</sub> at low temperatures. *Appl Catal A Gen* 327:261–269
48. Shigemoto N, Moffat JB (2000) Characterization and activity of copper-on-carbon catalysts for low-temperature selective reduction of nitric oxide with ammonia. *Catal Lett* 69:1–10
49. Ouzzine M, Cifredo GA, Gatica JM, Harti S, Chafik T, Vidal H (2008) Original carbon-based honeycomb monoliths as support of Cu or Mn catalysts for low-temperature SCR of NO: effects of preparation variables. *Appl Catal A Gen* 342:150–158
50. Grzybek T (2007) Layered clays as SCR DeNO<sub>x</sub> catalysts. *Catal Today* 119:125–132
51. Moreno-Tost R, Oliveira ML, Eliche-Quesada D, Jiménez-Jiménez J, Jiménez-López A, Rodríguez-Castellón E (2008) Evaluation of Cu-PPHs as active catalysts for the SCR process to control NO<sub>x</sub> emissions from heavy duty diesel vehicles. *Chemosphere* 72:608–615
52. Held W, Koenig A, Richter T, Puppe L (1990) Catalytic NO<sub>x</sub> reduction in net oxidizing exhaust gas. SAE Paper, Document Number: 900496
53. Held W, Koenig A (1987) Deuschens Patent, DE 3642018 A1
54. Iwamoto M, Yahiro H (1994) Novel catalytic decomposition and reduction of NO. *Catal Today* 22:5–18 (and references herein)
55. Inui T, Iwamoto M, Kojo S, Shimizu S, Hirabayashi T (1994) Removal of nitric oxide on metallosilicate catalysts. *Catal Today* 22:41–57; Iwamoto M (1994) Preface. *Catal Today* 22:1–2
56. Tabata T, Kokitsu M, Okada O (1994) Study on patent literature of catalysts for a new NO<sub>x</sub> removal process. *Catal Today* 22:147–169
57. Armor JN (1995) Catalytic reduction of nitrogen oxides with methane in the presence of excess oxygen: a review. *Catal Today* 26:147–158
58. Cant NW, Liu IOY (2000) The mechanism of the selective reduction of nitrogen oxides by hydrocarbons on zeolite catalysts. *Catal Today* 63:133–146
59. Iwamoto M (1994) Zeolites in environmental catalysis. *Stud Surf Sci Catal* 84:1395–1410
60. Li Y, Armor JN (1993) Selective catalytic reduction of NO<sub>x</sub> with methane over metal exchanged zeolites. *Appl Catal B Environ* 2:239–256; Li Y, Armor JN (1994) Selective reduction of NO<sub>x</sub> by methane on co-ferrierites .1. Reaction and kinetic-studies. *J Catal* 150:376–387
61. Li Y, Battavio PB, Armor JN (1993) Effect of water-vapor on the selective reduction of NO by methane over cobalt-exchanged ZSM-5. *J Catal* 142:561–571
62. Li Y, Slager TL, Armor JN (1994) Selective reduction of NO<sub>x</sub> by methane on co-ferrierites .2. Catalyst characterization. *J Catal* 150:388–399; Li Y, Armor JN (1993) Simultaneous, catalytic removal of nitric-oxide and nitrous-oxide. *Appl Catal B Environ* 3:55–60
63. Yokoyama C, Misono M (1994) Catalytic reduction of nitrogen monoxide by propene in the presence of oxygen over cerium ion-exchanged zeolites .1. General-characteristics of the reaction and effects of alkaline-earth metal addition. *B Chem Soc Jpn* 67:557–562
64. Joyner RW, Stockenhuber M (1997) Unusual structure and stability of iron-oxygen nano-clusters in Fe-ZSM-5 catalysts. *Catal Lett* 45:15–19
65. Chen HY, Sachtler WMH (1998) Promoted Fe/ZSM-5 catalysts prepared by sublimation: De-NO<sub>x</sub> activity and durability in H<sub>2</sub>O-rich streams. *Catal Lett* 50:125–130
66. Hirabayashi H, Yahiro H, Mizuno N, Iwamoto M (1992) High catalytic activity of platinum-ZSM-5 zeolite below 500-K in water-vapor for reduction of nitrogen monoxide. *Chem Lett* 2235–2236

67. Iwamoto M, Yahiro H, Shin HK, Watanabe M, Guo I, Konno M, Chikahisa T, Murayama T (1994) Performance and durability of Pt-MFI zeolite catalyst for selective reduction of nitrogen monoxide in actual diesel-engine exhaust. *Appl Catal B Environ* 5:L1–L6
68. Choi BC, Foster DE (2005) State-of-the-art of de-NO<sub>x</sub> technology using zeolite catalysts in automobile engines. *J Ind Eng Chem* 11:1–9
69. Wichterlova B (2004) Structural analysis of potential active sites in metallo-zeolites for selective catalytic reduction of NO<sub>x</sub>. An attempt for the structure versus activity relationship. *Top Catal* 28:131–140
70. Salgado ALSM, Passos FB, Schmal M (2003) NO reduction by ethanol on Pd and Mo catalysts supported on HZSM-5. *Catal Today* 85:23–29
71. Kikuchi E, Ogura M, Aratani N, Sugiura Y, Hiromoto S, Yogo K (1996) Promotive effect of additives to In/H-ZSM-5 catalyst for selective reduction of nitric oxide with methane in the presence of water vapour. *Catal Today* 27:35–40
72. Ogura M, Kage S, Hayashi M, Matsukata M, Kikuchi E (2000) Remarkable enhancement in durability of Pd/H-ZSM-5 zeolite catalysts for CH<sub>4</sub>-SCR. *Appl Catal B-Environ* 27:L213–L216
73. Shimizu KI, Satsuma A, Hattori T (2000) Metal oxide catalysts for selective reduction of NO<sub>x</sub> by hydrocarbons: toward molecular basis for catalyst design. *Catal Surv Jpn* 4:115–123 (and references herein)
74. Hamada H (1994) Selective reduction of NO by hydrocarbons and oxygenated hydrocarbons over metal oxide catalysts. *Catal Today* 22:21–40
75. Kung MC, Kung HH (2004) Selective lean NO<sub>x</sub> reduction over metal oxides. *Top Catal* 28:105–110
76. Bethke KA, Kung MC, Yang B, Shah M, Alt D, Li C, Kung HH (1995) Metal oxide catalysts for lean NO<sub>x</sub> reduction. *Catal Today* 26:169–183
77. Kintaichi Y, Hamada H, Tabata M, Sasaki M, Ito T (1990) Selective reduction of nitrogen oxides with hydrocarbons over solid acid catalysts in oxygen-rich atmospheres. *Catal Lett* 6:239–244
78. Hamada H, Kintaichi Y, Tabata M, Sasaki M, Ito T (1991) Sulfate-promoted metal oxide catalysts for the selective reduction of nitrogen monoxide by propane in oxygen-rich atmosphere. *Chem Lett* 20:2179–2182
79. Bethke KA, Alt D, Kung MC (1994) NO reduction by hydrocarbons in an oxidizing atmosphere over transition metal-zirconium mixed oxides. *Catal Lett* 25:37–48
80. Hamada H, Kintaichi Y, Sasaki M, Ito T, Tabata M (1991) Transition metal-promoted silica and alumina catalysts for the selective reduction of nitrogen monoxide with propane. *Appl Catal* 75:L1–L8
81. Amin NSA, Tan EF, Manan ZA (2003) Selective reduction of NO<sub>x</sub> with C<sub>3</sub>H<sub>6</sub> over Cu and Cr promoted CeO<sub>2</sub> catalysts. *Appl Catal B Environ* 43:57–69
82. Torikai Y, Yahiro H, Mizuno N, Iwamoto M (1991) Enhancement of catalytic activity of alumina by copper addition for selective reduction of nitrogen monoxide by ethene in oxidizing atmosphere. *Catal Lett* 9:91–95
83. Iliopoulou EF, Evdou AP, Lemonidou AA, Vasalos IA (2004) Ag/alumina catalysts for the selective catalytic reduction of NO<sub>x</sub> using various reductants. *Appl Catal A Gen* 274:179–189
84. Miyadera T (1993) Alumina-supported silver catalysts for the selective reduction of nitric oxide with propene and oxygen containing organic compounds. *Appl Catal B Environ* 2:199–205
85. Tabata M, Hamada H, Suganuma F, Yoshinari T, Tsuchida H, Kintaichi Y, Sasaki M, Ito T (1994) Promotive effect of Sn on the catalytic activity of Al<sub>2</sub>O<sub>3</sub> for the selective reduction of NO by methanol. *Catal Lett* 25:55–60
86. Ukisu Y, Sato S, Abe A, Yoshida K (1993) Possible role of isocyanate species in NO<sub>x</sub> reduction by hydrocarbons over copper-containing catalysts. *Appl Catal B Environ* 2:147–152



87. Kotsifa A, Kondarides DI, Verykios XE (2008) A comparative study of the selective catalytic reduction of NO by propylene over supported Pt and Rh catalysts. *Appl Catal B Environ* 80:260–270
88. Bamwenda GR, Ogata A, Obuchi A, Oi J, Mizuno K, Skrzypek J (1995) Selective reduction of nitric oxide with propene over platinum-group based catalysts: studies of surface species and catalytic activity. *Appl Catal B Environ* 6:311–323
89. Obuchi A, Ohl A, Nakamura M, Ogata A, Mizuno K, Ohuchi H (1993) Performance of platinum-group metal catalysts for the selective reduction of nitrogen oxides by hydrocarbons. *Appl Catal B Environ* 2:71–80
90. Burch R, Millington PJ, Walker AP (1994) Mechanism of the selective reduction of nitrogen monoxide on platinum-based catalysts in the presence of excess oxygen. *Appl Catal B Environ* 4:65–94
91. Burch R, Ottery D (1996) Selective catalytic reduction of NO<sub>x</sub> by hydrocarbons on Pt/Al<sub>2</sub>O<sub>3</sub> catalysts at low temperatures without the formation of N<sub>2</sub>O. *Appl Catal B Environ* 9: L19–L24
92. Burch R, Millington PJ (1996) Selective reduction of NO<sub>x</sub> by hydrocarbons in excess oxygen by alumina- and silica-supported catalysts. *Catal Today* 29:37–42
93. Obuchi A, Ogata A, Takahashi H, Oi J, Bamwenda GR, Mizuno K (1996) Selective reduction of nitrogen oxides with various organic substances on precious metal catalysts under a high GHSV condition. *Catal Today* 29:103–107
94. Pietraszek A, Da Costa P, Marques R, Kornelak P, Hansen TW, Camra J, Najbar M (2007) The effect of the Rh–Al, Pt–Al and Pt–Rh–Al surface alloys on NO conversion to N<sub>2</sub> on alumina supported Rh, Pt and Pt–Rh catalysts. *Catal Today* 119:187–193
95. Denton P, Giroir-Fendler A, Praliaud H, Primet M (2000) Role of the nature of the support (alumina or silica), of the support porosity, and of the Pt dispersion in the selective reduction of NO by C<sub>3</sub>H<sub>6</sub> under lean-burn conditions. *J Catal* 189:410–420
96. Kotsifa A, Kondarides DI, Verykios XE (2007) Comparative study of the chemisorptive and catalytic properties of supported Pt catalysts related to the selective catalytic reduction of NO by propylene. *Appl Catal B Environ* 72:136–148
97. Adamowska M, Muller S, Da Costa P, Krzton A, Burg P (2007) Correlation between the surface properties and DeNO<sub>x</sub> activity of ceria-zirconia catalysts. *Appl Catal B Environ* 74:278–289
98. Thomas C, Gorce O, Fontaine C, Krafft JM, Villain F, Djéga-Mariadassou G (2006) On the promotional effect of Pd on the propene-assisted decomposition of NO on chlorinated Ce<sub>0.68</sub>Zr<sub>0.32</sub>O<sub>2</sub>. *Appl Catal B Environ* 63:201–214
99. Liotta LF, Longo A, Macaluso A, Martorana A, Pantaleo G, Venezia AM, Deganello G (2004) Influence of the SMSI effect on the catalytic activity of a Pt(1%)/Ce<sub>0.6</sub>Zr<sub>0.4</sub>O<sub>2</sub> catalyst: SAXS, XRD, XPS and TPR investigations. *Appl Catal B Environ* 48:133–149
100. Liu Z, Wang K, Zhang X, Wang J, Cao H, Gong M, Chen Y (2009) Study on methane selective catalytic reduction of NO on Pt/Ce<sub>0.67</sub>Zr<sub>0.33</sub>O<sub>2</sub> and its application. *J Nat Gas Chem* 18:66–70
101. Adamowska M, Krztoń A, Najbar M, Camra J, Djéga-Mariadassou G, Da Costa P (2009) Ceria–zirconia-supported rhodium catalyst for NO<sub>x</sub> reduction from coal combustion flue gases. *Appl Catal B Environ* 90:535–544
102. Twigg MV (2007) Progress and future challenges in controlling automotive exhaust gas emissions. *Appl Catal B Environ* 70:2–15
103. Rewick RT, Wise H (1975) Reduction of nitric-oxide by carbon-monoxide on copper catalysts. *J Catal* 40:301–311
104. London JW, Bell AT (1973) Simultaneous infrared and kinetic study of reduction of nitric-oxide by carbon-monoxide over copper oxide. *J Catal* 31:96–109
105. Chen JC, Fang GC, Shi SS (2009) Activities of different metal oxide catalysts on NO reduction and CO oxidation. *Int J Environ Pollut* 37:86–96

106. Xiaoyuan J, Huijuan L, Xiaoming Z (2008) Catalytic activity of CuO-loaded TiO<sub>2</sub>/gamma-Al<sub>2</sub>O<sub>3</sub> for NO reduction by CO. *J Mat Sci* 43:6505–6512
107. Bellido JDA, Assaf EM (2009) Reduction of NO by CO on Cu/ZrO<sub>2</sub>/Al<sub>2</sub>O<sub>3</sub> catalysts: characterization and catalytic activities. *Fuel* 88:1673–1679
108. Khristova M, Ivanov B, Spassova I, Spassov T (2007) NO reduction with CO on copper and ceria oxides supported on alumina. *Catal Lett* 119:79–86
109. Cheng X, Zhu A, Zhang Y, Wang Y, Au CT, Shi C (2009) A combined DRIFTS and MS study on reaction mechanism of NO reduction by CO over NiO/CeO<sub>2</sub> catalyst. *Appl Catal B Environ* 90:395–404
110. Hu Y, Griffiths K, Norton PR (2009) Surface science studies of selective catalytic reduction of NO: progress in the last 10 years. *Surf Sci* 603:1740–1750 (and references herein)
111. Shelef M, Graham GW (1994) Why rhodium in automotive Three-Way Catalysts? *Catal Rev* 36:433–457
112. Busca G, Larrubia MA, Arrighi L, Ramis G (2005) Catalytic abatement of NO<sub>x</sub>: chemical and mechanistic aspects. *Catal Today* 107–108:139–148
113. Fernández-García M, Martínez-Arias A, Iglesias-Juez A, Hungría AB, Anderson JA, Conesa JC, Soria J (2003) Behavior of bimetallic Pd-Cr/Al<sub>2</sub>O<sub>3</sub> and Pd-Cr/(Ce,Zr)O<sub>x</sub>/Al<sub>2</sub>O<sub>3</sub> catalysts for CO and NO elimination. *J Catal* 214:220–233
114. Hungría AB, Fernández-García M, Anderson JA, Martínez-Arias A (2005) The effect of Ni in Pd–Ni/(Ce,Zr)O<sub>x</sub>/Al<sub>2</sub>O<sub>3</sub> catalysts used for stoichiometric CO and NO elimination. Part 2: catalytic activity and in situ spectroscopic studies. *J Catal* 235:262–271
115. Herman GS, Peden CHF, Schmiege SJ, Belton DN (1999) A comparison of the NO–CO reaction over Rh(100), Rh(110) and Rh(111). *Catal Lett* 62:131–138
116. Alas SJ, Rojas F, Kornhauser I, Zgrablich G (2006) Dynamic Monte Carlo simulation of oscillations and pattern formation during the NO + CO reaction on the Pt(100) surface. *J Mol Catal A-Chem* 244:183–192
117. Ward TR, Alemany P, Hoffman R (1993) Adhesion of rhodium, palladium, and platinum to alumina and the reduction of nitric oxide on the resulting surfaces: a theoretical analysis. *J Phys Chem* 97:7691–7699
118. Winter ERS (1971) The catalytic decomposition of nitric oxide by metallic oxides. *J Catal* 22:158–170
119. Haneda M, Nakamura I, Fujitani T, Hamada H (2005) Catalytic active site for NO decomposition elucidated by surface science and real catalyst. *Catal Surv Asia* 9:207–215
120. Haneda M, Kintaichi Y, Bion N, Hamada H (2003) Alkali metal-doped cobalt oxide catalysts for NO decomposition. *Appl Catal B Environ* 46:473–482
121. Iwamoto S, Takahashi R, Inoue M (2007) Direct decomposition of nitric oxide over Ba catalysts supported on CeO<sub>2</sub>-based mixed oxides. *Appl Catal B Environ* 70:146–150
122. Iwamoto M, Furukawa H, Mine Y, Uemura F, Mikuriya S, Kagawa S (1986) Copper (II) ion-exchanged ZSM-5 zeolites as highly active catalysts for direct and continuous decomposition of nitrogen monoxide. *J Chem Soc Chem Comm* 11:1272–1273; Iwamoto M, Yahiro H, Tanda K, Mizuno N, Mine Y, Kagawa S (1991) Removal of nitrogen monoxide through a novel catalytic process. 1. Decomposition on excessively copper-ion-exchanged ZSM-5 zeolites. *J Phys Chem* 95:3727–3730
123. Kustova MY, Rasmussen SB, Kustov AL, Christensen CH (2006) Direct NO decomposition over conventional and mesoporous Cu-ZSM-5 and Cu-ZSM-11 catalysts: improved performance with hierarchical zeolites. *Appl Catal B Environ* 67:60–67
124. Lee DK (2006) Thermodynamic features of the Cu-ZSM-5 catalyzed NO decomposition reaction. *Korean J Chem Eng* 23:547–554
125. Murray HH (1995) Clays in industry and the environment. In: Churchman GJ, Fritzpatrick RW, Egleton RA (eds) *Clays controlling the environment*, 10th International Clay Conference. CSIRO, Melbourne
126. Vaughan DEW (1988) Pillared clays – a historical perspective. *Catal Today* 2:187–198
127. Burch R (1988) Pillared clays. *Catal Today* 2:185–367

128. Pinnavaia TJ (1983) Intercalated clay catalysts. *Science* 220:365–371
129. Figueras F (1988) Pillared clay as catalysts. *Catal Rev* 30:457–499
130. Gil A, Korili SA, Vicente MA (2008) Recent advances in the control and characterization of the porous structure of pillared clay catalysts. *Catal Rev* 50:153–221
131. Vaccari A (1999) Clays and catalysis: a promising future. *Appl Clay Sci* 14:161–198
132. Centi G, Perathoner S (2008) Catalysis by layered materials: a review. *Micropor Mesopor Mat* 107:3–15
133. Yang RT, Chen JP, Kikkinides ES, Cheng LS, Cichanowicz JE (1992) Pillared clays as superior catalysts for selective catalytic reduction of nitric oxide with ammonia. *Ind Eng Chem Res* 31:1440–1445
134. Yang RT, Cichanowicz JE (1995) Pillared interlayered clay catalysts for the selective reduction of nitrogen oxides with ammonia. US Patent 5415850
135. Chen JP, Hausladen MC, Yang RT (1995) Delaminated Fe<sub>2</sub>O<sub>3</sub>-pillared clay: its preparation, characterization, and activities for selective catalytic reduction of NO by NH<sub>3</sub>. *J Catal* 151:135–146
136. Pinnavaia TJ, Tzou MS, Landau SD, Raythatha RH (1984) On the pillaring and delamination of smectite clay catalysts by polyoxo cations of aluminium. *J Mol Catal* 27:195–212
137. Ocelli ML, Landau SD, Pinnavaia TJ (1987) Physicochemical properties of a delaminated clay cracking catalyst. *J Catal* 104:331–338; Ocelli ML (1988) Surface properties and cracking activity of delaminated clay catalysts. *Catal Today* 2:339–355
138. Chmielarz L, Kuśtrowski P, Zbroja M, Asocha W, Dziembaj R (2004) Selective reduction of NO with NH<sub>3</sub> over pillared clays modified with transition metals. *Catal Today* 90:43–49
139. del Castillo HL, Gil A, Grange P (1996) Selective catalytic reduction of NO by NH<sub>3</sub> on titanium pillared montmorillonite. *Catal Lett* 36:237–239
140. Yang RT, Li W (1995) Ion-exchanged pillared clays: a new class of catalysts for selective catalytic reduction of NO by hydrocarbons and by ammonia. *J Catal* 155:414–417
141. Perathoner S, Vaccari A (1997) Catalysts based on pillared interlayered clays for the selective catalytic reduction of NO. *Clay Miner* 32:123–134
142. Long RQ, Yang RT, Zammit KD (2003) Superior pillared clay catalysts for selective reduction of nitrogen oxides for power plant emission control. US patent 6,521,559 B1
143. Long RQ, Yang RT (1999) Selective catalytic reduction of nitrogen oxides by ammonia over Fe<sup>3+</sup>-exchanged TiO<sub>2</sub>-pillared clay catalysts. *J Catal* 186:254–268 (and references herein)
144. Long RQ, Yang RT (1999) Acid- and base-treated Fe<sup>3+</sup>-TiO<sub>2</sub>-pillared clays for selective catalytic reduction of NO by NH<sub>3</sub>. *Catal Lett* 59:39–44
145. Ramis G, Yi L, Busca G, Turco M, Kotur E, Willey RJ (1995) Adsorption, activation, and oxidation of ammonia over SCR catalysts. *J Catal* 157:523–535
146. Bergaya F, Ouad A, Mandalia T (2006) Pillared clays and clay minerals. In: Bergaya F, Theng BKG, Lagaly G (eds) *Handbook of clay science. Developments in clay science*, vol 1. Elsevier, Amsterdam
147. Vicente MA, Bañares-Muñoz MA, Toranzo R, Gandía LM, Gil A (2001) Influence of the Ti precursor on properties of Ti-pillared smectites. *Clay Miner* 36:125–138
148. He MY, Liu Z, Min E (1988) Acidic and hydrocarbon catalytic properties of pillared clay. *Catal Today* 2:321–338
149. Komadel P, Madejova J (2006) Acid activation of clay minerals. In: Bergaya F, Theng BKG, Lagaly G (eds) *Handbook of clay science. Developments in clay science*, vol 1. Elsevier, Amsterdam
150. Vicente MA, Suárez M, Bañares-Muñoz MA, López González JD (1996) Comparative FT-IR study of the removal of octahedral cations and structural modifications during acid treatment of several silicates. *Spectrochimic Acta A* 52:1685–1694
151. Long RQ, Yang RT (2000) FTIR and kinetic studies of the mechanism of Fe<sup>3+</sup>-exchanged TiO<sub>2</sub>-pillared clay catalyst for selective catalytic reduction of NO with ammonia. *J Catal* 190:22–31

152. Long RQ, Yang RT (2000) The promoting role of rare earth oxides on Fe-exchanged TiO<sub>2</sub>-pillared clay for selective catalytic reduction of nitric oxide by ammonia. *Appl Catal B Environ* 27:87–95
153. Chmielarz L, Kuśtrowski P, Zbroja M, Rafalska-Asocha A, Dudek B, Dziembaj R (2003) SCR of NO by NH<sub>3</sub> on alumina or titania-pillared montmorillonite variously modified with Cu or Co: part I. General characterization and catalysts screening. *Appl Catal B Environ* 45:103–116
154. Chmielarz L, Kuśtrowski P, Zbroja M, Gil-Knap B, Datka J, Dziembaj R (2004) SCR of NO by NH<sub>3</sub> on alumina or titania pillared montmorillonite modified with Cu or Co. Part II. Temperature programmed studies. *Appl Catal B Environ* 53:47–61
155. Chmielarz L, Kuśtrowski P, Michalik M, Dudek B, Czajka M, Dziembaj R (2007) Phlogophites intercalated with Al<sub>2</sub>O<sub>3</sub> pillars and modified with transition metals as catalysts of the DeNO<sub>x</sub> process. *React Kinet Catal Lett* 91:369–378
156. Chmielarz L, Kuśtrowski P, Michalik M, Dudek B, Piwowarska Z, Dziembaj R (2008) Vermiculites intercalated with Al<sub>2</sub>O<sub>3</sub> pillars and modified with transition metals as catalysts of DeNO<sub>x</sub> process. *Catal Today* 137:242–246
157. Bergaya F, Lagaly G (2006) General introduction: clays, clay minerals, and clay Science. In: Bergaya F, Theng BKG, Lagaly G (eds) *Handbook of clay science. Developments in clay science, vol 1*. Elsevier, Amsterdam
158. Brigatti MF, Galan E, Theng EKG (2006) Structures and mineralogy of clay minerals. In: Bergaya F, Theng BKG, Lagaly G (eds) *Handbook of clay science. Developments in clay science, vol 1*. Elsevier, Amsterdam
159. Newman ACD, Brown G (1987) The chemical constitution of clays. In: Newman ACD (ed) *Chemistry of clays and clay minerals. Mineralogical Society Monograph*, London
160. Cheng LS, Yang RT, Chen N (1996) Iron oxide and chromia supported on titania-pillared clay for selective catalytic reduction of nitric with ammonia. *J Catal* 164:70–81
161. Olszewska D (2006) Ammonia and water sorption properties of the mineral-layered nanomaterials used as the catalysts for NO<sub>x</sub> removal from exhaust gases. *Catal Today* 114:326–332
162. Long RQ, Yang RT (2000) Selective catalytic reduction of NO with ammonia over V<sub>2</sub>O<sub>5</sub> doped TiO<sub>2</sub> pillared clay catalysts. *Appl Catal B Environ* 24:13–21
163. Long RQ, Yang RT (2000) Catalytic performance and characterization of VO<sup>2+</sup>-exchanged Titania-pillared clays for selective catalytic reduction of nitric oxide with ammonia. *J Catal* 196:73–85
164. Boudali LK, Ghorbel A, Grange P, Figueras F (2005) Selective catalytic reduction of NO with ammonia over V<sub>2</sub>O<sub>5</sub> supported sulfated titanium-pillared clay catalysts: influence of V<sub>2</sub>O<sub>5</sub> content. *Appl Catal B-Environ* 59:105–111
165. Arfaoui J, Boudali LK, Ghorbel A, Delahay G (2009) Effect of vanadium on the behaviour of unsulfated and sulfated Ti-pillared clay catalysts in the SCR of NO by NH<sub>3</sub>. *Catal Today* 142:234–238
166. Boudali LK, Ghorbel A, Grange P (2006) SCR of NO by NH<sub>3</sub> over V<sub>2</sub>O<sub>5</sub> supported sulfated Ti-pillared clay: reactivity and reducibility of catalysts. *Appl Catal A Gen* 305:7–14
167. Arfaoui J, Boudali LK, Ghorbel A, Delahay G (2008) Influence of the nature of titanium source and of vanadia content on the properties of titanium-pillared montmorillonite. *J Phys Chem Solids* 69:1121–1124
168. Grzybek T, Klinik J, Krzyzanowski A, Papp H (2002) Carbon-covered clays as catalytic supports. 1. Iron-promoted samples as DeNO<sub>x</sub> catalysts *Catal Lett* 81:193–197
169. Chmielarz L, Dziembaj R, Grzybek T, Klinik J, Łojewski T, Olszewska D, Papp H (2000) Pillared smectite modified with carbon and manganese as catalyst for SCR of NO<sub>x</sub> with NH<sub>3</sub>. Part I. General characterization and catalyst screening. *Catal Lett* 68:95–100
170. Chmielarz L, Dziembaj R, Grzybek T, Klinik J, Łojewski T, Olszewska D, Wegrzyn A (2000) Pillared smectite modified with carbon and manganese as catalyst for SCR of NO<sub>x</sub> with NH<sub>3</sub>. Part II. Temperature-programmed studies. *Catal Lett* 70:51–56; Chmielarz L,

- Dziembaj R, Łojewski T, Wegrzyn A, Grzybek T, Klinik J, Olszewska D (2001) Effect of water vapour and SO<sub>2</sub> addition on stability of zirconia-pillared montmorillonites in selective catalytic reduction of NO with ammonia. *Solid State Ionics* 141–142:715–719
171. Grzybek T, Motak M, Papp H (2004) The structure of prospective DeNO<sub>x</sub> catalysts based on carbon–montmorillonite nanocomposites. *Catal Today* 90:69–76
  172. Motak M (2008) Montmorillonites modified with polymer and promoted with copper as DeNO<sub>x</sub> catalysts. *Catal Today* 137:247–252
  173. Sato K, Fujimoto T, Kanai S, Kintaichi Y, Inaba M, Haneda M, Hamada H (1997) Catalytic performance of silver ion-exchanged saponite for the selective reduction of nitrogen monoxide in the presence of excess oxygen. *Appl Catal B Environ* 13:27–33
  174. Yang RT, Tharappiwattananon N, Long RQ (1998) Ion-exchanged pillared clays for selective catalytic reduction of NO by ethylene in the presence of oxygen. *Appl Catal B Environ* 19:289–304
  175. Li W, Sirilumpen M, Yang RT (1997) Selective catalytic reduction of nitric oxide by ethylene in the presence of oxygen over Cu<sup>2+</sup> ion-exchanged pillared clays. *Appl Catal B Environ* 11:347–363
  176. Chmielarz L, Zbroja M, Kuśtrowski P, Dudek B, Rafalska-Asocha A, Dziembaj R (2004) Pillared montmorillonites modified with silver – temperature programmed desorption studies. *J Therm Anal Calorim* 77:115–123
  177. Valverde JL, de Lucas A, Sánchez P, Dorado F, Romero A (2003) Cation exchanged and impregnated Ti-pillared clays for selective catalytic reduction of NO<sub>x</sub> by propylene. *Appl Catal B Environ* 43:43–56
  178. Valverde JL, de Lucas A, Dorado F, Romero A, García PB (2005) Influence of the operating parameters on the selective catalytic reduction of NO with hydrocarbons using Cu-Ion-Exchanged Titanium-Pillared interlayer clays (Ti-PILCs). *Ind Eng Chem Res* 44:2955–2965
  179. Valverde JL, de Lucas A, Dorado F, Romero A, García PB (2005) Study by in situ FTIR of the SCR of NO by propene on Cu<sup>2+</sup> ion-exchanged Ti-PILC. *J Mol Catal A Chem* 230:23–28
  180. Dorado F, de Lucas A, García PB, Romero A, Valverde JL (2006) Copper ion-exchanged and impregnated Fe-pillared clays – study of the influence of the synthesis conditions on the activity for the selective catalytic reduction of NO with C<sub>3</sub>H<sub>6</sub>. *Appl Catal A Gen* 305:189–196
  181. Dorado F, de Lucas A, García PB, Valverde JL, Romero A (2006) Preparation of Cu-ion-exchanged Fe-PILCs for the SCR of NO by propene. *Appl Catal B Environ* 65:5–184
  182. Lin Q, Hao J, Li J, Ma Z, Lin W (2007) Copper-impregnated Al–Ce-pillared clay for selective catalytic reduction of NO by C<sub>3</sub>H<sub>6</sub>. *Catal Today* 126:351–358
  183. Koch D, Kesore K, Tomlinson AAG (2009) Methods for the production of catalytically active layer silicates. US Patent 7476639–B2
  184. Konin GA, Ilichev AN, Matyshak VA, Khomenko TI, Korchak VN, Tretyakov VF, Doronin VP, Bunina RV, Alikina GM, Kuznetsova TG, Paukshtis EA, Fenelonov VB, Zaikovskii VI, Ivanova AS, Beloshapkin SA, Rozovskii AY, Tretyakov VF, Ross JRH, Breen JP (2001) Cu, Co, Ag-containing pillared clays as catalysts for the selective reduction of NO<sub>x</sub> by hydrocarbons in an excess of oxygen. *Top Catal* 16/17:193–197
  185. Matyshak VA, Tretyakov VF, Chernyshev KA, Burdeinaya TN, Korchak VN, Sadykov VA (2006) Reaction paths of the formation and consumption of nitroorganic complex intermediates in the selective catalytic reduction of nitrogen oxides with propylene on zirconia-pillared clays according to in situ spectroscopic data. *Kinet Catal* 47:747–755
  186. Tretyakov VF, Kuznetsova TG, Doronin VP, Bunina RV, Alikina GM, Batuev L, Matyshak VA, Rozovskii AY, Tretyakov VF, Burdeinaya TN, Lunin V, Ross JRH (2006) NO<sub>x</sub> SCR by decane and propylene on Pt + Cu/Zr-pillared clays in realistic feeds: performance and mechanistic features versus structural specificity of nanosized zirconia pillars. *Catal Today* 114:13–22
  187. Matyshak VA, Tretyakov VF, Burdeinaya TN, Chernyshov KA, Sadykov VA, Sil'chenkova ON, Korchak VN (2007) Effect of the modification of ZrO<sub>2</sub>-Containing pillared clay with Pt

- and Cu atoms on the properties of inorganic complex intermediates in the selective catalytic reduction of nitrogen oxides with propylene according to in situ IR-spectroscopic data. *Kinet Catal* 48:74–83
188. Belver C, Bñares-Muñoz MA, Vicente MA (2004) Fe-saponite pillared and impregnated catalysts I. Preparation and characterization. *Appl Catal B Environ* 50:101–112
  189. Belver C, Vicente MA, Fernández-García M, Martínez-Arias A (2004) Supported catalysts for DeNO<sub>x</sub> reaction based on iron clays. *J Mol Catal A Chem* 219:309–313
  190. Mata G, Trujillano R, Vicente MA, Belver C, Fernández-García M, Korili SA, Gil A (2007) Chromium-saponite clay catalysts: preparation, characterization and catalytic performance in propene oxidation. *Appl Catal A Gen* 327:1–12
  191. Belver C, Vicente MA, Martínez-Arias A, Fernández-García M (2004) Fe-saponite pillared and impregnated catalysts II. Nature of the iron species active for the reduction of NO<sub>x</sub> with propene. *Appl Catal B Environ* 50:227–234
  192. Belver C, Mata G, Trujillano R, Vicente MA (2008) Ni/pillared clays as catalysts for the selective catalytic reduction of nitrogen oxides by propene. *Catal Lett* 123:32–40
  193. Bahamonde A, Mohino F, Rebollar M, Yates M, Avila P, Mendioroz S (2001) Pillared clay and zirconia-based monolithic catalysts for selective catalytic reduction of nitric oxide by methane. *Catal Today* 69:233–239
  194. Mohino F, Avila P, Salerno P, Bahamonde A, Mendioroz S (2005) PILC-based monolithic catalysts for the selective catalytic reduction of nitrogen oxides by methane in oxygen excess. *Catal Today* 107–108:192–199
  195. Mendioroz S, Martín-Rojo AB, Rivera F, Martín JC, Bahamonde A, Yates M (2006) Selective catalytic reduction of NO<sub>x</sub> by methane in excess oxygen over Rh based aluminium pillared clays. *Appl Catal B Environ* 64:161–170
  196. Philippopoulos C, Gangas N, Papayannakos N (1996) Catalytic reduction of NO with CO over an Rh/Al pillared clay catalyst. *J Mater Sci Lett* 15:1940–1944
  197. Morfis S, Philippopoulos C, Papayannakos N (1998) Application of Al-pillared clay minerals as catalytic carriers for the reaction of NO with CO. *Appl Clay Sci* 13:203–212
  198. Qi G, Yang RT, Thompson LT (2004) Catalytic reduction of nitric oxide with hydrogen and carbon monoxide in the presence of excess oxygen by Pd supported on pillared clays. *Appl Catal A Gen* 259:261–267
  199. Sirilumpen M, Yang RT, Tharappiwattananon N (1999) Selective catalytic reduction of NO with hydrocarbon on Cu<sup>2+</sup>-exchanged pillared clay: an IR study of the NO decomposition mechanism. *J Mol Catal A Chem* 137:273–286
  200. Rives V, Ulbarri MA (1999) Layered double hydroxides (LDH) intercalated with metal coordination compounds and oxometalates. *Coord Chem Rev* 181:61–120
  201. Rives V (2002) Characterisation of layered double hydroxides and their decomposition products. *Mater Chem Phys* 75:19–25
  202. Vaccari A (1998) Preparation and catalytic properties of cationic and anionic clays. *Catal Today* 41:53–71
  203. Kannan S (2006) Catalytic applications of hydrotalcite-like materials and their derived forms. *Catal Surv Asia* 10:117–137
  204. Tichit D, Gerardin C, Durand R, Coq B (2006) Layered double hydroxides: precursors for multifunctional catalysts. *Top Catal* 39:89–96
  205. Mulukutla RS, Detellier C (1996) Thermally activated Mg, Fe layered double hydroxide as reductant for nitric oxide. *J Mater Sci Lett* 15:797–799
  206. Mulukutla RS, Detellier C (1997) Use of a calcined Ni(II), Al(III) layered double hydroxide for the reduction of nitric oxide in the presence of methane and oxygen. *J Mater Sci Lett* 16:752–754
  207. Montanari B, Vaccari A, Gazzano M, Käfher P, Papp H, Pasel J, Dziembaj R, Makowski W, Lojewski T (1997) Characterization and activity of novel copper-containing catalysts for selective catalytic reduction of NO with NH<sub>3</sub>. *Appl Catal B Environ* 13:205–217

208. Centi G, Fornasari G, Gobbi C, Livi M, Trifirò F, Vaccari A (2002) NO<sub>x</sub> storage-reduction catalysts based on hydrotalcite: effect of Cu in promoting resistance to deactivation. *Catal Today* 73:287–296
209. Basile F, Fornasari G, Livi M, Tinti F, Trifirò F, Vaccari A (2004) Performance of new Pt and Pt-Cu on hydrotalcite-derived materials for NO<sub>x</sub> storage/reduction. *Top Catal* 30:223–227
210. Alini S, Bologna A, Basile F, Montanari T, Vaccari A (2003) Catalytic decomposition of nitrous oxide involves contacting gaseous mixture containing nitrous oxide with catalytic system obtained by calcination and reduction with hydrogen of hydrotalcite compound. Patent number: EP1262224-A1; EP1262224-B1; DE60101461-E
211. Yu JJ, Cheng J, Ma CY, Wang HL, Li LD, Hao ZP, Xu ZP (2009) NO<sub>x</sub> decomposition, storage and reduction over novel mixed oxide catalysts derived from hydrotalcite-like compounds. *J Colloid Interf Sci* 333:423–430
212. Yu JJ, Wang XP, Li LD, Hao ZP, Xu ZP, Lu GQ (2007) Novel multi-functional mixed-oxide catalysts for effective NO<sub>x</sub> capture, decomposition, and reduction. *Adv Funct Mater* 17:3598–3606
213. Yu JJ, Tao YX, Liu CC, Hao ZP, Xu ZP (2007) Environmental novel NO trapping catalysts derived from Co-Mg/X-Al (X=Fe, Mn, Zr, La) hydrotalcite-like compounds. *Sci Tech* 41:1399–1404
214. Galarneau A, Barodawalla A, Pinnavaia TJ (2002) Porous clay heterostructures formed by gallery-templated synthesis. *Nature* 374:529–531
215. Polverejan M, Pauly TR, Pinnavaia TJ (2000) Acidic porous clay heterostructures (PCH): intragallery assembly of mesoporous silica in synthetic saponite clays. *Chem Mater* 12:2698–2704
216. Galarneau A, Barodawalla A, Pinnavaia TJ (1997) Porous clay heterostructures (PCH) as acid catalysts. *Chem Commun* 1661–1662
217. Chmielarz L, Kuśtrowski P, Piwowska Z, Gil B, Michalik M (2009) Montmorillonite, vermiculite and saponite based porous clay heterostructures modified with transition metals as catalysts for the DeNO<sub>x</sub> process. *Appl Catal B Environ* 88:331–340
218. Chmielarz L, Kuśtrowski P, Dziembaj R, Cool P, Vansant EF (2007) Selective catalytic reduction of NO with ammonia over porous clay heterostructures modified with copper and iron species. *Catal Today* 119:181–186

# Chapter 11

## Pillared Clay Catalysts in Green Oxidation Reactions

M.A. Vicente, R. Trujillano, K.J. Ciuffi, E.J. Nassar, S.A. Korili, and A. Gil

**Abstract** In this chapter, the use of pillared clays as catalysts in green oxidation reactions is considered. Several catalytic oxidation reactions have been selected, and special attention is given to the reaction products and to the yields achieved.

**Keywords** PILC · Pillared clays · Green oxidation reactions · Catalysts

### 11.1 Introduction

Pillared InterLayered Clays (PILCs, in short) are prepared by exchanging the charge-compensating cations present in the interlamellar space of the clays with hydroxy-metal polycations. On calcination, the inserted polycations yield rigid, thermally stable oxide species, which prop the clay layers apart and prevent their collapse. The intercalation and pillaring processes produce the development of a porous structure with the presence of particular surface sites. These solids have been used in catalytic, purification, and sorption-based separation applications.

The methods and the mathematical models used in the characterization of the porous structure of PILCs have been presented in a recent review [1]. From this study and all the references cited therein, it is clear that a great interest exists in the microporous structure of PILCs as well as in the effect of their structure on the applications of these materials. In summary, several researchers have suggested a bimodal micropore distribution for the microporous structure developed by the intercalated and the pillared clays, but this suggestion is open to questioning and can contribute to the expansion of this field in the coming years.

Interest in the application of PILCs as catalysts has undergone a huge increase over the last few years [1, 2]. One of the most studied subjects related to PILCs

---

A. Gil (✉)

Department of Applied Chemistry, Public University of Navarra, E-31006 Pamplona, Spain  
e-mail: andoni@unavarra.es



is their use as support for active catalytic phases in the preparation of supported catalysts and the applicability of the resulting solids in several reactions, particularly in environmental-friendly processes. In this respect, the selective reduction of NO<sub>x</sub> has been the reaction of environmental interest for which PILCs have been most widely used [3–22], as well as the complete oxidation of volatile organic compounds (VOCs) [23–34]. Wet hydrogen peroxide catalytic oxidation of wastewater [35–65] has also been studied.

The aims of sustainable development are to reduce the adverse consequences of the substances that we generate and use. The role of chemistry is essential in ensuring that the next generation of chemicals, materials, and energy will be more sustainable than the current one. Worldwide demand for environmental-friendly chemical processes and products requires the development of novel and cost-effective approaches to pollution prevention. One of the most attractive concepts in chemistry for sustainability is Green Chemistry, which is the utilization of a set of principles that reduces or eliminates the use or generation of hazardous substances in the design, manufacture, and applications of chemical products [66]. These ideas frequently require the redesign of chemical products or processes. The rapid development of Green Chemistry is due to the recognition that environmental-friendly products and processes will be economical in the long term. Heterogeneous catalysis remains one of the most important fields of Green Chemistry, since it is widely used to minimize pollution in chemical synthesis and processing.

This chapter presents the use of pillared clays in catalytic oxidation applications. In fact, various chapters of this book review related topics, but there is need for a focused overview discussing the oxidation reactions related to the concepts of Green Chemistry. Several catalytic oxidation reactions have been selected, and the main results concerning the use of pillared clays as catalysts are summarized.

## 11.2 Alkene Oxidation

### 11.2.1 Epoxidation

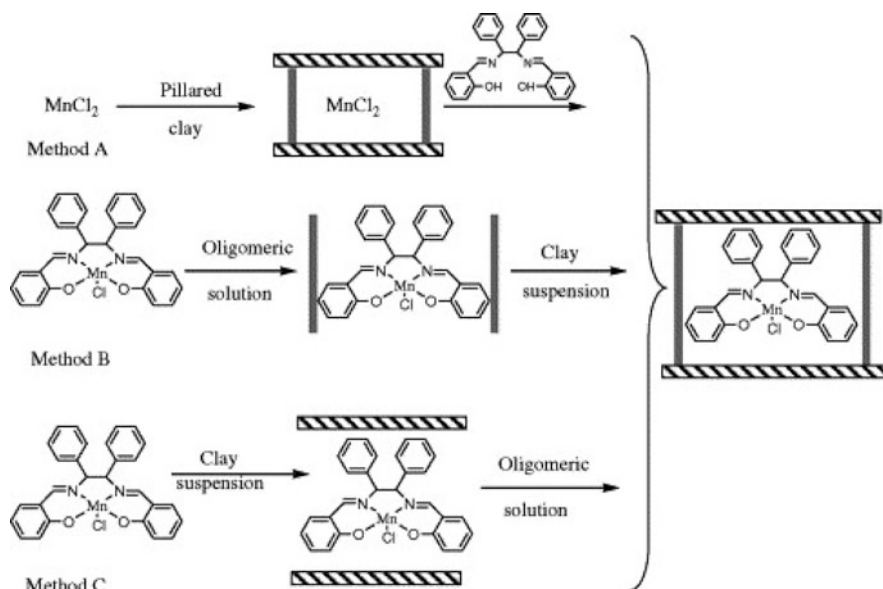
Epoxides are important intermediates in several chemical industries, being the starting point for the preparation of products such as drugs and paints, but the commercial process of epoxide production leads to co-products that cause environmental problems. In this context, hydrogen peroxide is an interesting oxidant because it is considered to be clean and environmental-friendly, safe, and cheap and the only by-products formed are water and oxygen.

Alkene epoxidation has attracted interest due to the use of epoxides as intermediates in organic synthesis applied to the pharmaceutical and the agrochemical industries [67]. Ethylene oxidation to ethylene oxide (oxirane) is by far the most important epoxidation reaction in commercial operation. The reaction is carried out at an elevated pressure over a silver catalyst supported on a non-porous alumina and promoted by alkali metals. Ethylene oxide can be used directly as fumigant

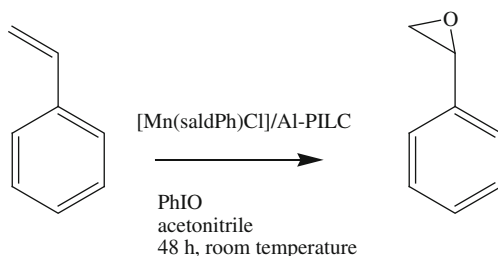
and sterilizing agent and in the synthesis of ethylene glycol and derivatives of this chemical. Propylene oxide can be commercially obtained from the chlorohydrin process and the hydroperoxide process. This chemical is used as a package fumigant for dried fruit and as acid scavenger and pH control agent because of its reaction with HCl, which produces propylene chlorohydrin. Polyether polyols, polyurethane, propylene glycol, surfactants, and isopropanolamines are derivatives of propylene oxide.

Freire et al. [68, 69] reported the encapsulation of Mn(III) salen complex into an alumina-pillared clay using various methodologies (see Scheme 11.1). These materials were employed in styrene epoxidation at room temperature, using iodosylbenzene (PhIO) as oxygen source (see Scheme 11.2). The solids presented high styrene epoxide selectivity and were reused several times. Only a small decrease in the catalytic performance was observed in each reuse. This behavior was related to complex leaching and metal deactivation occurring for all materials during the catalytic cycles. The authors extended these studies considering chiral counterparts and enantioselective styrene epoxidation by using two oxidants: iodosylbenzene (PhIO) and a mixture of *m*-chloroperoxybenzoic acid (*m*-CPBA) and *N*-methylmorpholine (NMO) as co-oxidant [70]. The encapsulated complexes gave alkene conversions ranging from 16 to 40%.

Mata et al. [71] described the use of Ni-saponite catalysts obtained by impregnation of an Al-pillared saponite with the following Ni salts: Ni(II) nitrate, Ni(II) chloride, and Ni(II) acetylacetonate. The resulting solids were employed as

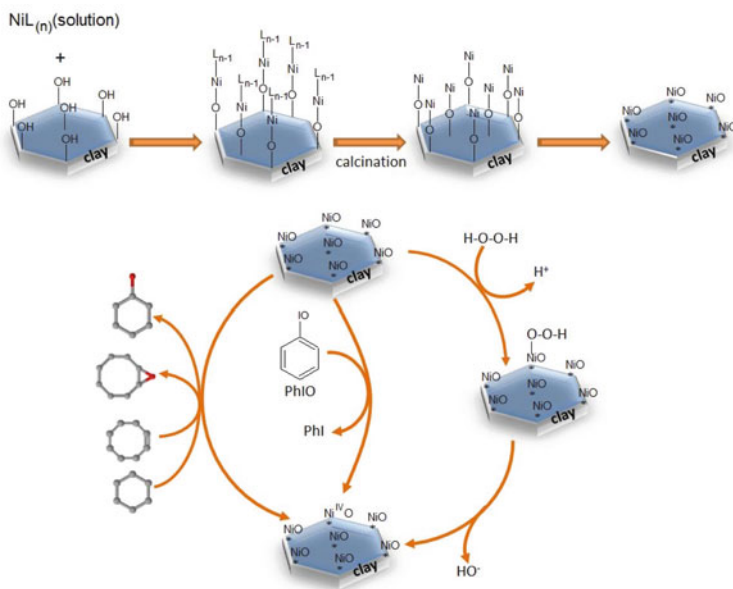


**Scheme 11.1** Methods for the encapsulation of Mn(III) salen complex into an alumina-pillared clay. Adapted from Ref. [68]

**Scheme 11.2** Styrene epoxidation

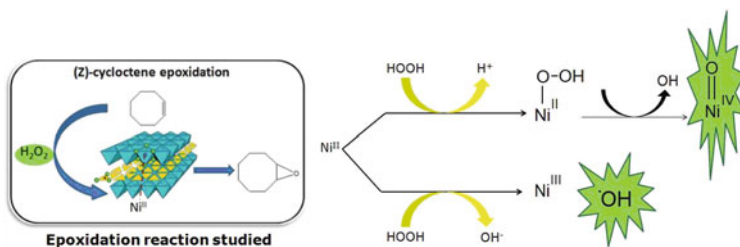
catalysts for (*Z*)-cyclooctene epoxidation, using iodosylbenzene as model oxidant and hydrogen peroxide as clean oxidant, at 25 °C and atmospheric pressure. With both oxidants there was 100% selectivity for the epoxide; no other products were found. Epoxide yields were between 29 and 32% when iodosylbenzene was used as oxidant, and the materials synthesized from Ni(II) acetylacetonate precursor showed the best catalytic efficiency. The nickel species present on the surface of the clay (NiO and NiAl<sub>2</sub>O<sub>4</sub>) play a crucial role in the catalytic process, since the nickel ions act as the active species responsible for oxygen atom transfer from the oxidant to the substrate. The active phases in this epoxidation are metal-oxo species, Ni<sup>IV</sup>=O (see Scheme 11.3).

With hydrogen peroxide as oxidant epoxide yields ranged from 13 to 25% and epoxide production was attributed to the formation of high-valence metal-oxo active

**Scheme 11.3** Mechanism proposed for cyclooctene and cyclohexene oxidation by iodosylbenzene over Ni-clay catalysts

species. It is noteworthy that no free radical mechanisms were observed even when hydrogen peroxide was employed as oxidant, which makes these materials potentially applicable in large-scale processes. A selective catalyst was achieved using cyclohexane, an inert substrate. The products resulting from its partial oxidation, cyclohexanol/cyclohexanone, also called K/A-oil, are very important for the production of adipic acid, which is used in the manufacture of textile fibres, such as nylon-6 and nylon-6.6. Normally the industrial process includes several reaction steps and produces toxic chlorinated by-products [72]. Using iodosylbenzene as oxidant and Ni-clay catalysts, Mata et al. [71] found a very interesting system that led to cyclohexanone as the only product, with yields ranging from 20 to 27%, and 100% selectivity, under mild conditions. The prepared catalysts overcame many typical disadvantages of the industrial process, in which the same reaction takes place at high temperatures and pressures, and only 4% cyclohexane conversion is obtained in a K/A-oil mixture (85% selectivity). Besides, the industrial process employs homogeneous catalysts, which are difficult to recycle, and produce waste. On the basis of the high selectivity for the ketone and the absence of radical mechanisms, ketone production was attributed to the formation of a high-valence metal-oxo active species (see Scheme 11.3).

Trujillano et al. [73] reported the preparation of a synthetic saponite containing  $\text{Ni}^{2+}$  as octahedral cations, using a simple hydrothermal methodology. The synthetic saponite was intercalated with  $\text{Al}_{13}^{7+}$  polycations and used as catalyst for (Z)-cyclooctene oxidation, employing the green oxidant hydrogen peroxide, at room temperature and atmospheric pressure. The only product was epoxide with 100% selectivity and the conversion ranged from 17 to 20%. Two oxidation mechanisms were taking place with synthetic saponite catalysts, and that there was a competition between the metal-oxo and the radical species, which were produced by heterolytic or homolytic  $\text{H}_2\text{O}_2$  cleavage (see Scheme 11.4).



**Scheme 11.4** Mechanisms proposed for cyclooctene oxidation with hydrogen peroxide over synthetic Ni-saponites

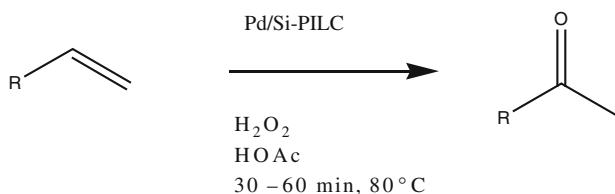
### 11.2.2 Oxidative Ketonization

The lower aliphatic ketones have excellent solvent properties. Because of their ability to form azeotropes with water and organic liquids, they are employed in

extractive distillation. Aromatic ketones are useful intermediates for the manufacture of pharmaceuticals, resins, or dyestuffs, among others [67].

A procedure for the allylic oxidation of cyclic and acyclic alkenes to the corresponding  $\alpha,\beta$ -unsaturated carbonyl compounds has been described in detail by Choudary et al. [74]. Cr-PILCs were used as catalysts and *tert*-butyl hydroperoxide as oxidant.

The intercalation of a montmorillonite with silylpropylethylenediamine palladium(II) was reported by Subba Rao et al. [75]. The obtained solid, with a basal spacing of 2.01 nm, was used in the selective oxidation of olefins to methyl ketones with  $\text{H}_2\text{O}_2$  as oxidant. Several olefins were studied by the authors, who found that the oxidation proceeds very rapidly and selectively with quantitative yields in the range of 92–97% (see Scheme 11.5). The results can be attributed to the orientation and spatial requirements of the complex formed between the substrate and the metal in the interlamellar space of montmorillonite. Under the reaction conditions presented in Scheme 11.5, decomposition of  $\text{H}_2\text{O}_2$  occurs and excess molar quantities were required. After a simple filtration, the catalysts could be reused for four cycles, showing consistent performance.



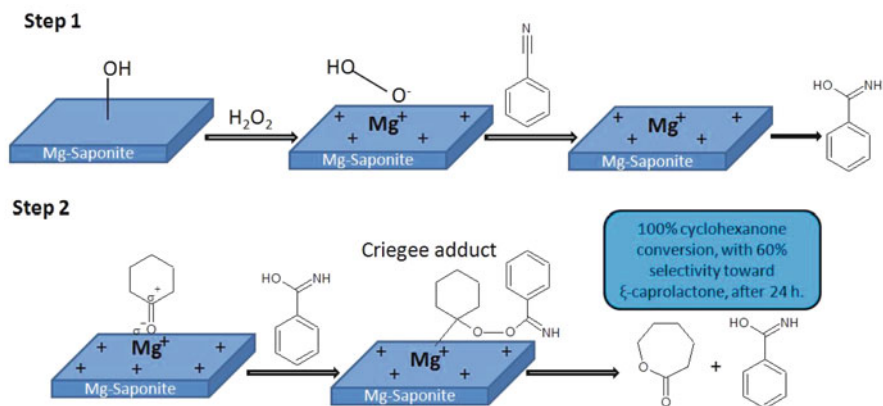
**Olefins:** 1-octene, 1-hexene, 1-decene, 1-dodecene, allyl acetate, styrene, benzal acetone, cinnamaldehyde, allyl alcohol.

**Scheme 11.5** Oxidative ketonization of olefins

Trujillano et al. [73] prepared a synthetic saponite with  $\text{Mg}^{2+}$  as octahedral cation, observing that it has great potential as catalyst in an important oxidation reaction, the Baeyer–Villiger oxidation of ketones. The products of this reaction, lactones or esters, are important intermediates in the agrochemical, chemical, and pharmaceutical industries. The cyclohexanone conversion achieved with hydrogen peroxide was 100%, with 60% selectivity toward  $\epsilon$ -caprolactone. Magnesium plays an essential role in the catalytic process, as presented in Scheme 11.6.  $\text{Mg}^{2+}$  is described as the promoter of the link between the Brønsted basic sites on the surface of the clay and hydrogen peroxide.

### 11.2.3 Allylic Oxidation

Romanenko et al. [76] found that the reaction of  $\alpha$ -pyrene with *tert*-butyl hydroperoxide can proceed via allylic oxidation or  $\alpha$ -pyrene isomerization,



**Scheme 11.6** Mechanism proposed for the cyclohexanone oxidation over synthetic Mg-saponite

depending on the structural features of the catalysts based on Fe-PILC. After 50 h of reaction, Fe-PILC mainly gives isomerization products (limonene and camphene). When mechanochemically activated Fe-PILC was considered, the presence of allylic oxidation products was observed.

## 11.3 Alkylaromatic Oxidation

### 11.3.1 Aromatic Ring Oxidation

Phenol is one of the most important chemicals in industry, widely used in the synthesis of resins and fibres, among others [67]. Phenol is currently produced via the Hock process, which is an indirect multistage process that produces equimolar acetone as a by-product. The economic aspects of this process depend mainly on the market price of acetone. For this reason, it is desirable that direct hydroxylation of benzene to phenol under mild conditions with high yield is developed. Several materials have been reported as catalysts and supported catalysts for the liquid-phase hydroxylation process with  $\text{H}_2\text{O}_2$  as oxidant [77–82]. The direct hydroxylation of benzene to phenol using  $\text{H}_2\text{O}_2$  as oxidant and various metals supported on Al-PILC has been reported by Pan et al. [83], who studied the effects of solvent nature, reaction temperature, and benzene/ $\text{H}_2\text{O}_2$  molar ratio on the conversion of benzene to phenol.

## 11.4 Oxidation of Compounds Containing Oxygen

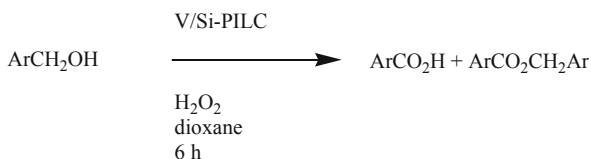
### 11.4.1 Alcohol Oxidation

Benzaldehyde, benzoic acid, and benzyl benzoate can be obtained from benzyl alcohol oxidation. Benzaldehyde is used in the pharmaceutical industry and may

be utilized as raw material in the manufacture of herbicides. Substantial quantities of benzoic acid are used to improve the properties of various alkyd resins coating formulations [67].

The oxidation of several substituted benzyl alcohols using V-PILC as catalyst and  $\text{H}_2\text{O}_2$  as oxidant has been reported by Choudary and Valli [84] (see Scheme 11.7). Benzyl alcohols and *para*-substituted benzyl alcohols are oxidized to acids and esters. The formation of esters should be related to the presence of acid sites on montmorillonite. *ortho*-Substituted alcohols are not oxidized. The same authors have presented several examples of selective alcohol oxidation to the carbonyl compounds using a Cr-PILC catalyst [85].

**Scheme 11.7** Benzyl alcohol oxidation



Ar- :  $\text{CH}_3\text{C}_6\text{H}_4$ -,  $\text{ClC}_6\text{H}_4$ -,  $\text{O}_2\text{NC}_6\text{H}_4$ -,  $\text{CH}_3\text{OC}_6\text{H}_4$ -,  $(\text{CH}_3)_2\text{C}_6\text{H}_4$ -,  $\text{C}_6\text{H}_5$ -.

The oxidation of 1-phenylpropan-1-ol to propiophenone using Cr,Al-PILCs as catalysts and *tert*-butyl peroxide has been studied by Palinko et al. [86]. The mixed Cr,Al-PILCs show a higher conversion of the alcohol than Cr-PILC.

### 11.4.2 Phenol Oxidation

Phenol oxidation by  $\text{H}_2\text{O}_2$  is widely used in the chemical industry for preparation of the dihydroxylated derivatives [67]. The oxidation process takes place via the decomposition of  $\text{H}_2\text{O}_2$ , with formation of an unstable electrophilic intermediate which attacks the phenol nucleus to give a phenoxy ion. This ion can be considered as the precursor of the products usually formed by this process, which are hydroquinone, catechol, and benzoquinone, all being important intermediates for the production of fine chemicals used in photography and polymer industries [87]. The initial classic route to hydroquinone starts from aniline, sulfuric acid, and manganese oxide, but this process produces high amounts of ammonium and manganese sulfates. When the reaction is carried out in the presence of  $\text{H}_2\text{O}_2$ , the main waste product is water. The selectivity of the products is affected by the solvent nature (see Fig. 11.1) [88, 89]. With protic solvents such as methanol, hydroquinone prevails over catechol, whereas with an aprotic solvent such as acetone, catechol prevails over hydroquinone. Other conditions leading to good activities concerning phenol hydroxylation over substituted molecular sieves are typically the presence of Ti species [90] and a hydrophobic character of the support. Del Castillo et al. [91] have reported the catalytic performance and selectivity in phenol hydroxylation of

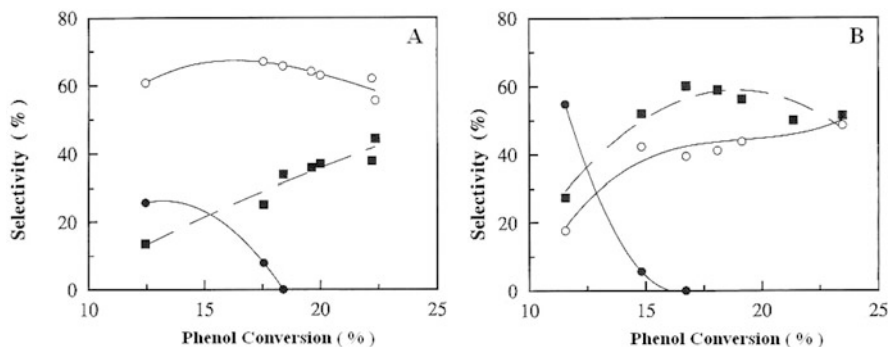
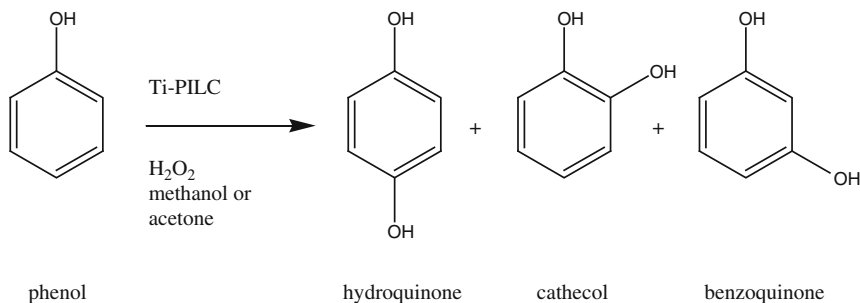


**Fig. 11.1** Selectivity toward hydroquinone (○), catechol (■), and benzoquinone (●) during phenol hydroxylation. Methanol (a) and acetone (b) as solvents, respectively

a Ti-PILC and its modified derivative by sulfation (SNTi-PILC). The effect of the solvent, methanol, or acetone on the distribution of the products at 70 °C was studied (see Scheme 11.8). It was found that Ti-PILC and SNTi-PILC-modified pillared clays result in the same phenol conversion after 24 h in both methanol and acetone; however, an important effect on selectivity is observed when the effect of the solvent is considered (see Fig. 11.1): hydroquinone was the main product when methanol was used while catechol was the one obtained with acetone. The hydroxylation of phenol to form hydroquinone and catechol has been postulated to occur via formation of titanium-peroxo species, which facilitate the direct insertion of oxygen into the aromatic ring. So the selectivities observed in methanol and acetone can be related to the nature of the solvents. It seems that hydroquinone is the main product in the case of a protic solvent such as methanol, because of the formation of a H-bond between methanol and phenol. When the reaction takes place in acetone, an aprotic solvent, the interaction between the Brönsted sites of the surface catalyst and the phenol is favored.



**Scheme 11.8** Phenol hydroxylation

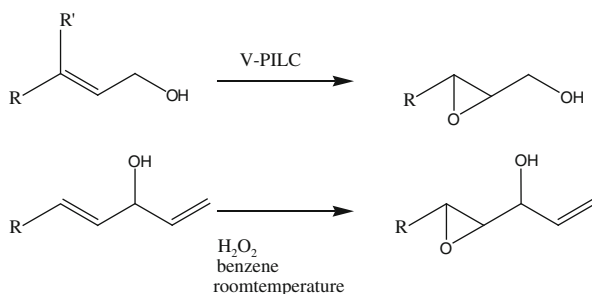
The catalytic behavior of Fe–Al-PILC in this reaction, under conventional heating and microwave irradiation, has been studied by Letaïf et al. [92]. The presence



of redox centers in the layers or in the galleries of the materials, together with a Brønsted acid environment in the galleries of the PILCs, induces phenol hydroxylation. Conversions up to 40% and selectivities of 65% for catechol and 35% for hydroquinone were found.

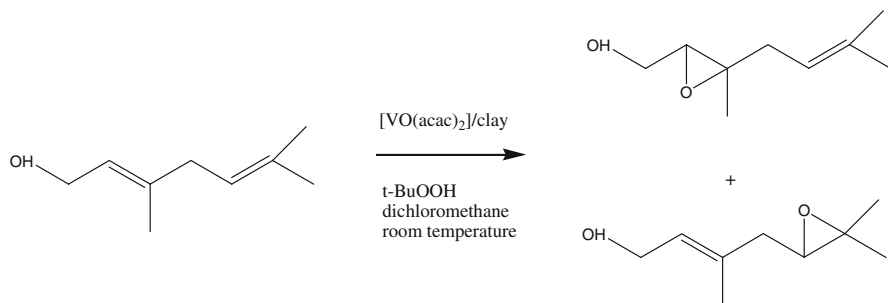
### 11.4.3 Allylic Alcohol Epoxidation

An unusual regioselectivity toward internal allylic double bonds over terminal ones in allylic alcohol epoxidation has been described by Choudary et al. [93] (see Scheme 11.9). Using  $\text{H}_2\text{O}_2$  to oxidize several allylic alcohols over a V-PILC catalyst, the authors obtained only monoepoxides when allylic double bonds were used as reactants. The same authors [94] used Ti-PILC in order to obtain better enantiomeric purities.



**Scheme 11.9** Allylic alcohol epoxidation

Several PILCs have been used by Ghorbel et al. [95–97] as catalysts for the epoxidation of 2-hexen-1-ol and 3-phenyl-2-propenol. When Ti-PILCs were employed as catalysts, Khalfalleh-Boudali et al. [95] found that at temperatures below 25 °C there was a considerable formation of by-products, acids, and aldehydes, while at higher temperatures the main product was the epoxide. The authors attributed the changes of the selectivity to the high activation energy of the epoxidation. In the case of V-PILC catalysts, infrared (IR) and electron spin resonance (ESR) studies showed the presence of  $\text{VO}^{2+}$  species in the interlayer of the clay, which could be the active sites for the epoxidation reaction [96]. The effects of catalyst calcination temperature, reaction temperature, and *tert*-butyl hydroperoxide/alcohol ratio on the catalytic performance have been studied. The best conditions for high yields were calcination temperature of 300 °C, reaction temperature of 77 °C, and 8:7 *tert*-butyl hydroperoxide/alcohol ratio. The catalytic performance of Ti-PILCs was significantly improved by vanadia doping [97]. The Ti-source did not play an important role in the epoxidation process. The alcohol conversion on vanadia-doped Ti-PILC initially increased with increasing V content and then decreased, probably due to pore blockage by vanadia species.



**Scheme 11.10** Geraniol epoxidation

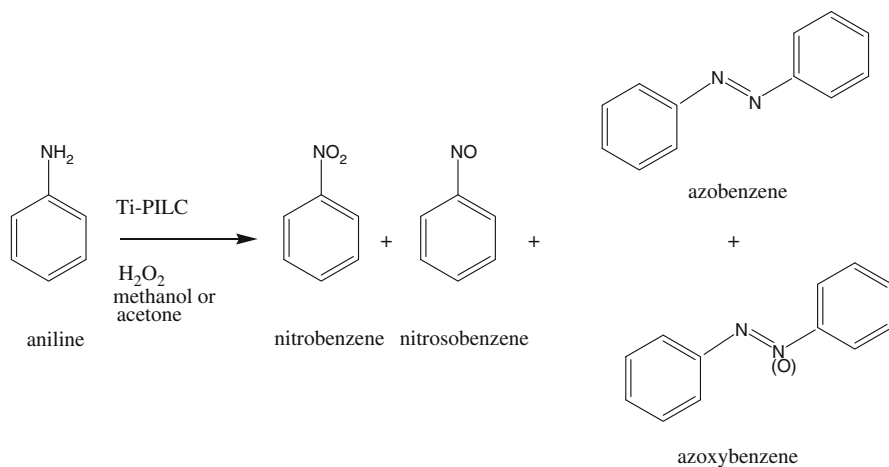
The geraniol epoxidation at room temperature, using *tert*-butyl hydroperoxide as oxygen source (see Scheme 11.10) was studied over clay-supported vanadyl(IV) acetylacetonate ( $\text{VO}(\text{acac})_2$ ) catalysts [98]. The supports were two parent clays, K10-montmorillonite and laponite, and those resulting from functionalization of the parent ones with (3-aminopropyl)triethoxysilane (APTES). All the materials catalyzed geraniol epoxidation, with the following geraniol conversion: K10 (100%) > laponite (68%) > APTES-K10 (49%) > APTES-laponite (7%). The regioselectivity values toward 2,3-epoxygeraniol were high (97–99%), comparable to those of homogeneous reactions. The authors claim that in the case of K10, grafting through APTES leads to a more chemically and catalytically stable material, while laponite is better support for the anchoring of  $\text{VO}(\text{acac})_2$ .

## 11.5 Heteroatom Oxidation

### 11.5.1 Amine Oxidation

Aniline oxidation is an interesting reaction for the synthesis of oxygenated derivatives such as hydroxylamine, nitroso, azo, and azoxy compounds. Among them, nitroso and azoxy compounds have special importance as synthesis intermediates. Aromatic nitroso compounds are used in the vulcanization of rubber, stabilization of halogenated materials, and as antioxidants in lubricating oil [67], whereas azoxybenzenes are used as dyes, reducing agents, chemical stabilizers, and polymerization inhibitors. Derivatives of azoxybenzenes are employed as liquid crystals and medicines [99]. In this way, several oxidation methods have been reported.

Jagtap and Ramaswamy [100] have investigated the effect of synthesis conditions on the properties of Ti-PILCs, prepared by ultrasonic and conventional techniques. The materials were tested as catalysts in aniline oxidation to azoxybenzene at room temperature with aqueous  $\text{H}_2\text{O}_2$  as oxidant (see Scheme 11.11). The aniline conversion and the product selectivity depend on the nature of the solvent and the oxidant, on catalyst concentration, and on the  $\text{H}_2\text{O}_2$ /aniline molar ratio. The best performance was obtained with methanol as a solvent.

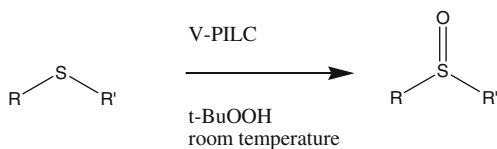


**Scheme 11.11** Aniline oxidation

### 11.5.2 Sulfoxidation

Choudary and Rani [101] obtained an efficient catalytic system for the highly selective oxidation of aryl sulfides to sulfoxides at room temperature using vanadium-pillared clay as catalyst and *tert*-butyl hydroperoxide as oxidant (see Scheme 11.12). The developed methods overcame many disadvantages associated with other systems, such as formation of sulfones, low yields, long reaction times, and tedious workup procedures. The reaction products were selectively sulfoxides in excellent yields.

**Scheme 11.12** Sulfoxidation of aryl sulfides



**R** :  $\text{CH}_3^-$

**R'** :  $\text{CH}_3\text{C}_6\text{H}_4^-$ ,  $\text{C}_6\text{H}_5^-$ ,  $\text{XC}_6\text{H}_4^-$ ,  $\text{NO}_2\text{C}_6\text{H}_4^-$ ,  $\text{C}_6\text{H}_5\text{-CH}_2^-$ ,  $\text{CH}_3(\text{CH}_2)_7^-$ .

## 11.6 Conclusions

The number of published works where pillared layered clays are considered as catalysts for green oxidation reactions is continuously expanding. Starting from natural, inexpensive clays, it is possible to develop new materials with a

microporous structure that can be controlled during the intercalation process and incorporate to it metal cations to create catalytic sites. The possibility of catalyst design and the control of active site distribution are the two main reasons that make pillared clays challenging as stable and selective catalysts in green oxidation reactions.

## References

1. Gil A, Korili SA, Vicente MA (2008) Recent advances in the control and characterization of the porous structure of pillared clay catalysts. *Catal Rev – Sci Eng* 50:153–221
2. Gil A, Gandia LM, Vicente MA (2000) Recent advances in the synthesis and catalytic applications of pillared clays. *Catal Rev – Sci Eng* 42:145–212
3. Yang RT, Chen JP, Kikkini ES, Cheng LS, Cichanowicz JE (1992) Pillared clays as superior catalysts for selective catalytic reduction of NO with NH<sub>3</sub>. *Ind Eng Chem Res* 31:1440–1445
4. Cheng LS, Yang RT, Chen N (1996) Iron oxide and chromia supported on titania-pillared clay for selective catalytic reduction of nitric oxide with ammonia. *J Catal* 164:70–81
5. Del Castillo HL, Gil A, Grange P (1996) Selective catalytic reduction of NO by NH<sub>3</sub> on titanium pillared montmorillonite. *Catal Lett* 36:237–239
6. Li W, Sirilumpen M, Yang RT (1997) Selective catalytic reduction of nitric oxide by ethylene in the presence of oxygen over Cu<sup>2+</sup> ion-exchanged pillared clays. *Appl Catal B* 11:347–363
7. Yang RT, Tharappiwattananon N, Long RQ (1998) Ion-exchanged pillared clays for selective catalytic reduction of NO by ethylene in the presence of oxygen. *Appl Catal B* 19:289–304
8. Sirilumpen M, Yang RT, Tharapiwattananon N (1999) Selective catalytic reduction of NO with hydrocarbon on Cu<sup>2+</sup>-exchanged pillared clay: and IR study of the NO decomposition mechanism. *J Mol Catal A* 137:273–286
9. Chmielarz L, Dziembaj R, Grzybek T, Klinik J, Lojewski T, Olszewska D, Papp H (2000) Pillared smectite modified with carbon and manganese as catalyst for SCR of NOx with NH<sub>3</sub>. Part I. General characterization and catalyst screening. *Catal Lett* 68:95–100
10. Lee D-K, Kim S-C, Kim S-J, Kang J-K, Kim D-S, Oh S-S (2002) Preparation of iron-doped titania-pillared clays and their application to selective catalytic reduction of NO with ammonia. *Stud Surf Sci Catal* 142:895–902
11. Khalfallah Boudali L, Ghorbel A, Grange P (2003) Selective catalytic reduction of NO by NH<sub>3</sub> on sulfated titanium-pillared clay. *Catal Lett* 86:251–256
12. Khalfallah Boudali L, Ghorbel A, Grange P, Jung SM (2002) Vanadia-doped titanium pillared clay: preparation, characterization and SCR activity of NO by ammonia. *Stud Surf Sci Catal* 143:873–880
13. Chmielarz L, Kustrowski P, Zbroja M, Rafalska-Lasocha A, Dudek B, Dziembaj R (2003) SCR of NO by NH<sub>3</sub> on alumina or titania-pillared montmorillonite various modified with Cu or Co. Part I. General characterization and catalysts screening. *Appl Catal B* 45:103–116
14. Valverde JL, de Lucas A, Sánchez P, Dorado F, Romero A (2003) Cation exchanged and impregnated Ti-pillared clays for selective catalytic reduction of NOx by propylene. *Appl Catal B* 43:43–56
15. Qi G, Yang RT, Thompson LT (2004) Catalytic reduction of nitric oxide with hydrogen and carbon monoxide in the presence of excess oxygen by Pd supported on pillared clays. *Appl Catal A* 259:261–267
16. Dorado F, de Lucas A, García PB, Romero A, Valverde JL (2006) Copper ion-exchanged and impregnated Fe-pillared clays. Study of the influence of the synthesis conditions on the activity for the selective catalytic reduction of NO with C<sub>3</sub>H<sub>6</sub>. *Appl Catal A* 305:189–196
17. Khalfallah Boudali L, Ghorbel A, Grange P (2006) SCR of NO by NH<sub>3</sub> over V<sub>2</sub>O<sub>5</sub> supported sulfated Ti-pillared clay: reactivity and reducibility of catalysts. *Appl Catal A* 305:7–14

18. Olszewska D (2006) Ammonia and water sorption properties of the mineral-layered nanomaterials used as the catalysts for NO<sub>x</sub> removal from exhaust gases. *Catal Today* 114:326–332
19. Chmielarz L, Kustrowski P, Michalik M, Dudek B, Czajka M, Dziembaj R (2007) Phlogophites intercalated with Al<sub>2</sub>O<sub>3</sub> pillars and modified with transition metals as catalysts of the DeNO<sub>x</sub> process. *React Kinet Catal Lett* 91:369–378
20. Li Q, Hao J, Li J, Ma Z, Lin W (2007) Copper-impregnated Al–Ce-pillared clay for selective catalytic reduction of NO by C<sub>3</sub>H<sub>6</sub>. *Catal Today* 126:351–358
21. Chmielarz L, Kustrowski P, Michalik M, Dudek B, Piwowarska Z, Dziembaj R (2008) Vermiculites intercalated with Al<sub>2</sub>O<sub>3</sub> pillars and modified with transition metals as catalysts of DeNO<sub>x</sub> process. *Catal Today* 137:242–246
22. Arfaoui J, Khalfallah Boudali L, Ghorbel A, Delahay G (2009) Effect of vanadium on the behaviour of unsulfated and sulfated Ti-pillared clay catalysts in the SCR of NO by NH<sub>3</sub>. *Catal Today* 142:234–238
23. Storaro L, Ganzerla R, Lenarda M, Zanoni R (1995) Vapor-phase deep oxidation of chlorinated hydrocarbons catalyzed by pillared bentonites. *J Mol Catal A* 97:139–143
24. Gil A, Toranzo R, Bañares MA, Vicente MA, Gandia LM (1998) Preparation, characterization and catalytic activity in the deep oxidation of acetone of Cr,Al-pillared saponites. *J Chem Technol Biotechnol* 72:131–136
25. Gil A, Vicente MA, Lambert J-F, Gandia LM (2001) Platinum catalysts supported on Al-pillared clays. Application to the catalytic combustion of acetone and methyl-ethyl-ketone. *Catal Today* 68:41–51
26. Gandia LM, Vicente MA, Gil A (2002) Complete oxidation of acetone over manganese oxide catalysts supported on alumina- and zirconia-pillared clays. *Appl Catal B* 38:295–307
27. Vicente MA, Bañares-Muñoz MA, Lambert J-F, Korili SA, Gil A, Gandia LM (2002) Aplicación de catalizadores soportados Pt/arcillas intercaladas en la oxidación completa de acetona. *Afinidad* 499:262–266
28. Jinjun L, Zheng J, Zhengping H, Xiuyan X, Yahui Z (2005) Pillared laponite clays-supported palladium catalysts for the complete oxidation of benzene. *J Mol Catal A* 225:173–179
29. Zuo S, Zhou R (2006) Al-pillared clays supported rare earths and palladium catalysts for deep oxidation of low concentration of benzene. *Appl Surf Sci* 253:2508–2514
30. Mata G, Trujillano R, Vicente MA, Belver C, Fernandez M, Korili SA, Gil A (2007) Chromium-saponite clay catalysts: preparation, characterization and catalytic performance in propene oxidation. *Appl Catal A* 327:1–12
31. Anisia KS, Kumar A (2007) Oxidation of cyclohexane with molecular oxygen in presence of characterized macrocyclic heteronuclear FeCu complex catalyst ionically bonded to zirconium pillared montmorillonite clay. *J Mol Catal A* 271:164–179
32. Carriazo JG, Centeno MA, Odriozola JM, Moreno S, Molina R (2007) Effect of Fe and Ce on Al-pillared bentonite and their performance in catalytic oxidation reactions. *Appl Catal A* 317:120–128
33. Oliveira LCA, Lago RM, Fabris JD, Sapag K (2008) Catalytic oxidation of aromatic VOCs with Cr or Pd-impregnated Al-pillared bentonite: byproduct formation and deactivation studies. *Appl Clay Sci* 39:218–222
34. Ramaswamy V, Malwadkar S, Chilukuri S (2008) Cu–Ce mixed oxides supported on Al-pillared clay: effect of method of preparation on catalytic activity in the preferential oxidation of carbon monoxide. *Appl Catal B* 84:21–29
35. Barrault J, Abdellaoui M, Bouchoule C, Mejesté A, Tatibouet JM, Louloudi A, Papayannakos N, Gangas NH (2000) Catalytic wet peroxide oxidation over mixed (Al–Fe) pillared clays. *Appl Catal B* 27:L225–L230
36. Chirchi L, Ghorbel A (2002) Use of various Fe-modified montmorillonite samples for 4-nitrophenol degradation by H<sub>2</sub>O<sub>2</sub>. *Appl Clay Sci* 21:271–276
37. Guélou E, Barrault J, Fournier J, Tatibouët J-M (2003) Active iron species in the catalytic wet peroxide oxidation of phenol over pillared clays containing iron. *Appl Catal B* 44:1–8

38. Guo J, Al-Dahhan M (2003) Catalytic wet oxidation of phenol by hydrogen peroxide over pillared clay catalyst. *Ind Eng Chem Res* 42:2450–2460
39. Carriazo J, Guelou E, Barrault J, Tatibouet J.M, Moreno S. (2003) Catalytic wet peroxide of phenol over Al–Cu or Al–Fe modified clays. *Appl Clay Sci* 22:303–308
40. Nikolopoulos AN, Igglessi-Markopoulou O, Papayannakos N (2004) Degradation of 4-hydroxybenzoic acid by combined ultrasound irradiation and catalytic wet peroxide oxidation. *Ultrason Sonochem* 11:183–186
41. Sum OSN, Feng J, Hu X, Yue PL (2004) Pillared laponite clay-based Fe nanocomposites as heterogeneous catalysts for photo-Fenton degradation of Acid Black 1. *Chem Eng Sci* 59:5269–5275
42. Mei JG, Yu SM, Cheng J (2004) Heterogeneous catalytic wet peroxide oxidation of phenol over delaminated Fe–Ti-PILC employing microwave irradiation. *Catal Commun* 5:437–440
43. Kim S-C, Lee D-L (2004) Preparation of Al–Cu pillared clay catalysts for the catalytic wet oxidation of reactive dyes. *Catal Today* 97:153–158
44. Timofeeva MN, Khankhasaeva STs, Badmaeva SV, Chuvilin AL, Burgina EB, Ayupov AB, Panchenko VN, Kulikova AV (2005) Synthesis, characterization and catalytic application for wet oxidation of phenol of iron-containing clays. *Appl Catal B* 59:243–248
45. Molina CB, Casas JA, Zazo JA, Rodríguez JJ (2006) A comparison of Al–Fe and Zr–Fe pillared clays for catalytic wet peroxide oxidation. *Chem Eng J* 118:29–35
46. Chen J, Zhu L (2006) Catalytic degradation of Orange II by UV–Fenton with hydroxyl-Fe-pillared bentonite in water. *Chemosphere* 65:1249–1255
47. Tabet D, Saidi M, Houari M, Pichat P, Khalaf H (2006) Fe-pillared clay as a Fenton-type heterogeneous catalyst for cinnamic acid degradation. *J Environ Manage* 80:342–346
48. Liu S, Yang J-H, Choy J-H (2006) Microporous SiO<sub>2</sub>–TiO<sub>2</sub> nanosols pillared montmorillonite for photocatalytic decomposition of Methyl Orange. *J Photochem Photobiol A* 179:75–80
49. Caudo S, Centi G, Genovese C, Perathoner S (2007) Copper- and iron-pillared clay catalysts for the WHPCO of model and real wastewater streams from olive oil milling production. *Appl Catal B* 70:437–446
50. Azabou S, Najjar W, Gargoubi A, Ghorbel A, Sayadi S (2007) Catalytic wet peroxide photo-oxidation of phenolic olive oil mill wastewater contaminants. Part II. Degradation and detoxification of low-molecular mass phenolic compounds in model and real effluent. *Appl Catal B* 77:166–174
51. Caudo S, Genovese Ch, Perathoner S, Centi G (2008) Copper-pillared clays (Cu-PILC) for agro-food wastewater purification with H<sub>2</sub>O<sub>2</sub>. *Micropor Mesopor Mater* 107:46–57
52. Chen J, Zhu L (2007) Heterogeneous UV–Fenton catalytic degradation of dyestuff in water with hydroxyl-Fe pillared bentonite. *Catal Today* 126:463–470
53. Giordano G, Perathoner S, Centi G, De Rosa S, Granato T, Katovic A, Siciliano A, Tagarelli A, Tripicchio F (2007) Wet hydrogen peroxide catalytic oxidation of olive oil mill wastewaters using Cu-zeolite and Cu-pillared clay catalysts. *Catal Today* 124: 240–246
54. Herney Ramirez J, Costa CA, Madeira LM, Mata G, Vicente MA, Rojas-Cervantes ML, López-Peinado AJ, Martín-Aranda RM (2007) Fenton-like oxidation of Orange II solutions using heterogeneous catalysts based on saponite clay. *Appl Catal B* 71:44–56
55. Najjar W, Azabou S, Sayadi S, Ghorbel A (2007) Catalytic wet peroxide photo-oxidation of phenolic olive oil mill wastewater contaminants. Part I. Reactivity of tyrosol over (Al–Fe)PILC. *Appl Catal B* 74:11–18
56. Sanabria N, Álvarez A, Molina R, Moreno S (2008) Synthesis of pillared bentonite starting from Al–Fe polymeric precursor in solid state, and its catalytic evaluation in the phenol oxidation reaction. *Catal Today* 133–135:530–533
57. Herney-Ramirez J, Lampinen M, Vicente MA, Costa CA, Madeira LM (2008) Experimental design to optimize the oxidation of Orange II dye solution using a clay-based Fenton-like catalyst. *Ind Eng Chem Rev* 47:284–294

58. de León MA, Castiglioni J, Bussi J, Sergio M (2008) Catalytic activity of an iron-pillared montmorillonitic clay mineral in heterogeneous photo-Fenton process. *Catal Today* 133–135:600–605
59. Ben Achma R, Ghorbel A, Dafinov A, Medina F (2008) Copper-supported pillared clay catalysts for the wet hydrogen peroxide catalytic oxidation of model pollutant tyrosol. *Appl Catal A* 349:20–28
60. Iurascu B, Siminiceanu I, Vione D, Vicente MA, Gil A (2009) Phenol degradation in water through a heterogeneous photo-Fenton process catalyzed by Fe-treated laponite. *Water Res* 43:1313–1322
61. Luo M, Bowden D, Brimblecombe P (2009) Catalytic property of Fe–Al pillared clay for Fenton oxidation of phenol by H<sub>2</sub>O<sub>2</sub>. *Appl Catal B* 85:201–206
62. Martínez LM, Domínguez MI, Sanabria N, Hernández WY, Moreno S, Molina R, Ordiozola JA, Centeno MA (2009) Deposition of Al–Fe pillared bentonites and gold supported Al–Fe pillared bentonites on metallic monoliths for catalytic oxidation reactions. *Appl Catal A* 364:166–173
63. Damardji B, Khalaf H, Duclaux L, David B (2009) Preparation of TiO<sub>2</sub>-pillared montmorillonite as photocatalyst. Part II. Photocatalytic degradation of a textile azo dye. *Appl Clay Sci* 45:98–104
64. Timofeeva MN, Khankhasaeva STs, Chesalov Yu A, Tsybulya SV, Panchenko VN, Dashinamzhilova ETs (2009) Synthesis of Fe, Al-pillared clays starting from the Al,Fe-polymeric precursor: effect of synthesis parameters on textural and catalytic properties. *Appl Catal B* 88:127–134
65. Sun S-P, Li C-J, Sun J-H, Shi S-H, Fan M-H, Zhou Q (2009) Decolorization of an azo dye Orange G in aqueous solution by Fenton oxidation process: effect of system parameters and kinetic study. *J Hazard Mater* 161:1052–1057
66. Anastas PT, Warner J (1998) *Green chemistry: theory and practice*. Oxford University Press, Oxford
67. Kirk-Othmer (1982) *Encyclopedia of chemical technology*. In: Mark HF, Othmer DF, Overberger ChG, Seaborg GT (eds) Wiley, New York, NY
68. Cardoso B, Pires J, Carvalho AP, Kuzniarska-Biernacka I, Silva AR, de Castro B, Freire C (2005) Mn(III) salen complex immobilised into pillared clays by in situ and simultaneous pillaring/encapsulation procedures: application in the heterogeneous epoxidation of styrene. *Micropor Mesopor Mater* 86:295–302
69. Kuzniarska-Biernacka I, Silva AR, Carvalho AP, Pires J, Freire C (2007) Direct immobilisation versus covalent attachment of a Mn(III) salen complex onto an Al-pillared clay and influence in the catalytic epoxidation of styrene. *J Mol Catal A* 278:82–91
70. Das P, Kuzniarska-Biernacka I, Silva AR, Carvalho AP, Pires J, Freire C (2006) Encapsulation of chiral Mn(III) salen complexes into aluminium pillared clays: application as heterogeneous catalysts in the epoxidation of styrene. *J Mol Catal A* 248:135–143
71. Mata G, Trujillano R, Vicente MA, Korili SA, Gil A, Belver C, Ciuffi KJ, Nassar EJ, Ricci GP, Cestari A, Nakagaki S (2009) (Z)-Cyclooctene epoxidation and cyclohexane oxidation on Ni/alumina-pillared clay catalysts. *Micropor Mesopor Mater* 124:218–226
72. Mishra G, Sinha S (2008) Oxidation of cyclohexane with molecular oxygen catalyzed by SiO<sub>2</sub> supported palladium catalysts. *Catal Lett* 125:139–144
73. Trujillano R, Vicente MA, Rives V, Korili SA, Gil A, Ciuffi KJ, Nassar EJ (2009) Preparation, alumina-pillaring and oxidation catalytic performance of synthetic Ni-saponite. *Micropor Mesopor Mater* 117:309–316
74. Choudary BM, Prasad AD, Swapna V, Valli VLK, Bhuma V (1992) Chromium pillared clay catalysed allylic oxidation and oxidative deprotection of allyl ethers and amines: a simple and convenient procedure. *Tetrahedron* 48:953–962
75. Subba Rao YV, Rani SS, Choudary BM (1992) New montmorillonite silylpropylethylenediamine palladium(II) complex in oxidation of terminal olefins. *J Mol Catal* 15:141–146

76. Romanenko EP, Taraban EA, Tkachev AV (2006) Catalytic oxidation of  $\alpha$ -pinene with *tert*-butyl hydroperoxide in the presence of Fe-pillared montmorillonite. *Russ Chem Bull Int Ed* 55:993–998
77. Bhaumik A, Mukherjee P, Kumar R (1998) Triphase catalysis over titanium–silicate molecular sieves under solvent-free conditions: I. Direct hydroxylation of benzene. *J Catal* 178:101–107
78. Parvulescu V, Su B-L (2001) Iron, cobalt or nickel substituted MCM-41 molecular sieves for oxidation of hydrocarbons. *Catal Today* 69:315–322
79. Dubey A, Kannan S (2005) Liquid phase hydroxylation of benzene over Cu-containing ternary hydrotalcites. *Catal Commun* 6:394–398
80. Choi JS, Kim TH, Choo KY, Sung JS, Saidutta MB, Ryu SK, Song SD, Ramachandra B, Rhee Y-W (2005) Direct synthesis of phenol from benzene on iron-impregnated activated carbon catalysts. *Appl Catal A* 290:1–8
81. Masumoto Y-H, Hamada R, Yokota K, Nishiyama S, Tsuruya S (2002) Liquid-phase oxidation of benzene to phenol by vanadium catalysts in aqueous solvent with high acetic acid concentration. *J Mol Catal A* 184:215–222
82. Lemke K, Ehrlich H, Lohse U, Berndt H, Jähnisch K (2003) Selective hydroxylation of benzene to phenol over supported vanadium oxide catalysts. *Appl Catal A* 243:41–51
83. Pan J, Wang C, Guo S, Li J, Yang Z (2008) Cu supported over Al-pillared interlayer clays catalysts for direct hydroxylation of benzene to phenol. *Catal Commun* 9:176–181
84. Choudary BM, Valli VLK (1990) A novel vanadium pillared montmorillonite catalyst for molecular recognition of benzyl alcohols. *J Chem Soc Chem Commun* 1115–1116
85. Choudary BM, Durga Prasad A, Valli VLK (1990) Selective oxidation of alcohols by chromia-pillared montmorillonite catalyst. *Tetrahedron Lett* 31:5785–5788.
86. Palinko I, Molnar A, Nagy JB, Bertrand J-C, Lazar K, Valyon J, Kiricsi I (1997) Mixed-metal pillared layer clays and their pillaring precursors. *J Chem Soc Faraday Trans* 93:1591–1599
87. Clark JH (1999) Green chemistry: challenges and opportunities. *Green Chem* 1:1–8
88. Thangaraj A, Kumar R, Ratnasamy P (1991) Catalytic properties of crystalline titanium silicalites II. Hydroxylation of phenol with hydrogen peroxide over TS-1 zeolites. *J Catal* 131:294–297
89. Tuel A, Moussa-Khouzami S, Ben Yaarit Y, Naccache CM (1991) Hydroxylation of phenol over titano silicalite-1 (TS-1): surface and solvent effects. *J Mol Catal* 68:45–52
90. del Castillo HL, Gil A, Grange P (1997) Influence of the nature of titanium alkoxide and of the acid of hydrolysis in the preparation of titanium-pillared montmorillonites. *J Phys Chem Sol* 58:1053–1062
91. del Castillo HL, Gil A, Grange P (1996) Hydroxylation of phenol on titanium pillared montmorillonite. *Clays Clay Miner* 44:706–709
92. Letaïef S, Casal B, Aranda P, Martín-Luengo MA, Ruiz-Hitzky E (2003) Fe-containing pillared clays as catalysts for phenol hydroxylation. *Appl Clay Sci* 22:263–277
93. Choudary BM, Valli VLK, Durga Prasad A (1990) A new vanadium-pillared montmorillonite catalyst for the regioselective epoxidation of allylic alcohols. *J Chem Soc Chem Commun* 721–722
94. Choudary BM, Valli VLK, Durga Prasad A (1990) An improved asymmetric epoxidation of allyl alcohols using titanium-pillared montmorillonite as a heterogeneous catalyst. *J Chem Soc Chem Commun* 1186–1187
95. Khalfallah-Boudali L, Ghorbel A, Figueras F, Pinel C (2000) Characterization and catalytic properties of titanium pillared clays in the epoxidation of allylic alcohols. *Stud Surf Sci Catal* 130:1643–1648
96. Khedher I, Ghorbel A (2000) Epoxidation of allylic alcohol by vanadium-montmorillonite catalyst. *Stud Surf Sci Catal* 130:1649–1654
97. Arfaoui J, Khalfallah-Boudali L, Ghorbel A. (2006) Vanadia-doped titanium-pillared clay: preparation, characterization and reactivity in the epoxidation of allylic alcohol (*E*)-2-hexen-1-ol. *Catal Commun* 7:86–90



98. Pereira C, Silva AR, Carvalho AP, Pires J, Freire C (2008) Vanadyl acetylacetonate anchored onto amine-functionalised clays and catalytic activity in the epoxidation of geraniol. *J Mol Catal A* 283:5–14
99. Sakuae S, Tsubakino T, Nishiyama Y, Ishii Y (1993) Oxidation of aromatic amines with hydrogen peroxide catalyzed by cetylpyridinium heteropolyoxometalates. *J Org Chem* 58:3633–3638
100. Jagtap N, Ramaswamy V (2006) Oxidation of aniline over titania pillared montmorillonite clays. *Appl Clay Sci* 33:89–98
101. Choudary BM, Rani SS (1992) Vanadium-pillared montmorillonite catalyst for selective oxidation of sulfides to sulfoxides. *J Mol Catal* 75:L7–L12

# Chapter 12

## Heterogeneous Catalysis by Polyoxometalate-Intercalated Layered Double Hydroxides

Vicente Rives, Daniel Carriazo, and Cristina Martín

**Abstract** The preparation, characterisation and catalytic performance of layered double hydroxides (LDH) with the hydrotalcite-type structure containing different polyoxometalates (POM) in the interlayer are studied. Special attention is paid to the preparation procedures, as they control the properties of the solids formed and thus their catalytic behaviour. The study is extended to solids prepared upon thermal decomposition of these POM-LDH systems. It is concluded that the LDH does not act as a simple support, but that its specific properties, such as nature of the cations in the brucite-like layers, specific surface area and the method followed for its preparation, have an outstanding effect on the final catalytic properties of the POM-LDH systems.

**Keywords** Pillared clays · Heterogeneous catalysis · LDH · POM

### 12.1 Introduction

Layered double hydroxides (LDHs), also known as anionic clays due to the similarities shared with cationic clays, or hydrotalcite-like materials, as derived from the natural hydroxycarbonate of Mg and Al discovered in Sweden in 1842, constitute a broad family of lamellar solids which in the last decades have deserved an increasing interest because of their applications in different fields [1, 2]. A search in Google™ on 22 February 2009 for “hydrotalcite” returned 92,000 entries, while for “layered double hydroxide(s)” they were 21,000; a search for “LDH” is not valid (more than 2 million entries were returned) as this acronym stands also for *Lactate DeHydrogenase*. Their properties have been reviewed in the last 8 years in different books and monographs [2–4].

---

V. Rives (✉)

GIR-QUESCAT, Departamento de Química Inorgánica, Universidad de Salamanca,  
Salamanca 37008, Spain  
e-mail: vrives@usal.es

Their structure is similar to that of brucite,  $\text{Mg}(\text{OH})_2$  (a  $\text{CdI}_2$ -type structure), where hydroxyl anions are hexagonal close packed and magnesium cations are filling all octahedral sites every two layers. A different way to describe this structure is as edge-sharing octahedra of magnesium cations surrounded by six hydroxyl groups forming infinite sheets; these layers are stacked on top of each other and held together by weak hydrogen bonds.

The isomorphous substitution of some of the cations by others with similar size, but with higher valence, develops a positive charge in these brucite-like sheets. In order to recover the electroneutrality, anions, together with water molecules, are incorporated between the layers, Fig. 12.1. There are different ways in which brucite-like sheets can arrange [5], the most typical ones being rhombohedral (3R symmetry) and hexagonal (2H symmetry).

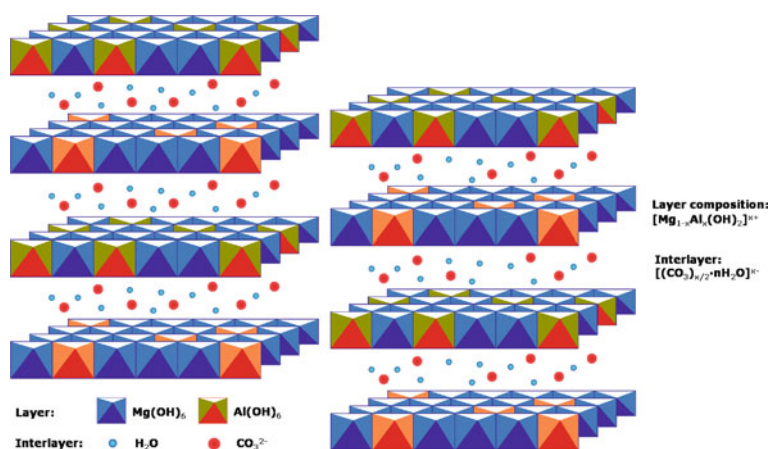


**Fig. 12.1** Idealised structure of a layered double hydroxide with the hydroxalite structure

Many different metal cations may be located in the brucite-like layers. The most commonly found are  $\text{Mg}^{2+}$ ,  $\text{Zn}^{2+}$ ,  $\text{Co}^{2+}$ ,  $\text{Ni}^{2+}$ ,  $\text{Cu}^{2+}$  or  $\text{Mn}^{2+}$  as divalent cations and  $\text{Al}^{3+}$ ,  $\text{Cr}^{3+}$ ,  $\text{Co}^{3+}$ ,  $\text{Fe}^{3+}$ ,  $\text{V}^{3+}$ ,  $\text{Y}^{3+}$  or  $\text{Mn}^{3+}$  among the trivalent ones. All these elements, with the exception of  $\text{Al}^{3+}$  (0.50 Å), have similar ionic radii as that of  $\text{Mg}^{2+}$  (0.62–0.69 Å), thus accounting for the isomorphous substitution without a substantial distortion of the structure. In addition to these cations, other LDHs containing monovalent and tetravalent metal cations within the brucite-like layers have also been synthesised [6–9]. Although most of the systems reported so far contain only two different metal cations in the layers, other systems containing three or even four different metal cations have also been described [10–17].

Regarding the anions in the interlayer, there are no strict limitations to their nature, and systems with many different anionic species have been described: simple inorganic anions (carbonate, nitrate, halides, etc.) [18], organic anions (terephthalate, acrylate, lactate, etc.) [19–21], coordination compounds [22], polyoxometalates [23] biomolecules such as nucleoside monophosphates (AMP, CMP,

GMP or ATP) or even DNA fragments [24–26] have been successfully intercalated between the brucite-like layers.

The only restriction concerning the nature of the anions to be intercalated makes reference to their size/charge ratio. Large anions with low charge are unable to balance properly the positive charge in the layers. Pinnavaia et al. [27] claimed that, in some cases, polyoxometalates (POMs) with the Keggin structure with a charge less than  $-4$  are unable to be intercalated between brucite-like layers with a  $M^{2+}/M^{3+}$  molar ratio close to 2, since these molecules are not spatially able to balance the host layer charge.

In all natural occurring LDHs and in most of the synthetic hydrotalcite-like materials, the  $M^{2+}/M^{3+}$  molar ratio ranges between 2 and 4. Solids containing larger concentrations of the trivalent cations may destabilise the structure, due to repulsion forces affording between them. On the other hand, high  $M^{2+}/M^{3+}$  ratios require a lower amount of very well-dispersed anionic species between the layers for balancing the positive charge of the layers, and this may lead to the collapse of the structure. It cannot be forgotten that the positive charge of the layers is associated with the  $M^{3+}$  cations and is not delocalised along the layer. Different authors have reported the synthesis of these sort of solids with lower or higher molar ratios than those considered usual [28], although it should be taken into account that for this sort of materials it is difficult to know the accurate layer composition, since for such extreme ratios formation of dispersed amorphous oxides cannot be discarded.

These materials have deserved a great interest in recent decades because of their applications in different fields due to their peculiar properties:

- *Acid–base properties.* LDH solids are in general basic materials with surface basic hydroxyl groups; this basic character mainly depends on the chemical composition of the layers (nature and molar fraction on metal cations) and can be modulated in a given range through the substitution of some cations by others with a higher acidic ability. The basicity of carbonate-intercalated LDHs has been related to the electronegativity of the cations in the layers [29, 30]. The mixed oxides formed upon thermal decomposition of LDHs exhibit even more basicity than that observed for the pristine materials, probably because of the existence of strong oxide basic sites. Additionally, the intercalation of different species can give rise to the development of acid sites providing systems with unique acid–base properties.
- The possibility to prepare *homogeneous mixtures* containing well-dispersed elements in both – the layer and the interlayer – domains in a wide range of composition and ratios allows to synthesise solids with tailored properties.
- They exhibit the so-called *memory effect* [27, 31], consisting of the ability to recover their original layered structure when mixed oxides, obtained upon calcination at moderate temperatures (usually not exceeding  $500\text{ }^{\circ}\text{C}$ ), are put in contact with solutions containing anions. If a Mg, Al LDH is calcined in these conditions and immersed in pure water, the solid formed contains hydroxyl anions in the interlayer and is known as meixnerite.

- They show a good *anion exchange* capacity (AEC) associated with the non-divalent layer cation, usually higher than that shown by cationic clays, and ranging between 2 and 4 mEq g<sup>-1</sup>.

Diverse synthetic routes to prepare LDHs have been described in the literature [32–34], the most widely used being coprecipitation, anionic exchange, sol–gel, salt oxide, reconstruction and topochemical synthesis. Selection of one or another greatly depends on the specific material to be prepared.

The most commonly used method is the *coprecipitation* one, which consists in the slow addition of a solution containing salts of the divalent and trivalent metal cations in the required molar ratio into a reactor containing water; an alkaline solution is simultaneously added to keep the pH within a selected, narrow range, at which both metal cations precipitate as hydroxides.

The *anionic exchange* method is very useful to obtain LDHs intercalated with anions of different nature. According to some authors this is not properly a synthesis method, but a post-synthesis modification, since it is necessary to have a LDH precursor. This is usually a carbonate-free LDH, since due to the extreme affinity between carbonate and LDHs, it is very difficult to achieve a complete exchange when starting from carbonate-containing LDHs. Anions of different nature having various sizes, shapes and formal charges have been successfully intercalated by using this method. Thermodynamically, the feasibility of exchanging the anions in LDHs depends on the electrostatic interactions between the positively charged layers and the interlayer anions. Another important feature to be taken into account is that the equilibrium constants increase as the ionic radius of the anion decreases, and consequently the exchange is favoured for anions with high charge densities. From a kinetics point of view, the rate-determining step is the diffusion of the in-going anions within the interlayer. Exchange reactions are usually carried out by stirring the LDH precursor in a solution containing an excess of the anion to be intercalated; ultrasounds have been also applied to speed up the exchange process [35].

The *salt oxide* method consists of the reaction between a metal oxide and a metal salt (usually nitrate or chloride). Although this procedure was firstly applied to prepare Zn,Cr LDHs with intercalated chloride anions using ZnO and CrCl<sub>3</sub>, other hydrotalcite-type solids have been successfully prepared through this method [36].

The *sol–gel* method is also useful to synthesise this kind of solids. It involves the formation of a mobile colloidal suspension of particles with a size in the 1–100 nm range (sol) that then gels through internal cross-linking. The LDH is formed by hydrolysis and subsequent condensation of a solution typically containing metal alkoxides and/or acetylacetonates [37]. Materials prepared through this method exhibit good homogeneity, high specific surface areas and high porosity, although in some cases impurities related to the alcoholates used remain strongly held to the crystallites.

A method known as SNAS (*separate nucleation and ageing steps*) has been developed and applied rather recently to prepare LDHs [38]. By using this method,

LDHs with a strict control of size and particle size distribution can be prepared, combining a fast mixing of the parent solutions and a nucleation process, followed by a separate ageing process. Hydrotalcites with different Mg/Al ratios can be prepared using this method [39].

The *reconstruction* method is based on the above-mentioned memory effect. It involves several steps: first the preparation of a hydrotalcite-type solid containing the desired metal cations in the brucite-like layer, commonly intercalated with carbonate (as the carbonate-containing LDHs are easily formed because of the affinity between them). Second, the solid is calcined at temperatures usually not above 500 °C (preferable under dynamic inert gas atmosphere to avoid contamination by CO<sub>2</sub>). Finally, the mixed oxide formed is stirred in an aqueous solution of the anions to be intercalated, usually in a concentration several times higher than that required for a stoichiometric reaction.

Highly crystalline LDHs have been recently prepared through topochemical synthesis. This procedure uses well-crystallised, pure or mixed metal hydroxides (e.g. Co(OH)<sub>2</sub> or Fe(OH)<sub>2</sub>) as precursors; then some of the cations are oxidised to the trivalent state through reaction with bromine or iodine. The resulting LDHs which host the halides in the interlayer exhibit high crystallinity and can undergo exchange with other anions [40, 41].

All these methods provide only a limited control over the particle size, morphology, surface area and pore architecture, a series of parameters which strongly define their particular performance. In recent years, other routes, not typically used to prepare this sort of materials, have been applied for a better design and tailoring of the LDHs textural properties. In this regard, Hu et al. [42] have reported the preparation of nanoplatelets of dodecylsulphate-intercalated MgAl-LDHs by using an isooctane-sodium dodecylsulphate reverse emulsion; Géraud et al. [43] have prepared macroporous LDHs containing different metals within the brucite-like layers through self-assembled colloidal template assisted with polystyrene nanoparticles; Li et al. [44] have reported the preparation of LDHs thin films through delamination of nitrate-intercalated MgAl-LDHs in formamide and then layer-by-layer assembling with an anionic polymer. Inverse micelles have also been used [42, 45].

Hydrothermal and microwave treatments have been applied to process LDHs previously prepared through one of the methods above described. Although the excitation method differs between both techniques, the outcome is similar, improving the crystallinity of the LDH materials and other properties, especially upon microwave treatment [46–61].

The fields of applications of LDHs are very broad. Only a few of them will be outlined below.

*Medicine.* Due to its basic nature, hydrotalcite is commonly used as an antacid, since it produces a prolonged neutralising effect; hydrotalcite can be found in different commercial drugs, such as Talcid© or Almax©. MgAl-LDHs have been also used to adsorb intestinal phosphate to prevent hyperphosphatemia, sometimes arising during haemodialysis treatments on patients afflicted with kidney diseases [62]. Hydrotalcite-type materials have also been proposed for the controlled release of

intercalated drugs. It has been reported that drug intercalation into LDH matrices does not only reduce stomach irritation but, in some cases, an increase in drug solubility is also observed [63–65]. Choy et al. [66] proposed to use LDH materials as non-viral vectors for DNA release inside the cell. The ion exchange capability of LDHs allows encapsulating functional negatively charged biomolecules such as antisense DNA to form bio-LDH nanohybrids, a system where the hydroxide layers protect the intercalated molecules from degradation: once the LDH–DNA hybrids have entered into the cell through endocytosis, the hydroxide layers are dissolved in the lysosome, with a slightly acid pH, and the encapsulated biomolecules are released inside the cell.

*Materials science.* The main commercial application of LDHs involves their use as additives in polyvinyl chloride polymers (PVC). It has been reported that the dispersion of a certain amount of LDH within this polymer improves its strength and helps to maintain the original white colour of the polymer [67, 68]. Several authors have claimed that incorporation of LDH into polymer matrices enhances their mechanical properties and may provide them with novel ones: colour [69], flame retardant [70–72] or barrier effect [73–75]. Regarding the field of analytical chemistry, hydrotalcite-type materials have been used as electrode surface modifiers. These materials show many advantages on comparing them with the widely used organic polymers such as chemical inertness, better stability and tolerance to high temperatures and oxidising conditions, making LDHs very interesting materials for the development of amperometric sensors [76, 77].

*Water decontamination.* Adsorption is the most common process for the uptake of heavy metals from polluted reservoirs. However, depending on the pH conditions, metals can exist as cations or in several anionic forms. The large AEC together with the memory effect exhibited by hydrotalcite-type solids, make them promising adsorbents for the removal of harmful species in anionic form. Moreover, while other adsorbents show the maximum adsorption capacities at extremely low pH values, hydrotalcites and systems formed upon their calcination can be used at pHs close to that at which pollutants are usually found in the environment [78]. Layered double hydroxides were proposed as adsorbents for the capture of inorganic anions such as arsenate, chromate or phosphate from waste water [79], but in recent years their use has been extended also for adsorptive removal of organic toxic species, such as phenolic compounds, pesticides or even nuclear residues. This issue has been recently reviewed [80].

*Separation processes.* O'Hare [81] has recently reported the use of these materials for the separation or purification of isomeric compounds. This separation can be achieved due to the differences of affinity shown by the isomers. The compound is separated from the mixture by intercalation into the layered material, and it can be readily recovered by treatment of the material with an anion which is intercalated between the layers in the material displacing the compound. Carbonate is preferred in most cases on account of its strong affinity to LDH materials, thus allowing the guest compound to be recovered in a substantially quantitative and allows the material to be regenerated by calcining the carbonate-intercalated solid and hydrating the resulting product.

*Catalysis.* Most of the applications of LDHs are within the field of catalysis. The easiness to incorporate a wide number of elements homogeneously dispersed with controlled proportions, thus allowing the synthesis of tailored catalysts, makes hydrotalcite-type materials very interesting solids for the application within this field [82]. Hydrotalcites can play up to three different roles in heterogeneous catalysis: as synthesised, as catalyst supports and as catalyst precursors. Catalysis by LDHs has been reviewed by Jacobs et al. [83] and more recently by Centi and Perathoner [84], and basic catalysis processes by LDHs have been also summarised by Tichit and Coq [85] and Figueras [86] for several reactions (aldolisation, Meerwin–Ponndorf–Verley hydrogenation, epoxidation and oxidation, as well as Michael and Wadsworth–Emmons additions), finding excellent yields under mild conditions and easy separation from the reaction medium and regeneration. Regarding the use of LDHs with intercalated POMs, it is worth mentioning the pioneer works by Nijs et al. [87], Pinnavaia [88] and others [23].

– *Supports.* LDHs with different pairs of cations in the brucite-like layers calcined at 250–450 °C have been used as supports for Ziegler catalysts for olefins polymerisation [89]. Calcined MgAl-LDHs have been also used to support CeO<sub>2</sub> for the removal of SO<sub>x</sub> from emissions in fluid cracking units; these systems are very stable even after severe steam treatments and also show good catalytic regeneration [90, 91].

Catalysts prepared by impregnation of solids derived from calcination of LDHs with platinum or palladium salts have been studied in the one-step synthesis of methyl isobutyl ketone (MIBK) from acetone and hydrogen at atmospheric pressure; it has been claimed that the support itself catalyses the condensation of acetone and diacetone alcohol and its subsequent dehydration to mesityl oxide, while Pd and Pt catalyse the selective hydrogenation of mesityl oxide to MIBK [92, 93].

– *Precursors.* Most of the catalytic applications involving hydrotalcite-type materials as catalysts use the oxides formed upon their calcination. These oxides exhibit some features such as wide compositional ranges, homogeneous dispersion of the elements, preserved even after moderate thermal treatments or reduction, high specific surface areas (100–130 m<sup>2</sup> g<sup>-1</sup>) or memory effect, making them more attractive than other oxides obtained through conventional methods. These oxides, well as amorphous or crystallised phases, have shown high catalytic activity in diverse reactions. The main routes followed for the preparation of catalysts starting from hydrotalcite-type materials are shown in Fig. 12.2 [85].

Common uses of the oxides obtained through calcination of hydrotalcite-type materials include basic catalysed reactions, such as aldol condensation of aldehydes and ketones [94, 95] or polymerisation of alkene oxides. Kohjiya et al. [96] investigated the polymerisation of propylene oxide using carbonate-intercalated MgAl LDHs calcined at different temperatures. These authors have reported that calcined LDHs where the lamellar structure is preserved were inactive in this process and concluded that the maximum activity corresponded to LDHs calcined at 450 °C.



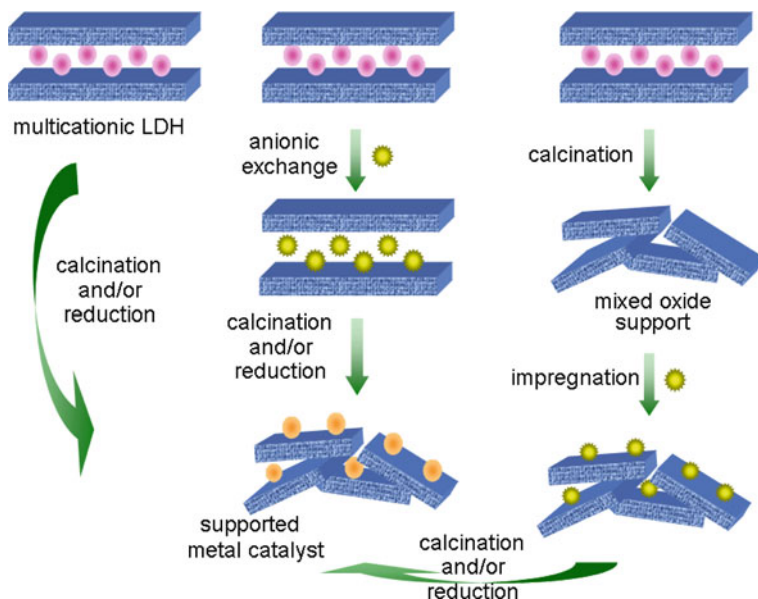


**Fig. 12.2** Simplified representation of the main routes leading to supported metal catalysts from LDH precursors. Reprinted from [85] (figure 2), with kind permission from Springer Science+Business Media

Promising applications in the field of fine chemicals and intermediates have been also reported, e.g. one-step synthesis of citronitril (fragrance as well as detergent and soap industry) [97], chalcones and flavonoids (pharmaceutical industry) [98], alkylated phenols (octane boosters and organic intermediates) [99] and some high volume chemicals as diacetone alcohol [100].

Oxidative steam reforming of methanol has been also studied over oxides formed upon calcination of Cu,Zn,Al(Zr) hydrotalcite-type materials at 450 °C, for selective production of hydrogen for fuel cells. Replacement of aluminium by zirconium was found to greatly enhance the catalytic performance, due to the improved copper reducibility and its higher dispersion [101]. Mixed oxides prepared upon calcination of carbonate-intercalated Mg,Al,Fe, Zn,Al,Fe or Cu,Al,Fe LDHs have been successfully used as seeds for the catalytic synthesis of carbon nanotubes [17, 102]. Oxides formed upon calcination of Co,Ni,Mg,Al or Ni,Mg,Al LDHs have been used for the gas-phase hydrogenation of acetonitrile, and a good correlation between the selectivity to monoethylamine and the acidity has been found [103, 104]. Selective hydrogenation of acetylene to ethylene has been studied on calcined Ni,Zn,Al,Cr or Ni,Zn,Al,Fe LDHs [13, 14], finding a decrease in coke formation in the presence of Zn or Cr, while an increase in nickel concentration led to a decrease in conversion, selectivity and yield to ethylene.

– *As synthesised.* As such, LDHs exhibit lower basicity than that shown by their derived products obtained upon calcination; however, carbonate or

hydroxyl-intercalated LDHs have shown good performances on different basic catalysed processes, such as aldol condensation of acetone [46, 105, 106], isomerisation [107, 108], phenol hydroxylation [109], Baeyer–Villiger oxidation [110], Knoevenagel condensation [111] or olefin epoxidation [112].

In this chapter we review the preparation, characterisation and catalytic properties of LDHs with intercalated polyoxometalates, POMs. It should be recalled that according to IUPAC [113] rules, swelling of a layered material is the main characteristic of the intercalation compounds, resulting from insertion of guest species in the interlayer region, while the term “pillared” should apply to the solid obtained by thermal or chemical transformation of a layered compound, showing microporosity or mesoporosity and being chemically and thermally stable. This is not usually the case of the POM–LDH systems, which are thermally less stable than the compounds formed with cationic clays.

It has been shown that the catalyst activities and selectivities can be controlled to a large extent by the preparation method [114] and, consequently, special attention will be paid in this review to the preparation procedures used. Our review goes back roughly around the beginning of the century, as previous reviews on this subject can be found in the literature [23, 84–88, 115, 116]. In order to provide a systematic study, we have chosen to review the literature following the groups and periods of the periodic table of the elements, which seems to be adequate from a chemical point of view.

## 12.2 Vanadium-Containing LDHs

As mentioned above, one of the methods used to incorporate these metal-containing anions into the LDH matrix is coprecipitation, even from sodium aluminate solutions [117], and it is a pH-dependent process. In some cases, the solid is preswelled by intercalation of organic bulk anions such as terephthalate [118]. If raw intercalation, without preswelling, is intended, it has been reported [117] that only monomeric or dimeric oxyanions are able to be intercalated, while intercalation of larger polymeric forms is impeded.

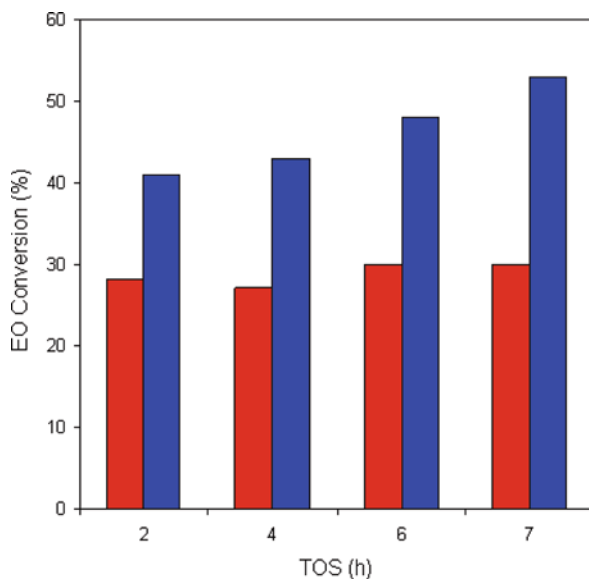
Due to the known affinity of carbonate anions for these solids, a study on the competitive adsorption of carbonate or vanadate has been carried out [119], by using a mixed solution of sodium carbonate and vanadate ( $\text{NaVO}_3$ ). The exchange is pH dependent, and it has been found that only  $\text{VO}_4^{3-}$ ,  $\text{HV}_2\text{O}_7^{3-}$  and  $(\text{VO}_3)_n^{x-}$  are intercalated, while  $\text{V}_2\text{O}_7^{4-}$  species are excluded; together with these species, three different types of carbonate species (hydrogen bonded to interlayer water molecules, hydrogen bonded to layer hydroxyl groups and free carbonate anions) have been identified.

Malherbe et al. [116] have studied the performance of Cu,Cr LDHs containing intercalated pyrovanadate or decavanadate in the interlayer in alkoxylation reactions, namely reaction of *n*-butanol with ethylene oxide (EO), under flow conditions.

The reaction between EO and *n*-butanol may proceed according to a base- or acid-catalysed mechanism. Due to the different stability of oxovanadate species with pH (nuclearity of the POM increases as pH is decreased), the samples with intercalated  $[V_2O_7]^{4-}$  was prepared at pH 10, while that containing  $[V_{10}O_{28}]^{6-}$  was prepared at pH 4.5.

Both samples showed 100% selectivity to butoxymonoethyleneglycol ether,  $CH_3-(CH_2)_3-O-(CH_2)_2-OH$  (BMGE), EO conversion changing as shown in Fig. 12.3. The different conversion found (ca. twice for the decavanadate than for the pyrovanadate catalyst) should be related to the vanadium loading.

**Fig. 12.3** Ethylene oxide conversion vs. time on stream on catalysts containing intercalated  $V_2O_7^{4-}$  (red bars) or  $V_{10}O_{28}^{6-}$  (blue bars). Constructed from data in [116], with permission from Elsevier



Layered double hydroxides are usually considered to be basic materials, resulting from the metallic hydroxides, the basicity being associated with the presence of free hydroxyl groups ( $OH^-$ ). However, a small, but detectable, amount of dioxane was formed in all cases; as this compound is only formed in acidic media [120], it should be concluded that these materials behave as bifunctional catalysts, exhibiting neither purely acid nor basic character.

When these catalysts are suspended in a liquid medium (as here to perform these catalysis studies) two different processes can take place:

- (i) a mechanism can be triggered to keep pH around the same value (thus accounting for the stability and lack of polymerisation/depolymerisation of the interlayered POM), considering that the interlamellar domain behaves as a semi-fluid region where the presence of protons or hydroxyls can act as a buffer, or

- (ii) if such a buffering is not possible, a reaction between the POM and surrounding water molecules will take place, and well via polymerisation/depolymerisation or protonation, a change in pH will occur, thus accounting for the acid-basic character of these materials: the different properties would result from the different nature of the interlayer POM, in some sort of way tuning the properties of the LDH matrix.

Brønsted basicity results from surface hydroxyls, but other possible active sites are most probably due to the presence of transition metal cations; as  $V^{5+}$  species are  $d^0$ , they are able to provide some Lewis acidity to the LDH.

On the other hand, the size of the anion can also be a limiting factor on the catalytic activity; it is strongly believed that most of the catalytic activity takes place at the edges on the interlayer space and/or through the adsorbed anions; the interlayer accessibility will mostly depend on the size of the anionic species as well as on their charge density and orientation within the interlayer.

Jacobs et al. [121] have studied Mg,Al LDHs containing decavanadate as catalysts for selective epoxidation of allylic and homoallylic alcohols. Among the many different procedures to prepare decavanadate-containing LDHs [122], two approaches were selected to prepare the samples: exchange of a nitrate precursor with an aqueous  $NaVO_3$  solution at pH 4.5 or without pH control (sample V), in both cases with or without preswelling with terephthalate, following the method described by Drezdron [118]. The PXRD diagrams of samples prepared at pH 4.5 were essentially identical, with diffraction maxima close to 10.6, 5.86 and 3.94 Å, corresponding to diffraction by planes (003), (006) and (009), respectively; Raman spectroscopic analysis demonstrated that the decavanadate moiety was maintained at pH 4.5 (although small residues of terephthalate persisted when preswelling was used), while for the samples prepared without pH control cyclic species  $(VO_3)_n^{n-}$  ( $n \geq 3$ ) formed by  $[VO_4]$  tetrahedra sharing two corners were formed.

Best yield and selectivity for conversion of geraniol were achieved for the decavanadate-containing LDHs (without or with preswelling) when toluene was used as solvent and *t*-BuOOH as oxidant dissolved in decane, with minimal formation of geranial, suggesting that maximum effectiveness is achieved if anhydrous conditions are applied; no leaching was either observed, probably because hydrolysis of the decavanadate anions is prevented by the anhydrous conditions used. In contrast, low conversions and selectivities were obtained if vanadate is introduced in the LDH without pH control, in other words, when polymers with low nuclearity are formed. These authors also demonstrated that the reaction actually occurs on the solid surface and not under homogeneous conditions and that successive runs could be applied without noticeable loss in catalytic performance.

When the decavanadate-containing samples were used in toluene with *t*-BuOOH/decane as an oxidant for epoxidation of different terpenic allylic alcohols, high conversions and epoxide selectivities were obtained for geraniol, nerol, perillyl alcohol, myrtenol and *trans*-pinocarveol, and regioselectivity to the double bond close to the alcohol group was observed for substrates with two double bonds; probably the reaction proceeds via coordination of the allylic alcohol group to the

active V atom before oxygen transfer takes place. These authors have also highlighted the importance of maintaining a small cluster of oxovanadium species to achieve these results (only very low activity is observed for quaternary ammonium decavanadate in toluene) to permit simultaneous coordination of the oxidant and of the alcohol without destruction of the cluster.

Mild oxidation of tetrahydrothiophene (THT) to sulfolane has been studied on vanadium-containing LDHs by Hulea et al. [123]. The samples were prepared following the method described by Dula et al. [124], direct ion exchange from a Mg,Al-NO<sub>3</sub> LDH with aqueous NaVO<sub>3</sub> at pH 4.5. As also observed by other authors [23], the Mg/Al ratio decreases upon incorporation of decavanadate, due to extraction of Mg<sup>2+</sup> cations in acid solution, forming a polyoxometalate salt impurity, as concluded from the PXRD diagrams, which show additional diffraction maxima to those expected for the decavanadate-intercalated phase, which (003) plane gives rise to a maximum at 10.2 Å. These authors also observe that the specific surface area increases from 16 m<sup>2</sup> g<sup>-1</sup> for the original nitrate sample to 50 m<sup>2</sup> g<sup>-1</sup> for the decavanadate intercalated one, and the nitrogen adsorption isotherm reveals the presence of mesopores and micropores, with development of interparticle and intragallery porosity. Thermal decomposition of the sample takes place in two stages [125], namely dehydration and dehydroxylation, with final formation of mixed oxides. The UV-Vis/DR spectrum exhibits a broad band extending from 550 to 200 nm which can be deconvoluted into two components at 300–320 nm due to coordinated V in pseudo-tetrahedral geometry, V<sub>2</sub>O<sub>7</sub><sup>4-</sup> (representing 30% of total vanadium), and a second band at 420–450 nm due to V in octahedral coordination, V<sub>10</sub>O<sub>28</sub><sup>6-</sup> [126], responsible for 70% of V species.

Oxidation was highly selective towards the sulfoxidation reaction, resulting exclusively in sulfoxide and sulfone, without direct hydrogen peroxide decomposition, probably due to the mild conditions used (20–30 °C and dilute medium). Although the V-oxospecies have an essential contribution to the activation of the oxidising agent, the performance was lower than that exhibited by samples containing Mo or W (see below), as approximately all the vanadium-containing species have at least two metal atoms or more (V<sub>2</sub>O<sub>7</sub><sup>4-</sup> and V<sub>10</sub>O<sub>28</sub><sup>6-</sup>) and, in addition, a portion of the vanadium species are involved in the formation of the Mg oxovanadate detected by PXRD which probably has no catalytic activity. The catalyst can be reused and no loss in catalytic performance was observed even after four runs (conversion at 5 and 10 min was 17.7 and 30.2%, respectively, in the first run and 16.2 and 29.2%, respectively, in the fourth run).

Catalytic oxidative desulfurisation (ODS) has been claimed as a promising alternative technology to the current hydrodesulfurisation (HDS) process for reducing sulfur in gasoline and diesel fuels. To gain insight in its suitability, these authors have also studied [127] the use of decavanadate-containing Mg,Al LDHs for mild oxidation of sulfides and thiophenes using dilute hydrogen peroxide under mild conditions (40 °C) in the presence of acetonitrile as a solvent; oxidation of sulfides led to the corresponding sulfoxides and sulfones as major products, while oxidation of thiophenes led to the corresponding sulfones. The observed reactivity was the following:

Benzo-thiophene (BT) < dibenzo-thiophene (DBT) < diphenyl-sulfide (PPS) < benzyl-phenyl-sulfide (BPS) < methyl-phenyl-sulfide (MPS)

which runs parallel to the electron density (nucleophilicity) at the sulfur atom in each of these compounds. Conversion was only around 20%, suggesting a good accessibility inside the porous structure of the vanadate-LDH catalyst for these large molecules. As for the former studies, conversion remained almost constant even after four catalytic cycles (tested for methyl-phenyl-sulfide oxidation).

In addition to these studies, performed under liquid–solid regime, many studies have been also carried out in solid–gas regime, using calcined LDHs intercalated with POMs. Thermal treatment of these systems introduces important changes in the structure and precise nature of the chemical, reactive species. In other cases the catalytically active species (V-containing units) are not intercalated, but incorporated into a hydrotalcite support prepared by impregnation or even solid phase mixing. Rabello de Castro et al. have studied [128] systems prepared by impregnation of a Mg,Al LDH (with intercalated carbonate or hydroxyl groups) with vanadyl sulphate solutions at different pHs or mixing with  $V_2O_5$ .

The V species formed upon thermal treatment of LDH precursors have been studied by ESR by Serwicka et al. [129]. These authors have studied three different samples: one (A) prepared by coprecipitation and anion exchange containing intercalated decavanadate [130, 131], while two other samples contained  $V^{3+}$  in the layers together with Mg and Al (molar fraction of V 12%, sample B) or only Mg (molar fraction of V 61%, sample C) [129]. The PXRD patterns [124] indicate the presence of decavanadate in the interlayer of sample A, although formation of a co-product, presumably a magnesium oxovanadate, has been also observed. Calcination leads to formation of MgO and different vanadates: pyrovanadate from sample A, but orthovanadate from sample C, as previously reported by Rives et al. [132]. Pyrovanadate is formed by partial depolymerisation of interlayer decavanadate existing in sample A, while orthovanadate is formed from isolated V species existing in the brucite-like layers of sample C.

Formally the original samples should contain exclusively  $V^{5+}$  (sample A) or  $V^{3+}$  (samples B and C). Pentavalent vanadium,  $d^0$ , is diamagnetic, while  $V^{3+}$  is a non-Kramer's ion with the unpaired electrons and as such not likely to give ESR signals under the experimental conditions used. However, all starting materials showed ESR signals with a characteristic eight-line hyperfine pattern due to the interaction of the unpaired electron with the  $^{51}V$  nucleus ( $I = 7/2$ ), pointing to the presence of  $V^{4+}$ , i.e. during preparation an oxidation (samples B and C) or reduction (sample A) has taken place. The values for the ESR signals indicate the formation of a vanadyl bond in the vanadium species. The initial relative content of  $V^{4+}$  species is higher in samples B and C (especially in sample B, which specific surface area is twice that for sample C) than in sample A. The signals are very sensitive to structural changes induced by thermal treatments and, for samples B and C, on the amount of V existing in the sample, with a well-resolved signal for sample B and a well-resolved one superimposed on a broad structureless one – typical of  $V^{4+}$  species in close proximity to each other – for sample C.

When these samples were tested for oxidative dehydrogenation (ODH) of propane to propene [133], the catalyst obtained from sample A was much more active than those derived from samples B and C; as the specific surface areas (after calcination) and V content were very similar for samples A and B, these results suggest that the better performance stems from the presence of centres of a higher specific activity. The trends in selectivity can be easily understood in terms of a consecutive (propane – propene – carbon oxides) – consecutive (propane – carbon oxides) mechanism, typical of selective oxidation of hydrocarbons. The different intrinsic activity of the V species formed in these catalysts is in agreement with the ESR results described above, which pointed to a difference in the covalency of in-plane  $V^{4+}$ -O  $\pi$ -bonds existing in samples A and B. Pyrovanadate formed upon calcination of sample A is more reducible than orthovanadate detected in calcined sample B, and thus prone to participate in the ODH process via a Mars–van Krevelen mechanism, where the source of oxygen for the oxidation is lattice oxygen from the catalyst, and the lattice defect is removed by reaction with dissociatively adsorbed oxygen [134, 135]. Total oxidation is favoured by electrophilic  $O_2^-$  and  $O^-$  radicals formed during reduction of an oxygen molecule to oxide anions; their fast transformation to  $O^{2-}$  species would enhance selectivity to partial oxidation products (propene). The existence of low reducible, isolated V sites in orthovanadate would stabilise these electrophilic species, and thus total oxidation, while more reducible pyrovanadate species (formed by calcination of the  $V_{10}O_{28}^{6-}$  LDH, sample A, precursor) provide conditions for the formation of nucleophilic oxygen species, thus suppressing total oxidation of propane.

Regarding the role of Al (from the brucite-like layers), it seems to improve the selectivity to propene (Al exists in sample B, but not in sample C), contrary to the previous results by Blasco and López-Nieto [136], who claimed that the increase in acidity due to the presence of aluminium would hold strongly the basic propene molecule, favouring its total oxidation; for these exLDH samples, Serwicka et al. claim [124] that the different long-range ordering observed for orthovanadate in sample C but not in sample B might affect the properties of individual V sites, in agreement with the ESR results [129], evidencing small changes of bond lengths around the respective sites.

The nature of the V polyoxometalate existing in the interlayer space affects also the catalytic performance of the solids obtained upon calcination. Serwicka et al. [137] have studied the catalytic activity of oxides prepared by calcination at 550 °C of Mg,Al LDHs containing  $V_{10}O_{28}^{6-}$  or  $V_2O_7^{4-}$  in oxidative dehydrogenation of propane. To obtain the samples by anion exchange from Mg,Al- $NO_3$  LDH precursors, the impregnating  $NaVO_3$  solution was adjusted at pH 4.5 (to stabilise decavanadate species, sample V10-LDH) or 9.5 (to stabilise pyrovanadate species, sample V2-LDH), and the solids were then calcined at 550 °C for 24 h in air to produce the corresponding mixed oxides (V10-MO and V2-MO, respectively). A reference catalyst was also prepared by impregnation of MgO and calcination under the same experimental conditions. As mentioned above for other studies, a depletion in Mg content is observed in the sample prepared at pH 4.5 (which PXRD pattern suggests the simultaneous presence of a Mg oxovanadate salt), while

for sample V2-LDH the V content is larger than expected; this last finding has been explained on the grounds of the easy protonation these POMs can undergo by small pH changes, probably in the vicinity of the LDH (highly basic) particles. Moreover, FTIR spectra suggest the presence of  $(\text{VO}_3)_n^{n-}$  species, together with  $\text{V}_2\text{O}_7^{4-}$ , in sample V2-LDH, and the gallery heights calculated from the PXRD patterns can be consistent also with both oxovanadium species, although some sort of grafting [138] should be assumed. Upon calcination only broad diffraction maxima due to MgO are recorded, sharper for catalyst V10-MO, where the presence of crystalline  $\text{Mg}_2\text{V}_2\text{O}_7$  can be also envisaged. XPS shows surface Mg enrichment in all samples, and the surface V/O ratio is two times higher for V10-MO than for V2-MO.

Regarding the catalytic performance in ODH of propane, the areal reaction rate (per surface unit) is much larger for sample V10-MO than for the other two catalysts tested, a difference which cannot be accounted only by the different surface density of V centres, but should be related to a larger intrinsic reactivity of the V species existing in sample V10-MO. This sample shows a high selectivity to CO, formed by consecutive oxidation of propene. To explain this behaviour, these authors have also measured the activity of their catalysts in isopropanol decomposition, which leads to formation of propene on acid type sites, but of acetone on basic redox sites, finding that propene formation is higher and the acetone/propene ratio lower on sample V10-MO than in the other two catalysts. As the propene molecule exhibits basic properties, it is concluded that it should be more strongly held on the more acidic and less basic surface, i.e. sample V10-MO, thus enhancing its further oxidation and increasing the selectivity to CO.

Similar samples with intercalated decavanadate, but prepared via intermediate swelling of the layers with terephthalate, have been also studied by Rives et al. for ODH of propane [139]. For comparison, samples with the same V content were prepared by impregnation of MgO with an aqueous solution of ammonium vanadate, with or without added alumina. The PXRD pattern of the LDH sample shows the same features as discussed above for other Mg,Al LDHs with interlayer decavanadate, with the (003) maximum at 11.6 Å, which might correspond to the presence in the interlayer of  $\text{V}_{10}\text{O}_{28}^{6-}$  or  $\text{V}_4\text{O}_{12}^{4-}$  species, the former species being more stable at the pH the sample had been prepared (4.5). Calcination at 550 °C rendered different mixed oxides: MgO and mostly amorphous Mg pyrovanadate from the LDH sample, MgO and pyrovanadate from the vanadate-impregnated MgO sample, and metavanadate ( $\beta\text{-MgV}_2\text{O}_6$ ) and some orthovanadate for the vanadate-impregnated MgO–Al<sub>2</sub>O<sub>3</sub> sample. Surface Mg enrichment is observed for the exLDH sample by XPS, while the other oxides show a surface V enrichment, probably because diffusion of V species into the MgO or Al<sub>2</sub>O<sub>3</sub> crystallites should be very slow; the surface composition changes after the ODH of propane tests, suggesting that coke is preferentially deposited on surface exposed V species. Surface acidity, as qualitatively measured by FTIR monitoring of pyridine adsorption, shows the presence of Lewis acid sites in the exLDH sample, Brønsted sites in the MgO-impregnated sample and both sorts of acid sites in the MgO–Al<sub>2</sub>O<sub>3</sub> impregnated one.



The largest activity in propane ODH was observed for the exLDH sample. However, on considering the areal values, the largest normalised activity was measured for the MgO–Al<sub>2</sub>O<sub>3</sub> impregnated sample, with the largest surface density of V/O sites, which remain active during the reaction; the larger acidity of this catalyst is also responsible for the larger selectivity to CO observed; on the contrary, the MgO-impregnated sample favours formation of CO<sub>2</sub>, as the Brønsted sites existing in this sample do not only favour propene formation but also its combustion, as olefins are highly reactive on electrophilic sites [140].

ODH of *n*-butane has been studied by Wegrzyn et al. [141] on nanostructured vanadium oxides prepared by calcination at 700 °C from decavanadate Mg<sub>3</sub>Al LDHs prepared at pH 4.5 from carbonate-containing precursors. In this case, the experimental conditions were tuned to prepare samples with different degrees of carbonate/decavanadate exchange. If this was less than 40%, the PXRD patterns suggest the formation of two phases, with intercalated carbonate or a partially depolymerised vanadate, while above this value the presence of decavanadate seems to be evident (lattice parameter 35 Å). The intensities of the typical FTIR bands due to carbonate and decavanadate are in agreement with these results and those from element chemical analysis. On calcination, MgO is detected by PXRD for the V-poor samples, MgO, Mg<sub>3</sub>V<sub>2</sub>O<sub>8</sub> and α-Mg<sub>2</sub>V<sub>2</sub>O<sub>7</sub> for the 40% exchanged sample, and MgO and α-Mg<sub>2</sub>V<sub>2</sub>O<sub>7</sub> for the V-rich samples, in agreement with previous studies [137, 142] and with FTIR results [141]. Temperature-programmed desorption (TPD) of CO<sub>2</sub> and FTIR were applied to measure surface basicity, this parameter decreasing (per surface area) for low V-loading, increasing for the highest V-loading, while surface acidity (from ammonia adsorption) increases with respect to a reference, V-free sample and remains almost constant whichever the V content.

Specific activity in *n*-butane ODH on the calcined solids increases with the V content; however, the highest selectivity to ODH products and lowest selectivity to CO<sub>x</sub> were observed for the V-poor samples. These results can be explained from the larger nucleophilic character (basicity) of oxygen atoms in Mg–O–V units existing in orthovanadate (leading to hydrogen abstraction) than in V–O–V units (thus leading to total oxidation) existing in α-Mg<sub>2</sub>V<sub>2</sub>O<sub>7</sub> and MgV<sub>2</sub>O<sub>6</sub>. The decrease in 1,3-butadiene selectivity for high-V loading should be related to the presence of highly crystalline α-Mg<sub>2</sub>V<sub>2</sub>O<sub>7</sub>. Although both acid and basic sites are necessary for high activity and selectivity in this reaction, total selectivity for the dehydrogenated products was higher on the highly basic catalysts.

In situ DXAS (dispersive X-ray absorption spectroscopy) has been also applied to ascertain the precise nature of the V species existing in V-LDH systems [128]. For these studies, two commercial (AkzoNobel) Mg<sub>3</sub>Al LDHs, containing interlayer carbonate or hydroxyl groups, were used, and vanadium incorporation was carried out by impregnation with aqueous solutions of VOSO<sub>4</sub> at different pHs or physical mixture of the carbonate LDH with solid VOSO<sub>4</sub>·5H<sub>2</sub>O or V<sub>2</sub>O<sub>5</sub>. FTIR monitoring of the samples showed formation of different V-oligomeric species, depending on the pH during impregnation, while DAXS undoubtedly showed the presence of V<sup>5+</sup> species, indicating that oxidation from V<sup>4+</sup> to V<sup>5+</sup> takes place during impregnation. Calcination at 800 °C led to an increase of the specific surface area of the

solids and formation of a mixture of oxides. Wong et al. [143] showed that the main-edge position in the XAS spectra of V compounds provides information about the valence of the V cation, while the pre-edge intensity informs about the vanadium coordination: pre-edges are absent for symmetrical coordination (strict, undistorted  $[\text{VO}_6]$  octahedra), while very intense signals are recorded for tetrahedral coordination. Consequently, in situ DXAS allows verification of changes in vanadium closest neighbourhood, due to the oxides mixture formed, as well as oxidation processes. From the spectra of the carbonate LDH and  $\text{VOSO}_4$  physical mixture, it is concluded that vanadium is oxidised from +4 to +5 at 350 °C and above this temperature no shift of the pre-edge peak is observed, indicating that the vanadium neighbourhood becomes stable; the spectrum for the sample calcined at 600 °C is similar to that for a carbonate LDH and  $\text{V}_2\text{O}_5$  mixture. On the other hand, the spectra of the samples prepared by impregnation have comparable features to the spectra of vanadates [144], although depending on the pH during impregnation, which affects the polymerisation degree of the V species. As expected, dispersion of the vanadium species increases for samples prepared by impregnation in aqueous solution at alkaline pH (where formation of V monomers is favoured). These V species show different reducibility, an important aspect to be taken into account if the solids are to be used in catalytic processes running through the Mars–van Krevelen mechanism.

Dinka et al. [145] have studied the reaction of methanol and *n*-propanol over LDHs and hydrotalcite-like compounds containing  $\text{V}_2\text{O}_5$ , incorporated well by intercalation using the method described by Drezdzonek [118] with different (2–5) Mg/Al molar ratios, or by impregnation with aqueous solutions of  $\text{NH}_4\text{VO}_3$  containing oxalic acid, the solids being finally calcined in air at 550 °C to yield mixed oxides. It was found that increasing the V content led to a decrease in the specific surface area (e.g. from 175 to 59  $\text{m}^2 \text{g}^{-1}$  for samples prepared by intercalation with a Mg/Al ratio of 2 and V contents ranging from 5 to 50% weight), as well as a decrease in surface basicity (from 0.16 to 0.03  $\text{mmol g}^{-1}$  for the same set of samples). Also reducibility, as measured by temperature-programmed reduction, decreased as the V content was increased, i.e. reduction started at higher temperatures.

While the V-free LDH produced mainly 2-butanol and isobutanol (together with a small amount of propene), the presence of vanadium changed dramatically the reaction products distribution: higher conversion and selectivity were obtained for samples prepared by intercalation, while impregnated samples favoured formation of propionaldehyde and isobutanol. The activity of the catalysts for isobutyric aldehyde formation is probably associated with the acid–base properties of the catalyst: those with higher basicity produce this compound with low selectivity as a consequence of transformation of the aldehyde into isobutanol by a Meerwein–Ponndorf–Verley reaction, and formation of enolates seems to be an essential step in the reaction mechanism.

Alkoxylation of *n*-butanol with ethylene oxide (EO) to produce 2-butoxy ethanol has been also studied on this sort of calcined LDHs [146], analysing the effect of enhanced basicity. A commercial (Süd-Chemie AG, Germany) Mg,Al LDH was calcined and the structure reconstructed with intercalated decavanadate at pH

4.5 (sample MAV), which was then calcined at 450 °C (sample MAV-CAL) and rehydrated in water (MAV-HYD) or in a 1 M KOH solution (MAV-KOH). The aim of rehydration under these two conditions was not to reconstruct the MAV layered structure, which is unique for LDHs containing simple anionic species like carbonate or nitrate, but to evaluate how rehydration could hopefully modulate the reactivity of the mixed oxides. Actually, the PXRD diagrams of the calcined and rehydrated samples were rather similar, showing only broad diffraction maxima due to periclase (MgO) and a broad reflection which could probably correspond to mostly amorphous Mg vanadates. Quite interestingly, the intensities of the periclase maxima decrease in sample MAV-CAL with respect to the parent calcined solid, and such a decrease is more evident in the rehydrated samples (even more for sample MAV-KOH than for sample MAV-HYD). The specific surface areas were of the same order for all three catalysts (42–60 m<sup>2</sup> g<sup>-1</sup>). Conversion of EO in a batch reactor increases with reaction time in the order MAV < MAV-HYD < MAV-KOH. However, the calcined solid shows better conversion for low reaction times, reaching a plateau (74% conversion) and being deactivated after 20 h reaction. This is attributed to formation of a gelatinous solid, polyethylene glycol and polyethoxylates, which strongly adsorb on the surface of the catalyst and would likely be the origin of deactivation. Following the mechanism proposed by Chibwe [120], formation of butoxide intermediates is favoured by the presence of acid–strong base pair sites, associated respectively with cations (Al<sup>3+</sup>, Mg<sup>2+</sup>, V<sup>5+</sup>) and oxide anions. Reaction of these oxide anions with EO would account for formation of polyethoxylates; to diminish its formation, a ButOH/EO ratio of 5 was used.

Formation of polyethoxylates can be alternatively explained on the basis of the intrinsic properties of the catalyst: glycol ethers are much more polar than butanol and would be preferentially adsorbed on the surface of the highly ionic surface of catalyst MAV-CAL, blocking the active sites. Rehydration would protonate surface oxide anions to less basic, but still catalytically active, hydroxyl ones; if rehydration is made in a basic media either increases the amount of OH groups or forms stronger ones.

The rehydrated catalysts show similar EO conversion than after an induction period of 30 h when the reaction was studied in a fixed-bed flow reactor. The origin of this induction period is not clear, but these authors suggest it is needed to form an intermediate reactive species (e.g. butoxide anions) which saturate the catalyst surface providing a hydrophobic character which favours diffusion of the reactant molecules to the active sites; the rather small difference observed between both catalysts is probably related to the stronger basicity (better performance) of the surface sites in sample MAV-KOH. Nevertheless, both catalysts exhibit much better selectivity to the monoglycol adduct than commercially used potassium acetate. Finally, conversion rate decreases as LHSV is increased, but selectivity to BMGE (butoxy monoethylene glycol ether) remains almost constant (88%), suggesting that the selectivity could be related to the adsorptive properties of the catalyst rather than to the kinetics of the reaction, the calcined support providing a basic support for the oxovanadium species, between which some sort of synergetic interaction seems to develop.

Regarding oxidation reactions of other substrates, only one paper, as far as we know, has reported the N-oxidation of tertiary amines on a  $\text{Mg}_3\text{Al-VO}_3$  LDH [147] with 7% (weight) V prepared by ionic exchange of a nitrate precursor, although XRD data indicate that intercalation does not actually take place, but the vanadate anions lie on edge-on positions of the LDH. Yield of *N*-methylmorpholine N-oxide from *N*-methylmorpholine was 40% vs. 15% for unsupported  $\text{NaVO}_3$ .

These authors have used this same catalyst for oxidation of thioanisole with  $\text{H}_2\text{O}_2$  in aqueous medium [148]. The conversion to the sulfoxide and the sulfone was only slightly larger than for  $\text{NaVO}_3$  (42 vs. 35%), but total selectivity to the sulfoxide was observed for the immobilised catalyst, with an important decrease in TOF.

Table 12.1 summarises the reactions catalysed by LDHs with intercalated POMs containing vanadium species.

**Table 12.1** Summary of reactions catalysed by LDHs with intercalated vanadium-containing POMs

Layer cations	Intercalated species	Reaction	Substrate	Reference
Cu,Cr	$[\text{V}_2\text{O}_7]^{4-}$	Alkoxylation	BuOH	[116]
Cu,Cr	$[\text{V}_{10}\text{O}_{28}]^{6-}$	Alkoxylation	BuOH	
Mg,Al	$[\text{V}_{10}\text{O}_{28}]^{6-}$	Epoxidation	Geraniol	[121]
Mg,Al	$[\text{V}_{10}\text{O}_{28}]^{6-}$	Epoxidation	Nerol	
Mg,Al	$[\text{V}_{10}\text{O}_{28}]^{6-}$	Epoxidation	Perillyl alcohol	
Mg,Al	$[\text{V}_{10}\text{O}_{28}]^{6-}$	Epoxidation	Myrtenol	
Mg,Al	$[\text{V}_{10}\text{O}_{28}]^{6-}$	Epoxidation	<i>trans</i> -Pinocarveol	
Mg,Al	$[\text{V}_{10}\text{O}_{28}]^{6-}$	Epoxidation	Isopulegol	
Mg,Al	$[\text{V}_{10}\text{O}_{28}]^{6-}$	Epoxidation	Nopol	
Mg,Al	$[\text{V}_{10}\text{O}_{28}]^{6-}$	Epoxidation	$\beta$ -Citronellol	
Mg,Al	$[\text{V}_{10}\text{O}_{28}]^{6-}$	Epoxidation	Verbenol	
Mg,Al	$[\text{V}_{10}\text{O}_{28}]^{6-}$	Epoxidation	Crotyl alcohol	
Mg,Al	$[\text{V}_{10}\text{O}_{28}]^{6-}$	Epoxidation	Cinnamyl alcohol	
Mg,Al	$[\text{V}_{10}\text{O}_{28}]^{6-}$	Epoxidation	2-cyclohexen-1-ol	
Mg,Al	$[\text{V}_{10}\text{O}_{28}]^{6-}$	Epoxidation	Carveol	
Mg,Al	$[\text{V}_{10}\text{O}_{28}]^{6-}$	Sulfoxidation	Tetrahydrothiophene	123
Mg,Al	$[\text{V}_{10}\text{O}_{28}]^{6-}, [\text{V}_2\text{O}_7]^{4-}$	Oxidation	Benzothiophene	127
Mg,Al	$[\text{V}_{10}\text{O}_{28}]^{6-}, [\text{V}_2\text{O}_7]^{4-}$	Oxidation	Dibenzothiophene	
Mg,Al	$[\text{V}_{10}\text{O}_{28}]^{6-}, [\text{V}_2\text{O}_7]^{4-}$	Oxidation	Diphenyl sulfide	
Mg,Al	$[\text{V}_{10}\text{O}_{28}]^{6-}, [\text{V}_2\text{O}_7]^{4-}$	Oxidation	Benzyl-phenyl sulfide	
Mg,Al	$[\text{V}_{10}\text{O}_{28}]^{6-}, [\text{V}_2\text{O}_7]^{4-}$	Oxidation	Methyl-phenyl sulfide	
Mg,Al	$[\text{V}_{10}\text{O}_{28}]^{6-}$	ODH	Propane	133
(calcined)				
Mg,Al (550 °C)	$[\text{V}_{10}\text{O}_{28}]^{6-}$	ODH	Propane	124
Mg,Al (550 °C)	$[\text{V}_{10}\text{O}_{28}]^{6-}, [\text{V}_2\text{O}_7]^{4-}$	ODH	Propane	137
Mg,Al (550 °C)	$[\text{V}_{10}\text{O}_{28}]^{6-}, [\text{V}_4\text{O}_{12}]^{4-}$	ODH	Propane	139
Mg,Al (700 °C)	$[\text{V}_{10}\text{O}_{28}]^{6-}$	ODH	<i>n</i> -Butane	141
Mg,Al (550 °C)	$[\text{V}_{10}\text{O}_{28}]^{6-}$	Propanol + MeOH	Propanol	145
Mg,Al (550 °C)	$\text{VO}_3^-$	Propanol + MeOH	Propanol	
Mg,Al (450 °C)	$[\text{V}_{10}\text{O}_{28}]^{6-}$	Alkoxylation	<i>n</i> -Butanol	146

## 12.3 Chromium-Containing LDHs

Incorporation of chromates into LDHs has deserved much interest not only because of the application of the products obtained in catalysis but also as a method for scavenging highly noxious chromate from water. Prasanna et al. [149] have studied several LDHs with intercalated chromate containing different pairs of divalent/trivalent cations in the brucite-like layers. A detailed study of the PXRD patterns and their simulation using DIFFaX has permitted to understand the stacking of the layers: Mg,Al–CrO<sub>4</sub> and Mg,Fe–CrO<sub>4</sub> show a basal spacing of 10.8 Å with turbostratic disorder (i.e. rotation of the layers within their plane); hydrothermal treatment of the first solid induces structural ordering, but stacking disorder consisting of intergrowth of different polytypes (2H and 3R), distinguishable from turbostratic disorder is observed. Stacking disorder of chromate-containing LDHs arises from a mismatch of the tetrahedral chromate anion (T<sub>d</sub>) within the trigonal prismatic sites (D<sub>3h</sub>) in the interlayer region, and turbostraticity can be considered an extreme case for stacking disorder. FTIR spectroscopy evidences the lack of grafting, as only a single absorption due to the antisymmetric  $\nu_3$  mode is recorded at 886 cm<sup>-1</sup> for the Mg,Al–CrO<sub>4</sub> LDH (765 cm<sup>-1</sup> for free chromate), which remains unchanged after hydrothermal treatment.

Zn,Al–CrO<sub>4</sub> LDH also contains stacking faults with local rhombohedral symmetry, but in this case the interlayer spacing is only 7.3 Å, indicating grafting of the chromate units to the hydroxyl layers; this is also confirmed by FTIR spectroscopy, with two absorptions at 922 and 876 cm<sup>-1</sup>, as a result of decrease of symmetry from T<sub>d</sub> (a single mode with T<sub>2</sub> symmetry) to C<sub>3v</sub> (two modes with A<sub>1</sub> + E symmetries). Ni,Al–CrO<sub>4</sub>, Ni,Fe–CrO<sub>4</sub>, Co,Al–CrO<sub>4</sub> and Co,Fe–CrO<sub>4</sub> LDHs show turbostratic disorder, which persists after hydrothermal treatment, but this treatment gives rise to an increase in crystallite size and favours also grafting ( $\nu_3$  splitting leading to two IR absorptions at 933 and 876 cm<sup>-1</sup>). Upon thermal treatment at 500–800 °C, Cr<sup>6+</sup> is reduced to Cr<sup>3+</sup> and mixed oxides are formed. These are crystalline ones in all cases but for the Mg,Al system, which is the only one reconstructing back the layered structure on soaking in water. This difference has been ascribed to the added stability of the mixed oxides formed with transition metal cations because of the crystal field effect [150, 151].

The importance of grafting arises from the fact that once grafted the chromate anion cannot be replaced by anion exchange nor leached, thus permitting a true anchoring to the brucite-like layers. Grafting can be also achieved by mild calcination in the solid state [152] instead of under hydrothermal conditions, provided the temperature is not high enough to destroy the layered structure, a process taking place at 400 °C for Mg,Al–CrO<sub>4</sub>, but at 300 °C for the Zn,Al–CrO<sub>4</sub> one. A detailed analysis by Raman spectroscopy has also evidenced the grafting process of chromate in Mg,Al LDHs [149]. The Raman spectrum of chromate in solution shows four bands at 848 ( $\nu_1$ ), 348 ( $\nu_2$ ), 884 ( $\nu_3$ ) and 363 cm<sup>-1</sup> ( $\nu_4$ ). The band due to the  $\nu_1$  mode is recorded in the same position for Mg,Al–CrO<sub>4</sub>, while the antisymmetric  $\nu_3$  mode splits into two bands at 884 and 928 cm<sup>-1</sup>; a splitting is also observed for mode  $\nu_2$  at 363 and 237 cm<sup>-1</sup>, and, finally, mode  $\nu_4$  is recorded at 474 cm<sup>-1</sup>.

Incorporation of chromate in the interlayers of a Mg,Al LDH yields larger loadings by the reconstruction method than through the conventional coprecipitation or exchange procedures and is accelerated under ultrasound treatment. However, when using calcined Mg,Al,Fe LDHs a larger adsorption is observed, probably because of the larger specific surface of the calcined precursor [153].

Chromate and dichromate-containing Cu,Cr LDHs prepared by coprecipitation and anion exchange have been used for alkoxylation of *n*-butanol with ethylene oxide (EO) [116]. The nature of the interlayer anion was fixed by using different pHs during synthesis, namely 8.5 for chromate and 4.5 for dichromate. Despite the known Brønsted basicity of LDHs associated with hydroxyl groups, and that selectivity in glycol ether was very high in all cases (93–96% to BMGE), detection of dioxane, which can be only formed in acidic media, evidences the presence of acid sites in these catalysts, probably related to the chromium cations themselves (Lewis type acid sites). The activity of the Cu,Cr–Cr<sub>2</sub>O<sub>7</sub> catalyst was larger than that shown by systems with the same cations in the brucite-like layers, but with decavanadate or heptamolybdate in the interlayer [116]. EO conversion increased with time on stream in batch reactor studies, and for a given reaction, the activity was always larger for the dichromate than for the chromate-containing LDH.

Calcined LDHs containing chromate species in the interlayer have been also used as catalysts. Thermal decomposition of polyoxometalate-containing LDHs has been previously reported [125], but a detailed study using a very slow heating schedule (2 °C min<sup>-1</sup>) has shown that thermal decomposition of a Mg,Al–CrO<sub>4</sub> LDH takes place in five mass losses steps [154]; according to analysis of evolved gases, the first two (99 and 192 °C) correspond to loss of water from the interlayer, while the three remaining losses at 354, 427 and 452 °C are due to dehydroxylation of the brucite-like layers; in addition, oxygen evolution (from chromate decomposition) is also observed at 498 °C.

The ability of LDHs to incorporate chromate in the interlayer depends on the nature of the brucite-like cations (Mg and Al, or Zn and Al) and the anion existing in the interlayer (nitrate or carbonate) to be exchanged [155], as well as the incorporation method (anion exchange or reconstruction). In most of the cases, however, a small impurity due to intercalated carbonate remains. Calcination at increasing temperatures gives rise to a decrease in the value of the spacing for the (003) diffraction maximum (which corresponds to the sum of the gallery height and the thickness of the brucite-like layer, 4.8 Å [118]) up to 300 °C (above this temperature, collapsing of the structure occurs) for the Mg,Al samples, but for the Zn,Al samples a decrease in the spacing is also observed, and collapsing takes place in this case at 300 °C. This lower stability of the Zn-containing sample might be related to the fact that ZnO crystallises at a lower temperature than MgO does.

Shrinkage of the gallery could be due to grafting of the chromate anion to the brucite-like layers or to removal of interlayer water [156]. To elucidate the actual reason, a sample calcined at 200 °C was equilibrated with water vapour at room temperature, but after several hours no swelling was observed, confirming that grafting had taken place and shrinkage was not due to dehydration. Grafting upon calcination is also evidenced by FTIR spectroscopy, showing splitting of the band due to

the antisymmetric  $\nu_3$  mode of chromate at  $880\text{ cm}^{-1}$  into two bands at  $930$  and  $864\text{ cm}^{-1}$  because of the change in symmetry from  $T_d$  to  $C_{3v}$ .

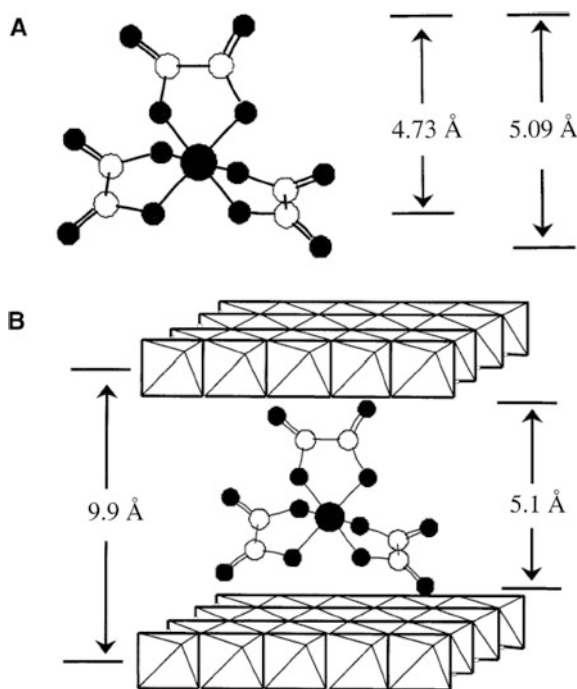
Both series of samples (with Mg,Al or Zn,Al in the brucite-like layers) also behave differently upon calcination once the layered structure has been destroyed. So, the PXRD diagram of Mg,Al–CrO<sub>4</sub> precursors calcined at  $800\text{ }^\circ\text{C}$  shows broad diffraction maxima of periclase and weak peaks of a Mg–Al–Cr spinel, while for the Zn,Al–CrO<sub>4</sub> samples the diffraction maxima are much sharper and are due to MgO and ZnAl<sub>2</sub>O<sub>4</sub>, but the Cr-containing species should be in an amorphous state.

The changes in the oxidation state of chromium species upon calcination can be also observed by UV–Vis/DR spectroscopy [155]; the spectra show intense bands due to charge transfer processes involving Cr<sup>6+</sup> species and only after high-temperature calcination bands due to octahedral Cr<sup>3+</sup> species (together with a change in the colour from yellow to green) develop; in agreement with the results commented above, such a change is observed at lower temperature for the Zn,Al samples than for the Mg,Al ones. The decrease in the content of Cr<sup>6+</sup> species as the calcination temperature is increased is further confirmed from TPR experiments, which show an increase in hydrogen consumption for samples precalcined below  $400\text{ }^\circ\text{C}$  (samples Mg,Al), and then a decrease, being almost unobservable for samples calcined at  $800\text{ }^\circ\text{C}$ ; reduction of Cr(VI) takes place at lower temperatures for the Zn,Al samples than for the Mg,Al ones.

FTIR monitoring of pyridine adsorption on the samples calcined at  $300\text{ }^\circ\text{C}$  and above has demonstrated the presence of Lewis acid sites on these samples; bands are recorded at  $1609$ ,  $1589$ ,  $1575$ ,  $1489$  and  $1443\text{ cm}^{-1}$  and are due to modes 8a, 8b, 19a and 19b of pyridine adsorbed on surface Lewis acid sites. However, the bands are much weaker for the samples precalcined above  $400\text{ }^\circ\text{C}$  and disappear upon outgassing at  $200\text{ }^\circ\text{C}$ , indicating the weakness of these sites, surface acidity being slightly weaker for the Zn-containing samples. These sites are associated with coordinatively unsaturated Cr<sup>6+</sup> and Mg<sup>2+</sup> (or Zn<sup>2+</sup>) cations. Although Brønsted acid sites have been detected in Cr<sup>3+</sup>/TiO<sub>2</sub> systems [157], they were not detected in the LDH samples, probably due to the large basicity of the existing oxide anions.

Another way to incorporate metal cations in the interlayer of LDHs is using coordination complexes. Besse et al. [158, 159] have intercalated trioxalate and dioxalate complexes in Zn,Al LDHs, concluding that the experimental conditions during synthesis control the type of interlayer anion in the final solids. Cr malonate complexes have been intercalated by Gutmann et al. [160], and co-intercalation of carbonate and oxalate-iron(III) complex has been also described [161]. The problem of this sort of compounds arises from the easiness with which these ligands coordinate metal cations, so being able to dissolve partially the brucite-like layers. Mg,Al LDHs with intercalated  $[\text{Cr}(\text{C}_2\text{O}_4)_3]^{3-}$  have been prepared by del Arco et al. [162] by reconstruction (and with or without further hydrothermal treatment) from a calcined carbonate precursor and by anion exchange from a nitrate precursor. The Mg/Al molar ratios in the reconstructed samples were lower than in the starting precursor, indicating partial dissolution of Mg(II) cations, and the Cr/oxalate ratios were also lower than three; these results, in addition to the FTIR spectra, suggest that the Cr complex is partially destroyed (actually, the presence of traces of

**Fig. 12.4** Molecular dimensions of free  $[\text{Cr}(\text{C}_2\text{O}_4)_3]^{3-}$  anion (**a**) and that intercalated between the sheets of the layered double hydroxide (**b**) Reprinted from [162], with permission from American Chemical Society



magnesium oxalate can be concluded from the FTIR spectra) and co-intercalation of free oxalate anions (to balance the positive charge of the layers) takes place. The PXRD data indicate that the Cr complex is intercalated with one of its  $\text{C}_2$  axes perpendicular to the brucite-like layers, Fig. 12.4, and the inversion observed in the relative intensities of the (003) and (006) maxima has been related to an increase in the electron density in the (00l) planes at a distance equal to one half of the spacing of the (003) planes [27, 150, 151, 158, 163]. On thermal decomposition, transient chromate species are formed, whose maximum concentration (according to the TPR curves) is achieved in the sample calcined at 400 °C, then progressively decreasing as the calcination temperature is increased. As for the samples described above [152, 155] prepared directly with chromate in the interlayer, surface Lewis acid sites are detected on the samples calcined at or above 400 °C, but Brønsted sites are not detected.

A different approach has been used by Wei et al. to incorporate chromium complexes in the interlayer of a Mg,Al LDH, namely by incorporating first the anionic salen-like ligand and then forming the complex in situ by reaction with  $\text{Cr}^{3+}$  chloride [164]; the calcined solids have been used for oxidation of benzyl alcohol to benzaldehyde using  $\text{H}_2\text{O}_2$  as oxidant. These authors have tested three different Schiff bases, prepared by reaction of salicylaldehyde with three diamines (ethylenediamine, diethyltriamine and *o*-phenylenediamine). These compounds were reacted with sulfuric acid for obtaining the corresponding phenyl ring-sulphonated compounds,



and then with the LDH (which layers had been previously swelled by intercalation of benzoate anions) and the solid thus obtained was finally soaked with a  $\text{CrCl}_3$  aqueous solution, forming the corresponding intercalated  $[\text{Cr}(\text{SO}_3\text{-salen})]^{2-}$  complexes, as confirmed by FTIR and UV-Vis spectroscopy results. The PXRD patterns show formation of intensively swelled structures, with  $d_{003}$  spacings ca. 20 Å, Fig. 12.5.

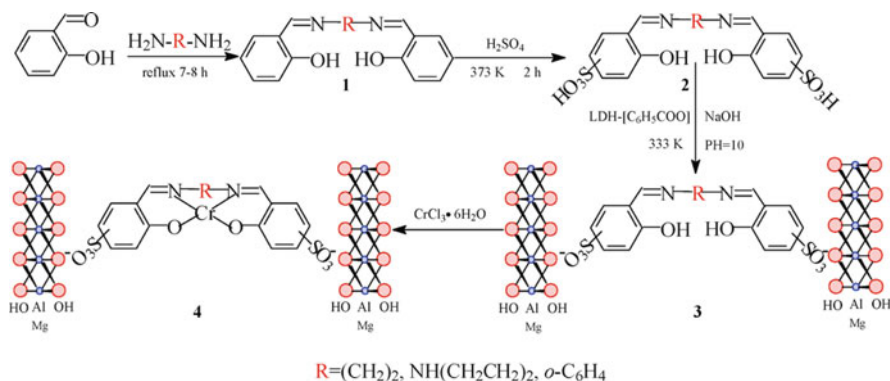


**Fig. 12.5** Preparation of Mg,Al-[Cr(SO<sub>3</sub>-salen)] LDH. Reprinted from [164], with permission from Elsevier

The unintercalated complexes showed a conversion of  $\text{C}_6\text{H}_5\text{-CH}_2\text{OH}$  ranging from 19.5 to 28.8, and the benzoate-LDH of 3.1%, but in all cases selectivity to benzaldehyde was lower than 80% and benzoic acid (ca. 15%) and benzyl benzoate (ca. 8%) were also formed. However, with the  $[\text{Cr}(\text{SO}_3\text{-salen})]$ -LDH catalysts the conversion increased up to 65.8% for the *o*-phenylenediamine derivative and in all three cases selectivity to formation of benzaldehyde was 100%. The electron-withdrawing ability of the *o*- $\text{C}_6\text{H}_4$  groups contributes to the formation of a  $\pi$ -extended coordination structure, decreasing the electron density around the central metal ion and increasing the stability of the heterogenised complex; furthermore, the resulting planar structure favours approaching of the  $\text{H}_2\text{O}_2$  molecule to the catalytic active site. On the contrary, the backbones in the other complexes are electron donating, increasing the electron density around the central metal ion and unfavouring the formation of the oxochromium intermediate. Conversion and selectivity remained unaltered even in the presence of radical scavengers (pyrocatechol, resorcinol and hydroquinone), indicating that the reaction proceeds via an ionic mechanism.

A complete study on the use of calcined Mg,Al LDHs containing chromium in three different structural sites: as  $\text{Cr}^{3+}$  in the brucite-like layers (A), as an intercalated  $\text{Cr}^{3+}$ -EDTA complex (B) and as intercalated chromate (C), in non-oxidative dehydrogenation of ethane to ethylene (EDH), has been reported by Sayari et al. [165]. The preparation procedure is outlined in Fig. 12.6. Four type-A samples were prepared with different Al/Cr molar ratios or even without Al. These authors report that in the absence of Al no pure hydrotalcite-type Mg,Cr phase could be

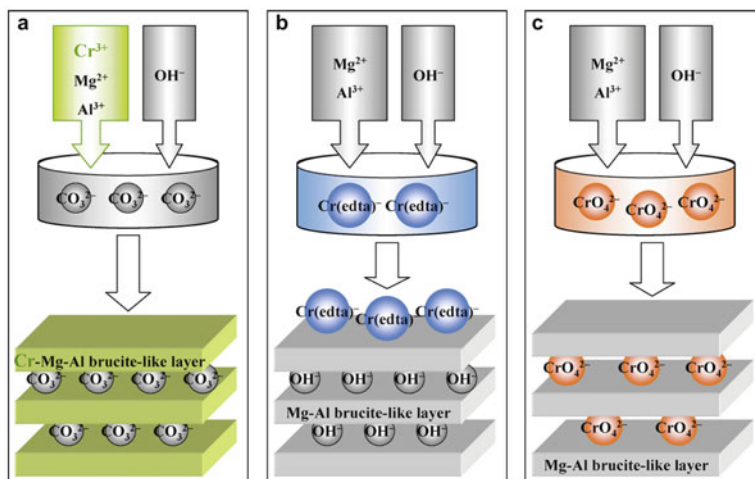


**Fig. 12.6** Non-oxidative dehydrogenation of ethane to ethylene over chromium catalysts prepared from layered double hydroxide precursors. Reprinted from [165], with permission from Elsevier

formed (segregation of brucite was observed by PXRD and Mg surface enrichment by XRF), despite formation of such a pure phase has been described previously [166]. The basal spacing for sample B was close to 7.8 Å, indicating that the Cr–EDTA complex is not inserted in the interlayer (while Ni and Cu complexes were [167]), but should be adsorbed on the external surface of the crystallites; no grafting was concluded from the Raman spectrum for sample C. On calcination at 500 °C partial oxidation to Cr<sup>6+</sup> species was observed, and XPS indicated that the molar Cr<sup>6+</sup>/Cr<sup>3+</sup> ratio was always larger than 1.0.

Ethane dehydrogenation was studied at 700 °C during 5 h tests; a decrease in activity was observed due to catalyst deactivation, especially during the first hour of time on stream. Samples prepared by method (A) displayed the largest selectivity to ethylene (79–84%) but only 12–15% ethane conversion, while larger conversions (26–30%) for samples B and C correlated with lower selectivity (71–74%). Along these experiments coke deposition was observed, and its amount was quantified after tests by temperature-programmed oxidation (TPO) using CO as oxidant. Carbon content was very low (ca. 5%) for the Al-free samples and amounted up to 42% for sample B. After exposure to the EDH reaction and TPO experiments the specific surface areas of the samples decreased sharply, especially for the Al-free samples (ca. 75% decrease), but this result should be taken cautiously, as the reference-specific surface areas correspond to the solids calcined at 500 °C and the samples were subsequently heated at 700 °C during the catalytic runs and up to 940 °C during TPO experiments; consequently, we do not know if the reduction in specific surface area actually is a consequence of these treatments or merely from sintering after submitting the sample to higher temperatures.

Table 12.2 summarises the reactions catalysed by LDHs with intercalated POMs containing chromium species.

**Table 12.2** Summary of reactions catalysed by LDHs with intercalated chromium-containing LDHs

Layer cations	Intercalated species	Reaction	Substrate	Reference
Cu,Cr	$\text{CrO}_4^{2-}$	Alkoxylation	<i>n</i> -Butanol	[116]
Cu,Cr	$\text{Cr}_2\text{O}_7^{2-}$	Alkoxylation	<i>n</i> -Butanol	
Mg,Al	$[\text{Cr}(\text{SO}_3\text{-salen})]^{2-}$	Oxidation	Benzyl alcohol	[164]
Mg,Al,Cr (500 °C)	$\text{CO}_3^{2-}$	EDH	Ethane	[165]
Mg,Cr (500 °C)	$\text{CO}_3^{2-}$	EDH	Ethane	
Mg,Al (500 °C)	$\text{CrO}_4^{2-}$	EDH	Ethane	
Mg,Al (500 °C)	$\text{Cr}(\text{EDTA})^-$	EDH	Ethane	

## 12.4 Molybdenum-Containing LDHs

Polymerisation–depolymerisation processes are very important for oxomolybdates, as different species can be formed in narrow pH ranges. As the immediate vicinity of the brucite-like layers has a rather high pH, formation of POMs with different nuclearities will not only depend on the experimental conditions fixed but also depend on kinetics aspects related to the interaction with the layers.

As for the systems above described, molybdate can be incorporated in Mg,Al LDHs from sodium aluminate solutions in a pH-dependent process [117]. Synthetic Mg,Al LDHs containing  $\text{MoO}_4^{2-}$  prepared by direct synthesis have been studied by Raman spectroscopy [149]. The spacing for the first basal diffraction is 7.97 Å, almost coincident within experimental error with those for sulphate (7.99 Å) or chromate (7.98 Å); however, the diffraction peak shows some sort of asymmetry. In aqueous solution all four modes of  $\text{MoO}_4^{2-}$  ( $T_d$  symmetry) are Raman active and are recorded at 894 ( $\nu_1$ ), 407 ( $\nu_2$ ), 833 ( $\nu_3$ ) and 320 ( $\nu_4$ )  $\text{cm}^{-1}$ . However, for the molybdate-LDH the  $\nu_1$  band splits into an intense one at 896  $\text{cm}^{-1}$  and a weaker one at 904  $\text{cm}^{-1}$ . Such a splitting also affects to mode  $\nu_4$ , which splits into an intense one at 322  $\text{cm}^{-1}$  and a weak one at 354  $\text{cm}^{-1}$ . These results suggest that two structurally different molybdate species coexist in the interlayer, thus accounting for the broadening observed in the PXRD pattern. These authors [149] tentatively suggest the existence of hydrated molybdate species (responsible for the intense components), together with a second type, probably bonded to the brucite-like hydroxyl surface. However, this situation does not correspond to the grafting status above described, as in such a case the decrease in the spacing of the PXRD maximum would be much more marked. Grafting of  $\text{Mo}_2\text{O}_7^{2-}$  species upon calcination at 200 °C onto the slabs of a Ni,Co LDH has been demonstrated by Delmas et al. [168] from XRD and Mo K-edge EXAFS measurements.

Thermal decomposition of these molybdate-intercalated LDHs takes place in five steps [154], the first two ones corresponding to removal of adsorbed and intercalated water, respectively, followed by dehydroxylation (also in two consecutive steps) and finally a recrystallisation step, leading to the formation of MgO,  $\text{MgMoO}_4$  and  $\text{MgAl}_2\text{O}_4$  spinel. No weight loss is recorded above 500 °C. This sort of studies

are important, as they permit to determine the temperature ranges at which given crystalline species are stabilised.

One of the problems found when intercalation POMs in the interlayer of LDHs by anionic exchange is that the acidic properties of the POM solutions give rise to a partial dissolution of the LDH layers. However, by performing the process in an ethanol/water solution, Hibino and Tsunashima [169] have been able to preserve the highly ordered structure of parent LDH during exchange to incorporate paramolybdate,  $\text{Mo}_7\text{O}_{24}^{6-}$ , species. Adipate- and chloride-containing Mg,Al LDHs (with different Mg/Al molar ratios and always with nitrate impurities) were prepared by coprecipitation and submitted to hydrothermal treatment to obtain more ordered crystals. It was found that the adipate/nitrate ratio depended on the Mg/Al ratio. Intercalation of paramolybdate was achieved regardless the size of the anion in the precursor LDH without any sort of preswelling. Regarding exchange in water, dissolution of Mg was observed for samples with Mg/Al = 2, but in a much lesser extension if Mg/Al = 3 or 4. No dissolution was, however, observed, when a water/ethanol mixture (containing the minimum amount of water needed to dissolve paramolybdate) was used and Mg/Al = 3 or 4, giving rise to a solid with basal PXRD reflections corresponding to spacings of 6 and 4 Å (an impurity characterised by reflections with spacings of 6.8 and 4 Å was also formed for Mg/Al = 4, but its origin remains obscure). As a basal spacing of 12 Å had been previously reported [118, 170] for paramolybdate-LDHs, the reflections at 6 and 4 Å were attributed to planes (006) and (009), respectively. These authors also discuss about the origin of the broad reflection recorded at lower angles in the PXRD diagrams of POM-LDH systems, usually attributed to a Mg POM, but they conclude that it should correspond to some sort of LDH structure (probably with intercalated lower nuclearity molybdates formed through hydrolysis). Model calculations have proved that the (003) reflection actually exists, but its intensity is extremely low because of the large scattering factor of molybdenum atoms; consequently, if this reflection is recorded, one should conclude that the solid has a poor crystallinity. Thermal decomposition gives rise to structural rearrangements even at 80 °C, although they are reverted upon exposure to water.

Another way to overcome the problem arising from the acido-base reaction between the POM and the LDH is to select less basic LDHs, i.e. Zn,Al instead of Mg,Al ones. This approach was used by Gardner and Pinnavaia in a classic study to elucidate the actual nature of the active species in cyclohexene oxidation with  $\text{H}_2\text{O}_2$  [171]. They studied a  $\text{Mg}_2\text{Al-Mo}_7\text{O}_{24}$  LDH prepared by ion exchange from a precursor preswelled with terephthalate and  $\text{MoO}_4^{2-}$  lowering the pH to 4.4 to polymerise the molybdate anion and to favour release of the protonated organic anion through protonation; the solid was prepared as powder or as a thin film and was dried at 120 °C. Alternatively, a  $\text{Zn}_2\text{Al-Mo}_7\text{O}_{24}$  LDH was prepared by a modification [27] of the induced hydrolysis method [172] by exchange of a nitrate precursor with aqueous  $(\text{NH}_4)_6\text{Mo}_7\text{O}_{24}\cdot 4\text{H}_2\text{O}$ , without pH control and digestion at 80 °C for 18 h. The PXRD pattern of the Mg sample showed the reflections due to basal planes, although the first one (expected at 12 Å) was extremely weak and buried in a broad diffraction centred at ca. 10.2 Å, whose intensity was much higher in

the diagram of unoriented powder. The Raman spectrum showed only the bands due to heptamolybdate, and so it should be concluded that this was the intercalated species and that the broad diffraction was due to a Mg (or Al) heptamolybdate salt. However, the PXRD diagram of the solid dried at 120 °C (a treatment given prior to the catalytic runs) demonstrated that the sample had undergone decomposition, as the diffraction due to the basal planes had disappeared. The activity shown by this catalyst could not be then related to interlayer heptamolybdate species, as they do not further exist in the 120 °C heated sample.

As mentioned above, stable phases were obtained when intercalating heptamolybdate in Zn<sub>2</sub>Al LDH; the PXRD lines were sharp and the basal spacing (12.1 Å) and the Raman spectra confirmed the presence of heptamolybdate, although a very weak impurity peak (10.8 Å) was also recorded in the PXRD diagram; as for the Mg<sub>2</sub>Al sample, decomposition was also observed at 120 °C, affecting not only to the LDH gallery (dehydration) but also to the precise nature of the POM, as concluded from Raman spectroscopy studies.

These LDH intercalated POMs were less reactive than the unsupported catalysts for peroxide oxidation of cyclohexene to the corresponding epoxide and diol in (BuO)<sub>3</sub>PO (the carbonate form of the Mg,Al LDH was inactive). This is consistent with the inaccessibility of the gallery POM centres under reaction conditions, even if the LDH–POM structure was retained, and consequently the activity observed should be attributed to the by-phase (Mg or Al heptamolybdate) or to the decomposition products formed after heating at 120 °C. Selectivities to epoxide and diol also differ for the intercalated and unsupported catalysts, and shape selectivity cannot be expected due to the named limited access to the gallery. It should be noticed, however, that the Raman spectrum of the used catalyst is consistent with a layered structure, probably a MoO<sub>4</sub><sup>2-</sup> intercalate.

In their study on the activity of Cu,Cr LDHs intercalated with POMs for *n*-butanol alkoxylation with ethylene oxide (EO), Malherbe et al. [116] have also studied a system intercalated with Mo<sub>7</sub>O<sub>24</sub><sup>6-</sup> prepared by coprecipitation and anionic exchange. Conversion of EO decreased with time on stream from 58% (2 h) to 51% (7 h) with total selectivity to butoxymonoethyleneglycol ether (BMGE) and a small amount of dioxane, which formation is again explained on the basis of the presence of Brønsted acidic sites, probably formed through reaction of POM with interlayer water molecules in the catalyst surface or Lewis acidic sites (the d<sup>0</sup> cations). Other active sites could be related to the Mo ions themselves, which can undergo reduction reactions (from the initial +6 state) in the reductive reaction medium. The activity trend observed on comparing three different POMs is as follows:



Also in this case lack of accessibility has been claimed, due to the overpopulation of the interlayer (which depend on the POM size and formal charge, as well as on its orientation within the gallery), as a limiting factor, the reaction probably taking place only at the edges of the interlayer space and/or through adsorbed POM anions.

Zavoianu et al. have carried out a detailed study on the effect of the preparation conditions on the physicochemical properties and catalytic performance of Mg,Al-molybdate-LDHs in cyclohexene oxidation with hydrogen peroxide [173]. Five samples were prepared by (i) ionic exchange with aqueous  $\text{Na}_2\text{MoO}_4$  at pH 10 from a carbonate precursor following the method proposed by Pinnavaia et al. [174] at pH 10; (ii) competitive ionic exchange at pH 10 using a carbonate precursor in water containing  $\text{Na}_2\text{MoO}_4$  and *p*-toluene sulfonic acid (*p*TOS) [175, 176]; (iii) exchange of the carbonate precursor with *p*TOS at pH 4.5 and then exchange with molybdate at pH 4.5 for 24 h and then at pH 10; (iv) direct synthesis at high supersaturation and pH 10 [1]; and (v) low supersaturation, by adding a solution containing magnesium and aluminium nitrates and molybdate to water. Unfortunately, all samples displayed a basal spacing of  $7.809 \pm 0.15 \text{ \AA}$ , roughly coincident with that measured for the carbonate precursor,  $7.905 \text{ \AA}$ , thus suggesting that no intercalation was achieved in any case. Several techniques (FTIR, Raman and UV–Vis spectroscopies) suggest the presence of  $\text{MoO}_4^{2-}$  and smaller amounts of  $\text{Mo}_7\text{O}_{24}^{6-}$  species in all samples. The catalytic performance seems to be strongly influenced by the basicity (as measured by benzoic acid titration using bromothymol blue and phenolphthalein as indicators), which decreases with the increase in Mo loading (2.8–9.3% weight); the activity of molybdate is related to its ability to produce singlet oxygen.

POM-LDHs with different divalent cations in the brucite-like layers (Mg, Zn, Ni, trivalent being Al in all cases) have been tested in epoxidation of norbornadiene and benzonorbornadiene [177]. The catalysts had been prepared by anion exchange from preswelled (terephthalate) precursors and heptamolybdate, keeping pH at 4.5 to avoid depolymerisation of the POM and to favour release of protonated terephthalate. Following the findings of Gardner and Pinnavaia [171] the broad PXRD peak close to  $11 \text{ \AA}$  was almost absent for the Zn,Al– $\text{Mo}_7\text{O}_{24}$  sample, which PXRD diagram showed the sharpest diffraction maxima. From Raman spectroscopy studies for similar samples [178], such an impurity has been claimed to correspond to a  $\text{MoO}_4^{2-}$  intercalate, as observed by Gardner and Pinnavaia after the catalytic runs [171]. The gallery height ( $7.2 \text{ \AA}$ ) was in all cases consistent with intercalation of the heptamolybdate anion oriented with its  $\text{C}_2$  axis perpendicular to the layers, and FTIR spectroscopy also supported the presence of heptamolybdate.

Conversion of norbornadiene was 100% in all cases (three solvents were tested, dioxane, acetone and dioxane-butyl maleate) with a substrate:oxidant ratio of 1:8, except on Zn,Al and Mg,Al in acetone. Highest selectivities in exo-epoxide were found with Ni,Al and Zn,Al in acetone, and the worst performance was observed for all catalysts in dioxane-butyl maleate, by-products being the ketone and an alcohol (mostly exo-norborneol, as concluded from  $^1\text{H}$  and  $^{13}\text{C}$  NMR spectroscopy). No significant difference was observed for  $\text{H}_2\text{O}_2$  efficiency (54–59%) among all catalysts and solvents. Total conversion of benzonorbornadiene was observed in all cases, but on Mg,Al in acetone, with total selectivity to epoxide and total conversion on Ni,Al and Zn,Al in acetone and dioxane,  $\text{H}_2\text{O}_2$  efficiency was similar as for norbornadiene oxidation (52–55%). Finally, oxidation of cyclohexene has been also studied on these catalysts. Conversion was 66–85% (depending on the solvent

and the catalyst), varying in the order Ni,Al > Zn,Al > Mg,Al and H<sub>2</sub>O<sub>2</sub> efficiency was 75% in all cases; this order can be related to the increasing basicity of the LDH matrix. Only a small loss of active phase was observed in the reaction medium, but these authors attribute this to attrition and not to leaching, and recyclability tests over six runs indicated that the activity was preserved, probably because of the small capability of these catalysts to induce polymerisation of these substrates.

A yield of 90% in *N*-methylmorpholine *N*-oxide was obtained by Choudary et al. upon oxidation of *N*-methylmorpholine on Mg<sub>3</sub>Al–MoO<sub>4</sub> (48% for Na<sub>2</sub>MoO<sub>4</sub>) containing 21% (weight) Mo, although no proper intercalation took place, as the XRD pattern on the solid was essentially the same as that for the Mg<sub>3</sub>Al–NO<sub>3</sub> precursor used [147]. These authors have used this same catalyst for oxidation of thioanisole with H<sub>2</sub>O<sub>2</sub> in aqueous medium [148]. No major differences in conversion were found between MoO<sub>4</sub>-LDH (80%) and Na<sub>2</sub>MoO<sub>4</sub> (89%), with identical selectivity to the sulfoxide (94%), although a fourfold increase in TOF was found for the immobilised catalyst.

Hulea et al. [123] have studied the mild oxidation of tetrahydrothiophene to sulfolane on a Mg<sub>3</sub>Al–Mo<sub>7</sub>O<sub>24</sub> LDH prepared [178] by anionic exchange of a nitrate precursor with an aqueous solution of Na<sub>2</sub>MoO<sub>4</sub>·2H<sub>2</sub>O at pH 4.5. As for many of the systems described so far, the Mg/Al ratio strongly decreases (1.61 vs. 2 for the original nitrate phase) upon exchange due to extraction of Mg<sup>2+</sup> cations in the acidic medium; the specific surface area increases from 16 (nitrate phase) to 45 m<sup>2</sup> g<sup>-1</sup>, and the shape of the nitrogen adsorption–desorption isotherms suggests development of mesopores and micropores and formation of a new interparticle and intragallery microporosity. As for the vanadate-containing sample studied also by these authors, the TG curve shows two weight losses (dehydration and dehydroxylation, respectively [125]), and as for the tungstate sample (also studied, see below), total weight loss is ca. one-third of that for the nitrate precursor, as in this last case also the anion is evolved as a mixture of nitrogen oxides. The PXRD diagram shows the typical pattern of a layered material, but with a broad reflection at ca. 11.5 Å indicating the presence of, at least, two intercalating species. These were identified from the UV–Vis/DR spectrum, which shows a broad absorption in the near UV range, which can be deconvoluted into two components close to 255 [MoO<sub>4</sub>] species and 325 nm [MoO<sub>6</sub>] species as in the heptamolybdate anion, with relative intensities 63/37.

Oxidation of tetrahydrothiophene was highly selective towards the sulfoxidation reaction, resulting exclusively in sulfoxide and sulfolane. A conversion of 98% was reached after 45 min reaction, with a selectivity to sulfolane of 78%, values much larger than for the corresponding decavanadate-containing LDH (see above). Despite the large nuclearity of heptamolybdate species, only terminal Mo=O bonds are able to form easier peroxo rings; this means that about 37% (according to the UV–Vis/DR results) of the species are less active. Contrary to the reasoning of Gardner and Pinnavaia above given [171], these authors [123] claim that swelling of the structure is enough to permit accessibility of the reagent molecules to the POM species in the interlayer. It should be noticed that the V- and Mo-containing samples displayed similar basal distances (10.2 and 11.5 Å, respectively) but very different

catalytic performances (ca. 50 and 98% conversion after 45 min reaction, respectively), despite their similar specific surface areas (50 and 45  $\text{m}^2 \text{g}^{-1}$ , respectively); on the contrary, the W-containing sample (see details below) showed a similar basal distance (10.5 Å), the same performance as the Mo-containing catalyst, but its specific surface area was ca. one half (25  $\text{m}^2 \text{g}^{-1}$ ). Consequently, it seems that the different catalytic performances are much more related to the intrinsic nature of the catalytic sites. Leaching is very important, conversion decreasing from 86% after 5 min in a first run to 81% in a fourth run, as confirmed by the observed activity of the solution attributed to the dissolved Mo species, after filtering off the solid.

Mild oxidation of sulfides and thiophenes using dilute hydrogen peroxide under mild conditions (40 °C) in the presence of acetonitrile as a solvent has been also studied [127] on these same catalysts. Sulfides lead to sulfoxides and sulfones as major products, while thiophenes led exclusively to sulfones. The Mo catalyst was much more active than the V-containing one, and conversion of 100% was measured for methyl-phenyl-sulfide (MPS) and benzyl-phenyl-sulfide (BPS) after 45 min reaction, Fig. 12.7. Regarding the whole series of substrates studied, the overall conversion changes as for the V-containing catalyst (see above). Leaching of Mo species was also observed.

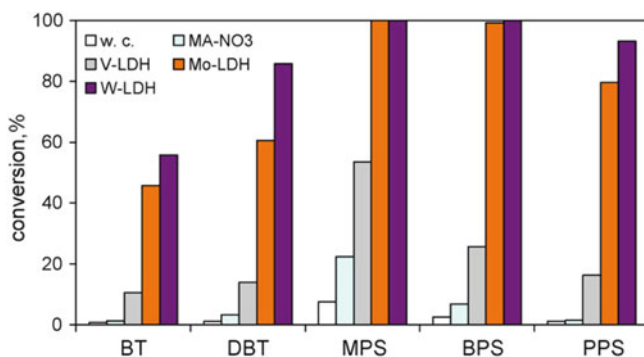


**Fig. 12.7** Effect of the catalyst on the organic sulfur compounds conversion;  $T = 40^\circ\text{C}$ ,  $\text{H}_2\text{O}_2/\text{substrate} = 5$  (mol mol $^{-1}$ ), solvent = MeCN,  $t = 45$  min for MPS, BPS and PPS,  $t = 3$  h for DBT and  $t = 18$  h for BT. Reprinted from [127], with permission from Elsevier

It is well known that oxidative dehydrogenation of propane to propene goes through a Mars-van Krevelen mechanism on catalysts possessing both red-ox and acid-base sites [137], so typically being red-ox active early transition metal oxides (V and Mo oxides mostly) associated with divalent cations (see above for V–Mg–O systems). Efficient Mo-containing catalysts in these reactions contain a certain excess of  $\text{MoO}_3$  over  $\text{MgMoO}_4$ . Mitchell and Wass [179] have prepared molybdate-containing LDHs catalysts to be used in propene ODH using different preparative protocols: (i) commercial (Reheis Ireland) or calcined  $\text{Mg,Al-CO}_3$  LDH (hydrotalcite) added to an aqueous solution of heptamolybdate at pH 4.5; (ii) calcined  $\text{Mg,Al}$  LDH reconstructed in a basic solution of terephthalic acid, and added to a solution of ammonium dimolybdate ( $\text{Mo}_2\text{O}_7^{2-}$ ) at pH 4.5; (iii) from a slurry of terephthalate



Mg,Al LDH (exchange is more difficult if the solid crystallises [163]) prepared by direct synthesis, to which a solution of  $\text{Na}_2\text{MoO}_4 \cdot 2\text{H}_2\text{O}$  and nitric acid was added (pH value not provided). In some cases, swelling of the hydrotalcite was attained by intercalating glycerol or terephthalic acid to precalcined hydrotalcite. In addition, a reference magnesium molybdate,  $\text{Mg}_2\text{Mo}_3\text{O}_{11}$ , was also prepared.

Intercalation of Mo species led to noisy PXRD diagrams, indicating a loss of crystallinity upon intercalation and the broad feature at 10–11 Å characteristic of Mg (or Al) polyoxomolybdates; the presence of  $\text{MoO}_3$  could not be concluded from the PXRD patterns. The highest Mo uptake (25–30% weight) was found for catalysts prepared at pH 4.5, whichever the starting molybdates, as these will converge to the same solution species at a given pH. Uptake was larger for the calcined materials, but when impregnation was carried out at pH 4.5 (nitric acid) both the calcined and uncalcined materials yield large Mo contents, probably because nitric acid protonates and displaces interlayer carbonate, expelled as  $\text{CO}_2$ . The use of glycerol did not enhance Mo uptake and was disadvantageous, as the particles became sticky and difficult to filter and wash. No advantage was observed when using terephthalic acid in terms of Mo uptake or increased gallery height. When the reaction temperature was increased from room temperature to 70 °C more Mo was incorporated. Despite catalysts with high Mo content and large  $d$  spacings (prepared at pH 4.5) were yellow, as  $\text{MgMoO}_4$ , but neither PXRD nor IR spectroscopy evidenced its presence.

Conversions larger than 5% were observed only after heating the catalysts at 550 °C or above, where  $\text{MgAl}_2\text{O}_4$ ,  $\text{MgMo}_2\text{O}_7$  and  $\text{MgMoO}_4$  have been formed [13, 180]. However, formation of these species depends on the layered precursor; the material which was most active in propane ODH and the most selective towards propene was that prepared from a calcined commercial hydrotalcite and ammonium dimolybdate with prior impregnation with terephthalic acid and pH adjusted to 4.5 (nitric acid).

Halodecarboxylation of carboxylic acids is a useful and selective reaction to produce halogenated organic substrates. Bhattacharjee et al. [181] have reported the formation of  $\beta$ -bromostyrenes using KBr and  $\text{H}_2\text{O}_2$  in the presence of  $\text{Na}_2\text{MoO}_4$  in an aqueous medium; to avoid the negative conditions of this reaction (e.g. use of complex reagents, environmentally undesirable solvents and long reaction times under homogeneous conditions generating heavy metal/solid wastes), Choudary et al. have reported the use of molybdate-containing Mg,Al LDHs for this reaction [182]. The Mg,Al-Cl LDH precursor was prepared by coprecipitation, and molybdate was intercalated by adding the LDH solid to an aqueous solution of sodium molybdate. Similar compounds were prepared with sodium tungstate and sodium vanadate, but no indication of the precise conditions (e.g. pH) were provided. The PXRD patterns showed no important change and since no new phase is detected clearly in the PXRD patterns, authors conclude that intercalation must proceed homogeneously by local structural distortion of the layers, yielding to irregular stacking of the layers.

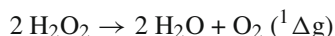
Halodecarboxylation of cinnamic acid to  $\beta$ -bromostyrene showed a yield of 80% on the molybdate-LDH, while yields were much lower for the tungstate (30%) or

vanadate (25%) analogues [182]. When using the pure sodium salts, also this order of yield was found ( $\text{Na}_2\text{MoO}_4 > \text{Na}_2\text{WO}_4 > \text{NaVO}_3$ ), and the absolute values were smaller than for the corresponding LDH derivatives.

Good to moderate yields were obtained on  $\text{MoO}_4$ -LDH with different substrates [182]. It was observed that acids with electron-donating substituents were particularly reactive compared to those having electron-withdrawing groups; when using substituted benzoic acid lower yields were obtained with electron-releasing substituents. These findings can be correlated to the inherent basic character and large positive charge of the LDH lattice. No loss of activity was observed even after five runs, indicating that leaching does not occur.

Selective oxyfunctionalisation of organic substrates by singlet oxygen ( $^1\text{O}_2$ ) has been receiving much attention. Photosensitisation for the generation of singlet molecular oxygen is well documented in the literature, but an intensive search exists for alternative dark systems. Although molybdate catalysts are able to produce singlet oxygen in homogeneous conditions, soluble bases and large solvent volumes are needed. Molybdate-LDHs have been used for these purposes, avoiding the use of dissolved bases [175], since the LDH surface locally provides the optimal basicity for  $^1\text{O}_2$  generation at a high rate [183]. A Mg,Al-Cl LDH precursor was prepared by coprecipitation and molybdate was incorporated by exchange at room temperature for 24 h in a  $\text{Na}_2\text{MoO}_4$  aqueous solution at pH 10. The Mg/Al ratio was changed from 7:3 to 8:2 and 9:1; basal spacing was 7.6 Å for all samples and the 9:1 sample showed co-formation of brucite. XPS showed formation of an Al-rich LDH phase on top of the brucite phase, probably because of the strong deviation of the chemical composition from that for hydrotalcite (Mg/Al ratio 3:1). Surface basicity (from the pH of a suspension, the amount of adsorbed indicators and XPS O(1s) measurement) decreased when increasing the amount of aluminium. Most of Mo was as  $\text{MoO}_4^{2-}$  and only the presence of a small amount of heptamolybdate could be concluded from Raman spectra.

Exposure of this catalyst to  $\text{H}_2\text{O}_2$  in dioxane turned the suspension brick-red; time-resolved UV-Vis/DR spectroscopy showed bands at 330–310 and 350–345 nm typical of  $[\text{MoO}(\text{O}_2)_2]^{2-}$  and  $[\text{Mo}(\text{O}_2)_4]^{2-}$  species, as well as a shoulder at 365 nm typical of triperoxospecies [184, 185], which are known to release easily singlet oxygen, which is slower for the other two species; the infrared luminescence spectrum shows an emission at 1276 nm, due to the weak, spin forbidden relaxation process  $[^1\text{O}_2, ^1\Delta_g] \rightarrow [^3\text{O}_2, 3\Sigma_g^-]$ . Formation of singlet oxygen is related to the basic nature of the LDH matrix and no leaching of the molybdate species was observed (reaction stopped after filtering off the solid). When a wider series of samples differing in the Mo content was studied, the decomposition rate of  $\text{H}_2\text{O}_2$  according to reaction



correlates with the molybdate content in the LDH [186].

Oxidation of 1-methyl-1-cyclohexene was studied on these catalysts with varying Mo content (12.5, 25 and 37.5% of total AEC). Compared to homogeneous

molybdate, Mo-LDHs show slightly lower or comparable oxidant efficiency but significantly higher activity in  $^1\text{O}_2$  generation, with minimal interference by non-desired reactive oxygen species [187]. The highest yield was achieved with the catalyst containing less Mo. Too much Mo could produce an excessive amount of  $^1\text{O}_2$ , causing a depletion of the substrate around the catalytic site or  $^1\text{O}_2$ – $^1\text{O}_2$  annihilation to produce  $\text{O}_2$  ( $3\Sigma_g^-$ ).

Co-intercalation of *p*-toluenesulfonate (*p*TOS) yielded a sample with a basal spacing of 17.25 Å, suggesting that the organic anion is perpendicular to the layers; this was a more hydrophobic catalyst, with a more gradual consumption of  $\text{H}_2\text{O}_2$  due to repulsion between *p*TOS and  $\text{H}_2\text{O}_2$ . Overall yield of oxygenated species increases, with a fivefold increase in epoxide formation; the lower surface  $\text{H}_2\text{O}_2$  concentration seems to favour formation of monoperoxo or diperoxo epoxidising species, instead of the triperoxomolybdate, which releases  $^1\text{O}_2$  fastest.

Concerning the effect of basicity provided by the LDH matrix, this was tested in oxidation of 2,3-dimethyl-2-butene. The epoxide was preferentially formed than the enylhydroperoxide on the less basic catalyst (Mg/Al ratio 7:3), as formation of epoxidising species (monoperoxo or diperoxo molybdate) is favoured at lower pH.

It should be noticed that  $^1\text{O}_2$  yield during oxygenation of 2,3-dimethyl-2-butene or 1-methyl-1-cyclohexene increased with the reaction temperature, but decreased after reaching a maximum around 35 °C. This could result from a decrease in  $^1\text{O}_2$  lifetime with increasing environment temperature. By choosing the appropriate conditions (Mg/Al ratio, Mo loading and reaction temperature 35 °C), these authors have been able to oxygenate several substrates via  $^1\text{O}_2$  formation with a very marginal (1–4%) formation of the corresponding epoxide.

These authors have reported further studies on the disproportionation of  $\text{H}_2\text{O}_2$  into singlet oxygen [188]. They kept the Mg/Al ratio between 1.5 and 5; lower ratios yield to crystallisation of bohemite,  $\text{Al}(\text{OH})_3$ , while larger values yielded co-formation of brucite,  $\text{Mg}(\text{OH})_2$ . The Mg/Al ratio rules the AEC of the LDH and thus the Mo loading. The rate of  $\text{H}_2\text{O}_2$  disproportionation was tested on these catalysts by cerimetry. A rate of  $30 \times 10^{-5} \text{ M s}^{-1}$  was measured for the sample with Mg/Al = 1.5, rapidly decreasing to ca.  $1 \times 10^{-5} \text{ M s}^{-1}$  for Mg/Al = 3 and higher. Production of singlet oxygen was assessed by chemical trapping (CT) of  $^1\text{O}_2$  with  $\beta$ -citronellol;  $\text{H}_2\text{O}_2$  efficiency increased from Mg/Al = 1.5 to 2, then keeping roughly constant values. Generation of  $^1\text{O}_2$ , as studied by chemiluminescence (CL), showed a yield of 30–35%, whichever the Mg/Al ratio. The higher activity of the Mo-LDHs in disproportionation of  $\text{H}_2\text{O}_2$  might be due to the electrostatic field exerted by the highly charged LDH support, resulting in enhanced polarisation of the Mo–O<sub>2</sub> and O–O bonds in the immobilised peroxomolybdate complexes, compared to the corresponding dissolved species [186]. The  $^1\text{O}_2$  yields determined by CL are slightly larger than those determined by CT, probably by physical quenching by  $\beta$ -citronellol.

The rate of  $\text{H}_2\text{O}_2$  disproportionation decreases sharply when the Mo loading is increased; the efficiency of  $\text{H}_2\text{O}_2$  use is less affected by the Mo loading than the rate of  $\text{H}_2\text{O}_2$  disproportionation. These findings can be explained by the restricted access

of  $\beta$ -citronellol to the  $\text{MoO}_4^{2-}$  anions in the interlayer space at high Mo loadings, and a part of the  $^1\text{O}_2$  produced within the LDH crystals will be lost by quenching and consequently the rate of  $\text{H}_2\text{O}_2$  disproportionation and  $^1\text{O}_2$  yield decreases with increasing Mo loading.

On the other hand, it has been reported [189] that the oxidant efficiency of Mg,Al LDHs containing molybdate can be improved by pretreatment with polyols, by increasing the  $\text{H}_2\text{O}_2$  efficiency, yielding the best heterogeneous catalysts in terms of  $\text{H}_2\text{O}_2$  use [190]. This was checked by chemical trapping of the formed  $^1\text{O}_2$  with  $\beta$ -citronellol, whose complete conversion to allylic hydroperoxides requires two equivalents of  $\text{H}_2\text{O}_2$ . The molybdate-LDH, however, requires eight equivalents for complete conversion, but pretreatment of the catalyst with 1,3-propanediol, glycerol, ethylene glycol or 1,2-propanediol increases the efficiency; treatment with 2-methoxyethanol, 2,2,2-trifluoroethanol, simple alcohols (e.g. *tert*-butanol or ethanol) or DMF did not result in an improvement of the oxidant efficiency compared to the unmodified molybdate-LDH. Physicochemical characterisation has shown that the glycol is not intercalated, but interacting with aluminium located at the outer surface and the edges of the LDH crystals. Peroxidation of several olefins with this glycol-modified catalyst led conversions above 88% and selectivities up to 99%.

The structural and texture evolution of LDHs intercalated with paramolybdate anions has been reported [178]. The study permits to identify the species formed at different stages of thermal decomposition and could be useful to select experimental conditions to prepare specific catalytically active species. The samples were prepared by impregnation of five precursors with an aqueous solution of ammonium heptamolybdate at pH 4.5. One precursor was meixnerite, prepared by rehydration of a calcined Mg,Al- $\text{CO}_3$  LDH; two were Mg,Al and Zn,Al LDHs in the nitrate form [163, 171], prepared by coprecipitation; and two were Mg,Al and Zn,Al LDHs too, with intercalated terephthalate [118, 191]. As for the other POM-LDH systems here reviewed, the  $\text{M}^{2+}/\text{Al}$  ratio was lower (1.5–1.6) than the nominal one (2) for the Mg,Al systems, but rather close (1.9–2.0) for the Zn,Al ones; the larger acidity of Zn with respect to Mg favours dissolution of  $\text{Mg}^{2+}$  in a larger extent than that of  $\text{Zn}^{2+}$ . The Al/Mo ratio is roughly equal to 6/7, indicating the presence of heptamolybdate in the interlayer. The PXRD patterns demonstrate formation of solids with the hydrotalcite-type structure in all cases. Basal diffraction at ca. 12, 6 and 4 Å were recorded for all molybdenum-containing samples, with the already observed [27, 150, 151, 158, 163] inversion in the relative intensities of the (003) and (006) diffraction lines; the gallery height indicates that the heptamolybdate units are located with their  $\text{C}_2$  axis perpendicular to the layers, so maximising the interactions with the layer hydroxyl groups. The ex-nitrate samples show a diffraction at 4.9 Å and a broad diffraction at 11–9.8 Å, whose intensity increases with the synthesis temperature and upon calcination up to 200 °C. Collapsing of the structure is observed upon calcination at 300 °C, with almost flat PXRD patterns.  $\text{MgMoO}_4$  crystallises at 600 °C, but contrary to the findings of Twu and Dutta [180], formation of  $\text{MgAl}_2\text{O}_4$  or  $\text{MgMo}_2\text{O}_7$  was not observed. Formation of  $\text{ZnMoO}_4$  is already observed at 450 °C and additional diffraction maxima due to  $\text{ZnAl}_2\text{O}_4$  and

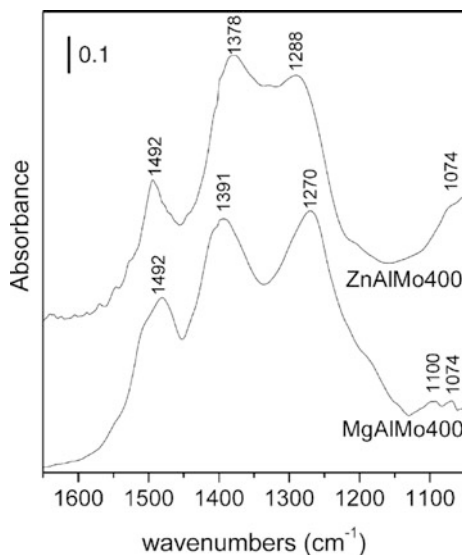
$\text{Zn}_3\text{Mo}_2\text{O}_9$  are observed at 800 °C. The broad diffraction and the maximum at 4.9 Å are not due to Mg (or Zn or Al) molybdates as the solid formed upon reaction between Mg (or Zn or Al) nitrate and ammonium heptamolybdate at pH 4.5 did not show these signals. These PXRD signals are not either due to new phases formed through grafting, as the line at 4.9 Å disappears on equilibrating the solid calcined at 120 °C with decarbonated water at room temperature for 1 day.

All the samples were microporous, but microporosity decreases when the calcination temperature is increased. They show similar Raman spectra, with bands coincident with those of heptamolybdate and a very small amount of discrete  $[\text{MoO}_4]$  species formed through hydrolysis of heptamolybdate, which could be responsible for the broad diffraction at 11–9.8 Å, while the maximum at 4.9 Å should correspond to a distorted structure. On calcination at 150 °C the band due to the stretching Mo–O mode slightly shifts towards larger wavenumbers, which has been ascribed to a shortening of the Mo–O bonds, as a consequence of a stronger interaction with the layers. Major changes occur above 200 °C, indicating a lower polymerisation degree and increasing the concentration of tetrahedral  $[\text{MoO}_4]$  species in dimolybdate units (formed by a tetrahedron and an octahedron), finally leading to formation of discrete  $\text{MMoO}_4$  ( $\text{M} = \text{Mg}, \text{Zn}$ ). The increased basicity of the LDH matrix on dehydration and dehydroxylation could also enhance the depolymerisation process.

Surface red-ox and acid–base properties of the ex-nitrate and molybdate-containing LDH samples calcined at 400 °C have been studied by FTIR monitoring of the adsorption of several probe molecules [192]. Surface acidity has been studied by pyridine (Py) adsorption. The bands recorded indicate the presence of surface Lewis acid types, ascribed to coordinatively unsaturated (cus)  $\text{Mo}^{6+}$  cations, as the bands characteristic of Py adsorbed on  $\text{Al}^{3+}$  cations [193] were not recorded. For the Mg-containing samples additional bands at 1638 and 1538  $\text{cm}^{-1}$  are due to protonated pyridine and are ascribed to surface Brønsted acid sites, absent in the calcined nitrate precursor [193]. Both Lewis and Brønsted acid sites are relatively strong, as the bands persist even after outgassing at 300 °C.

Surface basicity was studied by adsorption of trimethyl borate (BATE), whose FTIR spectrum shows three sharp bands at 1485 (methyl deformation), 1360 (B–O stretching) and 1063 (C–O stretching)  $\text{cm}^{-1}$  [194]. The first band is recorded at 1492  $\text{cm}^{-1}$  upon adsorption on the samples, but the other two bands split into 1390 and 1270  $\text{cm}^{-1}$ , and 1100 and 1074  $\text{cm}^{-1}$ , respectively, for the Mg sample; only the first band splits (1378 and 1288  $\text{cm}^{-1}$ ) for the Zn sample, while the C–O stretching band is recorded as a single one at 1074  $\text{cm}^{-1}$ , Fig. 12.8. Interaction with surface basic sites takes place through electron density donation into the  $p_z$  orbital of the boron atom (assuming a  $sp^2$  hybridisation) and then strength of this donation is directly related to the strength of the surface basic sites, and distortion of the BATE molecule from  $D_{3h}$  to  $C_{3v}$  around the boron atom. The red-ox properties were tested through temperature-programmed reduction (TPR) and FTIR monitoring of isopropanol (ISP) adsorption. TPR experiments show a single reduction maximum at ca. 715 °C for the Mg sample (untreated and calcined at 400 °C), but at 535 °C for the Zn samples. Tetrahedral  $[\text{MoO}_4]$  units are reduced at ca. 900 °C,

**Fig. 12.8** FTIR spectra recorded after adsorption of bate at room temperature on samples MgAlMo400 and ZnAlMo400 and outgassed at room temperature. Reprinted from [192], with permission from Elsevier



while octahedral  $[\text{MoO}_6]$  ones are reduced around  $760^\circ\text{C}$  or  $450\text{--}550^\circ\text{C}$  if they are dispersed [195]. Consumption of hydrogen (due exclusively to reduction of Mo species) indicates a larger reducibility in the Zn- than on the Mg-containing samples.

As oxidation of ISP can lead to formation of acetone or acetic acid, the adsorption of these two species was also studied. Adsorption of acetic acid takes place dissociatively (mostly on the Mg sample) and molecularly or through weak adsorption (mostly on the Zn sample). Dissociated species persist even after outgassing at  $300^\circ\text{C}$ . Only physisorption of acetone was observed at room temperature, but on heating at  $200^\circ\text{C}$  formation of enol species or those resulting from aldol condensation was observed, as reported by Figueras et al. after acetone interaction with meixnerite [196]; in addition, bands due to acetate species are also observed on the Mg sample. Adsorption of ISP on both samples takes place dissociatively, leading to formation of isopropoxide species; upon heating at  $300^\circ\text{C}$  the same bands as recorded after adsorption of acetone adsorbed on weak surface Lewis acid sites are recorded, while the intensities of the alcoxide bands decrease and those due to molecularly adsorbed ISP disappear; formation of acetate species was observed only on the Mg sample after heating at  $250^\circ\text{C}$ . It should be noticed that propene formation was not observed, probably because of the very low Brønsted type surface acidity. Acetone production is larger on the Zn sample, probably because of its larger reducibility (larger  $\text{H}_2$  consumption at lower temperature). TPR experiments on samples pretreated in ISP at  $300^\circ\text{C}$  showed a lower  $\text{H}_2$  consumption, indicating that the catalysts become reduced with this treatment, supporting a Mars-van Krevelen mechanism for the reactions observed. Aldolic condensation yielding mesityl oxide has been observed on both catalysts at  $200\text{--}250^\circ\text{C}$ , the activity increasing as the basic strength increases [196, 197].

Das and Parida [198] have studied the esterification of acetic acid with *n*-butanol on Zn,Al LDHs exchanged with molybdophosphoric acid (MPA). The Zn,Al LDH in the nitrate form was prepared by direct synthesis, then exchanged with terephthalic acid in a basic medium (leading to an increase in the basal spacing from 7.65 to 13.9 Å) and finally incorporation of the molybdophosphate anion (MPA) by exchange at pH 4.5–5, preparing samples with MPA weight loadings of 5, 10, 15 and 20% (spacings  $14.1 \pm 0.1$  Å). The crystallite size decreased from 94 to 64 Å as the MPA loading was increased, and the specific surface area showed a maximum value ( $89 \text{ m}^2 \text{ g}^{-1}$ ) for the 15 wt% sample. Typical MPA FTIR bands were recorded at 1026, 964, 827 and  $754 \text{ cm}^{-1}$  (1067, 1021, 992, 893, 822 and  $771 \text{ cm}^{-1}$  for unloaded MPA), indicating that MPA was retained in the interlayer. Surface Brønsted acidity was measured by quantifying the amount of irreversibly adsorbed bases (pyridine and 2,6-dimethyl-pyridine), maximum values being found for the 15 wt% sample. Conversion of acetic acid was also maximum (84%) for this sample, although selectivity to the ester was 100% in all cases (it should be noticed that a conversion of 31% was measured in the absence of catalyst and that the Zn,Al LDH in the nitrate form showed a conversion of 56%). This behaviour might be ascribed to the maximum surface Brønsted acidity and maximum specific surface area shown by this sample. Conversion decreased from 84 to 59% when the acid/alcohol molar ratio decreased from 1/10 to 1/20, while selectivity was maintained at 100%. It seems that an excess of alcohol blocks the active sites or prevents a nucleophilic attack by shielding the protonated alcohol due to its own excess. Conversion also increased with the reaction temperature (66 to 84% on passing from 80 to 110 °C), as formation of carbonium ions for the nucleophilic reaction results favoured. These authors conclude a first-order dependence of the reaction rate on acetic acid concentration.

Finally, regarding the studies on intercalation of bulk POMs, in addition to the intercalation of semispherical Keggin-type ones and others which structure originates from the polymerisation of Keggin fragments (e.g. Wells – Dawson and Finke structures), intercalation of a POM with a rather unique structure, namely decamolybdodocobaltate(III),  $[\text{H}_4\text{Co}_2\text{Mo}_{10}\text{O}_{38}]^{6-}$ , briefly  $[\text{Co}_2\text{Mo}_{10}]$  has been also studied. The interest arises from its distinctive structure and the fact that it has been claimed [199] as a possible precursor for the synthesis of Co-Mo/ $\gamma$ - $\text{Al}_2\text{O}_3$  hydrotreating catalysts, and also on titania and zirconia supports [200]. The anion is formed by putting together two Andersen chiral fragments of  $[\text{CoMo}_5]$ ; consequently, its intercalation can produce a completely inorganic chiral microporous material. Intercalation of  $[\text{Co}_2\text{Mo}_{10}]$  has been attained [201] by anionic exchange in a Mg,Al (molar ratio 2) meixnerite at pH 4.7 (lower pH values led to partial dissolution of the LDH, while higher values led to depolymerisation of the POM). As predicted by modellisation [202], low microporosity solids were obtained because of close packing of the pillars; according to the PXRD results, the intercalated  $[\text{Co}_2\text{Mo}_{10}]$  anions presented two different orientations whose gallery heights were 7.4 and 9.7 Å, the lower of which was more stable. The intercalated anion was stable up to 250 °C and collapsing of the layered structure was observed at 300 °C, forming amorphous phases, although maintaining their external morphology up to 500 °C.

**Table 12.3** Summary of reactions catalysed by LDHs with intercalated molybdenum-containing POMs

Layer cations	Intercalated species	Reaction	Substrate	References
Mg,Al	Mo <sub>7</sub> O <sub>24</sub> <sup>6-</sup>	Epoxidation	Cyclohexene	[171]
Zn,Al	Mo <sub>7</sub> O <sub>24</sub> <sup>6-</sup>	Epoxidation	Cyclohexene	
Cu,Cr	Mo <sub>7</sub> O <sub>24</sub> <sup>6-</sup>	Alkoxylation	<i>n</i> -Butanol	[116]
Mg,Al	Mo <sub>7</sub> O <sub>24</sub> <sup>6-</sup>	Epoxidation	Norbornadiene	[177]
Mg,Al	Mo <sub>7</sub> O <sub>24</sub> <sup>6-</sup>	Epoxidation	Benzenorbornadiene	
Zn,Al	Mo <sub>7</sub> O <sub>24</sub> <sup>6-</sup>	Epoxidation	Norbornadiene	
Zn,Al	Mo <sub>7</sub> O <sub>24</sub> <sup>6-</sup>	Epoxidation	Benzenorbornadiene	
Ni,Al	Mo <sub>7</sub> O <sub>24</sub> <sup>6-</sup>	Epoxidation	Norbornadiene	
Ni,Al	Mo <sub>7</sub> O <sub>24</sub> <sup>6-</sup>	Epoxidation	Benzenorbornadiene	
Mg,Al	Mo <sub>7</sub> O <sub>24</sub> <sup>6-</sup>	Oxidation	Tetrahydrothiophene	[123]
Mg,Al	Mo <sub>7</sub> O <sub>24</sub> <sup>6-</sup>	Oxidation	Benzothiophene	[127]
Mg,Al	Mo <sub>7</sub> O <sub>24</sub> <sup>6-</sup>	Oxidation	Dibenzothiophene	
Mg,Al	Mo <sub>7</sub> O <sub>24</sub> <sup>6-</sup>	Oxidation	Diphenyl sulfide	
Mg,Al	Mo <sub>7</sub> O <sub>24</sub> <sup>6-</sup>	Oxidation	Benzyl-phenyl sulfide	
Mg,Al	Mo <sub>7</sub> O <sub>24</sub> <sup>6-</sup>	Oxidation	Methyl-phenyl sulfide	
Mg,Al	Mo <sub>7</sub> O <sub>24</sub> <sup>6-</sup>	ODH	Propane	[179]
Mg,Al	MoO <sub>4</sub> <sup>2-</sup>	Halodecarboxylation	Cinnamic acid	[182]
Mg,Al	MoO <sub>4</sub> <sup>2-</sup>	Oxyfunctionalisation	1-Methylcyclohex-1-ene	[175]
Mg,Al	MoO <sub>4</sub> <sup>2-</sup>	Oxyfunctionalisation	2,3-Dimethylbut-2-ene	
Mg,Al	MoO <sub>4</sub> <sup>2-</sup>	Oxyfunctionalisation	$\alpha$ -Terpinene	
Mg,Al	MoO <sub>4</sub> <sup>2-</sup>	Hydroperoxidation	$\beta$ -Citronellol	[188]
Zn,Al	PMo <sub>12</sub> O <sub>40</sub> <sup>3-</sup>	Esterification	Acetic acid	[198]

Table 12.3 summarises the reactions catalysed by LDHs with intercalated POMs containing molybdenum species.

## 12.5 Tungsten-Containing LDHs

Polyoxotungstates constitute a larger family than chromates, vanadates and molybdates. The precise nature of the W-POM formed is highly dependent on pH, Fig. 12.9, and thus preparation of POM-LDH compounds is a difficult task.

As mentioned above, the acid–base interaction between the POM anions (which are hydrolytically unstable at weakly acid to basic pH) and the LDH (which provides the medium with a basic character) leads to a partial dissolution of the layers affecting the M<sup>2+</sup>/M<sup>3+</sup> ratio of the final product; this ratio is essential since it determines the charge density of the LDH layers and therefore the void volume between POM units within the gallery. It has been also mentioned that the partial dissolution might give rise to formation of a co-phase which is thought to be a Mg-rich salt of the POM that deposits on the surface of the LDH crystallites, blocking the access to the interlayer galleries [203]. In order to minimise these problems, several approaches have been used [203, 204]. Yun and Pinnavaia [203] intercalated



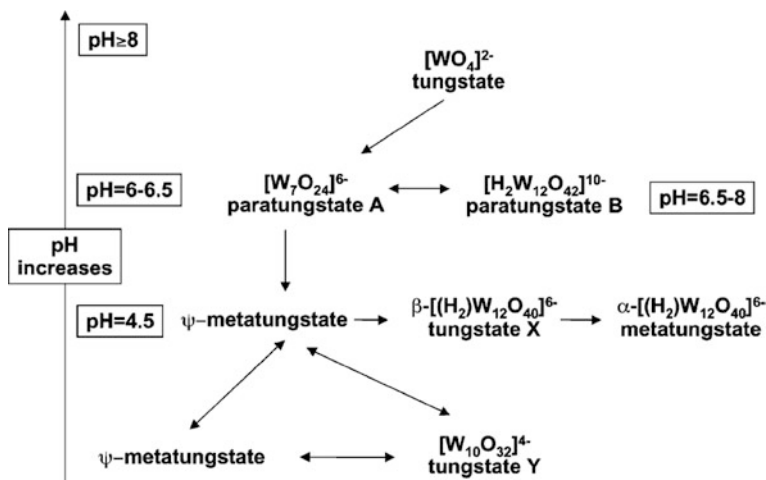


**Fig. 12.9** pH ranges corresponding to the stability of different tungsten POMs. Reprinted from [207], with permission from American Chemical Society

POMs with the Keggin, Dawson and Finke structures, but only succeeded with systems with a  $M^{2+}/M^{3+}$  molar ratio of 3:1. Weir and Kydd [204] have succeeded in intercalating metatungstate anions,  $H_2W_{12}O_{40}^{6-}$  into Mg,Al LDHs with ratios 2, 3 and 4. The method consists of preparing a Mg,Al- $CO_3$  LDH precursor, decomposing it by calcination at 500 °C under flowing nitrogen, reconstruct the structure to the meixnerite form (with intercalated hydroxyl groups) by slurring in water for 5 days, then exchanging with adipate using a large excess (up to 218%) of this anion and finally exchanging with metatungstate solution. In this way the presence of strongly held carbonate is avoided, and swelling by adipate favours intercalation of the POM units. The spacing ( $d_{003}$ ) is ca. 14.9 Å, indicating pillaring by intact Keggin anions. The intensity of the diffraction peak of the co-phase at 7.89 Å results very low. Although incorporation of the POM units is facilitated by using a two- or three-fold excess of adipate to convert the meixnerite phase to the adipate one, complete exchange was achieved by using only a slight (5%) excess of the POM with an ageing time of 5–10 min at reflux temperature. Nevertheless, the W/Al ratio (theoretical value 2) reaches a value of 2.36 when the Mg/Al ratio is equal to 4, suggesting a partial protonation of the tungstate anions within the LDH galleries. The specific surface areas result rather large (110–140 m<sup>2</sup> g<sup>-1</sup>) and a bimodal microporosity suggests the presence of interlayer and intercrystalline pores.

Intercalation of metatungstate,  $H_2W_{12}O_{42}^{6-}$ , has been scarcely studied [171, 205, 206], although with somewhat random success. We have studied its intercalation following different routes [207], namely anion exchange from a Mg,Al- $NO_3$  precursor at different temperatures and contact times, anion exchange from a Mg,Al adipate precursor (similar to the method described by Pinnavaia [203]), reconstruction from a calcined Mg,Al- $CO_3$  precursor and direct synthesis from precursor salts. The precise conditions are summarised in Table 12.4.

**Table 12.4** Synthesis details, chemical composition and X-ray diffraction data

Sample	Method	Precursor	pH/T/t <sup>a</sup>	wt% W <sup>b</sup>	Mg/Al <sup>c</sup>	W/Al <sup>c</sup>	<i>d</i> (003) <sup>d</sup>
WN1	Anion exchange	Mg <sub>2</sub> Al–NO <sub>3</sub>	6.5/50/15	37.4	2.0	1.2	14.6
WN2	Anion exchange	Mg <sub>2</sub> Al–NO <sub>3</sub>	6.5/50/60	36.9	2.1	1.2	14.6; 10.4
WN5	Anion exchange	Mg <sub>2</sub> Al–NO <sub>3</sub>	6.5/100/30	37.2	2.0	1.1	12.6; 10.4
WN6	Anion exchange	Mg <sub>2</sub> Al–NO <sub>3</sub>	6.5/100/360	37.9	2.0	1.1	10.0
WADP	Anion exchange	Mg <sub>2</sub> Al–adipate	6.5/70/30	35.4	1.95	1.1	10.4
WR	Reconstruction	Mg <sub>2</sub> Al–CO <sub>3</sub>	7/70/360	32.7	1.9	1.0	10.1
WCOP	Direct coprecipitation	coprecipitation	6.5/70/360	27.0	1.6	0.8	10–11 <sup>e</sup>

<sup>a</sup>pH, temperature (°C) and contact time (min)

<sup>b</sup>Weight percentage

<sup>c</sup>Molar ratio

<sup>d</sup>In Å

<sup>e</sup>Poorly crystallised

Source: Adapted with permission from Synthesis and characterization of new Mg<sub>2</sub>Al–paratungstate layered double hydroxides [207]

Regarding the different Mg/Al ratios measured for the different solids, Weir et al. [208] have suggested that the coprecipitation method is worse than anion exchange due to sequential precipitation (first the trivalent and then the divalent one) instead of simultaneous precipitation at pH lower than 10. Sample WN1 (prepared by anion exchange at room temperature and short reaction time) shows a basal reflection of 14.6 Å; although this value has been previously reported for intercalated metatungstate species [27, 87, 203] suggesting that, despite reaction started from paratungstate, it was transformed into metatungstate during the reaction, such a transformation is hardly expected, as pH was maintained at 6–6.5, and so it was concluded that the POM species corresponds to upwards oriented paratungstate A units, while in sample WN5 (prepared at 100 °C for 30 min) the spacing is 12.6 Å, corresponding to paratungstate A with its C<sub>2</sub> axis parallel to the brucite-like layers. Samples WADP, WN6 and WR (see Table 12.1) show a spacing of 10 Å, which could correspond to a poorly ordered Mg polyoxometalate phase [209], or products formed upon partial hydrolysis of the starting POM [209, 210, 211]. However, the recorded XRD maxima do not coincide with those of magnesium paratungstate, nor their FTIR spectra show coincident bands. These authors conclude [207] that intercalated species correspond to W<sub>7</sub>O<sub>24</sub><sup>6-</sup> species with their C<sub>2</sub> axis parallel to the brucite layers and grafted to them, as previously suggested by Clearfield for other POM–LDH systems [210] and demonstrated from XRD and W L(III)-edge EXAFS measurements by Delmas et al. [168] for W<sub>2</sub>O<sub>7</sub><sup>2-</sup> species onto the slabs of a Ni,Co LDH upon calcination at 200 °C; the strong interactions arising upon grafting were demonstrated by the lack of shift of the diffraction maxima upon equilibrating the samples with water vapour.

Oxidation of ethanol on the sample prepared by anion exchange at 100 °C for 30 min and calcined at 500 or 700 °C has been studied by FTIR monitoring of ethanol, acetaldehyde and acetic acid adsorption [212]. According to their PXRD diagrams, the sample calcined at 500 °C is mostly amorphous, but sharp diffraction

peaks develop after calcination at 700 °C, which correspond to wolframite,  $\text{MgWO}_4$  (with octahedrally coordinated  $\text{Mg}^{2+}$  and  $\text{W}^{6+}$  cations) and a similar phase with the same chemical composition, but with tetrahedrally coordinated  $\text{W}^{6+}$  species. Oxidative dehydrogenation on these solids to acetaldehyde or acetic acid may take place on Lewis acid sites ( $\text{W}^{6+}$  and  $\text{Al}^{3+}$ ) whose presence is evidenced by FTIR monitoring of pyridine adsorption, as well as on strongly basic sites,  $\text{O}^{2-}$  or  $\text{OH}^-$ , which presence is evidenced by formation of enolate species ( $\text{CH}_2=\text{CHO}^-$ ) or crotonaldehyde, detected after acetaldehyde adsorption. Although red-ox sites ( $\text{W}^{6+} \rightarrow \text{W}^{4+}$ ) also exist, reducibility (from TPR results) is very low. Acetaldehyde is formed through intermediate ethoxy species, formed by dissociative adsorption of ethanol on acid–base sites with simultaneous formation of hydroxyl groups and water molecules. As reducibility is very low, especially for the sample calcined at 700 °C, acetaldehyde should be formed through simple dehydrogenation, which is favoured on basic sites. However, the sample calcined at 500 °C being more easily reducible, oxidative dehydrogenation is also possible, following a Mars-van Krevelen mechanism [213]. Acetate is not formed on the sample calcined at 500 °C, while Cannizzaro disproportionation of acetaldehyde into ethoxy and acetate species has been observed on both samples at room temperature and 100 °C.

Several tungsten-containing POMs have been intercalated in meixnerite, namely lacunary Dawson ion ( $\alpha\text{-P}_2\text{W}_{17}\text{O}_{61}$ ) $^{10-}$ , the Finke  $[\text{Zn}_4(\text{H}_2\text{O})_2(\text{AsW}_9\text{O}_{34})_2]^{10-}$  and  $[\text{WZn}_3(\text{H}_2\text{O})_2(\text{ZnW}_9\text{O}_{34})_2]^{12-}$  ions, the double Dawson  $[\text{P}_4\text{W}_{30}\text{Zn}_4(\text{H}_2\text{O})_2\text{O}_{112}]^{16-}$  and the polyoxocryptates ( $\text{NaSb}_9\text{W}_{21}\text{O}_{86}$ ) $^{18-}$  and ( $\text{NaP}_5\text{W}_{30}\text{O}_{110}$ ) $^{14-}$  [88]. Meixnerite had been prepared by rehydration of a carbonate precursor calcined at 500 °C and was suspended in an aqueous solution containing a threefold excess of dissolved POM, in  $\text{N}_2$  at 70 °C. According to FTIR and in some cases  $^{31}\text{P}$  MAS-NMR spectroscopies, all POMs keep their integrity after intercalation, and the molecules are intercalated with their  $\text{C}_2$  axis orthogonal to the layer stacking direction, while the cryptate POMs are intercalated with the major axes parallel to the LDH layer. The samples exhibit a wide range of specific surface areas (30–120  $\text{m}^2 \text{g}^{-1}$ ) and up to ca. 60% of the total surface is due to the presence of gallery micropores.

A Zn,Al LDH in the nitrate form was used as a precursor to intercalate ( $\text{NaP}_5\text{W}_{30}\text{O}_{110}$ ) $^{14-}$  by anion exchange at 95 °C and pH 6 and tested for the oxidation of cyclohexene with  $\text{H}_2\text{O}_2$  in  $(\text{BuO})_3\text{PO}$  [88]. As for the previous set of samples, microporous surface area was lower than expected, probably by the deposition of a POM salt impurity characterised by a PXRD signal at ca. 15 Å, together with that of the intercalated product at ca. 22.0 Å. The activity in the named reaction (mostly forming cyclohexanediol) was different from that for the unsupported ( $\text{NaP}_5\text{W}_{30}\text{O}_{110}$ ) $^{14-}$  anion, and the turnover number for epoxide formation increased with the relative amount of the impurity, which is probably dispersed on the surface and edges of the LDH particles. The change in selectivity is mainly attributable to the less acidic nature of the LDH–POM system.

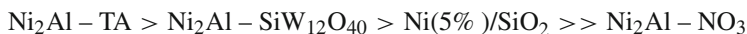
Jitkarna et al. [214] have intercalated Keggin-type POMs,  $\text{PW}_{12}\text{O}_{40}^{3-}$  and  $\text{SiW}_{12}\text{O}_{40}^{4-}$ , in Mg,Al LDHs previously swelled with deoxycholate (DA), the anion of a secondary biliar acid which provides a gallery height of 28 Å by formation

of a bilayer of anions with their carboxylate groups pointing towards the brucite-like layers [215]. The DA LDH had been prepared by direct synthesis at pH 8–10, while the POM-containing samples were prepared by anion exchange at pH 8. Exchange is extremely easy, as the gallery heights for these POMs is ca. 13–15 Å, one half of the free height in the DA LDH precursor. The solids prepared have been calcined at increasing temperatures and have been characterised by PXRD and thermal analyses and tested in SCR of NO with NH<sub>3</sub>. Five consecutive decomposition stages have been identified, forming different phases: (i) the original dried layered materials (which were not tested as catalysts in the named reaction), (ii) dehydrated layered solids at 250 °C, (iii) dehydroxylated layered solids with specific surface areas ranging between 48 and 79 m<sup>2</sup> g<sup>-1</sup> at 350 °C, (iv) amorphous mixed oxides with specific surface areas between 108 and 125 m<sup>2</sup> g<sup>-1</sup> at 500 °C, and (v) crystalline – MgO, MgAl<sub>2</sub>O<sub>4</sub> spinel and MgWO<sub>4</sub> – mixed oxides at 900 °C. All clay catalysts gave over 99% N<sub>2</sub>/N<sub>2</sub>O selectivity at all temperatures tested, the highest activities (which increased with the reaction temperature) being measured for the catalysts calcined at 500 °C, for which surface Brønsted sites associated with Mg–O–Al units exist. Probably, crystalline phases (spinel and MgWO<sub>4</sub>) formed at higher calcination temperatures suppress the activity, while Brønsted acidity also decreases. NO conversion was increased from a maximum of 31.2% at 450 °C for catalyst PW<sub>12</sub>O<sub>40</sub><sup>3-</sup>-POM calcined at 500 °C to 46.3% on the same catalyst doped (by impregnation) with 5% Fe, probably because of development of Brønsted acid sites related to Fe=O or Fe-OH moieties.

The easiness with which intercalation of POMs in LDHs is achieved has been related to a compatibility between the positive charge density of the layers, the formal charge of the POM and its molecular size. According to Kwon and Pinnavaia [216] only those POMs whose negative charge is more than five could be easily exchanged with nitrate in Zn<sub>2</sub>Al–NO<sub>3</sub>; no exchange was observed for SiW<sub>12</sub>O<sub>40</sub><sup>4-</sup> and only partial exchange occurred for PCuW<sub>11</sub>O<sub>39</sub><sup>5-</sup>. The reason is that the area per unit charge in Zn<sub>2</sub>Al–NO<sub>3</sub> is ca. 16.6 Å<sup>2</sup> and the diameter of a Keggin anion is ca. 9.8 Å; if the Keggin anions are close packed, the cross-section of each anion is estimated to be 83.1 Å<sup>2</sup>, occupying the area corresponding to five positive charges in the brucite-type layer of Zn<sub>2</sub>Al. To overcome this problem, Tatsumi et al. [217] have prepared systems where the Zn/Al molar ratio has been increased, thus resulting in an increase in the space/charge ratio in the interstices between LDHs; for comparison, other LDHs have been prepared and several Keggin and lacunary Keggin ions have been intercalated, and the solids been tested as catalysts for epoxidation of alkenes. Zn<sub>*n*</sub>Al–NO<sub>3</sub> (*n* = 2, 3, 4), Mg<sub>2</sub>Al–NO<sub>3</sub> and Ni<sub>2</sub>Al–NO<sub>3</sub> were prepared by the induced hydrolysis method [172] at pH 7; SiW<sub>12</sub>O<sub>40</sub><sup>4-</sup> was incorporated by ion exchange at pH 4, but according to XRD data it was unsuccessful; Zn<sub>2</sub>Al–SiW<sub>9</sub>O<sub>34</sub> was prepared by the same method without added HNO<sub>3</sub>; and Zn<sub>3</sub>Al–SiW<sub>11</sub>O<sub>39</sub> was prepared following the method described by Narita et al. [209]. For the Zn<sub>3</sub>Al and Zn<sub>4</sub>Al exchanged systems a basal spacing of 14.7 Å was measured, confirming intercalation, although the by-product characterised by a XRD line at 6.5–10° (2θ) was also detected. Exchange led to an increase in the BET surface area from 11 m<sup>2</sup> g<sup>-1</sup>

for  $\text{Zn}_3\text{Al-NO}_3$  to  $46 \text{ m}^2 \text{ g}^{-1}$  for  $\text{Zn}_3\text{Al-SiW}_{12}\text{O}_{40}$ , although no data is reported about the possible microporosity of the sample.

Oxidation of cyclohexene with  $\text{H}_2\text{O}_2$  led to cyclohexene oxide, 1,2-cyclohexanediol and 1,2-cyclohexanedione,  $\text{SiW}_{11}\text{O}_{39}^{8-}$  showing larger activity than  $\text{SiW}_{12}\text{O}_{40}^{4-}$  whether intercalated or not, although total TON was larger for the unintercalated system and hydrolysis of epoxide was retarded for the intercalates, probably because of the lowered acidity of the catalyst. A definitive proof demonstrating that the reaction occurred inside the LDH galleries arised from the study of the oxidation of cyclohexene, cyclooctene and cyclododecene, the relative reaction rate decreasing as the size of the substrate was increased because of lowered diffusivity. When the oxidation of cyclohexene was performed with  $\text{O}_2$  in the presence of isobutyraldehyde,  $\text{SiW}_{12}\text{O}_{40}^{4-}$  was superior to  $\text{SiW}_{11}\text{O}_{39}^{8-}$ , and on changing the LDH matrix the activity decreased in the order  $\text{Ni}_2\text{Al} \gg \text{Mg}_2\text{Al} > \text{Zn}_3\text{Al}$ ; actually, for a  $\text{Ni}(5\%)/\text{SiO}_2$  catalyst prepared by impregnation,  $\text{Ni}_2\text{Al-NO}_3$  and a  $\text{Ni}_2\text{Al-LDH}$  with intercalated terephthalate (TA), the activity decreased in the order.

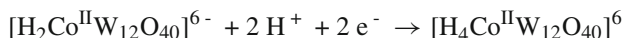
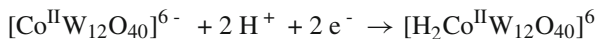
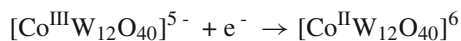


Thus concluding that the reaction was actually catalysed by Ni in the brucite-type layers. Swelling of the layers by intercalated terephthalate anion is probably responsible for the enhanced activity of this catalyst if compared to the nitrate analogue.

Metatungstate and tungstoniobate-containing Mg,Al and Zn,Al LDHs have been studied for cyclooctene epoxidation at  $60^\circ\text{C}$  [218] using different solvents (acetone, ethanol or acetonitrile) and oxidants (aqueous  $\text{H}_2\text{O}_2$  or *t*-BuOOH); the samples were prepared by anion exchange from the nitrate precursors using  $(\text{NH}_4)_6\text{H}_2\text{W}_{12}\text{O}_{40}$  (samples MgAl-W and ZnAl-W) and  $\text{N}(\text{CH}_3)_4\text{Na}_3\text{W}_4\text{Nb}_2\text{O}_{19}$  (samples MgAl-W/Nb and ZnAl-W/Nb) at pH 5.5 or 4.5 and  $80^\circ\text{C}$  or room temperature, respectively. The solids show gallery heights of 9.7 and 7.2 Å, respectively, and the PXRD diagrams showed in both cases the broad diffraction peak at 9–11 Å usually ascribed to a  $\text{M}^{2+}$  POM salt. The FTIR spectra showed the characteristic bands due to the POM, indicating that the molecular structures do not undergo any significant change upon intercalation. Thermal decomposition takes place in the expected [125] two steps (dehydration and dehydroxylation combined with collapsing of the structure), followed by an exothermic effect ascribed to crystallisation of Mg ( $573^\circ\text{C}$ ) or Zn ( $482$  and  $668^\circ\text{C}$ ) tungstates, and no crystalline phase containing Al or Nb was detected. The original samples show BET surfaces areas of 20–25 (tungstate) or 70–90 (tungsto-niobate)  $\text{m}^2 \text{ g}^{-1}$ , with an appreciable microporosity content, especially in the tungsto-niobate samples. The pristine Mg,Al and Zn,Al LDHs show cyclooctene conversions lower than 7% using any of the solvents tested. When using EtOH as a solvent and hydrogen peroxide as an oxidant, the ZnAl-W and ZnAl-W/Nb catalysts showed both epoxidation and catalase (disproportionation of  $\text{H}_2\text{O}_2$  into  $\text{H}_2\text{O}$  and  $\text{O}_2$ ) activities, the latter significantly large than the former, and similar results were observed for the Mg samples. However, when *t*-BuOOH was

used as an oxidant, negligible activity was observed. On the contrary, the unsupported POM salts produced only 1,2-cyclooctanediol. These differences between the intercalated and the free POMs can be ascribed to subtle changes in basicity arising from the presence of the LDH matrix. Leaching was, however, observed, as reaction proceeded with the liquid (EtOH–H<sub>2</sub>O<sub>2</sub>) after filtering the solid.

A tungstocobaltate POM with the Keggin-type structure [CoW<sub>12</sub>O<sub>40</sub>]<sup>5-</sup> has been intercalated in a Mg,Al LDH trying to prepare solids with multifunctional properties, considering the strong oxidising ability of Co<sup>3+</sup> cations [219]. The solid was prepared by anion exchange from a Mg,Al nitrate LDH precursor at pH 6.5 at 90 °C. The PXRD diagram shows a gallery height of 10.1 Å, in agreement with the size (10.2 Å) of the anion along its C<sub>2</sub> axis; as for most of POM–LDH systems, a broad diffraction close to 9 Å is also recorded. FTIR spectra showed bands in the same positions as for K<sub>5</sub>[CoW<sub>12</sub>O<sub>40</sub>] and the absence of those of nitrate, indicating complete exchange and that the structure of the Keggin anion is maintained. Collapsing of the structure is observed at 400 °C, after dehydration and dehydroxylation. The electrochemical behaviour of CoW<sub>12</sub>O<sub>40</sub>–LDH was investigated by using a CPE (carbon paste electrode) in 2 M H<sub>2</sub>SO<sub>4</sub> by cyclic voltammetry. It exhibits one reversible 1-electron and two 2-electron redox processes corresponding to Co<sup>3+</sup>/Co<sup>2+</sup> couple and W waves, respectively:



similar to the electrochemical behaviour observed for pure K<sub>5</sub>[CoW<sub>12</sub>O<sub>40</sub>].

Additional information about the structure of the POM–LDH was obtained from magnetic susceptibility measurement. The  $\chi_m T$  value remains basically constant at 2.97 cm<sup>3</sup> K (mol Co)<sup>-1</sup> from room temperature down to 100 K, only very slightly less than the expected value (3.00 cm<sup>3</sup> K (mol Co)<sup>-1</sup>) for one non-interacting Co<sup>3+</sup> centre with  $S = 2$ , and then slowly decreases, indicating an antiferromagnetic interaction between the transition metal ions; the Curie–Weiss constants were  $C = 3.03 \text{ cm}^{-1} \text{ K (mol Co)}^{-1}$  and  $\theta = -8.54 \text{ K}$ , indicating a weak antiferromagnetic coupling between Co<sup>3+</sup> centres, probably affected by the ordered arrangement of the anions in the interlayer space of the LDH.

Oxidation of benzaldehyde with H<sub>2</sub>O<sub>2</sub> showed an increase in conversion with the reaction temperature, the selectivity and conversion decreasing at 90 °C. Yield reached a value of 98.8% for the POM–LDH catalyst, markedly larger than for the unloaded LDH (75%) and the free POM (77%), although the activity decreased after 5 h reaction, probably from an unknown by-reaction.

As already shown along this review, heteropoly compounds are active oxidation catalysts, their performance being increased by the incorporation of transition metals, especially when these metals occupy the lacunary or defect position of the POM structure; actually, these compounds can be also viewed as transition metal complexes where the POM unit acts as a ligand. Jana et al. [220] have prepared Mg,Al LDHs intercalated with  $\alpha$ -[SiW<sub>9</sub>O<sub>37</sub>(Co(H<sub>2</sub>O)<sub>3</sub>)]<sup>10-</sup> following different routes and have tested them in liquid-phase oxidation of cyclohexanol and other substrates with molecular oxygen. As expected, direct exchange with a Mg,Al-CO<sub>3</sub> LDH precursor (sample I) was unsuccessful; exchange with a meixnerite form (prepared by rehydration of the carbonate precursor calcined at 450 °C for 15 h) also failed (sample II), and intercalation was only achieved by exchange after swelling the meixnerite form with adipate (sample III). Probably the adipate-containing precursor somewhat limits the acid-base reaction with POM, as dissolution of Mg<sup>2+</sup> (measured from the magnesium content in the solids) decreased in the order I > II > III. The small amounts of cobalt found in samples I and II (ca. 3% of the content in sample III) might correspond to species adsorbed on the external surface of the crystallites. Microporosity also developed in sample III. FTIR and UV-Vis spectroscopies demonstrated the integrity of the POM after intercalation.

Only sample III was tested for selective oxidation of cyclohexanol to cyclohexanone with oxygen at atmospheric pressure using 1,4-dioxane as a solvent. Conversion increased linearly with time, reaching a value of 67% (62% for the unintercalated POM) after 12 h reaction, always with selectivity of 100% to cyclohexanone; a small amount of by-products (keto-1,4-dioxane) was found even in the absence of cyclohexanol, indicating that they arise from the solvent used. Lower performances were measured for POMs with similar structures containing Cu, Fe, Ni or Cr. The activity of sample III was larger than those shown by Pt(10%)/MgO, RuO<sub>2</sub>(10%)/FAU, Ru<sub>0.35</sub>MnFe<sub>1.5</sub>Cu<sub>0.15</sub>O<sub>x</sub> and Ru<sub>0.3</sub>Co<sub>2</sub>CeO<sub>x</sub>, but lower than that shown by Ru-tungstosilicate (although showing a larger selectivity to cyclohexanone). The Co-POM-LDH catalyst resulted unaltered (according to the spectroscopic results) after the catalytic runs, and no leaching was either observed, and could be used four times without noticeable decrease in selectivity. The catalyst was also successful for oxidation of benzyl alcohol, showing higher conversion and selectivity (79 and 98.4%, respectively) to benzaldehyde than the unintercalated POM (68 and 85.9%).

Gardner and Pinnavaia [171] have prepared Mg,Al and Zn,Al LDHs intercalated with polyoxotungstate. Two approaches were followed: (i) exchange of the terephthalate-preswelled LDH with Na<sub>2</sub>WO<sub>4</sub> at pH 4.4 or (ii) exchange of a Zn<sub>2</sub>Al-NO<sub>3</sub> LDH with aqueous (NH<sub>4</sub>)<sub>6</sub>H<sub>2</sub>W<sub>12</sub>O<sub>40</sub> at pH 4.3 and digestion at 80 °C for 18 h. The X-ray diffraction pattern of the first sample showed two typical signals, one at 10.1 Å due to the salt-like impurity and another one at 12.1 Å, which is not consistent with the value, 14.1 Å, previously reported [27] for H<sub>2</sub>W<sub>12</sub>O<sub>42</sub><sup>10-</sup> intercalated into an LDH.

Hydrolysis reactions of WO<sub>4</sub><sup>2-</sup> are very complex: at pH 9 the predominant species is WO<sub>4</sub><sup>2-</sup>; W<sub>7</sub>O<sub>24</sub><sup>6-</sup> is formed at pH 5–6, but is converted into H<sub>2</sub>W<sub>12</sub>O<sub>42</sub><sup>10-</sup> at pH 4.4. The spacing value measured (12.1 Å) is consistent with

intercalation of  $W_7O_{24}^{6-}$ . On the contrary, the sample prepared by exchange of the nitrate precursor showed a spacing of 14.6 Å, again with the impurity characterised by a diffraction at 11.1 Å, and shows microporosity (i.e. it is actually pillared) after outgassed at 150 °C.

The intercalated LDH are far less reactive than the unsupported POMs in peroxide oxidation of cyclohexene, consistently with their accessibility to the gallery POM centres under reaction conditions; leaching was not observed and the  $H_2W_{12}O_{40}^{6-}$  catalyst yielded a mixture of epoxide and the diol when unsupported, but exclusively the diol when intercalated, probably because the acid–base properties of the LDH may promote ring opening of the epoxide to the diol. Finally, these authors [171] stress that an aluminium salt of  $H_2W_{12}O_{40}^{6-}$  gave a XRD pattern similar to that of the impurity phase observed for the intercalated compounds and also showed activity in the tested reaction, so its contribution to the activity results found cannot be ignored.

Tungstate-intercalated LDHs have been also used as biomimetic catalysts for mild oxidative bromination and bromide-assisted epoxidation reactions, finding that the activity is one hundred times larger than that shown by the homogeneous analogue. These studies are very important from the environmental point of view, as conventional bromination methods typically use elemental bromine, a pollutant and health hazard, and alternate compounds, such as haloperoxidase enzymes, have been used. Jacobs et al. [221] have used M,Al–Cl (M = Mg, Ni) LDHs exchanged with tungstate; XRD data show no swelling upon exchange, despite Raman spectroscopy showed the typical features of tetrahedral  $WO_4^{2-}$  units, which indicates that  $WO_4^{2-}$  should be mainly located in edge positions. Conversion of phenol red (phenolsulphonphthalein) into bromophenol blue (tetrabromophenolsulphonphthalein) was complete in the presence of the catalyst,  $NH_4Br$  and  $H_2O_2$ , reaction probably proceeding through  $H_2O_2$  coordination on the metal and formation of peroxo species, identified in the UV–Vis reflectance spectrum (colour changing from white to yellow); their reaction with bromide recovers tungstate forming bromine, which brominate phenol red, Fig. 12.10. The reaction was not observed to proceed in the absence of tungstate-LDH [222]. When LDHs containing different divalent

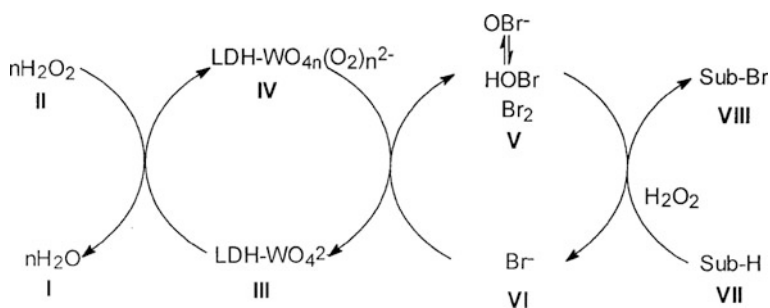


**Fig. 12.10** Plausible reaction mechanism for the oxybromination by Mg,Al-WO<sub>4</sub>-LDH. Reprinted from [225], with permission from Elsevier



cations in the interlayer were used, the activity decreased in the order  $\text{Mg}^{2+} > \text{Ni}^{2+} > \text{Zn}^{2+}$  when the counteranion was chloride and  $\text{Mg}^{2+} > \text{Zn}^{2+}$  when it was nitrate, although no definitive explanation for this behaviour was reported [222].

Catalytic decomposition of  $\text{H}_2\text{O}_2$  into singlet oxygen ( $^1\text{O}_2$ ) can be achieved by haloperoxidase assisted by bromide anions in the absence of any organic substrate. An analogous effect is observed for  $\text{Mg,Al-WO}_4^{2-}$  LDH, although  $^1\text{O}_2$  production is considerably slower than on  $\text{Mg,Al-MoO}_4^{2-}$  [187]. The reaction is extremely low with LDH containing exclusively nitrate anions; however, a slight increase in the decomposition rate is observed with cointercalated nitrate-tungstate samples, due to the thermal instability of peroxotungstate and the formation of  $^1\text{O}_2$ ;  $\text{H}_2\text{O}_2$  decomposition in the presence of bromide proceeds more than 60 times faster. Singlet molecular oxygen was identified by its luminiscence at ca. 1268 nm due to the forbidden  $^1\text{O}_2 (^1\Delta_g) \rightarrow ^3\text{O}_2 (^3\Sigma_g^-)$  transition [221, 222].

Regarding mild oxidative bromination and bromide-assisted epoxidation with  $\text{H}_2\text{O}_2$ , it has been found that the high halogenation activity of the  $\text{Ni,Al-WO}_4^{2-}$  catalyst mimics the activity of V-bromoperoxidase enzymes [223]. Bromination of dimethoxytoluene (DMT) with  $\text{Ni,Al-WO}_4^{2-}$  LDH in the presence of  $\text{NH}_4\text{Br}$  and  $\text{H}_2\text{O}_2$  in methanol yielded exclusively ring-substituted bromo-DMT, indicating that the oxidised bromine species is  $\text{Br}^+$  rather than  $\text{Br}^\bullet$  [183], as a radical reaction would also yield dimethoxybenzylbromide [222, 223]. On comparing the bromination performance of this catalyst to those of several homogeneous or heterogeneous mimics, it has been found that (i) tungstate has a much higher activity when supported on the LDH than in solution, the reaction proceeds in mild pH conditions (6–8), in sharp contrast with previous mimics which require strong acidic conditions ( $\text{pH} < 2.5$ ); probably the large positive electric potential of the tungstate-LDH surface induces an enrichment of bromide ions close to the surface. (ii) The activity of the  $\text{Mg,Al-WO}_4^{2-}$  system is much larger than any other solid inorganic mimic or any heterogeneous redox catalyst. (iii) Immobilisation of the enzymes is preferred in industrial applications than their use in homogeneous conditions to improve reusability and stability, but this reduces the activity, a drawback not shown by the  $\text{WO}_4^{2-}$  LDH system. Bromide-assisted epoxidation proceeds via intermediate bromohydrin and becomes the main reaction (against bromination) by switching from biphasic conditions to a single liquid phase [223].

The tungstate-containing takovite,  $\text{Ni,Al-WO}_4^{2-}$  LDH, catalyst – prepared by direct exchange with a  $\text{Ni,Al-NO}_3$  precursor without pH control – has been also used for oxidative halogenation of anhydrosugars and related dihydropyrans [224] in view of replacing hazardous or polluting agents such as elemental halogens or hypervalent  $\text{I}^{3+}$  or  $\text{I}^{5+}$  reagents, starting from  $\text{NH}_4\text{Br}$  or  $\text{NH}_4\text{I}$ . Delivery of  $\text{BrO}^-$  or  $\text{IO}^-$  from  $\text{H}_2\text{O}_2$  and the immobilised tungstate leads to reaction with the enol ether substrates. The role of the LDH matrix, in addition to immobilisation of the peroxotungstate species, is to compensate the charge repulsion between the halides and the peroxotungstate. No leaching of tungstate was observed [190], despite the expected competition for intercalation with  $\text{Br}^-$  or  $\text{I}^-$ , but the stronger electrostatic interactions of the former with the brucite-like layers probably prevents such a leaching.

The importance of tungstate-LDH catalysts in environmental respectful bromination reactions has been also enhanced by Choudary et al. [22] during bromination of aromatic compounds. These authors also studied Ni,Al and Mg,Al LDHs in their chloride forms as precursors, incorporation of tungstate being carried out by exchange at room temperature for 24 h. As for Jacobs et al. catalysts [221–223], exchange does not occur and tungstate species are believed to be at edge-on positions of the LDH structure. Bromination of several substrates (e.g. anisole, acetanilide, methylenedioxybenzene, phenyl-dimethyl-amine, *p*-methylphenol) was achieved with yields 74–92% at 72 °C. Bromination of bisphenol-A (BA) to tetrabromobisphenol-A (TBBA), an important fire retardant, was tested on these catalysts and other tungsten-based homogeneous and heterogeneous catalysts (e.g. Mg, Al or Na tungstate), Fig. 12.11.

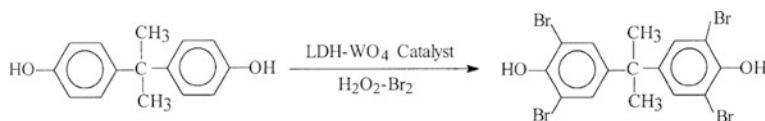


**Fig. 12.11** Bromination of bisphenol-A to tetrabromobisphenol-A catalysed by Mg,Al-WO<sub>4</sub>-LDH. Reprinted from [225], with permission from Elsevier

The LDH-based catalysts showed the largest yields (95–96%), purity (>99.5%) and TOF (five times larger than Al<sub>2</sub>(WO<sub>4</sub>)<sub>3</sub>). The reaction proceeds with only a slight excess of H<sub>2</sub>O<sub>2</sub> and Br<sub>2</sub> above the stoichiometric values. The mechanism proposed by these authors [225] is essentially identical to that proposed by Jacobs et al. for phenol red bromination [221]; formation of singlet oxygen is ruled out as the consumption of H<sub>2</sub>O<sub>2</sub> approximates to the amount predicted by the stoichiometric requirement. Lower yields were observed when using toluene or other hydrocarbons as solvents, and the best results were obtained with 1,2-dichloroethane, which could be recovered (97–98%) and reused for five to six cycles without any loss of activity or selectivity.

Applications of POM-LDH systems as heterogeneous thermal acid–base or oxidation catalysts have been limited in some aspects by the relatively low thermal stability of the pillared compounds; however, they are very suitable for photocatalysis processes, usually taking place at room temperature. Actually, POMs have a number of features in common with semiconductor metal oxides (the most widely used TiO<sub>2</sub>) [226], such as low toxicity, and are also environmentally benign catalysts. Such a photochemical activity has been observed for heptatungstate or paratungstate A, W<sub>7</sub>O<sub>24</sub><sup>6-</sup> (briefly W<sub>7</sub>). Hu et al. [227] have reported that a Mg<sub>2</sub>Al-W<sub>7</sub> system shows good photocatalytic activity for degradation of hexachlorocyclohexane (HCH), without undergoing deactivation after five cycles. The sample was prepared by anion exchange at pH 6.5 and 70 °C of Mg<sub>2</sub>Al-LDH containing terephthalate in the interlayer with an aqueous solution of Na<sub>2</sub>WO<sub>4</sub>·2H<sub>2</sub>O acidified (to polymerise the tungstate anion) at pH 6–7; simultaneous protonation of terephthalate anion assists its removal from the interlayer space. It should be stressed that at this pH paratungstate A (W<sub>7</sub>O<sub>24</sub><sup>6-</sup>) is in equilibrium with paratungstate B

( $\text{H}_2\text{W}_{12}\text{O}_{42}^{10-}$ ), the concentration of the former increasing at pH close to 6, low concentrations, low ionic strength and high temperature. The solid is characterised by the expected diffraction maximum at 12.3 Å (although a maximum at 10.2 Å suggests the formation of the know by-product), suggesting insertion of the POM with its  $C_2$  axis perpendicular to the LDH layers, thus providing maximum hydrogen bonding interactions with the hydroxyl groups of the layers. The integrity of the POM was confirmed by FTIR and UV/DR spectroscopies. However, the W/Mg content was slightly larger than expected due to (i) partial dissolution of  $\text{Mg}^{2+}$  in the acidic medium or (ii) an excess of  $\text{W}_7\text{O}_{24}^{6-}$  ions physically adsorbed on the positively charged layers. The specific surface area was ca.  $44 \text{ m}^2 \text{ g}^{-1}$  (ca.  $10 \text{ m}^2 \text{ g}^{-1}$  for the unsupported POM), without accessible microporous or mesoporous structure (contrary to previous findings for POM-LDH systems which exhibited some or appreciable microporosity [88, 124, 171, 178, 218, 220]), probably because of crowding of the interlayer by the POM units.

Photodegradation of HCH was not observed upon irradiation in the absence of  $\text{Mg}_2\text{Al-W}_7$  or in the presence of the LDH support (without POM loading), but complete mineralisation was achieved by recovery of 97.6% chlorine after 10 h irradiation. The authors assume that the interlayer  $\text{W}_7$  anion is photoexcited and the HCH molecules diffuse into the interlayer space and are photoactivated by the photoexcited  $\text{W}_7$  and then degraded and totally mineralised. However, this process can be hardly accepted, if no microporosity nor mesoporosity exist and access to the interlayer is hindered by an excessive crowding of the interlayer. Disappearance of HCH followed a Langmuir-Hinshelwood first-order kinetics law. From GC/MS and ion chromatography authors conclude a reaction where HCH is first transformed into hexachlorobenzene, then hexahydroxybenzene and tetrahydroxybenzoquinone, this forming acetic and formic acids, which are fully mineralised to  $\text{CO}_2$  and  $\text{H}_2\text{O}$ ; formation of hexanediacid was also observed. Leaching amounts only 5% of the initial  $\text{W}_7$  content.

These authors have also studied this same photocatalytic reaction (photodegradation of HCH) on calcined POM-LDH systems [228].  $\text{Zn/Al/W(Mn)}$  mixed oxides were prepared by calcination at 600–700 °C of a  $\text{Zn}_2\text{Al}$  LDH containing  $\text{SiW}_{11}\text{O}_{39}^{8-}$  or  $\text{SiW}_{11}\text{O}_{39}\text{Mn}(\text{H}_2\text{O})^{6-}$  (briefly  $\text{SiW}_{11}$  and  $\text{SiW}_{11}\text{Mn}$ , respectively). These authors claim that an improvement of the photocatalytic activity is expected (if compared to the layered, uncalcined structures), and also loss of POM (weakly held to the layers by electrostatic forces and hydrogen bonding) during the catalytic runs would be avoided; moreover, separation of POM-LDH from the reaction system is difficult because of its milky dispersion. The POM-LDH precursors were prepared by exchange at pH 4.5 and 90 °C for 6 h of a Zn,Al-nitrate precursor with the potassium salts of the POMs. The gallery heights were close to 10 Å, suggesting again an orientation of the POM (unaltered, according to FTIR spectroscopy results) with its  $C_2$  axis perpendicular to the LDH layers, and formation of the co-phase was also observed. The specific surface areas changed from  $20 \text{ m}^2 \text{ g}^{-1}$  for the as-synthesised POM-LDH samples to  $83 \text{ m}^2 \text{ g}^{-1}$  upon calcination at 400 °C (forming a mostly amorphous phase together with  $\text{ZnO}$  and  $\text{ZnAl}_2\text{O}_4$ ) and finally dropping

to  $35 \text{ m}^2 \text{ g}^{-1}$  at  $600\text{--}700^\circ\text{C}$  for the mixed oxides (samples ZnAl–SiW<sub>11</sub>–MO and ZnAl–SiW<sub>11</sub>Mn–MO), with simultaneous crystallisation of spinels ZnAl<sub>2</sub>O<sub>4</sub> and ZnWO<sub>4</sub>; according to EPR results, manganese is in the tetravalent state.

Conversions of HCH on different catalysts are shown in Fig. 12.12 (blank reaction on LDH without tungsten species or in the dark yielded no conversion). All these compounds are formed by  $d^0$  cations and can be photoexcited and form oxygen-to-metal charge transfer (OMCT) excited states with considerable oxidising ability; therefore, HCH molecules were photoexcited by these metal oxides and then photooxidised into CO<sub>2</sub> and H<sub>2</sub>O. Although the performance might be related to the OMCT values for these catalysts, the reason for the best performance observed for the calcined POM–LDH systems remains unclear, and the role of specific surface area and porosity features cannot be ignored.

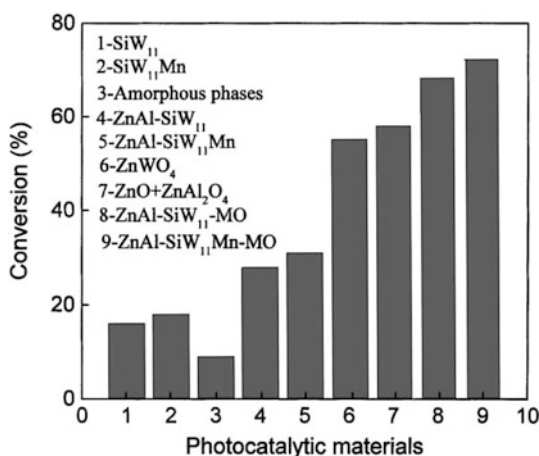


**Fig. 12.12** Photocatalytic activity of various photocatalytic materials to the degradation of an aqueous HCH (0.14 mM). The content of each active component in the solids or aqueous solutions was  $\approx 0.015$  mM. Turnover number was  $\approx 9.3$ . Irradiation time was 4 h. Conversion (%) =  $(1 - [\text{HCH}]_t / [\text{HCH}]_0) \times 100$ , where  $[\text{HCH}]_t$  and  $[\text{HCH}]_0$  represent  $t$  time and initial concentration of HCH, respectively. Reprinted from [228], with permission from Elsevier

Propene epoxidation has been also studied on POM–LDHs. Liu et al. [229] have reported on a complex system, consisting of a M,Al LDH ( $M = \text{Mg}, \text{Zn}$ ) with a small (5% atomic) Pd content isomorphically substituting the divalent cations (larger contents would segregate extra-lattice Pd species [8]), and with peroxo-polyoxometalates derived from  $\text{PW}_{11}\text{O}_{39}^{7-}$  (briefly  $\text{PW}_{11}$ ) in the interlayer. The sample was prepared by anion exchange at pH 4.5 and  $60^\circ\text{C}$  for 6 h of a Pd,Mg,Al–NO<sub>3</sub> precursor in an aqueous  $\text{Na}_7\text{PW}_{11}\text{O}_{39}$  solution. Upon reaction with 30% H<sub>2</sub>O<sub>2</sub>,  $\text{PW}_{11}\text{O}_{39}^{7-}$  undergoes in situ decomposition to peroxo-polyoxometalates,  $\text{PO}_4[\text{WO}(\text{O}_2)_2]_4^{3-}$  (briefly  $\text{PW}_4$ ) and  $\text{W}_2\text{O}_3(\text{O}_2)_4(\text{H}_2\text{O})_2^{2-}$  (briefly  $\text{W}_2$ ), which are immediately fixed in the interlayer region between the brucite-like layers by electrostatic interactions and hydrogen bonding. These

changes are confirmed by XRD, showing spacings of 8.9 Å for the nitrate precursor, 14.6 Å for the  $\text{PW}_{11}$ -containing LDH and 11.2 and 10.3 Å for those containing  $\text{PW}_4$  and  $\text{W}_2$ , respectively, in agreement with the diameters for these species. It is noteworthy that XRD data did not show formation of the common by-product in this case. Formation of these species was concluded from FTIR spectroscopy, on comparing the spectra of the samples with reference compounds, namely (i)  $\text{Na}_7\text{PW}_{11}\text{O}_{39}$  with five characteristic bands at 1100 and 1050 ( $\text{P-O}_a$ ), 950 ( $\text{W-O}_d$ ), 890 ( $\text{W-O}_b\text{-W}$ ) and 810 and 740  $\text{cm}^{-1}$  ( $\text{W-O}_c\text{-W}$ ); (ii)  $(\text{TBA})_4\text{PO}_4[\text{WO}(\text{O}_2)_2]_4$  with bands at 1075 and 1045 ( $\nu_{\text{P-O}}$ ), 940 ( $\nu_{\text{W-O}}$ ) and 840  $\text{cm}^{-1}$  ( $\nu_{\text{O-O}}$ ); and (iii)  $\text{K}_2[\text{W}_2\text{O}_3(\text{O}_2)_4(\text{H}_2\text{O})_2]$ , with bands at 980, 960, 850, 835, 775 and 615  $\text{cm}^{-1}$ .  $^{31}\text{P}$  MAS-NMR spectra show a single band ( $\delta = -10.4$  ppm) for  $\text{Na}_7\text{PW}_{11}\text{O}_{39}$  and  $\text{PdMgAl-PW}_{11}$  LDH, but three signals (3.6, 5.6 and 5.8 ppm) upon treatment with 30%  $\text{H}_2\text{O}_2$ . However,  $^{27}\text{Al}$  MAS-NMR showed in all cases a single line at 8 ppm due to octahedrally coordinated Al. The authors claim that as no chemical bond is formed between the LDH layers and the interlayer anions, decomposition of  $\text{PW}_{11}\text{O}_{39}^{7-}$  proceeds equally in the homogeneous system and in the interlayer.

Epoxidation of propene [229] with molecular oxygen proceeded on this catalyst only in methanol, but not in acetonitrile, and only in a minor extent (4.3% conversion and 8.9% selectivity) when using the  $\text{PdMgAl-NO}_3$  precursor (i.e. the peroxopolyoxometalate species is essential). The Pd K-edge EXAFS FT spectra showed a band at 1.6 Å, coincident with that recorded for PdO, but the first Pd-Pd interaction at 2.5 Å was almost negligible and the second Pd-Pd at 2.9 Å was absent, confirming that  $\text{Pd}^{2+}$  ions are isomorphically substituting  $\text{Mg}^{2+}$  cations and not forming PdO crystals. After the reaction the Pd-O interaction disappeared, whereas an interaction attributed to the Pd-Pd bond (coincident with that for a Pd foil) appeared at 2.3 Å, indicating that zerovalent  $\text{Pd}^0$  particles formed during the reaction should be considered the active species for propene epoxidation by molecular oxygen in methanol. Extraction of  $\text{Pd}^{2+}$  cations from the octahedral sites does not give rise to collapsing of the LDH structure because of the low Pd loading, thus permitting reuse of the catalyst without loss of activity.

If the reaction catalysed by the POM-LDH system takes place inside the interlayer space, a decrease in hydrophobicity would enhance diffusion of the substrate and/or the products. With this aim, Figueras et al. [230] have studied the epoxidation of cyclohexene with hydrotalcite-intercalated organotungstic complexes prepared following different routes. A  $\text{Mg}_3\text{Al-CO}_3$  LDH (HT) was prepared by coprecipitation, and a meixnerite phase (MX) was prepared by calcination at 450 °C and immersion in decarbonated water. The tungstate catalysts (HT-W, MX-Wa and MX-Wb) were prepared by impregnation of the HT or MX solids with aqueous  $\text{Na}_6\text{W}_7\text{O}_{24}$  at pH 7. Suspensions of MX or HT with phenylphosphonic (P) or dodecylphosphonic (D) acid led to solids MX-P, MX-D, HT-P and HT-D; the first two solids were treated with a solution of  $(\text{Oct}_3\text{MeN})_2\text{W}_2\text{O}_{11}$  in dichloromethane in such an amount to complex only 10% of the phosphonate involved. Intercalation was not achieved with the carbonate-containing precursors, but succeeded for the

meixnerite ones. The specific surface areas of the catalysts ranged from 58 to 85 m<sup>2</sup> g<sup>-1</sup> and the <sup>31</sup>P MAS-NMR spectra showed the presence of a small amount of free organophosphonic acid.

Simple tungstates afforded 100% selectivity in cyclohexene epoxidation, conversion ranging from 12 to 40% after 6 h reaction, but for those prepared from a carbonate LDH precursor (where tungstate was not intercalated) only superficial species were active, while the yield was larger for MX-Wa, prepared from meixnerite, where real intercalation had taken place. The complexing ability of D was larger than that of P, confirming the importance of lipophilicity around the catalytic site, which ensures good diffusion of the alkene. No diol is formed in anhydrous conditions, and high selectivities to cyclohexenol and cyclohexenone were measured, mainly with anhydrous H<sub>2</sub>O<sub>2</sub>. Changing the nature of the phosphonic acid or using anhydrous H<sub>2</sub>O<sub>2</sub> has little influence on the rate, suggesting that the solid is indeed hydrophobic. The main reaction is an allylic oxidation, resulting from the reaction of OH• radical which formed by the homolytic cleavage of WO–OH species, related to the charge of the W atom. Overall, the efficiency of the phosphonate-peroxotungstate species results from the intrinsic reactivity of the WO<sub>5</sub>–O=P subunits, associated with the lipophilic behaviour afforded by the long chains of the ligands.

Self-assembled WZn<sub>3</sub>(ZnW<sub>9</sub>O<sub>34</sub>)<sub>2</sub><sup>12-</sup> (briefly ZnWO) was immobilised in a Mg<sub>3</sub>Al–NO<sub>3</sub> LDH by directly adding a twofold excess to a LDH slurry at pH 7.5 for 3 h at 60 °C [231]. The FTIR spectrum shows three peaks at 930, 875 and 770 cm<sup>-1</sup>, coinciding with those of the sodium salt of the ZnWO anion, with only very weak peaks of nitrate or tungstate, suggesting a selective intercalation of the anion and that its structure was retained after exchange. The XRD pattern indicates a gallery height of 10.2 Å, in agreement with the diameter of the short axis of the sandwich-type ZnWO anion, together with an additional XRD peak at ca. 12 Å probably due to ZnWO immobilised on the external surface of the LDH layers. Hydrothermal treatment at 120 °C for 7 days did not alter the structure of the ZnWO-LDH solid. The selective intercalation observed may origin from (i) the large negative charge of the ZnWO anion, larger than the other two competing anions in the medium (nitrate and tungstate), and (ii) the high positive charge of the LDH layers.

Epoxidation of (E)-2-hexen-1-ol with aqueous H<sub>2</sub>O<sub>2</sub> at 50 °C was solvent dependent and despite selectivity was 97–99%, the largest yield (80%) was obtained when using acetonitrile as a solvent, and only a negligible decrease in activity was observed after even seven catalytic runs. The larger selectivity of the supported than the unsupported catalyst may arise from the basic properties of the layered material, which may suppress the acid-catalysed epoxide hydrolysis [232]. Similar large (99%) selectivities and yields up to 86–96% were measured for epoxidation of various allylic alcohols with aqueous H<sub>2</sub>O<sub>2</sub> with high TOFs.

These authors have extended their studies on epoxidation of olefins with aqueous H<sub>2</sub>O<sub>2</sub> in the absence of any organic solvent [233] using other POMs, namely WC<sub>3</sub>(CoW<sub>9</sub>O<sub>34</sub>)<sub>2</sub><sup>12-</sup> (briefly CoWO), WZnMn<sub>2</sub>(ZnW<sub>9</sub>O<sub>34</sub>)<sub>2</sub><sup>12-</sup> (MnZnWO) and PW<sub>11</sub>O<sub>39</sub><sup>7-</sup> (PWO), intercalated in Mg,Al and Zn,Al LDHs by anion exchange

from nitrate precursors at 60 °C. While PWO was incorporated at pH 5, all other POMs were intercalated at pH 7. FTIR spectra demonstrated selective intercalation with retention of the POM structure and the swelling of the brucite-like layers was in agreement with the sizes of the POM entities, although a broad diffraction with  $d = 11\text{--}13 \text{ \AA}$  was recorded in all cases, which is probably due to POM anions immobilised on the external surface of the LDH crystallites. The  $\text{N}_2$  adsorption isotherms corresponded to type I at low relative pressure, with type H3 hysteresis loop at higher relative pressures, indicating the presence of both interlayer micropores and interparticle mesopores; actually, ca. 10–40% of the surface area arises from micropores, absent for the nitrate LDH precursors. The degree of exchange of POM was 103–147%, exceeding the maximum AEC of the LDH; this might be ascribed to the unavailability of partial negative charge of POM for balancing the LDH host charge or to a partial protonation of the POM anions, thus decreasing their formal negative charge.

These LDH–POM catalysts exhibit comparable reactivity and much higher selectivity (81–98%) than the sodium POM salt under identical conditions in epoxidation of prenil [233]. The  $\text{H}_2\text{O}_2$  efficiency increased in the order  $\text{CoWO} < \text{MnZnWO} < \text{PWO} < \text{ZnWO}$ , indicating that ZnWO species show relatively slower decomposition of  $\text{H}_2\text{O}_2$  than other POM species. On changing the nature of the LDH, it was found that MgAl–ZnWO shows a higher selectivity to epoxide than ZnAl–ZnWO, and the same trend was observed for MgAl–MnZnWO (97%) and ZnAl–MnZnWO (92%). These differences may arise from the different basicity of both supports: the pH of a suspension of MgAl–ZnWO or ZnAl–ZnWO (0.1 g in 10 ml distilled water) was 7.8 and 7.2, respectively, and the concentration of surface sites (using bromothymol blue as indicator and titrating with benzoic acid) was 380 and 250  $\mu\text{mol g}^{-1}$ , respectively. It should be recalled that the LDHs, in the nitrate form, showed negligible (<5%) activity, as well as physical mixtures of the  $\text{NO}_3$ -LDH and the POM. In other words, basicity of the LDH support plays an outstanding role on the reaction tested [233].

Hydrolysis of prenil oxide was slow in the presence of Na–ZnWO, but faster in the presence of  $\text{H}_2\text{O}_2$ ; addition of Na–ZnWO did not slowdown the hydrolysis, but addition of LDH–ZnWO did. These results confirm that hydrolysis is due to the acidity of  $\text{H}_2\text{O}_2$ , but it occurs in solution rather than on the surface of ZnWO, and such an acidity of aqueous  $\text{H}_2\text{O}_2$  is suppressed by the basic LDH hosts. This buffer effect may arise from surface hydroxyl groups of the LDH host, which are able to trap protonic species in aqueous  $\text{H}_2\text{O}_2$ , thus decreasing epoxide hydrolysis. Reusability was also tested, finding encouraging results, and the catalysts were applied, with good performance, for epoxidation of other allylic alcohols; selectivity to the epoxide was always well above 90% and larger than that measured in homogeneous medium, with TOF values up to 37,000  $\text{h}^{-1}$ .

Das and Parida [198] have performed a parallel study of the esterification of acetic acid with *n*-butanol on Zn,Al LDHs exchanged with tungstophosphoric acid (TPA) similar to that carried out with molybdophosphoric acid (MPA) above described, obtaining slightly worse results. A Zn,Al– $\text{NO}_3$  LDH prepared by direct synthesis was exchanged with terephthalic acid in a basic medium (basal spacing 13.9  $\text{\AA}$ ) and finally tungstophosphate anion (TPA) was incorporated by exchange at

pH 4.5–5, preparing samples with TPA weight loadings of 5, 10, 15 and 20% (spacings  $14.1 \pm 0.1 \text{ \AA}$ ). The crystallite size ranged from 61 to 69  $\text{\AA}$ , and the specific surface area showed a maximum value ( $86 \text{ m}^2 \text{ g}^{-1}$ ) for the 15 wt% sample. Typical TPA FTIR bands were recorded at 1016, 892, 828 and  $751 \text{ cm}^{-1}$  (1067, 1021, 992, 893, 822 and  $771 \text{ cm}^{-1}$  for unloaded TPA) indicating that TPA was retained in the interlayer. However, two strong intense bands persist at  $1500\text{--}1400 \text{ cm}^{-1}$ , probably due to the antisymmetric and symmetric  $\nu_{\text{COO}}$  modes of terephthalate anions, still existing in the interlayer. Surface Brønsted acidity was measured from the amount of irreversibly adsorbed bases (pyridine and 2,6-dimethyl-pyridine), maximum values being found for the 15 wt% sample. Conversion of acetic acid was also maximum (77%) for this sample, although selectivity to the ester was 100% in all cases. This behaviour might be ascribed to the maximum surface Brønsted acidity and maximum specific surface area shown by this sample.

Choudary et al. [147] have also studied oxidation of *N*-methyl morpholine to *N*-methylmorpholine *N*-oxide on a  $\text{Mg}_3\text{Al}\text{-WO}_4$  catalyst (without intercalation) containing 11% (weight) W, with a yield of 96% (75% for  $\text{Na}_2\text{WO}_4$ ). This value was larger than that measured for vanadate or molybdate analogues, although a similar catalyst containing  $\text{PO}_4[\text{WO}(\text{O}_2)]_4^-$  showed only a yield of 40%, despite the W content was 21% (weight). Yields approached 100% for other tertiary amines. Although water was the best solvent, addition of dodecylbenzenesulfonic acid sodium salt increased by two or three times the reaction rate. This reaction takes place under liquid (organic *tert*-amine) – solid (catalyst) – liquid (aqueous phase) conditions, the role of the surfactant probably being to increase the contact area of the interface between the aqueous and the organic phases and to enhance the transfer of lipophilic amine from the organic to the aqueous phase. Formation of intermediate peroxotungstate species was confirmed by UV/DR spectroscopy (development of an absorption band at 325 nm), and the catalyst was reusable for six cycles without loss of activity or selectivity.

Oxidation of anisole was studied on these same catalysts [148]. Similar conversion levels were measured for unsupported  $\text{Na}_2\text{WO}_4$  (95% in 2.5 h),  $\text{LDH-PO}_4[\text{WO}(\text{O}_2)]_4$  (90%, 4 h) and  $\text{LDH-WO}_4$  (94% in 30 min). This last catalyst showed better selectivity (88%) to the sulfoxide, with a considerable increase in TOF ( $42.72 \text{ h}^{-1}$  vs. 15 for  $\text{LDH-PO}_4[\text{WO}(\text{O}_2)]_4$  and 9 for  $\text{Na}_2\text{WO}_4$ ). On testing oxidation of several sulfides, it was found that aromatic sulfides are selectively oxidised to sulfoxides at lower conversions and lower reaction times, but to sulfones on prolonging the reaction time; aliphatic sulfides are oxidised faster than the aromatic ones, without formation of sulfones even for long reaction times. This means that the oxidation rate increases with increased nucleophilicity on the sulfur atom. Among the different solvents tested, the best results were obtained with water, and in all cases only 0.3% leaching of tungstate was observed, the catalyst being reusable for several cycles. Formation of tungsten-peroxide species was confirmed by UV/DR spectroscopy, with a band at 325 nm.

Hulea et al. have also studied the oxidation of thiophenes and thioethers on tungstate-containing LDHs, but analysing the effect of the relative content of tungstate ( $\text{WO}_4^{2-}$ ) or heptatungstate ( $\text{W}_7\text{O}_{24}^{6-}$ ) species on the catalytic performance [234]. A nitrate precursor ( $\text{Mg}/\text{Al} = 2$ ) was prepared at pH 9.5, and



then tungstate was incorporated by direct ion exchange at pH 6.5 (sample PW-LDH) or 9.5 (sample W-LDH). Despite the total W loading was similar in both cases (Mg/Al/W molar ratios 2.05/1.00/0.23 and 2.10/1.00/0.26, respectively), it is hoped that the lower pH for the first sample would enhance the content of the heptatungstate anion. The basal spacings for the (003) planes were 10.01 and 10.53 Å, respectively, for samples W-LDH and PW-LDH. As for heptatungstate-containing samples values of 10.4 and 14.6 [207] and 12.1 Å [171] have been reported, the results obtained suggest that intercalation of tungstate species has actually taken place. UV–Vis spectroscopy confirms the presence of both tungstate species in both samples, and deconvolution of the charge transfer absorption reveals two components at 215–230 nm (tetrahedral  $[\text{WO}_4]$  species in  $\text{WO}_4^{2-}$ ) and 250 nm (octahedral  $[\text{WO}_6]$  species in  $\text{W}_7\text{O}_{24}^{6-}$ ) with relative intensities  $[\text{WO}_4]/[\text{WO}_6]$  of 5/1 and 3/1 for samples W-LDH and PW-LDH, respectively. Finally, Raman spectroscopy showed bands at  $980\text{ cm}^{-1}$  ( $\nu_{\text{W}=\text{O}}$ ) and 530, 405 and  $250\text{ cm}^{-1}$  ( $\delta_{\text{W}-\text{O}-\text{W}}$ ). Overall, both spectroscopies indicate that at pH 9.5 (sample W-LDH) the predominant species is tungstate and at pH 6.5 heptatungstate. The specific surface areas were  $60\text{ m}^2\text{ g}^{-1}$  for both samples, and microporosity was also found in both.

Sulfoxidation of sulfides in an organic solvent using 30%  $\text{H}_2\text{O}_2$  (partial decomposition to  $\text{O}_2$  was also observed) as an oxidant resulted in almost complete selectivity to sulfoxides and/or sulfones, while thiophene derivatives led directly to the corresponding sulfone, without leaching nor noticeable decrease in activity after four catalytic runs. The W-LDH catalyst exhibited higher activity than PW-LDH, probably due to the complex structure of the paratungstate anions, with a flat orientation in the interlayers [207], somewhat hindering the access of the organic substrate to the active sites of the polyanion. As also reported by Choudary [148], the faster oxidation of sulfides is related to the different nucleophilicity of the sulfur atoms. On increasing the reaction temperature, decomposition of  $\text{H}_2\text{O}_2$  to  $\text{O}_2$  is enhanced.

Sample W-LDH was used also [127] to oxidise several sulfur-containing compounds, finding that conversion increased in the order.

Benzo-thiophene < di-benzo-thiophene < di-phenyl-sulfide < benzyl-phenyl-sulfide < methyl-phenyl-sulfide

Again sulfides led to sulfoxides and sulfones, but thiophenes led to sulfones exclusively, and the change in rate reaction agrees well with electron density at the sulfur atom. The first reaction step is formation of peroxotungstate species (identified by UV/DR spectroscopy), followed by transfer of the electrophilic oxygen to the sulfide, forming the corresponding sulfoxide. The peroxo-bridged high-nuclearity metal species are less active towards oxygen atom transfer than the lower nuclearity species because, despite the former has more tungsten atoms, only terminal  $\text{W}=\text{O}$  bonds are able to form peroxo rings.

Tetrahydrothiophene (THT) oxidation on Hulea's sample W-LDH takes place in two consecutive steps [123] under mild conditions (20–30 °C) and dilute medium, forming first tetrahydrothiophene oxide, which then undergoes further complete oxidation to sulfolane, without direct decomposition of  $\text{H}_2\text{O}_2$ . Conversion and

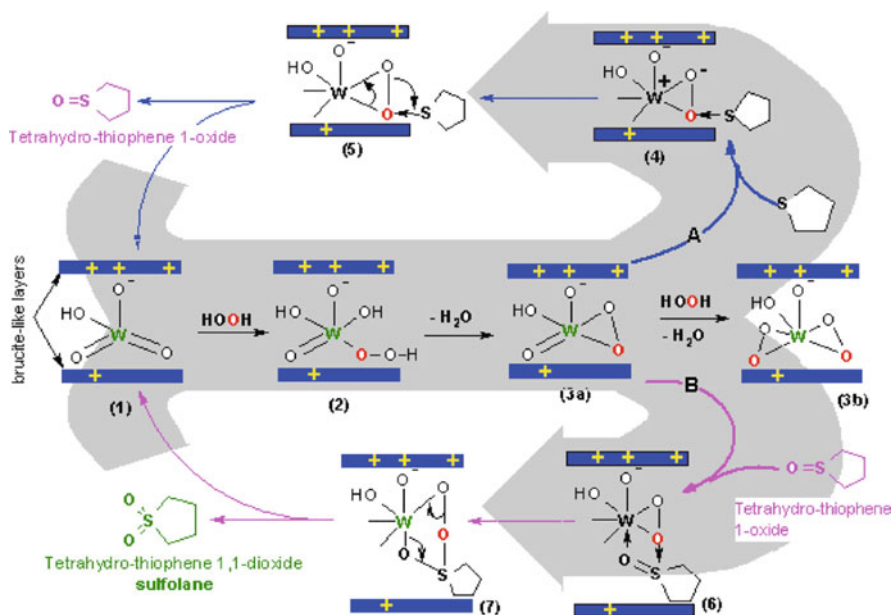


**Fig. 12.13** Proposed mechanism for the THT oxidation with  $\text{H}_2\text{O}_2$  over W-LDH catalyst. Reprinted from [123], with permission from Elsevier

selectivity were larger than for the vanadium and molybdenum analogues (see above), and the proposed reaction mechanism is summarised in Fig. 12.13. When different reaction conditions were used, the following summarised results were obtained after 60 min: (i) 100% conversion is reached at 25 °C; (ii) conversion (between brackets) decreased when using different solvents in the order dioxane (100%) = acetonitrile (100%) > acetone (69%) > ethanol (43%) > methanol (29%); (iii) total conversion was measured for  $\text{H}_2\text{O}_2/\text{THT}$  ratios equal to or larger than 2. Conversion did not decrease after four catalytic runs.

Catalytic oxidation of dimethylsulfoxide (DMSO) from wastewater has been also studied by Hulea et al. on tungstate-containing LDHs [235] on the samples named as W-LDH and PW-LDH [234], as well as on a Zn,Al LDH prepared at pH 9.5 (sample WZ-LDH). The specific surface areas were in the range 24 (WZ-LDH) to 37 (PW-LDH)  $\text{m}^2 \text{g}^{-1}$ , showing micro- and mesoporosity. Basal spacings for the (003) planes were 10.37, 10.26 and 10.16 Å, respectively, for samples W-LDH, PW-LDH and WZ-LDH, confirming replacement of the nitrate anions, although some structural disorder was observed (broader diffraction maxima). UV/DR and Raman spectroscopies confirmed the presence of octahedral and tetrahedral oxotungstate species, which molar fractions strongly depended on pH during synthesis: 85 and 77%  $[\text{WO}_4]$  species in W-LDH and WZ-LDH, but 8% in PW-LDH.

Oxidation of DMSO to dimethylsulfoxide was carried out with  $\text{H}_2\text{O}_2$ , whose efficiency was in all cases higher than 95%, resulting exclusively in dimethylsulfoxide,  $(\text{CH}_3)_2\text{S}(\text{O})_2$ . Conversion decreased in the order W-LDH > PW-LDH >

**Table 12.5** Summary of reactions catalysed by LDHs with intercalated tungsten-containing POMs

Layer cations	Intercalated species	Reaction	Substrate	References
Zn,Al	$\text{NaP}_5\text{W}_{30}\text{O}_{110}^{14-}$	Oxidation	Cyclohexene	[88]
Mg,Al (250–900 °C)	$\text{PW}_{12}\text{O}_{40}^{3-}$	Selective catalytic reduction	NO	[215]
Mg,Al (250–900 °C)	$\text{SiW}_{12}\text{O}_{40}^{4-}$	Selective catalytic reduction	NO	
Zn,Al	$\text{SiW}_{12}\text{O}_{40}^{4-}$	Epoxidation	Cyclohexene	[217]
Ni,Al	$\text{SiW}_{12}\text{O}_{40}^{4-}$	Epoxidation	Cyclohexene	
Zn,Al	$\text{SiW}_{11}\text{O}_{39}^{8-}$	Epoxidation	Cyclohexene	
Mg,Al	$\text{H}_2\text{W}_{12}\text{O}_{40}^{6-}$	Epoxidation	Cyclooctene	[218]
Mg,Al	$\text{W}_4\text{Nb}_2\text{O}_{19}^{4-}$	Epoxidation	Cyclooctene	
Zn,Al	$\text{H}_2\text{W}_{12}\text{O}_{40}^{6-}$	Epoxidation	Cyclooctene	
Zn,Al	$\text{W}_4\text{Nb}_2\text{O}_{19}^{4-}$	Epoxidation	Cyclooctene	
Mg,Al	$\text{CoW}_{12}\text{O}_{40}^{5-}$	Oxidation	Benzaldehyde	[219]
Mg,Al	$\alpha\text{-[SiW}_9\text{O}_{37}(\text{Co}(\text{H}_2\text{O})_3)]^{10-}$	Oxidation	Cyclohexanol	[220]
Mg,Al	$\text{H}_2\text{W}_{12}\text{O}_{40}^{6-}$	Epoxidation	Cyclohexene	[171]
Zn,Al	$\text{H}_2\text{W}_{12}\text{O}_{40}^{6-}$	Epoxidation	Cyclohexene	
Mg,Al	$\text{WO}_4^{2-}$	Mild oxidative bromination	Olefins, 1,3-diketones, aromatics	[221]
Ni,Al	$\text{WO}_4^{2-}$	Mild oxidative bromination	Olefins, 1,3-diketones, aromatics	
Ni,Al	$\text{WO}_4^{2-}$	Mild oxidative bromination	Olefins, 1,3-diketones, aromatics	
Ni,Al	$\text{WO}_4^{2-}$	Mild oxidative bromination	Aromatics olefins Aliphatic olefins	[223]
Mg,Al	$\text{WO}_4^{2-}$	Mild oxidative bromination	Cyclic enol ethers	[224]
Ni,Al	$\text{WO}_4^{2-}$	Mild oxidative bromination	Aromatics	[225]
Mg,Al	$\text{W}_7\text{O}_{24}^{6-}$	Photodegradation	Aromatics	[227]
Zn,Al (600–700 °C)	$\text{SiW}_{11}\text{O}_{39}^{8-}$	Photodegradation	Hexachlorocyclohexene	[228]
Zn,Al (600–700 °C)	$\text{SiW}_{11}\text{O}_{39}\text{Mn}(\text{H}_2\text{O})^{6-}$	Photodegradation	Hexachlorocyclohexene	
PdMgAl	$\text{PW}_{11}\text{O}_{39}^{7-}$	Epoxidation	Propene	[8]
PdZnAl	$\text{PW}_{11}\text{O}_{39}^{7-}$	Epoxidation	Propene	
Mg,Al	$\text{W}_7\text{O}_{24}^{6-}$	Epoxidation	Cyclohexene	[230]
Mg,Al	$\text{C}_6\text{H}_5\text{PO}_3(\text{WO}_5)_2$	Epoxidation	Cyclohexene	

Table 12.5 (continued)

Layer cations	Intercalated species	Reaction	Substrate	References
Mg,Al	$C_{12}H_{23}PO_3(WO_5)_2$	Epoxidation	Cyclohexene	
Mg,Al	$WZn_3(ZnW_9O_{34})_2^{12-}$	Epoxidation	Allylic alcohols	[231]
Mg,Al	$WCo_3(CoW_9O_{34})_2^{12-}$	Epoxidation	Prenol	[233]
Mg,Al	$WZnMn_2(ZnW_9O_{34})_2^{12-}$	Epoxidation	Prenol	
Mg,Al	$PW_{11}O_{39}^{7-}$	Epoxidation	Prenol	
Zn,Al	$WCo_3(CoW_9O_{34})_2^{12-}$	Epoxidation	Prenol	
Zn,Al	$WZnMn_2(ZnW_9O_{34})_2^{12-}$	Epoxidation	Prenol	
Zn,Al	$PW_{11}O_{39}^{7-}$	Epoxidation	Prenol	
Zn,Al	$PW_{12}O_{40}^{3-}$	Esterification	Acetic acid	[198]
Mg,Al	$WO_4^{2-}$	Oxidation	Anisole	[148]
Mg,Al	$PO_4[W(O)(O_2)]_4$	Oxidation	Anisole	
Mg,Al	$WO_4^{2-}$	Oxidation	Triophenes, thioethers	[234]
Mg,Al	$W_7O_{24}^{6-}$	Oxidation	Triophenes, thioethers	
Mg,Al	$WO_4^{2-}, W_7O_{24}^{6-}$	Oxidation	Triophenes, thioethers	
Mg,Al	$WO_4^{2-}, W_7O_{24}^{6-}$	Oxidation	Benzothiophene	[127]
Mg,Al	$WO_4^{2-}, W_7O_{24}^{6-}$	Oxidation	Dibenzothiophene	
Mg,Al	$WO_4^{2-}, W_7O_{24}^{6-}$	Oxidation	Diphenyl sulfide	
Mg,Al	$WO_4^{2-}, W_7O_{24}^{6-}$	Oxidation	Benzyl-phenyl sulfide	
Mg,Al	$WO_4^{2-}, W_7O_{24}^{6-}$	Oxidation	Methyl-phenyl sulfide	[123]
Mg,Al	$WO_4^{2-}, W_7O_{24}^{6-}$	Sulfoxidation	Tetrahydrothiophene	[235]
Mg,Al	$WO_4^{2-}, W_7O_{24}^{6-}$	Sulfoxidation	Dimethylsulfoxide	

WZ-LDH  $\gg$  Mg,Al-NO<sub>3</sub> > Zn,Al-NO<sub>3</sub>. The differences can be related to the differences in the WO<sub>4</sub><sup>2-</sup>/W<sub>7</sub>O<sub>24</sub><sup>6-</sup> ratio (much larger for W-LDH than for PW-LDH), but this fact does not justify the conversion measured for WZ-LDH, although it might be related to a larger acidity of the latter. The reaction rate increases with the reaction temperature. Even with a H<sub>2</sub>O<sub>2</sub>/DMSO ratio of 1/1 conversion of DMSO reached 97% after 3 h reaction, with H<sub>2</sub>O<sub>2</sub> efficiency of 98%, thus demonstrating that a large excess of hydrogen peroxide is not justified. Different solvents led to changes in reaction rate as above cited for tetrahydrothiophene (THT) oxidation. Reuse of the catalyst did not change the catalytic performance even after four runs.

Table 12.5 summarises the reactions catalysed by LDHs with intercalated POMs containing tungsten species.

## 12.6 Miscellaneous Systems

### 12.6.1 Boron-Containing LDHs

The synthesis of boron-containing LDHs is very appealing because the introduction of B-anions should provide these materials with Brønsted acid sites, thus allowing mild acid-catalysed reactions such as vapour-phase Beckmann rearrangement; moreover, intercalation of boron oxides in the LDH structure would avoid the easy borate volatilisation and leaching during catalytic tests. Direct synthesis or exchange with a nitrate precursor did not lead to the desired borate-intercalated materials [236], although it was then reported [237] that tetraborate could be intercalated by exchanging a nitrate precursor with Na<sub>2</sub>B<sub>4</sub>O<sub>5</sub>(OH)<sub>4</sub>·8H<sub>2</sub>O and hydrothermal treatment if the precursor is maintained in suspension; if dried, only a partial exchange is observed after a severe hydrothermal treatment. Direct synthesis with boric acid leads to a LDH-triborate solid [238]. It has been observed that the Mg/Al molar ratio somewhat determines the easiness with which exchange takes place: If such a ratio is high the interlayer concentration of nitrate anions is low and adopt a “flat” orientation, parallel to the brucite-like layers, exchange with bulk borate species being difficult. However, if such a ratio is low (e.g. Mg/Al = 2), then the nitrate anions adopt a tilted orientation, expanding the layers and then exchange with tetraborate species takes place [163]. Intercalated tetraborate does not undergo depolymerisation, as concluded from the <sup>11</sup>B MAS-NMR spectrum, which corresponds to the presence of trigonal [BO<sub>3</sub>] and tetragonal [BO<sub>4</sub>] units in a molar ratio of one. Calcination at 500 °C destroys completely the layered structure, leading to an amorphous material with a specific surface area of 55 m<sup>2</sup> g<sup>-1</sup>. FTIR monitoring of pyridine adsorption shows bands at 1590, 1575, 1490 and 1449 cm<sup>-1</sup>, which disappear on outgassing at room temperature, indicating that surface acid sites are very weak. Adsorption of ammonia was negligible. Monitoring of surface Lewis basic sites was carried out [239] by adsorption of boric acid trimethyl ester (bate); the spectrum shows bands at 1493, 1391 (shoulder), 1363, 1340 (shoulder) and 1040 cm<sup>-1</sup>, very close positions of those for bulk bate and disappearing on outgassing at room temperature, i.e. surface basicity is also very low. Adsorption of

acetaldehyde leads to FTIR bands typical of strongly adsorbed acetaldehyde and crotonaldehyde, formed through aldol condensation; no oxidation to acetate species is observed. Formation of crotonaldehyde was larger than on calcined solids with intercalated carbonate, nitrate or silicate, probably because it rehydrates more easily. Isopropanol is only adsorbed physically on the sample calcined at 500–600 °C, although at 300 °C acetone (identified by FTIR bands at 1740 and 1720  $\text{cm}^{-1}$ ) is formed [193].

Trifirò et al. have used calcined boron-containing LDHs for gas-phase Beckmann isomerisation of cyclohexanone oxime. In a first study [240] samples were prepared by direct synthesis with boric acid at different pHs. According to XRD measurements,  $[\text{B}(\text{OH})_4]^-$  or  $[\text{B}_3\text{O}_3(\text{OH})_4]^-$  parallel to the cationic layers are intercalated at pH 7.5 (spacing 8.07 Å), and the same species are responsible for a biphasic solid with spacings 10.87 and 8.07 Å at pH 9.0, but at pH 11 the spacing is 7.98 Å, due to  $[\text{B}(\text{OH})_4]^-$ . The solid prepared at pH 9.0 was selected for further studies, due to its larger B content. Upon calcination at 400 °C for 18 h led to a solid with a single XRD reflection at 6.9 Å, suggesting grafting of the borate species to the layers. XPS measurements showed the same binding energy in all cases, decreasing 0.4 eV upon calcination, without surface B enrichment (25–28%).  $^{11}\text{B}$  MAS-NMR spectroscopy shows that upon calcination  $\text{BO}_3$  is the most abundant species, strongly interacting with octahedral Al species. The low caprolactam selectivity observed is attributed by these authors to the low availability of boron atoms on the particle surface, the low B loading (merely 5% in the pristine solid) and the electrostatic interactions leading to grafting of the boron species.

In a second study [241] three different routes were used to prepare the catalyst, namely (i) exchange at pH 9.5 with a Mg,Al-adipate LDH precursor; (ii) coprecipitation with boric acid (and washing with a tetraborate solution to avoid loss of borate species) and (iii) impregnation of a Mg,Al-carbonate LDH calcined at 500 °C with boron anions at incipient wetness. All solids were calcined at 400 °C before the catalytic tests. Ion exchange allows a more homogeneous dispersion of the borates, resulting in higher availability of boron species on the catalyst surface and thus higher catalytic performance than that for the coprecipitated sample. In addition to caprolactam, cyclohexanone is formed as the major by-product, probably through hydrolysis of the oxime, together with small amounts of cyclohexen-2-one on stronger acid sites. Unfortunately, reaction proceeds with formation of tars, which require heating at 500 °C to be removed and to regenerate the catalyst, and this treatment destroys the layered structure; the mixed oxide formed show similar or even larger catalytic activity, probably because structural changes associated with formation of the amorphous phase also makes more B available at the surface, destroying the grafting effect observed for the un-used catalysts.

### 12.6.2 Manganese-Containing LDHs

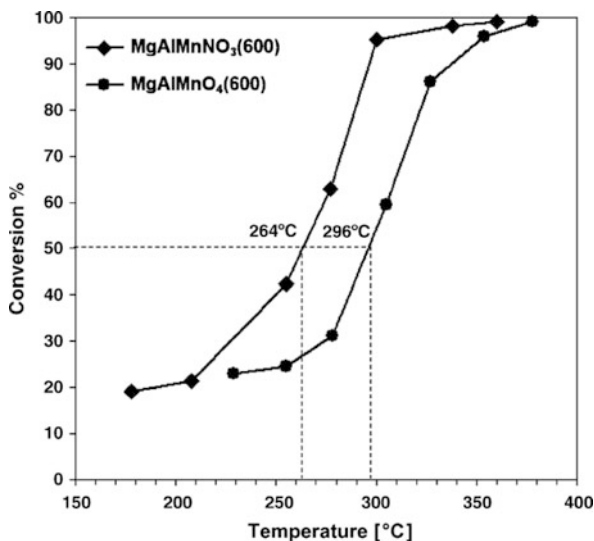
Very few studies have been devoted to LDHs with intercalated oxomanganate species. Suib et al. have reported the formation of  $\text{MnO}_x$  species in the interlayer

of a Mg,Al LDH [242]. Complete exchange was achieved from a nitrate precursor with permanganate and then reduction with glucose, ethanol and ascorbic acid. The spacing after reduction (which could be related to the size of the interlayer  $\text{MnO}_x$  species) was larger when reducing with ascorbic acid (9.93 Å) than with the other reagents.

Permanganate-containing LDHs have been used for selective oxidation of alkyl-aryl hydrocarbons to the corresponding aromatic ketones [243]. Samples with Mg/Al ratios ranging from 2 to 10 were prepared by reconstruction at 80 °C with aqueous  $\text{KMnO}_4$  of the LDH previously calcined at 600 °C. Calcination at 200 °C did not alter the layered structure. The spacing of the permanganate-containing sample was the same as for the original LDH, despite the large radius of the  $\text{MnO}_4^-$  ion, and was not altered after the catalytic runs. The specific surface area decreases from ca. 36 to 26  $\text{m}^2 \text{g}^{-1}$  as the Mg/Al ratio increased from 2 to 10. Although the surface basicity of the LDH precursor (as measured by titration with benzoic acid using phenolphthalein as indicator) increased sharply with the Mg/Al ratio, the pH of a slurry of the  $\text{MnO}_4^-$ -LDH was always close to 10; also in this sense decomposition of  $\text{H}_2\text{O}_2$  increased. Oxidation of ethylbenzene, diphenylmethane and *n*-propylbenzene by  $\text{O}_2$  proceeded with selectivity above 90% (100% for  $\text{CH}_2\text{Ph}_2$ ), the lowest reactivity found for *n*-propylbenzene. The largest activity was shown by the catalyst with a Mg/Al ratio of 10 (i.e. that with the highest basicity). The reaction rate was larger than in the presence of the same amount of  $\text{KMnO}_4$ , and no leaching was observed.

Products formed upon calcination of LDHs with intercalated POMs are usually different from those formed upon calcination of LDHs where the metal cation forming the POM is located in the brucite-like layers [132]. Serwicka et al. have studied the performance of solids prepared upon calcination at 600 °C of LDHs with layer  $\text{Mn}^{2+}$  or interlayer permanganate in total combustion of toluene [244]. In the first case (sample MgMnAl) a MgMnAl-nitrate LDH was prepared and the second sample ( $\text{MgAlMnO}_4$ ) was prepared by anion exchange of a MgAl-nitrate precursor at pH 10. Intercalation of permanganate leads to an increase of the basal spacing from 8.30 to 8.99 Å. Upon calcination at 600 °C, a  $\text{Mn}^{3+}$  spinel ( $\text{MgMn}_{1.75}\text{Al}_{0.25}\text{O}_4$ ) was formed from sample MgMnAl, whose crystallinity is increased upon calcination at 800 °C. However, calcination of sample  $\text{MgAlMnO}_4$  led to poorly crystallised MgO-MnO; calcination at 800 °C led to incipient crystallisation of a spinel phase, but it seems to be closer to  $\text{MgAl}_2\text{O}_4$  than to  $\text{MgMn}_{1.75}\text{Al}_{0.25}\text{O}_4$ . XPS and EPR measurements indicate the presence of different manganese species ( $\text{Mn}^{2+}$ ,  $\text{Mn}^{3+}$  and  $\text{Mn}^{4+}$ ). TPR analysis showed that sample  $\text{MgMnAlNO}_3$  calcined at 600 °C was more easily reduced than calcined sample  $\text{MgAlMnO}_4$ , probably due to the different nature of the spinels formed in both solids. Sample  $\text{MgMnAlNO}_3$  calcined at 600 °C was more active for toluene combustion; actually, light-off T50 (temperature of 50% conversion), Fig. 12.14, was 264 °C, 32 °C lower than for calcined sample  $\text{MgAlMnO}_4$ , probably by the easier reducibility of the surface amorphous layer containing  $\text{Mn}^{4+}$  and  $\text{Mn}^{3+}$ .

**Fig. 12.14** Temperature dependence of the toluene conversion at GHSV  $30,000 \text{ h}^{-1}$  for  $\text{MgAlMnAlNO}_3$  and  $\text{MgAlMnO}_4$  catalysts calcined at  $600^\circ\text{C}$ . Reprinted from [244], with permission from Elsevier



### 12.6.3 Niobium-Containing LDHs

Niobium compounds are extensively used in many heterogeneous catalytic processes where they can act as catalyst supports or as the active phase [245], e.g. in dehydration of sugars [246, 247]. Mixed Nb-W POMs have been intercalated in LDHs [218, 248] and studied in epoxidation of cyclooctene (see above). A single niobate POM with the Lindqvist structure,  $\text{H}_3\text{Nb}_6\text{O}_{19}^{5-}$ , has been also intercalated in a Mg,Al LDH and its activity in isopropanol oxidation has been studied [249]. The sample (Mg,AlNb) was prepared by ion exchange of a Mg,Al- $\text{NO}_3$  LDH precursor with aqueous  $\text{K}_8\text{Nb}_6\text{O}_{19}$  at pH 12 and  $90^\circ\text{C}$  for 16 h. Contrary to the general findings when intercalating POMs in acidic (typically pH 4.5) media, where a decrease in the Mg/Al ratio is observed, in this case a slight increase was found, probably because of a partial dissolution of amphoteric aluminium species in the strongly basic preparation medium. The gallery height,  $7.2 \text{ \AA}$ , is in agreement with location of the niobate anion with its  $C_3$  axis perpendicular to the layers, although again a broad peak at  $11 \text{ \AA}$  is also observed. Calcination at  $450\text{--}500^\circ\text{C}$  leads to an amorphous material, while at  $800^\circ\text{C}$  sharp peaks due to  $\text{Mg}_4\text{Nb}_2\text{O}_9$  were recorded. The sample shows a limited surface area ( $24 \text{ m}^2 \text{ g}^{-1}$ ), but ca. 40% corresponds to adsorption in micropores, which disappear, with an appreciable surface area development (up to  $157 \text{ m}^2 \text{ g}^{-1}$ ) upon calcination at  $500^\circ\text{C}$ , then decreasing at  $800^\circ\text{C}$  ( $45 \text{ m}^2 \text{ g}^{-1}$ ) due to formation of very crystalline  $\text{Mg}_4\text{Nb}_2\text{O}_9$ . Adsorption of pyridine at room temperature leads to FTIR bands due to adsorption on  $\text{Al}^{3+}$



cations, although a band at  $1608\text{ cm}^{-1}$  could be also due to adsorption on coordinatively unsaturated  $\text{Nb}^{5+}$  sites, as it coincides with that recorded after adsorption of pyridine on  $\text{Nb}_2\text{O}_5$  [250]; the bands are recorded even after outgassing at  $300^\circ\text{C}$ , indicating that pyridine is adsorbed on strong surface Lewis acid sites. Adsorption of isopropanol takes place dissociatively, forming isopropoxide species; on heating without outgassing bands due to acetone ( $1709$  and  $1230\text{ cm}^{-1}$ , due to  $\nu_{\text{C}=\text{O}}$  and  $\nu_{\text{as}(\text{C}-\text{C})}$ , respectively) weakly O-adsorbed to surface Lewis acid sites develop. Acetone is formed via simple dehydrogenation, since TPR experiments did not show any hydrogen consumption due to reduction of Nb species.

### 12.6.4 Osmium-Containing LDHs

Osmium is an active catalyst for asymmetric dihydroxylation of olefins, leading to chiral vicinal diols. However, the high cost, toxicity and possible contamination of osmium catalysts in the products restrict its use in industry. Heterogeneisation on resins or silica, microencapsulation and immobilisation on silica have been claimed as solutions to overcome some of these problems. Choudary et al. have prepared  $\text{Mg,Al-OsO}_4^{2-}$ -LDH by ion exchange from a  $\text{Mg,Al-Cl}$  LDH [251, 252]; however, no swelling was observed by XRD (basal spacing  $7.8\text{ \AA}$ ), indicating that  $\text{OsO}_4^{2-}$  species are mainly located in edge positions. IR ( $\nu_{\text{as}(\text{O}=\text{Os}=\text{O})}$  at  $800\text{--}855\text{ cm}^{-1}$ ), UV/DR ( $320\text{--}290\text{ nm}$ ) and XPS (Os  $4f_{7/2}$  line at  $53\text{ eV}$  due to  $\text{Os}^{\text{VI}}$  species) spectroscopies indicate that the POM entity is unaffected upon supporting. Achiral dihydroxylation of *trans*-stilbene was achieved with a large yield (96%) and 99% enantiomeric excess, and the catalyst could be used up to five times without significant activity loss.

Other olefins were also dihydroxylated, forming the corresponding diols with high yields, and with larger activity and enantioselectivity than previously reported catalysts [251]; the catalyst is also active for dihydroxylation of stilbene, cinamates and aryl-allyl ethers. In any case, no proper exchange exists, according to the XRD results above cited; moreover, dihydroxylation of 1,4-*bis*(9-O-dihydroquinidiny)phthalazine ((DHQ)<sub>2</sub>PHAL) would not be possible if the Os species are intercalated, with a gallery height of only  $3\text{ \AA}$  (after subtracting  $4.8\text{ \AA}$ , width of the brucite layers, from the experimental basal spacing of  $7.8\text{ \AA}$ ).

Activity was slightly improved on increasing the Mg/Al ratio from 2 to 3; co-intercalation of other anions increased also the activity in the order  $\text{CO}_3^{2-} > \text{acetate} > \text{Cl}^- > \text{NO}_3^-$ , i.e. both trends correspond to an increase in basicity, probably leading to a faster hydrolysis of monoglycolate ester. Regarding the use of different solvents, better enantioselectivities were obtained in the order  $\text{H}_2\text{O}-\text{CH}_3\text{CN} < \text{H}_2\text{O}-\text{CH}_3\text{CN}-\text{acetone} < \text{H}_2\text{O}-\text{acetone} < \text{H}_2\text{O}-\textit{tert}\text{-BuOH}$ . Recyclability depended on the cooxidant used, leaching being observed when this was hexacyanoferrate, probably due to a competitive intercalation/deintercalation reaction between  $\text{OsO}_4^{2-}$  and  $\text{Fe}(\text{CN})_6^{3-}$ , which depends on the formal charge of the anion.

This catalyst has been also used for asymmetric aminohydroxylation (AA) of olefins [253] using chloramine-T and (DHQ)<sub>2</sub>PHAL to afford chiral vicinal

N-protected amino alcohols. Strong electron-deficient methyl cinnamate and ethyl crotonate undergo AA with better yields than less electron-deficient species, like stilbene or cyclohexene, due to the greater polarisation of the Os=NT group in the former. On recycling, enantiomeric excess was maintained, but conversion drastically decreased from 60% in the first run to 10% in the third one, leaching being related to the presence of chloramine-T in the reaction medium.

Mg,Al LDH systems containing two POMs,  $\text{OsO}_4^{2-}$  and  $\text{WO}_4^{2-}$ , without (sample LDH-OsW) or with (sample LDH-PdOsW) the simultaneous presence of  $\text{PdCl}_4^{2-}$ , have been prepared by Choudary et al. and used to synthesise chiral diols via Heck coupling – N-oxidation – asymmetric dihydroxylation [254]. The samples were prepared by ionic exchange from a chloride-LDH precursor from  $\text{K}_2\text{OsO}_4 \cdot 2\text{H}_2\text{O}$ ,  $\text{Na}_2\text{WO}_4 \cdot 2\text{H}_2\text{O}$  and  $\text{Na}_2\text{PdCl}_4$  at 25 °C without pH control. No swelling of the LDH is observed, indicating that the guest anions are located on the edge positions. FTIR ( $\nu_{\text{O}=\text{Os}=\text{O}}$  and  $\nu_{\text{O}=\text{W}=\text{O}}$  bands at 860–830  $\text{cm}^{-1}$  and  $\nu_{\text{Pd}-\text{Cl}}$  at 335  $\text{cm}^{-1}$ ) and UV–Vis spectra (bands due to tungstate, osmate and chloropalladate at 253, 280 and 293 nm, respectively) confirm the integrity of these species upon supporting, and the formal oxidation states remained unaltered, according to XPS measurements, either during ion exchange and at the end of the reaction.

Catalyst LDH-OsW displays superior activity to afford diols with higher yields than when silica or a resin was used as a support, and then the homogeneous catalyst in achiral dihydroxylation reactions. Simultaneous asymmetric dihydroxylation of several olefins to yield chiral vicinal diols with high yields using  $\text{H}_2\text{O}_2$  was achieved with LDH-OsW and its homogeneous analogue. Chiral diols can be synthesised using the trifunctional LDH-PdOsW catalyst and  $\text{H}_2\text{O}_2$  as a terminal oxidant, Fig. 12.15.

Table 12.6 summarises the reactions catalysed by LDHs with intercalated POMs containing boron, manganese or osmium species.

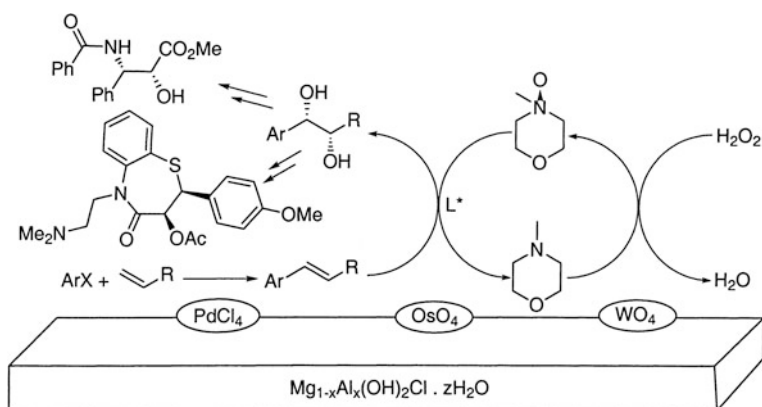


**Fig. 12.15** Catalytic cycle in the LDH-PdOsW-catalysed synthesis of chiral diols using  $\text{H}_2\text{O}_2$  as the terminal oxidant. Reprinted from [254], with permission from American Chemical Society

**Table 12.6** Summary of reactions catalysed by LDHs with intercalated boron, manganese or osmium-containing POMs

Layer cations	Intercalated species	Reaction	Substrate	References
Mg,Al	$[\text{B}(\text{OH})_4]^-$ , $[\text{B}_3\text{O}_3(\text{OH})_4]^-$	Beckmann isomerisation	Cyclohexanone oxime	[240]
Mg,Al (400 °C)	$[\text{B}(\text{OH})_4]^-$ , $[\text{B}_3\text{O}_3(\text{OH})_4]^-$	Beckmann isomerisation	Cyclohexanone	[241]
Mg,Al (400 °C)	$[\text{B}(\text{OH})_4]^-$ , $[\text{B}_3\text{O}_3(\text{OH})_4]^-$	Beckmann isomerisation	Cyclohexenone	[243]
Mg,Al	$\text{MnO}_4^-$	Selective oxidation	Ethylbenzene	
Mg,Al	$\text{MnO}_4^-$	Selective oxidation	Diphenylmethane	
Mg,Al	$\text{MnO}_4^-$	Selective oxidation	<i>n</i> -Propylbenzene	
Mg,Al	$\text{OsO}_4^{2-}$	Asymmetric dihydroxylation	Olefins	[251]
Mg,Al	$\text{OsO}_4^{2-}$	Dihydroxylation	<i>trans</i> -Stilbene	[252]
			$\alpha$ -Methylstyrene	
Mg,Al	$\text{OsO}_4^{2-}$	Asymmetric aminohydroxylation	Olefins	[253]
Mg,Al	$\text{OsO}_4^{2-}$ , $\text{WO}_4^{2-}$	Asymmetric hydroxylation	Olefins (aromatic, cyclic and mono, di- and trisubstituted)	[254]
Mg,Al	$\text{OsO}_4^{2-}$ , $\text{WO}_4^{2-}$ , $\text{PdCl}_4^{2-}$	Asymmetric hydroxylation	Olefins (aromatic, cyclic and mono, di- and trisubstituted)	

## 12.7 Conclusions

An overview of the results above summarised shows that the immobilisation of polyoxometalate species in the interlayers of layered double hydroxides with the hydrotalcite-type solids allows the preparation of heterogeneous catalysts with tailored red-ox and acidity properties. As it has been described, these properties can be finely tuned through the modification of both components (the cations in the brucite-like layers and the polyoxometalate in the interlayer) making them suitable materials in many different catalytic processes.

Although along this chapter we have extensively described a wide number of catalytic processes where these LDH–POM materials have been successfully tested, there is still a long way to be explored in this field; novel polyoxometalates are continuously being synthesised and layered double hydroxides offer them a suitable inorganic environment for their confinement at the nanometric level, modulating its pristine properties and in most of the cases improving their catalytic performances in a specific process.

On the other hand, parameters such as polarity modulation or the uses of different solvents that can strongly influence the reactivity of the LDH–POM tandem for a given catalytic process are not so far widely documented. The research in this field is widely open and the new expected findings will keep it as a very attractive field in the near future.

**Acknowledgements** Authors thank for financial support from Ministerio de Educación y Ciencia (grant MAT2009-08526) and ERDF. DC acknowledges a grant from Junta de Castilla y León.

## References

1. Cavani F, Trifirò F, Vaccari A (1991) Hydrotalcite-type anionic clays: preparation, properties and applications. *Catal Today* 11:173
2. Rives V (ed) (2001) Layered double hydroxides: present and future. Nova Science, New York, NY
3. Duan X, Evans DG (eds) (2006) Layered double hydroxides. Springer, Berlin
4. Wypych F, Satyanarayana KG (eds) (2004) Clay surfaces; fundamentals and applications. Elsevier, Amsterdam
5. Drits VA, Bookin AS (2001) Crystal structure and X-ray identification of layered double hydroxides. In: Rives V (ed) Layered double hydroxides: present and future. Nova Science, New York, NY, p 39
6. Fogg AM, Freij AG, Parkinson FM (2002) Synthesis and anion exchange chemistry of rhombohedral Li/Al layered double hydroxides. *Chem Mater* 14:232
7. Tichit D, Das N, Coq B, Durand R (2002) Preparation of Zr-containing layered double hydroxides and characterization of the acido-basic properties of their mixed oxides. *Chem Mater* 14:1530
8. Basile F, Fornasari G, Gazzano M, Vaccari A (2000) Synthesis and thermal evolution of hydrotalcite-type compounds containing noble metals. *Appl Clay Sci* 16:185
9. Dobrosz I, Jiratova K, Pitchon V, Rynkowski JM (2005) Effect of the preparation of supported gold particles on the catalytic activity in CO oxidation reaction. *J Molec Catal A* 234:187
10. Rives V, Kannan S (2000) Layered double hydroxides with the hydrotalcite-type structure containing  $\text{Cu}^{2+}$ ,  $\text{Ni}^{2+}$  and  $\text{Al}^{3+}$ . *J Mater Chem* 10:489

11. Rives V, Dubey A, Kannan S (2001) Synthesis, characterization and catalytic hydroxylation of phenol over CuCoAl ternary hydrotalcites. *Phys Chem Chem Phys* 3:4826
12. Morpugo S, Jacono M, Porta P (1996) Copper–zinc–cobalt–aluminium–chromium hydroxycarbonates and mixed oxides. *J Solid State Chem* 122:324
13. Monzón A, Romeo E, Royo C, Trujillano R, Labajos FM, Rives V (1999) Use of hydrotalcites as catalytic precursors of multimetallic mixed oxides. Application in the hydrogenation of acetylene. *Appl Catal A General* 185:53
14. Rives V, Labajos FM, Trujillano R, Romeo E, Royo C, Monzón A (1998) Acetylene hydrogenation on Ni–Al–Cr oxide catalysts: the role of added Zn. *Appl Clay Sci* 13:363
15. Monzón A, Romeo E, Royo C, Trujillano R, Labajos FM, Rives V (1998) Development of Ni mixed oxides as catalysts for selective hydrogenation. *Av Ing Quim* 8:24
16. Romeo E, Royo C, Monzón A, Trujillano R, Labajos FM, Rives V (2000) Preparation and characterisation of Ni–Mg–Al hydrotalcites as hydrogenation catalysts. *Stud Surface Sci Catal* 130:2099
17. Benito P, Herrero M, Labajos FM, Rives V, Royo N, Latorre N, Monzón A (2009) Production of carbon nanotubes from methane. Use of Co–Zn–Al catalysts prepared by microwave-assisted synthesis. *Chem Eng J* 149:455
18. Constantino VRL, Pinnavaia TJ (1995) Basic properties of  $Mg^{2+}_{1-x}Al^{3+}_x$  layered double hydroxides intercalated by carbonate, hydroxide, chloride, and sulfate anions. *Inorg Chem* 34:883
19. Newman SP, Jones W (1998) Synthesis, characterization and applications of layered double hydroxides containing organic guests. *New J Chem* 22:105
20. San Román MS, Holgado MJ, Jaubertie C, Rives V (2008) Synthesis, characterisation and delamination behaviour of lactate-intercalated Mg,Al-hydrotalcite-like compounds. *Solid State Sci* 10:1333
21. Jaubertie C, Holgado MJ, San Román MS, Rives V (2006) Structural characterization and delamination of lactate-intercalated Zn,Al-layered double hydroxides. *Chem Mater* 18:3114
22. Bhattacharjee S, Anderson JA (2006) Comparison of the epoxidation of cyclohexene, dicyclopentadiene and 1,5-cyclooctadiene over LDH hosted Fe and Mn sulfonato-salen complexes. *J Molec Catal A* 249:103
23. Rives V, Ulibarri MA (1999) Layered double hydroxides (LDH) intercalated with metal coordination compounds and oxometalates. *Coord Chem Rev* 181:61
24. Choy JH, Kwak SY, Park JS, Jeong JY (2001) Cellular uptake behavior of [-32P] labeled ATP–LDH nanohybrids. *J Chem Mater* 11:1671
25. Choy JH, Kwak SY, Park JS, Jeong JY, Portier J (1999) Intercalative nanohybrids of nucleoside monophosphates and DNA in layered metal hydroxide. *J Am Chem Soc* 121:1399
26. Desigaux L, Ben Belkacem M, Richard P, Cellier J, Leone P, Cario L, Leroux F, Taviot-Gueho C, Pitard B (2006) Self-assembly and characterization of layered double hydroxide/DNA hybrids. *Nanolett* 6:199
27. Kwon T, Pinnavaia TJ (1989) Pillaring of a layered double hydroxide by polyoxometalates with Keggin-ion structures. *Chem Mater* 1:381
28. López-Salinas E, García-Sánchez M, Montoya JA, Acosta DR, Abasolo JA, Schifter I (1997) Structural characterization of synthetic hydrotalcite-like  $[Mg_{1-x}Ga_x(OH)_2] (CO_3)_{x/2} \cdot mH_2O$ . *Langmuir* 13:4748
29. Valente JS, Figueras F, Gravelle M, Kumbhar P, López J, Besse JP (2000) Basic properties of the mixed oxides obtained by thermal decomposition of hydrotalcites containing different metallic compositions. *J Catal* 189:370
30. Rousselot I, Taviot-Gueho C, Leroux F, Leone P, Palvadeau P, Besse JP (2002) Insights on the structural chemistry of hydrocalumite and hydrotalcite-like materials: investigation of the series  $Ca_2M^{3+}(OH)_6Cl \cdot 2H_2O$  ( $M^{3+}$ :  $Al^{3+}$ ,  $Ga^{3+}$ ,  $Fe^{3+}$ , and  $Sc^{3+}$ ) by X-ray powder diffraction. *J Solid State Chem* 167:137

31. Chibwe K, Jones W (1989) Intercalation of organic and inorganic anions into layered double hydroxides. *J Chem Soc Chem Comm* 926
32. De Roy A, Forano C, Besse JP (2001) Layered double hydroxides: synthesis and post-synthesis modification. In: Rives V (ed) *Layered double hydroxides: present and future*. Nova Science, New York, NY, p 1
33. Kanazaki E (2004) Preparation of layered double hydroxides. In: Wypych F, Satyanarayana KG (eds) *Clay surfaces; fundamentals and applications*. Elsevier, Amsterdam, p 345
34. He J, Wei M, Li B, Kang Y, Evans DG, Duan X (2006) Preparation of double layered hydroxides. In: Duan X, Evans DG (eds) *Layered double hydroxides*. Springer, Berlin, p 89
35. Kooli F, Jones W, Rives V, Ulibarri MA (1997) An alternative route to polyoxometalate-exchanged layered double hydroxides: the use of ultrasound. *J Mater Sci Lett* 16:27
36. Taviot-Gueho C, Leroux F, Payen C, Besse JP (2005) Cationic ordering and second-staging structures in copper-chromium and zinc-chromium layered double hydroxides. *Appl Clay Sci* 28:111
37. Prinetto F, Ghiotti G, Graffin P, Tichit D (2000) Synthesis and characterization of sol-gel Mg/Al and Ni/Al layered double hydroxides and comparison with co-precipitated samples. *Micropor Mesopor Mater* 39:229
38. Zhao Y, Li F, Zhang R, Evans DG, Duan X (2002) Preparation of layered double-hydroxide nanomaterials with a uniform crystallite size using a new method involving separate nucleation and aging steps. *Chem Mater* 14:4286
39. Evans DG, Duan X (2006) Preparation of layered double hydroxides and their applications as additives in polymers, as precursors to magnetic materials and in biology and medicine. *Chem Comm* 485
40. Ma R, Takada K, Fukuda K, Iyi N, Bando Y, Sasaki T (2008) Topochemical synthesis of monometallic (Co<sup>2+</sup>-Co<sup>3+</sup>) layered double hydroxide and its exfoliation into positively charged Co(OH)<sub>2</sub> nanosheets. *Angew Chem Int Ed Engl* 47:86
41. Ma R, Takada K, Fukuda K, Iyi N, Bando Y, Sasaki T (2007) Synthesis and exfoliation of Co<sup>2+</sup>/Fe<sup>3+</sup> layered double hydroxides: an innovative topochemical approach. *J Am Chem Soc* 129:5257
42. Hu G, Wang N, O'Hare D, Davis J (2007) Synthesis of magnesium aluminium layered double hydroxides in reverse microemulsions. *J Mater Chem* 17:2257
43. Gérard E, Prevot V, Ghanbaja J, Leroux F (2006) Macroscopically ordered hydrotalcite-type materials using self-assembled colloidal crystal template. *Chem Mater* 18:238
44. Li L, Ma R, Ebin A, Iyi N, Sasaki T (2005) Positively charged nanosheets derived via total delamination of layered double hydroxides. *Chem Mater* 17:4386
45. Pérez-Bernal ME, Ruano-Casero RJ, Benito F, Rives V (2009) Nickel-aluminum layered double hydroxides prepared via inverse micelles formation. *J Solid State Chem* 182:1593
46. Climent MJ, Corma A, Iborra S, Epping K, Veltz A (2004) Increasing the basicity and catalytic activity of hydrotalcites by different synthesis procedures. *J Catal* 225:316
47. Herrero M (2008) *Nanomateriales híbridos orgánicos/inorgánicos con hidróxidos dobles laminares*. Ph D Thesis, University of Salamanca, Spain
48. Benito P (2007) *Influencia de la radiación microondas en el proceso de síntesis de compuestos tipo hidrotalcita y óxidos relacionados*. Ph D Thesis, University of Salamanca, Spain
49. Benito P, Labajos FM, Mafra L, Rocha J, Rives V (2009) Carboxylate-intercalated layered double hydroxides aged under microwave-hydrothermal treatment. *J Solid State Chem* 182:18
50. Herrero M, Labajos FM, Rives V (2009) Size control and optimisation of intercalated layered double hydroxides. *Appl Clay Sci* 42:510
51. Benito P, Herrero M, Barriga C, Labajos FM, Rives V (2008) Microwave-assisted homogeneous precipitation of hydrotalcites by urea hydrolysis. *Inorg Chem* 47:5453
52. Benito P, Guinea I, Labajos FM, Rives V (2008) Microwave-assisted reconstruction of Ni,Al hydrotalcite-like compounds. *J Solid State Chem* 181:987

53. Herrero M, Benito P, Labajos FM, Rives V (2007) Nanosize cobalt oxide-containing catalysts obtained through microwave-assisted methods. *Catal Today* 128:129
54. Benito P, Guinea I, Herrero M, Labajos FM, Rives V (2007) Incidence of microwave hydrothermal treatments on the crystallinity properties of hydrotalcite-like compounds. *Z Anorg Allg Chem* 633:1815
55. Benito P, Labajos FM, Rives V (2007) Microwave-assisted synthesis of layered double hydroxides. In: Buckley RW (ed) *Solid state chemistry research trends*. Nova Science, New York, NY, p 173
56. Herrero M, Benito P, Labajos FM, Rives V (2007) Stabilization of  $\text{Co}^{2+}$  in layered double hydroxides (LDHs) by microwave-assisted ageing. *J Solid State Chem* 180:873
57. Benito P, Labajos FM, Rives V (2006) Microwave-treated layered double hydroxides containing  $\text{Ni}^{2+}$  and  $\text{Al}^{3+}$ : the effect of added  $\text{Zn}^{2+}$ . *J Solid State Chem* 179:3784
58. Benito P, Labajos FM, Rocha J, Rives V (2006) Influence of microwave radiation on the textural properties of layered double hydroxides. *Micropor Mesopor Mater* 94:148
59. Benito P, Labajos FM, Rives V (2006) Uniform fast growth of hydrotalcite-like compounds. *Crystal Growth Design* 6:1961
60. Benito P, Labajos FM, Rives V (2006) Influence of microwave radiation on the thermal properties of Ni,Al hydrotalcite-like compounds. *Mater Sci Forum* 514–516:1284
61. Benito P, Herrero M, Labajos FM, Rives V (2006) Co-containing LDHs synthesized by the microwave-hydrothermal method. *Mater Sci Forum* 514–516:1241
62. Ookubo A, Ooi K, Hayashi H (1992) Hydrotalcites as potential adsorbents of intestinal phosphate. *J Pharm Sci* 81:1139
63. Del Arco M, Cebadera E, Gutiérrez S, Martín C, Montero MJ, Rives V, Rocha J, Sevilla MA (2004) Mg,Al layered double hydroxides with intercalated indomethacin: synthesis, characterization, and pharmacological study. *J Pharm Sci* 93:1649
64. Yang JH, Han YS, Park M, Park T, Hwang SJ, Choy JH (2007) New inorganic-based drug delivery system of indole-3-acetic acid-layered metal hydroxide nanohybrids with controlled release rate. *Chem Mater* 19:2679
65. O'Hare DM (2003) European Patent 1341556
66. Choy JH, Kwak SY, Jeong JY, Park JS (2000) Inorganic layered double hydroxides as nonviral vectors. *Angew Chem Int Ed Engl* 39:4041
67. Wang X, Zhang Q (2004) Effect of hydrotalcite on the thermal stability, mechanical properties, rheology and flame retardance of poly(vinyl chloride). *Polymer Int* 53:698
68. Kaluskova R, Novota M, Vymazal Z (2004) Investigation of thermal stabilization of poly(vinyl chloride) by lead stearate and its combination with synthetic hydrotalcite. *Polym Degr Stab* 85:903
69. Taviot-Gueho C, Illaïk A, Vuillermoz C, Commereuc S, Vernay V, Leroux F (2007) LDH-dye hybrid material as coloured filler into polystyrene: structural characterization and rheological properties. *J Phys Chem Solids* 68:1140
70. Stelandre L, Foulon M, Le Goff PY (2004) US Patent 6790895
71. Chen W, Qu BJ (2003) Structural characteristics and thermal properties of PE-g-MA/MgAl-LDH exfoliation nanocomposites synthesized by solution intercalation. *Chem Mater* 15:3208
72. Pereira CMC, Herrero M, Labajos FM, Marques AT, Rives V (2009) Preparation and properties of new flame retardant unsaturated polyester nanocomposites based on layered double hydroxides. *Polym Degrad Stab* 93:939
73. Sorrentino A, Gorrasi G, Tortora M, Vittoria V, Costantino U, Marmottini F, Padella F (2005) Incorporation of Mg–Al hydrotalcite into a biodegradable Poly( $\gamma$ -caprolactone) by high energy ball milling. *Polymer* 46:1601
74. Martínez-Gallegos S, Herrero M, Rives V (2008) Preparation of composites by in situ polymerisation of PET-hydrotalcite using dodecylsulphate. *Mater Sci Forum* 587–588:568
75. Martínez-Gallegos S, Herrero M, Rives V (2008) In situ microwave-assisted polymerization of polyethylene terephthalate in layered double hydroxides. *J Appl Polym Sci* 109:1388

76. Scavetta E, Balalrin B, Berettoni M, Caprani I, Giorgetti M, Tonelli D (2006) Electrochemical sensors based on electrodes modified with synthetic hydrotalcites. *Electrochim Acta* 51:2129
77. Shan D, Mousty C, Cosnier S (2004) Subnanomolar cyanide detection at polyphenol oxidase/clay biosensors. *Anal Chem* 76:178
78. Kovanda F, Kovacsova E, Kolousek D (1999) Removal of anions from solution by calcined hydrotalcite and regeneration of used sorbents in repeated calcination-rehydration-anion exchange processes. *Collect Czech Chem Comm* 64:1517
79. Miyata S (1983) Anion-exchange properties of hydrotalcite-like compounds. *Clays Clay Min* 31:305
80. Goh KH, Lim TT, Dong Z (2008) Application of layered double hydroxides for removal of oxyanions: a review. *Water Res* 42:1343
81. O'Hare DM, Lotsch B (2001) EP Patent 20010954187
82. Vaccari A (1998) Preparation and catalytic properties of cationic and anionic clays. *Catal Today* 41:53
83. Sels BF, de Vos DE, Jacobs PA (2001) Hydrotalcite-like anionic clays in catalytic organic reactions. *Catal Rev Sci Eng* 43:443
84. Centi G, Perathoner S (2008) Catalysis by layered materials: a review. *Micropor Mesopor Mater* 107:3–15
85. Tichit D, Coq B (2003) Catalysis by hydrotalcites and related materials. *CATTECH* 7:206
86. Figueras F (2004) Base catalysis in the synthesis of fine chemicals. *Topics Catal* 29:189
87. Nijss H, de Bock N, Vansant EF (1999) Comparative study of the synthesis and properties of polyoxometalate pillared layered double hydroxides (POM-LDHs). *J Porous Mater* 6:101
88. Gardner EA, Yun SK, Pinnavaia TJ (1998) Layered double hydroxides pillared by macropolyoxometalates. *Appl Clay Sci* 13:479
89. Müller-Tamm H, Frielingsdorf H, Schweier G, Reuter L (1971) German Patent 2163851
90. Bhattacharyya AA, Woltermann GM, Yoo JS, Karch A, Cormier WE (1988) Catalytic SO<sub>x</sub> abatement: the role of magnesium aluminate spinel in the removal of SO<sub>x</sub> from fluid catalytic cracking (FCC) flue gas. *Ind Eng Chem Res* 27:1356
91. Yoo JS, Bhattacharyya AA, Radiowski CA (1991) De-SO<sub>x</sub> catalyst: an XRD study of magnesium aluminate spinel and its solid solutions. *Ind Eng Chem Res* 30:1444
92. Das N, Tichit D, Durand R, Graffin P, Coq B (2001) Influence of the metal function in the "one-pot" synthesis of 4-methyl-2-pentanone (methyl isobutyl ketone) from acetone over palladium supported on Mg(Al)O mixed oxides catalysts. *Catal Lett* 71:181
93. Nikolopoulos AA, Jang BWL, Spivey JJ (2005) Acetone condensation and selective hydrogenation to MIBK on Pd and Pt hydrotalcite-derived MgAl mixed oxide catalysts. *Appl Catal A General* 296:128
94. Reichle WT (1980) Pulse microreactor examination of the vapor-phase aldol condensation of acetone. *J Catal* 63:295
95. Reichle WT (1985) Catalytic reactions by thermally activated, synthetic, anionic clay minerals. *J Catal* 94:547
96. Kohjiya S, Sato T, Nakayama T, Yamashita S (1981) Polymerization of propylene oxide catalyzed by calcined hydrotalcite. *Makromol Chem Rapid Comm* 2:231
97. Corma A, Iborra S, Primo J, Rey F (1994) One-step synthesis of citrinitril on hydrotalcite derived base catalysts. *Appl Catal A General* 114:215
98. Corma A, Fornés V, Rey F (1994) Hydrotalcites as base catalysts: influence of the chemical composition and synthesis conditions on the dehydrogenation of isopropanol. *J Catal* 148:205
99. Velu S, Swamy CS (1994) Alkylation of phenol with methanol over magnesium-aluminium calcined hydrotalcites. *Appl Catal A General* 119:241
100. Tichit D, Naciri Bennani M, Figueras F, Tessier R, Kervenal J (1998) Aldol condensation of acetone over layered double hydroxides of the meixnerite type. *Appl Clay Sci* 13:401
101. Velu S, Suzuki K, Okazaki M, Kapoor MP, Osaki T, Ohashi F (2000) Oxidative steam reforming of methanol over CuZnAl(Zr)-oxide catalysts for the selective production of



- hydrogen for fuel cells: catalyst characterization and performance evaluation. *J Catal* 194:373
102. Zhao Y, Jiao QZ, Li CH, Liang J (2007) Catalytic synthesis of carbon nanostructures using layered double hydroxides as catalyst precursors. *Carbon* 45:2159
  103. Coq B, Tichit D, Ribet S (2000) Co/Ni/Mg/Al layered double hydroxides as precursors of catalysts for the hydrogenation of nitriles: hydrogenation of acetonitrile. *J Catal* 189:117
  104. Dung NT, Tichit D, Chiche BH, Coq B (1998) Influence of the thermal treatments of a (Ni+Mg)/Al layered double hydroxide in the hydrogenation of acetonitrile. *Appl Catal A General* 169:179
  105. Rowlofs JCAA, Lensveld CJ, Van Dillen AJ, De Jong KP (2001) On the structure of activated hydrotalcites as solid base catalysts for liquid-phase aldol condensation. *J Catal* 203:184
  106. Abelló S, Medina F, Tichit D, Pérez-Jiménez J, Groen JC, Sueiras JE, Salagre P, Cesteros Y (2005) Aldol condensations over reconstructed Mg-Al hydrotalcites: structure-activity relationships related to the rehydration method. *Chem Eur J* 11:728
  107. Kishore D, Kannan S (2004) Double bond migration of eugenol to isoeugenol over as-synthesized hydrotalcites and their modified forms. *Appl Catal A General* 270:227
  108. Kishore D, Kannan S (2006) Catalytic isomerization of estragole to anethole over hydrotalcites and HT-like compounds. *J Molec Catal A Chemical* 244:83
  109. Rives V, Prieto O, Dubey A, Kannan S (2003) Synergistic effect in the hydroxylation of phenol over CoNiAl ternary hydrotalcites. *J Catal* 220:161
  110. Kaneda K, Yamashita T (1996) Heterogeneous Baeyer-Villiger oxidation of ketones using m-chloroperbenzoic acid catalyzed by hydrotalcites. *Tetrahedron Lett* 37:4555
  111. Costantino U, Curini M, Montanari F, Nocchetti M, Rosati O (2003) Hydrotalcite-like compounds as catalysts in liquid phase organic synthesis: I. Knoevenagel condensation promoted by  $[\text{Ni}_{0.73}\text{Al}_{0.27}(\text{OH})_2](\text{CO}_3)_{0.135}$ . *J Molec Catal A Chemical* 195:245
  112. Ueno S, Yamaguchi K, Yoshida K, Ebitani K, Kaneda K (1998) Hydrotalcite catalysis: heterogeneous epoxidation of olefins using hydrogen peroxide in the presence of nitriles. *Chem Comm* 295
  113. Schoonheydt RA, Pinnavaia TJ, Lagaly G, Gangas N (1999) Pillared clays and pillared layered solids. *Pure Appl Chem* 71:2367
  114. Mamedov EA, Cortés Corberán V (1995) Oxidative dehydrogenation of lower alkanes on vanadium oxide-based catalysts. The present state of the art and outlooks. *Appl Catal A General* 127:1
  115. Hu C, Li D, Guo Y, Wang E (2001) Supermolecular layered double hydroxides. *Chin Sci Bull* 46:1061
  116. Malherbe F, Depège C, Forano C, Besse JP, Atkins MP, Sharma B, Wade SR (1998) Alkoxylation reaction catalysed by layered double hydroxides. *Appl Clay Sci* 13:451
  117. Smith HD, Parkinson GM, Hart RD (2005) In situ absorption of molybdate and vanadate during precipitation of hydrotalcite from sodium aluminate solutions. *J Crystal Growth* 275:1665
  118. Drezdron MA (1988) Synthesis of isopolymetalate-pillared hydrotalcite via organic-anion-pillared precursors. *Inorg Chem* 27:4628
  119. Palmer SJ, Nguyen T, Frost RL (2007) Synthesis and Raman spectroscopic characterisation of hydrotalcite with  $\text{CO}_3^{2-}$ - and  $\text{VO}_3^-$ - anions in the interlayer. *J Raman Spec* 38:1602
  120. Chibwe M (1990) Ph D Thesis, University of Cambridge, UK
  121. Villa AL, de Vos DE, Verpoort F, Sels BF, Jacobs PA (2001) A study of V-pillared layered double hydroxides as catalysts for the epoxidation of terpenic unsaturated alcohols. *J Catal* 198:223
  122. Ulibarri MA, Labajos FM, Rives V, Trujillano R, Jones W, Kooli F (1994) Comparative study of the synthesis and properties of vanadate-exchanged layered double hydroxides. *Inorg Chem* 33: 2592

123. Maciuca AL, Dumitriu E, Fajula F, Hulea V (2008) Mild oxidation of tetrahydrothiophene to sulfolane over V-, Mo- and W-containing layered double hydroxides. *Appl Catal A General* 338:1
124. Dula R, Wcislo K, Stoch J, Grzybowska B, Serwicka EM, Kooli F, Bhranowski K, Gawel A (2002) Layered double hydroxide-derived vanadium catalysts for oxidative dehydrogenation of propane: influence of interlayer-doping versus layer-doping. *Appl Catal A General* 230:281
125. Rives V (2001) Study of layered double hydroxides by thermal methods. In: Rives V (ed) *Layered double hydroxides: present and future*. Nova Science, New York, NY, p 115
126. Kantcheva M (2000) Spectroscopic characterization of vanadium(V) oxo species deposited on zirconia. *Phys Chem Chem Phys* 2:3043
127. Maciuca AL, Ciocan CE, Dumitriu E, Fajula F, Hulea V (2008) V-, Mo- and W-containing layered double hydroxides as effective catalysts for mild oxidation of thioethers and thiophenes with H<sub>2</sub>O<sub>2</sub>. *Catal Today* 138:33
128. De Castro FR, Lam YL, Herbst MH, Santos FM, Mereira MM (2008) Thermal treatment study of vanadium-loaded hydrotalcites employing in situ DXAS. *Catal Today* 133–135:210
129. Bhranowski K, Dula R, Kooli F, Serwicka EM (1999) ESR study of the thermal decomposition of V-containing layered double hydroxides. *Colloids Surf A Physicochem Eng Aspects* 158:129
130. Serwicka EM, Nowak P, Bhranowski K, Jones W, Kooli F (1997) Insertion of electrochemically reduced Keggin anions into layered double hydroxides. *J Mater Chem* 7:1937
131. Bhranowski K, Kooli F, Poltowicz J, Serwicka EM (1998) Polyvanadate-exchanged hydrotalcites as catalysts for selective oxidation of cyclohexene with molecular oxygen. *React Kinet Catal Lett* 64:3
132. Kooli F, Crespo I, Barriga C, Ulibarri MA, Rives V (1996) Precursor dependence of the nature and structure of non-stoichiometric magnesium aluminium vanadates. *J Mater Chem* 6:1199
133. Bhranowski K, Brzybowska B, Kooli F, Serwicka EM, Wcislo K (1997) In: Haber J, Dyrek K, Lagan J (eds) *Third European congress on catalysis Europacat-3, Book of Abstracts vol 1, Drukarnia TEXT, Krakow*
134. Boudeville Y, Kolb M, Pantazidis A, Márquez Álvarez C, Mirodatos C, Elokhin V (1999) Monte-Carlo methods for simulating the catalytic oxidative dehydrogenation of propane over VMgO catalyst. *Chem Eng Sci* 54:4295
135. Creaser D, Andersson B, Hudgins RR, Silverston PL (1999) Transient kinetic analysis of the oxidative dehydrogenation of propane. *J Catal* 182:264
136. Blasco MT, López-Nieto JM (1997) Oxidative dehydrogenation of short chain alkanes on supported vanadium oxide catalysts. *Appl Catal A General* 157:117
137. Bhranowski K, Bueno G, Cortés Corberán V, Kooli F, Serwicka EM, Valenzuela RX, Wcislo K (1999) Oxidative dehydrogenation of propane over calcined vanadate-exchanged Mg,Al-layered double hydroxides. *Appl Catal A General* 185:65
138. Depège C, Bigey L, Forano C, de Roy A, Besse JP (1996) Synthesis and characterization of new copper-chromium layered double hydroxides pillared with polyoxovanadates. *J Solid State Chem* 126:314
139. Blanco S, Carrazán SRG, Rives V (2008) Oxidative dehydrogenation of propane on Mg-V-Al mixed oxides. *Appl Catal A General* 342:93
140. Aramendía MA, Borau V, Jiménez C, Marinas JM, Porras A, Urbano J (1996) Magnesium oxides as basic catalysts for organic processes: study of the dehydrogenation–dehydration of 2-propanol. *J Catal* 161:829
141. Wegrzyn A, Rafalska-Lasocha A, Dudek B, Dziembaj R (2006) Nanostructured V-containing hydrotalcite-like materials obtained by non-stoichiometric anion exchange as precursors of catalysts for oxidative dehydrogenation of n-butane. *Catal Today* 116:74

142. Del Arco M, Holgado MJ, Martín C, Rives V (1987) New route for the synthesis of  $V_2O_5$ -MgO oxidative dehydrogenation catalysts. *J Mater Sci Lett* 6:616
143. Wong J, Lytle FW, Messmer RP, Maylotte DH (1984) K-edge absorption spectra of selected vanadium compounds. *Phys Rev B* 30:5596
144. Malet P, Odriozola JA, Labajos FM, Rives V, Ulibarri MA (1995) XAS study of transition metal ions in hydrotalcite-like compounds. *Nuclear Instr Methods Phys Res B* 97:16
145. Dinka P, Prandova K, Hronec M (1998) Reaction of methanol and n-propanol over hydrotalcite-like catalysts containing vanadium oxide. *Appl Clay Sci* 13:467
146. Malherbe F, Besse JP, Wade SR, Smith WJ (2000) Highly selective synthesis of 2-butoxy ethanol over Mg/Al/V mixed oxides catalysts derived from hydrotalcites. *Catal Lett* 67:197
147. Choudary BM, Bharathi B, Venkat Reddy Ch, Lakshmi Kantam M, Raghavan KV (2001) The first example of catalytic N-oxidation of tertiary amines by tungstate-exchanged Mg-Al layered double hydroxide in water: a green protocol. *Chem Comm* 1736
148. Choudary BM, Bharathi B, Venkat Reddy Ch, Lakshmi Kantam M (2002) Tungstate-exchanged Mg-Al-LDH catalyst: an eco-compatible route for the oxidation of sulfides in aqueous medium. *J Chem Soc Perkin Trans 1* 2069
149. Prasanna SV, Kamath PV, Shivakumara C (2007) Synthesis and characterization of layered double hydroxides (LDHs) with intercalated chromate ions. *Mater Res Bull* 42:1028
150. Kooli F, Rives V, Ulibarri MA (1995) Preparation and study of decavanadate-pillared hydrotalcite-like anionic clays containing transition metal cations in the layers. 1. Samples containing nickel-aluminum prepared by anionic exchange and reconstruction. *Inorg Chem* 34:5114
151. Kooli F, Rives V, Ulibarri MA (1995) Preparation and study of decavanadate-pillared hydrotalcite-like anionic clays containing transition metal cations in the layers. 2. Samples containing magnesium-chromium and nickel-chromium. *Inorg Chem* 34:5122
152. Del Arco M, Carriazo D, Martín C, Pérez-Gruoso AM, Rives V (2006) Characterization of chromate-intercalated layered double hydroxides. *Mater Sci Forum* 514–516:1541
153. Carriazo D, del Arco M, Martín C, Rives V (2007) A comparative study between chloride and calcined carbonate hydrotalcites as adsorbents for Cr(VI). *Appl Clay Sci* 37:231
154. Frost RL, Musumeci AW, Bostrom T, Adebajo MO, Weier ML, Martens W (2005) Thermal decomposition of hydrotalcite with chromate, molybdate or sulphate in the interlayer. *Thermochim Acta* 429:179
155. Del Arco M, Carriazo D, Martín C, Pérez-Gruoso AM, Rives V (2005) Acid and redox properties of mixed oxides prepared by calcination of chromate-containing layered double hydroxides. *J Solid State Chem* 178:3571
156. Stanimirova St, Vergilov I, Kirov G, Petrova N (1999) Thermal decomposition products of hydrotalcite-like compounds: low-temperature metaphases. *J Mater Sci* 34:4153
157. Venezia AM, Palmisano L, Schiavello M, Martín C, Rives V (1994) Characterization of chromium ion-doped titania by FTIR and XPS. *J Catal* 147:115
158. Prevot V, Forano C, Besse JP (1999) Reactivity of oxalate with ZnAl layered double hydroxides through new materials. *J Mater Chem* 9:155
159. Prevot V, Forano C, Besse JP (2000) Intercalation of anionic oxalato complexes into layered double hydroxides. *J Solid State Chem* 153:301
160. Gutmann N, Müller B, Tiller HJ (1995) Malonate intercalation into layered chromium—zinc double hydroxides. *J Solid State Chem* 119:331
161. Carlino S, Hudson M (1998) A thermal decomposition study on the intercalation of tris-(oxalato) ferrate(III) trihydrate into a layered (Mg/Al) double hydroxide. *Solid State Ionics* 110:153
162. Del Arco M, Gutiérrez S, Martín C, Rives V (2003) Intercalation of  $[Cr(C_2O_4)_3]^{3-}$  complex in Mg,Al layered double hydroxides. *Inorg Chem* 42:4232
163. Del Arco M, Gutiérrez S, Martín C, Rives V, Rocha J (2000) Effect of the Mg: Al ratio on borate (or silicate)/nitrate exchange in hydrotalcite. *J Solid State Chem* 151:272
164. Wu G, Wang X, Li J, Zhao N, Wei W, Sun Y (2008) A new route to synthesis of sulphonato-salen-chromium(III) hydrotalcites: highly selective catalysts for oxidation of benzyl alcohol to benzaldehyde. *Catal Today* 131:402

165. Tsyganok A, Green RG, Giorgi JB, Sayari A (2007) Non-oxidative dehydrogenation of ethane to ethylene over chromium catalysts prepared from layered double hydroxide precursors. *Catal Comm* 8:2186
166. Labajos FM, Rives V (1996) Thermal evolution of chromium(III) ions in hydrotalcite-like compounds. *Inorg Chem* 35:5313
167. Tsyganok A, Sayari A (2006) Incorporation of transition metals into Mg–Al layered double hydroxides: Coprecipitation of cations vs. their pre-complexation with an anionic chelator. *J Solid State Chem* 179:1830
168. Vaysse C, Guerlou-Demourgues L, Demourgues A, Delmas C (2002) Thermal behavior of oxometalate (Mo, W)-intercalated layered double hydroxides: study of the grafting phenomenon. *J Solid State Chem* 167:59
169. Hibino T, Tsunashima A (1997) Synthesis of paramolybdate intercalates of hydrotalcite-like compounds by ion exchange in ethanol/water solution. *Chem Mater* 9:2082
170. Xu ZP, Zeng HC (2001) Abrupt structural transformation in hydrotalcite-like compounds  $Mg_{1-x}Al_x(OH)_2(NO_3)_x \cdot nH_2O$  as a continuous function of nitrate anions. *J Phys Chem B* 105:1743
171. Gardner E, Pinnavaia TJ (1998) On the nature of selective olefin oxidation catalysts derived from molybdate- and tungstate-intercalated layered double hydroxides. *Appl Catal A General* 167:65
172. Taylor RM (1984) The rapid formation of crystalline double hydroxy salts and other compounds by controlled hydrolysis. *Clay Miner* 19:591
173. Zavoianu R, Birjega R, Pavel OD, Cruceanu A, Alifanti M (2005) Hydrotalcite like compounds with low Mo-loading active catalysts for selective oxidation of cyclohexene with hydrogen peroxide. *Appl Catal A General* 286:211
174. Kwon T, Tsigdinos GA, Pinnavaia TJ (1988) Pillaring of layered double hydroxides (LDH's) by polyoxometalate anions. *J Am Chem Soc* 110:3653
175. Van Laar F, de Vos D, Vanoppen D, Sels B, Jacobs PA, del Guerzo A, Pierard F, Kirsch-de Mesmacker A (1998) Heterogeneous molybdate catalysts for the generation of singlet molecular oxygen ( $^1\Delta_g$ ) from  $H_2O_2$ . *Chem Comm* 267
176. Van Laar FM, de Vos DE, Pierard E, Kirsch-de Mesmacker A, Fiermans L, Jacobs PA (2001) Generation of singlet molecular oxygen from  $H_2O_2$  with molybdate-exchanged layered double hydroxides: effects of catalyst composition and reaction conditions. *J Catal* 197:139
177. Carriazo D, Martín C, Rives V, Popescu A, Cojocaru B, Mandache I, Parvulescu VI (2006) Hydrotalcites composition as catalysts: preparation and their behavior on epoxidation of two bicycloalkenes. *Micropor Mesopor Mater* 95:39
178. Carriazo D, Domingo C, Martín C, Rives V (2006) Structural and texture evolution with temperature of layered double hydroxides intercalated with paramolybdate anions. *Inorg Chem* 45:1243
179. Mitchell PCH, Wass SA (2002) Propane dehydrogenation over molybdenum hydrotalcite catalysts. *Appl Catal A General* 225:153
180. Twu J, Dutta PK (1992) Raman spectroscopic studies of intercalated molybdate ions in layered metal hydroxides. *Chem Mater* 4:398
181. Sinha J, Layek S, Mandal GC, Bhattacharjee M (2001) A green Hunsdiecker reaction: synthesis of bromostyrenes from the reaction of unsaturated aromatic carboxylic acids with KBr and  $H_2O_2$  catalysed by  $Na_2MoO_4 \cdot 2H_2O$  in aqueous medium. *Chem Comm* 1916
182. Choudary BM, Someshwar T, Kantam ML, Reddy Ch V (2004) Molybdate-exchanged Mg–Al–LDH catalyst: an eco-compatible route for the synthesis of  $\alpha$ -bromostyrenes in aqueous medium. *Catal Comm* 5:215
183. Wahlen J, de Vos DE, Jacobs PA, Alsters PL (2004) Solid materials as sources for synthetically useful singlet oxygen. *Adv Synth Catal* 346:152
184. Nardello V, Marko J, Vermeersch G, Aubry JM (1995)  $^{90}Mo$  NMR and kinetic studies of peroxomolybdic intermediates involved in the catalytic disproportionation of hydrogen peroxide by molybdate ions. *Inorg Chem* 34:4950

185. Csányi LJ, Horváth I, Galbács ZM (1989) Peroxide derivatives of molybdenum(VI) in neutral and alkaline media. *Transition Metal Chem* 14:90
186. Sels BF, de Vos DE, Grobet PJ, Jacobs PA (2001) Kinetic and spectroscopic study of  $^1\text{O}_2$  generation from  $\text{H}_2\text{O}_2$  catalyzed by LDH- $\text{MoO}_4^{2-}$  (LDH=Layered Double Hydroxide). *Chem Eur J* 2547
187. Sels BF, de Vos DE, Grobet PJ, Pierard F, Kirsch-de Mesmaeker A, Jacobs PA (1999) Molybdate- and tungstate-exchanged layered double hydroxides as catalysts for  $^1\text{O}_2$  formation: characterization of reactive oxygen species and a critical evaluation of  $^1\text{O}_2$  detection methods. *J Phys Chem B* 103:11114
188. Wahlen J, de Vos DE, Sels BF, Nardello V, Aubry JM, Alsters PL, Jacobs PA (2005) Molybdate-exchanged layered double hydroxides for the catalytic disproportionation of hydrogen peroxide into singlet oxygen: evaluation and improvements of  $^1\text{O}_2$  generation by combined chemiluminescence and trapping experiments. *Appl Catal A General* 293:120
189. Wahlen J, de Vos D, Jary W, Alsters P, Jacobs P (2007) Glycol-modified molybdate catalysts for efficient singlet oxygen generation from hydrogen peroxide. *Chem Comm* 2333
190. Alaerts L, Wahlen J, Jacobs PA, de Vos DE (2008) Recent progress in the immobilization of catalysts for selective oxidation in the liquid phase. *Chem Comm* 1727
191. Crespo I, Barriga C, Rives V, Ulibarri MA (1997) Intercalation of iron hexacyano complexes in Zn,Al-hydrotalcite. *Solid State Sci* 101:729
192. Carriazo D, Martín C, Rives V (2007) An FT-IR study of the adsorption of isopropanol on calcined layered double hydroxides containing isopolymolybdate. *Catal Today* 126:153
193. Del Arco M, Gutiérrez S, Martín C, Rives V (2001) FTIR study of isopropanol reactivity on calcined layered double hydroxides. *Phys Chem Chem Phys* 3:119
194. Li C, Fu Sh, Zhang H (1994) An infrared spectroscopic study on the Lewis base properties of metal oxides by using a novel probe molecule: boric acid trimethyl ester. *Chem Comm* 17
195. Del Arco M, Carrazán SRG, Martín C, Rives V (1996) The effect of the preparation method on the nature and dispersion of surface species formed upon reaction of molybdenum trioxide with alumina and titania. *J Mater Sci* 31:1561
196. Tessier R, Tichit D, Figueras F, Kervennal J (1995) FR Patent 9500094
197. Chisem IC, Jones W, Martín C, Martín I, Rives V (1998) Probing the surface acidity of lithium aluminium and magnesium aluminium layered double hydroxides. *J Mater Chem* 8:1917
198. Das J, Parida KM (2007) Heteropoly acid intercalated Zn/Al HTlc as efficient catalyst for esterification of acetic acid using n-butanol. *J Molec Catal A Chemical* 264:248
199. Cabello CI, Cabrerizo FM, Alvarez A, Thomas HJ (2002) Decamolybdodicobaltate(III) heteropolyanion: structural, spectroscopical, thermal and hydrotreating catalytic properties. *J Molec Catal A Chemical* 186:89
200. Mazurelle J, Lamonier C, Lancelot C, Payen E, Pichon C, Guillaume D (2008) Use of the cobalt salt of the heteropolyanion  $[\text{Co}_2\text{Mo}_{10}\text{O}_{38}\text{H}_4]^{6-}$  for the preparation of CoMo HDS catalysts supported on  $\text{Al}_2\text{O}_3$ ,  $\text{TiO}_2$  and  $\text{ZrO}_2$ . *Catal Today* 130:41
201. Bravo-Suárez JJ, Páez-Mozo EA, Oyama ST (2004) Intercalation of decamolybdodicobaltate(III) anion in layered double hydroxides. *Chem Mater* 16:1214
202. Bravo-Suárez JJ, Páez-Mozo EA, Oyama ST (2004) Microtextural properties of layered double hydroxides: a theoretical and structural model. *Micropor Mesopor Mater* 67:1
203. Yun SK, Pinnavaia TJ (1996) Layered double hydroxides intercalated by polyoxometalate anions with kegglin ( $\alpha\text{-H}_2\text{W}_{12}\text{O}_{40}^{6-}$ ), dawson ( $\alpha\text{-P}_2\text{W}_{18}\text{O}_{62}^{6-}$ ), and finke ( $\text{Co}_4(\text{H}_2\text{O})_2(\text{PW}_9\text{O}_{34})_2^{10-}$ ) structures. *Inorg Chem* 35:6853
204. Weir MR, Kydd RA (1998) Synthesis of metatungstate pillared layered double hydroxides with variable layer composition. Effect of the Mg:Al ratio on the microporous structure. *Micropor Mesopor Mater* 20:339
205. Tatsumi T, Yamamoto K, Tajima H, Tominaga H (1992) Shape selective epoxidation of alkenes catalyzed by polyoxometalate-intercalated hydrotalcite. *Chem Lett* 815

206. Guo Y, Li D, Hu C, Wang Y, Wang E (2001) Layered double hydroxides pillared by tungsten polyoxometalates: synthesis and photocatalytic activity. *Int J Inorg Mater* 3:347
207. Del Arco M, Carriazo D, Gutiérrez S, Martín C, Rives V (2004) Synthesis and characterization of new Mg<sub>2</sub>Al-paratungstate layered double hydroxides. *Inorg Chem* 43:375
208. Weir MR, Moore J, Kydd RA (1997) Effects of pH and Mg:Ga ratio on the synthesis of gallium-containing layered double hydroxides and their polyoxometalate anion exchanged products. *Chem Mater* 9:1686
209. Narita E, Kaviratna PD, Pinnavaia TJ (1993) Direct synthesis of a polyoxometallate-pillared layered double hydroxide by coprecipitation. *J Chem Soc Chem Comm* 60
210. Wang J, Tian Y, Wang RC, Clearfield A (1992) Pillaring of layered double hydroxides with polyoxometalates in aqueous solution without use of preswelling agents. *Chem Mater* 4:1276
211. Weber RS, Gallezot P, Lefebvre F, Suib SL (1993) Partial pillaring of layered double hydroxides by [SiW<sub>9</sub>V<sub>3</sub>O<sub>40</sub>]<sup>7-</sup>. *Micropor Mater* 1:223
212. Del Arco M, Carriazo D, Gutiérrez S, Martín C, Rives V (2004) An FT-IR study of the adsorption and reactivity of ethanol on systems derived from Mg<sub>2</sub>Al-W<sub>7</sub>O<sub>24</sub><sup>6-</sup> layered double hydroxides. *Phys Chem Chem Phys* 6:465
213. Mars P, van Krevelen DW (1954) Oxidations carried out by means of vanadium oxide catalysts. *Chem Eng Sci* 3:41
214. Wongkerd T, Puengnaruemitchai A, Jitkarna S (2008) Phase change of catalysts derived from a LDH-deoxycholate intercalated compound and its impacts on NO reduction from stationary source emissions. *Appl Catal B Environmental* 78:101
215. Ogawa M, Asai S (2000) Hydrothermal synthesis of layered double hydroxide/deoxycholate intercalation compounds. *Chem Mater* 12:3253
216. Kwon T, Pinnavaia TJ (1992) Synthesis and properties of anionic clays pillared by [XM<sub>12</sub>O<sub>40</sub>]<sup>n-</sup> Keggin ions. *J Molec Catal* 74:23
217. Watanabe Y, Yamamoto K, Tatsumi T (1999) Epoxidation of alkenes catalyzed by heteropolyoxometalate as pillars in layered double hydroxides. *J Molec Catal A Chemical* 145:281
218. Carriazo D, Lima S, Martín C, Pillinger M, Valente AA, Rives V (2007) Metatungstate and tungstoniobate-containing LDHs: preparation, characterisation and activity in epoxidation of cyclooctene. *J Phys Chem Solids* 68:1872
219. Wei X, Fu Y, Xu L, Li F, Bi B, Liu X (2008) Tungstocobaltate-pillared layered double hydroxides: preparation, characterization, magnetic and catalytic properties. *J Solid State Chem* 181:1292
220. Jana SK, Kubota Y, Tatsumi T (2008) Cobalt-substituted polyoxometalate pillared hydroxide: synthesis and catalysis in liquid-phase oxidation of cyclohexanol with molecular oxygen. *J Catal* 255:40
221. Sels BF, de Vos DE, Buntinx M, Pierard F, Kirsch-de Mesmaeker A, Jacobs P (1999) Layered double hydroxides exchanged with tungstate as biomimetic catalysts for mild oxidative bromination. *Nature* 400:855
222. Sels BF, de Vos DE, Buntinx M, Jacobs PA (2003) Transition metal anion exchanged layered double hydroxides as a bioinspired model of vanadium bromoperoxidase. *J Catal* 216:288
223. Sels BF, de Vos DE, Jacobs PA (2001) Use of WO<sub>4</sub><sup>2-</sup> on layered double hydroxides for mild oxidative bromination and bromide-assisted epoxidation with H<sub>2</sub>O<sub>2</sub>. *J Am Chem Soc* 123:8350
224. Sels BF, Levecque P, Brosius R, de Vos DE, Jacobs P, Gammon DW, Kinfe HH (2005) A new catalytic route for the oxidative halogenation of cyclic enol ethers using tungstate exchanged on takovite. *Adv Synth Catal* 347:93
225. Choudary BM, Someshwar T, Reddy Ch V, Kantam ML, Ratnam KJ, Sivaji LV (2003) The first example of bromination of aromatic compounds with unprecedented atom economy using molecular bromine. *Appl Catal A General* 251:397

226. Herrmann JM (1999) Heterogeneous photocatalysis: fundamentals and applications to the removal of various types of aqueous pollutants. *Catal Today* 53:115
227. Guo Y, Li D, Hu C, Wang Y, Wang E, Zhou Y, Feng S (2001) Photocatalytic degradation of aqueous organochlorine pesticide on the layered double hydroxide pillared by Paratungstate A ion,  $Mg_{12}Al_6(OH)_{36}(W_7O_{24}) \cdot 4H_2O$ . *Appl Catal B Environmental* 30:337
228. Guo Y, Li D, Hu C, Wang E, Zou Y, Ding H, Feng S (2002) Preparation and photocatalytic behavior of Zn/Al/W(Mn) mixed oxides via polyoxometalates intercalated layered double hydroxides. *Micropor Mesopor Mater* 56:153
229. Liu Y, Murata K, Hanaoka T, Inaba M, Sakanishi K (2007) Synthesis of new peroxo-polyoxo metalates intercalated layered double hydroxides for propene epoxidation by molecular oxygen in methanol. 248:277
230. Palomeque J, Figueras F, Gelbard G (2006) Epoxidation with hydrotalcite-intercalated organotungstic complexes. *Appl Catal A General* 300:100
231. Liu P, Wang C, Zeng F, Ying P, Li C (2008) Direct immobilization of self-assembled polyoxometalate catalyst in layered double hydroxide for heterogeneous epoxidation of olefins. *J Catal* 256:345
232. De Vos DE, Wahlen J, Sels BF, Jacobs PA (2002) Peroxide reactions with anion-exchanged layered double hydroxide catalysts. *Synlett* 367
233. Liu P, Wang C, Li C (2009) Epoxidation of allylic alcohols on self-assembled polyoxometalates hosted in layered double hydroxides with aqueous  $H_2O_2$  as oxidant. *J Catal* 262:159
234. Hulea V, Maciucă AL, Fajula F, Dumitriu E (2006) Catalytic oxidation of thiophenes and thioethers with hydrogen peroxide in the presence of W-containing layered double hydroxides. *Appl Catal A General* 313:200
235. Maciucă AL, Dumitriu E, Fajula F, Hulea V (2007) Catalytic oxidation processes for removing dimethylsulfoxide from wastewater. *Chemosphere* 68:227
236. Cheng S, Lin JT (1992) Preparation and characterization of borate pillared anionic clay. In: Ocelli ML, Robson HE (eds) *Synthesis of microporous materials, vol 2. Expanded clays and other microporous solids*, Van Nostrand Reinhold, New York, NY, p 170
237. Li C, Ma S, Liu X, Yue Y, Hui J, Xu R, Bao Y, Rocha J (1996) Synthesis and characterization of tetraborate pillared hydrotalcite. *Chem Mater* 8:204
238. Bhattacharyya AA, Hall DB (1992) New triborate-pillared hydrotalcites. *Inorg Chem* 31:3869
239. Del Arco M, Gutiérrez S, Martín C, Rives V (2000) Sistemas LDHs de Mg Y Al con distinto anión en la interlámina calcinados: Reactividad en la aldolización del acetaldehído. In: Orfao JM, Faria JL, Figueiredo JL (eds) *Proceedings of XVII Iberoamerican symposium on catalysis, Porto, Portugal, FEUP Ed., CD-ROM edition*
240. Bechara R, D'Huysser A, Fournier M, Forni L, Fornasari G, Trifirò F, Vaccari A (2002) Synthesis and characterization of boron hydrotalcite-like compounds as catalyst for gas-phase transposition of cyclohexanone-oxime. *Catal Lett* 82:59
241. Forni L, Fornasari G, Trifirò F (2008) Intercalation of hydrotalcite-like anionic clays with boron anions and their effect on cyclohexanone oxime isomerization. *Micropor Mesopor Mater* 107:39
242. Villegas JC, Giraldo OH, Laubernds K, Suib SL (2003) New layered double hydroxides containing intercalated manganese oxide species: synthesis and characterization. *Inorg Chem* 42:5621
243. Choudary VR, Indurkar JR, Narkhede VS, Jha R (2004)  $MnO_4^{-1}$  exchanged Mg–Al hydrotalcite: a stable and reusable/environmental-friendly catalyst for selective oxidation by oxygen of ethylbenzene to acetophenone and diphenylmethane to benzophenone. *J Catal* 227:257
244. Dula R, Janik R, Machej T, Stoch J, Grabowski R, Serwicka EM (2007) Mn-containing catalytic materials for the total combustion of toluene: the role of Mn localisation in the structure of LDH precursor. *Catal Today* 119:327

245. Nowak I, Ziolek M (1999) Niobium compounds: preparation, characterization, and application in heterogeneous catalysis. *Chem Rev* 9:3603
246. Carlini C, Giuratti M, Galletti AMR, Sbrana G, Armaroli T, Busca G (1999) Selective saccharides dehydration to 5-hydroxymethyl-2-furaldehyde by heterogeneous niobium catalysts. *Appl Catal A General* 183:295
247. Dias AS, Lima S, Carriazo D, Rives V, Pillinger M, Valente AA (2006) Exfoliated titanate, niobate and titanoniobate nanosheets as solid acid catalysts for the liquid-phase dehydration of d-xylose into furfural. *J Catal* 244:230
248. Evans J, Pillinger M, Zhang JJ (1996) Structural studies of polyoxometalate-anion-pillared layered double hydroxides. *J Chem Soc Dalton Trans* 2963
249. Carriazo D, Martín C, Rives V (2006) Thermal evolution of a MgAl hydrotalcite-like material intercalated with hexaniobate. *Eur J Inorg Chem* 4608
250. Martín C, Solana G, Malet P, Rives V (2003) Nb<sub>2</sub>O<sub>5</sub>-supported WO<sub>3</sub>: a comparative study with WO<sub>3</sub>/Al<sub>2</sub>O<sub>3</sub>. *Catal Today* 78:365
251. Choudary BM, Chowdari NS, Kantam ML, Raghavan KV (2001) Catalytic asymmetric dihydroxylation of olefins with new catalysts: the first example of heterogenization of OsO<sub>4</sub><sup>2-</sup> by ion-exchange technique. *J Am Chem Soc* 123:9220
252. Choudary BM, Chowdari NS, Jyothi K, Kantam ML (2002) Catalytic asymmetric dihydroxylation of olefins with reusable OsO<sub>4</sub><sup>2-</sup> on ion-exchangers: the scope and reactivity using various cooxidants. *J Am Chem Soc* 124:5341
253. Choudary BM, Chowdari NS, Jyothi K, Kantam ML (2003) Heterogeneous catalytic asymmetric aminohydroxylation of olefins using LDH-supported OsO<sub>4</sub>. *J Molec Catal A Chemical* 196:151
254. Choudary BM, Chowdari NS, Madhi S, Kantam ML (2003) A trifunctional catalyst for one-pot synthesis of chiral diols via heck coupling-N-oxidation-asymmetric dihydroxylation: application for the synthesis of diltiazem and taxol side chain. *J Org Chem* 68:1735



# Chapter 13

## Basicity, Catalytic and Adsorptive Properties of Hydrotalcites

Francois Figueras

**Abstract** Solid bases have numerous potential applications, not only as catalyst for the manufacture of fine chemicals, in refining and petrochemistry, but also for adsorption and anion exchange. The present processes use liquid bases, typically alcoholic potash, and require neutralisation of the reaction medium at the end of the reaction, with production of salts. The substitution of these liquid bases by solids would provide cleaner and safer processes, due to the reduction of salts, and facilitate separation of the products and recycling of the catalyst. This chapter reviews the recent ideas on the modification of the basic properties of hydrotalcites by anion exchange and on the catalytic properties of solid bases as catalysts. Many examples of successful applications are given, with emphasis to industrial processes recently presented such as isomerisation of olefins. The basic properties of hydrotalcites can also be used to carry the exchange of toxic anions, humic acids or dyes, and have driven recent developments proposing HDT as drug carriers.

**Keywords** PILC · Pillared clays · Catalysts · Hydrotalcites

### 13.1 Introduction

Hydrotalcite (HDT) is an anionic clay, also known as layered double hydroxide (LDH), of composition  $\text{Mg}_6\text{Al}_2(\text{CO}_3)(\text{OH})_{16}\cdot 4(\text{H}_2\text{O})$ , showing a layered structure of brucite in which Mg is partially substituted by Al. The metal hydroxide layers are positively charged, with balancing anions and water molecules located interstitially [4]. Isomorphous structures are obtained by the substitution of divalent cations (Mg, Cu, Ni, Mn), by trivalent cations. Hydrotalcite-like structures can be obtained using other trivalent (Al, Fe, Cr) and divalent cations (Mg, Ni, Cu, Co, Zn, Mn) [1]. The HDTs used industrially are now synthetic, and several methods have been reported for their synthesis [2–5], including sol–gel [6].

---

F. Figueras (✉)

IRCELYON-CNRS-Université Lyon, 2 avenue Albert Einstein, 69626 Villeurbanne Cedex, France  
e-mail: francois.figueras@ircelyon.univ-lyon1.fr

The compensating anions, which are carbonates in the natural mineral, can be exchanged and their substitution by  $\text{OH}^-$  allows the synthesis of a Bronsted base, while calcination yields a solid Lewis base. The basic strength is related to the density of charge, which can be calculated from Sanderson's theory of electronegativity [7] or determined by XPS [8]. According to Sanderson's model, the intermediate electronegativity of a compound is defined as a geometrical mean of the atomic electronegativities of the components. The average charge on an element can then be defined as

$$\delta_i = (\chi - \chi_i) / \eta_i$$

where  $\chi$  and  $\eta_i$  are the electronegativity and hardness of the element  $i$  under consideration. The calculation was done for HDTs of different chemical composition using the electronegativity values of Allred and Rochow [9]. A linear correlation can be obtained between the temperature of decarbonation of hydrotalcites and the partial charge of oxygen (Fig. 13.1) [10]; thus in a first approximation, the basic properties of hydrotalcites are controlled by the electronegativity of the components. The model predicts that basicity also changes with the chemical composition; however, the  $M2/M3$  ratio in hydrotalcites can be changed in a small range only, so that the effect of this ratio on the average charge on oxygen is relatively small, leading to small variations of the decarbonation temperature with the Mg/Al ratio [11].

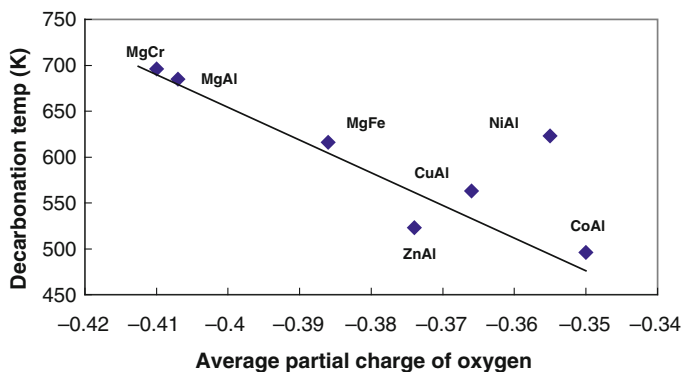


**Fig. 13.1** Relation between the average charges on oxygen according to Sanderson with the decarbonation temperature, for a series of hydrotalcites. Reprinted from [10], with permission from Elsevier

## 13.2 Activation of HDT

The properties of HDT for anionic exchange have been described by Miyata [12]. The equilibrium constants of monovalent anions are in the sequence  $\text{OH}^- > \text{F}^- > \text{Cl}^- > \text{Br}^- > \text{NO}_3^- > \text{I}^-$  and those for divalent anions  $\text{CO}_3^{2-} > \text{SO}_4^{2-}$ . The

ion-exchange equilibrium constants tend to increase as the diameter of the anions decreases. These rules are useful for the determination of potential applications and of conditions of activation. Due to these rules, the exchange of carbonates for  $\text{OH}^-$  is unfavoured, and the simpler method of activation is based on the decarbonation by calcination at about 450–500 °C, followed by rehydration either in the gas or liquid phase [13, 14]. This method has been later improved by using rehydration in the liquid phase using ultrasounds or a high stirring speed, leading to nanoplatelets with surface areas of 400 m<sup>2</sup>/g, displaying catalytic activities in aldol condensations up to eight times higher than the catalysts rehydrated in the gas phase [15, 16]. The basic properties of HDT can also be modified introducing F [17, 18] or *tert*-butyrate anions [19] both leading to a higher activity for base-catalysed reactions. In both cases the preparation is based on the reconstruction of the HDT structure of a calcined sample in the presence of solutions of KF or Kt-OBu. Kantam et al. [20] have reported the modification of HDT by reaction with Li-diisopropylamide which also gives a rather strong base, as evidenced by the catalytic properties for Michael additions for instance.

Several attempts have been made to increase the reactivity of HDT by decreasing the particle size in the synthesis. In that case, sonication was used in the preparation of HDT at 298 K. These HDT samples prepared under sonication were formed by dispersed and homogenous particles of 80 nm average particle size [21]. After calcinations the surface area increases up to 300 m<sup>2</sup>/g, slightly above the usual value of 230–280 m<sup>2</sup>/g. A recent advance in the preparation of HDT has been to grow it on a carbon nanofiber as support [22, 23]. Very small crystallites, of about 20 nm in size, are then obtained, which exhibit a much higher number of basic sites and higher activity [23].

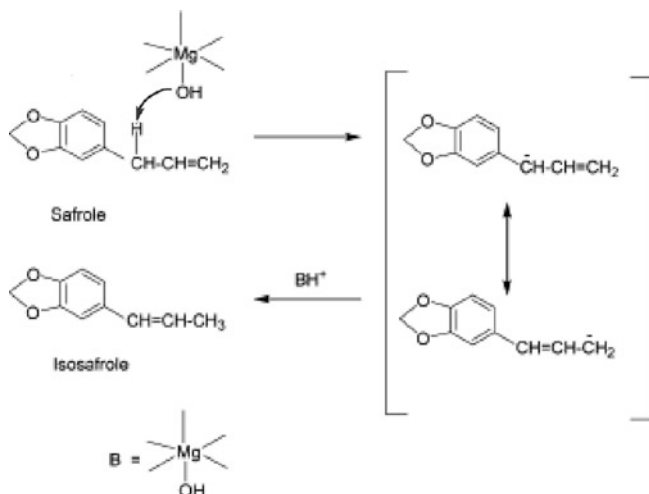
### 13.3 Recent Applications of HDT as Basic Catalyst

The catalytic properties of HDT for base-catalysed reactions have recently been reviewed [24], and the present report will be limited to very recent work.

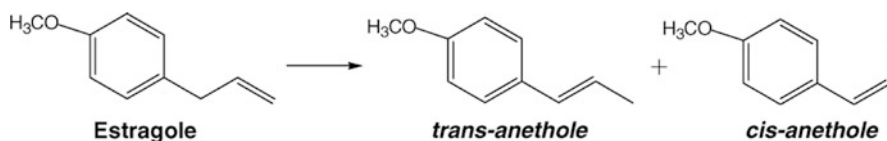
#### 13.3.1 Isomerisation of Olefins

The isomerisation of olefins can be catalysed by SrO [25], MgO [26] and La<sub>2</sub>O<sub>3</sub> [27]. It is not then quite surprising that eugenol and safrole can also be isomerised selectively over HDT [28, 29]. The mechanism proposed by the authors for safrole isomerisation is reported in Scheme 13.1.

Estragole can also be isomerised to anethole (Scheme 13.2) in a batch reactor at 200 °C: in DMF as solvent, the conversion after 6 h using MgAl-HDT was 97% and the selectivity to *trans* anethole 88% [30].



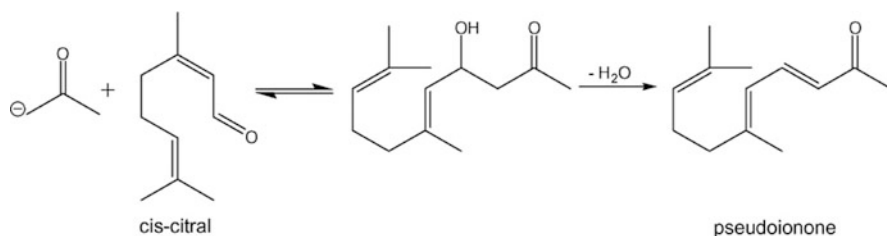
**Scheme 13.1** Base-catalysed mechanism of safrole isomerisation



**Scheme 13.2** Isomerisation of estragole to anethole

### 13.3.2 Aldolisation

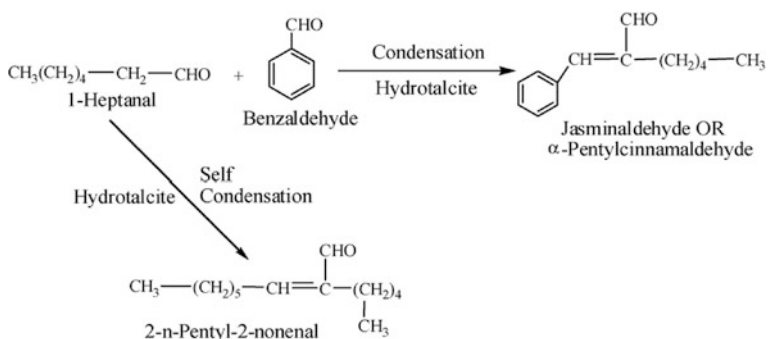
After the original work devoted to the aldolisation of acetone [19, 31–34], many reports have been devoted to the synthesis of perfumes by cross aldolisation reactions [35]. Aldolisation is an exothermic process which is favoured at low temperature. It is also a slow reaction, usually investigated in batch reactors in the liquid phase. For instance the aldol condensation of citral and acetone to pseudoionones (Scheme 13.3) has been investigated on MgAl-HDT at 273 K [36–39]. The ratio



**Scheme 13.3** Condensation of citral with acetone

acetone/citral was found to be a key factor of the reaction. The initial rate of pseudoionone formation exhibited a maximum at A/C = 3, leading to a selectivity to pseudoionone of 100%. At higher or lower A/C ratios, diacetone alcohol was the main by-product and at A/C < 2 the product of citral self-condensation was additionally formed. Due to this, the pseudoionone selectivity at extreme A/C ratios decreased to 70–80% [40].

The synthesis of jasminaldehyde (Scheme 13.4) by solvent-free condensation of 1-heptanal with benzaldehyde has been shown to work better on weak acid–base catalysts [41] and Mg–Al hydrotalcite samples of varied Mg/Al molar ratio [42]. A maximum selectivity of jasminaldehyde of 86% at 98% conversion of 1-heptanal was observed using a hydrotalcite of Mg/Al molar ratio of 3.5 as a catalyst. The catalyst could be recycled three times without loss of activity.



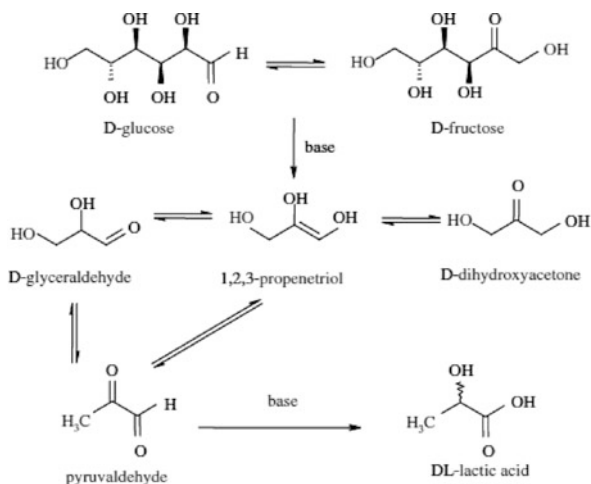
**Scheme 13.4** Synthesis of jasminaldehyde from heptanal and benzaldehyde

The solvent-free aldol condensation of propanal to 2-methylpentenal has been reported using MgAl-HDT as catalyst [43]. The cross aldolisation of acetaldehyde and heptanal was achieved on NiMgAl-HDT. The best selectivity was observed for the Ni-free sample [44]. Biologically active compounds have been obtained by the aldolisation of fluorine-containing benzaldehydes on HDT, reaching a yield of 80% in a semi-continuous process [45].

In the gas phase, Reichle first reported the aldolisation of acetone to isophorone on calcined HDT, at about 573 K [46, 47]. Suzuki and Ono [48] obtained methyl vinyl ketone by reaction of acetone and formaldehyde at 673 K, with a highest yield of 20% on acetone basis with the heat-treated hydrotalcites.

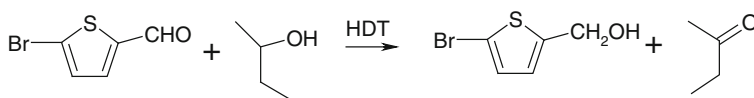
The principle of micro-reversibility teaches us that the same catalyst should catalyse retroaldolisation. Indeed the retroaldolisation of glucose in solution is catalysed by basic salts such as  $\text{Zn}^{2+}$  [49]. In heterogeneous catalysis, the conversion of glucose to lactic acid in water (Scheme 13.5), using HDT first calcined then rehydrated, reaches about 20% at 57% conversion of glucose [50].

**Scheme 13.5**  
Retroaldolisation of glucose  
leading to lactic acid on HDT



### 13.3.3 Meerwein–Ponndorff–Verley Reductions of Carbonyls

The Meerwein–Ponndorff–Verley hydrogenation of aldehydes and ketones has been achieved on calcined HDT using isopropanol as reductant [51]. When the substrate contains several reactive groups, the selective reduction becomes particularly difficult. The selective hydrogenation of aldehydes containing sulfur moieties has been performed quantitatively using isobutanol as hydrogen source (Scheme 13.6) and MgAl mixed oxides as catalysts [52]. The reaction was achieved in butan-2-ol at its boiling point, and the results are compared in Table 13.1 with those reported with a Rh diferrocenyl complex anchored on alumina [53].



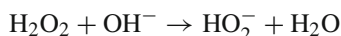
**Scheme 13.6** Hydrogen transfer reduction of bromothiophenecarboxaldehyde by isobutanol

**Table 13.1** Comparison of the results of hydrogen transfer hydrogenations using butan-2-ol at its boiling point and hydrogenation on Rh/Al<sub>2</sub>O<sub>3</sub> catalysts

Substrate	Catalyst	Alc. yield (%)	Reaction time (h)
Thiophenecarboxaldehyde	Rh(DiPFc)/Al <sub>2</sub> O <sub>3</sub>	100	18
	HDT	100	3
Bromo-5-thiophene-2-carboxaldehyde	Rh(DiPFc)/Al <sub>2</sub> O <sub>3</sub>	37.2	18
	HDT	100	3
4-Methylthiobenzaldehyde	Rh(DiPFc)/Al <sub>2</sub> O <sub>3</sub>	100	18
	HDT	100	3

### 13.3.4 Oxidations

The epoxidation of unsaturated ketones or aldehydes by  $\text{H}_2\text{O}_2$  or organic peroxides is base catalysed and goes through a nucleophilic addition by a Michael-type mechanism involving an attack by  $\text{HO}_2^-$ . This anion results from the attack of hydrogen peroxide by hydroxyls according to the reaction



which accounts for the role of basicity. Yadav and Kapoor first reported the epoxidation of activated alkenes by *t*-butylhydroperoxide (TBHO) using  $\text{KF}/\text{Al}_2\text{O}_3$  as catalyst [54]. With  $\text{H}_2\text{O}_2$ , this solid would dissolve in the reaction medium, which is not the case for HDT [55]. Indeed HDTs show activities comparable to that of titanasilicates for the epoxidation of isophorone. Yamaguchi et al. [56] investigated the effect of the Mg/Al ratio of HDT on the rate of epoxidation of unsaturated ketones. 2-Cyclohexen-1-one gave 2,3-epoxycyclohexanone in 91% yield at 313 K for 5 h with high efficiency in hydrogen peroxide. The catalytic activity of hydrotalcites increased as the basicity of their surfaces increased. For less reactive substrates, adding a cationic surfactant such as *n*-dodecyl-trimethylammonium bromide to the oxidation system accelerated the epoxidation reaction.

Raw MgAl mixed oxides are not active for the epoxidation of unsaturated ketones by TBHO. However, upon decarbonation and rehydration of the surface these solids become active for the epoxidation of cyclohexen-2-one with TBHO (Fig. 13.2) and reach quantitative yields. No correlation was found between the reaction rate or final conversion and basicity since solids such as  $\text{KF}/\text{Al}_2\text{O}_3$  and HDT-OH showing large differences in their number of sites showed the same properties [57]. The only solid base active for the epoxidation of isophorone with  $\text{H}_2\text{O}_2$  was a MgLa mixed oxide. HDT-OtBu can epoxidise cyclohexene-2-one at 273 K in 5 min instead of 6 h for HDT, which confirms its higher basicity compared to HDT [58].

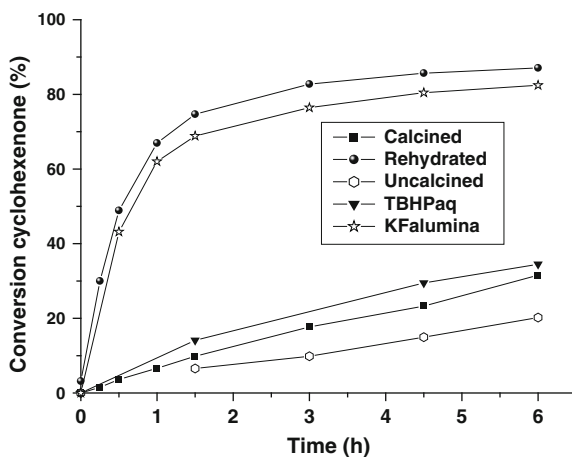
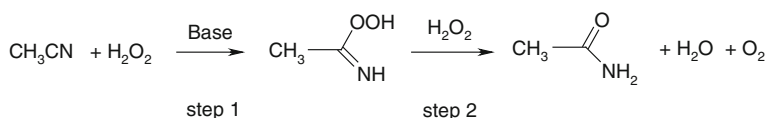


**Fig. 13.2** Effect of activation on the catalytic properties of hydrotalcite, and comparison with KF/alumina for the epoxidation of cyclohexene-2-one by TBHO at room temperature

In the presence of a nitrile, epoxidation can be extended to unfunctionalised olefins [59]. HDT acts then as a catalyst to form a perhydroxyl anion species ( $\text{HOO}^-$ ), which in turn nucleophilically attacks the nitrile to generate a peroxy-carboximidic acid as an active intermediate oxidant (Scheme 13.7). The best additive is benzonitrile [60] or an amide [61]. The spectrum of substrates is then enlarged but the reaction consumes the nitrile or amide additive.



**Scheme 13.7** Formation and decomposition of peroxy-carboximidic acid

It can also be applied to the oxidation of sulfur compounds to sulfones. The MgAl mixed oxides catalyse the oxidation of thioethers but not of dibenzothiophene to the corresponding sulfone [62]. By contrast the HDT-OH obtained by rehydration shows properties comparable to titanosilicates for the conversion of dibenzothiophene to sulfone in acetonitrile as solvent, as illustrated in Fig. 13.3 [63]. In the case of oxidation in presence of nitriles, a too high basicity leads to the decomposition of  $\text{H}_2\text{O}_2$  by the secondary reaction of Scheme 13.7. Strong bases are inactive in the reaction because hydrogen peroxide is decomposed to oxygen. Indeed the selectivity to  $\text{O}_2$  decreases from 90 to 17% after hydration. Therefore a very long rehydration can be supposed to yield a well-ordered solid of lower basicity because it contains an excess of water inhibiting the stronger basic sites. In turn the low basicity decreases

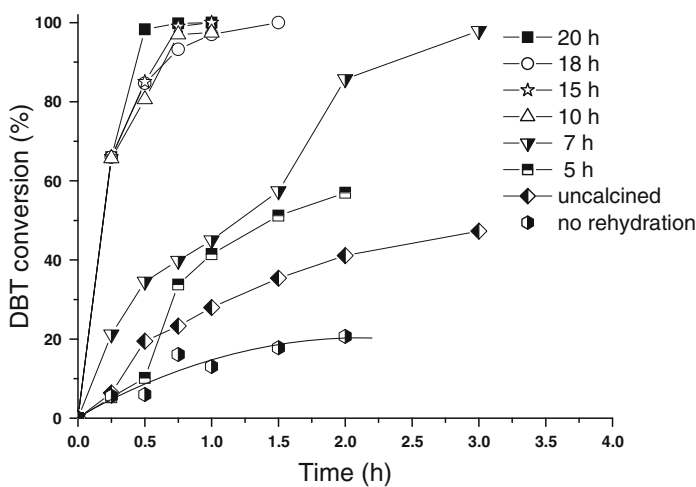


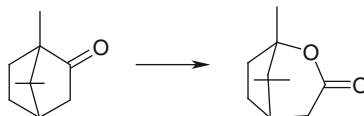
**Fig. 13.3** Effect of activation of hydrotalcites on the rate of oxidation of DBT by hydrogen peroxide using acetonitrile as solvent



the rate of decomposition and more  $\text{H}_2\text{O}_2$  is available for the desired reaction of step 1.

The peroxycarboximide acid of Scheme 13.7 can also be used to achieve epoxidation of non-allylic olefins, such as styrene [64], and Baeyer–Villiger oxidation of ketones to lactones (Scheme 13.8) [65–67]. The reaction, applied to a variety of ketones at 343 K, provided conversions above 70% with 100% selectivity after 6 h. The addition of Sn increased the activity and allowed recycling of the catalyst without loss of activity.

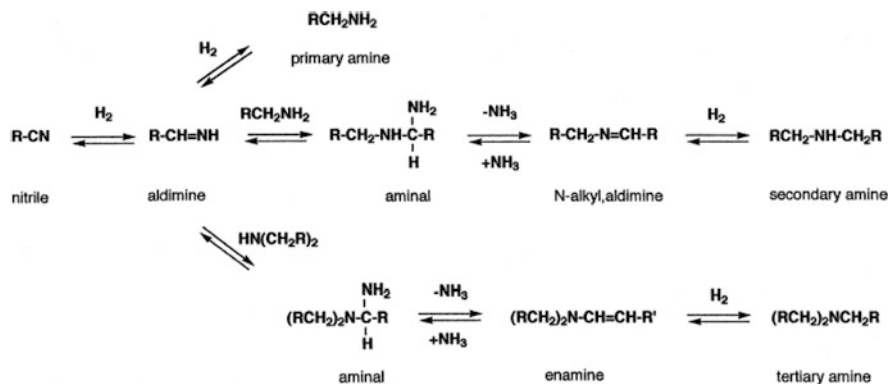
**Scheme 13.8**  
Baeyer–Villiger oxidation of ketones



### 13.4 Bifunctional Catalysis

As pointed out above, the aldol condensation often gives an unsaturated ketone by dehydration of the aldol, therefore the coupling of this reaction with hydrogenation opens the route for a synthesis of methyl-isobutylketone from acetone. In the first experiments the selectivity reached 60–70% at 35–40% conversion [68]. In a liquid-phase batch microreactor at 118 °C and 400 psig, a 0.1 wt% Pd/HDT gave a higher selectivity to MIBK (82%) at 38% conversion [69]. From their kinetic study, Winter et al. [70] concluded that although the hydrogenation of one of the intermediates, mesityl oxide (MO), at 1.2 bar suffers from severe mass transfer limitations in  $\text{H}_2$ , the catalytic activity in the single-stage synthesis is stable over several hours if the steady-state concentration of MO is kept low. Under the presented conditions the dehydration reaction of diacetone alcohol to MO is rate limiting in the production of MIBK. This conclusion agrees with the fact that the net yield of MIBK is independent of metal type and loading, depending only on the wt% of exposed metal [71]. However, the by-products differ according to the metal: Pt/HDT is more selective for the direct hydrogenation to isopropanol, while Pd/HDT forms more of the intermediate diacetone alcohol. Very recently, Tichit et al. reported the synthesis of 2-methyl-3-phenyl-propanal (MPPAL) from benzaldehyde and propanal, by cross aldolisation of the two substrates, followed by  $\text{C}=\text{C}$  hydrogenation of the intermediate unsaturated aldehyde [72]. The selectivity into the desired product was 77% at 64% benzaldehyde conversion.

Bifunctionality is sometimes undesired, for instance in the selective hydrogenation of nitriles to primary amines because the primary amine reacts fast to yield a secondary or tertiary amine (Scheme 13.9). This side process is acid catalysed, therefore basic supports are preferred, and the selectivity to primary amine increases up to 95% at 99% conversion using a basic CoNiAlMg HDT [73, 74]. In the liquid-phase hydrogenation of adiponitrile into aminocapronitrile, MgNi-HDT



**Scheme 13.9** Reaction scheme for the hydrogenation of nitrile on Ni catalysts (from Ref. [74])

(Mg/(Mg+Ni) = 0.20) reaches 66% selectivity into ACN at 70% conversion (50% yield at 85% conversion). With acetonitrile the EtNH<sub>2</sub> selectivity was 92.6% at 99% MeCN conversion [75].

The IR spectroscopy of adsorbed CO provided evidence of the presence of smaller Ni<sup>0</sup> ensembles on the sample with Mg/(Mg + Ni)=0.20, and larger back-donation from Ni<sup>0</sup> sites to the 2π\* orbitals of CO. It was proposed that the lower formation of by-products was due to (i) a faster desorption of ACN from the Ni<sup>0</sup> surface before deeper hydrogenation and (ii) the decrease of transimination reactions which need large Ni<sup>0</sup> ensembles to proceed [76].

## 13.5 Support Effects on Palladium

### 13.5.1 Electronic Effects

Queau and Poilblanc first investigated the effect of electron donors or acceptors on the chemisorption of CO on Pd and Pt evaporated films [77, 78]; CO chemisorbed on transition metals forms a σ-bond by donation of the lone pair of the C atom and a π-bond by back-donation of metallic d electrons to the antibonding π\*-orbital of CO. By addition of electron acceptors, the stretching frequency of the CO molecules progressively shifts to higher wavenumbers, corresponding to an increase of the CO bond strength, due to a lowering of the electron back-donation from the metal to the antibonding orbitals of the chemisorbed CO molecules. This electron-withdrawing ligand effect of halogen is a long-range effect which uses the collective properties of the metal surface. The addition of electron donors provokes the reverse effect. Indeed supporting Pd on acid zeolites induces a shift of the CO vibration to higher wavenumbers, while basic zeolites shift the band to lower wavenumbers [79]. For Pt, HDT has the same effect as basic zeolites [80, 81]. The adsorption of CO followed

by IR spectroscopy therefore shows that a basic support has the same effect as a basic additive on the electron density at the surface.

### ***13.5.2 Catalytic Properties for Hydrogenations***

Pd is very efficient for the hydrogenation of alkynes to alkenes and the selectivity can even be promoted by the addition of electron donor compounds, such as piperidine, which favours the desorption of the olefin [82]. In the partial hydrogenation of 2-butyne-1,4-diol, the highest activities and selectivities to 2-butene-1,4-diol were thus obtained by increasing the pH of the reaction medium with additives such as organic bases, KOH [83]. An alternative is to use Pd catalysts supported on HDT, which yield 88% selectivity to butane diol at 90% conversion [84].

### ***13.5.3 Dechlorination of Trichlorobenzene***

Catalytic hydrodechlorination is an efficient way to remove chloride species from chlorinated hydrocarbons. Hydrodechlorination reaction of 1,2,4-trichlorobenzene was studied over a series of palladium (1 wt%) catalysts supported on calcined Mg/Al hydrotalcite-like materials (HT) prepared with different Mg/Al ratios [85]. It was observed that the activity, stability and selectivity of the catalysts were strongly dependent on the Mg/Al molar ratio in the Mg(Al)O support. The sample with Mg/Al ratio of 4 exhibited the highest activity and selectivity towards total hydrodechlorination reaction giving benzene. Rehydration of the calcined hydrotalcite catalyst resulted in an enhancement of the hydrodechlorination performance. It was demonstrated that catalyst deactivation was mainly due to coke formation, and the decrease of the amount of coke with the base character of the support agrees with an acid catalysis in coke formation. The coke formed during the reaction could be eliminated by combustion recovering the initial activity.

### ***13.5.4 Catalysis of C–C Coupling Reactions***

Many reactions, in particular the reactions of C–C coupling such as Heck, Suzuki or Sonogashira reactions [86, 87], require an activation of the noble metal by basic additives such as phosphines or phosphites, which are toxic and expensive. Under Heck reaction conditions, phosphines and their palladium complexes are prone to decomposition so that excesses of phosphine and palladium are required. The excess of phosphine reduces the reaction rate while the higher amount of palladium increases the cost of the process. Moreover, the product has to contain less than a few ppm of palladium to respect the regulations.

Attempts have been made to support Pd by zeolites, carbon or oxides [88–92]. The reactivity thus observed for chloroarenes, the cheaper reactants, is low.

Choudary et al. [93] reported the immobilisation of nanocrystallites of palladium on layered double hydroxide, which showed a higher activity in non-aqueous ionic liquid media and microwave conditions for the Heck reaction. These results have been reproduced by Zhou et al. [94] using fluorinated hydrotalcite as support. Palladium on basic zeolites has also been reported to be more active, for Heck coupling, than Pd on acid zeolites [95]. The most active Pd catalysts reported up to now for C–C coupling are those supported on MgLaO mixed oxides [96–98]. The activity for Heck coupling using chloroarenes as substrates is related to the basicity of the support, since the catalysts work at 80 °C for MgLaO mixed oxides, 130 °C for HDT, 160 °C for Pd/zeolites [89], and 170 °C for Pd/MCM-41 [99, 100]. It can be pointed out that both Heck reaction and dechlorination are supposed to involve the oxidative addition of the substrate on the Pd atom to form an intermediate adsorbed species. The fact that both reactions have a faster rate on Pd/HDT is then satisfactory.

### ***13.5.5 Merox Process***

Mercaptans (RSH) are present in petroleum, and their presence, even in very small quantities, gives rise to an unpleasant odour and corrosion. Their removal, also called sweetening, is thus necessary. The mercaptan oxidation (merox) process developed by UOP has been most widely practiced in the refining industry. It involves catalytic oxidation of the mercaptans to disulfides with air by cobalt phthalocyanines in the presence of caustic soda as a co-catalyst. However, the spent caustic soda is recognised as a hazardous waste, and its disposal is becoming more difficult and expensive due to environmental regulations. The ideal solution to this problem is to substitute caustic soda by solid bases to develop a more environmentally friendly effluent-free process for the mercaptan sweetening. Marcilly et al. proposed alkaline silico-aluminates as supports [101], but Holmgren et al. [102–104] and Liu et al. [105] reported that Mg(Al)O-supported cobalt phthalocyanine bifunctional catalysts, which possess Co<sup>2+</sup> oxidation sites and Mg(Al)O base sites in cooperative interaction, can effectively oxidise mercaptans to disulfides, in the absence of NaOH. Recent results show that the support must exhibit a mild basicity [106]. This therefore permits to design cleaner processes.

## **13.6 Solid Bases as Adsorbents and Anionic Exchangers**

### ***13.6.1 Trapping of Organic Compounds and Anions***

Humic substances create problems in drinking water production from surface waters and in water treatment in general because of the colour, taste and odour that accompany it, of the forming potential of carcinogenic disinfection by-products (DPBs) (e.g. trihalomethanes, haloacetic acids) during the chlorination of drinking water,

and of the fouling potential of membranes and ion-exchange resins. Lower molecular weight humic and fulvic acids were preferentially adsorbed because these fractions can more easily enter the mesoporous LDHs and contain more carboxylic groups [107]. By contrast, the higher molecular weights are trapped at the surface in low amounts.

Organic dyes themselves, their metabolites or their decomposition by-products have been recognised to be mutagenic, so that increasingly stringent regulations have prompted the development of more efficient dyestuff waste treatment procedures. Bascialla and Regazzoni [108] have investigated the uptake of the diazo dye Acid Blue 113 by hydrotalcite (HT) and calcined hydrotalcite (CHT) as a function of reaction time and equilibrium concentration. The adsorption of the dye obeys a Langmuir model, and the adsorption constant  $K_L$  determined for CHT is 4.2 l/mg, about three times that of HT. The maximum sorption capacity is larger by a factor of 50 for CHT, and reaches 2544 mg/g. Non-toxic dyes such as methyl orange have also been intercalated with stabilisation of the dye towards air oxidation. This permits the obtention of a new pigment [109].

Endocrine active compounds (EACs) are natural or synthetic compounds that adversely affect the endocrine system of many organisms ranging from nematodes to fish to polar bears. Two common EACs found in the waterways are the biogenic hormone  $17\beta$ -estradiol (E2) and the synthetic hormone  $17\alpha$ -ethynylestradiol (EE2), which have both been identified downstream from municipal or agricultural waste treatment plants in concentrations as high as 200 and 831 ng/l, values at which the reproductive physiology and (or) behaviour of many organisms can be affected. Morris et al. [110] have shown that these EACs can be scavenged from water by interaction with HDT: after one pass through a packed column decreased the estrogenic activity of the river water from 519 to 387 ng E2 equiv./l. A slurry treatment reduced the E2 concentration in water from 317 ng/l to below detection limit.

HDTs can trap toxic mineral anions such as arsenates [111], chromates [112, 113] and phosphates [114]. The literature in this field has recently been reviewed [115]. The affinities of LDHs for oxyanions were estimated in the following ranges: 0.1–87.5 mg/g LDHs for arsenite (As(III)); 5–615 mg/g for arsenate (As(V)); 9–160 mg/g for chromate (Cr(VI)); 7.3–81.6 mg/g for phosphate (as P); 29–270 mg/g for selenite (Se(IV)); 14–20 mg/g for borate (as B); and 2.3–4.6 mg/g for nitrate (as N). LDHs offer technical as well as economical merits in treating waters and wastewaters containing harmful oxyanions. One of the most competitive advantages of LDHs is that they consist of hydroxides of common and abundant metals on the earth and can be synthesised economically. Oxyanion adsorption process using LDHs also shows considerably faster kinetics in comparison to most of the biological treatment processes. The main advantages of LDHs over the conventional anionic exchange resins include their higher anion exchange capacity for certain oxyanions and their good thermal stability. Furthermore, LDHs can be fully regenerated in a short time for reuse. However, LDHs have several shortcomings that may limit their large-scale applications for oxyanion removal. First, precursor metals of LDHs could be released into the solution, particularly at lower pH values.

Second, regeneration of the spent LDHs can be costly. Third, high basicity would be introduced to the product water if the calcined LDHs are used.

According to the authors, prior to full-scale application of LDHs in water and wastewater treatment, additional studies are still required to develop the most economical synthesis method to produce at large scale the LDHs with the optimum surface area, anion exchange capacity and thermal stability. Hydrotalcite can be modified by anchoring of tannins and become then a trap for heavy metals. The selectivity order was  $\text{Cu(II)} > \text{Zn(II)} > \text{Cd(II)}$ , and the maximum adsorption capacities were 81.47 mg/g for Cu (II), 78.91 mg/g for Zn(II) and 74.97 mg/g for Cd(II) [116].

A difficult problem is the elimination of fluoride anions from drinking water. The presence of  $\text{F}^-$  induces fluorosis among human beings and is a worldwide problem. Mandal and Mayadevi [117] propose a trap consisting of cellulose-supported layered double hydroxides. The solid having an LDH loading of 27% showed maximum fluoride uptake capacity (5.29 mg/g of supported material, corresponding to 25.18 mg/g of LDH) in fixed-bed column study. However, competitive exchanges in the presence of sulfates and carbonates are required to establish the practical interest of the method.

### 13.6.2 $\text{SO}_x$ Additives for FCC

The flue gases generated by fluid catalytic cracking units (FCC units) used to crack petroleum feedstocks contain many types of contaminants, in particular sulfur oxides formed by the oxidation of sulfur-containing compounds. In FCC units, microspheroidal catalyst particles having chemical activities towards sulfur oxide gases are circulated in admixture with the microspherical particles used to carry out the petroleum cracking function. These hydrocarbon cracking catalyst particles are often referred to as “bulk” or “FCC” catalysts while the sulfur catalyst particles are often referred to as “ $\text{SO}_x$  additives”. During the hydrocarbon cracking process, a coke-like material that also contains a sulfur component coming from the petroleum feedstock is deposited on the  $\text{SO}_x$  additive particles as well as on the FCC catalyst particles. Both kinds of particles, and hence the coke and sulfur deposited on them, are carried from the FCC unit’s reactor to its catalyst regenerator. Here, the coke and sulfur are burned off catalyst particles. The sulfur component of such coke/sulfur deposits forms sulfur oxide gases (e.g. sulfur dioxide and sulfur trioxide which are often collectively referred to as “ $\text{SO}_x$ ” gases). Unless captured, these  $\text{SO}_x$  gases would be emitted to the atmosphere along with other flue gases given off by the catalyst regenerator (e.g. carbon monoxide, carbon dioxide and nitrous oxides). The  $\text{SO}_x$  additive is transferred to the reactor unit where the sulfate is reduced to  $\text{H}_2\text{S}$ . The hydrogen sulfide gas produced in the FCC reactor unit is eventually captured and ultimately reduced to elemental sulfur. In other kinds of industrial facilities (e.g. coal-fired power plants and certain chemical manufacturing plants)  $\text{SO}_x$  additives are usually employed in the form of larger particles such as pellets that are better used in fixed-bed reactors.

Since sulfur oxides are acidic,  $\text{SO}_x$  additives are solid bases containing an oxidising function to convert  $\text{SO}_2$  to  $\text{SO}_3$ , more acidic. These  $\text{SO}_x$  additives must also easily reduce to  $\text{H}_2\text{S}$  at cracking temperature (about  $630^\circ\text{C}$ ).  $\text{MgO}$  and  $\text{Ce}$  are the most common components [118], but  $\text{MgFe}$  [119],  $\text{CeO}_2$  supported by  $\text{MgAl}$  hydrotalcites [120],  $\text{Zn-HDT}$  [121] and  $\text{MgAlFe}$  hydrotalcites, with  $\text{Ce}$  additive [122], have been recently proposed. It was demonstrated that the isomorphic incorporation of iron increased its reduction capability which was reflected in higher reduction rates and metal sulfate reduction grade at  $550^\circ\text{C}$ . Moreover, when cerium was present in the iron-containing materials the saturation rate was improved, because cerium oxide promotes the oxidation of  $\text{SO}_2$  to  $\text{SO}_3$ . The way cerium was incorporated influenced the  $\text{SO}_2$  adsorption capacity.

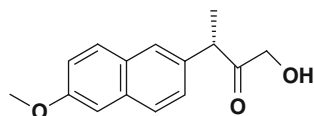
### 13.6.3 $\text{NO}_x$ Traps

Lean burn and diesel engines can decrease fuel consumption up to 30% compared to stoichiometric engines [123]. However, the lean operating conditions have been limited so far because the oxides of nitrogen ( $\text{NO}_x$ ) emitted under oxidising conditions could not be purified using conventional three-way catalysts [124, 125]. Toyota has developed at a large scale a new technology called the “ $\text{NO}_x$  storage-reduction” based on  $\text{Pt/Ba-Al}_2\text{O}_3$  catalysts [124, 126, 127], used with engines operating alternately under lean and rich conditions.  $\text{NO}_x$  is stored as nitrate in the catalyst under lean conditions and subsequently released and reduced under rich conditions. This technology requires low sulfur fuels because  $\text{Pt}$  also oxidises  $\text{SO}_2$  to  $\text{SO}_3$  [128]. Sulfates, more stable than nitrates, inhibit trapping and decompose only at temperatures above 926 K which causes a fuel penalty [129].  $\text{Pt}$  catalysts also show maximum activity around 523 K and lose efficiency above 673 K, temperature at which  $\text{NO}_x$  emissions are high.  $\text{PtCu/HDT}$  catalysts which show improved thioreistance are also less active above 673 K [130]. In this system, HDT plays the role of solid base for the trapping of nitrates.

## 13.7 Hydrotalcites as Reservoirs for Drugs

A recent evolution has been the description of HDT as carrier for drugs. Many drugs are organic acids, for instance naproxen or flurpiribofen, a non-steroidal anti-inflammatory drug (NSAID) (Scheme 13.10), and can be intercalated in  $\text{MgAl}$  [131] and  $\text{MgFe-HDT}$  [132]. Different methods of preparation were compared. The products were analysed by thermal and infrared analysis and X-ray diffraction. The

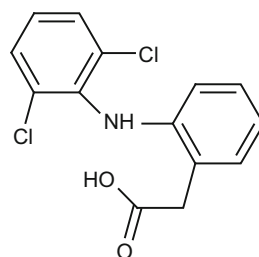
**Scheme 13.10** Structural formula of naproxene



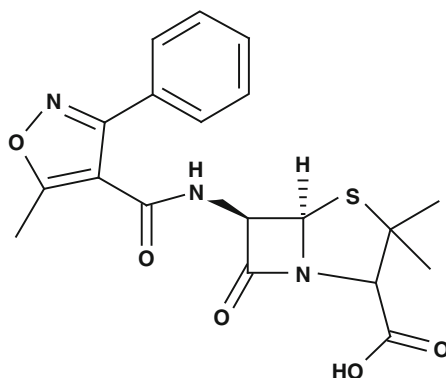
addition of the drug in the coprecipitation of the hydroxides was found to be better than reconstruction to obtain intercalated monophase nanocomposites. In acidic medium HDT dissolves and the intercalated drug starts to release in a molecular form which is suitable for adsorption. The drug solubility has been investigated before and after intercalation. It has been found that HDT improved the drug solubility and its dissolution rate. The same phenomenon has been reported for another NSAID, meclofenamic acid, loaded on HDT [133]. Indomethacin, a NSAID commonly used to reduce fever, pain, stiffness and swelling, has also been intercalated and the pharmacological studies *in vivo* show that intercalation of the drug in the HDT reduces the ulcerating damage of the drug [134].

Bonina et al. [135] reported the encapsulation of diclofenac (Scheme 13.11) on HDT calcined or not. Hydrotalcite pretreated at 500 °C showed a higher adsorption capacity, but a slow release of the drug, whereas diclofenac adsorbed from ethanolic solution by untreated hydrotalcite released faster. This sample was selected for *in vivo* experiments. Ten healthy volunteers participated in the *in vivo* experiments: the diclofenac-hydrotalcite appeared to be useful for an efficient application on human skin as inhibitor of the UV-induced erythemas, also better than the usual gel samples.

**Scheme 13.11** Structural formula of diclofenac



Oxacillin sodium (Scheme 13.12) is a betalactam antibiotic in the penicillin class widely used in the treatment of infections such as osteomyelitis and septicaemia. This drug shows toxic side effects of oxacillin (e.g. cholestatic hepatitis, upset stomach, diarrhoea, acute interstitial nephritis), aggregation process in aqueous solution



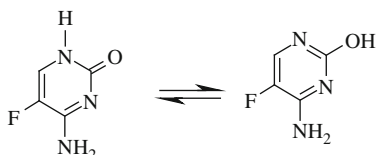
**Scheme 13.12** Structural formula of oxacillin



and low stability which are undesired. The use of hydrotalcite-like anionic clay as a host matrix for oxacillin is an attempt to obtain a novel therapeutic delivery system able to overcome the drug problems [136]. The oxacillin–clay formulations were prepared reacting a calcined HDT with a solution of oxacillin. From the XR patterns HDT was only partially intercalated. The rate of release is higher from MgFe-HDT than from MgAl-HDT and is of higher basic strength [10] which suggests that the process is thermodynamically controlled.

The intercalation of 5-fluorocytosine, 5-FC (Scheme 13.13) into a layered inorganic host, Zn–Al layered double hydroxide (LDH), has been carried out using coprecipitation method to obtain nanohybrids. The *in vitro* drug release from the nanohybrids is remarkably lower than that from the corresponding physical mixture and pristine 5-FC at either pH 4.8 or pH 7.5. In addition, the release rate of 5-FC from the nanohybrid at pH 7.5 is remarkably lower than that at pH 4.8, and this composite might be used as drug delivery system [137].

**Scheme 13.13** Structural formula of 5-fluorocytosine



Potential cancer chemotherapy agents have been investigated using the encapsulation of an anticancer drug 5-fluorouracil (5-Fu) into LDH through coprecipitation method. The X-ray pattern of the 5-Fu-LDH nanohybrid showed interlayer distances of 0.58 nm, in agreement with the size of the drug molecule, thus indicating a successful intercalation. The drug efficiency of the composite was evaluated on several cancer cell lines such as human lung cancer, osteosarcoma and hepatoma cells. Free 5-Fu, methotrexate (MTX), MTX-LDH and doxorubicin (Dox) were also used for comparative studies. The results demonstrated that both 5-Fu-LDH and MTX-LDH nanohybrids were more efficient for the inhibition of cancer cell proliferation than free 5-Fu and MTX, respectively, leading to cell death in a concentration-dependent manner. The highest drug efficiency was achieved by MTX-LDH nanohybrid, even higher than Dox, one of the most effective chemotherapy agents against a variety of cancers. Moreover, LDH itself did not exhibit acute cytotoxic effect up to 500 mg/ml as measured by 3-(4,5-dimethylthiazol-2-yl)-2,5-diphenyltetrazolium bromide (MTT) assay [138].

## 13.8 Conclusions

Hydrotalcites have now been proposed for a large variety of uses spanning from catalysis to adsorption and drugs carriers. Among the applications,  $\text{SO}_x$  additives are probably the largest scale process and have driven the research of cheap and clean synthesis of HDT at a large scale [139]. The availability of the starting material at the industrial scale will favour new applications.

## References

1. Vaccari A (1998) Preparation and catalytic properties of cationic and anionic clays. *Catal Today* 41:53–71
2. Miyata S, Kumura T (1973) Synthesis of new hydrotalcite-like compounds and their physicochemical properties. *Chem Lett* 8:843–848
3. Miyata S (1975) The syntheses of hydrotalcite-like compounds and their structures and physico-chemical properties. I. The systems magnesium(2+)-aluminum(3+)-nitrate(1-), -chloride(1-) and -perchlorate(1-), nickel(2+)-aluminum(3+)-chloride(1-), and zinc(2+)-aluminum(3+)-chloride(1-). *Clays Clay Miner* 23:369–375
4. Reichle WT (1986) Synthesis of anionic clay minerals (mixed metal hydroxides, hydrotalcite). *Solid State Ionics* 22:135–141
5. Cavani F, Trifiro F, Vaccari A (1991) Hydrotalcite-type anionic clays: preparation, properties and applications. *Catal Today* 11:173–301
6. Lopez T, Bosch P, Ramos E, Gomez R, Novaro O, Acosta D, Figueras F (1996) Synthesis and characterization of sol-gel hydrotalcites. Structure and texture. *Langmuir* 12:189–192
7. Sanderson RT (1976) *Inorganic chemistry*. Reinhold, New York, NY
8. Vinek H, Noller H, Ebel M, Schwarz K (1977) X-Ray photoelectron-spectroscopy and heterogeneous catalysis, with elimination-reactions as an example. *J Chem Soc Faraday Trans I* 73:734–746
9. Allred AL, Rochow EG (1958) A scale of electronegativity based on electrostatic force. *J Inorg Nucl Chem* 5:264–268
10. Sanchez-Valente J, Figueras F, Gravelle M, Kumbhar P, Lopez J, Besse JP (2000) Basic properties of the mixed oxides obtained by thermal decomposition of hydrotalcites containing different metallic compositions. *J Catal* 189:370–381
11. Tichit D, Lhouty MH, Guida A, Chiche BH, Figueras F, Auroux A, Bartolini D, Garrone E (1995) Textural properties and catalytic activity of hydrotalcites. *J Catal* 151:50–159
12. Miyata S (1983) Anion-exchange properties of hydrotalcite-like compounds. *Clays Clay Miner* 31:305–311
13. Tichit D, Naciri Bennani M, Figueras F, Tessier R, Kervennal J (1998) Aldol condensation of acetone over layered double hydroxides of the meixnerite type. *Appl Clay Sci* 13:401–415
14. Tessier R, Tichit D, Figueras F, Kervennal J (1995) Aldolisation sélective de l'acétone en diacétonalcool par un catalyseur basique solide. *FR2729137*
15. Abello S, Medina F, Tichit D, Perez-Ramirez J, Cesteros Y, Salagre P, Sueiras JE (2005) Nanoplatelet-based reconstructed hydrotalcites: towards more efficient solid base catalysts in aldol condensations. *Chem Commun* 11:1453–1455
16. Abello S, Medina F, Tichit D, Perez-Ramirez J, Groen JC, Sueiras JE, Salagre P, Cesteros Y (2005) Aldol condensations over reconstructed Mg–Al hydrotalcites: structure-activity relationships related to the rehydration method. *Chem Eur J* 11:728–739
17. Choudary BM, Lakshmi Kantam M, Neeraja V, Koteswara Rao K, Figueras F, Delmotte L (2001) Layered double hydroxide fluoride: a novel solid base catalyst for C–C bond formation. *Green Chem* 3:257–260
18. Figueras F, Choudary BM, Lakshmi Kantam M, Neeraja V, Koteswara Rao K (2001) Use of a solid hydrotalcite structure incorporating fluorides for basic catalysis of Michael or Knoevenagel reactions. *Wo0166246*
19. Choudary BM, Kantam ML, Kavita B, Reddy CV, Rao KK, Figueras F (1998) Aldol condensations catalyzed by novel Mg–Al–O-t-Bu hydrotalcite. *Tetrahedron Lett* 39:3555–3558
20. Kantam ML, Ravindra A, Reddy CV, Sreedhar B, Choudary BM (2006) Layered double hydroxides-supported diisopropylamide: synthesis, characterization and application in organic reactions. *Adv Synth Catal* 348:569–578
21. Climent MJ, Corma A, Iborra S, Epping K, Veltz A (2004) Increasing the basicity and catalytic activity of hydrotalcites by different synthesis procedures. *J Catal* 225:316–326

22. Winter F, van Dillen AJ, de Jong KP (2005) Supported hydrotalcites as highly active solid base catalysts. *Chem Commun* 31:3977–3979
23. Winter F, Koot V, van Dillen AJ, Geus JW, de Jong KP (2005) Hydrotalcites supported on carbon nanofibers as solid base catalysts for the synthesis of MIBK. *J Catal* 236:91–100
24. Figueras F (2004) Base catalysis in the synthesis of fine chemicals. *Topics Catal* 29:189–196
25. Mohri M, Tanabe K, Hattori H (1974) Isomerization of 1-butene catalyzed by strontium oxide. *J Catal* 32:144–147
26. Hattori H (1995) Heterogeneous basic catalysis. *Chem Rev* 95:537–558
27. Rosynek MP, Fox JS (1977) Characterization of catalytic lanthanum oxide for double bond isomerization of *n*-butenes. *J Catal* 49:285–293
28. Kishore D, Kannan S (2004) Environmentally benign route for isomerization of safrole-hydrotalcite as solid base catalyst. *J Mol Catal A* 223:225–230
29. Kishore D, Kannan S (2002) Isomerization of eugenol and safrole over MgAl hydrotalcite, a solid base catalyst. *Green Chem* 4:607–610
30. Kishore D, Kannan S (2006) Catalytic isomerization of estragole to anethole over hydrotalcites and HT-like compounds. *J Mol Catal A* 244:83–92
31. Teissier R, Tichit D, Figueras F, Kervennal J (1996) Preparation of diacetone alcohol. *EP 720977*
32. Figueras F, Tichit D, Naciri MB, Ruiz R (1998) Selective aldolization of acetone into diacetone alcohol using hydrotalcites as catalysts. *Chem Ind* 75:37–49
33. Rao KK, Gravelle M, Valente, JS, Figueras F (1998) Activation of Mg–Al hydrotalcite catalysts for Aldol condensation reactions. *J Catal* 173:115–121
34. Lopez J, Jacquot R, Figueras F (2000) Heterogeneous catalysis of aldolizations on activated hydrotalcites. *Stud Surf Sci Catal (International Congress on Catalysis, (2000) Pt. A)* 130A:491–496
35. Corma Canos A, Climent Olmedo MJ, Vely AIL, Iborra Chornet S, Susarte Rogel M (2001) Method and catalysts for obtaining alpha,beta-unsaturated carbonyl compounds used in the perfume and scent industry. *Wo0138278*
36. Noda C, Alt GP, Werneck RM, Henriques CA, Monteiro JLF (1998) Aldol condensation of citral with acetone on basic solid catalysts. *Braz J Chem Eng* 15:120–125
37. Roelofs JCAA, Geus JW, Van Dillen AJ, De Jong KP, Jastrzebski JTBH (2000) Method for the condensation of an aldehyde and a ketone. *EP 1029844 99-200450 1029844, 19990216*
38. Roelofs JCAA, van Dillen AJ, de Jong KP (2000) Base-catalyzed condensation of citral and acetone at low temperature using modified hydrotalcite catalysts. *Catal Today* 60:297–303
39. Climent MJ, Corma A, Iborra S, Vely A (2002) Synthesis of pseudoionones by acid and base solid catalysts. *Catal Lett* 79:157–163
40. Abello S, Dhir S, Colet G, Perez-Ramirez J (2007) Accelerated study of the citral-acetone condensation kinetics over activated Mg–Al hydrotalcite. *Appl Catal A* 325:121–129
41. Climent MJ, Corma A, Fornes V, Guil-Lopez R, Iborra S (2002) Aldol condensations on solid catalysts: a cooperative effect between weak acid and base sites. *Adv Synth Catal* 344:1090–1096
42. Sharma SK, Parikh PA, Jasra RV (2008) Eco-friendly synthesis of jasminaldehyde by condensation of 1-heptanal with benzaldehyde using hydrotalcite as a solid base catalyst. *J Mol Catal A* 286:55–62
43. Sharma SK, Parikh PA, Jasra RV (2007) Solvent free aldol condensation of propanal to 2-methylpentenal using solid base catalysts. *J Mol Catal A* 278:135–144
44. Lutic D, Hulea V, Coq B, Durand R, Tichit D (2006) The aldol condensation of acetaldehyde and heptanal on NiMg(Al)O mixed oxides obtained from LDH precursors. *Prog Catal* 15: 31–38
45. Campanati M, Franceschini S, Piccolo O, Vaccari A, Zicmanis A (2004) Catalytic condensation of aromatic aldehydes with acetone on activated Mg–Al mixed oxides. *Catal Commun* 5:145–150
46. Reichle WT (1985) Catalytic reactions by thermally activated, synthetic anionic clay minerals. *J Catal* 94:547–557

47. Reichle WT, Kang SY, Everhardt DS (1986) The nature of the thermal decomposition of a catalytically active anionic clay mineral. *J Catal* 101:352–359
48. Suzuki E, Ono Y (1988) Aldol condensation reaction between formaldehyde and acetone over heat-treated synthetic hydrotalcite and hydrotalcite-like compounds. *Bull Chem Soc Jpn* 61:1008–1010
49. Bicker M, Endres S, Ott L, Vogel H (2005) Catalytical conversion of carbohydrates in subcritical water: a new chemical process for lactic acid production. *J Mol Catal A* 239:151–157
50. Onda A, Ochi T, Kajiyoshi K, Yanagisawa K (2008) Lactic acid production from glucose over activated hydrotalcites as solid base catalysts in water. *Catal Commun* 9:1050–1053
51. Kumbhar PS, Sanchez Valente J, Lopez J, Figueras F (1998) Meerwein-Ponndorf-Verley reduction of carbonyl compounds catalysed by Mg–Al hydrotalcite. *Chem Commun* 7: 535–536
52. Vu TTH, Kumbhar PS, Figueras F (2003) Base-catalyzed hydrogenation of sulfur-containing aldehydes. *Adv Synth Catal* 345:493–496
53. Burk MJ, Gerlach A, Semmeril D (2000) An immobilized homogeneous catalyst for efficient and selective hydrogenation of functionalized aldehydes, alkenes, and alkynes. *J Org Chem* 65:8933–8939
54. Yadav VK, Kapoor KK (1994) Al<sub>2</sub>O<sub>3</sub> supported KF: an efficient mediator in the epoxidation of electron deficient alkenes with t-BuOOH. *Tetrahedron Lett* 35:9481–9484
55. Fraile JM, Garcia J, Mayoral J, Figueras F (1996) Comparison of several heterogeneous catalysts in the epoxidation of [alpha]-isophorone with hydroperoxides. *Tetrahedron Lett* 37:5995–5996
56. Yamaguchi K, Mori K, Mizugaki T, Ebitani K, Kaneda K (2000) Epoxidation of alpha,beta-unsaturated ketones using hydrogen peroxide in the presence of basic hydrotalcite catalysts. *J Org Chem* 65:6897–6903
57. Palomeque J, Lopez J, Figueras F (2002) Epoxydation of activated olefins by solid bases. *J Catal* 211:150–156
58. Choudary BM, Kantam ML, Bharathi B, Reddy CV (1998) Superactive Mg–Al–O–tBu hydrotalcite for epoxidation of olefins. *Synlett* 11:1203–1204
59. Ueno S, Yamaguchi K, Yoshida K, Ebitani K, Kaneda K (1998) Hydrotalcite catalysis: heterogeneous epoxidation of olefins using hydrogen peroxide in the presence of nitriles. *Chem Commun* 2:295–296
60. Aramendia MA, Borau V, Jimenez C, Luque JM, Marinas JM, Ruiz JR, Urbano FJ (2001) Epoxidation of limonene over hydrotalcite-like compounds with hydrogen peroxide in the presence of nitriles. *Appl Catal A* 216:257–265
61. Yamaguchi K, Ebitani K, Kaneda K (1999) Hydrotalcite-catalyzed epoxidation of olefins using hydrogen peroxide and amide compounds. *J Org Chem* 64:2966–2968
62. Dumitriu E, Guimon C, Cordoneanu A, Casenave S, Hulea T, Chelaru C, Martinez H, Hulea V (2001) Heterogeneous sulfoxidation of thioethers by hydrogen peroxide over layered double hydroxides as catalysts. *Catal Today* 66:529–534
63. Palomeque J, Clacens JM, Figueras F (2002) Oxidation of dibenzothiophene by hydrogen peroxide catalyzed by solid bases. *J Catal* 211:103–108
64. Kirm I, Medina F, Rodríguez X, Sueiras J, Cesteros Y, Salagre P (2004) Epoxidation of styrene with hydrogen peroxide using hydrotalcites as heterogeneous catalysts. *Appl Catal A* 272:175–185
65. Pillai UR, Sahle-Demessie E (2003) Sn-exchanged hydrotalcites as catalysts for clean and selective Baeyer-Villiger oxidation of ketones using hydrogen peroxide. *J Mol Catal A* 191:93–100
66. Jimenez-Sanchidrian C, Hidalgo JM, Llamas R, Ruiz JR (2006) Baeyer-Villiger oxidation of cyclohexanone with hydrogen peroxide/benzonitrile over hydrotalcites as catalysts. *Appl Catal A* 312:86–94

67. Ruiz JR, Jimenez-Sanchidrian C, Llamas R (2006) Hydrotalcites as catalysts for the Baeyer-Villiger oxidation of cyclic ketones with hydrogen peroxide/benzonitrile. *Tetrahedron* 62:11697–11703
68. Chen YZ, Hwang CM, Liaw CW (1998) One-step synthesis of methyl isobutyl ketone from acetone with calcined Mg/Al hydrotalcite-supported palladium or nickel catalysts. *Appl Catal A* 169:207–214
69. Nikolopoulos AA, Jang BWL, Subramanian R, Spivey JJ, Olsen DJ, Devon TJ Culp RD, Subramanian R (2000) Environmentally-benign liquid-phase acetone condensation process using novel heterogeneous catalysts. *ACS Symp Ser* 767:194–205
70. Winter F, Jos Van Dillen A, De Jong KP (2004) Single-stage liquid-phase synthesis of methyl isobutyl ketone under mild conditions. *J Mol Catal A* 219:273–281
71. Nikolopoulos AA, Jang BWL, Spivey JJ (2005) Acetone condensation and selective hydrogenation to MIBK on Pd and Pt hydrotalcite-derived MgAl mixed oxide catalysts. *Appl Catal A* 296:128–136
72. Tichit D, Ortiz MdJM, Francova D, Gerardin C, Coq B, Durand R, Prinetto F, Ghiotti G (2007) Design of nanostructured multifunctional Pd-based catalysts from layered double hydroxides precursors. *Appl Catal A* 318:170–177
73. Tichit D, Coq B, Ribet S, Durand R, Medina F (2000) Tailoring of acido-basic properties and metallic function in catalysts obtained from LDHs for the hydrogenation of nitriles and of a,b-unsaturated aldehydes. *Stud Surf Sci Catal (International Congress on Catalysis, (2000), Pt. A)* 130A:503–508
74. Coq B, Tichit D, Ribet S (2000) Co/Ni/Mg/Al layered double hydroxides as precursors of catalysts for the hydrogenation of nitriles: hydrogenation of acetonitrile. *J Catal* 189:117–128
75. Medina Cabello F, Tichit D, Coq B, Vaccari A, Dung NT (1997) Hydrogenation of acetonitrile on nickel-based catalysts prepared from hydrotalcite-like precursors. *J Catal* 167:142–152
76. Tichit D, Durand R, Rolland A, Coq B, Lopez J, Marion P (2002) Selective half-hydrogenation of adiponitrile to aminocapronitrile on Ni-based catalysts elaborated from lamellar double hydroxide precursors. *J Catal* 211:511–520
77. Queau R, Poilblanc R (1972) Interactions between Lewis bases chemisorbed on transition metal surfaces. Infrared spectroscopic studies. *J Catal* 27:200–206
78. Queau R, Labroue D, Poilblanc R (1981) Interactions of chlorine and bromine with chemisorbed carbon monoxide on evaporated platinum, rhodium, and iridium films. *J Catal* 69:249–253
79. Figueras F, Gomez R, Primet M (1973) In: Meier WM, Uytterhoeven JB (eds) Adsorption and catalytic properties of palladium supported by silica, alumina, magnesia, and amorphous and crystalline silica-aluminas. *Molecular Sieves, International Conference, 3rd, Zurich, 1973, American Chemical Society, Zurich*, pp 480–488
80. Kazansky VB, Borovkov VY, Serykh AI, Figueras F (1997) Diffuse reflectance IR study of noble metals supported on basic carriers. Part I: Pt supported on Al-Mg hydrotalcite. *Catal Lett* 49:35–41
81. Zhang G, Coq B, de Menorval LC, Tichit D (1996) Comparative behavior of extremely dispersed Pt/Mg(Al)O and Pt/Al<sub>2</sub>O<sub>3</sub> for the chemisorption of hydrogen, CO and CO<sub>2</sub>. *Appl Catal A* 147:395–406
82. Boitiaux JP, Cosyns J, Vasudevan S (1985) Hydrogenation of highly unsaturated hydrocarbons over highly dispersed Pd catalyst. Part II: ligand effect of piperidine. *Appl Catal* 15:317–326
83. Telkar MM, Rode CV, Rane VH, Chaudhari RV (2005) Influence of alkali metal doping on selectivity behaviour of platinum catalysts for hydrogenation of 2-butyne-1,4-diol. *Catal Commun* 6:725–730
84. Francova D, Tanchoux N, Gerardin C, Trens P, Prinetto F, Ghiotti G, Tichit D, Coq B (2007) Hydrogenation of 2-butyne-1,4-diol on supported Pd catalysts obtained from LDH precursors. *Micropor Mesopor Mater* 99:118–125

85. Meshesha BT, Chimentão RJ, Medina F, Sueiras JE, Cesteros Y, Salagre P, Figueras F (2009) Catalytic hydrodechlorination of 1,2,4-trichlorobenzene over Pd/Mg(Al)O catalysts. *Appl Catal B* 87:70–77
86. Beletskaya IP, Cheprakov AV (2000) The Heck reaction as a sharpening stone of palladium catalysis. *Chem Rev* 100:3009–3066
87. Crisp GT (1998) Variations on a theme: recent developments on the mechanism of the Heck reaction and their implications for synthesis. *Chem Soc Rev* 27:427–436
88. Augustine RL, O'Leary ST (1992) Heterogeneous catalysis in organic chemistry. Part 8. The use of supported palladium catalysts for the Heck arylation. *J Mol Catal* 72:229–242
89. Djakovitch L, Koehler K (2001) Heck reaction catalyzed by Pd-modified Zeolites. *J Am Chem Soc* 123:5990–5999
90. Kohler K, Wagner M, Djakovitch L (2001) Supported palladium as catalyst for carbon–carbon bond construction (Heck reaction) in organic synthesis. *Catal Today* 66: 105–114
91. Dams M, Drijkoningen L, Pauwels B, Van Tendeloo G, De Vos DE, Jacobs PA (2002) Pd-Zeolites as heterogeneous catalysts in Heck chemistry. *J Catal* 209:225–236
92. Heidenreich RG, Kohler K, Krauter JGE, Pietsch J (2002) Pd/C as a highly active catalyst for Heck, Suzuki and Sonogashira reactions. *Synlett* 7:1118–1122
93. Choudary BM, Madhi S, Chowdar, NS, Kantam ML, Sreedhar B (2002) Layered double hydroxide supported nanopalladium catalyst for Heck-, Suzuki-, Sonogashira-, and Stille-type coupling reactions of chloroarenes. *J Am Chem Soc* 124:14127–14136
94. Zhou H, Zhuo GL, Jiang XZ (2006) Heck reaction catalyzed by Pd supported on LDH-F hydrotalcite. *J Mol Catal A* 248:26–31
95. Corma A, Garcia H, Leyva A, Primo A (2003) Basic zeolites containing palladium as bifunctional heterogeneous catalysts for the Heck reaction. *Appl Catal A* 247:41–49
96. Cwik A, Hell Z, Figueras F (2006) Palladium/magnesium-lanthanum mixed oxide catalyst in the Heck reaction. *Adv Synth Catal* 348:523–530
97. Cwik A, Hell Z, Figueras F (2005) Suzuk-Miyaura cross-coupling reaction catalyzed by Pd/MgLa mixed oxide. *Org Biomol Chem* 3:4307–4309
98. Cwik A, Hell Z, Figueras F (2006) A copper-free Sonogashira reaction using a Pd/MgLa mixed oxide. *Tetrahedron Lett* 47:3023–3026
99. Mehnert CP, Weaver DW, Ying JY (1998) Heterogeneous Heck catalysis with palladium-grafted molecular sieves. *J Am Chem Soc* 120:12289–12296
100. Mehnert CP, Ying JY (1997) Palladium-grafted mesoporous MCM-41 material as heterogeneous catalyst for Heck reactions. *Chem Commun* 2215–2216
101. Marcilly C, Courty P, Leporq S (1993) Sweetening of petroleum cuts without addition of an aqueous alkaline solution using a basic solid catalyst. US Patent 2,688,223
102. Arena BJ, Holmgren JS (1993) Catalyst for sweetening a sour hydrocarbon fraction. US Patent 5,232,887
103. Gillespie RD, Bricker JC, Arena BJ, Holmgren JS (1995) Sweetening sour petroleum fractions using a supported metal chelate and a solid base catalyst. US Patent 5,413,704
104. Alcaraz JJ, Arena BJ, Gillespie RD, Holmgren JS (1998) Solid base catalysts for mercaptan oxidation. *Catal Today* 43:89–99
105. Liu HC, Yang XY, Ran GP, Min EZ (2000) Novel bifunctional catalysts of cobalt phthalocyanine bonded to organic-functionalized basic calcined Mg–Al hydrotalcite for autoxidation of mercaptans. *J Chem Res S* 6:294–295
106. Liu HC, Min EZ (2006) Catalytic oxidation of mercaptans by bifunctional catalysts composed of cobalt phthalocyanine supported on Mg–Al hydrotalcite-derived solid bases: effects of basicity. *Green Chem* 8:657–662
107. Vreysen S, Maes A (2008) Adsorption mechanism of humic and fulvic acid onto Mg/Al layered double hydroxides. *App Clay Sci* 38:237–249
108. Bascialla G, Regazzoni AE (2008) Immobilization of anionic dyes by intercalation into hydrotalcite. *Coll Surf A* 328:34–39

109. Laguna H, Loera S, Ibarra IA, Lima E, Vera MA, Lara V (2007) Azoic dyes hosted on hydrotalcite-like compounds: non-toxic hybrid pigments. *Micropor Mesopor Mater* 98: 234–241
110. Morris JM, Jin S, Cui K (2008) Removal of endocrine active compounds using layered double hydroxide material. *Chem Eng J* 145:160–163
111. Wang SL, Liu CH, Wang MK, Chuang YH, Chiang PN (2009) Arsenate adsorption by Mg/Al-NO<sub>3</sub> layered double hydroxides with varying the Mg/Al ratio. *Appl Clay Sci* 43:79–85
112. Prasanna SV, Rao RAP, Kamath PV (2006) Layered double hydroxides as potential chromate scavengers. *J Coll Interf Sci* 304:292–299
113. Prasanna SV, Vishnu Kamath P (2008) Chromate uptake characteristics of the pristine layered double hydroxides of Mg with Al. *Solid State Sci* 10:260–266
114. Chitrakar R, Tezuka S, Sonoda A, Sakane K, Ooi K, Hirotsu T (2005) Adsorption of phosphate from seawater on calcined MgMn-layered double hydroxides. *J Coll Interf Sci* 290:45–51
115. Goh KH, Lim TT, Dong Z (2008) Application of layered double hydroxides for removal of oxyanions: a review. *Water Res* 42:1343–1368
116. Anirudhan TS, Suchithra PS (2008) Synthesis and characterization of tannin-immobilized hydrotalcite as a potential adsorbent of heavy metal ions in effluent treatments. *Appl Clay Sci* 42:214–223
117. Manda S, Mayadevi S (2008) Cellulose supported layered double hydroxides for the adsorption of fluoride from aqueous solution. *Chemosphere* 72:995–998
118. Evans M (2003) SO<sub>x</sub> reduction. *Hydrocarbon Eng* 8:43–46
119. Zhuo GL, Chen YF, Ge ZH, Jiang XZ (2002) Study on Mg/Fe mixed oxides derived from hydrotalcite as De-SO<sub>x</sub> catalyst. *Chinese Chem Lett* 13:279–282
120. Polato CMS, Henriques CA, Neto AA, Monteiro JLF (2005) Synthesis, characterization and evaluation of CeO<sub>2</sub>/Mg,Al-mixed oxides as catalysts for SO<sub>x</sub> removal. *J Mol Catal A* 241:184–193
121. Andersson POF, Pirjamali M, Jaras SG, Boutonnet Kizling M (1999) Cracking catalyst additives for sulfur removal from FCC gasoline. *Catal Today* 53:565–573
122. Cantu M, Lopez-Salinas E, Valente JS (2005) SO<sub>x</sub> removal by calcined MgAlFe hydrotalcite-like materials: effect of the chemical composition and the cerium incorporation method. *Environ Sci Technol* 39:9715–9720
123. Heck RML, Farrauto RJ (1994) Catalysts for environmental control. *Royal Soc Chem [Special Publication]* 139 (chemically modified surfaces):120–38
124. Matsumoto S, Ikeda Y, Suzuki H, Ogai M, Miyoshi N (2000) NO<sub>x</sub> storage-reduction catalyst for automotive exhaust with improved tolerance against sulfur poisoning. *Appl Catal B* 25:115–124
125. Burch R, Breen JP, Meunier FC (2002) A review of the selective reduction of NO<sub>x</sub> with hydrocarbons under lean-burn conditions with non-zeolitic oxide and platinum group metal catalysts. *Appl Catal B* 39:283–303
126. Matsumoto SI (1996) DeNO<sub>x</sub> catalyst for automotive lean-burn engine. *Catal Today* 29: 43–45
127. Matsumoto SI (2004) Recent advances in automobile exhaust catalysts. *Catal Today* 90: 183–190
128. Matsumoto S, Yokota K, Doi H, Kimura M, Sekizawa K, Kasahara S (1994) Research on new DeNO<sub>x</sub> catalysts for automotive engines. *Catal Today* 22:127–146
129. Guyon M, Blejean F, Bert C, Le Faou P (1998) Impact of sulfur on NO<sub>x</sub> trap catalyst activity. Study of the regeneration conditions. *Soc Automot Eng [Special Publication]* 1399 (direct injection: engines, emissions, and after treatment):87–95
130. Centi G, Fornasari G, Gobbi C, Livi M, Trifiro F, Vaccari A (2002) NO<sub>x</sub> storage-reduction catalysts based on hydrotalcite. Effect of Cu in promoting resistance to deactivation. *Catal Today* 73:287–296

131. Berber M.R, Minagawa K, Katoh M, Mori T, Tanaka M (2008) Nanocomposites of 2-arylpropionic acid drugs based on Mg–Al layered double hydroxide for dissolution enhancement. *Eur J Pharm Sci* 35:354–360
132. del Arco M, Fernández A, Martín C, Rives V (2009) Release studies of different NSAIDs encapsulated in Mg, Al, Fe-hydrotalcites. *Appl Clay Sci* 42:538–544
133. Del Arco M, Fernandez A, Martin C, Sayalero ML, Rives V (2008) Solubility and release of fenamates intercalated in layered double hydroxides. *Clay Miner* 43:255–265
134. Del Arco M, Cebadera E, Gutierrez S, Martin C, Montero MJ, Rives V, Rocha, J, Sevilla MA (2004) Mg,Al layered double hydroxides with intercalated indomethacin: synthesis, characterization, and pharmacological study. *J Pharm Sci* 93:1649–1658
135. Bonina FP, Giannossi ML, Medici L, Puglia C, Summa V, Tateo F (2008) Diclofenac-hydrotalcite: in vitro and in vivo release experiments. *Appl Clay Sci* 41:165–171
136. Carja G, Kameshima Y, Ciobanu G, Chiriac H, Okada K (2009) New hybrid nanostructures based on oxacillin-hydrotalcite-like anionic clays and their textural properties. *Micron* 40:147–150
137. Liu CX, Hou WG, Li LF, Li Y, Liu SJ (2008) Synthesis and characterization of 5-fluorocytosine intercalated Zn–Al layered double hydroxide. *J Solid State Chem* 181: 1792–1797
138. Choi SJ, Oh JM, Choy JH (2008) Anticancer drug-layered hydroxide nanohybrids as potent cancer chemotherapy agents. *J Phys Chem Solids* 69:1528–1532
139. Valente JS, Cantu MS, Figueras F (2008) A simple environmentally friendly method to prepare versatile hydrotalcite-like compounds. *Chem Mater* 20:1230–1232



# Chapter 14

## Mesoporous Phosphate Heterostructures: Synthesis and Application on Adsorption and Catalysis

Ramón Moreno-Tost, José Jiménez-Jiménez, Antonia Infantes-Molina, Celio L. Cavalcante, Jr., Diana C.S. Azevedo, María Dolores Soriano, José Manuel López Nieto, Antonio Jiménez-López, and Enrique Rodríguez-Castellón

**Abstract** Porous phosphate heterostructures (PPHs) are solids formed by a layered metal(IV) phosphate expanded with silica galleries obtained by combining the two main strategies for obtaining mesoporous materials [pillared layered structures (PLS') and MCM-41]. The different synthetic pathways for obtaining mesoporous phosphate structures with silica galleries with Zr- or Ti-doped silica, the study of their structural, textural and acid properties, its functionalisation with different organic substances such as propionitrile, 3-aminopropyl triethoxysilane, (3-mercaptopropyl)trimethoxysilane, vinyltrimethoxysilane, phenyltriethoxysilane and 3-(triethoxysilyl)propionitrile are discussed. The preparation of metal-supported catalysts and their application in gas separation, adsorption and catalysis are reviewed. Specifically, the use of Cu- and Fe-exchanged PPH for the adsorption of benzothiophene and the separation of propane/propene is the main application as adsorbent. The hydrotreating of aromatic hydrocarbons using ruthenium-impregnated catalysts via hydrogenation and hydrogenolysis/hydrocracking for the production of clean diesel fuels, the selective catalytic reduction of NO from stationary and mobile sources by using Cu-PPH with 1, 3 and 7 wt% of Cu and the selective oxidation of hydrogen sulphide to sulphur with vanadium-containing PPH are the three catalytic reactions of environmental interest studied.

**Keywords** Phosphates · Heterostructures · Adsorption · Catalysis · Pillared · Mesoporous

---

E. Rodríguez-Castellón (✉)

Departamento de Química Inorgánica, Cristalografía y Mineralogía, Unidad Asociada al Instituto de Catálisis (CSIC), Universidad de Málaga, 29071 Málaga, Spain  
e-mail: castellon@uma.es

## 14.1 Introduction

Layered compounds have been closely related to catalysis since the beginning of the petrochemical industry. The first hydrocracking process came on stream with acid-treated clays in 1936 [1–3]. Although the role of clays as cracking catalysts was replaced by zeolites and aluminosilicates in 1964 [4], salt-loaded, acid-treated and ion-exchanged clays were still found to be efficient catalysts in many organic reactions [5, 6]. The rising of oil prices in 1973 forced the oil industry to face an entirely new problem: how to process heavy crude oils rich in metals and large refractory molecules. The concept of pillared clays (PILCs) emerged in the 1970s of the past century as a result of the search for large pore catalysts capable of cracking heavy oils [7]. Basically, it consists of converting layered clay minerals into highly porous structures by exchanging the interlayer cations with oligomeric oxo/hydroxyl cationic species which, after calcination, produce oxide pillars expanding the silicate layers. These materials demonstrate high activity in cracking process and a selectivity for products with larger molecules [8, 9]. However, the original objective of applying these materials as catalysts for FCC was unsuccessful due to their low hydrothermal stability. The main use of pillared clays was in acid catalysis [10], production of fine chemicals [11] and for the reduction of pollutants (selective catalytic reduction of  $\text{NO}_x$  and catalytic removal of volatile organic compounds [12, 13]).

This procedure to expand the interlayer region of clays was also applied to other layered materials as metal(IV) phosphates. These pillared layered solids can be considered as two-dimensional zeolite-like structures, which are prepared by cation exchange with inorganic polyhydroxocations. Upon heating, these oligomeric cations give rise to oxide nanoparticles, which sustain the layers permanently apart and create zeolite-like interlayer and interpillar spaces, thus yielding materials with high surface areas and acidity [14]. For example, pillared materials prepared from layered  $\alpha$ -zirconium phosphate have been extensively studied and they have been shown to be active in acid-catalysed reactions [15], in oxidative dehydrogenation of light alkanes [16] and as a support of active phases in reactions such as hydrogenation of aromatic hydrocarbons [17] and hydrodesulphurisation of thiophene [18].

At the beginning of the 1990s of the past century, Mobil Oil scientists reported a new method for preparation of mesoporous materials using surfactant molecules as a template for inorganic silica arrays [19]. By interaction of surfactant micelles with inorganic species, three geometries can be obtained: hexagonal (MCM-41), cubic (MCM-48) and lamellar (MCM-50), with subsequent applications as catalysts and adsorbents [20]. Only for the first and second geometries, after the surfactant molecules are removed, generally by calcination, porous materials with high specific surface areas and well-defined porous diameters are obtained. However, in the case of materials with a lamellar geometry, the removal of the surfactant gives rise to the collapse of the structure and a non-porous material occurs. In 1995 Galarneau et al. [21] proposed a new way to obtain thermally stable porous materials from cationic layered clays by combining the two main strategies for

obtaining mesoporous materials [pillared layer structures (PLS<sup>+</sup>) and MCM-41]. The synthesis of such materials consists of intercalating cationic templates and neutral amine co-templates in the interlayer space of clays forming micelle structures; then, the silica pillars are created by in situ hydrolysis and condensation of a silica source around the micelle structures and finally the organic templates are removed from the material by a classical calcination, producing materials with a high surface area and combined micro- and mesoporous structure. This new class of materials was called porous clay heterostructures (PCHs).

The synthesis of an MCM-50-type lamellar zirconium phosphate, expanded with cationic surfactant molecules, was firstly reported by Jiménez-Jiménez et al. [22]. This phosphate was used as a starting material for the insertion of gallium oxide into its interlayer space by cationic exchange of the surfactant guest with oligomeric gallium species, leading to a porous structure, as is the case for PLS materials. Here, we have studied the use of a surfactant-expanded zirconium phosphate for the formation of silica galleries into the interlayer space, analogous to the PCH material, which shall be named a porous phosphate heterostructure (PPH). With this method, MCM-50 zirconium phosphate materials can be used as precursor for the synthesis of mesoporous solids and a new field for application of these materials can be opened. Thus, this chapter reviews PPH materials focusing on the synthesis, characterisation and their applications.

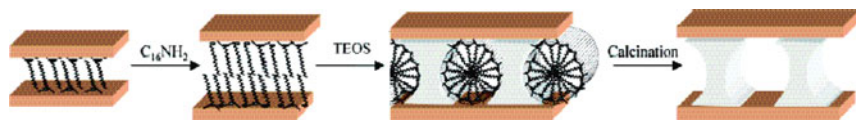
## 14.2 Synthesis of Si-PPH

The synthesis of Si-PPH materials is based on the method developed by Jiménez-Jiménez et al. [23]. Briefly, the synthesis was carried out by using cetyltrimethylammonium (CTMA)-expanded zirconium phosphate as precursor, which was prepared with a solution of CTMABr in *n*-propanol, H<sub>3</sub>PO<sub>4</sub> and zirconium(IV) *n*-propoxide. The solid thus obtained (CTMA-ZrP) [22] was suspended in water and a solution of hexadecylamine in *n*-propanol was added as co-surfactant. After 1 day under stirring, a solution of TEOS in *n*-propanol was added as reactant to generate the silica galleries. This suspension was stirred at room temperature for 3 days. The solid obtained was then centrifuged, washed with ethanol and dried at 333 K in air. This as-prepared material was calcined at 823 K for 6 h. These materials were prepared by varying the hexadecylamine/P and TEOS/P molar ratios.

The starting material CTMA-ZrP has an expanded MCM-50 structure where the cationic molecules of cetyltrimethylammonium are inserted into the interlayer space of zirconium phosphate, with a basal spacing of 33 Å. From this basal spacing of 33 Å, it is possible to deduce that surfactant molecules are forming a double layer in the interlayer space with the alkyl chains slanted at 55° with respect to the layers. This basal spacing is shorter than expected, which supposes an imbrication of alkyl chains. On the other hand, due to the fact that the cross section of the polar head of CTMA is larger than that corresponding to an exchange site, and since the alkyl chains are imbricated, only two of every three acid sites will be neutralised [22].

When hexadecylamine is added, this basic molecule can enter between the chains of CTMA and neutralise the remaining acid sites on the  $\alpha$ -zirconium phosphate layer.

These expanded materials (with and without the neutral co-surfactant) are used for the formation of silica galleries in the interlayer space using these organic molecules themselves as templates (Scheme 14.1). The preservation of the  $d_{001}$  diffraction peak at low angle after calcination indicates that the structure does not collapse after the removal of the surfactant; thus the formation of the silica galleries in the interlayer space of the phosphate holds the zirconium phosphate layers apart. In contrast to the method previously used in the synthesis of PCH [21], these PPH materials can also be obtained without the addition of the neutral co-surfactant. This is made possible due to the high cation exchange capacity (CEC) of zirconium phosphate (6.63 meq/g) in comparison with clay minerals, which exhibit much lower CEC values (0.7–1.12 meq/g).

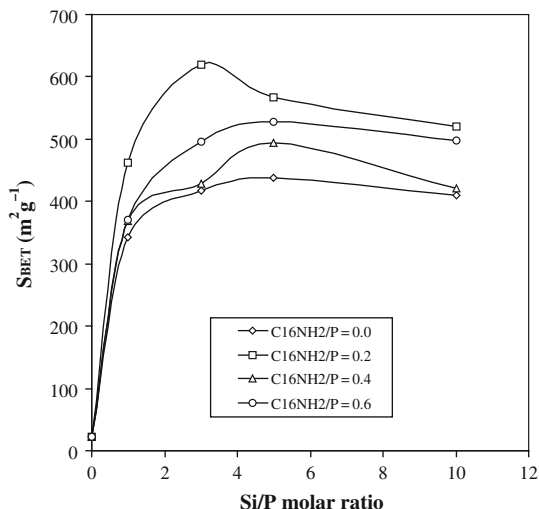


**Scheme 14.1** Synthesis of the mesoporous zirconium phosphate heterostructure. From [23], with permission from The Royal Society of Chemistry

Several materials were synthesised by varying the TEOS/P and the co-surfactant/P molar ratios. Four co-surfactant/P ratios were tested (0, 0.2, 0.4 and 0.6). The most significant difference is that of the definition and intensity of the  $d_{001}$  diffraction peak. The most intense peaks are observed for the solid with a  $C_{16}NH_2/P$  molar ratio of 0.2. This behaviour can be explained taking into account that a critical amount of surfactant is necessary for templating the silica galleries. The influence of the added amount of TEOS (molar ratios of 1, 3, 5 and 10) was also studied showing that with the lowest molar ratio, the obtained material exhibits a low intensity  $d_{001}$  diffraction peak due to the small amount of added TEOS which is insufficient for the adequate formation of the galleries. However, for the other materials of this series, relatively high-intensity  $d_{001}$  diffraction peaks are obtained, this being indicative of the existence of quite well-ordered structures.

These materials have been characterised by  $N_2$  adsorption–desorption at 77 K, showing type IV isotherms, which correspond to mesoporous materials. The BET surface values observed (340–619  $m^2/g$ ) are quite high in comparison to those observed for CTMA–ZrP after calcination at 823 K (22  $m^2/g$ ). These values indicate the presence of a silica structure in the interlayer space of the zirconium phosphate, resulting in a porous system accessible to the  $N_2$  molecules. The highest value of BET surface (619  $m^2/g$ ) was obtained with a co-surfactant/P molar ratio of 0.2 and an added TEOS/P molar ratio of 3 (Fig. 14.1). The lamellar nature of this material can clearly be observed in the TEM image [23]. Materials synthesised without co-surfactant show the lowest surface area values. This is probably due to the existence of an insufficient amount of surfactant for the adequate formation of the galleries.

**Fig. 14.1** BET surface evolution with co-surfactant/P and TEOS/P molar ratio added. Reproduced from [23], with permission from The Royal Society of Chemistry



The acidity of these materials was evaluated by TPD-NH<sub>3</sub>. The acidity of these materials comes from the presence of free P–O–H groups located on the layers of zirconium phosphate, as well as from the presence of silanol groups on the surface of the silica galleries. Moreover, silanol groups will display enhanced acidity due to the inductive effect from the layer. When the total acidity is normalised by taking into account the surface area of the acid solids, the surface density of acid sites of the studied materials is obtained. According to this parameter, the density of acid sites decreases with the increase in the TEOS/P molar ratio used in the synthetic process. This indicates that when TEOS molecules are hydrolysed into the interlayer space of zirconium phosphate, the P–O–H groups are either neutralised or covered by the silica framework and in this case the acidity generally arises from free Si–O–H groups only. This produces a decrease in the number of the available P–O–H groups and thus a concomitant reduction of the acidity. The material with a TEOS/P molar ratio of 3 and hexadecylamine/P molar ratio of 0.2 [3-SiPPH(0.2)] was chosen as a representative material taking into account its high surface area, acidity and crystallinity. The 3-SiPPH(0.2) material exhibits 1.70 mmol NH<sub>3</sub>/g desorbed between 373 and 823 K, revealing it to be a very acidic solid, especially having strong acid centres, since 58% of the total ammonia desorption takes place in the temperature range of 573–823 K [23].

The physical and chemical properties of these new materials named PPH can be modified by different procedures. The silica galleries have been doped with other chemical elements to improve acid or redox characteristics so as to enhance their potential application on specific catalytic reactions. Also, the silica galleries can be functionalised with different organic groups and hybrid porous phosphate heterostructures can be obtained. Finally, pristine PPH material can be used as support of other chemical species, which can be incorporated by classical wet impregnation or by cationic exchange because of the high CEC of PPH material (1.7 meq/g).

In the following sections, a summary of the procedures used to obtain these new derivatives of PPH materials is presented.

### 14.3 Doping the Silica Galleries

Several studies have been carried out after the publication of the synthesis of mesoporous silica MCM-41 doped with Zr [24] or Ti [25]. For Zr–MCM-41, acid properties are useful in its applications as acid catalyst [26] or as support of noble metals for hydrogenation and hydrogenolysis/hydrocracking reactions [27]. However, for Ti–MCM-41, their redox properties prompt this material to be used as catalyst for the selective oxidation of organic compounds such as epoxidation reactions using  $\text{H}_2\text{O}_2$  [28]. We have considered the possibility of obtaining analogous solids by doping a silica PPH with Zr or Ti [29], which can be used for the same catalyst application as Zr–MCM-41 and Ti–MCM-41 when higher acidities are required. Chemical (acid and/or redox) properties of these materials can be modified by doping the silica galleries with different elements. In this case, zirconium or titanium ions have been incorporated into the silica array due to the potential effect of these elements in the acid and redox properties of the obtained solids.

As stated above, the best experimental conditions were hexadecylamine/P and TEOS/P molar ratios of 0.2 and 3.0, respectively, in order to obtain a solid with high surface area and acidity [23]. These molar ratios were also used in the preparation of mixed Si/Zr– and Si/Ti–PPH. Thus, the molar ratio of (Si+M)/P used was 3, where M is the doping element (Zr or Ti in this case). For each type, two solids were synthesised using Si/M molar ratios of 5 and 25.

For the material doped with titanium, the intensity and definition of the  $d_{001}$  diffraction peak is analogous to that of pure silica. However, when it is doped with zirconium, a less ordered structure is obtained. In general, the  $d_{001}$  values, in all cases, are close to those of the pristine pure Si–PPH material, which is indicative that hydrolysis and condensation of the respective mixed alkoxide give rise to a similar inorganic structure, with basal spacing values similar to those of Si–PPH [29].

The Si/M atomic ratio was calculated by XPS to determine the distribution of the doping agent in the silica framework. The surface Si/M molar ratio is lower than the theoretical values for the Si/Zr–PPH solids; however, the opposite occurs in the case of Si/Ti–PPH solids. This can be explained by taking into account the different hydrolysis rate of the alkoxides used as source of Zr and Ti with respect to TEOS. The hydrolysis rate of titanium(IV) propoxide is slower than that of TEOS, and not all are hydrolysed, thus yielding a surface Si/Ti molar ratio higher than the theoretical amounts that were added. Nevertheless, for Zr/Si PPH the inverse situation is observed because of the high hydrolysis rate of zirconium(IV) propoxide, leading to zirconium species located inside the inorganic galleries.

The textural properties of these materials show in all cases relatively high BET surface areas ( $>400 \text{ m}^2/\text{g}$ ), but in comparison with pure silica PPH ( $620 \text{ m}^2/\text{g}$ ), the incorporation of Zr or Ti causes a decrease in the BET surface area. This decrease

can be due to the formation of less ordered structures upon the incorporation of Zr or Ti. The pore size distribution indicates a narrow range of pore diameters in the materials with the maximum centred at 17 Å, therefore lying within the mesoporous range.

The evaluation of acid activity of these materials by means of the isopropanol test shows that doped materials are more readily deactivated than pristine Si-PPH. This fact is due to the presence of Lewis acid sites generated by the presence of Zr and Ti, which favour the formation of coke poisoning and partial deactivation of the solid.

Vanadium was also successfully incorporated into the silica galleries [30]. Several solids were prepared in *n*-propanol by varying the Si/V molar ratio from 1 to 25. Materials, both with and without TEOS, were also prepared by using water, instead of *n*-propanol, as solvent. The solid with the lower vanadium loading shows the characteristic low-angle diffraction peak at 2.5°. In this case, the inorganic galleries of silica/vanadia are well formed in an analogous way as pure silica PPH material. However, with a further incorporation of vanadium, the diffraction peak at low angle disappears. This can be attributed to the formation of amorphous structures in which the crystalline order was destroyed due to the formation of a mixed silica/vanadia inorganic framework in the interlayer space. The XRD patterns at high angle show the V<sub>2</sub>O<sub>5</sub> characteristic diffraction peaks for samples with Si/V molar ratios of 2 or lower. The presence of V<sub>2</sub>O<sub>5</sub> crystallites is proved by the drastic decrease of BET surface with the V loading, varying from 795 m<sup>2</sup>/g for Si/V = 25 to only 60 m<sup>2</sup>/g for Si/V = 1. Both the sample synthesised without TEOS (NT-5PPH) and the sample obtained in aqueous media (Vw-5PPH) exhibit strong reflection lines assigned to V<sub>2</sub>O<sub>5</sub> (Fig. 14.2), but also those due to the presence of ZrP<sub>2</sub>O<sub>7</sub> (JCPDF-85-0896) formed by the collapse of the interlayer space, and formation of P-O-P bounds between neighbour layers by condensation of P-OH groups. The presence of pyrophosphate is also observed for pure silica PPH. The presence of

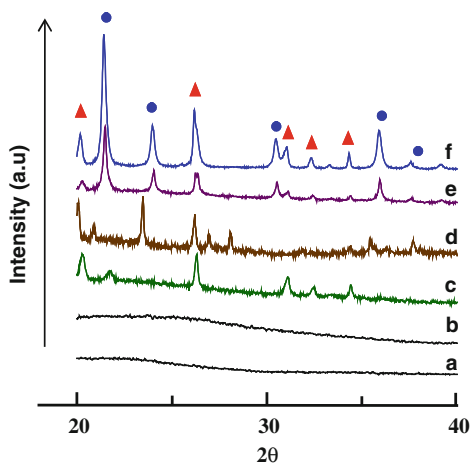


**Fig. 14.2** XRD patterns of catalysts: (a) V-25PPH; (b) V-5PPH; (c) V-2PPH; (d) V-1PPH; (e) Vw-PPH; (f) NT-5PPH. Symbols: (▲) V<sub>2</sub>O<sub>5</sub> (JCPDS: 41-1426); (●) ZrP<sub>2</sub>O<sub>7</sub> (JCPDS: 85-896)

V<sub>2</sub>O<sub>5</sub> crystallites is also confirmed by Raman spectroscopy by the bands at 998, 706, 530, 489, 410, 305, 289, 203 and 159 cm<sup>-1</sup>, which are related to the presence of V<sub>2</sub>O<sub>5</sub> crystallites [31], while the appearance of a band at 1020 cm<sup>-1</sup> is related to the presence of isolated V<sup>5+</sup> species (terminal V=O bond of an amorphous cluster of V<sub>2</sub>O<sub>5</sub>) [32]. Accordingly, isolated species and V<sub>2</sub>O<sub>5</sub> crystallites are observed in the sample with Si/V = 5, while V<sub>2</sub>O<sub>5</sub> crystallites are formed on samples prepared with lower Si/V ratios.

## 14.4 Functionalisation of Silica Galleries

Another way of modulating the properties of silica PPH is to incorporate functional groups [33], i.e. propionitrile groups, in the silica galleries to provide new properties to these solids. The presence of propionitrile (CN) groups on the silica galleries is achieved by adding to the expanded zirconium phosphate a triethoxysilyl propionitrile precursor together with TEOS under a TEOS/CN molar ratio of 5 or 50, while maintaining the Si/P molar ratio of 3. In this case, the calcination of the solid with the surfactant would lead to the destruction of the propionitrile group, therefore the elimination of the surfactant from inside the silica galleries is achieved by extraction with a EtOH/HCl solution.

The presence of nitrile groups in the synthesised solids is verified by CNH analysis and IR spectroscopy by the stretching vibration of the C≡N bond at 2256 cm<sup>-1</sup>. The BET areas of the pristine Si-PPH and the functionalised solids are quite high, 620 and 530 m<sup>2</sup>/g for Si-PPH and CN5-PPH, respectively, in spite of the presence of propionitrile groups. However, the application of pressure to the powder for preparing disks clearly reduces these values (around 65% for pure silica heterostructure Si-PPH and between 95 and 99% for hybrid materials). The dramatic decrease of the surface area (around 500 m<sup>2</sup>/g for powder and less than 20 m<sup>2</sup>/g for pressured discs) as well as the vanishing of the *d*<sub>001</sub> reflection line in the XRD diffractograms seems to indicate the collapse of the hybrid solid structure. This fact may be attributed to (i) the formation of bonds among the nitrile groups with the surface P-O-H groups, or with the less acidic surface Si-O-H groups, giving rise to cross-linking and the consequent reduction of the surface area and (ii) the blocking of pores by flexible -CH<sub>2</sub>-CH<sub>2</sub>-CN groups. Moreover, propionitrile groups can migrate to the external surface. This fact is proved by XPS analysis, which shows an enrichment of the surface with C and N, suggesting that the pressure produces the departure or the segregation of propionitrile groups out to the surface.

On the other hand, various organic compounds have been introduced into the silica galleries providing new properties to the PPH. The precursors of the organic moieties were 3-aminopropyl triethoxysilane; (3-mercaptopropyl)-trimethoxysilane; vinyltrimethoxysilane; phenyltriethoxysilane and 3-(triethoxysilyl)propionitrile, which functionalise the surface of silica galleries due to the co-condensation of TEOS and the respective organosilane. The solids obtained were named X<sub>*n*</sub>-PPH, where X indicates the organic groups (N, S, V, Ph and CN for 3-aminopropyl,



3-mercaptopropyl, vinyl, phenyl and propionitrile, respectively) and  $n$  denotes the TEOS/organosilyl-derived molar ratio used.

The incorporation of the different organic groups was carried out by co-condensation of a mixture of corresponding organosilane and TEOS into the interlayer space of the surfactant-expanded zirconium phosphate. The incorporation of organic groups into the structure was studied using several techniques. Thus, CNHS or CNH elemental analyses were used for the determination of mercaptopropyl, propionitrile and 3-aminopropyl, whereas UV spectrophotometry was used for detecting the presence of vinyl and phenyl groups. The tendency of the incorporation of organic groups as a function of their nature is shown in Fig. 14.3. A high incorporation of organic groups is observed for polar groups such as propionitrile and aminopropyl. However, for non-polar groups, such as phenyl derivatives, low incorporation is observed. This suggests that the polarity of organic molecules can be a determining factor in the incorporation of organic groups in the inorganic galleries, which can be explained by the mechanism proposed in the formation of these PPH materials (see Scheme 1). When the rod-like surfactant molecules used as templates for the silica galleries accommodate inside the interlayer space, the polar heads of the surfactant molecules are oriented towards the surface where the silica precursors (TEOS and organosilane) will be hydrolysed and condensed. In the case of polar organic groups, their presence favours such mechanism, which causes a high incorporation of polar organic molecules in the hybrid material, contrary to what happens with non-polar molecules, for which a low incorporation is observed. Additionally, the largest size of phenyl groups with respect to the other organic groups used may also determine their low incorporation.

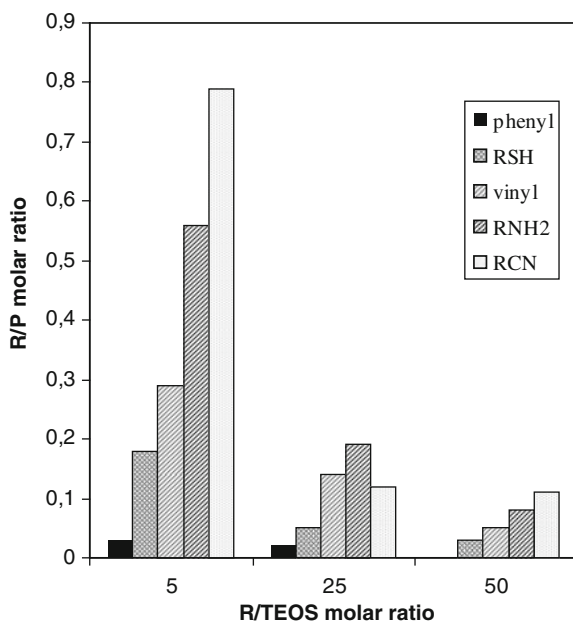
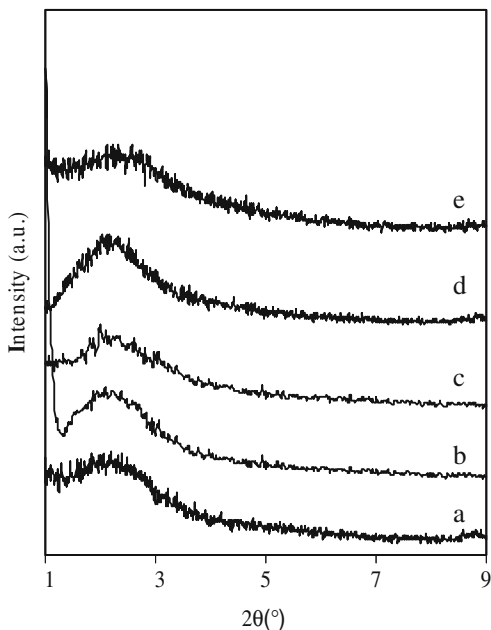


**Fig. 14.3** Incorporation of different organic groups as a function of TEOS/organosilane molar ratio added

**Fig. 14.4** XRD patterns for (a) CN25–PPH, (b) Ph25 PPH, (c) S25–PPH, (d) N25–PPH and (e) V25–PPH



In all cases, after the extraction process, a broad peak at low angle is observed, corresponding to the  $d_{001}$  diffraction (Fig. 14.4). This is indicative that zirconium phosphate layers are expanded by the formation of silica galleries in interlayer space. Thus, when the TEOS/organosilane molar ratio decreases, the intensity of the diffraction peak decreases, and for the N5–PPH material, no diffraction peak is observed. Also, for organic groups with low polarity (vinyl and phenyl), the intensity of the  $d_{001}$  reflection line decreases, which is more evident for the material with the highest amount of incorporated organic groups (corresponding to a TEOS/organosilane molar ratio of 5).

The  $N_2$  adsorption–desorption isotherms at 77 K of this kind of materials are of type IV corresponding to mesoporous materials. The observed BET surface area values of these hybrid materials are high (see Table 14.1), which indicates that silica galleries are present into the interlayer space of zirconium phosphate. However, in all the cases these BET surface areas are lower than those of the pristine PPH pure silica materials. This indicates that the incorporation of organic molecules on the surface of silica galleries hinders the correct formation of silica galleries, as observed in the XRD patterns.

Regarding the pore volume, these hybrid solids present high values. In this case, some materials show higher values of pore volume and average pore diameter than does the pristine PPH material. This can be due to the contribution of pores of larger sizes formed by the face–edge or edge–edge interaction of different particles, which is characteristic of pillared layered structures.

**Table 14.1** Basal spacing and textural properties of different hybrid PPH materials

Material	R/P (molar ratio)	$d_{001}$ (Å)	$S_{\text{BET}}$ (m <sup>2</sup> /g)	$V_p$ (cm <sup>3</sup> /g)	$d_p$ (Å)
PPH	–	40	620	0.543	30.9
S-5PPH	0.18	40	472	0.513	37.9
S-25PPH	0.05	40	506	0.521	37.8
S-50PPH	0.03	44	537	0.522	36.8
N-5PPH	0.56	–	223	0.411	63.9
N-25PPH	0.19	40	355	0.437	47.5
N-50PPH	0.08	42	556	0.618	37.4
CN-5PPH	0.79	38	516	0.607	42.9
CN-25PPH	0.12	40	565	0.658	43.9
CN-50PPH	0.11	37	513	0.567	40.1
V-5PPH	0.29	36.5	556	0.609	42.2
V-25PPH	0.14	38	475	0.495	39.2
V-50PPH	0.05	38	574	0.495	39.9
Ph-5PPH	0.03	33	498	0.516	39.1
Ph-25PPH	0.02	39	545	0.596	41.8
Ph-50PPH	0.001	39	571	0.657	44.6

N, S, V, Ph and CN for 3-aminopropyl, 3-mercaptopropyl, vinyl, phenyl and propionitrile, respectively.

## 14.5 PPH as Support of Other Chemical Species

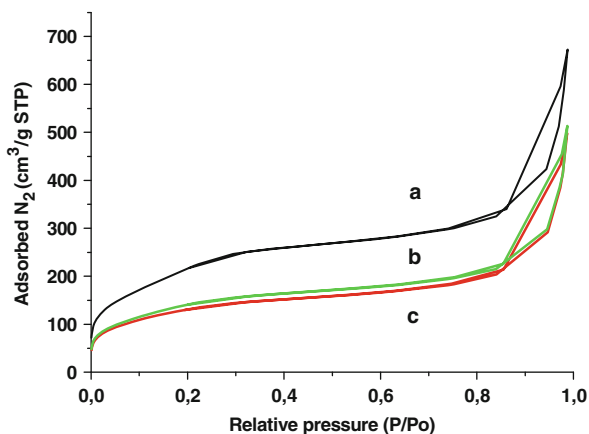
Given the physical and chemical properties of the PPH material, it may be used as support for other chemical species with potential applications in catalysis or adsorption. Thus, as the PPH material presents high ionic exchange capacity (1.73 meq/g), Cu(II) and Cu(I) were incorporated using such procedure [34]. These exchanged materials preserve the diffraction peak at low angle, which indicates that the silica gallery structure is preserved into the interlayer space. However, a decrease of the BET surface area is observed compared to the pristine PPH material. Thus, values of 409 and 325 m<sup>2</sup>/g are reported for Cu(II) and Cu(I) exchanged materials, respectively. These materials have been studied for gas separations [34].

Although new materials derived from PPH can be obtained by cation exchange, the preparation of new materials by wet impregnation of PPH with solutions containing other chemical species is profusely used. Fe(III) was impregnated into the mesoporous structure of Si-PPH by mixing the support with aqueous and organic (ethanol) Fe(NO<sub>3</sub>)<sub>3</sub>•9H<sub>2</sub>O solutions. Added metal salt in solution was calculated so as to incorporate around 2 wt% of iron in the impregnated material. The solvent was evaporated to dryness under constant stirring (80 °C) and the obtained solid was dried and then calcined at 550 °C. Table 14.2 summarises the textural properties obtained from N<sub>2</sub> adsorption/desorption measurements and in this case a Si-PPH with a much higher BET surface area was obtained. As mentioned before, the impregnation process tends to decrease the surface area and pore volume, whereas a slight increase in average pore diameter is observed. However, the

**Table 14.2** Textural properties of Si-PPH and Fe/Si-PPH materials determined from N<sub>2</sub> adsorption/desorption isotherms at 77 K

Sample	$S_{\text{BET}}$ (m <sup>2</sup> /g)	$V_{\text{pore}}$ (cm <sup>3</sup> /g)	Average pore diameter (nm)
Si-PPH	772	1.041	3.5
Fe-PPH (H <sub>2</sub> O)	428	0.633	4.0
Fe-PPH (ethanol)	482	0.650	3.7

isotherm shape (see Fig. 14.5) and X-ray diffractogram at low angle confirm that the porous framework is maintained despite the incorporation of Fe. Table 14.3 brings atomic concentrations for the various elements detected on the material surface. Iron may be found in very small concentration on the surface; however, the mass concentration as determined by ICP reveals that most of the iron is present in the bulk of the material, rather than on the surface. This is particularly true for the impregnation carried out in aqueous solution. Nevertheless, in both cases, incorporation of iron into the bulk material was about the same for both impregnation procedures and reached around 85% of the intended metal concentration (2 wt%).

**Fig. 14.5** Nitrogen adsorption/desorption isotherms at 77 K for Si-PPH (a) and Fe/Si-PPH impregnated from ethanolic (b) and aqueous (c) ferric nitrate solutions**Table 14.3** Atomic concentrations of Si-PPH and Fe/Si-PPH materials determined from XPS

Sample	O	Si	Fe	P	Zr
Si-PPH	68.1	25.7	–	4.2	2.0
Fe/Si-PPH (impregnated in H <sub>2</sub> O)	66.9	26.4	0.2 (0.5) <sup>a</sup> (1.7) <sup>b</sup>	4.4	2.1
Fe/Si-PPH (impregnated in EtOH)	67.6	25.7	0.4 (1.04) <sup>a</sup> (1.7) <sup>b</sup>	4.2	2.1

<sup>a</sup>Mass concentration converted from XPS atomic concentration

<sup>b</sup>Mass concentration as determined from ICP-OES

XPS analysis reveals that iron is present on the surface as Fe(III), very likely as ferric oxide. The XRD at low angle reveals that the incorporation of iron from aqueous solution does not change significantly the broad peak observed at around  $2\theta = 2^\circ$ , which is characteristic of the mesoporous arrangement and formation of silica galleries. However, for the material impregnated from ethanolic solution, this peak is nearly indistinguishable. These materials have been tested for the adsorption of benzothiophene in order to estimate their potential as selective adsorption of refractory sulphur cyclic compounds from hydrotreated naphtha streams. The adsorption isotherm of benzothiophene from solution (in hexane) is shown in Fig. 14.6, together with other inorganic adsorbents. Adsorption capacity is comparable to other mesoporous materials proposed in the literature [35]. Infrared spectra of Fe/Si-PPH submitted to benzothiophene vapours at  $25^\circ\text{C}$  were recorded in order to investigate the type of interaction of these materials with BT upon adsorption. Before passing BT vapours over the sample, the adsorbent was activated in situ at  $350^\circ\text{C}$  under He flow for 1 h. Each of the curves shown in Fig. 14.7 represents the measured spectrum at a given contact time subtracted from the spectrum of the clean sample. Increasing absorbance peaks may be observed at the following regions:  $3750$ ,  $1670$  and  $1530\text{ cm}^{-1}$ . In the first region, around  $3750\text{ cm}^{-1}$ , the absorbance peaks may be assigned to stretching vibrations of terminal silanol groups, which may indicate that either the sulphur atom or the cyclic thiophenic ring interacts with terminal hydroxyl groups, as suggested by Gutierrez-Alejandre et al. [36]. At  $1670\text{ cm}^{-1}$ , absorbance peaks may be due to stretching vibrations of the C=O bond, possibly as a result of interactions between carbon atoms in the thiophenic ring and oxygen atoms from the adsorbent structure. The peak around  $1530\text{ cm}^{-1}$  is generally correlated to stretching vibrations of C=C bonds present in aromatic molecules. The increasing intensity of this peak without changes in position and shape suggests that BT is adsorbed without aromatic ring opening.

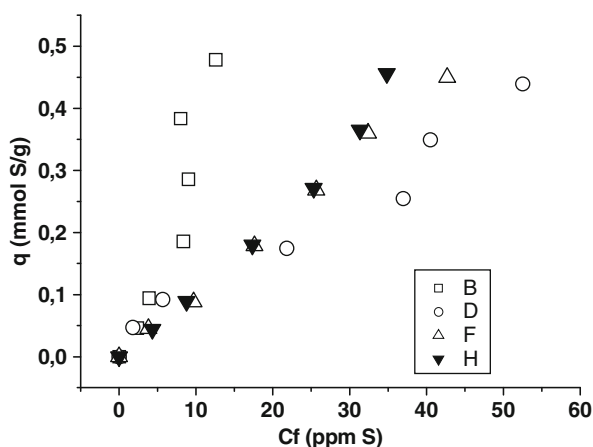


**Fig. 14.6** Adsorption isotherm of benzothiophene from solution (hexane) at  $25^\circ\text{C}$  for Si-PPH as compared to other mesoporous inorganic solids

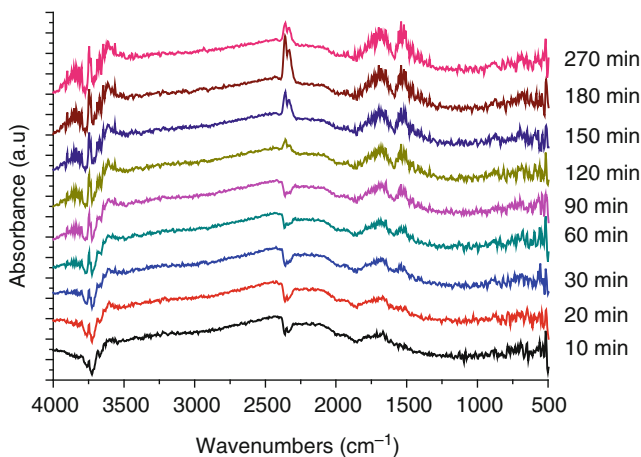


**Fig. 14.7** FTIR spectra for increasing contact time of Fe/Si-PPH with benzothiophene vapours at 25°C. Each spectrum is the result of the subtraction of the measured spectrum from that obtained with the clean and activated sample

Finally, several materials such as PPH with Cu [37], Ru [38] and V [39] were prepared by wet impregnation. These new materials are mainly synthesised to be used as catalysts, and their performance will be described in the next section.

## 14.6 Applications in Catalysis and Adsorption of Si-PPH

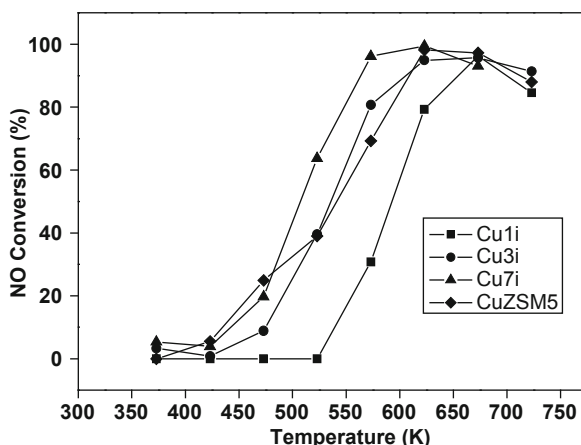
As mentioned previously, this porous phosphate heterostructure may be considered as a layered material, synthesised using a variation of the synthesis procedure typical of MCM-41 materials. This solid presents high thermal stability, surface area and acidity, which is appropriate to disperse an active phase or to be used directly in acid reactions. In the literature there are numerous papers published on applications of layered materials (clays, hydrotalcites, PILCs) in catalysis. Thus, one of the first examined applications of PPH was in the selective catalytic reduction (SCR) of NO<sub>x</sub> [37], hydrotreating processes [38] and selective oxidation of H<sub>2</sub>S to sulphur [30, 39], to avoid (or decrease) NO<sub>x</sub> emissions to the atmosphere from stationary or mobile sources or to treat hydrogen sulphide (H<sub>2</sub>S) emissions originated from petroleum refineries and gas plants. These are three of the most significant catalytic reactions with considerable environmental impact. Other application fields were the separation of propane and propene [34] and in electrochemistry [33].

Over recent years an amazing increase in the number of vehicles equipped with diesel engines has taken place in Europe. Among the disadvantages of these engines are the emissions of nitrogen oxides (NO<sub>x</sub>) and particulate matter. The current and future European legislation for the control of NO<sub>x</sub> emissions from heavy-duty vehicles foresees the obligatory treatment of exhaust gases in order to reduce the emissions of NO<sub>x</sub> to pre-established levels. The EURO V regulations took effect

in 2008 and have obliged a decrease in  $\text{NO}_x$  emissions from the previous level of 3.5 down to 2 g kW/h. At present, the urea-SCR process is considered to be the most promising way to decrease  $\text{NO}_x$  emissions produced by heavy-duty vehicles, especially trucks. Companies such as Siemens and MAN have developed catalytic systems employing urea as a reductor for these vehicles. The disadvantages of ammonia are avoided by using urea since the latter is non toxic, widely used in agriculture as a fertiliser and it is utilised in solution.

Within this context, Cu-PPH (1, 3 and 7 wt% of Cu) catalysts were prepared by the impregnation method and tested in the selective catalytic reduction of NO with ammonia as active catalysts for the control of the  $\text{NO}_x$  emissions from heavy-duty vehicles. At present, the Cu-zeolite catalysts are some of the most commonly studied materials for their role as active catalysts in the SCR of NO using ammonia or hydrocarbons as reducing agents. Therefore, a CuZSM5 (Si/Al ratio of 20) catalyst was prepared as a reference catalyst.

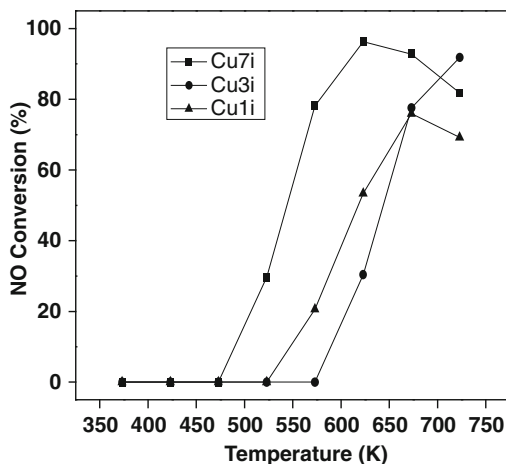
**Fig. 14.8** NO conversion as a function of the reaction temperature for the Cu $_x$ i and CuZSM5 catalysts. Experimental conditions: NO (1000 ppm),  $\text{NH}_3$  (1000 ppm),  $\text{O}_2$  (2.5 vol%); total flow 150 ml/min. Reproduced from [37], with permission from Elsevier



These catalysts are highly active, achieving 100% of NO conversion in some cases. Interestingly, with only 1 wt% Cu, this Cu1i catalyst reached 96% of NO conversion at 673 K and a higher metal loading had a minor effect on NO conversion (see Fig. 14.8). This fact points out that very active copper species are present over CuPPH catalysts. On the other hand, the Cu7i and Cu3i catalysts are more active than CuZSM5 catalyst at lower temperatures. The pristine Si-PPH support shows no catalytic activity over the entire range of temperatures assayed, meaning that the activity is due to the presence of copper as CuO particles or  $\text{Cu}^{2+}$  ions associated with surface oxygen. This fact implies that the presence of acid sites (Brønsted or Lewis) on the support is not enough to promote SCR of NO with  $\text{NH}_3$  over these catalysts.

For SCR technology, it is necessary to know the behaviour of the catalysts when  $\text{H}_2\text{O}$  is present in the feed because water is a by-product of the SCR reaction. Water accounts for up to 18% of the exhaust gas volume in diesel engines, therefore the

**Fig. 14.9** NO conversion as a function of the reaction temperature for the Cu<sub>7</sub>i and CuZSM5 catalysts in the presence of 14 vol% H<sub>2</sub>O. Experimental conditions were the same as reported in Fig. 14.8. Reproduced from [37], with permission from Elsevier



catalysts must not suffer any deactivation in the presence of water in the feed. Figure 14.9 shows the catalytic results when 14% (v/v) of H<sub>2</sub>O is added to the feed. In general a slight decrease in NO conversion is observed, although the NO conversion still reaches values above 92%, whilst maintaining excellent catalytic activity. This effect is reversible, with the initial activity being resumed when water is removed from the feed.

In addition to the effect of water on the catalytic behaviour of these copper catalysts, the effect of the presence of SO<sub>2</sub> has also been studied, since SO<sub>2</sub> is also present in diesel engine exhaust gases. The current SO<sub>2</sub> concentration in gases emitted by diesel engines ranges around 15 ppm. Nevertheless, more severe conditions have been applied in order to simulate the poisoning of the catalysts with this substance. Figure 14.10 shows the main catalytic results when 100 ppm of SO<sub>2</sub> is added to the feed. In general, a smooth reduction in activity is observed for all catalysts, this reduction being larger for catalysts with lower copper loading. The maximum activity temperatures are also observed to rise. The Cu-PPH catalysts show an increase of N<sub>2</sub>O production. Moreover, XPS results revealed no presence of sulphated species on the catalysts, which could lead to deactivation. The catalysts can be shaped as monoliths using Metocell, demonstrating the ease with which these catalysts can be moulded.

The application of current and future environmental legislations concerning exhaust emissions in the European Union implies the use of cleaner diesel fuels to avoid high particle emissions. The main focus of the legislation is on the reduction of polyaromatic hydrocarbons and sulphur content as well as an increase in the cetane number of diesel. These types of emissions are mainly related to the aromatic content of fuels [40] which on combustion produce particulate matter in the size range between 0.08 and 1 μm. They are breathable and have a significant health impact. On the other hand, the increased demand of diesel in the European Union has led to the use of fuels which are derived from the fractions of light cycle oil



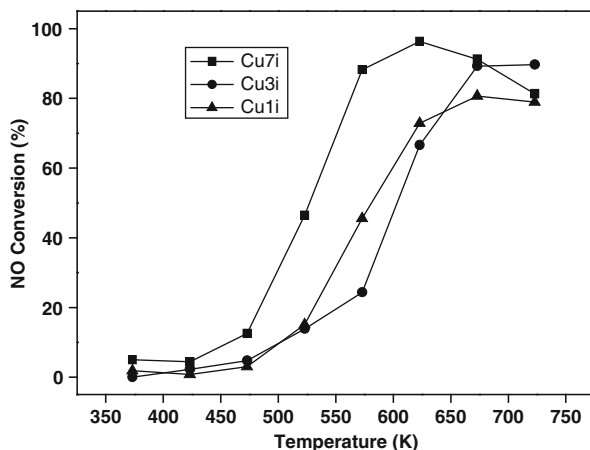


**Fig. 14.10** NO conversion as a function of the reaction temperature for the  $\text{Cu}_x\text{i}$  catalysts in the presence of 100 ppm  $\text{SO}_2$ . Experimental conditions were the same as reported in Fig. 14.8. Reproduced from [37], with permission from Elsevier

(LCO) produced in fluid catalytic cracking (FCC) plants [41]. The improvement of the LCO fractions may be achieved by (i) reducing the aromatic content, which also increases the cetane number; (ii) decreasing the sulphur content and (iii) increasing the cetane number with hydrogenolysis/hydrocracking reactions.

Regarding this issue, PPH materials could be adequate candidates to be used as support for active phases in hydrotreating processes. Mesoporous phosphate heterostructure (PPH) materials have been used as supports of ruthenium catalysts with a 5 wt% metal content (RuPPH) [38]. A pristine support (SiPPH) was used, as well as a potassium-exchanged material (denoted as KSiPPH), which was prepared by cation exchange of the pristine support to reduce its original acidity by 20%. Ruthenium supported on both SiPPH and KSiPPH was obtained by incipient wetness impregnation method using an aqueous solution of ruthenium(III) chloride and reduction at 400 °C without previous calcinations.

Both catalysts (RuPPH and KRuPPH) were tested in the hydrogenation and hydrogenolysis/hydrocracking of tetralin under high hydrogen pressure in the temperature range of 240–375 °C. This reaction was chosen as a model reaction to evaluate the catalytic performance of this family of supported ruthenium catalysts in the hydrogenation of aromatic hydrocarbons. The conversion of tetralin and the yields of the different reaction products obtained with both catalysts are shown in Fig. 14.11. They show a similar catalytic performance, although the RuSiPPH catalyst displays better activity at 350 °C, presenting 95% steady-state conversion and a very good balance between yields of hydrogenation (55%) and hydrogenolysis/hydrocracking products (28%). Considering the influence of the reaction temperature on selectivity towards the different reaction products, the formation of hydrogenation products is favoured at low temperatures due to the exothermic

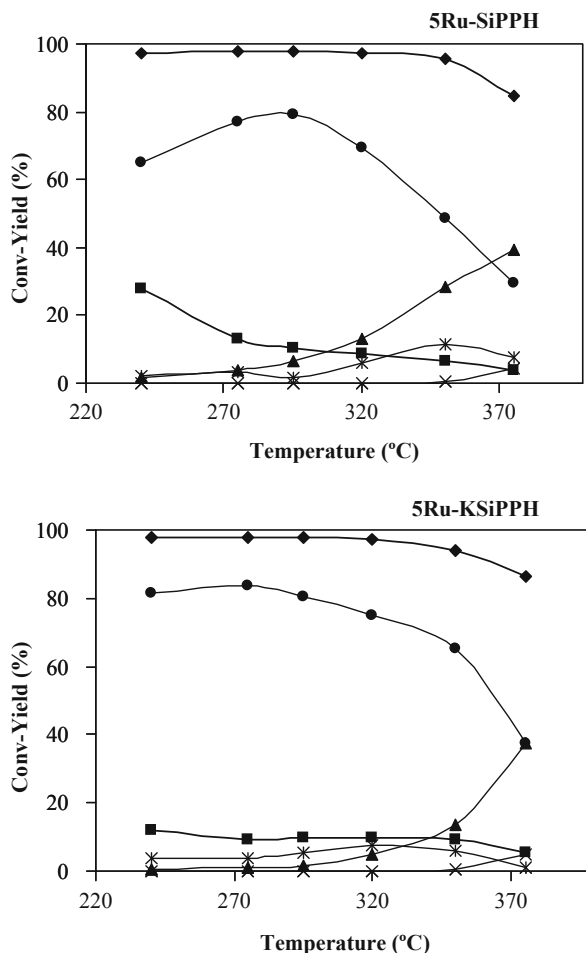
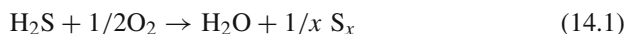


**Fig. 14.11** Evolution of the conversion of tetralin hydrogenation and hydrogenolysis/hydrocracking and yield of the different reaction products as a function of the reaction temperature on ruthenium catalysts: (◆) conversion, (●) *trans*-decalin, (■) *cis*-decalin, (▲) HCC, (×) naphthalene and (\*) VC. Experimental conditions:  $H_2/THN$  molar ratio = 10.1,  $P(H_2) = 4.5$  MPa,  $P(N_2) = 1.5$  MPa, LHSV =  $6\text{ h}^{-1}$ ; GHSV =  $1300\text{ h}^{-1}$ ; contact time = 2.8 s. Reproduced with permission from Elsevier

character of the hydrogenation reaction. In fact, the yield of hydrogenation products (*trans*- and *cis*-decalins) decreases from 93% at 240 °C to 33% at 375 °C for the RuPPH catalysts and from 93% at 240 °C to 43% for the RuKPPH catalysts. It is clear that hydrogenation reactions take place on metal particles and, since both catalysts have the same metal content, the hydrogenation performance is similar. The *trans*- to *cis*-decalin ratio is also very high for both catalysts over the complete range of temperatures studied. The thermodynamics associated with the catalytic

process favours the formation of *trans*-decalins, which means that the hydrogenation process is governed by thermodynamic equilibrium. However, the decrease in the formation of decalins at higher reaction temperatures could be due to their conversion into HHC (hydrocracking) products. These reactions are favoured at higher temperatures owing to the endothermic character of the reactions involving the C–C bond cleavage. The hydrocracking reaction requires bifunctional catalysts consisting of a dispersed metal, where hydrogen molecules are activated, with acid sites in the vicinity, where the tetralin molecules are retained and where H<sub>2</sub> is spilled over from the metallic centres. This fact is noticeable at 350°C when the RuPPH catalyst, with greater acidity and higher metallic dispersion, gives a HHC product yield of 28.4%, whilst the RuPPH catalyst gives a HHC product yield of only 13.3%. The formation of naphthalene as dehydrogenation product is very low for both catalysts. In addition, the thiotolerance of the best catalyst was assessed with a feed containing dibenzothiophene (DBT), a sulphur-containing molecule, at concentrations of 300 and 600 ppm. This catalyst shows an excellent performance with 300 ppm of DBT after 6 h on stream.

Current stringent environmental regulations oblige to treat hydrogen sulphide (H<sub>2</sub>S) emissions from petroleum refineries and gas plants. Claus and SuperClaus processes are the most commonly used but, due to thermodynamic limitations, a relevant percentage of H<sub>2</sub>S is not converted to sulphur in the Claus process, and high concentrations of H<sub>2</sub>S (2% vol) cannot be treated with the SuperClaus technology [42]. The selective oxidation of hydrogen sulphide by using oxygen from air is necessary [42, 43] to avoid the formation of SO<sub>2</sub> according to reaction (14.1):



Supported vanadium oxides using supports such as alumina or titania have been recently reported as catalysts for this oxidative process [44–46]. This is because vanadium-based catalysts are active and selective for the oxidation of H<sub>2</sub>S to sulphur at relatively low temperatures [45, 46]. The nature of the vanadium species and the characteristics of the metal oxide support influence the catalytic performance of vanadium-containing catalysts. New catalytic systems for this oxidative process with high activity and stability at moderate temperatures and resistant to sulphidation with low selectivity to the formation of SO<sub>2</sub> are required. Following this reasoning, PPH materials containing structural vanadium oxide have been proposed. Solids with vanadium incorporated into the silica galleries have been synthesised using similar procedures as described previously. The Si/V molar ratio ranged between 5 and 25. Additionally, a material without silica galleries was synthesised using water or *n*-propanol as solvent so as to test the effect of the synthesis medium.

Figure 14.12 shows the variation of the H<sub>2</sub>S conversion with time on stream (TOS) achieved over V-containing catalysts at 200°C. It may be seen that the conversion of H<sub>2</sub>S increases with the vanadium content. In addition, relatively fast catalyst decay is observed for samples prepared in *n*-propanol with Si/V ratios between 25 and 5, whereas the loss of H<sub>2</sub>S conversion with the time on stream is very low in

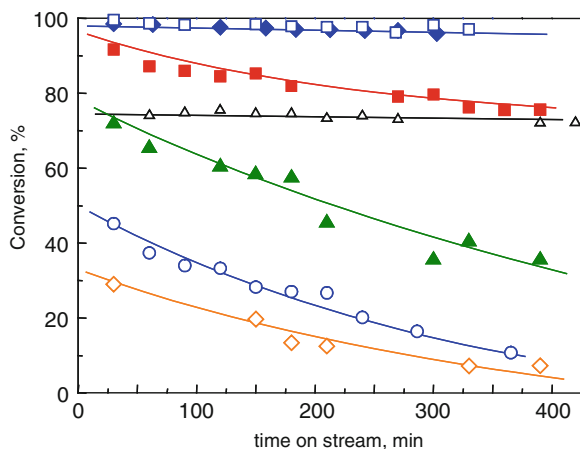


**Fig. 14.12** Variation of the H<sub>2</sub>S conversion with the time on stream (TOS) obtained over MZP-supported vanadium oxide catalysts. Reaction conditions: 0.1 g of catalyst; total flow of 130 ml/min; H<sub>2</sub>S/air/He molar ratio of 1.2/5.0/93.8 (i.e. H<sub>2</sub>S/O<sub>2</sub> ratio of 1/0.9); W/F = 31.2 g<sub>cat</sub>/h/mol<sub>H<sub>2</sub>S</sub>. Symbols: (◇) 0 V-MZP; (●) 2 V-MZP; (▲) 4 V-MZP; (■) 8 V-MZP; (□) 12 V-MZP; (◆) 16 V-MZP; V<sub>2</sub>O<sub>5</sub> (Δ). Reproduced with permission from Elsevier

samples with lower Si/V ratio. This way, the H<sub>2</sub>S conversion decreases from ~95% (at TOS of 5 min) to ~87% (at TOS of 800 min). According to these results, it can be concluded that both the catalytic activity and the catalyst stability are favoured on catalysts having V<sub>2</sub>O<sub>5</sub> crystallites. A similar conclusion may be drawn from the catalytic results obtained over Vw-PPH and NT-PPH catalysts, although this depends on the accessible V sites.

On the other hand, the selectivity towards sulphur of ~99% is observed in all catalysts. However, note that SO<sub>2</sub> (with selectivities lower than 3%) is observed in the first minutes of the reaction. This is in agreement with previous results in which V-containing materials have been proposed as active and selective catalysts for the partial oxidation of H<sub>2</sub>S to elemental sulphur.

The separation of olefin/paraffin mixtures is a subject of current interest, and several types of zeolites (NaX, ZSM-5) exchanged with Co(II), Cu(II) and Zn(II) have been tested [47, 48]. Other porous solids, such as  $\gamma$ -Al<sub>2</sub>O<sub>3</sub> and SiO<sub>2</sub>, ion-exchanged or impregnated with monovalent cations, proved to be efficient for this separation process [49, 50]. MCM-41 ion exchanged with Cu(II) and Ag(I) [50], mesoporous Cu(II)- and Ag(I)-derivatised aluminosilicate materials [51], mesoporous Ag(I)-impregnated SBA-15 [52] and SBA-15 ion exchanged with Ag(I) and K<sup>+</sup> natural erionite [53] have also been used. In such cases, the idea is the separation of propylene/propane mixtures via  $\pi$ -complexation.

In addition to the adsorption of benzothiophene reported above, an interesting potential application of PPH solids is the separation of gases. Recently, the adsorbents Cu<sup>+</sup>-PPH and Cu<sup>2+</sup>-PPH were prepared starting from a silica-expanded zirconium phosphate heterostructure (PPH), which was subjected to ion exchange

with Cu(I) and Cu(II) salts [34]. The starting material, SiPPH, presented high acidity and irreversible chemisorption of the olefin, which increased with temperature. Unlike the support, the irreversible adsorption of the olefin on the  $\text{Cu}^+$ -PPH and  $\text{Cu}^{2+}$ -PPH samples decreases with increasing temperature and disappears at 393 K, showing a very high selectivity towards propylene. The  $\text{C}_3\text{H}_8$  adsorption in all the samples was always reversible. On the basis of the results of this study, both  $\text{Cu}^+$ -PPH and  $\text{Cu}^{2+}$ -PPH samples can be efficiently applied in the separation of a  $\text{C}_3\text{H}_6/\text{C}_3\text{H}_8$  mixture at 393 K.  $\text{Cu}^+$ -PPH would have the highest efficiency, because its capacity for  $\text{C}_3\text{H}_6$  adsorption was higher than that for the  $\text{Cu}^{2+}$ -PPH sample.

Adsorption equilibrium and kinetic measurements of pure  $\text{C}_3\text{H}_6$  and  $\text{C}_3\text{H}_8$  in the three samples have been performed at different temperatures in the range between 273 and 393 K. A marked influence of Cu cations on the adsorption behaviour of the olefin was established. It was also established that the adsorption process of propylene in the support occurs by a mechanism similar to that of chemisorption, leading to a polymerisation reaction at 423 K. This is attributable to the high acidity of the adsorbent. Unlike the support, the irreversible adsorption of the olefin on the samples with Cu decreases with increasing temperature and disappears at 393 K, showing a high selectivity towards propylene.

**Acknowledgements** The authors gratefully acknowledge financial support from CICYT, Spain (NAN20004-09267-C01 and NAN2004-09267-C03-02). MDS thanks a fellowship from the Universidad Politécnica de Valencia. D.C.S. RMT would like to thank the Ministry of Science and Innovation (Spain) for the financial support under the Program Ramón y Cajal (RYC-2008-03387). Azevedo thanks CAPES, Brazil, for sponsoring a grant (1145/08-8) for visiting professor at UMA, Spain. AIM would like to thank the Ministry of Science and Innovation (Spain) for the financial support under the Program Juan de la Cierva (JCI-2009-05821).

## References

1. Voge HH (1983) In: David BH, Hettinger WP (eds) Heterogeneous catalysis, selected American histories, ACS symposium series, no. 222. American Chemical Society, Washington, DC, p 235
2. Swift HE (1977) In: Burton JT, Garten RL (eds) Advanced material in catalysis. Academic, New York, NY, p 209
3. Occelli ML, Rennard RJ (1988) Hydrotreating catalysts containing pillared clays. *Catal Today* 2:309
4. Csicsery SM (1984) Shape-selective catalysis in zeolites. *Zeolites* 4:202
5. Laszlo P (1986) Catalysis of organic reactions by inorganic solids. *Acc Chem Res* 19:121
6. Delaude L, Laszlo P, Smith K (1993) Heightened selectivity in aromatic nitrations and chlorinations by the use of solid supports and catalysts. *Acc Chem Res* 26:607
7. Vaughan DEW (1988) Pillared clays – a historical perspective. *Catal Today* 2:187
8. Vaughan DEW, Maher PK, Albers EW (1974) US Patent 3,838,037
9. Parthasarthy R, Vaughan DEW (1974) British Patent 1,483,466
10. Flessner U, Jones DJ, Rozière J Zajac J, Storaro L, Lenarda M Pavan M, Jiménez-López A, Rodríguez-Castellón E, Trombetta M, Busca G (2001) A study of the surface acidity of acid-treated montmorillonite clay catalysts. *J Mol Catal A* 168:247
11. Narayanan BN Sugunan S (2006) Selective formation of cumene on pillared clays by isopropylation of benzene. *React Kinet Catal Lett* 89:45

12. Storaro L, Ganzerla R, Lenarda M, Zanoni R, Jiménez López A, Olivera-Pastor P, Rodríguez Castellón E (1997) Catalytic behavior of chromia and chromium-doped alumina pillared clay materials for the vapor phase deep oxidation of chlorinated hydrocarbons. *J Mol Catal A* 115:329
13. Storaro L, Ganzerla R, Lenarda M, Zanoni R (1995) Vapour phase deep oxidation of chlorinated hydrocarbons catalyzed by pillared bentonites. *J Mol Catal A* 97:139
14. Mitchell IV (ed) (1990) Pillared layered structures: current trends and applications. Elsevier, London
15. Jiménez-López A, Maza-Rodríguez J, Rodríguez-Castellón E, Olivera-Pastor P (1996) Mixed alumina chromia pillared layered  $\alpha$ -zirconium phosphate materials: acidity and catalytic behaviour for isopropyl alcohol decomposition. *J Mol Catal A* 108:175
16. Pérez-Reina FJ, Rodríguez-Castellón E, Jiménez-López A (1999) Dehydrogenation of propane over chromia-pillared zirconium phosphate catalysts. *Langmuir* 15:8421
17. Mérida-Robles J, Olivera-Pastor P, Rodríguez-Castellón E, Jiménez-López A (1997) Fluorinated alumina pillared  $\alpha$ -zirconium phosphates as supports for metallic nickel catalysts. *J Catal* 169:317
18. Mérida-Robles J, Rodríguez-Castellón E, Jiménez-López A (1999) Characterization of Ni, Mo and Ni–Mo catalysts supported on alumina-pillared  $\alpha$ -zirconium phosphate and reactivity for the thiophene HDS reaction. *J Mol Catal A* 145:169
19. Kresge CT, Leonowicz ME, Roth WJ, Vartuli JC, Beck JS (1992) Ordered mesoporous molecular sieves synthesized by a liquid-crystal template mechanism. *Nature* 359:710
20. (a) Corma A (1997) From microporous to mesoporous molecular sieve materials and their use in catalysis. *Chem Rev* 97:2373; (b) Ciesla U, Schüth F (1999) Ordered mesoporous materials. *Micropor Mesopor Mater* 27:131
21. Galarneau A, Barodawalla A, Pinnavaia TJ (1995) Porous clay heterostructures formed by gallery-templated synthesis. *Nature* 374:529
22. Jiménez-Jiménez J, Maireles-Torres P, Olivera-Pastor P, Rodríguez-Castellón E, Jiménez-López A (1997) Sol–Gel synthesis of dodecyltrimethylammonium-expanded zirconium phosphate and its application to the preparation of acidic porous oligomeric gallium(III)-exchanged materials. *Langmuir* 13:2857
23. Jiménez-Jiménez J, Rubio-Alonso M, Eliche Quesada D, Rodríguez-Castellón E, Jiménez-López A (2005) Synthesis and characterisation of acid mesoporous phosphate heterostructure (PPH) materials. *J Mater Chem* 15:3466
24. Jones DJ, Jiménez-Jiménez J, Jiménez-López A, Maireles-Torres P, Olivera-Pastor P, Rodríguez-Castellón E, Rozière J (1997) Surface characterisation of zirconium-doped mesoporous silica. *Chem Commun* 431
25. Corma A, Navarro MT, Pérez-Pariente J (1994) Synthesis of an ultralarge pore titanium silicate isomorphous to MCM-41 and its application as a catalyst for selective oxidation of hydrocarbons. *J Chem Soc Chem Commun* 147
26. Rodríguez-Castellón E, Jiménez-López A, Maireles-Torres P, Jones DJ, Rozière J, Trombetta M, Lenarda M, Storaro L (2003) Textural and structural properties and surface acidity characterization of mesoporous silica-zirconia molecular sieves. *J Solid State Chem* 175:159
27. Eliche-Quesada D, Mérida-Robles JM, Rodríguez-Castellón E, Jiménez-López A (2005) Ru, Os and Ru–Os supported on mesoporous silica doped with zirconium as mild thio-tolerant catalysts in the hydrogenation and hydrogenolysis/hydrocracking of tetralin. *Appl Catal A* 279:209
28. Cagnoli MV, Casuscelli SG, Alvarez AM, Bengoa JF, Gallegos NG, Samaniego NM, Crivello ME, Ghione GE, Pérez CF, Herrero ER, Marchetti SG (2005) “Clean” limonene epoxidation using Ti-MCM-41 catalyst. *Appl Catal A* 287:227
29. Jiménez-Jiménez J, Rubio-Alonso M, Eliche-Quesada D, Rodríguez Castellón E, Jiménez-López A (2006) Synthesis and characterization of mixed silica/zirconia and silica/titania porous phosphate heterostructures (PPH). *J Phys Chem Solids* 67:1007

30. Soriano MD, Jiménez-Jiménez J, Concepción P, Jiménez-López A, Rodríguez-Castellón E, López Nieto JM (2010) Vanadium oxide-porous phosphate heterostructure catalysts for the selective oxidation of H<sub>2</sub>S to sulphur. *Solid State Sci* 12:996
31. Alov N, Kutsko D, Spirovová I, Bastl Z (2006) XPS study of vanadium surface oxidation by oxygen ion bombardment. *Surf Sci* 600:1628
32. Wachs IE, Deo G, Wenchuysen B, Andreini MA, Vuurman MA, De Boer M, Amiridis MD (1996) Selective catalytic reduction of NO with NH<sub>3</sub> over supported vanadia catalysts. *J Catal* 161:211
33. Piazuelo R, Rodríguez-Castellón E, Jiménez-Jiménez J, Jiménez-López A, Benavente J (2008) Chemical surface and electrochemical characterization of zirconium phosphate heterostructures. *Micropor Mesopor Mater* 115:23
34. Aguilar-Armenta G, Patino-Iglesias ME, Jiménez-Jiménez J, Rodríguez-Castellón E, Jiménez-López A (2006) Application of porous phosphate heterostructure materials for gas separation. *Langmuir* 22:1260
35. Wang Y, Yang RT, Heinzel JM (2008) Desulfurization of jet fuel by  $\pi$ -complexation adsorption with metal halides supported on MCM-41 and SBA-15 mesoporous materials. *Chem Eng Sci* 63:356
36. Gutierrez-Alejandre A, Larrubia MA, Ramirez J, Busca G (2006) FT-IR evidence of the interaction of benzothiophene with the hydroxyl groups of H-MFI and H-MOR zeolites. *Vibr Spectr* 41:42
37. Moreno-Tost R, Oliveira ML, Eliche-Quesada D, Jiménez-Jiménez J, Jiménez-López A, Rodríguez-Castellón E (2008) Evaluation of Cu-PPHs as active catalysts for the SCR process to control NOx emissions from heavy duty diesel vehicles. *Chemosphere* 72:608
38. Eliche-Quesada D, Macías-Ortiz MI, Jiménez-Jiménez J, Rodríguez-Castellón E, Jiménez-López A (2006) Catalysts based on Ru/mesoporous phosphate heterostructures (PPH) for hydrotreating of aromatic hydrocarbons. *J Mol Catal A* 255:41
39. Soriano MD, Jiménez-Jiménez J, Concepción P, Jiménez-López A, Rodríguez-Castellón E, López Nieto JM (2009) Selective oxidation of H<sub>2</sub>S to sulfur over vanadia supported on mesoporous zirconium phosphate heterostructure. *Appl Catal B Environ* 92:271
40. Karonis D, Lois E, Stournas S, Zannikos F (1998) Correlations of exhaust emissions from a diesel engine with diesel fuel properties. *Energy Fuels* 12:230
41. Cooper BH, Donniss BBL (1996) Aromatic saturation of distillates: an overview. *Appl Catal A* 137:203
42. Pieplu A, Saur O, Lavalley JC (1998) Claus catalysis and H<sub>2</sub>S selective oxidation. *Catal Rev Sci Eng* 40:409
43. Uhm JH, Shin MY, Zhidong J, Chung JS (1999) Selective oxidation of H<sub>2</sub>S to elemental sulfur over chromium oxide catalysts. *Appl Catal B* 22:293; Yasyerly S, Dogu G, Dogu T (2006) Selective oxidation of H<sub>2</sub>S to elemental sulfur over Ce-V mixed oxide and CeO<sub>2</sub> catalysts prepared by the complexation technique. *Catal Today* 117:271
44. Bineesh KV, Cho DR, Kim SY, Jermy BR, Park DW (2008) Vanadia-doped titania-pillared montmorillonite clay for the selective catalytic oxidation of H<sub>2</sub>S. *Catal Commun* 9:2040
45. Li KT, Huang CH (2006) Selective oxidation of hydrogen sulfide to sulfur over LaVO<sub>4</sub> catalyst: promotional effect of antimony oxide addition. *Ind Eng Chem Res* 45:7096
46. Park DW, Byung BH, Ju WD, Kim MI, Kim KH, Woo HC (2005) Selective oxidation of hydrogen sulfide containing excess water and ammonia over Bi-V-Sb-O catalysts. *Korean J Chem Eng* 22:190
47. Corma A, Rey F, Rius J, Sabater MJ, Valencia S (2004) Supramolecular self-assembled molecules as organic directing agent for synthesis of zeolites. *Nature* 431:287
48. Khelifa A, Derriche Z, Bengueddach A (1999) Adsorption of propene on NaX zeolite exchanged with Zn<sup>2+</sup> and Cu<sup>2+</sup>. *Appl Catal A* 178:61
49. Masuda T, Okubo Y, Mukai SR, Kawase M, Hashimoto K, Shichi A, Satsuma A, Hattori T, Kiyozumi Y (2001) Effective diffusivities of lighter hydrocarbons in Cu- and Co-MFI-type zeolite catalysts. *Chem Eng Sci* 56:889

50. Blas FJ, Vega LF, Gubbins KE (1998) Modeling new adsorbents for ethylene/ethane separations by adsorption via  $\pi$ -complexation. *Fluid Phase Equilib* 150–151:117
51. Kargol M, Zajac J, Jones DJ, Steriotis Th, Rozière J, Vitse P (2004) Porous silica materials derivatized with Cu and Ag cations for selective propene–propane adsorption from the gas phase: aluminosilicate ion-exchanged monoliths. *Chem Mater* 16:3911
52. Grande C, Araújo JDP, Cavenati S, Firpo N, Basaldella E, Rodrigues AE (2004) New  $\pi$ -complexation adsorbents for propane–propylene separation. *Langmuir* 20:5291
53. Aguliar-Armenta G, Patino-Iglesias ME (2002) Adsorption equilibria and kinetics of propylene and propane on natural erionite and on erionite exchanged with  $K^+$  and  $Ag^+$ . *Langmuir* 18:7456



# Chapter 15

## Recent Advances in the Preparation and Application of Mesoporous Aluminophosphate-Based Materials

Kathleen O'Malley, Wiebke Reimann, and Teresa Curtin

**Abstract** The synthesis of aluminophosphates has significantly advanced in recent years and in particular the synthesis of mesoporous aluminophosphate. This chapter reviews this advancement and outlines progress in the synthesis of metal-containing mesoporous aluminophosphates and the advances in the applications of these solids particularly in the area of catalysis.

**Keywords** Aluminophosphate · Mesoporous · Synthesis · Catalysis

### 15.1 Introduction

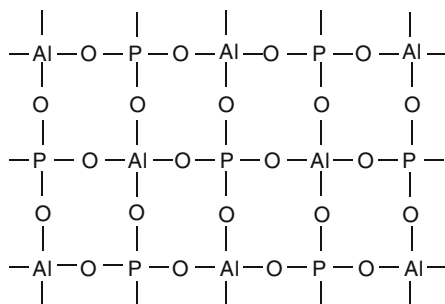
Microporous aluminophosphates, of pore size typically less than 1.2 nm, were first reported by Wilson et al. [1]. The structure consisted of alternating tetrahedral  $\text{AlO}_4$  and  $\text{PO}_4$  connected by shared oxygen atoms. Indeed, the Al–O–P bond structure of these solids, as presented in Fig. 15.1, was a significant departure from the corresponding Si–O–Si and Si–O–Al bonds of silicates and aluminosilicates, respectively. This represented a major development in terms of producing a non-silica-based microporous solid and subsequently opened up a vast body of research particularly in the area of catalysis and adsorption [2]. The main difficulty encountered during the synthesis of these non-silica-based solids was the ordered organisation of two different units (Al and P) on the surface of surfactant assemblies, without the formation of the single oxides. A further key development in the area was the successful synthesis of mesoporous aluminophosphates (AlPOs) [3–6] with pores in the range of 1.8–4 nm. The larger pores facilitate catalytic reactions or adsorption of larger molecules and also alleviate diffusion problems. Long-chained cationic *n*-alkyl trimethylammonium surfactants were primarily used as templates to

---

T. Curtin (✉)

Department of Chemical and Environmental Sciences, Materials and Surface Science Institute, SFI-SRC in Solar Energy Materials, University of Limerick, Limerick, Ireland  
e-mail: teresa.curtin@ul.ie

**Fig. 15.1** Schematic of an aluminophosphate



synthesise these mesoporous aluminophosphates [3, 7]. Other surfactant types have also been used, including *n*-alkylamines [7, 8] and anionic surfactants [9, 10]. In the majority of the earlier reports, these aluminophosphate solids were not particularly stable and the mesoporous structure collapsed when the surfactant was removed.

A number of reviews in this area chart the development of these solids from the initial studies regarding the synthesis of lamellar-type solids and the advancement in procedures for the synthesis of the more applicable non-lamellar mesoporous aluminophosphates [11, 12]. They outline synthetic procedures used to control the structure of the APOs and the difficulties encountered in maintaining the mesostructural ordering of the hexagonal phases following removal of the surfactant. Also included are developments regarding the synthesis of stable mesoporous solids using novel approaches and surfactants [11]. This chapter aims to review more recent progress regarding the synthesis of mesoporous aluminophosphates, developments regarding modification of their physicochemical properties by metal substitution into their framework and the attempts to use them for viable applications particularly in the area of catalysis.

## 15.2 Synthesis

Mesoporous aluminophosphate solids are composed of both  $\text{AlO}_4$  and  $\text{PO}_4$  units and have interesting physicochemical properties particularly for applications in catalysis and adsorption. They are generally prepared under hydrothermal conditions from gels containing sources of aluminium, phosphorous and an organic surfactant. The surfactant can be cationic, anionic or neutral [5, 13]. Overall, the procedure is lengthy and requires careful pH adjustment before hydrothermal treatment. Figure 15.2 outlines the general synthesis procedure. Typically, the aluminium source (e.g. aluminium propoxide) is dissolved in a solvent (i.e. water) and stirred. Then the appropriate amount of orthophosphoric acid is added. This mixture is well mixed before adding the surfactant (typically cetyltrimethylammonium bromide – CTAB). Finally, the tetramethylammonium hydroxide (TMAOH) solution is slowly added until a pH of about 8.5 is attained. The mixture is then stirred for a further 2 h before being transferred into a stainless-steel autoclave where it is placed in

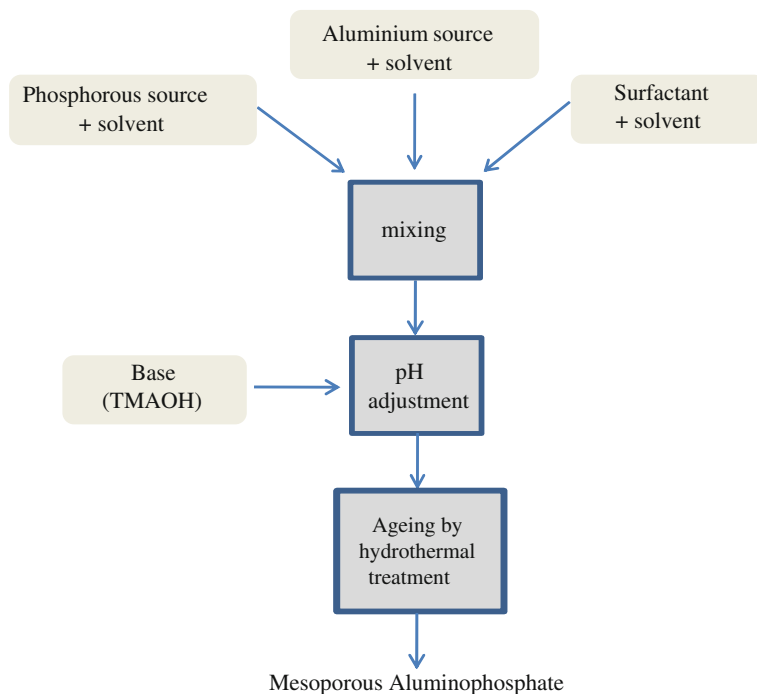


**Fig. 15.2** Preparation of mesoporous aluminophosphate using surfactant

an oven at 70 °C for up to 5 days. The resultant solid is then extensively washed with deionised water and finally with ethanol, and dried at 100 °C. The final step in the procedure involves removal of the surfactant, usually by treatment at high temperature.

### 15.3 Surfactant Removal

Even though a large number of procedures exist that can successfully synthesise mesoporous aluminophosphates, the step involving the removal of the organic structure-directing agent can result in complete collapse of the ordered material. Conventionally, calcination at high temperature is used to remove the surfactant. The negative effect of calcination has been linked to the incomplete condensation in the pore walls of the mesoporous solid during the synthesis procedure [14–16]. A less harsh method of surfactant removal is by solvent extraction. This method of extraction can only be used if the interaction between the surfactant and the solid is not particularly strong. Typical extracting liquids include HCl/methanol [16], *n*-butylamine/ethanol [17, 18], acetic acid/ethanol [19] and sodium acetate/methanol [9].

In general, however, poor stability, compared to the analogous mesoporous silica materials, is a feature of these mesoporous aluminophosphate solids and this consequently has severely limited their potential uses as catalysts and adsorbents. The origin of this instability lies in the synthesis step. The inorganic component is simply not stable enough to maintain its mesostructure following removal of the organic template. To tackle this problem, research has focused on a more complete condensation of the aluminophosphate component within the mesoporous structure therefore yielding a more stable and robust solid. A variety of strategies have been recently employed to do this. Tiemann et al. successfully increased the stability of aluminophosphates using a mild thermal treatment following synthesis. The post-synthesis procedure was carried out at 90 °C in a water vapour atmosphere for 12 h. The treatment was thought to result in a more complete framework condensation therefore improving stability and structural order of the mesoporous solid [16].

A three-stage calcination process was also shown to successfully remove the cetyltrimethylammonium bromide surfactant from a mesoporous aluminophosphate solid [20]. The first stage involved heat treatment at low temperature (140 °C) with the aim of continuing condensation of the inorganic precursors therefore strengthening the pore walls. The second and third heat treatment steps aimed to decompose and remove the surfactant in addition to promoting condensation of hydroxyl groups within the inorganic framework.

## 15.4 Block Copolymers as Surfactants

Block copolymers are made up of blocks of different polymerised monomers. They belong to a family of surfactants used widely in industry in applications such as coatings, detergents and emulsifiers. Block copolymers have been successfully used as templates for the synthesis of ordered large-pore silica and other metal oxides [21]. The synthesis has been successfully adapted to produce ordered mesoporous aluminophosphates, not only improving the thermal stability, but also extending the pore size of the hexagonal or disordered aluminophosphate structure [22].

Figure 15.3 shows the structure of a typical tri-block copolymer used in the preparation of mesoporous solids. This amphiphilic PEO–PPO–PEO or poly(ethylene oxide)–poly(propylene oxide)–poly(ethylene oxide) contains three sequences or blocks of monomers. The first and third blocks have the same chemical nature (hydrophilic) and molecular weight whereby the middle block differs in chemical nature (hydrophobic). During solid synthesis the hydrophobic PPO block clusters together since it is incompatible with the solvent (usually ethanol).

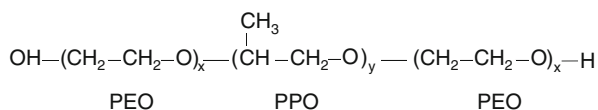


Fig. 15.3 Schematic of a tri-block copolymer

The hydrophilic PEO blocks expand into the surrounding solvent, protecting the hydrophobic micelle interior, and interact with the inorganic component in solution where condensation occurs. In this way the condensation of the inorganic species builds up around the micelle ultimately resulting in the formation of the mesoporous solid. The interaction between the PEO blocks and the inorganic precursors is through hydrogen bonding which is a relatively weak interaction.

In the synthesis of aluminophosphates using block copolymers, the mechanism of formation can be explained by an 'acid–base pair' formation and the solids synthesised present high thermal stability (600–900 °C) [22, 23]. An 'acid' precursor must couple with a 'base' counterpart forming the 'acid–base' pair. The pairs generate proper acidic conditions for the reaction of the inorganic species and are also critical for the development of the homogeneous growth of the overall framework. Therefore, the key to the successful synthesis of this solid is the appropriate choice of Al and P sources. A typical combination of inorganic pairings is  $\text{AlCl}_3$  and  $\text{H}_3\text{PO}_4$ , as these interact readily with each other forming a rigid and stable framework before calcination [24].

Block copolymers Pluronic F68 ( $\text{EO}_{80}\text{PO}_{30}\text{EO}_{80}$ ), Pluronic F127 ( $\text{EO}_{106}\text{PO}_{70}\text{EO}_{106}$ ), Pluronic P123 ( $\text{EO}_{20}\text{PO}_{70}\text{EO}_{20}$ ) and Pluronic F108 ( $\text{EO}_{132}\text{PO}_{50}\text{EO}_{132}$ ) are typical copolymers reported to date for the synthesis of mesoporous aluminophosphates [22, 24–27]. In addition to producing a relatively stable solid with large pores (up to 12 nm), the procedure is simple and relatively cheap, easily sourced chemicals are used and mild reaction conditions are employed. In a typical synthesis, as summarised in Fig. 15.4, the block copolymer,  $\text{AlCl}_3$  and  $\text{H}_3\text{PO}_4$  are dissolved in ethanol. The mixture is stirred for up to 2 h at room temperature. This is followed by a slow evaporation step at 40 °C and subsequently 80 °C. In general calcination at 550 °C for up to 12 h is used to remove the template and the mesoporous structure is retained following this heat treatment. The interaction between the surfactant and inorganic framework is relatively weak, therefore it is also possible to remove the surfactant by solvent extraction. Extraction liquids include dehydrated acetone. This is particularly relevant for the removal of surfactant from mesoporous aluminium organophosphonates where heat treatment at high temperatures may destroy the organic component of the framework structure [27, 28].

Other surfactants commonly reported for the formation of stable aluminophosphates are the simple alkyl poly(ethylene oxide) non-ionic surfactant and the semi-fluorinated analogue. The structures of these are shown in Fig. 15.5. The polyethylene oxide surfactant  $\text{C}_{16}\text{H}_{33}(\text{PEO})_{10}\text{OH}$  has been used to prepare stable aluminophosphates and aluminium organophosphonates with ordered mesoporous structure [27–30].

Some success also has been reported regarding the preparation of large surface area stable aluminophosphates ( $581 \text{ m}^2/\text{g}$ ) using a semi-fluorinated surfactant,  $\text{CF}_3(\text{CF}_2)_4(\text{EO})_{10}\text{OH}$ . The solids retained their mesoporous characteristics even after calcination at 700 °C [30]. The Al:P ratio was close to 1 and a significant portion of the Al was in the six coordinated state. This indicated a coordination with not only  $\text{PO}_4$  units but also water molecules or residual chloride ions, a factor also

**Fig. 15.4** Preparation of mesoporous aluminophosphate using block copolymers

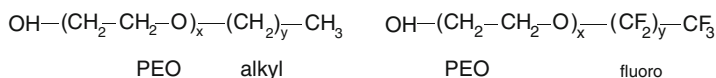
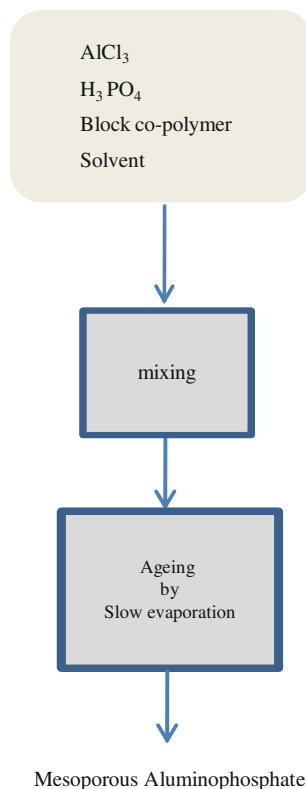


**Fig. 15.5** Alkyl poly(ethylene oxide) and semi-fluorinated surfactant

observed by other groups [16, 31]. It is reported that the hydrophobicity of the short fluorocarbon chain is much stronger than that of the hydrocarbon and results in the formation of solids with higher surface area but relatively small pores [32].

The ability to synthesise a thermally stable aluminophosphate mesoporous solid is an interesting exercise, however, the catalytic activity of such solids is relatively limited since they are essentially composed of a neutral framework and have low acidity primarily associated with exposed surface P–OH and Al–OH groups. In addition, they lack redox properties. However, the properties can be modified by incorporation of metal ions into their framework structure. Depending on the metal incorporated, catalysts with novel acidic or oxidative properties can be synthesised. The most important issue is the synthesis of a relatively stable solid that will tolerate use in relatively harsh reaction conditions. With the improvements in the stability of

mesoporous aluminophosphates, the number of reports on the synthesis of modified AlPO solids has increased.

## 15.5 Aluminophosphate Modification

Since the first report of microporous aluminophosphate solids [1], interest in these materials for use as adsorbents and catalysts has increased. The ability to incorporate other elements into the framework has opened up a vast area of research in terms of acid/base and oxidation/reduction catalysis [2]. For example, the incorporation of silicon into the framework of aluminophosphate molecular sieves imparts acidity, ion exchange capacity and enhanced hydrophilicity. These are important characteristics in catalysis and adsorption. In terms of metal incorporation into the larger-pore mesoporous aluminophosphate, the body of reported research is significantly less. However, much progress has been made over the past few years, particularly now that synthesis procedures have advanced to levels whereby relatively stable mesoporous structures can be produced.

There have been several reports regarding the incorporation of silicon into the framework of mesoporous aluminophosphate. Chakraborty et al. prepared a mesoporous silicoaluminophosphate (SAPO) with varying Si/Al ratios using the surfactant CTAB [33, 34]. From characterisation studies there was no evidence of Si–O–Al linkages. There was evidence, however, that Si-rich regions existed and that Si replaced P on a random basis.

Studies have been reported regarding the mechanism of silicon incorporation into the aluminophosphate framework. In a report by Zhao et al., two different mechanisms were thought to occur similar to the microporous analogues: an SM2 mechanism, whereby Si atoms replace P atoms in the framework (see Fig. 15.6a) and an SM3 mechanism whereby Si atoms replace Al–P pairing in the framework (see Fig. 15.6b) [35]. In the SM2 mechanism, the replacement of some phosphorous atoms with silicon results in a negative charge within the framework and this charge

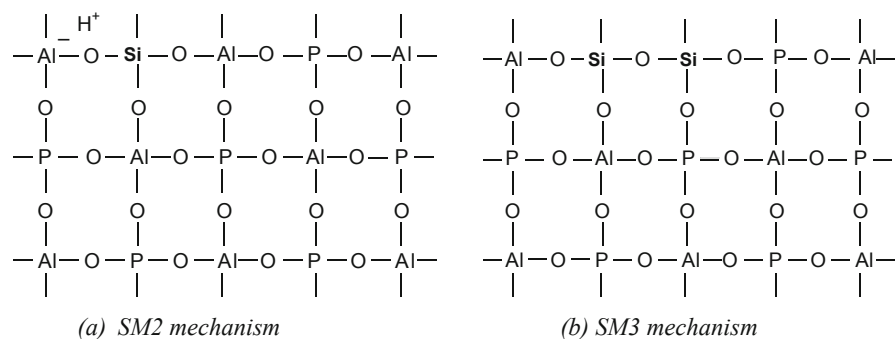


**Fig. 15.6** Schematic of silicoaluminophosphate. (a) SM2 mechanism and (b) SM3 mechanism

is compensated by extra-framework protons following calcination. These  $H^+$  ions can be a source of acidity for acid-catalysed reactions and can also be exchanged for transition metal ions.

The acidity of mesoporous SAPO materials was studied using Fourier transform infrared (FTIR) spectroscopy coupled with adsorbed CO and  $NH_3$ . Al–OH, P–OH and Si–OH groups are found on the surface of these porous solids, however, the overall acidity was found to be weaker than the Bronsted acid sites found on zeolites [36, 37].

Recently, a new approach to the synthesis of mesoporous SAPO materials has been reported [38]. The approach involves the incorporation of aluminophosphate units into the framework of aluminosilicate MCM-41, resulting in the formation of a mesoporous SAPO.

One of the first reports of iron incorporation into mesoporous aluminophosphates used cetyltrimethylammonium chloride (CTAC) as surfactant and ferric nitrate as the iron source [39]. Compared to the aluminophosphate, the high surface area and porosity of the iron-incorporated solid was retained following calcination at 550 °C. The location of the iron within the framework of the aluminophosphates was verified using electron paramagnetic resonance (EPR) spectroscopy where a strong signal at  $g_{\text{eff}} = 4.3$  was assigned to the high spin  $Fe^{3+}$  in a distorted tetrahedral environment. The stability of the iron species was not compromised by heat treatment indicating the stability of the  $Fe^{3+}$  ions within this tetrahedral matrix [40, 41]. A small amount of the iron species was present as  $Fe^{2+}$ . In a study by Tušar et al., detailed characterisation of the local environment of iron in a mesoporous hexagonal aluminophosphate catalyst prepared hydrothermally in a microwave oven was presented [42]. Iron was found to be predominately in the form of octahedrally coordinated  $Fe^{3+}$  ions with about 10% of the iron in the tetrahedral form. Removal of water by evacuation increased the level of  $Fe^{3+}$  in the tetrahedral form. In addition, it was noted that a significant level of iron reduction ( $Fe^{3+} \rightarrow Fe^{2+}$ ) took place during evacuation indicating that redox processes can easily proceed over these solids.

Iron was successfully incorporated into the framework of aluminophosphates using block copolymers [24]. The procedure involved using  $AlCl_3$ ,  $FeCl_3$ ,  $H_3PO_4$ , F127 and ethanol in the synthesis solution. The structure was retained following calcination at 500 °C. Iron was also incorporated into the aluminophosphate framework using a semi-fluorinated surfactant [30] and these solids were stable up to 600 °C. The iron replaces Al atoms in the framework structure as indicated by UV–vis spectra and the molar ratio of P to (Al + Fe) of close to 1. There was also evidence of extra-framework Fe–O clusters.

There are different approaches reported for the preparation of titanium-containing aluminophosphates. These include the incorporation of Ti into the framework [43–45], grafting of Ti onto the surface of pre-formed mesoporous aluminophosphate [46] and the preparation of pure mesoporous  $TiPO_4$  [47]. The incorporation of Ti into the aluminophosphate framework was achieved using CTAC (cetyltrimethylammonium chloride) as surfactant and titanium isopropoxide as the source of titanium [45]. The increase in Al/P ratio with titanium content indicated that  $Ti^{4+}$  replaced  $P^{5+}$  in the framework. Overall a maximum of



3.25% titanium could be incorporated into the tetrahedral framework mesoporous aluminophosphate matrix without forming a  $\text{TiO}_2$  phase.

Titanium grafting onto a calcined mesoporous aluminophosphate was achieved using titanocene dichloride ( $\text{Cp}_2\text{TiCl}_2$ ) as the grafting precursor [46]. From FTIR it was shown that the titanocene dichloride grafted to both the P–OH and the Al–OH groups on the surface of the aluminophosphate forming tetrahedral  $\text{Ti}^{4+}$  sites. However, not all –OH groups are occupied by the grafting agent therefore the mesoporous Ti – aluminophosphates still exhibited some acidity.

Stable mesoporous aluminophosphates containing zirconium were successfully prepared using tri-block copolymer P123 as the structure-directing agent [25]. The aluminium, phosphorus and zirconium sources were aluminium-tri-*sec*-butoxide, phosphoric acid and zirconium(IV) propoxide, respectively. Calcined samples show electron spin resonance (ESR) signals corresponding to  $\text{Zr}^{3+}$  at framework tetrahedral sites. The Zr ions isomorphously substitute for either Al or P.

Work has been reported on the modification of the aluminophosphate structure with magnesium [17, 48, 49]. Mesoporous magnesium-aluminophosphates were prepared using CTAB as the structure-directing agent [17]. The surfactant could be removed from the prepared solid by extraction with ethanol/*n*-butylamine, whereby direct calcination or extraction with HCl/ethanol resulted in collapse of the mesoporous structure. A report on magnesium and cobalt-substituted mesoporous aluminophosphates showed the incorporation of  $\text{Mg}^{2+}$  and  $\text{Co}^{2+}$  into the framework [48]. From pyridine adsorption studies this modification resulted in an increase in the acidic properties of the aluminophosphate. In particular there was clear evidence of the presence of Bronsted acidity, a characteristic not present in the pure aluminophosphate. Mohapatra and Selvam also reported on the synthesis and characterisation of mesoporous cobalt aluminophosphate [50]. The cobalt ions were reported to exhibit a divalent oxidation state in a tetrahedral coordination within the mesoporous aluminophosphate. The stability of this solid was verified following calcination.

Mesoporous aluminophosphate has been modified with other metals and these include magnesium, vanadium, molybdenum and boron. Mesoporous boroaluminophosphates (BAPOs) were prepared using CTAC as surfactant and  $\text{H}_3\text{BO}_3$  as the boron source [51]. Boron was shown to be incorporated into the structure primarily in the tetrahedral coordination with some evidence of the trigonal-coordinated species also present. The incorporation of boron into the framework had an effect of reducing the thermal stability of the solid. Manganese was also found to be incorporated into the AIPO framework using cationic surfactant as structure-directing agent [52]. A more recent study on the stability and electrochemical characteristics of a calcined mesoporous aluminophosphate with incorporated Mn showed the solid to be very unstable, dissolving over time in the electrolyte [53]. An attempt to incorporate molybdenum into AIPO has been reported using primary amines as templating agents [18]. The surfactant removal is accomplished using a solvent extraction technique where the extracting solvent was *n*-butylamine/ethanol. Acidic solvent extraction resulted in a collapse of the porous structure. From ESR and FTIR the molybdenum species were found to be in the form of  $\text{Mo}^{4+}$  and  $\text{Mo}^{6+}$  in a

tetrahedral position within the aluminophosphate. Evidence of bulk  $\text{MoO}_3$  was not present.

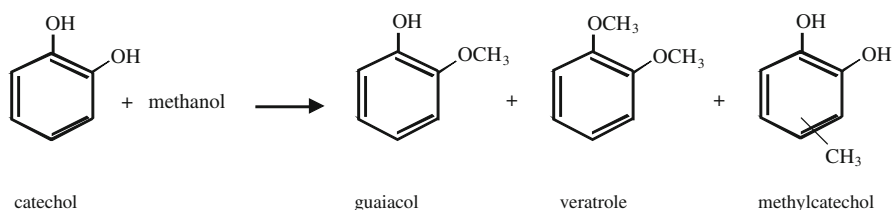
Vanadium could be incorporated into the framework of mesoporous AlPO [54]. Chemical and FTIR studies indicated that the vanadium replaced the phosphorous in the aluminophosphate network. The redox behaviour of the vanadium species ( $\text{V}^{4+} \leftrightarrow \text{V}^{5+}$ ) was demonstrated, which may be beneficial for oxidation catalysis.

## 15.6 Applications of Mesoporous Aluminophosphates and Metal Aluminophosphates

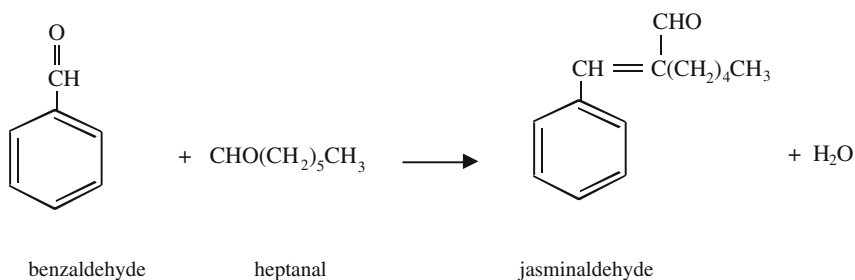
Some reports regarding the ability of mesoporous aluminophosphates and related structures to catalyse specific reactions have been recently reported in the literature. It is clear that the limited acidity associated with aluminophosphates can restrict their use as catalysts. However, the weak acid–base character of these solids can be exploited for a variety of reactions.

One such reaction is the selective O-methylation of catechol to form guaiacol (see Scheme 15.1 which also includes some possible side products). This reaction is industrially important as guaiacol is a valuable compound in the medical, fragrance and food sectors. Conventionally, guaiacol is produced through the methylation of catechol with  $(\text{CH}_3)_2\text{SO}_4$  [55] or with  $\text{CH}_3\text{I}$  in the presence of sodium hydride as the homogeneous catalyst [56]. These processes produce large quantities of waste, and the chemicals used are both toxic and corrosive. The use of a solid acid catalyst offers many advantages over the conventional route, including convenient separation of catalyst and product, catalyst reusability, reduction of waste, etc. Indeed mesoporous aluminophosphate solids have been reported to possess appropriate weak acid–base pairs to facilitate this reaction [57]. The vapour-phase reaction was carried out at  $280^\circ\text{C}$  and the primary product was guaiacol. A product yield of 74.3% was achieved with by-product veratrole, and methyl catechol also observed. Other catalysts have also been reported to be active for this reaction, including modified zirconia catalysts and base catalysts [58, 59].

Another reaction that can use the weak acid–base character of mesoporous aluminophosphates is the condensation of heptanal with benzaldehyde to form jasminaldehyde (see Scheme 15.2). Jasminaldehyde is a fine chemical of commercial



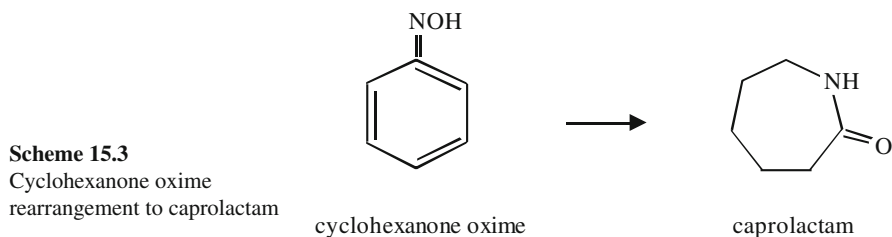
**Scheme 15.1** Methylation of catechol to form guaiacol and by-products



**Scheme 15.2** Condensation of benzaldehyde with heptanal to form jasminaldehyde

interest in the fragrance industry and its synthesis is normally carried out in the presence of alkali, such as sodium hydroxide or potassium hydroxide, as catalysts. One of the major problems associated with this reaction is the unwanted formation of relatively large amounts of by-product amylcinnamaldehyde and 2-*n*-pentyl-2-*n*-nonenal. Several solids have been tested as potential catalysts for this reaction including zeolites and aluminosilicates [60, 61]. The best results, however, were obtained using amorphous aluminophosphate catalysts. This was thought to be due to the acid–base bifunctional character of the solid where both the weak acid sites and the weak base sites have a cooperative effect in driving the reaction. Mesoporous aluminophosphate catalysts were also shown to be active for this reaction [62]. The activity of the catalysts could be increased by incorporating silicon into the aluminophosphate's structure. The increased activity was linked to the increased number of acid sites available for reaction.

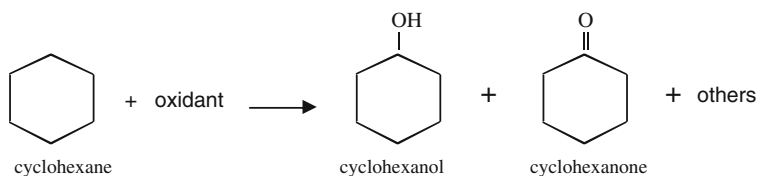
Silicon-incorporated aluminophosphates (SAPOs) have also been used for the Beckmann rearrangement of cyclohexanone oxime into caprolactam [63]. Caprolactam is an important monomer for the formation of nylon, a polymer with many applications [64]. Cyclohexanone oxime can be rearranged into caprolactam in the gas phase using a variety of acid catalysts [65–67], see Scheme 15.3, and is currently commercially produced by Sumitomo chemical co. using an MFI (mordenite framework inverted) type zeolite composed of silica [68]. One of the main issues of the process is the rapid deactivation of the catalyst and this requires periodic regeneration. Conesa et al. reported on the use of mesoporous silicoaluminophosphates for the Beckmann rearrangement of cyclohexanone and



**Scheme 15.3**  
Cyclohexanone oxime  
rearrangement to caprolactam

clycododecanone oximes both in the liquid and gas phases [63]. The prepared catalysts were found to be active and selective to the corresponding lactam although catalyst deactivation was observed. Overall, the yields are not at a level to compete with the catalysts currently used in the commercial process [68].

The liquid phase oxidation of cyclohexane into valuable products has attracted some attention in literature. The oxidation reaction, presented in Scheme 15.4, forms cyclohexanol, cyclohexanone and some other minor by-products. Work in this area up to the year 2001 has been reviewed in a work presented by Schuchardt et al. [69]. Recently, attention has been focused on developing new heterogeneous catalysts for the oxidation of cyclohexane under mild conditions. Traditional processes for this kind of synthesis involved using stoichiometric amounts of inorganic oxidants, resulting in the production of large amounts of waste. Selvam et al. reported on a series of metal-modified mesoporous aluminophosphates for the oxidation of cyclohexane. The catalysts investigated included Co-AIPO [50, 70], Cr-AIPO [71], V-AIPO [72], Ti-AIPO [45] and Fe-AIPO [40]. All were tested in a similar way: 100 °C, atmospheric pressure, 50 mg catalyst, 18 mmol cyclohexane, 18 mmol H<sub>2</sub>O<sub>2</sub> oxidant, 10 mmol acetic acid solvent. All catalysts, irrespective of the modifying metal, presented similar activities following 12 h reaction. In general the cyclohexane conversion was high (~90%) and the primary product was cyclohexanol (in most cases with a selectivity >90%). In general the selectivity to cyclohexanone was relatively low (<10%) with the exception of Fe-AIPO which presented selectivities of approx. 30%. For all catalysts some leaching was reported mostly because of the presence of a small amount of loosely bound extra-framework metal species in the mesoporous solid. This leaching was only observed in the initial test run and further leaching was not observed in subsequent tests. Unmodified mesoporous aluminophosphate resulted in a cyclohexane conversion of only 10%.

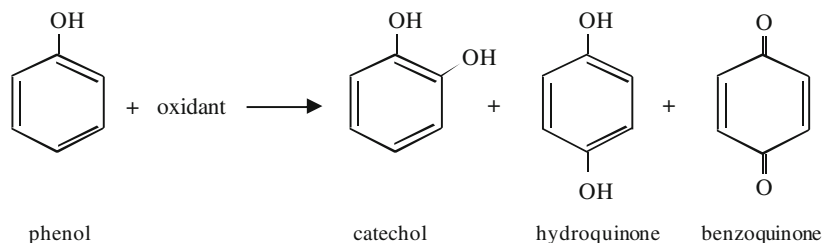


**Scheme 15.4** Cyclohexane oxidation

Cyclohexane oxidation over mesoporous AIPO has also been reported in the presence of air. Activities are much lower using this cheap oxidant source. Subrahmanyam et al. tested a Fe-AIPO for the oxidation of cyclohexane at 130 °C and 20–30 bar for 24 h [41]. High selectivities to the cyclohexanol product were observed but the conversion of the cyclohexane was relatively low (7–14%).

Hydroquinone and catechol are also important chemicals and intermediates used in the chemical, polymer and pharmaceutical industry. Similar to the oxidation of cyclohexane, the current industrial process for their synthesis uses various catalysts such as mineral acids, soluble metal ions and metal complexes. The process is complicated, requires a variety of process steps and produces large quantities of waste.

Consequently, much effort has been made to directly form these compounds from the hydroxylation of phenol with  $\text{H}_2\text{O}_2$  using heterogeneous catalysts such as titanium silicalite [73] and mesoporous silica [74]. Iron-modified AIPOs have also been reported as a potential catalyst for phenol hydroxylation with hydrogen peroxide [30]. The catalytic activity is strongly influenced by the iron content of the catalyst. Phenol conversion of 23% was achieved after 5 h reaction at 80 °C. The products of the reaction included catechol, hydroquinone and benzoquinone at selectivities of 60.7, 34.8 and 4.5%, respectively (see Scheme 15.5). No information is given regarding the usability of the catalyst.



**Scheme 15.5** Phenol hydroxylation

From the literature, it can be seen that mesoporous aluminophosphates can be used as catalysts for a variety of reactions. These reactions are primarily those that require mild acidic/basic conditions (catalysed by AIPO or SAPO) and reactions that require the redox capabilities of the metal-modified AIPOs. Overall the work in this area is very much in its infancy, and frequently there are catalysts other than mesoporous aluminophosphate that can perform at a better level than the optimum mesoporous AIPO, however, further developments in this relatively new area will offer potential.

## 15.7 Conclusions

The synthesis of mesoporous aluminophosphates has significantly advanced in recent years. The advancements have resulted in solids with greater stability and tuneable pore sizes. Pore sizes in the mesoporous range are important for reactions involving bulky molecules and in overcoming diffusion problems during reaction. The ability to incorporate other elements into the framework has opened up a vast area of research particularly in the area of catalysis. Silicon has been successfully incorporated into the aluminophosphate framework, resulting in increased acidity. This property can be exploited for acid-catalysed reactions such as the Beckmann rearrangement. Species commonly used in redox reactions can also be incorporated into the mesoporous network and these have been extensively characterised and tested for a variety of reactions. There is, however, scope for further development in the synthesis procedures and investigating the applications of these solids.

## References

1. Wilson TS, Lok BM, Messina CA, Cannan TR, Flanigen EM (1982) Aluminophosphate molecular-sieves – A new class of microporous crystalline inorganic solids. *J Am Chem Soc* 104:1146–1147
2. Hartmann M, Kevan L (1999) Transition-metal ions in aluminophosphate and silicoaluminophosphate molecular sieves: location, interaction with adsorbates and catalytic properties. *Chem Rev* 99:635–663
3. Zhao DY, Luan ZH, Kevan L (1997) Synthesis of thermally stable mesoporous hexagonal aluminophosphate molecular sieves. *Chem Commun* 11:1009–1010
4. Kimura T, Sugahara Y, Kuroda K (1999) Synthesis and characterization of lamellar and hexagonal mesostructured aluminophosphates using alkyltrimethylammonium cations as structure-directing agents. *Chem Mater* 11:508–518
5. Sayari A, Karra VR, Reddy JS, Moudrakovski IL (1996) Synthesis of a mesostructured lamellar aluminophosphate. *Chem Commun* 3:411–412
6. Feng PY, Xia Y, Feng JL, Bu XH, Stucky GD (1997) Synthesis and characterization of mesostructured aluminophosphates using the fluoride route. *Chem Commun* 10:949–950
7. Eswaramoorthy M, Neeraj S, Rao CNR (1999) Synthesis of hexagonal microporous silica and aluminophosphates by supramolecular templating of a short-chain amine. *Micropor Mesopor Mater* 28:205–210
8. Cheng SF, Tzeng JN, Hsu BY (1997) Synthesis and characterization of a novel layered aluminophosphates of kanemite-like structure. *Chem Mater* 9:1788–1796
9. Kron DA, Holland BT, Wipson R, Maleke C, Stein A (1999) Anion exchange properties of a mesoporous aluminophosphate. *Langmuir* 15:5300–8308
10. Holland BT, Isbester PK, Blanford CF, Munson EJ, Stein A (1997) Synthesis of ordered aluminophosphates and galloaluminophosphate mesoporous materials with anion-exchange properties utilizing polyoxometalate cluster/surfactant salts as precursors. *J Am Chem Soc* 119:6796–6803
11. Kimura T (2005) Synthesis of mesostructured and mesoporous aluminium organophosphonates prepared by using diphosphonic acids with alkylene groups. *Chem Mater* 17:337–344
12. Tiemann M, Förba M (2001) Mesostructured porous aluminophosphates synthesized with supramolecular structure directors. *Chem Mater* 13:3211–3217
13. Kimura T, Sugahara Y, Kuroda K (1997) Synthesis of a hexagonal mesostructured aluminophosphate. *Chem Lett* 10:983–984
14. Luan ZH, Zhao DY, He HY, Klinowski J, Kevan L (1998) Characterization of aluminophosphate-based tubular mesoporous molecular sieves. *J Phys Chem B* 102:1250–1259
15. He J, Yang XB, Evans DG, Duan X (2003) New methods to remove organic templates from porous materials. *Mater Chem Phys* 77:270–275
16. Tiemann M, Schulz M, Jäger C, Förba M (2001) Mesoporous aluminophosphate molecular sieves synthesized under nonaqueous conditions. *Chem Mater* 13:2885–2891
17. Masson NC, Pastore HO (2001) Synthesis and characterization of tubular aluminophosphate mesoporous materials containing framework magnesium. *Micropor Mesopor Mater* 44:173–183
18. Ho LH, Ikegawa T, Nishiguchi H, Nagaoka K, Takita Y (2006) Synthesis and characterization of molybdenum incorporated mesoporous aluminophosphate. *Appl Surf Sci* 252:6260–6268
19. Sarkar K, Bhaumik A (2008) Hydrothermal transformation of a layered aluminophosphates into a mesoporous structure. *J Porous Mater* 15:445–450
20. Yu J, Wang A, Li X, Tan J, Hu Y (2007) An improved calcination route to obtain high quality mesoporous aluminophosphate materials. *Mater Lett* 61:2620–2623
21. Zhao DY, Huo QS, Feng JL, Chmelka BF, Stucky GD (1998) Nonionic triblock and star diblock copolymer and oligomeric surfactant syntheses of highly ordered, hydrothermally stable, mesoporous silica structures. *J Am Chem Soc* 120:6024–6036

22. Tian BZ, Liu XY, Tu B, Yu CZ, Fan J, Wang LM, Xie SH, Stucky GD, Zhao DY (2003) Self-adjusted synthesis of ordered stable mesoporous minerals by acid–base pairs. *Nat Mater* 2:159–163
23. Yu C, Tian B, Zhao D (2003) Recent advances in the synthesis of non-siliceous mesoporous materials. *Curr Opin Solid State Mater Sci* 7:191–197
24. Wang L, Tian B, Fan J, Liu X, Yang H, Yu C, Tu B, Zhao D (2004) Block copolymer templating syntheses of ordered large-pore stable mesoporous aluminophosphates and Fe-aluminophosphate based on an “acid–base pair” route. *Micropor Mesopor Mater* 67:123–133
25. Lü J-M, Ranjit KT, Rungrojchaipan P, Kevan L (2005) Synthesis of mesoporous aluminophosphate (AIPO) and investigation of zirconium incorporation into mesoporous AIPOs. *J Phys Chem* 109:9284–9293
26. Mazaj A, Costacurta S, Logar NZ, Mali G, Tušar NN, Innocenzi P, Malfatti L, Thibault-Starzyk F, Amenitsch H, Kaučič V, Soler-Illia GJAA (2008) Mesoporous aluminophosphate thin films with cubic pore arrangement. *Langmuir* 24:6220–6225
27. Kimura T, Kato K, Yamauchi Y (2009) Temperature-controlled and aerosol-assisted synthesis of aluminium organophosphonate spherical particles with uniform mesopores. *Chem Commun* 33:4938–4940
28. Kimura T, Kato K (2007) Simple removal of oligomeric surfactants and triblock copolymers from mesostructured precursors of ordered mesoporous aluminium organophosphonates. *Micropor Mesopor Mater* 101:207–213
29. Zhao GL, Zhang XJ, Chen TH, Yuan ZY (2006) Synthesis of aluminophosphates and silicoaluminophosphate in the presence of nonionic poly(ethylene oxide) surfactant. *Mater Sci Eng B* 131:263–266
30. Du Y, Yang Y, Liu S, Xiao N, Zhang Y, Xiao F-S (2008) Mesoporous aluminophosphates and Fe-aluminophosphates with highly thermal stability and large surface area templated from semi-fluorinated surfactant. *Micropor Mesopor Mater* 114:250–256
31. Kimura T, Sugahara, Kuroda K (1998) Synthesis of mesoporous aluminophosphates and their adsorption properties. *Micropor Mesopor Mater* 22:115–126
32. Han Y, Li DF, Zhao L, Song JW, Yang XY, Li N, Di Y, Li CJ, Wu S, Xu XZ, Meng XJ, Lin KF, Xiao FS (2003) High-temperature generalized synthesis of stable ordered mesoporous silica-based materials by using fluorocarbon–hydrocarbon surfactant mixtures. *Angew Chem Int Ed* 42:3633–3637
33. Chakraborty B, Pulikottil AC, Das S, Viswanathan B (1997) Synthesis and characterisation of a mesoporous SAPO. *Chem Commun* 10:911–912
34. Chakraborty B, Pulikottil AC, Viswanathan B (1998) Physico-chemical and MAS NMR characterization of mesoporous SAPOs. *Appl Catal A: Gen* 167:173–181
35. Zhao XS, Lu GQ, Whittaker AK, Drennan J, Xu H (2002) Influence of synthesis parameters on the formation of mesoporous SAPOs. *Micropor Mesopor Mater* 55:51–62
36. Pastore HO, Coluccia S, Marchese L (2005) Porous aluminophosphates: from molecular sieves to designed acid catalysts. *Annu Rev Mater Res* 35:315–395
37. Gianotti E, Oliveira EC, Coluccia S, Pastore HO, Marchese L (2004) The surface acidity of mesoporous silicoaluminophosphates: an FTIR study. *Stud Surf Sci Catal* 154:1498–1504
38. Conesa TD, Mokaya R, Campelo, JM, Romero AA (2006) Synthesis and characterization of novel mesoporous aluminosilicate MCM-41 containing aluminophosphates building blocks. *Chem Commun* 17:1839–1841
39. Mohapatra SK, Sahoo B, Keune W, Selvam P (2002) Synthesis, characterization and catalytic properties of trivalent iron substituted hexagonal mesoporous aluminophosphates. *Chem Commun* 14:1466–1467
40. Selvam P, Mohapatra SK (2006) Thermally stable trivalent iron-substituted hexagonal mesoporous aluminophosphate (FeHMA) molecular sieves: synthesis, characterization, and catalytic properties. *J Catal* 238:88–99
41. Subrahmanyam C, Viswanathan B, Varadarajan TK (2004) Synthesis, characterization and catalytic activity of mesoporous trivalent iron substituted aluminophosphates. *J Mol Catal A: Chem* 233:149–153

42. Tušar NN, Logar NZ, Arčon I, Mali G, Mazaj M, Ristić A, Lázár K, Kaučič V (2005) Local environment of iron in the mesoporous hexagonal aluminophosphate catalyst. *Micropor Mesopor Mater* 87:52–58
43. Zhao XS, Lu GQ. (2001) Aluminophosphate-based mesoporous molecular sieves: synthesis and characterization of TAPOs. *Micropor Mesopor Mater* 44:185–194
44. Kapoor MP, Raj A (2000) Synthesis of mesoporous hexagonal titanium aluminophosphate molecular sieves and their catalytic applications. *Appl Catal A: Gen* 203:311–319
45. Selvam P, Mohapatra SK (2004) Synthesis, characterization and catalytic properties of mesoporous TiHMA molecular sieves: selective oxidation of cycloalkanes. *Micropor Mesopor Mater* 73:137–149
46. Gianotti E, Oliveira EC, Coluccia S, Pastore HO, Marchese L (2003) Synthesis and surface properties of Ti-containing mesoporous aluminophosphates. A comparison with Ti-grafted mesoporous silica Ti-MCM-41. *Inorg Chem Acta* 349:259–264
47. Zhao J, Tian B, Yue Y, Hua W, Zhao D, Gao Z (2005) New catalysts for dichlorodifluoromethane hydrolysis: mesostructured titanium and aluminium phosphates. *J Mol Catal A: Chem* 242:218–223
48. Karthik M, Vinu A, Tripathi AK, Gupa NM, Palanichamy M, Murugesan V (2004) Synthesis, characterization and catalytic performance of Mg and Co substituted mesoporous aluminophosphates. *Micropor Mesopor Mater* 70:15–25
49. Khimyak YZ, Klinowski J (2001) Incorporation of magnesium in mesostructured and mesoporous aluminophosphates. *Phys Chem Chem Phys* 3:1533–1561
50. Mohapatra SK, Selvam P (2003). Synthesis, characterization and catalytic properties of mesoporous cobalt aluminophosphate molecular sieves. *Topics in Catal* 22:17–22
51. Khimyak YZ, Klinowski J (2002). Synthesis and characterisation of mesoporous aluminophosphates containing boron. *J Mater Chem* 12:1079–1085
52. Zhao D, Luan Z, Kevan L (1997) Electron spin resonance and electron spin echo modulation spectroscopy of aluminophosphate-based mesoporous molecular sieve containing framework manganese. *J Phys Chem* 243:218–266
53. Gerbaldi C, Bodoardo S, Fiorilli S, Piana M, Penazzi N (2004) Characterization of Mn species in mesoporous systems: an electrochemical study. *Electrochem Acta* 50: 5539–5545
54. Venkatathri N, Srivastava R (2005) Synthesis, characterization and catalytic properties of hexagonal mesoporous vanadium aluminophosphate molecular sieves. *Catal Commun* 6:177–183
55. Dorothea G, (1991) Phenol derivatives, Ullmann's Encyclopaedia of Industrial Chemistry. VCH, Verlagsgesellschaft, Weinheim
56. Stoochnoff BA and Benoiton NL (1973) Methylation of some phenols and alcohols with sodium hydride methyl iodide in tetrahydrofuran at room temperature. *Tetrahedron Lett* 1:21–24
57. Liu G, Wang Z, Jia M, Zou X, Zhu X, Zhang W, Jiang D (2006) Thermally stable amorphous mesoporous aluminophosphates with controllable P/Al ratio: Synthesis, characterization, and catalytic performance for selective O-methylation of catechol. *J Phys Chem B* 110: 16953–16960
58. Fu Z, Yu Y, Yin D, Xu Y, Liu H, Liao H, Xu Q, Tan F, Wang J (2005) Vapor-phase highly selective O-methylation of catechol with methanol over ZnCl<sub>2</sub> modified  $\gamma$ -Al<sub>2</sub>O<sub>3</sub> catalysts. *J Mol Catal A: Gen* 232:69–75
59. Vishwanathan V, Balakrishna G, Rajesh B, Jayasri V, Sikhwivilu LM, Coville HJ (2008) Alkylation of catechol with methanol to give guaiacol over sulphate-modified zirconia solid acid catalysts: the influence of structural modification of zirconia on catalytic performance. *Catal Commun* 9:2422–2427
60. Climent MJ, Corma A, Garcia H, Guil-Lopez R, Iborra S, Fornes V (2001) Acid-base bifunctional catalysts for the preparation of fine chemicals: synthesis of jasminaldehyde. *J Catal* 197:385–393



61. Climent MJ, Corma A, Fornes V, Guil-Lopez R, Iborra S, (2002) Aldol condensations on solid catalysts: a cooperative effect between weak acid and base sites. *Adv Syn Catal* 344: 1090–1096
62. O'Malley K (2008) Novel solid acid catalysts. PhD thesis, University of Limerick, Ireland
63. Conesa TD, Mokaya R, Yang Z, Luque R, Campelo JM, Romero AA (2007) Novel mesoporous silicoaluminophosphates as highly active and selective materials in the Beckmann rearrangement of cyclohexanone and cyclododecanone oximes. *J Catal* 252:1–10
64. Ritz J, Fuchs H, Kieczka H, Moran WC (2002) Caprolactam, in Ullmann's encyclopaedia of industrial chemistry. Wiley, Weinheim
65. Curtin T, McMonagle JB, Ruwet M, Hodnett BK (1993) Deactivation and regeneration of alumina catalysts for the rearrangement of cyclohexanone oxime into caprolactam. *J Catal* 142:172–181
66. Curtin T, McMonagle JB, Hodnett BK (1992) Influence of boria loading on the acidity of  $B_2O_3/Al_2O_3$  catalysts for the conversion of cyclohexanone oxime to caprolactam. *Appl Catal A: Gen* 93:91–101
67. Sato S, Hasebe S, Sakurai H, Urabe K, Izumi Y (1992) Vapor-phase Beckmann rearrangement over alumina-supported boria catalyst prepared by vapour decomposition method. *Appl Catal* 29:107–115
68. Izumi Y, Ichihashi H, Shimazu Y, Kitamura M, Sato H (2007) Development and industrialization of the vapour-phase Beckmann rearrangement process. *Bull Chem Soc Jpn* 80:1280–1287
69. Schuchardt U, Cardoso D, Sercheli R, Pereira R, da Cruz RS, Guerreiro MC, Mandelli D, Spinace EV, Pires EL (2001) Cyclohexane oxidation continues to be a challenge. *Appl Catal A: Gen* 211:1–17
70. Mohapatra SK, Selvam P (2005) Synthesis and characterization of divalent cobalt-substituted mesoporous aluminophosphate molecular sieves and their application as novel catalysts for the oxidation of cycloalkanes. *J Catal* 233:276–287
71. Mohapatra SK, Hussain SK, Selvam P (2003) Synthesis, characterization and catalytic properties of chromium-containing hexagonal mesoporous aluminophosphate molecular sieves. *Catal Lett* 85:217–222
72. Mohapatra SK, Selvam P (2004) Synthesis, characterization and catalytic properties of vanadium substituted hexagonal mesoporous aluminophosphate molecular sieves. *Catal Lett* 93:47–52
73. Rao PRHP, Ramaswamy AV (1993) Catalytic hydroxylation of phenol over vanadium silicate molecular sieve with MEL structure. *Appl Catal A: Gen* 93:123–130
74. Wu C, Kong Y, Gao F, Wu Y, Lu Y, Wang J, Dong L (2008) Synthesis, characterization and catalytic performance for phenol hydroxylation of Fe-MCM41 with high iron content. *Micropor Mesopor Mater* 113:163–170

# Chapter 16

## Heterogeneous Complex Catalysts Having Ionically Macrocyclic Complex Bonded to Montmorillonite Clay for Industrial Reactions

Sunder Lal, K.S. Anisia, and Anil Kumar

**Abstract** Macrocyclic complexes were synthesized and ionically bonded with montmorillonite clay. Such catalysts are found to have excellent thermal stability and can be used for the industrially important catalytic reactions. The oxidation of cyclohexane without any promoter or solvent has been carried out using molecular oxygen. Based on the catalytic mechanism, experimental data were fitted to determine various rate constants.

**Keywords** PILC · Pillared clays · Montmorillonite · Complex catalysts

### 16.1 Introduction

#### 16.1.1 Montmorillonite as Catalyst

Clays are class of materials which are abundantly available in nature and can be used as catalyst supports. They are available as cationic clays (or clay minerals) and anionic clays which are also known as layered double hydroxides (LDHs) [1, 2]. Cationic clays are prepared starting from minerals and have negatively charged aluminosilicate layers, with small exchangeable cations in the interlayer space to balance the charge. Anionic clays are usually synthesized and have positively charged brucite-type metal hydroxide layers with exchangeable anions to balance the charge and water molecules located interstitially.

Cationic clays are colloidal layered hydrous aluminosilicates made of Si (O, OH) tetrahedra and the M (O,OH)<sub>6</sub> octahedra (where M = Al<sup>3+</sup>, Mg<sup>2+</sup>, Fe<sup>3+</sup> or Fe<sup>2+</sup>) and belong to the class of phyllosilicates [2]. These are further classified based on their layer types and charge and may exhibit both Bronsted and Lewis

---

A. Kumar (✉)

Department of Chemical Engineering, Indian Institute of Technology Kanpur, Kanpur 208016, India

e-mail: anilk@iitk.ac.in

acid sites [3, 4], which are the exposed OH groups and the  $Al^{3+}$  ions substituting for the  $Si^{4+}$  ions in the tetrahedral sheet, respectively. Various combinations of the tetrahedral and octahedral layers give clays with different properties. The smectite group clays (montmorillonites, saponite, hectorite, laponite) generally find application in catalysis and on treating these clays with acid, acid-treated catalysts can be obtained [5]. Commercially available acid-treated clays are montmorillonites K10, KSF, F-13, and F-20 and can be further upgraded by pillaring with various pillaring agents: organic compounds, metal trischelates, organometallic complexes, metal cluster cations, polyoxocations, etc. [6–10]. Pillaring is achieved by insertion of the pillaring agent in the interlayer region of the clay and is known as intercalation. The mechanism of intercalation was proposed to be an ion exchange reaction, followed by solvent removal which is achieved by calcinations with the preservation of the clay mineral structure and the pillaring agent structure. The final properties of pillared clays depend on the nature of the pillaring agent, pillaring procedure, thermal treatments, particle size, etc.

We have carried out literature search of chemical reactions with montmorillonite (and its modifications) catalysts and presented as summary in Table 16.1 [11–50]. The study of this table suggests that clays are commonly used for removing organic impurities from waste water for water pollution control. Water impurities could be several and clay catalysts have been used for the oxidation of phenol [11–17, 19, 20, 23], benzene [18], orange dye [21, 22], EDTA, oxalic acid [23], diphenyl ether [24], olive oil [26], methanol [27], naphthalene [28], pentachlorophenol [29], bisphenol A [30], polystyrene [32], azo dyes [34], and chromic acid [35]. For industrial reactions, people have also used montmorillonite pillared with metal salts [37–40] and metal complexes [36, 41–50]. It can also be seen from this table that multimetallic catalysts are used to obtain higher activities. It has already been stated that these are normally prepared by mixing two (or more than two) salts and dispersing the solution on a suitable support. Depending on the heat of mixing  $\Delta H_m$ , the multimetallic catalyst systems would exist as mono- or multiphase or solid solutions. To overcome this specific problem, multimetallic complexes has been proposed as catalysts in which case the catalytic activity and specificity is not dependant upon  $\Delta H_m$ .

### 16.1.2 Complexes

A compound formed from a Lewis acid (an electron pair acceptor) and a Bronsted base (a proton acceptor) is called a metal complex or coordination compound [51]. The Bronsted bases attached to the metal ions are called ligands [52]. A ligand bound to a metal ion through a single donor atom (e.g.,  $Cl^-$ ,  $H_2O$ ,  $NH_3$ ) is called unidentate ligand, while a ligand bound to a metal ion through two carbon atoms is called bidentate ligand and a ligand bound to a metal ion through several (more than two) donor atoms is called polydentate ligands. When a bi- or polydentate ligands are used, there are two or more donor atoms to bind to a single metal ion and it is said

Table 16.1 Literature review of catalytic reactions published between 2000 and 2009

References	Catalyst	Raw material	Products and pressure	Temperature	Procedure of catalyst preparation	Oxidizing agent	Conversion (%)	Comments
[11]	Al-Fe-pillared clay	Phenol solution with conc. $5 \times 10^{-4}$ mol/l in water	CO <sub>2</sub>	25–70 °C/1 atm	Obtained by pillaring Greek bauxite clay with 2% Fe through intercalation solution prepared by titrating Al <sup>3+</sup> /Fe <sup>3+</sup> salt with NaOH	H <sub>2</sub> O <sub>2</sub>	28–100	Total organic carbons (TOCs) from waste water were measured by DC 190 Dohmann equipment and phenol conversion was analyzed by HPLC with a C <sub>18</sub> column
[12]	Fe, Al or Cu, Al FAZA or CAZA	Phenol conc. $5 \times 10^{-4}$ in water	CO <sub>2</sub>	70 °C/1 atm	Catalyst is prepared by pillaring a commercial Greek bentonite called Zenith N with intercalant solution containing (Al, Cu) or (Al, Fe)	H <sub>2</sub> O <sub>2</sub> + O <sub>2</sub>	80	TOC conversion is directly related to iron or copper content of the catalyst
[13]	Four-catalyst systems: Fe-TS-1, Fe-NaY, Fe-USY, Fe-ZSM-5	Phenolic solution conc. 1 g/l with water	CO <sub>2</sub> and water	100 °C/1 atm	Hydrothermal crystallization of wetness-impregnated Fe <sub>2</sub> O <sub>3</sub> -TiO <sub>2</sub> -SiO <sub>2</sub> xerogels, crystallization of basic hydrogels and finally ion exchange	H <sub>2</sub> O <sub>2</sub>	100	Maximum value of TOC conversion after 2 h of reaction is achieved
[14]	Extrudates of Al-Fe-pillared clays	Phenol concentration 100–2000 ppm in water	Removal of phenol	25–60 °C/1 atm	Catalyst prepared by extruding a pillared Greek bentonite called Zenith-N	H <sub>2</sub> O <sub>2</sub>	100	Al-Fe-pillared catalyst achieves total elimination of phenol and TOC

Table 16.1 (continued)

References	Catalyst	Raw material	Products and pressure	Temperature	Procedure of catalyst preparation	Oxidizing agent	Conversion (%)	Comments
[15]	Al-Fe- or Al-Cu-modified clays	Phenol $5 \times 10^{-4}$ M in water	CO <sub>2</sub> and water	20 °C	Al-Cu is prepared by mixing 0.1 M Al and Cu nitrates with 0.2 M NaOH and Al-Fe by Fe nitrate (0.1 M) and 0.1 M NaOH	H <sub>2</sub> O <sub>2</sub>	100	The clays modified with Fe, Al show very fast conversion of phenol into CO <sub>2</sub> and water
[16]	Fe-Ti-PILC	Phenol 2 mmol/l with water	CO <sub>2</sub> and water	Microwave irradiation	Titanium tetraisopropoxide was added to 80% acetic acid solution, then white slurry was added, and stirred at 50 °C. TiO <sub>2</sub> solution was mixed with raw clay at pH 0.7. Suspension was stirred for 3 h, product was washed, and centrifuged to remove excess TiO <sub>2</sub> solution. TiO <sub>2</sub> and montmorillonite interaction compound were dried and calcined at 300 °C. Then it was dispersed into solution of NaOH. The sample after drying is Fe-Ti-PILC	H <sub>2</sub> O <sub>2</sub>	20–90	High removal of COD and total removal of phenol under mild conditions without leaching of iron species. Microwave irradiations curtail the reaction time
[17]	Extrudate Al-Fe pillared with montmorillonite clay	Phenol 1000–2000 ppm	Complete phenol removal	150–170 °C/1.5–3.2 atm	The catalyst is directly obtained from University lab	Air	20–100	Packed bed reactor with co-current downflow and upflow conditions

Table 16.1 (continued)

References	Catalyst	Raw material	Products	Temperature and pressure	Procedure of catalyst preparation	Oxidizing agent	Conversion (%)	Comments
[18]	Zr- and Ce-pillared laponite clays are used as support for Pd catalyst	Benzene	CO <sub>2</sub> and water	210 °C/2.0 atm	ZrOCl <sub>2</sub> •8H <sub>2</sub> O was dissolved in 120 ml water and the solution was refluxed for 1 h. Meanwhile, 5 g of laponite clay was dispersed in 240 ml of water, 10 g of surfactant Tergitol was added and stirred for 2 h at 90 °C for 48 h. The precipitate was washed, dried, and calcined at 550 °C for 20 h. Pd was loaded through incipient wetness impregnation method	Air	50–100	Pd/Zr-Lap appears to be the most effective catalyst which converts benzene completely at less than 210 °C. It shows excellent stability during a long-term stability test of 70 h
[19]	Fe-containing clays	Phenol	CO <sub>2</sub> and water	30–70 °C	It was prepared from naturally occurring montmorillonites by exchanging interlayer ion with polyoxocations containing Al <sub>13</sub> -PILC, iron adsorbed onto Al <sub>13</sub> -PILC and Fe <sub>0.8</sub> Al <sub>12.2</sub> -PILCs	H <sub>2</sub> O <sub>2</sub>	50–100	It was found that Phenol reduce to leaching of iron ions significantly

Table 16.1 (continued)

References	Catalyst	Raw material	Products	Temperature and pressure	Procedure of catalyst preparation	Oxidizing agent	Conversion (%)	Comments
[20]	FeO/SBA-15	Phenol 1 g/l	CO <sub>2</sub> and water	80 °C	This catalyst is agglomerated by extrusion with different particle sizes (0.35–2 mm) using bentonite mineral clay and methyl cellulose as binders	H <sub>2</sub> O <sub>2</sub>	100	Oxidation treatment is evaluated by several parameters in outlet aqueous solution. It shows complete removal of phenol and TOC degradation is 60%
[21]	Iron-impregnated pillared saponite clay	Orange II dye solution	Color removal	6.4–73.6 °C	Pillared clay was impregnated with Fe (III) acetylacetonate by incipient wetness impregnation and calcined at 500 °C for 4 h	H <sub>2</sub> O <sub>2</sub>	100	Removal of dye is nearly 100% and TOC conversion is 65%
[22]	Fe and Cu montmorillonite clay	Hydrophobic organic matter	Adsorption	25 °C/1.0 atm	Crude montmorillonite was washed and dried with 1 N FeCl <sub>3</sub> . Finally it is washed with water to remove chlorides	H <sub>2</sub> O <sub>2</sub>	100	Adsorption and fractionation of DOM fractions by montmorillonite saturated with transition metals demonstrated the importance of surface-controlled reactions in the retention of DOM and transport of organic colloids in soils

Table 16.1 (continued)

References	Catalyst	Raw material	Products	Temperature and pressure	Procedure of catalyst and preparation	Oxidizing agent	Conversion (%)	Comments
[23]	Fenton-type Fe-MCM-41 mesoporous material	Ethylenediamine tetraacetic acid and oxalic acid	Adsorption	30–70 °C/ 1.0 atm	Mesoporous Fe-MCM-41 molecular sieves with various Si/Fe ratios (25, 50, 75 and 100) were synthesized using sol-gel technique	H <sub>2</sub> O <sub>2</sub>	100	Fe-MCM-41 catalyst is found suitable for complete oxidation of organics for pollution control
[24]	TiO <sub>2</sub> -immobilized montmorillonite	Decabromodiphenyl ether (BDE)	CO <sub>2</sub> and water	Sunlight	The photocatalysts were prepared by immobilizing TiO <sub>2</sub> onto surfactant-pillared montmorillonite via ion exchange reaction between sodium montmorillonite with cation surfactant, cetyltrimethyl ammonium bromide (CTMAB)	Tetrahydrofuran	80–90	Complete removal of BDE 209 was achieved within 180 min of irradiation
[25]	Copper-exchanged aluminum-pillared clay	Olive oil wastewater treatment	Adsorption of polyphenols and TOC	UV	Commercial montmorillonite clay was supplied by CECA (France). Aluminum and copper nitrates were used as precursors for the pillaring solution and copper exchange reaction	H <sub>2</sub> O <sub>2</sub>	100	TOC and polyphenols were removed



Table 16.1 (continued)

References	Catalyst	Raw material	Products	Temperature and pressure	Procedure of catalyst preparation	Oxidizing agent	Conversion (%)	Comments
[26]	Fe-impregnated pillared montmorillonite K10	2-Naphthol (1 mmol) is mixed with 10 ml water and 0.1 ml TBHP	Binol	25–28 °C	FePLS catalysts were prepared by pillaring of Fe <sup>3+</sup> using anhydrous sodium carbonate, then montmorillonite clay (10 g) was added to it for 10 min. This resulting slurry was kept for 5 h, finally washed, dried, and activated at 550 °C	TBHP	99	Pillaring Fe <sup>3+</sup> -impregnated, K10-FePLS120 was found to be the best recycle heterogeneous catalyst
[27]	Clay-supported ceric ammonium nitrate (CAN), supported clay	Methanol (3 ml) was placed in 0.148 g of styrene and 250 mg of CAN-supported montmorillonite K10	Benzaldehyde	Room temperature	Montmorillonite K10 clay was obtained from Fluka and used as received. The cerium was ion exchanged into the montmorillonite K10 clay by stirring with ceric ammonium nitrate at room temperature for 72 h. After exchange, the clay was filtered washed, and dried	Molecular O <sub>2</sub>	95	Selective oxidation of olefins, chalcones, and their derivative to the corresponding carbonyl compounds; CAN supported with montmorillonite clay first time is reported
[28]	Hastelloy-C, SUS-316, and Teflon	Naphthalene	CO <sub>2</sub> , organic acids	27–120 °C/ 2 atm	Directly obtained from market	H <sub>2</sub> O <sub>2</sub>	99	SUS-316 is preferable for complete oxidation of styrene

Table 16.1 (continued)

References	Catalyst	Raw material	Products	Temperature and pressure	Procedure of catalyst preparation	Oxidizing agent	Conversion (%)	Comments
[29]	Fe(III)-montmorillonite clay	Penta-chlorophenol	Octachlorodibenzodioxin	25 °C	The clay suspension was first titrated to pH 6.8 and 0.5 M sodium acetate buffer to remove carbonate impurities. It was centrifuged for 6 min and then treated with 0.1 M FeCl <sub>3</sub> solution six times. Finally, it was washed with water until free of chlorides (checked by AgNO <sub>3</sub> )	Acetone	100	Fe(III)-montmorillonite clay catalyst demonstrated the plausibility of PCDD formation in situ soil and clay deposits
[30]	Montmorillonite KSF	Bisphenol A	Adsorption	27 °C	Montmorillonite KSF clay was purchased from market	Carboxylic salts	81	In this work the photodegradation of BPA in the heterogeneous system with montmorillonite KSF reagent is investigated
[31]	Accelerated UV light and organophilic montmorillonite clay (OHMT)	Polystyrene/clay nanocomposites	Styrene	40 °C	PS/OMMT nanocomposites were prepared by melt mixing in a Brabender Plastli-Corder	UV		PS and PS/OMMT nanocomposites proceed mainly through chain scission

Table 16.1 (continued)

References	Catalyst	Raw material	Products	Temperature and pressure	Procedure of catalyst preparation	Oxidizing agent	Conversion (%)	Comments
[32]	Montmorillonite nanocomposites (MMT)	Polystyrene	Styrene	Room temperature	The PS was absorbed in MMY as PS/O-MMTS, PS/Na/MMT from standard alkyl solution	UV		The degradation of PS was found to be faster than pristine PS
[33]	Titania clay composites	Phenol (0.5 mM) in water	Degradation of reactants	Sunlight	TiO <sub>2</sub> /Ca–montmorillonite composites were prepared by wet grinding in an agate mill and TiO <sub>2</sub> nanoparticles were bound to the surface of the negatively charged montmorillonite layers via heterocoagulation	Water vapor	96	Phenol solution and VOCs are degraded at significantly higher efficiency on TiO <sub>2</sub> /Ca–montmorillonite composites than on pure TiO <sub>2</sub>
[34]	Ironporphyrin (FeP) immobilized on montmorillonite	Azo dye	Tributylamine and 4-nitro aniline	Room temperature	FeP was prepared through reaction of the free base porphyrin with iron chloride and montmorillonite K10 was first submitted to ion exchange with NaCl solution. Finally both of them were added in deionized water and kept for 24 h and the catalytic filter and dried for 8 h at 80 °C	<i>tert</i> -Butyl hydroperoxide and iodosylbenzene	35	The catalyst is relatively stable and can be easily separated from reaction mixture

Table 16.1 (continued)

References	Catalyst	Raw material	Products	Temperature and pressure	Procedure of catalyst preparation	Oxidizing agent	Conversion (%)	Comments
[35]	Kaolinite and montmorillonite clay	$\text{Cr}^{6+}$ , conc. 50 $\mu\text{M}$	$\text{Cr}^{3+}$	25 °C	Kaolinite and montmorillonite clay were provided by the Nanjing Center	Citric acid	98	Montmorillonite and illite catalyze the reduction of $\text{Cr}^{6+}$ by citric acid. The catalytic impact was greatly affected by pH
[36]	Fe-CuL( $\text{NO}_3$ ) <sub>2</sub> ·4H <sub>2</sub> O on Zr-pillared clay	Cyclohexane	Cyclohexanol	150–210 °C	Montmorillonite clay was pillared with zirconium ions and then intercalated with the complex (Fe-CuL( $\text{NO}_3$ ) <sub>2</sub> ·4H <sub>2</sub> O) in 1:1 solution by stirring the mixture for 5 h, finally centrifuged and dried. In the next step, clay was treated NaCl and aged for 24 h and freshly prepared zirconium oxychloride solution was added. Final step was the intercalation of complex in the clay layers refluxed with complex dissolved in acetonitrile for 24 h at 80 °C and washed with acetone	O <sub>2</sub>	14.4	Cyclohexanol shows up in the GC analysis and cyclohexyl hydroperoxide was not detected in product mixture

Table 16.1 (continued)

References	Catalyst	Raw material	Products	Temperature and pressure	Procedure of catalyst preparation	Oxidizing agent	Conversion (%)	Comments
[37]	LiCl on montmorillonite K10	Benzyl alcohol	Benzaldehyde	Room temperature	Lithium chloride (2 g) is added to deionized water (100 ml) and the mixture is stirred for 5 min until complete dissolution of the lithium chloride, then clay is added (8 g), the resulting suspension is refluxed and stirred vigorously for 2 h and the solvent is evaporated. Then the residue is kept at 120 °C for 24 h	H <sub>2</sub> O <sub>2</sub>	71–95	High yield, easy workup, and reusability of the catalyst are the advantages of this method
[38]	Zeolite H-Y and montmorillonite K10	Epoxidized methyl- <i>cis</i> -octadecenoate	Epoxide	30 °C	Catalysts were supplied by DuPont and Rohm and Haas	Isobutyric acid	28–60	K10 and SAC80 lead to higher eOME conversions, but process is very costly and hence it is not recommended
[39]	Cu–Ce mixed oxide on Al-pillared clay	CO, H <sub>2</sub> , and CH <sub>4</sub>	CO <sub>2</sub>	150 °C/100 psi	The preparation of the samples was done by three different methods, viz. amorphous citrate route (ACRI), deposition precipitation, and wet impregnation method		96	No methanation activity was observed at any reaction conditions on these clay catalysts

Table 16.1 (continued)

References	Catalyst	Raw material	Products	Temperature and pressure	Procedure of catalyst preparation	Oxidizing agent	Conversion (%)	Comments
[40]	Sodium ferrate in copper nanoparticle on montmorillonite K10	Benzyl alcohol, benzaldehyde	Benzaldehyde benzoic acids	30 °C	Catalyst sodium ferrate was prepared by taking 1 g ferric nitrate in a 50-ml flask and required amount of sodium hypochlorite solution was added with stirring. Purple red precipitate was obtained. Ferrate dianions, copper nanoparticles were prepared by adding borohydrate solution to 10 ml of sodium borohydrate solution	NaClO	70–87	The one-pot system does not require tedious separation of ferrate and is quick and environmentally benign
[41]	Zr–Zr complex on montmorillonite clay	Polystyrene (200 g) of commercial grade without solvent	Wax	300–400 °C/ 120 psi	The Zr–Zr complex is prepared by adding 0.95 g 2,6-diformyl 4 methylphenol, 1,2-phenylenediamine, and zirconium oxychloride in 50 ml of DMF. Then the product is dissolved in a solution containing 0.336 phenylenediamine and 50 ml methanol and finally kept for 2 weeks for precipitation	Polystyrene wax having M.P. of 60 °C	100	There is no gas formation during the depolymerization and only wax is obtained

Table 16.1 (continued)

References	Catalyst	Raw material	Products	Temperature and pressure	Procedure of catalyst preparation	Oxidizing agent	Conversion (%)	Comments
[42]	Mn(III)-salen complexes on Al-pillared clays	0.2 mmol styrene, 0.2 mmol chlorobenzene, and 0.1 mmol PhIO in 5 cm <sup>3</sup> of acetonitrile	Epoxide, benzaldehyde	0 °C/1 atm	The PILCs, Al-WYO, and Al-BEN were prepared by using an aluminum oligomeric solution made from AlCl <sub>3</sub> and NaOH by precipitation and then the solid material was calcined at 350 °C. The PILC Al-TERG was prepared from BEN clay using oligomer	Iodosylbenzene (PhIO) in acetonitrile	40	Al-pillared, clay-based materials acted in epoxidation of styrene with moderate alkene conversions
[43]	Cobalt porphyrin complex immobilized on montmorillonite	0.04 mol cyclohexene in 0.06 mol isobutyaldehyde	1,2-Epoxy-cyclohexane and cyclohexane stream	120 °C under nitrogen	200 ml of 0.1 M nitric acid solution, 4.2–100×10 <sup>-5</sup> mol of porphyrinato cobalt complex was dissolved, then Na-montmorillonite mixture (2.5 g in 200 ml water) was added. The solution was refluxed for 5 h and the obtained solid was filtered, washed, and finally dried at room temperature	Molecular oxygen and acetonitrile	17–60	The catalytic activity of these materials was found remarkably high in the oxidation of cyclohexene by oxygen in the presence of isobutyaldehyde compared with homogeneous complex catalyst

Table 16.1 (continued)

References	Catalyst	Raw material	Products	Temperature and pressure preparation	Procedure of catalyst and pressure preparation	Oxidizing agent	Conversion (%)	Comments
[44]	Cobalt-salen-intercalated montmorillonite	<i>p</i> -Cresol	<i>p</i> -Hydroxybenzaldehyde and <i>p</i> -hydroxybenzoic acid	65 °C and ambient pressure	A slurry of montmorillonite clay (5 g) in chloroform and N <sub>2</sub> gas is bubbled for inert atmosphere, then Co-salen solution in chloroform is added to this slurry under N <sub>2</sub> atmosphere. It is stirred for 6 h and aged for 12 h and then washed with chloroform and acetone	NaOH and CH <sub>3</sub> OH	10–36	Activity of cobalt-salen intercalated into montmorillonite catalyst gave a TON as high as 150 with a selectivity of 90% to the oxygenated products for air oxidation of <i>p</i> -cresol under ambient pressure conditions
[45]	Binuclear macrocyclic copper complex bonded ionically to the montmorillonite clay	Cyclohexane	Cyclohexanone	145–190 °C	The acid-treated montmorillonite (procured from Ashapura Minechem Ltd Mumbai, India) was pillared with zirconium ions and then intercalated with complex	O <sub>2</sub>	21	The heterogeneous catalyst in this case was stable at high temperatures as confirmed by TG analysis. And it showed very high selectivity of cyclohexanone



Table 16.1 (continued)

References	Catalyst	Raw material	Products	Temperature and pressure	Procedure of catalyst preparation	Oxidizing agent	Conversion (%)	Comments
[46]	Clay-anchored no-heme iron-salen	Olefins and chalcones	Aldehyde and its derivative of chalcone ketones	Room temperature	Clay-anchored iron-salen complex synthesized by direct exchange method	Acetonitrile and H <sub>2</sub> O <sub>2</sub>	76–98	The reaction has been carried out with olefin (50 mg), 3 ml acetonitrile, and 30% H <sub>2</sub> O <sub>2</sub> in water in the presence of heterogeneous catalyst
[47]	Mn(III) complex catalyst on aluminum-pillared clays	Styrene	Epoxide, benzaldehyde	Room temperature and atmosphere	0.8 g of dried Al-WYO were added to 0.098 g of Mn(II) chloride tetrahydrate in 100 ml methanol, refluxed for 6 h, then 0.021 g of H <sub>2</sub> salPh was added and refluxed for 6 h, finally washed and centrifuged with dichloromethane	PhIO in Acetonitrile	60	Epoxidation is carried out at room temperature and catalyst activity is sustained even after manganese content is reduced
[48]	Mn(III) porphyrin with Al, V, Si	Cyclohexane and styrene in acetonitrile	Epoxide and allylic	25 °C	Mn(III) porphyrin-supported catalyst were prepared by stirring an aqueous solution containing MnTAPP with Al-MCM-41 or V-MCM at room temperature for 24 h. Materials was filtered and washed with water	Acetonitrile iodosal-benzene	40.5	It is found that the conversion of alkene increases with decrease in the Si/Al or Si/V ratio

Table 16.1 (continued)

References	Catalyst	Raw material	Products	Temperature and pressure preparation	Procedure of catalyst and pressure preparation	Oxidizing agent	Conversion (%)	Comments
[49]	Cobalt salophen into montmorillonite clay	Cyclohexane	Epoxide	35 °C	An absolute alcohol solution (70 ml) of salicylaldehyde (1.5 g) was added dropwise with stirring for 1.5 h into a solution of phenylenediamine (0.65 g) in warm ethanol (40 ml), then heated under reflux at 80 °C, filtered, and dried at room temperature for 10 h. The final catalyst was prepared by adding 1.5 g montmorillonite in $\text{Co}(\text{NO}_3)_2 \cdot 6\text{H}_2\text{O}$ at 40 °C for 24 h, filtered, and dried; the Schiff base in hot ethanolic solution was added later. The slurry obtained was heated under reflux at 80 °C with stirring for 10 h. Finally, the Co-L/montmorillonite catalyst was dried in vacuum at 50 °C	Air	23.6–94.2	The immobilized catalyst showed high activity and epoxide selectivity for aerobic epoxidation of cyclohexane under Mukaiyama's conditions
[50]	Fe and Mn on porphyrins supported on aminofunctionalized montmorillonite	Carbamazepine (2.0 mg) is added to a mixture of 1.5 ml CAN and 2.6 mg PhIO	Carbamazepine-pinetrans diol	Room temperature	Mn and Fe (TFPP)Cl covalently immobilized on the aminofunctionalized supports montmorillonite K-10 (MontX) and silica (SiX), where X = 1 or 2 represents the length of the organic chain binding the metalloporphyrin to the support	PhIO and $\text{H}_2\text{O}_2$	90	CBZ-EP is the main metabolite produced during carbamazepine metabolism by P450 in vivo

to form a chelate complex. Nitrogen, phosphorus, oxygen, sulfur, and the halides are some of the common elements that act as donor atoms. The compounds that contain carbon donor atoms are called organometallic compounds. Cyclic compounds which contain donor atoms oriented so that they can bind to a metal ion and are large enough to encircle it are known as macrocyclic ligands. Sometimes ligands can bind to more than one metal ion in a bridging arrangement. Polydentate ligands which can link several metal ions together are referred to as polynucleating ligand. Synthetic macrocyclic ligands have attracted a great deal of attention because they can be used as models for more intricate biological macrocyclic systems. In the latter, difference in interaction between the protons, metal cations, and anions can be obtained with different donor atoms. Macrocyclic complexes are also known to possess significant thermodynamic stability and the selectivity of the metal ions into the ligand cavity can be varied by varying the donor atoms.

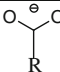
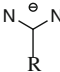
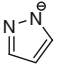
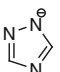
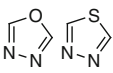
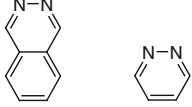
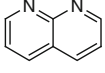
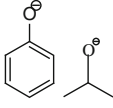
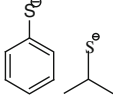
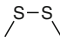
Different types of ligands can coordinate to transition metal ions and on doing so the reactivity of the metals may change drastically. Therefore, the rate and selectivity of a given process can be optimized by changing the ligand environment. It is also found that the multimetallic system provides new reactivity patterns and physical properties that are not achieved with similar monometallic complexes. The difference in their physical properties was thought to arise due to the electronic interactions between the metals.

Monometallic ligands are formed by the five-membered or six-membered chelate rings. The six-membered rings are less stable compared to the five-membered rings because of entropy considerations [52]. When the chelate rings are made up of aliphatic amine groups [which are donor atoms (denoted by D)], the rings undergo chiral, achiral chair, and chiral skew conformations [53]. If the donor nitrogen atoms are replaced by phosphines or arsines, divalent oxygen or sulfur groups, the rings undergo similar kind of transformations. When ternary amines, phosphines, and arsines are coordinated to a metal, the donor atom becomes a quaternary chiral center, while secondary sulfides form a tertiary chiral center. The chirality and the chiral stability of amines, phosphines, arsines, and sulfides have important consequences in controlling the topology of multidentate chelates [54]. Binucleating ligands have been classified based on the bridging groups that are used to assemble bimetallic complexes [52]. Various bridging groups that are used have been given in Table 16.2 [55–67] and can be classified as those that have single-atom bridges, those with two-atom bridges, and those with three-atom bridges as shown in this table.

### ***16.1.3 Scope of the Present Work***

It is seen that the complexes used in literature for catalysis decompose at low temperature and pressure due to chemical and thermal instability. To overcome this problem, we have prepared 10 macrocyclic complexes by reaction of 2,6-diformyl-4-methylphenol and 1,2-phenylenediamine to get the L-1 ligand (see Table 16.3) and 2,6-diformyl-4-methylphenol and 1,3-diaminopropane to get the L-2 ligand (see Table 16.4). The ionic bonding of these complexes with montmorillonite clay

**Table 16.2** Various bridging groups used for binucleating ligands

Bridging unit	Structure	Example	References
Carboxylate		$\text{Fe}_2(\text{I})_2(\text{CH}_3\text{OH})_2](\text{ClO}_4)_2$	[55]
Formamidinate		$\text{Pd}_2(\mu\text{-Cl})(\text{II})\text{Cl}_2$	[56]
Pyrazolate		$\text{Cu}_2(\text{III})_2(\text{BF}_3)_2\cdot(\text{CH}_3)_2\text{CO}$	[57]
Triazolate		$[\text{Cu}_2(\text{IV})_2\text{Br}_2(\text{H}_2\text{O})_2]^+$	[58]
Oxadiazole, thiadiazole		$[\text{Co}_2(\mu\text{-OAc})_2(\text{V})]\cdot\text{CH}_2\text{Cl}_2$	[59]
Pyridazine and pthalazine		$[\text{Co}_2^{2+}(\text{VI})(\text{CH}_3\text{CN})_4]$ $(\text{ClO}_4)_4\text{CH}_3\text{CN}$	[60, 61]
1,8-Naphthyridine		$[\text{Co}_2(\mu\text{-OH})-(\mu\text{-Cl})\cdot(89)]\text{Cl}_2$	[62]
Phenolate, alkoxide		$[\text{Fe}_2^{3+}(\mu\text{-OCH}_3)(103)(\text{Cl})_2\cdot(\text{CH}_3\text{OH})]$	[63]
Thiophenolate, thiolate		$[\text{Cr}_2^{2+}(165)_3](\text{ClO}_4)_2\text{Cl}\cdot\text{H}_2\text{O}\cdot\text{CH}_3\text{OH}$	[64–66]
Disulfide		$[(\text{Ir}(\text{SCH}_2\text{CH}_2\text{NH}_2)_2)_2\text{-}(176)]^{2+}$	[67]

**Table 16.3** Homodinuclear macrocyclic complexes synthesized

No.	Complex	M <sub>A</sub> M <sub>A</sub> L'	M <sub>A</sub> M <sub>A</sub> L
1	CuCuL-1 (CH <sub>3</sub> COO) <sub>2</sub>	Dialdehyde (2 g, 0.0122 mol) + <i>o</i> -phenylenediamine (0.65 g, 0.006 mol) + cupric acetate (2.44 g, 0.0122 mol) all in DMF (50 ml) at 40 °C. Kept for 3 h. Diethyl ether was added. Precipitate obtained (CuCuL-1'), collected by filtration and dried	CuCuL-1' (1.8 g, 0.0034 mol) + <i>o</i> -phenylenediamine (0.37 g, 0.0034 mol) in methanol (40 ml). Kept for 3 h. Diethyl ether was added. Precipitate obtained (1.68 g) was the final complex, collected by filtration and dried
2	MnMnL- 1•2H <sub>2</sub> O	Dialdehyde (2 g, 0.0122 mol) + <i>o</i> -phenylenediamine (0.65 g, 0.006 mol) + manganous chloride (2.41 g, 0.0122 mol) all in DMF (50 ml) at 40 °C. Kept for 3 h. Diethyl ether was added. Precipitate obtained (MnMnL-1'), collected by filtration and dried	MnMnL-1' (2.1 g, 0.0041 mol) + <i>o</i> -phenylenediamine (0.44 g, 0.0041 mol) in methanol (40 ml). Kept for 3 h. Diethyl ether was added. Precipitate obtained (1.82 g) was the final complex, collected by filtration and dried
3	NiNi L-1•2H <sub>2</sub> O	Dialdehyde (2 g, 0.0122 mol) + <i>o</i> -phenylenediamine (0.65 g, 0.006 mol) + nickel chloride (2.9 g, 0.0122 mol) all in DMF (50 ml) at 40 °C. Kept for 3 h. Diethyl ether was added. Precipitate obtained (NiNiL1-1'), collected by filtration and dried	NiNiL-1' (2.08 g, 0.004 mol) + <i>o</i> -phenylenediamine (0.43 g, 0.004 mol) in methanol (40 ml). Kept for 3 h. Diethyl ether was added. Precipitate obtained (1. 98 g) was the final complex, collected by filtration and dried
4	CuCuL-2	Dialdehyde (2 g, 0.0122 mol) + 0.5 ml 1,3-diaminopropane (0.4 g, 0.006 mol) + cupric acetate (2.44 g, 0.0122 mol) all in DMF (50 ml) at 40 °C. Kept for 1 h. Diethyl ether was added. Precipitate obtained (CuCuL-2'), collected by filtration and dried	CuCuL-2' (1.87 g, 0.0038 mol) + 0.3 ml 1,3-diaminopropane (0.282 g, 0.0038 mol) in methanol (40 ml). Kept for 1 h. Diethyl ether was added. Precipitate obtained (1.85 g) was the final complex, collected by filtration and dried
5	CoCoL-2 (Cl <sub>2</sub> ) <sub>2</sub> •4H <sub>2</sub> O	Dialdehyde (2 g, 0.0122 mol) + 0.5 ml 1,3-diaminopropane (0.4 g, 0.006 mol) + cobaltous chloride (2.9 g, 0.0122 mol) all in DMF (50 ml) at 40 °C. Kept for 1 h. Diethyl ether was added. Precipitate obtained (CoCoL-2'), collected by filtration and dried	CoCoL-2' (1.96 g, 0.004 mol) + 0.34 ml 1,3-diaminopropane (0.3 g, 0.004 mol) in methanol (40 ml). Kept for 1 h. Diethyl ether was added. Precipitate obtained (1.78 g) was the final complex, collected by filtration and dried
6	VVL-2•2H <sub>2</sub> O	Dialdehyde (2 g, 0.0122 mol) + 0.5 ml 1,3- diaminopropane (0.4 g, 0.006 mol ) + vanadyl sulfate (3.09 g, 0.0122 mol) all in DMF (50 ml) at 40 °C. Kept for 1 h. Diethyl ether was added. Precipitate obtained (VVL-2'), collected by filtration and dried	VVL-2' (1.79 g, 0.0038 mol) + 0.3 ml 1,3-diaminopropane (0.282 g, 0.0038 mol) in methanol (40 ml). Kept for 1 h. Diethyl ether was added. Precipitate obtained (1.71 g) was the final complex, collected by filtration and dried

**Table 16.4** Heterodinuclear macrocyclic complexes synthesized

No. Complex	M <sub>A</sub> L'	M <sub>A</sub> M <sub>B</sub> L'	M <sub>A</sub> M <sub>B</sub> L
1 CuFeL-1•4H <sub>2</sub> O	Dialdehyde (2 g, 0.0122 mol) + <i>o</i> -phenylenediamine (0.65 g, 0.006 mol) + cupric acetate (1.2 g, 0.006 mol) all in DMF (50 ml) at 40 °C. Kept for 3 h. Diethyl ether was added. Precipitate obtained (CuL-1'), collected by filtration and dried	Ferric nitrate (1.67 g, 0.004 mol) + CuL-1' (1.87 g, 0.004 mol) all in methanol (40 ml). Kept for 3 h. Diethyl ether was added. Precipitate obtained (CuFeL-1'), collected by filtration and dried	CuFeL-1' (1.97 g, 0.0038 mol) + <i>o</i> -phenylenediamine (0.41 g) all in methanol (30 ml). Kept for 3 h. Diethyl ether was added. Precipitate obtained (1.85 g) was the final complex, collected by filtration and dried
2 FeCuL-2 (NO <sub>3</sub> ) <sub>2</sub> •4H <sub>2</sub> O	Dialdehyde (2 g, 0.0122 mol) + 0.5 ml 1,3-diaminopropane (0.4 g, 0.006 mol) + ferric nitrate (2.5 g, 0.006 mol) all in DMF (50 ml) at 40 °C. Kept for 1 h. Diethyl ether was added. Precipitate obtained (FeL-2'), collected by filtration and dried	Cupric acetate (0.9 g, 0.0045 mol) + FeL-2' (1.9 g, 0.0045 mol) all in methanol (40 ml). Kept for 1 h. Diethyl ether was added. Precipitate obtained (FeCuL-2'), collected by filtration and dried	FeCuL-2' (1.83 g, 0.0038 mol) + 0.3 ml 1,3-diaminopropane (0.282 g, 0.0038 mol) all in methanol (30 ml). Kept for 1 h. Diethyl ether was added. Precipitate obtained (1.8 g) was the final complex, collected by filtration and dried
3 CuCoL-2 (Cl <sub>2</sub> ) <sub>2</sub> •4H <sub>2</sub> O	Dialdehyde (2 g, 0.0122 mol) + 0.5 ml 1,3-diaminopropane (0.4 g, 0.006 mol) + cupric acetate (1.2 g, 0.006 mol) all in DMF (50 ml) at 40 °C. Kept for 1 h. Diethyl ether was added. Precipitate obtained (CuL-2'), collected by filtration and dried	Cobaltous chloride (1.14 g, 0.0048 mol) + CuL-2' (2.07 g, 0.0048 mol) all in methanol (40 ml). Kept for 1 h. Diethyl ether was added. Precipitate obtained (CuCoL-2'), collected by filtration and dried	CuCoL-2' (1.93 g, 0.004 mol) + 0.34 ml 1,3-diaminopropane (0.3 g, 0.004 mol) all in methanol (30 ml). Kept for 1 h. Diethyl ether was added. Precipitate obtained (1.85 g) was the final complex, collected by filtration and dried
4 NiCuL-2•8H <sub>2</sub> O	Dialdehyde (2 g, 0.0122 mol) + 0.5 ml 1,3-diaminopropane (0.4 g, 0.006 mol) + nickel acetate (1.49 g, 0.006 mol) all in DMF (50 ml) at 40 °C. Kept for 1 h. Diethyl ether was added. Precipitate obtained (NiL-2'), collected by filtration and dried	Cupric acetate (0.88 g, 0.0044 mol) + NiL-2' (1.86 g, 0.0044 mol) all in methanol (40 ml). Kept for 1 h. Diethyl ether was added. Precipitate obtained (NiCuL-2'), collected by filtration and dried	NiCuL-2' (1.97 g, 0.0041 mol) + 0.34 ml 1,3-diaminopropane (0.3 g, 0.004 mol) all in methanol (30 ml). Kept for 1 h. Diethyl ether was added. Precipitate obtained (1.89 g) was the final complex, collected by filtration and dried

has been found to have thermal as well as chemical stability and the catalyst thus formed can be used for oxidation of cyclohexane as described below. The oxidation of cyclohexane has been studied using two catalysts, viz. FeCuL-2/montmorillonite and CuCuL-1/montmorillonite. In FeCu complex the L-2 ligand is more efficient, while in CuCu complex the L-1 ligand is more efficient. Experimental data were taken at regular intervals and the rate constants have been determined using genetic algorithm.

## 16.2 Experimental

### 16.2.1 Preparation of the Macrocyclic Complex

Homodinuclear (similar metals where  $M_A = M_B$ ) and heterodinuclear (i.e., dissimilar metals where  $M_A \neq M_B$ ) macrocyclic complexes of various metals were synthesized. For this, first 2,6-diformyl-4-methyl phenol was prepared following the procedure given in literature [68] given below. For the preparation of the complex, two equivalents of 2,6-diformyl-4-methyl phenol was condensed with two equivalents of 1,2-phenylenediamine to obtain the L-1 ligand. To obtain the L-2 ligand, two equivalents of 2,6-diformyl-4-methyl phenol were condensed with two equivalents of 1,3-diamino propane. This is done in two stages forming  $M_A L'$  and  $M_A M_B L'$  to form the final complex  $M_A M_B L$ .

#### 16.2.1.1 Preparation of 2,6-Diformyl-4-methylphenol (Dialdehyde)

*p*-Cresol (216 g, 2 mol) is added to NaOH solution (prepared by dissolving 100 g of NaOH in 400 ml water) which slowly turns into a gold color. A 37% formaldehyde (430 g) solution is added to it (step 1 of Fig. 16.1) and the mixture is stirred for 20 min and left for 24 h at ambient temperature (35°C). The yellow granular product obtained is 2,6-dimethylol-4-methylphenol which is collected by vacuum filtration and washed with saturated sodium chloride solution. This product is transferred to a three-necked, 5-l round-bottom flask fitted with an overhead stirrer. To the above mixture, 1300 ml double-distilled water and 130 ml of 33% NaOH are added and stirred for 0.5 h. Following this, 494 g (2.6 mol) of *p*-toluene sulfonyl chloride dissolved in toluene is added and stirred for 20 h at room temperature (step 2 of Fig. 16.1). This mixture is cooled in an ice bath and toluene (200 ml) is added with stirring. After 10 min, additional toluene (300 ml) is added and at this stage, white solid is formed. After 1 h, 100 ml of toluene and the slurry are added and stirred for 15 min. A white solid (which is tosylated phenol) is formed, is collected by vacuum filtration, and washed with toluene (400 ml) and dried under vacuum for 12 h.

The tosylated phenol (272 g, 0.8 mol) is now oxidized with sodium dichromate (208 g, 0.69 mol) and acetic acid (645 ml). Acetic acid (160 ml) is taken in a three-necked reactor vessel of 2 l volume, which is equipped with a stirrer, an addition

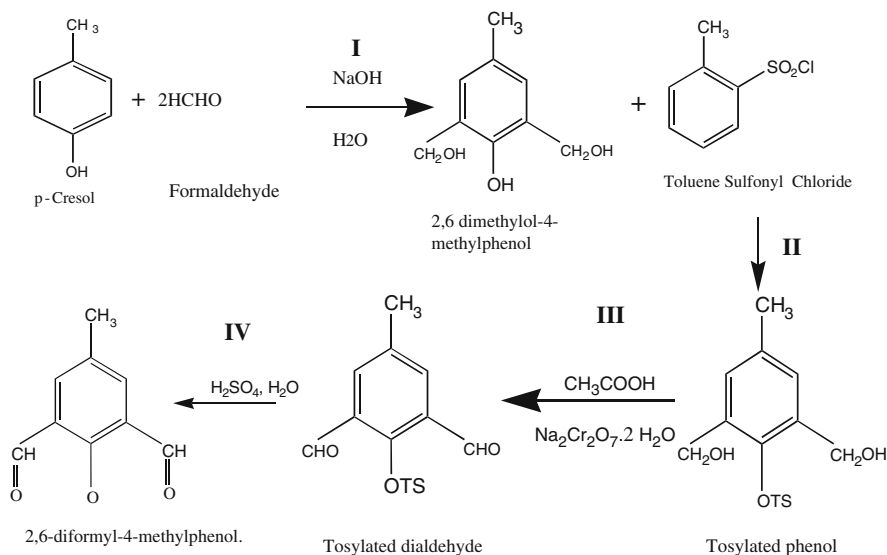


**Fig. 16.1** Synthesis of 2,6-diformyl-4-methylphenol (dialdehyde) used in complex preparation

funnel, and a water-cooled reflux condenser. The sodium dichromate is dissolved in the remaining acetic acid (485 ml) and is introduced through the addition funnel dropwise with stirring for about 40 min at 110 °C. The reaction mixture is cooled, filtered, and washed with water to get green-colored crystals of tosylated dialdehyde (250 g) (step 3 of Fig. 16.1). The tosylated dialdehyde is taken in a 5-l beaker and 900 ml of H<sub>2</sub>SO<sub>4</sub> is added to it. This mixture is stirred for 1 h and ice-water slurry is added till the volume becomes 4 l. The precipitated material is collected by vacuum filtration, washed with water, and dried. This is then dissolved in toluene and the liquid is recrystallized which gives brownish yellow-colored needle-like crystals. The product obtained is 2,6-diformyl-4-methylphenol; temperature (step 4 of Fig. 16.1) and the melting point of this compound is determined to be 130 °C (133.5 °C is the value reported in literature). The peaks in the NMR spectrum which shows singlets at 11.42 (phenolic), 10.18 (aldehyde), 7.74 (aromatic), and 2.36 (methyl) are matched with the literature values.

Two types of binucleating (homodinuclear and heterodinuclear) macrocyclic ligands are synthesized by varying the lateral chain. One complex is derived by condensing 2 equiv. of 2,6-diformyl-4-methylphenol with 2 equiv. of *o*-phenylenediamine, denoted as L-1, and the second one is formed by condensing 2 equiv. of 2,6-diformyl-4-methylphenol with 2 equiv. of 1,3-diaminopropane, denoted as L-2. Both these complexes have two identical N<sub>2</sub>O<sub>2</sub> sites. The procedures for the synthesis of homodinuclear and heterodinuclear complexes are given below.



### 16.2.1.2 Synthesis of Homonuclear $\text{CuCuL-1,2}(\text{CH}_3\text{COO}) [\text{L-1} = (\text{CH}_3\text{C}_6\text{H}_2(\text{CH})_2\text{ON}_2\text{C}_6\text{H}_4)_2]$ Macrocylic Complex

$\text{CuCuL-1}'$ . To 50 ml of *N,N*-dimethylformamide at 40 °C, 2,6-diformyl-4-methylphenol (1.95 g, 0.012 mol) and 1,2-phenylenediamine (0.65 g, 0.006 mol) are added. To this solution, cupric acetate (2.4 g, 0.012 mol) is added and the solution stirred till the cupric acetate dissolves completely (step 1 of Fig. 16.2). The solution is kept for 1 h and then diethyl ether (50 ml) is added after which a precipitate appears. The precipitate is collected by filtration and dried. The FTIR spectrum in Fig. 16.3a shows the presence of functional groups  $\text{C}=\text{N}$  at  $1533\text{ cm}^{-1}$  and  $\text{C}=\text{O}$  at  $1668\text{ cm}^{-1}$ .

The  $\text{CuCuL-1}'$  (1.8 g, 0.0034 mol) obtained from the previous step is dissolved in 30 ml of methanol and to this solution, 1,2-phenylenediamine (0.37 g, 0.0034 mol) is added (step 2 of Fig. 16.2). The solution is kept for 1 h and to this diethyl ether (50 ml) is added. The precipitate that appears is collected by filtration and dried. The FTIR spectrum shown in Fig. 16.3b gives  $\text{C}=\text{N}$  at  $1512\text{ cm}^{-1}$ , while the  $\text{C}=\text{O}$  peak (appearing at  $1664\text{ cm}^{-1}$ ) becomes weak as it forms  $\text{C}=\text{N}$  bond on reaction with 1,2-phenylenediamine.

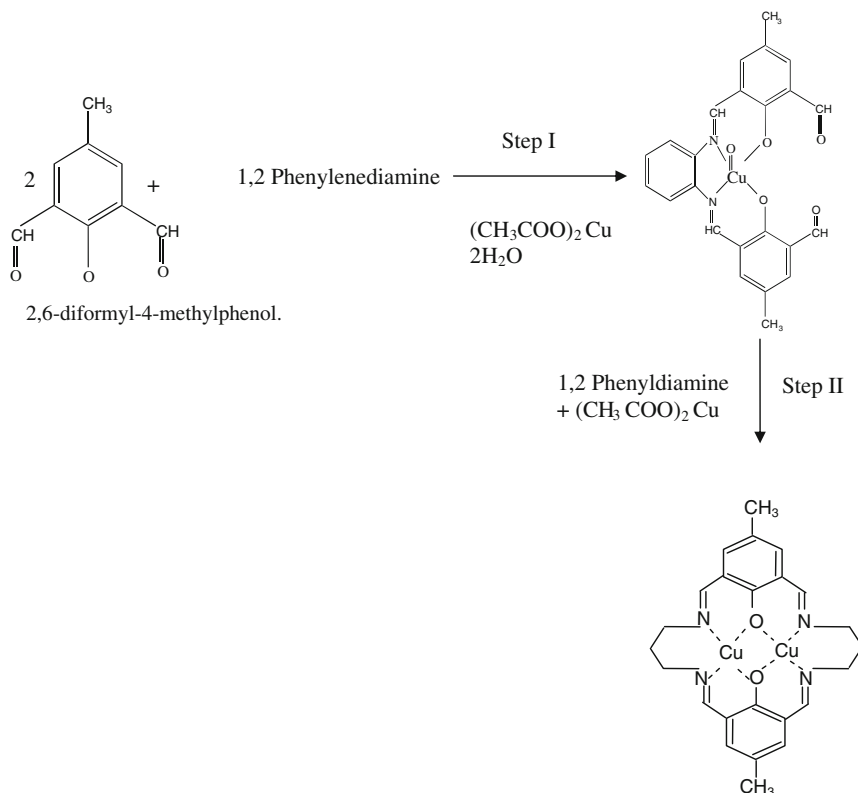


**Fig. 16.2** Synthesis of homonuclear macrocyclic copper complex of the L-1 ligand

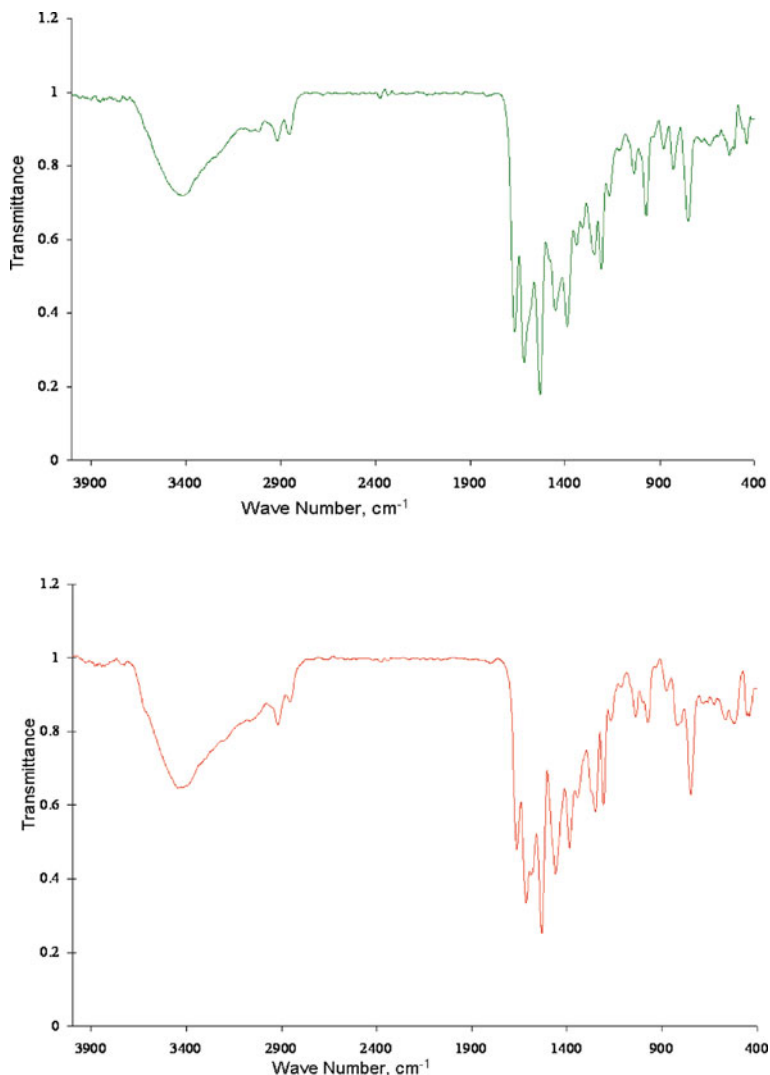


**Fig. 16.3** (a) FTIR spectra of CuCuL-1' which are formed in step 1 of Fig. 16.2. (b) FTIR spectra of CuCuL-1 complex which are formed in step 2 of Fig. 16.2

### 16.2.1.3 Synthesis of Heterobinuclear FeCuL-2 (NO<sub>3</sub>)<sub>2</sub>•4H<sub>2</sub>O Macrocylic Complex, L-2 = (CH<sub>3</sub>C<sub>6</sub>H<sub>2</sub>(CH)<sub>2</sub>O(CH<sub>2</sub>)<sub>3</sub>N<sub>2</sub>)<sub>2</sub>

*FeL-2'*: To 50 ml of *N,N*-dimethylformamide at 40 °C, 2,6-diformyl-4-methylphenol (1.95 g, 0.012 mol) is added first, followed by dropwise addition of 1,3-diaminopropane (0.5 ml, 0.006 mol) with stirring. To this solution, ferric nitrate (2.5 g, 0.006 mol) is added and the solution is stirred till all the ferric nitrate

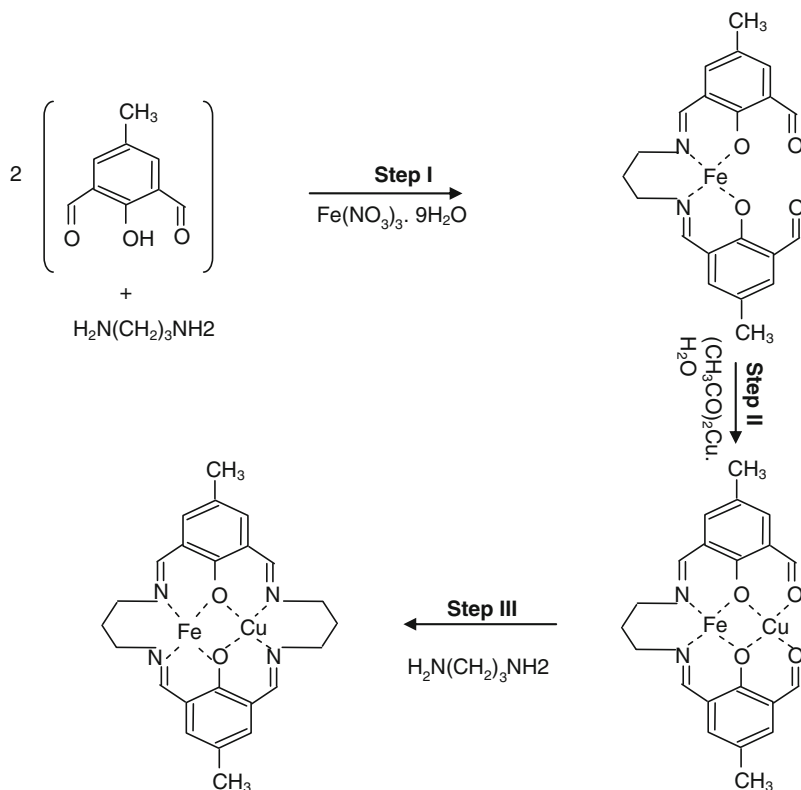


**Fig. 16.4** Synthesis of heterobinuclear macrocyclic FeCu complex of the L-2 ligand

dissolves completely (step 1 of Fig. 16.4). The solution is kept for 1 h after which diethyl ether is added, following which a precipitate appears which is filtered and dried. The FTIR spectrum shows the presence of functional groups  $\text{C}=\text{N}$  at  $1541\text{ cm}^{-1}$  and  $\text{C}=\text{O}$  at  $1671\text{ cm}^{-1}$ .

*FeCuL-2'*: The  $\text{FeL-2'}$  (1.9 g, 0.0045 mol) obtained from the previous step is dissolved in 30 ml of methanol and to this, cupric acetate (0.9 g, 0.0045 mol) dissolved in methanol is added with stirring (step 2 of Fig. 16.4). After 1 h, diethyl ether (50 ml) is added and within 30 min, olive green precipitate is formed which is filtered and dried. The FTIR spectrum once again shows the presence of functional groups  $\text{C}=\text{N}$  at  $1540\text{ cm}^{-1}$  and  $\text{C}=\text{O}$  at  $1666\text{ cm}^{-1}$ .

*FeCuL-2*: The  $\text{FeCuL-2'}$  (1.83 g, 0.0038 mol) is dissolved in 30 ml of methanol and to this, a solution of 1,3-diaminopropane (0.3 ml) is added dropwise with stirring. The solution is kept for 30 min and then diethyl ether (50 ml) is added to it (step 3 of Fig. 16.4). A precipitate is formed which is filtered from the solution and dried. The FTIR spectrum of the complex shows  $\text{C}=\text{N}$  at  $1532\text{ cm}^{-1}$  and the  $\text{C}=\text{O}$  peak does not appear as it forms  $\text{C}=\text{N}$  bond on reaction with 1,3-diaminopropane. To confirm the formation of the complex, the  $^1\text{H-NMR}$  spectrum of the complex

dissolved in  $d_6$ -DMSO is taken and it shows singlets at 9.149 ppm (phenolic), 3.378, and 2.072 ppm (aliphatic). The higher intensity at 2.072 ppm shows that the methyl peaks are overlapping with the aliphatic protons of the diaminopropane.

### 16.2.2 Synthesis of the Heterogeneous Complex Catalyst

In order to synthesize the heterogeneous catalyst, the acid (using HCl)-treated montmorillonite was procured from Ashapura Minechem Ltd, Mumbai, India. The montmorillonite clay was first pillared using zirconium ions and then was intercalated with the complex as shown in Fig. 16.5 The clay (20 g) was subjected

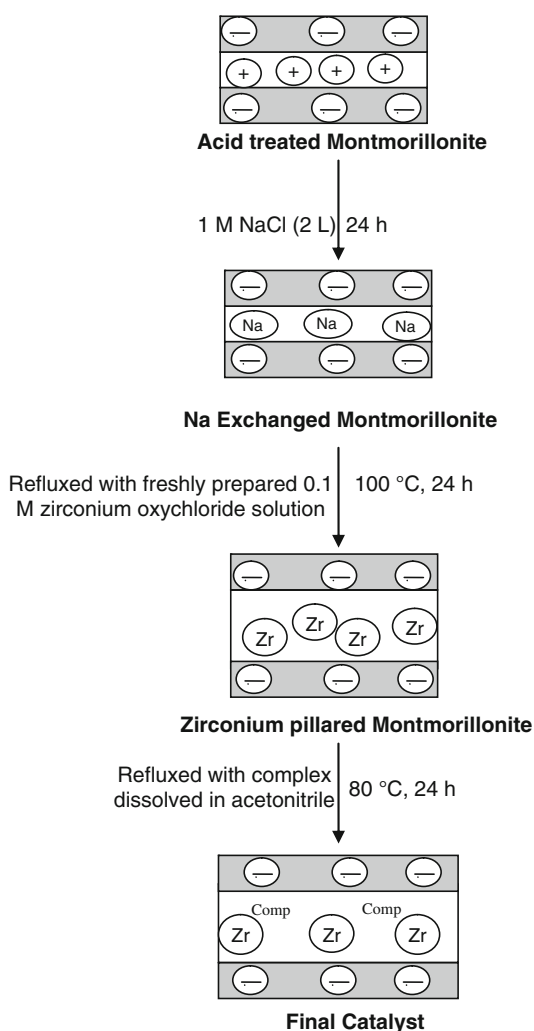


**Fig. 16.5** General scheme for complex catalyst preparation

to swelling by adding water (1 l) to the clay and stirring it for 5 h and the mixture was finally centrifuged and dried. In the next step, the clay was treated with NaCl solution (1 M) and this was aged for 24 h. The 20 g clay was separated, dried, and then refluxed with freshly prepared zirconium oxychloride (0.1 M) solution for 24 h at 100 °C to obtain zirconium-pillared montmorillonite. It was separated and dried after loading zirconium salt and its final weight was 28 g (an increase of 8 g). The final step is the intercalation of the complex in the clay layers and is shown in this figure. The clay (20 g) from this step was taken and refluxed with the metal complex (e.g., 1 g CuCu complex) dissolved in acetonitrile (250 ml) for 24 h at 80 °C. The final catalyst thus obtained was separated, washed with acetone, and dried. An increase in weight of 0.9 g was observed. The final weight of the catalyst was 20.9 g (an increase of 0.9 g).

## 16.3 Characterization of the Complexes and Their Catalysts

Tables 16.3 and 16.4 present the 10 complexes synthesized. Identical procedure has been used for the synthesis of all the complexes. The complexes have been characterized using (i) IR spectroscopy, (ii) C–H–N analysis (iii) TGA analysis, and (iv) single-crystal X-ray analysis.

### 16.3.1 FTIR Analysis of Complex

The FTIR analyses (Bruker Vector 22) of the complexes in Table 16.2 have been carried out in the range 400–4000  $\text{cm}^{-1}$ . The samples were ground with KBr (at about 1–3 wt%) and then pressed to 1-mm thick film. The analysis of the FTIR spectra is discussed below by taking the example of FeCuL-2 complex formation. The FTIR spectra of FeL-2', FeCuL-2', and FeCuL-2 confirm the formation of the complex and its intermediates by the frequencies of the C=N and C=O bonds. The C=N bond frequency for (i) FeL-2' appears at 1541  $\text{cm}^{-1}$  (Fig. 16.5a), (ii) FeCuL-2' appears at 1540  $\text{cm}^{-1}$ , and (iii) FeCuL-2 complex appears at 1532  $\text{cm}^{-1}$  (Fig. 16.5b). The C=O bond frequency for (i) FeL-2' appears at 1671  $\text{cm}^{-1}$  (Fig. 16.5c), (ii) FeCuL-2' appears at 1666  $\text{cm}^{-1}$  and disappears in the final step when the complex FeCuL-2' is reacted with 1,3-diaminopropane.

### 16.3.2 C–H–N Analysis of the Complex

The C–H–N analysis has been carried out on a CE-440 elemental analyzer (of Leimann Inc.). About 3–5 mg of the powdered sample is taken and first homogenized at 80 °C. Helium gas is used as a carrier and O<sub>2</sub> as oxidant and the sample is

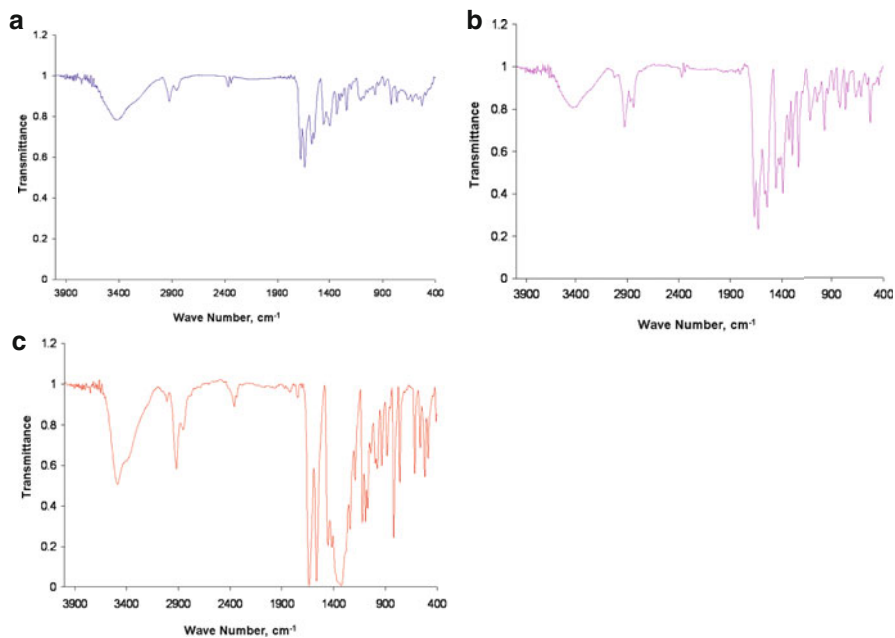
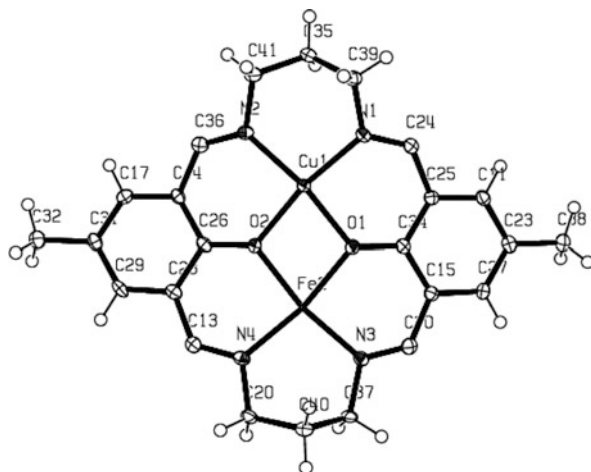


**Fig. 16.6** (a) FTIR spectra of  $\text{FeL-2'}$  which are formed in step 1 of the complex synthesis. (b) FTIR spectra of  $\text{FeCuL-2'}$  which are formed in step 2 of Fig. 16.4. (c) FTIR spectra of  $\text{FeCuL-2}$  complex which are formed in step 3 of Fig. 16.4

**Fig. 16.7** Molecular structure of the  $\text{FeCuL-2}$  macrocyclic complex as determined by single-crystal X-ray crystallography



heated to 950 °C. The percentage of carbon, hydrogen, and nitrogen present in the complexes is determined experimentally. The theoretical values (carbon, hydrogen, and nitrogen in the complex) are calculated from the molecular structure of the complex and are compared with the experimental values. The ligand L1 is  $C_{30}H_{22}N_4O_2$  and L2 is  $C_{24}H_{26}O_2N_4$  and one example of each ligand is discussed below. For the ligand L-1 the example of CuCu complex is given. Since it was prepared using cupric acetate, the complex was assumed to have  $CH_3COO$  attached to it and its molecular formula was taken as  $CuCuL-1(CH_3COO)_2$ . Thus the complex contains 34 carbon atoms, 28 hydrogen atoms, 6 oxygen atoms, 4 nitrogen atoms, and 2 copper atoms and the molecular weight of the complex is 715.092 g/mol. The theoretical values calculated for carbon, hydrogen, and nitrogen are 57.06, 3.92 and 7.83%, respectively. The experimentally obtained values are carbon 57.6%, hydrogen 3.9%, and nitrogen 6.9%. For the ligand L-2, the example of FeCu complex is given. Since the complex was prepared using ferric nitrate, the complex was assumed to have  $NO_3$  attached to it and its molecular formula was assumed to be  $FeCuL-2(NO_3)_2 \bullet 4H_2O$ . Thus the complex contains 24 carbon atoms, 34 hydrogen atoms, 12 oxygen atoms, 6 nitrogen atoms, 1 iron atom, and 1 copper atom. The molecular weight of the complex is 711.39 g/mol and the theoretical values calculated for carbon, hydrogen, and nitrogen are 40.15, 4.74, and 11.7%, respectively; the experimentally obtained values are 39.9% carbon, 3.995% hydrogen, and 11.93% nitrogen. A close agreement was observed between the experimental and theoretical values in the case of all the complexes as shown in Table 16.5.

**Table 16.5** C–H–N analysis of the complex synthesized. Comparison of experimentally obtained and theoretically calculated values is presented

Complex	Carbon		Hydrogen		Nitrogen	
	Experimental (%)	Theoretical (%)	Experimental (%)	Theoretical (%)	Experimental (%)	Theoretical (%)
CuCuL-1. ( $CH_3COO$ ) <sub>2</sub>	57.645	57.06	3.887	3.92	6.876	7.83
CuCuL-2	55.7	54.43	4.953	4.9	9.72	10.58
FeCuL-2. ( $NO_3$ ) <sub>2</sub> $\bullet 4H_2O$	39.914	40.145	3.995	4.74	11.931	11.7
CuCoL-2. ( $Cl_2$ ) <sub>2</sub> ( $H_2O$ ) <sub>4</sub>	38.49	39	4.953	4.6	7.647	7.59
CoCoL-2. ( $Cl_2$ ) <sub>2</sub> ( $H_2O$ ) <sub>4</sub>	38.206	39.25	4.861	4.63	8.129	7.63
NiNiL-1 $\bullet 2H_2O$	57.505	57.75	4.654	4.17	9.27	8.98
NiCuL-2 $\bullet 8H_2O$	43.204	43.099	6.464	6.29	7.443	8.38
MnMnL- 1 $\bullet 2H_2O$	58.076	58.44	3.728	4.22	10.549	10.39
VVL-2 $\bullet 2H_2O$	54.022	53.34	5.468	5.56	9.848	10.37
FeCuL-1 $\bullet 4H_2O$	53.771	54.43	4.283	4.54	8.742	8.47

### 16.3.3 Scanning Electron Microscopy of the Complex and the Catalyst

The SEM-EDX analyses of the complexes and the catalysts have been taken on a JEOL JSM-840A SEM and the presence of the metal on the catalyst has been confirmed. The sample is powdered and gold coated under vacuum to make it conducting for electrons. The metal content present in the sample is obtained from EDX analysis. The metal contents of the complexes are given in Table 16.6.

**Table 16.6** Metal content of the complexes obtained from EDAX

Complex	Metal 1 (%)	Metal 2
CuCuL-1	Cu = 16.89	–
CuCuL-2	Cu = 24.52	–
NiNiL-1	Ni = 18.02	–
MnMnL-1	Mn = 15.97	–
VVL-2	V = 17.68	–
CoCoL-2	Co = 15.65	–
FeCuL-2	Fe = 7.36	Cu = 8.43%
CuCoL-2	Cu = 8.17	Co = 6.87%
NiCuL-2	Ni = 8.34	Cu = 9.02%
FeCuL-1	Fe = 7.38	Cu = 9.46%

### 16.3.4 Single-Crystal X-Ray Analysis of the Complex

In order to grow the single crystal the following techniques were employed:

- Evaporation technique using methanol and dimethylformamide as solvents
- Solvent–nonsolvent diffusion technique using methanol, and
- n*-Hexane and vapor diffusion technique using methanol and diethyl ether

However, single crystals of all the complexes could not be obtained due to their low solubility. A single crystal of the FeCuL-2 complex was obtained. The crystals were obtained by dissolving the complex in methanol and then slowly evaporating the solvent at room temperature (28 °C). The single crystals thus obtained were used for data collection. Diffracted intensities were collected on a Bruker SMART APEX CCD diffractometer, with graphite-monochromated Mo K $\alpha$  ( $k = 0.71073 \text{ \AA}$ ) radiation at 100 K. For data reduction, “Bruker Saint Plus” program was used and the data were corrected for absorption. The structures were solved by SIR 92, expanded by Fourier-difference syntheses, and refined with the SHELXL-97 package incorporated into WinGX 1.64 crystallographic collective package [69]. The positions of the hydrogen atoms were calculated assuming ideal geometries. All non-hydrogen atoms were refined with anisotropic thermal parameters by full-matrix least-squares procedure. The structure of the complex obtained from this analysis is shown in Fig. 16.5 and the crystallographic parameters are summarized in Table 16.7. The selected bond lengths and bond angles are given in Table 16.8.



**Table 16.7** Crystal data and structure refinement parameters

Empirical formula	C <sub>24</sub> H <sub>22</sub> CuFeN <sub>6</sub> O <sub>9</sub>
Formula weight	657.87
Temperature	293(2) K
Wavelength	0.71069 Å
Crystal system space group	Orthorhombic, <i>P</i> -1
Unit cell dimensions	<i>a</i> = 8.565(5) Å, $\alpha$ = 90.000(5)° <i>b</i> = 18.262(5) Å, $\beta$ = 90.000(5)° <i>c</i> = 32.333(5) Å, $\gamma$ = 90.000(5)°
Volume	5057(3) Å <sup>3</sup>
<i>Z</i> , calculated density	8, 1.728 Mg/m <sup>3</sup>
Absorption coefficient	1.482 mm <sup>-1</sup>
<i>F</i> (000)	2680
Crystal size	0.1 mm × 0.1 mm × 0.05 mm
$\theta$ range for data collection	2.32–28.30°
Reflections collected / unique	32164/6232 [ <i>R</i> (int) = 0.0688]
Completeness to $\theta$ = 28.30	99.0%
Absorption correction	Empirical (SADABS)
Refinement method	Full-matrix least squares on <i>F</i> <sup>2</sup>
Data/restraints/parameters	6232/0/355
Goodness of fit on <i>F</i> <sup>2</sup>	1.053
Final <i>R</i> indices [ <i>I</i> > 2 $\sigma$ ( <i>I</i> )]	<i>R</i> 1 = 0.0645, <i>wR</i> 2 = 0.1518
<i>R</i> indices (all data)	<i>R</i> 1 = 0.0794, <i>wR</i> 2 = 0.1597
Largest diff. peak and hole	1.737 and -1.235

**Table 16.8** Selected bond lengths (Å) and angles (°)

Cu(1)–N(1)	1.956(4)
Cu(1)–O(1)	1.960(3)
Cu(1)–O(2)	1.961(3)
Cu(1)–N(2)	1.980(4)
Fe(2)–N(3)	1.949(4)
Fe(2)–O(1)	1.967(3)
Fe(2)–O(2)	1.970(3)
Fe(2)–N(4)	1.981(4)
N(1)–Cu(1)–O(1)	92.11(14)
N(1)–Cu(1)–O(2)	169.78(14)
O(1)–Cu(1)–O(2)	77.67(13)
N(1)–Cu(1)–N(2)	97.73(15)
O(1)–Cu(1)–N(2)	169.30(14)
O(2)–Cu(1)–N(2)	92.47(14)
N(3)–Fe(2)–O(1)	91.74(14)
N(3)–Fe(2)–O(2)	168.41(14)
O(1)–Fe(2)–O(2)	77.30(12)
N(3)–Fe(2)–N(4)	99.38(15)
O(1)–Fe(2)–N(4)	166.90(14)
O(2)–Fe(2)–N(4)	91.96(14)

### 16.3.5 Thermogravimetric Analysis (TGA) of the Complex and the Catalyst

The TGA of the complex as well as the final catalyst was carried out using a Perkin–Elmer instrument in N<sub>2</sub> atmosphere. The TGA graphs of the complexes and their corresponding catalysts are determined and repeated in Table 16.9. About 10–15 mg of the sample (complex/catalyst) was taken and heated from 40 to 950 °C at the rate of 10 °C/min and the weight loss was measured in this temperature range. This table gives the temperature until which the complex/catalyst is thermally stable. All the complexes showed considerable weight loss (more than 35%) on heating till 250 °C, while the corresponding complex catalysts were found to be stable till about 500 °C.

**Table 16.9** TGA analysis of different complex catalysts

Complex	Temperature (°C)	Catalyst	Temperature (°C)
CuCuL-1	250	CuCuL-1/montmorillonite	600
CuCuL-2	270	CuCuL-2/montmorillonite	438
NiNiL-1	250	NiNiL-1/montmorillonite	650
MnMnL-1	250	MnMnL-1/montmorillonite	310
VVL-2	175	VVL-2/montmorillonite	300
CoCoL-2	100	CoCoL-2/montmorillonite	606
FeCuL-2	250	FeCuL-2/montmorillonite	400
CuCoL-2	270	CuCoL-2/montmorillonite	650
NiCuL-2	230	NiCuL-2/montmorillonite	400
FeCuL-1	170	FeCuL-1/montmorillonite	420

### 16.3.6 Small-Angle X-Ray Diffraction Analysis of the Catalyst

Small-angle X-ray diffraction measurements were done on ARL X'TRA X-ray diffractometer (Thermo Electron Corporation) equipped with Cu K $\alpha$  ( $\lambda=1.54$  nm) radiation. The voltage and the current applied to the X-ray tube were 45 kV and 20 mA, respectively, and the sampling width was set at 0.05° with scanning speed as 1°/min ( $2\theta = 2^\circ$ – $10^\circ$ ). The result of the experiment is given in Fig. 16.8 and  $d$ -spacing is calculated Bragg's law from corresponding to (001) plane. The Bragg's law is given by  $n\lambda = 2d \sin \theta$ , where  $n$  is an integer,  $\lambda$  is the wavelength of the X-ray,  $d$  is the spacing between the planes in the atomic lattice, and  $\theta$  is the angle between the incident ray and the scattered plane. It was found that the  $d$ -spacing of the original montmorillonite was 15.48 Å ( $2\theta = 5.7$ ) while the  $d$ -spacing of the zirconium-pillared montmorillonite was 26.74 Å ( $2\theta = 3.3$ ). Thus there was an increase in  $d$ -spacing on pillaring the montmorillonite with zirconium and it further increased on incorporation of the complex. For example, the  $d$ -spacing of CuCuL-1 complexes incorporated into montmorillonite is 26.74 Å, while that of FeCuL-2 complex is 29.4 Å. The increase in  $d$ -spacing suggests that the complex has been intercalated between the layers of the clay.

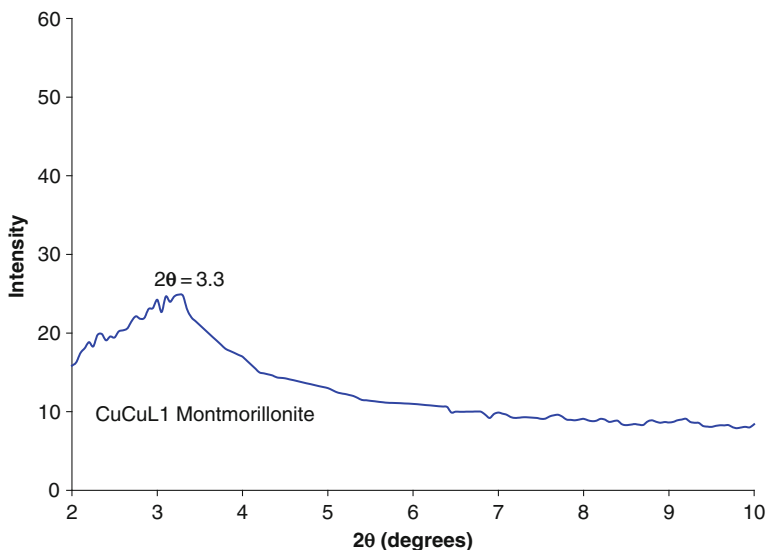


Fig. 16.8 Small-angle X-ray diffraction of CuCuL-1/montmorillonite catalyst

## 16.4 Catalytic Oxidation of Cyclohexane Using Oxygen

### 16.4.1 Introduction

The partial oxidation of hydrocarbons using oxygen is significant to the petrochemical industry in converting hydrocarbon feedstock into important functionalized chemicals. However in doing this, the desired partially oxidized products are further oxidized eventually converting it to  $\text{CO}_2$  and the C–H bond energies are different for primary, secondary, and tertiary (reducing in this order) positions. So in order to attain high selectivity for the target products, the conversions of the oxidation process are usually kept very low and the success of an industrial reaction depends on the stringent control of the temperature and pressure. The partial oxidation of cyclohexane to cyclohexanone and cyclohexanol is one of the industrially important processes as they serve as starting materials for the production of polymers such as nylon 6 and nylon 6,6 [84]. Cyclohexanone is used in the production of caprolactam which is utilized in the manufacture of nylon 6 and cyclohexanol is converted to adipic acid for the manufacture of nylon 6,6. The oxidation of cyclohexane is carried out industrially at a temperature of 150–180 °C and pressure of 1.0–1.6 MPa in the presence of Co salts (naphthenate, sterate, oleate) as catalyst. The cyclohexane conversion is kept low (about 3–4% per pass) as the cyclohexanol and cyclohexanone formed are more susceptible for further oxidation to  $\text{CO}_2$ . At industrial conditions, the products such as adipic, succinic, and oxalic acids and their cyclohexyl esters are always formed which need to be separated first [70, 71]. Experiments have shown

that water formed during the reaction has a retarding effect due to phase separation [72]. The alternate route to the formation of cyclohexanol and cyclohexanone involves the hydrogenation of phenol, a reaction that gives a selectivity of more than 97% at 99% conversion, but the process economics still favors the direct oxidation of cyclohexane [73]. In literature, catalytic oxidation studies have been conducted using stoichiometric oxidants such as hydrogen peroxide, *t*-butyl hydrogen peroxide (TBHP) other than molecular oxygen [74]. The leaching of the active species is low in the case of molecular oxygen in comparison with hydrogen peroxide and *t*-butyl hydrogen peroxide.

To overcome the problem of separating the catalyst from the reaction mass, many heterogeneous catalysts have been developed for this reaction. Generally these catalysts are either oxides or metal cations incorporated into inorganic matrices such as silica, alumina, zirconia, active carbon, zeolites [75], and aluminophosphates [76]. The activity of these systems also depends on the correct choice of the solvent, which determines the polarity of the medium and the size of the active metal that needs to be adsorbed on the surface of the support. For example, during the oxidation of cyclohexane in the presence of CoAPO-5 catalyst, the use of carboxylic acids (except formic acid) as the solvent is necessary and the use of propionic acid gives the highest reaction rate [77]. The other problems encountered in heterogeneous catalysis are leaching of active metal ions, extreme reaction conditions (2 MPa pressure and 177 °C temperature), and low activity [78]. An induction time is generally observed in the case of air oxidation of cyclohexane and is reduced by adding promoters or co-reactants such as acetaldehyde, cyclohexanone, cyclohexanol, and azobiz(isobutyronitrile) (AIBN) [79]. These also help in increasing the rate of cyclohexane oxidation (by decreasing the overall activation energy) and selectivity of the target products (a mixture of cyclohexanone and cyclohexanol).

Oxovanadium(IV) and copper(II) complexes of 1,2-diamino cyclohexane-based ligand encapsulated in zeolite Y have been used as catalysts using hydrogen peroxide as oxidant and 20 ml of CH<sub>3</sub>CN at 70 °C [80]. Supported complexes have been used such as metallophthalocyanine (Co, Fe, Mn) supported on  $\gamma$ -alumina [81], 6-2-(pyridyl methyl) amine Cu (II) complexes using hydrogen peroxide or *tert*-butyl hydroperoxide [82], pyrazole and trispyrazolylmethane rhenium complexes [83], and metallotetraphenyl porphyrins (Fe, Co, and Mn) supported on chitosan in the aerobic oxidation [84–98]. Patcas and Patcas [99] investigated the gas-phase oxidation of cyclohexane using NiO/ $\gamma$ -Al<sub>2</sub>O<sub>3</sub> catalyst in air at 390 °C product which later converted to cyclohexadiene, benzene, and carbon oxides. Anand et al. [100] studied the liquid-phase oxidation of cyclohexane over transition metals (Ti, Fe, Co, and Cr) incorporated into 3D mesoporous silicates.

The mechanism suggested in the literature assumes that cyclohexyl hydroperoxide (CHHP) is the intermediate formed in the presence of transition metal salts and sometimes a small quantity of this has been detected in the product stream [101–111]. The main products of its decomposition are cyclohexanol and cyclohexanone and are usually present in the product stream approximately in equimolar ratio. The primary effect of dissolved metal salts on the oxidation reaction is to increase the rate of reaction by catalyzing the homolytic decomposition

of hydroperoxides [87]. The mechanism of cyclohexane oxidation proposed in literature is a multistage, free radical chain reaction, comprising of initiation, chain propagation, and chain termination step. Tolman [102, 103] developed a reaction scheme consisting of 154 reactions which is impractical to analyze as it requires the determination of as many number of rate constants simultaneously with high accuracy. Hence lumped kinetic models which require lesser rate constants have been developed and the models available in literature are shown in Fig. 16.9 and are discussed below. In the first model, cyclohexane forms a hydroperoxide which is then converted into cyclohexanone, cyclohexanol, and unidentified waste products (D). In the second model, the formation of hydroperoxide is not considered, but further oxidation of cyclohexanol is terminated by the reaction with boric acid forming boric esters. Based on literature and experimental data, Literature has suggested an exhaustive model for non-catalytic oxidation which consisted of 19 reactions and 10 species. They estimated the rate constants and the concentration of the intermediate free radicals  $RO_2^\bullet$ ,  $RO^\bullet$ ,  $R^\bullet$ , and  $OH^\bullet$  in solution. Pohorecki et al. [106, 107] suggested a lumped kinetic model for the catalytic oxidation of cyclohexane. The reaction scheme consisted of seven reactions and the quasi-steady-state hypothesis was applied for estimating the free radical species  $RO_2^\bullet$ ,  $RO^\bullet$ , and  $R^\bullet$  in the solution. The reactive by-products in the liquid phase and the non-reactive by-products

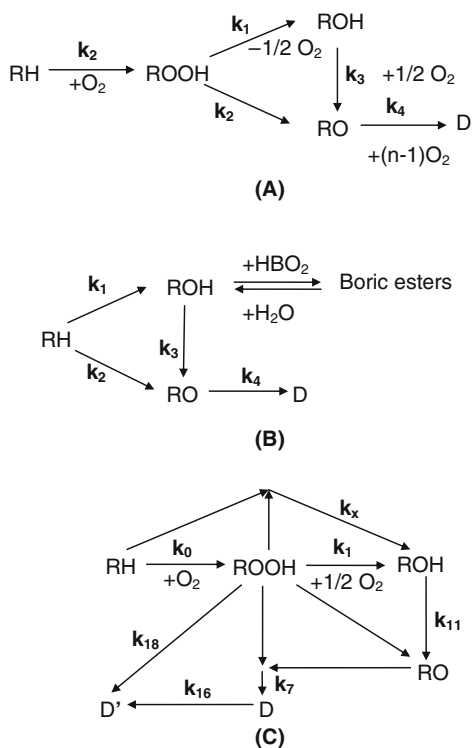


**Fig. 16.9** Kinetic models available in literature for oxidation of cyclohexane

in the gas phase were also incorporated into their model. The catalyst was thought to influence the initiation and the propagation steps and principal pathways were considered for global kinetics of the oxidation reaction. The role of the catalyst was introduced into the model by assuming specific forms of dependency of reaction rate constants on the catalyst concentrations.

Spielman [104] studied the influence of the reactor type on the selectivity and yield of the intermediate. Mass transfer limitations were not taken into account and a uniform concentration of dissolved oxygen was postulated. He found that, at any conversion level, selectivity and yield of intermediate were higher in a batch or plug flow reactor than in a continuous flow-stirred tank reactor. Steeman et al. [108] found that the optimum conditions for cyclohexane oxidation were 428–438 K temperature and 8–10 atm pressure. The efficiency of the oxidation to useful products decreased as the conversion was increased. Saunby and Kiff [109] studied the non-catalytic oxidation of cyclohexane and found that three CSTRs in series with equal conversion employed in each reactor were the optimum in terms of number of reactors, conversion per reactor, and overall conversion. This study failed to identify the rate-limiting steps as mass transfer effects were neglected. Suresh et al. [84] studied the autocatalytic oxidation of cyclohexane from 140 to 170 °C and reported that in this process, gas absorption is accompanied by chemical reaction. They studied the kinetics and the interaction of kinetics and mass transfer and found that the dissolved oxygen level rises to saturation and falls as the rate of reaction increases. They showed that the reaction is initially zero order in oxygen and becomes first order at low oxygen levels. Their kinetic model was based on the simplification of the accepted free radical mechanism and considered all the intermediates as one lump. Modén et al. [110] have investigated the kinetics and mechanism of cyclohexane oxidation in the presence of MnAPO-5 catalyst. They have proposed that cyclohexyl hydroperoxide is an intermediate in cyclohexanol and cyclohexanone formation. Their combined rates of formation were found to be first order in ROOH concentration and proportional to the redox-active Mn sites. Nunes et al. [111] have studied the mechanism and kinetics of cyclohexane oxidation (with iodobenzene) catalyzed by supramolecular manganese (III) porphyrins. They proposed a mechanism in which the cyclohexyl radical and OH groups combine rapidly to form cyclohexanol which is further oxidized to cyclohexanone. The free radical mechanism of cyclohexane oxidation occurs through the formation of cyclohexyl hydroperoxide intermediate in the reaction mass which decomposes to cyclohexanol and cyclohexanone (present in almost equimolar amounts).

### ***16.4.2 Reaction Procedure***

The oxidation reactions were performed in a high-pressure stainless steel reactor with a capacity of 300 ml equipped with gas delivery system and provision for sampling (see Fig. 16.10). The reactor was initially charged with 100 ml cyclohexane, 1 g of catalyst. It was pressurized with 1.38 MPa oxygen, then heated to the

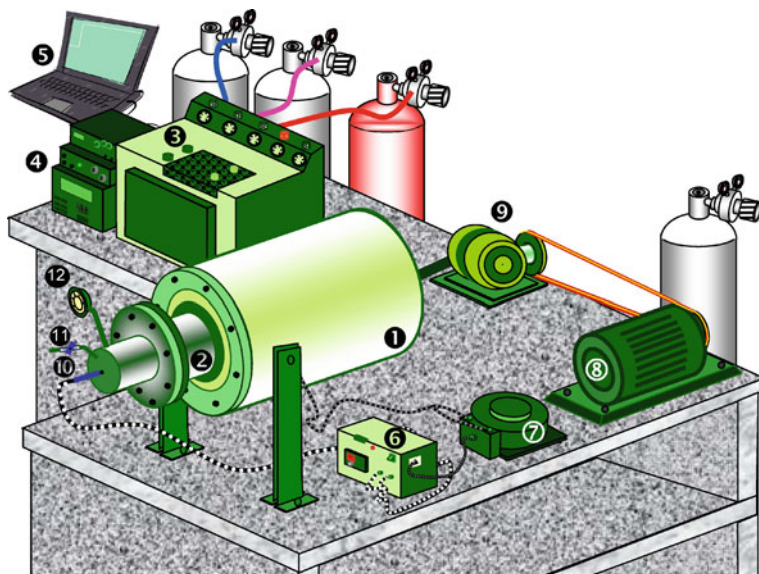


**Fig. 16.10** Schematic of the experimental setup. 1 furnace, 2 reactor, 3 gas chromatograph, 4 data station, 5 work station, 6 temperature controller, 7 variable auto transformer, 8 motor, 9 gear box, 10 thermocouple, 11 needle valve, 12 pressure gauge

required temperature for the desired reaction time using oxygen as the oxidant. An on/off controller was used for controlling the temperature with a chrome alloy thermocouple for temperature sensing. The product samples were withdrawn at regular intervals by means of a needle valve. The quantity withdrawn was less than 0.5 ml so that the total change in volume could be neglected. The products obtained after reaction were analyzed by gas chromatography (GC) using a fused silica capillary column (0.25 mm  $\times$  50 mm internal diameter, 0.25  $\mu$ m film thickness) with flame ionization detector, and the gas chromatography mass spectroscopy (GC-MS) was carried out using a Shimadzu QP-2000 instrument.

### ***16.4.3 Test for the Absence of Cyclohexyl Hydroperoxide in the Reaction Mass***

The presence of cyclohexyl hydroperoxide in the product mixture can be demonstrated by adding excess triphenylphosphine to the product formed due to which the former is converted to alcohol and can be detected as a peak corresponding to the alcohol in the GC analysis of the reduced sample confirmed the presence of cyclohexyl hydroperoxide molecule [98, 99]. In the presence of our catalyst, we have shown that on carrying similar experiments by adding triphenylphosphine, the peak intensity of the cyclohexanol in the GC analysis of the original product and the

reduced sample remains unchanged. Thus, it was concluded that in our case there is no cyclohexyl hydroperoxide in the product mixture.

#### ***16.4.4 Metal Leaching Test***

To confirm that the metal complex is not leaching at the reaction conditions studied, we carried out the following experiments.

1. The oxidation reactions were carried out using the spent catalyst and the conversion was found to remain unaltered.
2. From the product, the catalyst was filtered and the product mixture was once again subjected to the same temperature and pressure. The overall conversion was measured before and after the catalyst was filtered and found to be unchanged, indicating that there is no leaching of the active species.

#### ***16.4.5 Oxidation of Cyclohexane in the Presence of FeCuL-2/Montmorillonite and CuCuL-1/Montmorillonite Catalysts***

The oxidation of cyclohexane with molecular oxygen in the presence of FeCuL-2/montmorillonite and CuCuL-1/montmorillonite catalysts complex bonded to montmorillonite clay catalyst was studied in the temperature range of 140–210 °C. The above temperature range was chosen because below 140 °C the conversion was very low, while above 210 °C, though the conversion was high, a large amount of undesired products (D) were formed. The GC and GC-MS analyses were used for identifying the products and after confirming the products further analysis was done using GC. The product distribution was different with both these catalysts. In case of FeCuL-2/montmorillonite catalysts, cyclohexanone was obtained as the major product along with undesired product (D). The CuCuL-1/montmorillonite catalyst again gave cyclohexanone as the major product and the by-products were cyclohexanol and cyclohexene along with the undesired products (D). Based on the feed and the product concentration, the %conversion [=  $N_{RC}/N_{RF} \times 100$ ], %selectivity [=  $N_{PC}/N_{RC} \times 100$ ], and %yield [=  $N_{PC}/N_{RF} \times 100$ ] were calculated. In these,  $N_{RC}$  is the number of moles of cyclohexane consumed,  $N_{RF}$  is the number of moles of cyclohexane fed, and  $N_{PC}$  is the number of moles of product formed. In the case of FeCuL-2/montmorillonite catalyst, the overall conversion increases from 5.7 to 12.8% when the temperature was increased from 150 to 210 °C (160 min reaction time) and a conversion of 18% was obtained when the reaction was conducted at 210 °C for 260 min (see Fig. 16.11). At 150 °C the cyclohexanone was formed with high selectivity of 95.6% and with increase in temperature, its selectivity decreased to 83.7% at 210 °C due to the formation of undesired side products. At all temperatures the overall conversion and yield increased with reaction but there was a drop in selectivity with increase in reaction time.



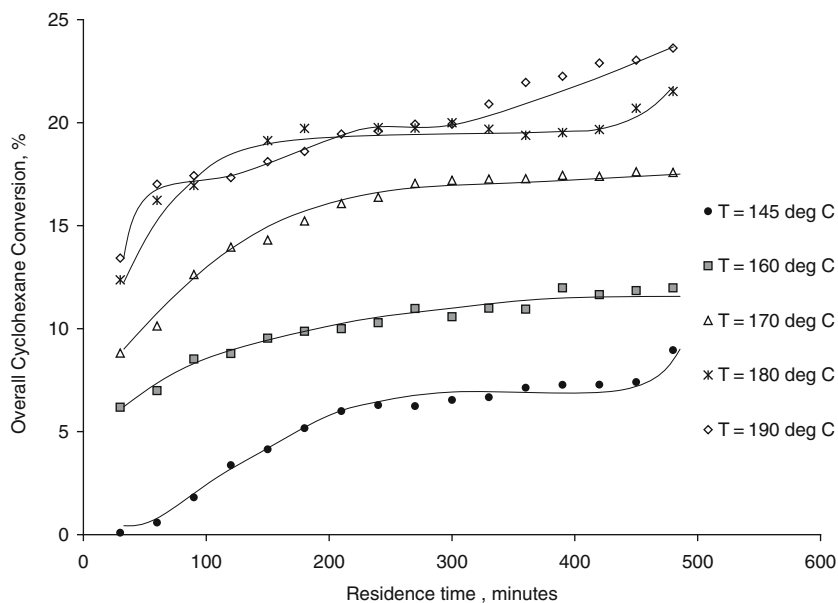


**Fig. 16.11** The variation of overall cyclohexane conversion with time for different temperatures in the presence of CuCuL-1/montmorillonite catalyst

For the CuCuL-1/montmorillonite catalyst the overall conversion increased from 9 to 23.6% when the temperature was increased from 145 to 190 °C (480 min reaction time) (see Fig. 16.11). At 145 °C, only cyclohexanone was formed as the product and after 480 min, the conversion was 9% and the selectivity toward the formation of cyclohexanone was 90.5%. When the temperature was increased to 160 °C, cyclohexanol and cyclohexene were formed in small amounts along with cyclohexanone as the major product. With increase in temperature, the selectivity toward the formation of cyclohexanone and cyclohexanol decreases as can be seen from Figs. 16.12 and 16.13 respectively. Cyclohexane was formed only in small amounts and its selectivity was below 10% in the temperature range studied. The yield of cyclohexanone and cyclohexanol increases with increase in temperature; so the decrease in the selectivity can be attributed to the increase in the rate of formation of the undesired product (D). The reaction was conducted for 8 h and a drastic change in conversion and yield is observed during the first 2.5 h.

### 16.4.6 Reaction Mechanism

Since we have experimentally shown that the cyclohexyl hydroperoxide is not present in the reaction mass, we have proposed a reaction mechanism in which this intermediate is produced in the adsorbed state. For this, a ligand-centered reaction

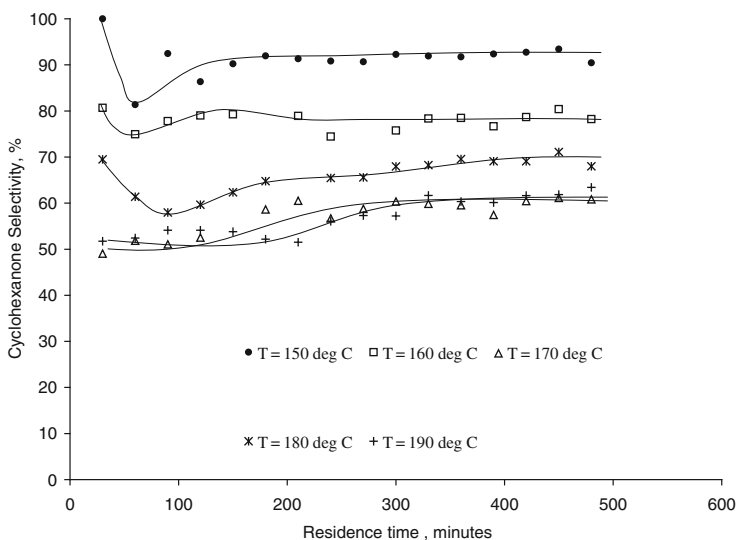


**Fig. 16.12** The variation of cyclohexanone selectivity with time for different temperatures in the presence of CuCuL-1/montmorillonite catalyst

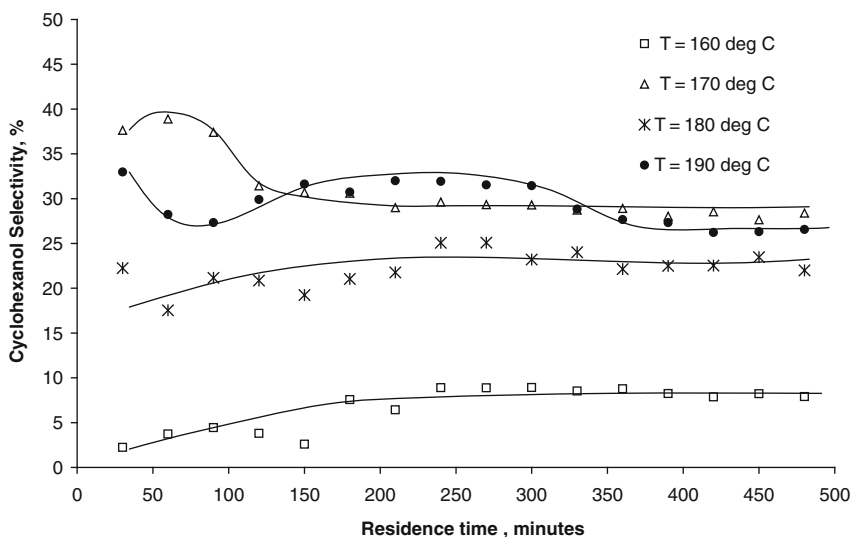


**Fig. 16.13** The variation of cyclohexanol selectivity with time for different temperatures in the presence of CuCuL-1/montmorillonite catalyst

mechanism has been proposed and shown in Fig. 16.14a, b. Since the concentrations of the product did not increase significantly as the reaction time was increased, some of the reactions were taken to be reversible in nature. A plausible mechanism with FeCuL-2/montmorillonite catalyst is shown in Fig. 16.14a. The cyclohexane

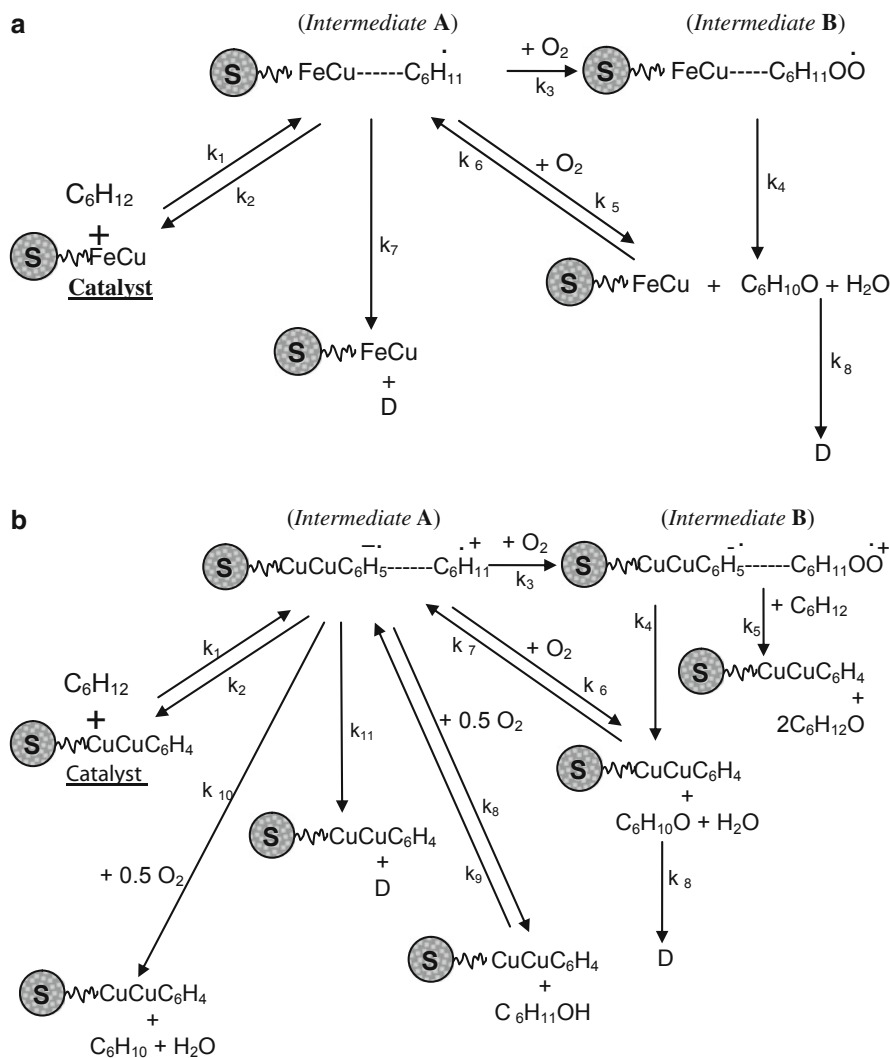


**Fig. 16.14** (a) A plausible reaction mechanism for the oxidation of cyclohexane in the presence of FeCuL-2 macrocyclic complex catalyst. (b) A plausible ligand-centered reaction mechanism for the oxidation of cyclohexane in the presence of CuCuL-1 macrocyclic complex catalyst

molecule in the presence of the catalyst first forms a cyclohexyl radical denoted as intermediate A (step 1). Intermediate A reacts with oxygen molecule forming a peroxy radical denoted as intermediate B (step 2) which forms cyclohexanone as shown in step 3. The intermediate A also leads to the formation cyclohexanone when it reacts with oxygen as shown in step 4. Reactions shown in steps 1 and 4 are taken to be reversible in nature as the concentration of cyclohexane and cyclohexanone

levels off and does not show significant increase with increase in reaction time after 2 h. Consistent with the approach adopted in the literature, unidentified side products (D) are assumed to be formed from intermediate A (step 5) and cyclohexanone (step 6).

A similar approach was followed in case of CuCuL-1/montmorillonite catalyst and a plausible mechanism with this catalyst is given in Fig. 16.14b. The cyclohexane molecule in the presence of the catalyst first forms a cyclohexyl radical cation intermediate A (step 1). Intermediate A reacts with oxygen molecule forming a peroxy radical cation intermediate B in the presence of the catalyst (step 2). This intermediate B forms cyclohexanone as shown in step 3 of Fig. 16.14b. This can also react with another molecule of cyclohexane forming cyclohexanone and cyclohexanol (see step 4). The intermediate A reacts with oxygen forming cyclohexanone in step 5 and cyclohexanol in step 6 and cyclohexane in step 7. Unidentified side products (D) are also formed from intermediate A (step 8) and cyclohexanone (step 9).

The mole balance equation for each component can be written based on the reaction mechanism and assuming that the overall reaction mass is homogeneous in nature. Since the concentration of the intermediate species is not taken as zero, the steady-state approximation is not valid. Equations (16.1)–(16.5) give the mole balance equation for FeCuL-2/montmorillonite catalyst:

$$d[\text{C}_6\text{H}_{12}]/dt = -k_1[\text{C}_6\text{H}_{12}] + k_2[\text{C}_6\text{H}_{11}^{\bullet-}] \quad (16.1)$$

$$\begin{aligned} d[\text{C}_6\text{H}_{11}^{\bullet-}]/dt = & k_1[\text{C}_6\text{H}_{12}] - k_2[\text{C}_6\text{H}_{11}^{\bullet-}] - k_3[\text{C}_6\text{H}_{11}^{\bullet-}][\text{O}_2] - k_5[\text{C}_6\text{H}_{11}^{\bullet-}][\text{O}_2] \\ & + k_6[\text{C}_6\text{H}_{10}\text{O}] - k_7[\text{C}_6\text{H}_{11}^{\bullet-}]d[\text{C}_6\text{H}_{11}\text{OO}^{\bullet-}]/dt = k_3[\text{C}_6\text{H}_{11}^{\bullet-}][\text{O}_2] \\ & - k_4[\text{C}_6\text{H}_{11}\text{OO}^{\bullet-}] \end{aligned} \quad (16.2)$$

$$d[\text{C}_6\text{H}_{10}\text{O}]/dt = k_4[\text{C}_6\text{H}_{11}\text{OO}^{\bullet-}] + k_5[\text{C}_6\text{H}_{11}^{\bullet-}][\text{O}_2] - k_6[\text{C}_6\text{H}_{10}\text{O}] - k_8[\text{C}_6\text{H}_{10}\text{O}] \quad (16.3)$$

$$d[\text{O}_2]/dt = -k_3[\text{C}_6\text{H}_{11}^{\bullet-}][\text{O}_2] - k_5[\text{C}_6\text{H}_{11}^{\bullet-}][\text{O}_2] + k_6[\text{C}_6\text{H}_{10}\text{O}] \quad (16.4)$$

$$d[D]/dt = k_7[\text{C}_6\text{H}_{11}^{\bullet-}] + k_8[\text{C}_6\text{H}_{10}\text{O}] \quad (16.5)$$

Similarly Eqs. 3.6–3.15 give the mole balance equations for CuCuL-1/montmorillonite catalyst:

$$d[\text{C}_6\text{H}_{12}]/dt = -k_1[\text{C}_6\text{H}_{12}] + k_2[\text{C}_6\text{H}_{11}^{\bullet-}] - k_5[\text{C}_6\text{H}_{12}][\text{C}_6\text{H}_{11}\text{OO}^{\bullet-}] \quad (16.6)$$

$$\begin{aligned} d[\text{C}_6\text{H}_{11}^{\bullet-}]/dt = & k_1[\text{C}_6\text{H}_{12}] - k_2[\text{C}_6\text{H}_{11}^{\bullet-}] - k_3[\text{C}_6\text{H}_{11}^{\bullet-}][\text{O}_2] - k_6[\text{C}_6\text{H}_{11}^{\bullet-}][\text{O}_2] \\ & + k_7[\text{C}_6\text{H}_{10}\text{O}] - k_8[\text{C}_6\text{H}_{11}^{\bullet-}][\text{O}_2]^{0.5} + k_9[\text{C}_6\text{H}_{12}\text{O}] - k_{10}[\text{C}_6\text{H}_{11}^{\bullet-}][\text{O}_2]^{0.5} \\ & - k_{11}[\text{C}_6\text{H}_{11}^{\bullet-}] \end{aligned} \quad (16.7)$$

$$d[\text{C}_6\text{H}_{11}\text{OO}^{\bullet-}]/dt = k_3[\text{C}_6\text{H}_{11}^{\bullet-}][\text{O}_2] - k_4[\text{C}_6\text{H}_{11}\text{OO}^{\bullet-}] - k_5[\text{C}_6\text{H}_{12}][\text{C}_6\text{H}_{11}\text{OO}^{\bullet-}] \quad (16.8)$$

$$d[\text{C}_6\text{H}_{10}\text{O}]/dt = k_4[\text{C}_6\text{H}_{11}\text{OO}^{\bullet-}] + k_6[\text{C}_6\text{H}_{11}^{\bullet-}][\text{O}_2] - k_7[\text{C}_6\text{H}_{10}\text{O}] - k_{12}[\text{C}_6\text{H}_{10}\text{O}] \quad (16.9)$$

$$d[\text{C}_6\text{H}_{12}\text{O}]/dt = k_5[\text{C}_6\text{H}_{12}][\text{C}_6\text{H}_{11}\text{OO}^{\bullet-}] + k_8[\text{C}_6\text{H}_{11}^{\bullet-}][\text{O}_2]^{0.5} - k_9[\text{C}_6\text{H}_{12}\text{O}] \quad (16.10)$$

$$d[\text{C}_6\text{H}_{10}]/dt = k_{10}[\text{C}_6\text{H}_{11}^{\bullet-}][\text{O}_2]^{0.5} \quad (16.11)$$

$$d[\text{O}_2]/dt = -k_3[\text{C}_6\text{H}_{11}^{\bullet-}][\text{O}_2] - k_6[\text{C}_6\text{H}_{11}^{\bullet-}][\text{O}_2] + k_7[\text{C}_6\text{H}_{10}\text{O}] - k_8[\text{C}_6\text{H}_{11}^{\bullet-}][\text{O}_2]^{0.5} + k_9[\text{C}_6\text{H}_{12}\text{O}] - k_{10}[\text{C}_6\text{H}_{11}^{\bullet-}][\text{O}_2]^{0.5} \quad (16.12)$$

$$d[D]/dt = k_{11}[\text{C}_6\text{H}_{11}^{\bullet-}] + k_{12}[\text{C}_6\text{H}_{10}\text{O}] \quad (16.13)$$

### 16.4.7 Optimal Data Fitting

Using these equations, we have carried out simulation employing Runge–Kutta 4 method (as needed for the genetic algorithm (GA) in this specific code for optimal curve fitting) with  $\Delta t = 0.01$  min for numerically stable solution and the concentration of each component was calculated. The results were optimized with the experimental values by using GA code. For this the objective function (given below) is written as the sum of squares of the difference of the simulated and the experimental values of cyclohexane and cyclohexanone for FeCuL-2/montmorillonite catalyst (Eq. 16.14):

$$\text{OF} = ([\text{CH}]_{\text{sim}} - [\text{CH}]_{\text{exp}})^2 + ([\text{CHone}]_{\text{sim}} - [\text{CHone}]_{\text{exp}})^2 \quad (16.14)$$

In the case of CuCuL-1/montmorillonite, the objective function OF (Eq. 16.15) is written as the sum of squares of the difference of simulated and experimental values of cyclohexane, cyclohexanone, cyclohexanol, and cyclohexene.

$$\text{OF} = ([\text{CH}]_{\text{sim}} - [\text{CH}]_{\text{exp}})^2 + ([\text{CHone}]_{\text{sim}} - [\text{CHone}]_{\text{exp}})^2 + ([\text{CHol}]_{\text{sim}} - [\text{CHol}]_{\text{exp}})^2 + ([\text{CHene}]_{\text{sim}} - [\text{CHene}]_{\text{exp}})^2 \quad (16.15)$$

In the GA optimization, the fitness function is taken as  $1/(1 + \text{OF})$  and its value of a single string is known as the string's fitness which is evaluated in each generation. The crossover and mutation probability were varied and finally taken at 0.9 and 0.05, respectively. The random population was created using a random number generator with a random seed equal to 0.887. The optimization was done for all

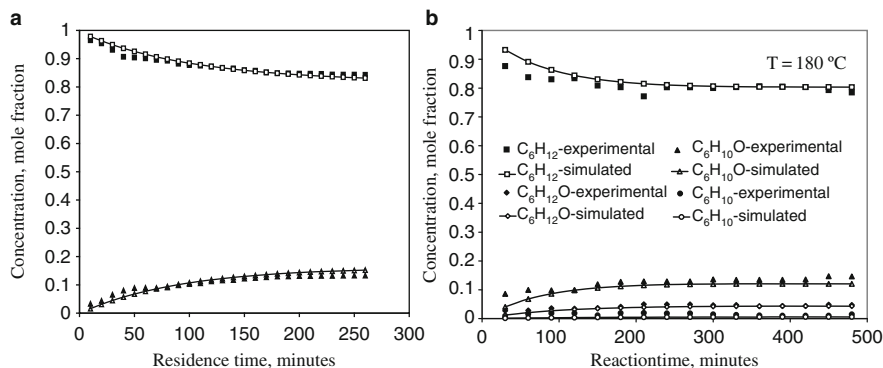


**Fig. 16.15** (a) Comparison of the simulated and the experimental results at  $T = 190\text{ }^{\circ}\text{C}$  for FeCuL-2/montmorillonite catalyst. The simulated results match the experimental data. (b) Comparison of the simulated and the experimental results at  $T = 180\text{ }^{\circ}\text{C}$  for CuCuL-1/montmorillonite catalyst. The simulated results match the experimental data

temperatures at which the reaction was performed for both the catalysts. The results of fitting the data at  $190\text{ }^{\circ}\text{C}$  for FeCuL-2/montmorillonite catalyst and at  $180\text{ }^{\circ}\text{C}$  for CuCuL-1/montmorillonite catalyst are given in Fig. 16.15, respectively. The simulated concentrations overlap the experimental data and the best-fit rate constants were determined. In Figs. 16.16 and 16.17 we have reported the concentrations of the intermediate species obtained from simulation and it was observed that these concentrations fall due to fall in the amount of oxygen present in the reaction mass. This suggests that a higher oxygen pressure would favor the forward reaction giving high yield of the products.

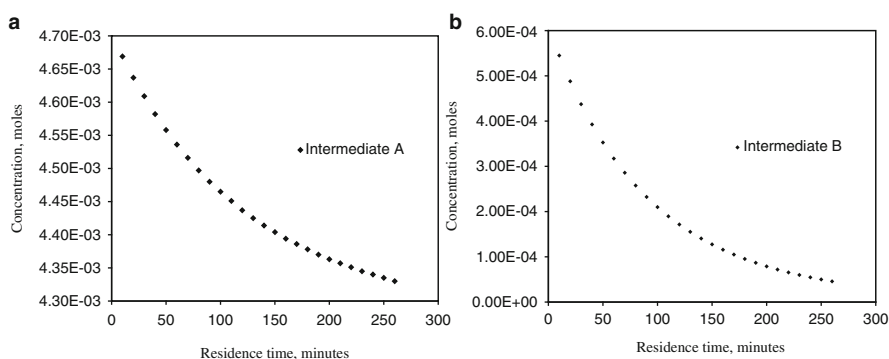


**Fig. 16.16** (a) The concentration of intermediate A obtained from simulation at  $T = 190\text{ }^{\circ}\text{C}$  for FeCuL-2/montmorillonite catalyst. (b) The concentration of intermediate B obtained from simulation at  $T = 190\text{ }^{\circ}\text{C}$  for FeCuL-2/montmorillonite catalyst

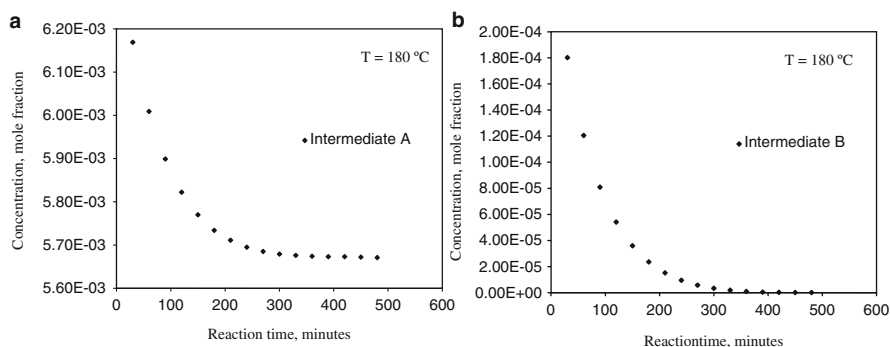


**Fig. 16.17** (a) The concentration of intermediate A obtained from simulation at  $T = 180\text{ }^{\circ}\text{C}$  for CuCuL-1/montmorillonite catalyst. (b) The concentration of intermediate B obtained from simulation at  $T = 180\text{ }^{\circ}\text{C}$  for CuCuL-1/montmorillonite catalyst

The reaction in the presence of CuCuL-2/montmorillonite was also studied at 170 and 190  $^{\circ}\text{C}$  and cyclohexanone was formed along with small amounts of cyclohexene; cyclohexanol was not formed as in the case of L1 ligand. The comparisons of the conversion obtained in the presence of CuCuL-1/montmorillonite and CuCuL-2/montmorillonite are given in Fig. 16.18a, b. At 170  $^{\circ}\text{C}$  and 260 min residence time, a conversion of 10% was obtained and the selectivity toward the formation of cyclohexanone and cyclohexene was 79 and 7.5%, respectively. On increasing the temperature to 190  $^{\circ}\text{C}$ , there was no major increase in conversion and it was 11%; the selectivities of cyclohexanone and cyclohexene were 81 and 8%, respectively. Thus it can be seen that the selectivity of cyclohexanone is higher in the presence of CuCuL-2/montmorillonite than in the presence of CuCuL-1/montmorillonite.

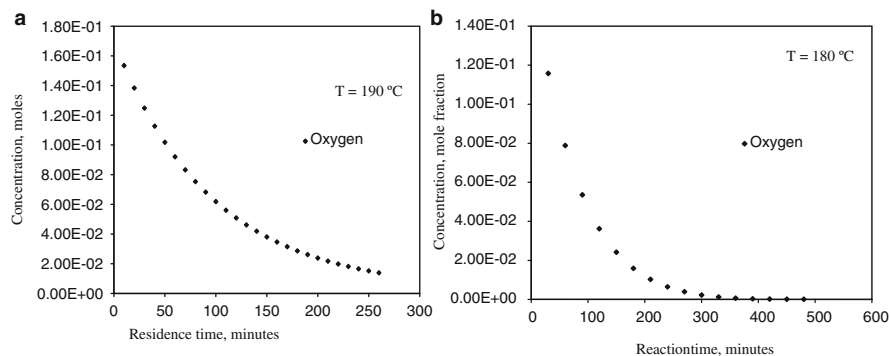


**Fig. 16.18** (a) The concentration of oxygen obtained from simulation at  $T = 190\text{ }^{\circ}\text{C}$  for FeCuL-2/montmorillonite catalyst. (b) The concentration of oxygen obtained from simulation at  $T = 180\text{ }^{\circ}\text{C}$  for CuCuL-1/montmorillonite catalyst

## 16.5 Conclusions

In this chapter, the oxidation of cyclohexane was studied using two catalysts, viz. FeCuL-2/montmorillonite and CuCuL-1/montmorillonite. The product distribution was different with both these catalysts and cyclohexanone was formed with high selectivity. In the case of FeCuL-2/montmorillonite catalyst the overall cyclohexane conversion was 18% and cyclohexanone was formed with 83% selectivity, the others being uncharacterizable side products. With CuCuL-1/montmorillonite catalyst the overall cyclohexane conversion was 23.6% and cyclohexanone, cyclohexanone, and cyclohexene (along with uncharacterizable side products) were formed with selectivity of 63.4, 26.5, and 5.65%, respectively. Based on the product formation, a plausible reaction mechanism was suggested in which the active site in the catalyst is the ligand site. The differential rate equations for each component have been written based on the reaction mechanism. These equations have been solved using fourth-order Runge–Kutta method and the optimum rate constants were determined using genetic algorithm. The concentrations obtained from simulation were matched with the experimental data.

## References

1. Reichle WT (1986) Synthesis of anionic clay minerals (mixed metal hydroxides, hydrotalcite). *Solid State Ionics* 22:135–141
2. Vaccari A (1998) Preparation and catalytic properties of cationic and anionic clays. *Catal Today* 41:53–71
3. Vaughan DEW (1988) Pillared clays – a historical perspective. *Catal Today* 2:87–198
4. Vaccari A (1999) Clays and catalysis: a promising future. *Appl Clay Sci* 14:161–198
5. Rhodes CN, Brown DR (1993) Surface properties and porosities of silica and acid-treated montmorillonite catalyst supports: influence on activities of supported ZnCl<sub>2</sub> alkylation catalysts. *J Chem Soc Faraday Trans 9*:1387–1391
6. Liu GH, Ko AN, Chang YC (1995) Synthesis and properties of pillared montmorillonite formed by intercalation of transition metal macrocyclic complexes. *Micropor Mater* 5:61–67
7. Mishra T, Parida K (1998) Transition metal oxide pillared clay: 5. Synthesis, characterization and catalytic activity of iron–chromium mixed oxide pillared montmorillonite. *Appl Catal A Gen* 174:91–98
8. Vicente MA, Belver C, Trujillano R, Rives V, Alvarez AC, Lambert JF, Korili SA, Gandia LM, Gil A (2004) Preparation and characterization of Mn and Co supported catalysts derived from Al pillared clays and Mn and Co complexes. *Appl Catal A* 267:47–58
9. Akcay M (2004) The catalytic acylation of alcohols with acetic acid by using Lewis acid character pillared clays. *Appl Catal A* 269:157–160
10. Belver C, Bañares-Muñoz MA, Vicente MA (2004) Fe-saponite pillared and impregnated catalysts I. Preparation and characterization. *Appl Catal A* 50:101–112
11. Carriazo JG, Guelou E, Barrault J, Tatibouet JM, Moreno S (2003) Catalytic wet peroxide oxidation of phenol over Al–Cu or Al–Fe modified clays. *Appl Clay Sci* 22:303–308
12. Barrault J, Tatibouet JM, Papayannakos N (2000) Catalytic wet peroxide oxidation of phenol over pillared clays containing iron or copper species. *C R Acad Sci Paris Serie IIc Chim Chem* 3:777–783
13. Ovejero G, Sotelo JL, Martinez F, Melero JA, Gordo L (2001) Wet peroxide oxidation of phenolic solutions over different iron-containing zeolitic materials. *Ind Eng Chem Res* 40(18):3921–3928



14. Guo J, Dahhan MA (2003) Catalytic wet oxidation of phenol by hydrogen peroxide over pillared clay catalyst. *Ind Eng Chem Res* 42(12):2450–2460
15. Carriazo JG, Guelou E, Barrault J, Tatiboue JM, Moreno S (2003) Catalytic wet peroxide oxidation of phenol over Al–Cu or Al–Fe modified clays. *Appl Clay Sci* 22:303–308
16. Mei JG, Yu SM, Cheng J (2004) Heterogeneous catalytic wet peroxide oxidation of phenol over delaminated Fe–Ti-PILC employing microwave irradiation. *Catal Commun* 5:437–440
17. Guo J, Dahhan MA (2005) Catalytic wet air oxidation of phenol in concurrent downflow and upflow packed-bed reactors over pillared clay catalyst. *Chem Eng Sci* 60:735–746
18. Jinjun L, Zheng J, Zhengping H, Xiuyan X, Yahui Z (2005) Pillared laponite clays-supported palladium catalysts for the complete oxidation of benzene. *J Mol Catal A Chem* 225: 173–179
19. Timofeeva MN, Khankhasaeva ST, Badmaeva SV, Chuvilin AL, Burgina EB, Ayupov AB, Panchenko VN, Kulikova AV (2005) Synthesis, characterization and catalytic application for wet oxidation of phenol of iron-containing clays. *Appl Catal B* 59:243–248
20. Martinez F, Melero JA, Botas J, Pariente MI, Molina R (2007) Treatment of phenolic effluents by catalytic wet hydrogen peroxide oxidation over Fe<sub>2</sub>O<sub>3</sub>/SBA-15 extruded catalyst in a fixed-bed reactor. *Ind Eng Chem Res* 46(13):4396–4405
21. Ramirez JH, Lampinen M, Vicente MA, Costa CA, Madeira LM (2008) Experimental design to optimize the oxidation of orange II dye solution using a clay-based Fenton-like catalyst. *Ind Eng Chem Res* 47(2):284–294
22. Polubesova T, Chen Y, Navon R, Chefetz B (2008) Interactions of hydrophobic fractions of dissolved organic matter with Fe<sup>3+</sup>- and Cu<sup>2+</sup>-montmorillonite. *Environ Sci Technol* 42(13):4797–4803
23. Gokulakrishnan N, Pandurangan A, Sinha PK (2009) Catalytic wet peroxide oxidation technique for the removal of decontaminating agents ethylenediaminetetraacetic acid and oxalic acid from aqueous solution using efficient Fenton type Fe-MCM-41 mesoporous materials. *Ind Eng Chem Res* 48(3):1556–1561
24. Chen TJ, Li G, Ding X, Sheng G, Mai JFB, O’Shea KE (2008) Characterization and the photocatalytic activity of TiO<sub>2</sub> immobilized hydrophobic montmorillonite photocatalysts. Degradation of decabromodiphenyl ether (BDE 209). *Catal Today* 139:69–76
25. Achma RB, Ghorbel A, Sayadi S, Dafinov A, Medina F (2008) A novel method of copper-exchanged aluminum-pillared clay preparation for olive oil mill wastewater treatment. *J Phys Chem Solids* 69:1116–1120
26. Onda A, Suzuki Y, Kajiyoshi K, Yanagisawa K (2006) Catalytic performance of autoclave liners in the wet oxidation of naphthalene. *Ind Eng Chem Res* 45(7):2194–2198
27. Gu C, Li H, Teppen BJ, Boyd S (2008) Octachlorodibenzodioxin formation on Fe(III)-montmorillonite clay. *Environ Sci Technol* 42(13):4758–4763
28. Anisia KS, Kumar A (2007) Oxidation of cyclohexane with molecular oxygen in presence of characterized macrocyclic heteronuclear FeCu complex catalyst ionically bonded to zirconium pillared montmorillonite clay. *J Mol Catal A Chem* 271:164–179
29. Kalilur Rahiman A, Rajesh K, Shanmuga Bharathi K, Sreedaran S, Narayanan V (2009) Catalytic oxidation of alkenes by manganese(III) porphyrin-encapsulated Al, V, Si-mesoporous molecular sieves. *Inorg Chim Acta* 362:1491–1500
30. Liu YX, Zhang X, Guo L, Wu F, Deng NS (2008) Photodegradation of bisphenol A in the montmorillonite KSF suspended solutions. *Ind Eng Chem Res* 47(19):7141–7146
31. Remili C, Kaci M, Kachbi S, Bruzaud S, Grohens Y (2009) Photo-oxidation of poly styrene/clay nanocomposites under accelerated UV exposure: effect on the structure and molecular weight. *J Appl Poly Sci* 112:2868–2875
32. Bottino FA, Pasquale GD, Fabbri E, Orestano A, Pollicino A (2009) Influence of montmorillonite nano-dispersion on polystyrene photo-oxidation. *Polym Degrad Stabil* 94:369–374
33. Menesi J, Korosi L, Bazso E, Zillmer V, Richardt A, Dekany I (2008) Photocatalytic oxidation of organic pollutants on titania–clay composites. *Chemosphere* 70:538–542

34. Barros VB, Faria AL, MacLeod TCO, Morales LAB, Assis MD (2008) Ironporphyrin immobilized onto montmorillonite as a biomimetic model for azo dye oxidation. *Int Biodeterior Biodegrad* 61:337–344
35. Lan Y, Li C, Mao J, Jun Sun A (2008) Influence of clay minerals on the reduction of  $\text{Cr}^{6+}$  by citric acid. *Chemosphere* 71:781–787
36. Jiang J, Ma K, Zheng Y, Cai S, Li R, Ma J (2009) Cobalt salophen complex immobilized into montmorillonite as catalyst for the epoxidation of cyclohexene by air. *Appl Clay Sci* 45: 117–122
37. Sis BE, Khalili B, Abdollahifar A, Hashemi M (2007) Transition metal free oxidation of alcohols to carbonyl compounds using hydrogen peroxide catalyzed with LiCl on montmorillonite K10. *Acta Chim Slov* 54:635–637
38. Schuster H, Rios LA, Weckes PP, Hoelderich WF (2008) Heterogeneous catalysts for the production of new lubricants with unique properties. *Appl Catal A Gen* 348:266–270
39. Rode CV, Kshirsagar VS, Nadgeri JM, Patil KR (2007) Cobalt–salen intercalated montmorillonite catalyst for air oxidation of *p*-cresol under mild conditions. *Ind Eng Chem Res* 46:8413–8419
40. Anisia KS, Kumar A (2008) Synthesis of heterogeneous copper complex catalyst for oxidation of cyclohexane using molecular oxygen. *Can J Chem Eng* 86:1054–1061
41. Lal S, Anisia KS, Jhansi M, Kishore L, Anil Kumar (2007) Development of heterogeneous catalyst by ionically bonding macrocyclic Zr–Zr complex to montmorillonite clay for depolymerization of polypropylene. *J Mol Catal A Chem* 265:15–24
42. Dhakshinamoorthy A, Pitchumani K (2006) Clay-anchored non-heme iron–salen complex catalyzed cleavage of C=C bond in aqueous medium. *Tetrahedron* 62:9911–9918
43. Cardoso B, Pires J, Carvalho AP, Biernacka IK, Silva AR, Castro B, Freire C, (2005) Mn(III) salen complex immobilised into pillared clays by in situ and simultaneous pillaring/encapsulation procedures application in the heterogeneous epoxidation of styrene. *Micropor Mesopor Mater* 86:295–302
44. Dasa P, Biernacka IKZ, Silva AR, Carvalho AP, Pires J, Freire C (2006) Encapsulation of chiral Mn(III) salen complexes into aluminium pillared clays: application as heterogeneous catalysts in the epoxidation of styrene. *J Mol Catal A Chem* 248:135–143
45. Kameyama H, Narumi F, Hattori T, Kameyama H (2006) Oxidation of cyclohexene with molecular oxygen catalyzed by cobalt porphyrin complexes immobilized on montmorillonite. *J Mol Catal A Chem* 258:172–177
46. Ramaswamy V, Malwadkar S, Chilukuri S (2008) Cu–Ce mixed oxides supported on Al-pillared clay: effect of method of preparation on catalytic activity in the preferential oxidation of carbon monoxide. *Appl Catal B* 84:21–29
47. Tandon PK, Singh SB, Srivastava M (2007) Synthesis of some aromatic aldehydes and acids by sodium ferrate in presence of copper nano-particles adsorbed on K 10 montmorillonite using microwave irradiation. *Appl Organometal Chem* 21:264–267
48. Faria AL, MacLeod TCO, Assis MD (2008) Carbamazepine oxidation catalyzed by iron and manganese porphyrins supported on aminofunctionalized matrices. *Catal Today* 133–135: 863–869
49. Bhor MD, Nandurkar NS, Bhanushali MJ, Bhanage BM (2008) Ultrasound promoted selective synthesis of 1,10-binaphthyls catalyzed by Fe impregnated pillared montmorillonite K10 in presence of TBHP as an oxidant. *Ultrason Sonochem* 15:195–202
50. Dhakshinamoorthy A, Pitchumani K, (2009) Clay-supported ceric ammonium nitrate as an effective, viable catalyst in the oxidation of olefins, chalcones and sulfides by molecular oxygen. *Catal Commun* 10:872–878
51. Das P, Kuźniarska-Biernacka I, Silva AR, Carvalho AP, Pires J, Freire C (2006) Encapsulation of chiral Mn(III) salen complexes into aluminium pillared clays: application as heterogeneous catalysts in the epoxidation of styrene. *J Mol Catal A Chem* 248:135–143
52. Vedrine JC, Millet JMM, Volta J (1996) Molecular description of active sites in oxidation reactions: acid–base and redox properties, and role of water. *Catal Today* 32:115–123

53. Corma A, Gracia H (2003) Lewis acids: from conventional homogeneous to green homogeneous and heterogeneous catalysis. *Chem Rev* 103:4307–4365
54. Ghorbel A, Hoang-Van C, Teichner SJ (1973) Catalytic activity of amorphous alumina prepared in aqueous media: I. Catalytic activity in isomerization of butene-1. *J Catal* 30:298–308
55. Adeeva V, Deehan JW, Janchen J, Lei GD, Schunemaron V, Vandevan LJM, Sachtler WMH, Vansanten RA (1995) Acid sites in sulfated and metal promoted zirconium dioxide catalysts. *J Catal* 151:364–372
56. Ponec V (2001) Alloy catalysts: the concepts. *Appl Catal A* 222:31–45
57. Huber GW, Dumesic JA (2005) An overview of aqueous – phase catalytic process for the production of hydrogen and alkanes in a biorefinery. *Catal Today* 111:119–132
58. Davda RR, Shabaker JW, Huber GW, Cortright RD, Dumesic JA (2003) Aqueous-phase reforming of ethylene glycol on silica-supported metal catalysts. *Appl Catal B* 43:13–26
59. Davda RR, Shabaker JW, Huber GW, Cortright RD, Dumesic JA (2003) Aqueous-phase reforming of ethylene glycol on silica-supported platinum catalysts. *Catal Lett* 88:1–8
60. Lotero E, Liu Y, Lopez DE, Suwannakern K, Bruce DA, Godwin JG (2005) Synthesis of biodiesel with acid catalysis. *Ind Eng Chem Res* 44:5353–5363
61. Srivastava A, Prasad R (2000) Triglycerides based diesel fuels. *Renew Sustain Energy Rev* 4:111–133
62. Wasmus S, Kuver A (1999) Methanol oxidation and direct methanol fuel cells: a selective review. *J Electroanal Chem* 461:14–31
63. Hamnett A (1997) Mechanism and electro catalysis in the direct methanol fuel cells. *Catal Today* 38:445–457
64. Wang CY (2004) Fundamental model for fuel cell engineering. *Chem Rev* 104:4727–4766
65. Jones CJ (2001) d- and f-Block chemistry. Royal Society of Chemistry, UK
66. Gavrilova AL, Bosnich B (2004) Principles mononucleating and binucleating ligand design. *Chem Rev* 104:349–383
67. Sargeson AM (1966) Conformations of Coordinated Chelates In: Karlin RL (ed) *Transition metal chemistry* (New York), vol 3. Marcel Dekker, New York, NY, pp 303–343
68. Senkler GH Jr, Mislow KJ (1972) Barrier to pyramidal inversion in ethylmethylphenylarsine. *J Am Chem Soc* 94:291–296
69. Emmert C, Vereslet M, Tuchagues JP (1996) Pentadentate dinucleating ligands affording bis( $\mu$ -carboxylato-*O,O*)diiron(II) complexes. *J Chem Soc Chem Commun* 66:617–619
70. Tsukada N, Tamura O, Inoue Y (2002) Synthesis and structures of palladium and platinum a-frame complexes bridged by a novel binucleating ligand, *N,N'*-bis[(2-diphenylphosphino)phenyl]-formamidine. *Organometallics* 21:2521–2528
71. van Koningsbruggen PJ, Gatteschi D, de Graaff RAG, Haasnoot JG, Reedijk J, Zanchini C (1995) Isotropic and anisotropic magnetic exchange interactions through  $\mu$ -*N1,N2* 1,2,4-triazole and  $\mu$ -sulfato bridges: X-ray crystal structure, magnetic properties, and single-crystal EPR study of ( $\mu$ -4-amino-3,5-bis(pyridin-2-yl)-1,2,4-triazole-*N',N1,N2,N''*)( $\mu$ -sulfato-*O,O'*)[(sulfato-*O*)aquacopper(II)] triaquacopper(II) hydrate. *Inorg Chem* 34:5175–5182
72. Incarvito C, Rheingold AL, Qin CJ, Bosnich ALB (2001) Bimetallic reactivity on the use of oxadiazoles as binucleating ligands. *Inorg Chem* 40:1386–1390
73. Brooker S, Kelly RJ, Moubaraki B, Murray KS (1996) First dicopper(II) complex to contain bridging macrocyclic pyridazine units: structure, electrochemistry and magnetochemistry of [Cu<sub>2</sub>L(MeCN)<sub>2</sub>(ClO<sub>4</sub>)<sub>2</sub>][ClO<sub>4</sub>]<sub>2</sub>. *J Chem Soc Chem Commun* 2579–2580
74. Rooker S, de Geest DJ, Kelly RJ, Plieger PG, Moubaraki B, Murray KS, Jameson GJ (2002) Exchange-coupled high-spin, low-spin and spin-crossover dicobalt (II) complexes of a pyridazine-containing Schiff-base macrocycle: control of cobalt (II) spin state by choice of axial ligands. *Chem Soc Dalton Trans* 2080–2087
75. Tikkanen WR, Kruger C, Bomben KD, Jolly WL, Kaska WC, Ford PC (1984) Synthesis, characterization, and X-ray molecular structures of mono- and dinuclear copper complexes with 2,7-bis(2-pyridyl)-1,8-naphthyridine. *Inorg Chem* 23:3633–3638

76. Gajda T, Kramer R, Jansco A (2000) Structure, equilibrium and ribonuclease activity of copper (II) and zinc (II) complexes formed with a dinucleating bis-imidazole ligand. *Eur J Inorg Chem* 1635–1644
77. Kersting B (1998) Preparation, structures, and properties of dinuclear Ni and Pd complexes of tridentate amine-chalcogenolate ligands. *Eur J Inorg Chem* 1071–1077
78. Kersting B, Siebert D (1998) First examples of dinickel complexes containing the  $N_3Ni(2-SR)_3NiN_3$  core. Synthesis and crystal structures of  $[L_2Ni_2][BPh_4]_2$  and  $[L_3Ni_2][BPh_4]_2$  ( $L = 2,6$ -di(aminomethyl)-4-*tert*-butyl-thiophenolate). *Inorg Chem* 37:3820–3828
79. Kersting B, Siebert D (1999) Preparation, structure, and properties of a mixed-valent  $Ni^{II}Ni^{III}$  amine-selenolate complex. *Eur J Inorg Chem* 189–193
80. Gange RR, Spiro CL, Smith TJ, Hamann CA, Thies WR, Shiemke AK (1981) The synthesis, redox properties and ligand binding of heterobinuclear transition-metal macrocyclic ligand complexes. Measurement of an apparent delocalization energy in a mixed-valent  $Cu^I Cu^{II}$  complex. *J Am Chem Soc* 103:4073–4081
81. Farrugia LJ, Win GX (2003) Ver 1.64: an integrated systems of windows programs for the solution, refinement and analysis of single-crystal X-ray diffraction data. Department of Chemistry, University Of Glasgow, UK
82. Berezin IV, Denisov ET, Emanuel NM (1966) The oxidation of cyclohexane. Transl. by Allen KA. Pergamon Press, Oxford
83. Emanuel NM, Denisov ET, Maizus ZK (1967) Liquid phase oxidation of hydrocarbons. Plenum press, New York, NY
84. Suresh AK, Sharma MM, Sridhar T (2000) Engineering aspects of industrial liquid-phase air oxidation of hydrocarbons. *Ind Eng Chem Res* 39:3958–3997
85. Schuchardt U, Cardoso D, Sercheli R, Pereira R, da Cruz RS, Guerreiro MC, Mandelli D, Spinacé EV, Pires EL (2001) Cyclohexane oxidation continues to be a challenge. *Appl Catal A* 211:1–17
86. Carvalho WA, Valardo PB, Wallau M, Schuchardt U (1997) Mesoporous redox molecular sieves analogous to MCM-41. *Zeolites* 18:408–416
87. Arends WCE, Sheldon RA, Wallau M, Schuchardt U (1997) Oxidative transformations of organic compounds mediated by redox molecular sieves. *Angew Chem Int Ed Engl* 36: 1144–1163
88. Lin SS, Weng HS (1994) Liquid phase oxidation of cyclohexane over CoAlPO-5. *Appl Catal A Gen* 118:21–31
89. Sakthivel A, Selvam P (2002) Mesoporous (Cr) MCM-41: a mild and efficient heterogeneous catalyst for selective oxidation of cyclohexane. *J Catal* 211:134–143
90. Steeman JWM, Kaarsemaker S, Hoftyzer PJ (1961) A pilot plant study of the oxidation of cyclohexane of air under pressure. *Chem Eng Sci* 14:139–149
91. Suresh AK, Sridhar T, Potter OE (1988) Autocatalytic oxidation of cyclohexane – modeling reaction kinetics. *AIChE J* 38:69–80
92. Mauryaa MR, Chandrakar AK, Chand S (2007) Oxovanadium (IV) and copper (II) complexes of 1,2-diaminocyclohexane based ligand encapsulated in zeolite-Y for the catalytic oxidation of styrene, cyclohexene and cyclohexane. *J Mol Catal A Chem* 270:225–235
93. Ebadi A, Safari N, Peyrovi MH (2007) Aerobic oxidation of cyclohexane with  $\gamma$ -alumina supported metallophthalocyanines in the gas phase. *Appl Catal A* 321:135–139
94. Silva AC, Fernandez TL, Carvalho NMF, Herbst MH, Bordinhao J, Horn A Jr, Wardell JL, Oestreicher EG, Antunes OAC (2007) Oxidation of cyclohexane catalyzed by bis-(2-pyridylmethyl)amine Cu(II) complexes. *Appl Catal A* 317:154–160
95. Alegria ECB, Kirillova MV, Martins LMDRS, Pombeiro AJL (2007) Pyrazole and trispyrazolylmethane rhenium complexes as catalysts for ethane and cyclohexane oxidations. *Appl Catal A* 317:43–52
96. Guan Huang G, Guo C, Tang S (2007) Catalysis of cyclohexane oxidation with air using various chitosan-supported metallotetraphenylporphyrin complexes. *J Mol Catal A* 261:125–130
97. Carvalho NMF, Horn A Jr, Antunes OAC (2006) Cyclohexane oxidation catalyzed by mononuclear iron (III) complexes. *Appl Catal A* 305:140–145

98. Esmelindro MC, Oestreicher EG, Marquez-Alvarez H, Dariva C, Egues SMS, Fernandes C, Bortoluzzi AJ, Drago V, Antunes OAC (2005) Catalytic oxidation of cyclohexane by a binuclear Fe(III) complex biomimetic to methane monooxygenase. *J Inorg Biochem* 99:2054–2061
99. Patcas F, Patcas FC. (2006) Reaction pathways and kinetics of the gas-phase oxidation of cyclohexane on NiO/ $\gamma$ -Al<sub>2</sub>O<sub>3</sub> catalyst. *Catal Today* 117:253–258
100. Anand R, Hamdy MS, Gkourgkoulas P, Maschmeyer Th, Jansen JC, Hanefeld U (2006) Liquid phase oxidation of cyclohexane over transition metal incorporated amorphous 3D-mesoporous silicates M-TUD-1 (M = Ti, Fe, Co and Cr). *Catal Today* 117:279–283
101. Wen Y, Potter OE, Sridhar T (1997) Uncatalyzed oxidation of cyclohexane in a continuous reactor. *Chem Eng Sci* 52:4593–4605
102. Tolman CA, Druliner JD, Krusic PJ, Nappa MJ, Siedel WC, Williams ID, Ittel SD (1988) Catalytic conversion of cyclohexylhydroperoxide to cyclohexanone and cyclohexanol. *J Mol Catal* 48:129–148
103. Tolman CA, Druliner JD, Nappa MJ, Herron N (1989). Alkane oxidation studies in DuPont's Central Research Department, Chap X. In: Hill CL (ed) *Activation and functionalization of alkanes*. Wiley, New York, NY
104. Spielman M (1964) Selectivity in hydrocarbon oxidation. *AIChE J* 10:496–501
105. Alagy J, Trombouze P, Van Landeghem H (1974) Designing a cyclohexane oxidation reactor. *Ind Eng Chem Proc Des Develop* 13:317–323
106. Pohorecki R, Baldgya J, Moniuk W, Podgorska W, Zdrojkowski A, Wierzchowski PT (2001) Kinetic model of cyclohexane oxidation. *Chem Eng Sci* 56:1285–1291
107. Pohorecki R, Baldgya J, Moniuk W, Krysztoforski A, Wojcik Z (1992) Liquid phase oxidation of cyclohexane – modeling and industrial scale process simulation. *Chem Eng Sci* 47:2559–2564
108. Steeman JWM, Kaarsemaker S, Hoftyzer PJ (1961) A pilot plant study of the oxidation of cyclohexane of air under pressure. *Chem Eng Sci* 14:139–149
109. Saunby JB, Kiff BW (1976) Liquid-phase oxidation – hydrocarbons to petrochemicals. *Hydrocarbon Process* 55:247
110. Modén B, Zhan B, Dakka J, Santiesteban JG, Iglesia E (2006) Kinetics and mechanism of cyclohexane oxidation on MnAPO-5 catalysts. *J Catal* 239:390–401
111. Nunes GS, Mayer I, Toma HE, Araki K (2005) Kinetics and mechanism of cyclohexane oxidation catalyzed by supramolecular manganese (III) porphyrins. *J Catal* 236:55–61

# Index

## A

- Adipic acid, 305, 498
- Adsorption
  - benzene, 25, 27, 245
  - carbon dioxide, 35, 39–40
  - ethane, 24, 30, 33, 38
  - n*-hexane, 25–27
  - methane, 33, 35, 38–39
  - methanol, 25–27
  - nitrogen, 24
  - water, 24, 28–30
- Advanced oxidation processes (AOPs), 129–131, 167
  - non-biodegradable organic pollutants, 130
- Al/Ce-PILC, 226–230, 243
- Al/Cr-PILC, 115, 248, 308
- Al/Fe-PILC, 173–175
- Alkylamines, 448
- Alkylammonium phyllosilicate hybrids, 75
- Alkyl poly(ethylene oxide), 451–452
- Alkyl trimethylammonium surfactant, 447–448
- Al/La-PILC, 236
- Aluminium organophosphonate, 451
- Aluminium oxide pillars, 111, 218
- Aluminophosphates, 447–459, 499
- Anionic surfactant, 448
- Arrhenius constant, 140

## B

- Beckmann rearrangement, 378, 457–459
- Beidellite, 2, 68, 134, 139, 150, 184
- Benzoquinone, 154, 308–309, 459
- Benzyl alcohol oxidation, 307–308
- Bi-functional catalysis
  - hydrogenation of nitriles, 407–408
  - synthesis of MIBK, 407
- Biogas, 24, 30–40
- Biototoxicity, 176
- Block copolymer

- Pluronic F68, 451
- Pluronic F127, 451
- Pluronic P123, 451
- poly(ethylene oxide)-poly(propylene oxide)-poly(ethylene oxide), 450

- Borate, 354, 378–379, 411
- Bragg's law, 497
- Bromination, 365–367, 376
- Brønsted
  - acidity, 112–113, 115, 118, 274, 278, 356, 361, 373, 455
  - basicity, 306, 329, 339, 400, 466

## C

- Catalytic application
  - acidic reaction, 115–116
  - hydrocarbon cracking, 115–116
  - photocatalytic reaction, 119–120
  - redox reaction, 116–117
  - selective catalytic reduction of NO<sub>x</sub>, 117–118
- Catalytic oxidation
  - complete oxidation, 225–251
  - deep oxidation, 226, 229–230, 235–241, 243–244, 246–249
- Catalytic wet peroxide oxidation (CWPO), 130, 171, 177, 201
- Cathecol, 309
- Cationic metal complex, 101
- CdS-PILCs, 84, 86
- CdS pillars, 86
- Cetyltrimethylammonium bromide (CTAB), 188–189, 448, 450, 453, 455
- Chemical oxygen demand (COD), 137, 143–144, 468
- Chromate, 249, 324, 338–342, 344, 357, 411, 486–487, 495
- Claus process, 441

- Continuous flow reactors, 153–154, 162, 177, 193, 202–203, 207, 213–214, 218, 222
- p*-coumaric acid, 179, 182–185
- Cr<sub>2</sub>O<sub>3</sub>/TiO<sub>2</sub>-PILC, 271, 277
- Cr-PILC, 25, 38, 113, 115, 248, 306, 308
- Cu<sup>2+</sup>-PILC, 179
- Cu-PILC, 180–183, 185–186
- Cyclohexane, oxidation, 458–459, 498–510
- Cyclohexanol, 305, 364, 376, 458, 475, 498–505, 507–508, 510
- Cyclohexanone, oxidation, 305, 364, 458, 498–499, 501
- Cyclohexyl hydroperoxide, 475, 499, 501–504
- D**
- Dawson, 356, 358, 360
- Decavanadate, 15, 327–335, 339, 348
- Delaminated pillared clays, 272–273
- DeNO<sub>x</sub> processes
- catalytic reduction with CO, 283–284
  - metal oxides, 263, 271
  - noble metals, 282–283, 285–287
  - selective catalytic reduction by ammonia, 271–279
  - selective catalytic reduction by hydrocarbons, 279–283
  - zeolites, 271
- Dialdehyde, 484–487
- Dichromate, 339, 486–487
- Dyehouse effluents, 185
- E**
- Electron spin resonance (ESR), 148, 177–178, 202, 205–207, 217–222, 271, 310, 331–332, 455–456
- Epoxidation
- of alkenes, 302–305, 361
  - of allylic alcohols, 7, 310–311
  - of cyclooctene, 304, 362, 381
  - of geraniol, 311, 329, 337
  - of styrene, 303–304, 478
- Epoxides, 302–305, 310, 329, 346–347, 352, 360, 362, 365, 371–372, 476, 478, 480–481
- Ethylene oxidation, 280, 302
- Ethylene oxide (EO), 302–303, 327–328, 335–336, 339, 346, 450–452
- F**
- FAZA, 147, 174–175, 177, 202–203, 206–213, 215–221, 467
- Fenton-like advanced oxidation processes
- acetic acid, 154
  - benzoquinone, 154
  - catechol, 154
  - cinnamic acid, 134, 138–140, 145–146
  - dye, 133–134, 137–141, 144, 152
  - hydroquinone, 154
  - hydroxyl radical, 130, 134–136, 139, 145
  - Langmuir–Hinshelwood, 155–159
  - nitrophenol, 134, 138, 149, 159
  - Orange II, 134, 137, 139–142, 144, 148, 160
  - oxalic acid, 130, 154
  - phenol, 133–134, 136–144, 146–151, 153–159, 206
- Fenton processes, 117, 136, 150, 191, 202
- reaction mechanism, 174
- Fe<sub>2</sub>O<sub>3</sub>/TiO<sub>2</sub>-PILC, 273–275
- Fe-PILC, 38–39, 106, 117, 132–133, 173–176, 178, 180–181, 185, 187–192, 307
- Fe pillared clay, 139, 272
- Fe/Si-PPH, 434–436
- Finke, 356, 358, 360
- G**
- Gas mixtures, 32–33, 261
- Grafting, 85, 311, 333, 338–339, 343–344, 354, 359, 379, 454–455
- Green Chemistry, 302
- Green oxidation reactions, 301–313
- H**
- Hectorite, 2, 13, 67–91, 103, 133, 188, 234, 466
- synthesis, 71–82
  - hydrothermal process, 77–82
- Heptamolybdate, 339, 346–349, 351, 353–354
- Hock process, 307
- Hydrodesulfurisation (HDS), 89, 330
- Hydrogen peroxide, 12, 111, 117, 130–131, 134–136, 139–143, 147–148, 153–155, 157, 167, 171–173, 175–188, 193, 201–204, 206–213, 221–222, 302, 304–306, 330, 347, 349, 362, 378, 405–406, 459, 499
- Hydroperoxyl radical, 12, 175
- Hydrophobic, 24, 26, 90, 172, 178, 187–190, 308, 336, 352, 370–371, 450–452, 470
- Hydroquinone, 154, 308–310, 342, 458–459
- Hydrotalcites, 339–415
- as reservoirs for drugs, 413–415
- Hydrothermal synthesis, 120
- Hydroxyl radicals, 6, 130, 134–136, 139, 145, 148, 168, 171–172, 174–176,

- 178–182, 186–187, 193, 202, 206, 211, 219–220, 222
- I**
- Ideal adsorbed solution theory (IAST), 30–34, 36–37
- Industrial waste aqueous streams, 186
- Iodosylbenzene (PhIO), 303–305, 474, 478, 480–481, 501
- J**
- Jasminaldehyde, 403, 456–457
- K**
- Keggin, 2, 7, 46, 63, 277, 321, 356, 358, 360–361, 363
- KRuPPH, 439
- L**
- Landfill gas, 35, 37–38
- Laponite, 13–14, 69–71, 73, 82–86, 88–89, 102, 115, 119, 133, 189, 191, 230, 280, 283, 311, 466, 469
- Layered double hydroxide (LDH)
- boron containing, 378–379
  - chromium containing, 338–344
  - manganese containing, 379–381
  - molybdenum containing, 344–357
  - niobium containing, 381–382
  - osmium containing, 382–384
  - structure, 319–327
  - tungsten containing, 357–378
  - vanadium containing, 327–337
- LDH in  $\text{DeNO}_x$
- CoAl-LDH, 286
  - MgAl-LDH, 323, 325
- Light cycle oil (LCO), 438–439
- M**
- Macrocyclic complexes, 465–511
- Macrocyclic ligands, 482, 487
- Magnesia silicate, 69–70
- Manganate, 379–380
- Mars-van Krevelen mechanism, 249, 332, 335, 349, 355, 360
- Memory effect, 321, 323–325
- Mesoporous phosphates heterostructures
- aluminophosphate, 447
  - condensation of heptanal with benzaldehyde, 456–457
  - oxidation of cyclohexane, 458
  - selective O-methylation of catechol, 456
- boroaluminophosphate, 455
  - magnesium-aluminophosphate, 455
  - silicoaluminophosphate, 453–454, 457–459
  - Beckmann rearrangement of cyclohexanone oxime, 457–458
- Metal cluster complex
- niobium oxide, 101–102
  - tantalum oxide, 101–102
- Metal oxide pillared clay
- chromium oxide, 108–110
  - iron oxide, 106–108
  - manganese oxide, 110
  - mixed oxides, 110–112
  - titanium oxide, 105–106
- Metatungstate, 358–359, 362
- Mica, 13, 68, 90, 187–188, 276
- Micropore size distribution, 24–25, 54
- Microwave irradiation, 3–17, 105, 111, 115, 309, 468
- Microwave synthesis
- clay to water ratio effect
    - alumina pillared montmorillonite, 8
    - iron oxide pillared montmorillonite, 8–9  - irradiation time effect
    - alumina pillared montmorillonite, 3–5
    - multimetallic pillared montmorillonite, 7
    - titania pillared montmorillonite, 6
    - zirconia pillared montmorillonite, 5–6  - metal to clay ratio effect
    - titanium pillared clays, 9
    - zirconium pillared montmorillonite, 9–10
- Mineral-carbonaceous nanocomposites, 279
- Mn-PILCs, 113
- Molecular sieve, 69, 91, 287, 308, 453, 471
- Molybdate, 344–345, 347, 350–353, 373
- Monometallic
- complexes, 482
  - ligands, 482
- Multimetallic complexes, 466
- N**
- Nanocomposites, 16, 68, 71, 77, 82, 86–87, 90–91, 172, 191, 279, 414, 473–474
- Nanoparticles
- $\text{SnO}_2$ , 90
  - $\text{ZnO}$ , 90
- Natural gas, 30, 34–35, 40
- $\text{NO}_x$  pollution
- catalytic technologies, 263–271
  - control pathways, 259–263



- NO<sub>x</sub> pollution (*cont.*)  
 legislative regulation, 259  
 non-catalytic technologies, 260
- O**
- Olive oil milling wastewater (OMW), 176,  
 179, 182, 185–186
- Orange II, 134, 137, 139–142, 144, 148, 160,  
 185, 188, 191, 470
- Organic surfactant, 448
- Organometallic complexes, 82, 466
- Orthovanadate, 331–334
- Other clays  
 aluminum intercalated samples, 13  
 chromia and tin oxide-pillared montmorillonites and laponites,  
 14–15  
 pillared anionic clays  
 PET-hydrocalcite nanocomposites, 16  
 PO<sub>4</sub><sup>3-</sup> and P<sub>2</sub>O<sub>7</sub><sup>4-</sup> intercalated  
 hydrocalcites, 16  
 polyvanadate intercalated  
 hydrocalcites, 15  
 saponite pillared with Fe-  
 organometallic by microwave  
 and ultrasound irradiation, 15
- Oxalate, 143, 148–149, 152, 340–341
- Oxidation  
 of alcohols, 307–308  
 of alkenes, 302–307  
 of alkylaromatics, 307  
 of allylic alkenes, 306–307  
 of aniline, 311–312  
 of aromatic rings, 307  
 of aryl sulphides, 312  
 of cyclohexanone, 305–306  
 of heteroatoms, 311–312  
 of ketones, 305–306
- Oxidative dehydrogenation (ODH), 332–334,  
 337, 342–343, 349–350, 357,  
 360, 424
- Oxidative desulfurisation (ODS), 330
- Oxidative ketonization, 305–306
- P**
- Palladium, 85, 230, 233, 264, 306, 325,  
 408–410
- Paramolybdate, 345, 353
- Paratungstate, 359, 367, 374
- Permanganate, 380
- Phase diagram, 31–33, 36–38
- Phenol, 111, 116–117, 133–134, 136–144,  
 146–148, 150–151, 153–159, 169,  
 173–174, 176–178, 184, 186–191,  
 201–222, 250, 307–310, 326, 459,  
 467–470, 474, 486–487, 499
- Photocatalysts, 6, 90, 105–106, 119–120,  
 187–191, 471
- Photocatalytic, 7, 9, 13–14, 86, 90, 103, 105,  
 119–120, 167–168, 172, 187–192  
 elimination of pollutants in water, 172
- Photo-Fenton, 117, 172, 191–192
- PILCs  
 in AOPs methods, 170–172  
 dehydration of 1-butanol, 44, 57, 60, 62  
 hydroisomerization and hydrocracking of  
*n*-heptane, 44, 57–58
- Pillared clays  
 acid activation, 113  
 acidity, 112–113  
 anion supported, 113–115  
 in AOPs methods, 170–172  
 in DeNO<sub>x</sub>  
 catalytic decomposition, 283–284  
 catalytic reduction with CO, 283  
 SCR by ammonia, 271–279  
 SCR by hydrocarbons, 279–283
- Pillared synthetic hectorites, 82–86
- Pollutants degradation, 133–134
- Polynuclear metal oxo-hydroxo cation, 101
- Polyoxometalate (POM), 319–385
- Polyphenolics, 176, 179, 182, 186
- Porous clay heterostructures (PCH) in DeNO<sub>x</sub>  
 Cu-PCH, 288  
 Fe-PCH, 288–289
- Porous material, 68, 82, 84, 99, 287, 424–425
- Porous phosphates heterostructures (PPH)  
 adsorption of benzothiophene, 435  
 Cu-PPH  
 selective catalytic reduction of NO, 437  
 hybrid PPH materials, 427, 433  
 propane/propene separation, 436  
 Ru-PPH  
 hydrogenation of tetralin, 439–440  
 hydrogenolysis/hydrocracking of  
 tetralin, 439  
 hydrotreating of aromatic hydrocarbons,  
 439  
 silica galleries, 430  
 3-aminopropyl-triethoxysilane, 430  
 (3-mercaptopropyl)-trimethoxysilane,  
 430  
 phenyltriethoxysilane, 430  
 3-(triethoxysilyl)propionitrile, 430  
 vinyltrimethoxysilane, 430  
 Si-PPH, 425–428, 436–443  
 V-PPH

- selective oxidation of hydrogen sulphide, 441
  - Porphyrins, 474, 478, 480–481, 499, 501
  - Positively charged colloidal particles, 100, 102
  - Probe-molecules, 24–26, 112–113, 233, 354
  - Propylene oxide, 303, 325, 450
  - Purification, 26–27, 30, 35, 167, 186, 201, 222, 301, 324
  - Pyridine adsorption, 54–55, 333, 340, 360, 378, 455
  - Pyrovanadate, 327–328, 331–333
- R**
- Reaction pathways
    - recent applications of HDT as basic catalyst
      - aldolisation, 402–404
      - isomerization of olefins, 401–402
      - Meerwein–Ponndorff–Verley
        - reductions of carbonyls, 404
      - oxidations, activated olefins, 406
      - oxidations, Baeyer–Villiger oxidation of ketones, 407
      - oxidations, sulfides, 406
      - retroaldolisation of glucose, 403–404
    - in WHPCO, 176–187
- S**
- Saponite, 2, 7, 13, 15–17, 68, 86, 88, 90, 113, 116, 133–134, 137, 142, 148, 185, 187–188, 234, 246–249, 283, 287–288, 303, 305–307, 466, 470
  - Scanning electron microscopy (SEM), 77–79, 85, 495
  - Selectivity, 11, 33–34, 36–38, 58–63, 84, 86, 90, 112, 115–116, 118, 130, 169, 188, 221, 249–250, 268–269, 273, 276–279, 281, 283, 285, 288–289, 303–306, 308–311, 326–329, 332–337, 339, 342–343, 346–348, 353, 356, 360–361, 363–364, 367, 370–375, 379–380, 382, 401, 403, 406–409, 412, 424, 439, 441–443, 458–459, 479, 481–482, 498–499, 501, 503–505, 510
  - Separation, 26–27, 30–39, 68, 70, 87, 99, 131, 150, 170, 301, 324–325, 368, 433, 436, 442–443, 456, 477, 499
  - Single-crystal X-ray analysis, 492, 495–496
  - Single-crystal X-ray crystallography, 493
  - Small-angle X-ray diffraction analysis, 497–498
  - Solid bases as adsorbents and anionic exchangers
    - NO<sub>x</sub> traps, 413
    - SO<sub>x</sub> additives for FCC, 412–413
    - trapping of organic compounds and anions, 410–412
  - Structure and activation of hydrotalcite, 399–401
  - Sulphated-TiO<sub>2</sub>-PILC, 278
  - Support effects
    - catalysis of C–C coupling reactions, 409–410
    - catalytic properties for hydrogenations, 409
    - dechlorination of trichlorobenzene, 409
    - electronic effects, 408–409
    - merox process, 410
  - Synthetic hectorite, 67–91, 133
- T**
- tert*-butyl hydroperoxide, 117, 306, 310–312, 474
  - Tetraborate, 378–379
  - TiO<sub>2</sub> nanoparticle, 188–189, 474
  - TiO<sub>2</sub> pillars, 6, 90, 102, 105, 119–120, 187–189, 191, 273, 275–276, 278, 280
  - Ti-PILC, 38–39, 105, 111–112, 118, 187–192, 246–247, 309–312
  - Titania pillared montmorillonite, 2, 6, 10, 105, 188, 273, 276
  - Titanocene dichloride, 455
  - Total organic carbon (TOC), 117, 136–138, 140–141, 144–145, 147–148, 152–153, 156, 160–161, 177–179, 185–186, 190–192, 203–214, 219–222, 250, 467, 470–471
  - Trischelates, 82, 466
  - Tungstate, 348, 350, 358, 362, 365–367, 370–371, 373–375, 383
  - Tungsten, 264, 272, 275, 357–378
  - Tungstocobaltate, 363
  - Tyrosol, 176, 185
- U**
- Ultrasound irradiation, 11–12, 15–17
- V**
- Vacancy solution theory (VST), 30–31, 33–34
  - Vanadate, 327, 329, 331, 333–337, 348, 350–351, 357, 373
  - Vermiculite, 68, 276–277, 287
  - Volatile organic compounds (VOC)
    - acetone, 231–232, 234, 249
    - benzene, 27, 226
    - chlorobenzene, 233–234
    - ethyl acetate, 231–232
    - methyl-ethyl-ketone, 234

Volatile organic compounds (VOC) (*cont.*)

toluene, [231–232](#)

V<sub>2</sub>O<sub>5</sub>/TiO<sub>2</sub>-PILC, [277–278](#)

## W

Waste water treatment, [129–162](#), [167–193](#),  
[412](#), [471](#)

Water treatment, [129–131](#), [167–169](#), [172–173](#),  
[201](#), [410–411](#)

Wet air catalytic oxidation (WACO), [167](#),  
[171–176](#)

Wet hydrogen peroxide catalytic oxidation  
(WHPCO), [130](#), [167](#), [171–187](#), [302](#)

Wet hydrogen peroxide oxidation (WHPO),  
[111](#), [171](#), [185](#)

Wet oxidation

by hydrogen peroxide, [176–187](#)

## Z

Zr/Si-PPH, [428–429](#)